

Sustainable Aviation

T. Hikmet Karakoc · József Rohács ·
Dániel Rohács · Selçuk Ekici ·
Alper Dalkiran · Utku Kale *Editors*

Solutions for Maintenance Repair and Overhaul

Proceedings of the International
Symposium on Aviation Technology,
MRO, and Operations 2021

 **SARES**
INTERNATIONAL SUSTAINABLE AVIATION
AND ENERGY RESEARCH SOCIETY




Springer

Sustainable Aviation

Series Editors

T. Hikmet Karakoc , Eskisehir Technical University, Eskisehir, Türkiye

C Ozgur Colpan , Department of Mechanical Engineering, Dokuz Eylöl University, Buca, Izmir, Türkiye

Alper Dalkiran , School of Aviation, Süleyman Demirel University, Isparta, Türkiye

The Sustainable Aviation book series focuses on sustainability in aviation, considering all aspects of the field. The books are developed in partnership with the International Sustainable Aviation Research Society (SARES). They include contributed volumes comprising select contributions to international symposiums and conferences, monographs, and professional books focused on all aspects of sustainable aviation. The series aims at publishing state-of-the-art research and development in areas including, but not limited to:

- Green and renewable energy resources and aviation technologies
- Aircraft engine, control systems, production, storage, efficiency, and planning
- Exploring the potential of integrating renewables within airports
- Sustainable infrastructure development under a changing climate
- Training and awareness facilities with aviation sector and social levels
- Teaching and professional development in renewable energy technologies and sustainability

* * *

T. Hikmet Karakoc • József Rohács
Dániel Rohács • Selçuk Ekici
Alper Dalkiran • Utku Kale
Editors


Solutions for Maintenance Repair and Overhaul

Proceedings of the International Symposium
on Aviation Technology, MRO,
and Operations 2021

 Springer


 **SARES**
INTERNATIONAL SUSTAINABLE AVIATION
AND ENERGY RESEARCH SOCIETY

Editors

T. Hikmet Karakoc 
Faculty of Aeronautics and Astronautics
Eskisehir Technical University
Eskisehir, Turkiye

Information Technology Research
and Application Center
Istanbul Ticaret University
Istanbul, Turkiye

Dániel Rohács 
Aeronautics and Naval Architecture
Budapest University of Technology
and Economics
Budapest, Hungary

Alper Dalkiran 
School of Aviation
Süleyman Demirel University
Keciborlu, Isparta, Turkiye

József Rohács 
Aeronautics and Naval Architecture
Budapest University of Technology
and Economics
Budapest, Hungary

Selçuk Ekici 
Aviation Department
Iğdır Üniversitesi
Iğdir, Turkiye

Utku Kale 
Aeronautics and Naval Architecture
Budapest University of Technology
and Economics
Budapest, Hungary

ISSN 2730-7778

Sustainable Aviation

ISBN 978-3-031-38445-5

<https://doi.org/10.1007/978-3-031-38446-2>

ISSN 2730-7786 (electronic)

ISBN 978-3-031-38446-2 (eBook)

© The Editor(s) (if applicable) and The Author(s), under exclusive license to Springer Nature Switzerland AG 2024

This work is subject to copyright. All rights are solely and exclusively licensed by the Publisher, whether the whole or part of the material is concerned, specifically the rights of translation, reprinting, reuse of illustrations, recitation, broadcasting, reproduction on microfilms or in any other physical way, and transmission or information storage and retrieval, electronic adaptation, computer software, or by similar or dissimilar methodology now known or hereafter developed.

The use of general descriptive names, registered names, trademarks, service marks, etc. in this publication does not imply, even in the absence of a specific statement, that such names are exempt from the relevant protective laws and regulations and therefore free for general use.

The publisher, the authors, and the editors are safe to assume that the advice and information in this book are believed to be true and accurate at the date of publication. Neither the publisher nor the authors or the editors give a warranty, expressed or implied, with respect to the material contained herein or for any errors or omissions that may have been made. The publisher remains neutral with regard to jurisdictional claims in published maps and institutional affiliations.

This Springer imprint is published by the registered company Springer Nature Switzerland AG
The registered company address is: Gewerbestrasse 11, 6330 Cham, Switzerland

Paper in this product is recyclable.

The Significance of Safety Factors in Maintenance Repair and Overhaul

The subject of aircraft technology can be defined as the possibility of dynamic flight at subsonic, supersonic, and hypersonic speeds. The aircraft designs with configuration examples for each speed category influence the material, propulsion, navigation, and even the expertise required for aircraft operation. Performance comparisons to analogous designs for aircraft utilizing conventional fuels, alternative fuels, and sustainable fuels alter the configurations for aircraft utilization. The aircraft maintenance and operation methods are modified based on the required level and operational mode for the data collection needs. Safety is another aspect of successful maintenance, repair, and overhaul (MRO) organization.

The quality of aviation maintenance training could become a major stumbling block for future growth in MRO safety. There are ongoing conversations to break the relationships that prevent the MRO business from advancing to the next level. Human factors in airplane maintenance programs and their impact on profitability and safety can be resolved through maintenance.

A previous body of research concluded that the frequency of passenger travel affected the quality of service that the aircraft received. After that, when all other factors were taken into account, the significance of safety finally overtook that of flying frequency. Moreover, safety management systems (SMS) are a crucial safety component for the transportation industry and many other industries. The fundamental purpose of an SMS program is to anticipate potentially hazardous situations before they escalate into accidents or incidents and to safeguard against human error. Integrating a concept focusing on safety considerations into the systems would boost safety from an MRO perspective. A risk in a technical system, for instance, is the potential failure of one or more subsystems, which could result in hazards or other adverse outcomes.

Human mistakes are responsible for eighty percent of all aviation accidents. Human factors can occasionally result in aviation maintenance groups' failure due

to a lack of planning, leading to defects. The absence of institutional human factor education contributes to the inefficiency of the aircraft maintenance industry within the global aviation market. European Aviation Safety Agency (EASA) would benefit if its aircraft maintenance division could adopt global standards and human factor training employing required educational programs. The inability to effectively prepare for human factors directly and negatively affects the maintenance's viability and safety atmosphere. Leadership in safety has a direct and beneficial effect on the safety atmosphere, which aids in managing human elements. Senior managers are responsible for building a culture of trust in their workforce by having faith in their people, validating their skills, and inspiring them to perform their jobs in a less risky manner. Proper communication has a direct positive effect, another essential element of a safe atmosphere. Increasing work safety, which reflects safety communication, and the need to urge employees to work more safely, which reflects a safe atmosphere, depend on upper management communicating with their teams using aviation accident case studies.

Another feature of MRO safety can be explained by the "Safety Differently" approach from Sidney Dekker as "a space in which individuals spontaneously negotiate and collaborate to generate the safest results for everyone." If an MRO organization possesses a suitable safety climate, the "Safety Differently" framework may be implemented to enhance the safety results.

An extra activity that must be completed to fulfill the safety program's requirements is the preparation of the participants. This preparation entails giving instructions from the top down and determining the setting where the experiments will take place. It is feasible to collect discoveries and actions, put them into action, and even potentially scale them up across the business to boost the possibility of successfully implementing higher levels of safety culture. This can be accomplished in a few different ways. However, technicians need to be encouraged to openly discuss their concerns and ideas so that the procedures can be personalized to account for the new safety concerns, allowing the processes to accommodate them. In this stage, it is possible to measure certain aspects of the safety performance of an MRO system using the RAMS factors (reliability, availability, maintainability, and supportability). These criteria are used to evaluate certain system components. The MRO safety is based upon the correctness of the data in case preventative maintenance is performed on the building. In addition, the data must be reliable; sensors must monitor and record thousands of parameters at rising sample rates to create numbers that can be relied upon. The RAMS method is the analysis that may be utilized to extract maximum value from obtained data. You can keep data analytics procedures simple by relying just on visuals or make them more complex by using complex statistical models and AI-based algorithmic frameworks. To tackle any problem, one must choose the approach that is both the most effective and the simplest. Two major categories of on-wing data analytics problems exist in maintenance, repair, and overhaul (MRO) operations. The first entails identifying patterns required for

categorizing and enhancing various maintenance and overhaul procedures. The second group of problems requires the detection of rare occurrences, such as the unplanned failure of specific components. The resolution of this collection of problems is dependent on the detection of notable outliers within vast data sets. However, the human effects are still the most significant case from the reliability point of view.

The percentage of competent technical safety specialists working in the safety management system was much lower than in other study areas. Positive aspects include the extent to which inspection personnel are given the authority to carry out their duties to resolve safety concerns and the fact that the organization had adequate plans to implement new technologies based on emerging trends by identifying and managing threats to aviation operations. Other positive aspects include the organization's adequate plans to implement new technologies based on emerging trends. The technology that supports the air traffic system for civil aviation is insufficient and has not been updated. In addition, it has not been implemented completely appropriately and with the smallest potential impact. In addition, the existing infrastructure maintenance methods or programs at established aerodromes are enough to assure continuing availability and conformity with international standards most effectively. Due to the technical nature of the aviation industry, which is defined by rapidly expanding technology, applications, and concerns, employees' professional skills are a crucial determinant of the overall level of aviation safety. It is vital to place a high premium on recruiting and retention policies to attract the appropriate personnel based on the organization's needs.

The MROs have been supporting the operational safety processes and have invested in education to help eliminate human variables. It may be determined that MROs have, on average, a very high degree of congruence between the components of social psychology. However, a few things may be altered to foster a more pleasant social environment. These include implementing a more robust system for effective communication and team collaboration, as well as increasing the frequency of incentives.

MRM, which stands for "Maintenance Resource Management," was created as a result of aircraft maintenance technicians' cooperation in safety enhancements. These technicians also received training to strengthen their communication skills, and they realized that both technicians and management needed to comprehend the significance of the enterprise's mission. Independent evidence indicates that employee participation, open communication, and a commitment to the mission have led to better maintenance safety, efficiency, and performance. MRM incorporates all of these components when seen within an organization's or sociotechnical system's framework.

Preface

The International Symposium on Aircraft Technology, Maintenance, Repair, Overhaul, and Operations (ISATECH) symposium papers analyze the global aviation industry's MRO industry prospects. There are many papers presented at ISATECH 2021 symposium. The 46 published papers of the ISATECH symposium cover many scientific topics. This conference was sponsored by Budapest University of Technology and Economics, Eskisehir Technical University, and the International Sustainable Aviation and Energy Research Society (SARES). It was held in Budapest, Hungary.

Aircraft, Flight trajectory, Airports, Design, Maintenance, Materials and composites, Performance, Propulsion, and Safety were recorded as the most frequently discussed subjects at this symposium. Furthermore, the subject of those articles has discussed every aspect of aviation, from energy management to flight creation, environmental research to operational performance. This symposium also covers conceptual designs of novel structures and finite elements for aircraft and fluid dynamics, maintenance, digitalization navigation, estimation, UAVs, autonomous, urban mobility, flight trajectory, maintenance-repair-and-overhaul (MRO), engines, tests, sustainability, airports, environment, multi-criteria decision making (MCDM), fuel types, performance, ground handling, operations, electric aircraft, optimization, and propellants.

The symposium also focuses on the future development of technology and MRO strategies in the global civil air transport business. We believe the readers get more updated information from the papers developed by the authors in this symposium.

However, we could not serve this proceedings book without the valuable help of our team. Kemal Keleş has communicated with all corresponding authors with

consistent track abilities. In contrast, the grand orchestration of the papers has managed by Hurşit Değirmenci with the help of Dilara Patatur and Güldeniz Bulut. We would like to thank this powerful team for their hard work gathering bits and pieces to build this book up.

Eskisehir, Turkiye
Budapest, Hungary
Budapest, Hungary
Iğdir, Turkiye
Isparta, Turkiye
Budapest, Hungary

T. Hikmet Karakoc
Jozsef Rohács
Dániel Rohács
Selçuk Ekici
Alper Dalkiran
Utku Kale

Contents

| | |
|--|-----------|
| Cork Composites in Aerospace Applications | 1 |
| Mohammad Rauf Sheikhi, Selim Gürgen, and Melih Cemal Kuşhan | |
| Low-Velocity Impact Resistance of Nylon 6.6 Nanofiber-Reinforced Epoxy Adhesives Used in Aircrafts | 7 |
| Musa Yılmaz and Mürsel Ekrem | |
| Determination of Optimum Mixing Parameter for Oil Flow Visualization | 17 |
| Aleyna Çolak, Mehmet Seyhan, and Mustafa Sarıoğlu | |
| An Assessment of Digitalization in Aircraft Maintenance | 25 |
| Kemal Ay and Ilkay Orhan | |
| Chip Breaking Applications and Chip Breaking Approach Using Variable Feed Rate in the Machining of Aviation Materials | 33 |
| Fatih Hayati Çakir | |
| SVD-Aided EKF for Nanosatellite Attitude Estimation Based on Kinematic Relations | 39 |
| Demet Cilden-Guler and Chingiz Hajiyev | |
| Developing New Concepts for the Integration of Drones into the General Air Transport Management and Urban Transport | 49 |
| Dung D. Nguyen, Utku Kale, and Dániel Rohács | |
| Development of Aircraft Maintenance Procedures Using Lean Tools | 61 |
| Tapdig Imanov, Melih Yildiz, and Elif Koruyucu | |
| Effect of Core Stitching on Flexural Properties of Lightweight Sandwich Composites | 67 |
| Çağrı Uzay | |

| | |
|--|------------|
| Environmental Impacts and Sustainability Practices of Airports | 75 |
| İrem Koçan and Gamze Orhan | |
| Evaluating Public Transport Development Projects by Multi-criteria Methods | 83 |
| Omar Alharasees | |
| Human Error Assessment and Reduction Technique in Aircraft Maintenance | 95 |
| Ebru Yazgan and Elif Kılıç Delice | |
| Assessment of Environmental Performance Indicators Based on Fuel Performance in an Aircraft Engine | 105 |
| Halil Yalcin Akdeniz | |
| Identification Performance Fields in Ground-Handling Operations to Corporate Performance | 113 |
| Ebru Yazgan, Vildan Durmaz, and Ayşe Küçük Yılmaz | |
| Impact Performance of the Kaolin-Filled Fiber-Reinforced Polymer Facing Sandwich Structures | 121 |
| Durmuş Can Acer and Necdet Geren | |
| Analysis of the Airport Sustainability Plan in the Context of EONS Components | 131 |
| Serap Gürsel and Hakan Rodoplu | |
| Optimizing Distributed Electric Aero-Propulsion Integration for a Novel Canard Aircraft Design | 139 |
| Omkar N. Walvekar and Satyanarayanan R. Chakravarthy | |
| Effects of Cruise Flight Conditions on Power and NOx Emissions for High Bypass Turbofan Engine | 151 |
| Hakan Aygun | |
| Conceptual Design and Sizing of LiDAR-Equipped Solar-Powered HALE UAV for Coastal Surveillance in India | 159 |
| Nouman Uddin and Rajkumar S. Pant | |
| Investigation of Heat Loss by Radiation from External Walls of Airport Buildings Depending on Different Sky Cloudiness Factor | 171 |
| Okan Kon and İsmail Caner | |
| Optimal Layout Design of Multi-Rotor Vehicle Based on PSO Algorithm | 181 |
| Yuke Huang, Mai Bando, and Shinji Hokamoto | |
| Development of Solar Sail for Interstellar Exploration | 193 |
| P. Suresh, Aadesh Varne, V. C. Jishnu, U. Kushal, and Parth Borse | |

Paperless Operations in Apron: A Case Study 199
 Eylem Turhan, Betül Kacar, İlkay Orhan, Alper Dalkiran,
 and Tahir Hikmet Karakoc

**Aircraft Inspection Using Drones – Benefits and Related
 Safety Concerns** 209
 Lidija Tomić and Olja Čokorilo

**Sizing and Performance Analysis of a Single-Seat
 Tandem Helicopter** 219
 Jelena Svorcan, Aleksandar Kovačević, Lazar Popović,
 and Aleksandar Simonović

**Optimization of the Surface of Drone Propeller Manufactured
 in 3D Printer** 229
 Ömer Seçgin and M. Ziya Sogut

Preparation of Smart Gels with Stiffening Behavior 237
 Selim Gürgen

Noise and Vibration Measurement System 243
 Anzhelika Stakhova

**A New Encryption Key Generator Design with True
 Random Bits** 249
 Taha Etem and Turgay Kaya

**A Case Study on Investigating Probabilistic Characteristics
 of Wind Speed Data for Green Airport** 259
 Ali Tatli, Ahmet Esat Suzer, Tansu Filik, and Tahir Hikmet Karakoc

**Enhancing Flight Safety Training and Prevention of Aviation
 Accidents with the Use of Physics and Aeronautics** 273
 Ioanna K. Lekea and Dimitrios G. Stamatelos

**Satellite Formation Flight Via NRM and EKF State
 Estimation Method** 281
 Tuncay Yunus Erkek and Chingiz Hajiye

**Evaluating the Effects of a Morphed Trailing Edge Flap
 for Aeroacoustics Applications** 289
 Joseph C. Watkins and Abdesslem Bouferrouk

**Modelling of Bird Strike for the Pilot Cabin Window
 in Side-By-Side-Seated Aircraft** 299
 Mustafa Zeki Yilmazoglu and Mehmet Berkay Luleci

Impact of Covid-19 on Air Traveler Behavior 315
 Volkan Yavas and Rustem Baris Yesilay

| | |
|--|-----|
| The Feasibility of Hydrogen Fuel Cells as a Solution Toward Zero Emissions in General Aviation Aircraft | 323 |
| Jonathan Charman and Abdessalem Bouferrouk | |
| Conceptual Design of Piezoelectric-Based Energy Harvesting Seats for Commercial Aircraft | 331 |
| Erfan Salami, Azadeh Salami, Elham Montazer, and Fairuz I. Romli | |
| Effects of Flow Pulsation on Shock Wave/Boundary Layer Interaction in Supersonic Isolator | 341 |
| Sardar Nafis Bin Ali, Abu Baker Siddque Rimon, and A. B. M. Toufique Hasan | |
| Effect of Bypass Mass Injection on Thrust Vectoring of a Supersonic Micro-Nozzle: A DSMC Investigation | 349 |
| Maruf Md. Ikram, Abu Taqui Md. Tahsin, and A. B. M. Toufique Hasan | |
| Research on Starting Optimizing Control and Active Load Fluctuation Control of More Electric Auxiliary Power Unit | 357 |
| Jiaming Zhang, Tianhong Zhang, Lingwei Li, and Xinglong Zhang | |
| Computational Analysis of Re-entry Space Vehicle at Supersonic and Hypersonic Speed | 367 |
| Jignesh Vala, Mehul K. Rana, Ayushi Mistry, Amit Parmar, Pritkumar Kathesiya, and Makadi Mahmmadsamad | |
| Sensor Fault Detection, Isolation, and Accommodation Applied to B-747 | 379 |
| Akan Guven and Chingiz Hajiyev | |
| Acoustic Emission and Acousto-Ultrasonic Monitoring in High-Temperature Environments | 387 |
| Luke Pollock and Graham Wild | |
| Explicit Dynamic Finite Element Simulation of Plate Impacts for Damage Localization | 397 |
| Luke Pollock, Noemi North, and Graham Wild | |
| Macroognition for Preparedness in Aviation | 407 |
| Maria Papanikou, Utku Kale, András Nagy, and Konstantinos P. Stamoulis | |
| Simulation of a 6DOF Nonlinear Missile | 415 |
| Kutaibah Srour and Sohayb Abdulkerim | |
| Advanced Data Analytics and Digital Technologies for Smart and Sustainable Maintenance | 425 |
| Konstantinos P. Stamoulis | |

Developing Models and Methods for Autonomous Drones in Urban Air Transport 433
 Dung D. Nguyen, Utku Kale, and Dániel Rohács

Using a New Kerosene Flame Bench Test to Analyze at Small Scales the Fire Reaction of Fiber-Reinforced Polymer Matrix Composites 447
 Alexis Coppalle, Eliot Schuhler, Avinash Chaudhary, and Benoît Vieille

Impacts of Aircraft on Environment in Europe 457
 Samer Al-Rabeei, Utku Kale, and Tawfik Mudarri

Hybrid Nanoparticle-Reinforced Polyurethane Composites Mechanical Behavior 467
 Safa Ak and Mürsel Ekrem

Design of Experiments for Wind Tunnel Testing of 53° Sweep Lambda UCAV Configuration 475
 Bilal Haider, Shuhaimi Mansor, Shabudin Mat, Wan Zaidi Wan Omar, and Nazri Nasir

Determination of Aerodynamic Characteristics for Leading-Edge Tubercle NACA 0015 Airfoil at Low Reynolds Number 487
 Mehmet Seyhan, Mustafa Sarioğlu, and Yahya Erkan Akansu

Comparison of GPS-Based Position Estimation Methods 495
 Mert Sever and Chingiz Hajiyev

Investigation of the Accuracy of Terrestrial Radio Navigation Methods for Determining Aircraft Position 507
 Alper Mehdi Sametoğlu and Chingiz Hajiyev

Development of an Efficient Finite Element Model for the Analysis of Buckling, Debonding, and Collapse Characteristics of Composite-Stiffened Panels Under Compressive Loading 517
 Vasileios Mantzaroudis and Dimitrios Stamatelos

A Conceptual Inventory of Entropy Management About Exergetic Sustainability Based on Different Cruise Altitude for Aircraft Engines 529
 M. Ziya Sogut, Enver Yalcin, and Tahir Hikmet Karakoc

Index 539

About the Editors

Siripong Atipan, Ph.D., received his B.Eng. in Mechanical Engineering from King Mongkut Institute of Technology Ladkrabang in 1994. He then joined the Department of Aerospace Engineering at Kasetsart University as a lecturer and was awarded a scholarship from the Royal Thai Government for his graduate study. Dr. Atipan received his M.Eng. in Aerospace Engineering from the Department of Aerospace Engineering, RMIT University, Australia, in 1997, and his Ph.D. in Aerospace Engineering from RMIT University in 2002. Under the supervision of Tom Steiner, his doctoral research focused on delaying vortex breakdown by steady and periodic part-length leading-edge blowing. He returned to the Department of Aerospace Engineering at Kasetsart University in 2002, where he is an Assistant Professor and continues his work in aerodynamics, aircraft performance, and design.

Can Özgür Çolpan, Ph.D., received his bachelor's and master's degrees from the Department of Mechanical Engineering at Middle East Technical University in 2003 and 2005, respectively. He conducted his Ph.D. studies at the Department of Mechanical and Aerospace Engineering of Carleton University between 2005 and 2009. He continued his studies as a post-doctoral researcher there between 2009 and 2010 and at Ryerson University between 2010 and 2012. He has been working as a faculty member in the Department of Mechanical Engineering of Dokuz Eylül University since 2012. In 2014 and 2019, he was appointed to the positions of associate professor and professor, respectively. Dr. Çolpan has conducted research in the field of fuel cells and hydrogen and the mathematical modeling of integrated energy systems. His areas of research include modeling of direct internal reforming solid oxide fuel cells, material development and mathematical modeling for direct methanol fuel cells, development of high-temperature PEM fuel cells, simulation and optimization of the fuel cell vehicle powertrains, catalytic dehydrogenation of solid hydrogen storage materials, analysis of organic Rankine cycle based systems, and analysis of biofuel fueled turbojet.

Alper Dalkıran, Ph.D., received his bachelor's degree from the Avionics Department at the Faculty of Aeronautics and Astronautics at Eskisehir Technical University (formerly known as Anadolu University). He completed his MSc degree in the School of Science from Anadolu University in 2004 in Aviation Maintenance. He earned his Ph.D. degree in 2017 in Environmental Sustainability on Airports from the School of Science at Anadolu University by developing a model of energy-based calculations of an aerodrome. Dr. Dalkıran has studied aircraft engines, sustainability, airports, and exergy. He has 17 years of professional experience in airports in information technology, automation, and integration. He has managed teams on system design, projects, tests, commissioning, operational readiness, and operations. He has been working in the School of Aviation at Suleyman Demirel University since 2019 and lecturing in flight theory, airline management, and airport design subjects.

Selcuk Ekici, Ph.D., received his B.S. in Mechanical Engineering from Eskisehir Osmangazi University, M.S. in Aeronautics and Astronautics from Anadolu University, and Ph.D. in Aeronautics and Astronautics from Eskisehir Technical University in 2008, 2015, and 2019, respectively. He is currently the Head of the Aviation Department at Iğdır University. Dr. Ekici has authored/co-authored books, book chapters, journal and conference papers, and numerous technical reports. He is an active member of various international scientific organizations and societies and serves as an associate editor and editorial board member for various international journals. An active researcher and supervisor, his research areas include aviation, thermodynamics, gas turbine engines, alternative/renewable fuels, and the environment.

Ismail Ekmeki, Ph.D., is a lecturer in the Department of Industrial Engineering at Istanbul Commerce University. He received his M.Sc. in Mechanical Engineering from the School of Science at Yildiz Technical University, M.Sc. in Industrial Engineering from İstanbul Technical University, and Ph.D. in Mechanical Engineering from Yildiz Technical University in 1982, 1983, and 1995, respectively. He has worked as a researcher, executive, and manager in academic positions on various industrial projects. His areas of research cover energy, optimization, decision making, safety, OHS, and HVAC-related topics.

Ali Haydar Ercan, Ph.D., received his bachelor's degree from the Mechanical Engineering Department, Faculty of Engineering at the University of Cumhuriyet, Sivas, and his M.Sc. degree from the Mechanical Engineering Department at the University of Gazi, Ankara, where he studied Heat Transfer. He earned his Ph.D. from the Department of Aerodynamics, University of Liverpool, England, where he worked on Boundary Layer Theory on Flat Plate Surfaces and developed empiric formulas for transition development distance from the leading edge. He completed his Ph.D. in 1997. He also earned a Postgraduate degree in Software Technologies from the University of Liverpool in 1999. He worked at the University of

Cumhuriyet as a lecturer, at the University of Liverpool as an assistant lecturer while studying for his Ph.D., and at Ondokuz Mayıs University as Head of the Junior Aviation Technical School, where he was one of the department's founders. Dr. Ercan works as a lecturer in the Department of Unmanned Aerial Vehicles in Electronics and Automation at Porsuk Vocational School at Eskisehir Technical University. He is also working on PIV (particle image velocimetry) related subjects and a new idea for wing design. He is a reviewer for four journals and a guest editor. He has held a wide range of managerial positions and has experience with international commercial private companies.

Aleksandar Grbović, Ph.D., has been a full professor in the Aeronautical Department of the Faculty of Mechanical Engineering at the University of Belgrade (UB-FME) since 2020. He graduated from UB-FME in 1994 and earned a Magister and Ph.D. from UB-FME in 2000 and 2012, respectively. His scientific field is aeronautics, focusing on engineering fracture mechanics and fatigue of aircraft structures. Professor Grbovic has supervised seven Ph.D. candidates and was a thesis defense committee member for an additional 15. He has contributed to developing several laboratory installations, including labs on numerical simulations and aircraft static and dynamic testing. He has published several chapters in monographs and more than 90 papers in international journals and conference proceedings. Professor Grbovic has worked on 20 engineering projects, numerous technical reports and reviews, and has delivered solutions to multiple problems in the Serbian aircraft industry and developing new constructions in the military sector.

Utku Kale, Ph.D., is an assistant professor at the Department of Aeronautics and Naval Architecture at the Budapest University of Technology and Economics (BME) in Hungary. He is currently training to become an airline pilot on the Airbus A320. In the framework of the ERASMUS program, he spent over a year at the University of Castilla La-Mancha, Spain. He has been involved in several international and national projects, including SESAR, Clean Sky, ERASMUS Plus, DU SPoC, and Hungarian EFOP. Dr. Kale is the author of over 40 articles. He received a Young Researcher Award in 2019 from the Sustainable Aviation Research Society (SARES) and a year-long success scholarship from Koc Holding. He was president of the Miskolc EAGE (European Association of Geoscientists and Engineers) Student Chapter in 2016/2017. He is currently a member of EAGE and SARES and is an associate editor of the *International Journal of Sustainable Aviation*.

T. Hikmet Karakoc, Ph.D., graduated from the Department of Mechanical Engineering, Anadolu University. He received his M.Sc. degree in Mechanical Engineering from the Yildiz Technical University. He received his Ph.D. from Anadolu University, where he started his full-time teaching and received his full professorship. He is currently researching at the Eskisehir Technical University. He has a wide range of research interests, including sustainable aviation, aircraft propulsion systems, insulation, heating, ventilating, and air conditioning (HVAC), indoor air quality, gas turbines, cogeneration systems, renewable energy, energy economics,

fuels, and combustion. He has participated in numerous industrial projects on these topics as a researcher, consultant, and project manager for over 30 projects and corporations. He also started a contest on special insulation applications among university students. He served as an editor-in-chief, guest editor, and editorial board member for international scientific journals. He published national and international papers in over 300 journals and 40 books. Professor Karakoc actively follows membership positions for the Chamber of Mechanical Engineers and many sectorial associations, international scientific organizations, and societies. He is an active Board of Directors member of the International Association for Green Energy. He is currently holding the presidency of the SARES organization, which is actively supporting scientists and students in the area of sustainable aviation. He also organizes four symposiums on aviation subject areas as a founding chair.

Navatasn Kongsamutr, Ph.D., works in the area of air transport management in the Department of Aerospace Engineering at Kasetsart University. He earned a B. Eng. in Aerospace Engineering from Kasetsart University, an MBA in Aviation Management from the Royal Melbourne Institute of Technology, and a Ph.D. in Air Transport Management from Cranfield University. His areas of expertise cover air transport management, business model development, strategic planning and management, policy, strategy, and competition analysis. Dr. Kongsamutr has conducted research and consulting work at both the national and corporate levels, including a strategic plan for the Royal Thai Government's Ministry of Transport, a national commercial airport master plan for the Civil Aviation Authority of Thailand, and the development of an aviation market intelligence system for Airports of Thailand PLC.

Ivan A. Kostić, Ph.D., is a Full Professor and Head of the Aerospace Department in the Faculty of Mechanical Engineering at the University of Belgrade. In addition, he is also a lecturer at the Serbian Military Academy of the University of Defence and was previously a lecturer at the Yugoslav Military Aeronautical Academy. He graduated from the University of Belgrade, Faculty of Mechanical Engineering, Aerospace Department, where he obtained his Magister and Doctoral degrees. Professor Kostić teaches courses in aerodynamic design, applied aerodynamics, high-speed aerodynamics, air vehicle design, flight dynamics, special topics in fluid mechanics, nonplanar lifting surfaces, airfoils and lifting surfaces of aircraft, aircraft weapon systems, and the theory of bombing and rocketing. He is the author or co-author of more than 150 publications, including scientific and technical papers in journals, conference proceedings, project reports, and books. Professor Kostić is a member of several domestic and international aeronautical associations. He holds his sport and private pilot licenses and has flying experience on single-engine aircraft and sailplanes.

Tomislav Letnik, Ph.D., is head of the Transport Economics Centre at the University of Maribor, where he has been a project manager since 2005. His work involves the management of several European and national projects in the field of logistics and transport economics. Dr. Letnik is also a lecturer at the University of Maribor for courses on logistics, transport economics, investment decisions, and system theory. He holds a B.S. degree in transport engineering and has successfully concluded postgraduate studies at the University of Maribor.

Maršenka Marksel is a research assistant with the Faculty of Civil Engineering, Transportation Engineering, and Architecture at the University of Maribor. She received a Bachelor's degree from the University of Maribor Faculty of Economics and Business. During her studies, she was actively involved in several research projects at the Institute of Economic Analysis and Forecasting and the Transport Economic Centre at the University of Maribor.

Ognjen Peković, Ph.D., is an associate professor with the Faculty of Mechanical Engineering at the University of Belgrade, where he also received his M.Sc. and Ph.D. degrees. He teaches courses on finite element methods, computational methods in aerospace engineering, aircraft performances, flight dynamics, aircraft control and systems, and aircraft armament. His research interests include structural design, drones, wind tunnel testing, wind turbines, renewable energy, and energy efficiency. Dr. Peković has participated in numerous research, innovation, and commercial projects on these topics as a researcher, consultant, and project manager over the past 15 years. He is a member of several national engineering associations, including the Serbian Chamber of Engineers, with three active licenses. He has a private pilot license and is a dedicated aviation enthusiast.

Daniel Rohacs, Ph.D., is head of the Department of Aeronautics and Naval Architecture at the Budapest University of Technology and Economics. He served for the Research Development and Simulation Department at HungaroControl – Hungarian Air Navigation Services as the head of the department for many years. He worked for Eurocontrol (Bretagne) as a doctoral researcher for three years as a Ph.D. student at École Pratique des Hautes Études, Sorbonne (2004–2005), and visiting Ph.D. student at Princeton University. He has good management practice as a research director of SME Rea-Tech Ltd (since 2006) and CEO of RDS-X Ltd. (2005–2007). Dr. Rohacs is very active in international cooperation and research, including the EU-supported projects EPATS, Sat-Rdmp, Sinbad, Pplane, Esposa, Innovate, SmartPolis, and as project manager of L1 Gabriel project, USIS SESAR UTM, SafeFly, IDEA-e, and special projects at HungaroControl, including the introduction of free-routing and remote tower concepts into operation, developing new ideas,

disruptive technologies, and solutions. He is active in international conference organizations and participates in IFAR (International Forum for Aviation Research). Dr. Rohacs is well known for combining solid technical and institutional backgrounds from academia and an open and dynamic business approach in the international market.

Jozsef Rohacs, Ph.D., is a full professor emeritus at the Department of Aeronautics and Naval Architecture at the Budapest University of Technology and Economics (BME). He served 12 years as Dean for Scientific Affairs and led the Department of Aircraft and Ships for over 20 years. He has extensive experience in high-level advising at large civil and military companies and managing small companies and foundations. Dr. Rohacs delivers lectures on numerical methods, numerical optimization, aerodynamics, flight mechanics, and control and development philosophies. He has an extensive practice in project management, including investigation, research technology, and product development. He was involved in many EU-supported projects (over 26 international projects), including EPATS, Sat-Rdmp, Sinbad, Pplane, Esposa, Innovate, SmartPolis, Nelui, and others, and coordinated the EU L1 level project, Gabriel. He is the professional and technical manager of the national project IDEA-e, developing the technology for electric and hybrid-electric propulsion systems and conceptual design for the 4-seater electric and hybrid cargo UAV aircraft.

Vis Sripawadkul is a lecturer in the Department of Aerospace Engineering at Kasetsart University, where he is primarily involved in aircraft design and optimization work. His areas of interest include airport engineering, and he is currently working as a consultant on several projects. He earned a B.Eng. in Aerospace Engineering from Kasetsart University, an M.Sc. in Computational Mechanics from Technical University Munich, and an M.Phil. in Engineering Design from Cranfield University.

Jelena Svorcan, Ph.D., is an associate professor in the Department of Aerospace Engineering in the Faculty of Mechanical Engineering at the University of Belgrade, where she also obtained her Ph.D. Over a decade-long scientific career, her research has mainly been focused on computational aerodynamics, rotating lifting surfaces, wind energy, turbulence, efficiency improvement, numerical simulations, aircraft design, and optimization. She has participated in several national research projects, including various collaborations with partners from industry. She has authored or co-authored over 70 scientific publications and technical solutions and regularly performs reviews for international scientific journals. Dr. Svorcan has prepared and delivered lectures in different courses at all three levels of study (B.Sc., M.Sc., Ph. D.), mentored students, and participated in several M.Sc. and Ph.D. thesis committees. She is a member of the AIAA, the APS, the Serbian Chamber of Engineers, the Serbian Society of Mechanics, and the Serbian Union of Mechanical and Electrical Engineering.

Cork Composites in Aerospace Applications



Mohammad Rauf Sheikhi, Selim Gürgen, and Melih Cemal Kuşhan

Contents

| | | |
|---|-------------------------|---|
| 1 | Introduction | 1 |
| 2 | Cork Applications | 3 |
| 3 | Conclusions | 4 |
| | References | 5 |

1 Introduction

Cork is a natural product that is the covering of the cork oak tree, *Quercus suber* L. It is composed of several cells such as 42 million cells per centimeter cube. The cells are generally structured with five wall layers, and the inside of the cells is filled with air. For this reason, the bigger part of the cork is just air, which makes this natural material very light. Cork is such a lightweight material that it floats on water. The density of cork is about 0.24 grams per cubic centimeter. Despite its low density, cork shows impermeable characteristics to fluids due to its closed-cell microstructure. In addition to these properties, cork is very flexible and durable under harsh environmental conditions. Moreover, cork is an imperishable material although it is a natural substance (Gil, 2009). Figure 1 shows the microstructural views of cork.

Cork is supplied from the cork oak forests on the Mediterranean coasts. Portugal and Spain are the biggest cork producers in the world because about 70% of the cork

M. R. Sheikhi (✉)

Eskişehir Technical University, Faculty of Aeronautics and Astronautics, Eskişehir, Türkiye
e-mail: mohammadraufsheikhi@eskisehir.edu.tr

S. Gürgen · M. C. Kuşhan

Department of Aeronautical Engineering, Eskişehir Osmangazi University, Eskişehir, Türkiye
e-mail: sgurgen@ogu.edu.tr; mkushan@ogu.edu.tr

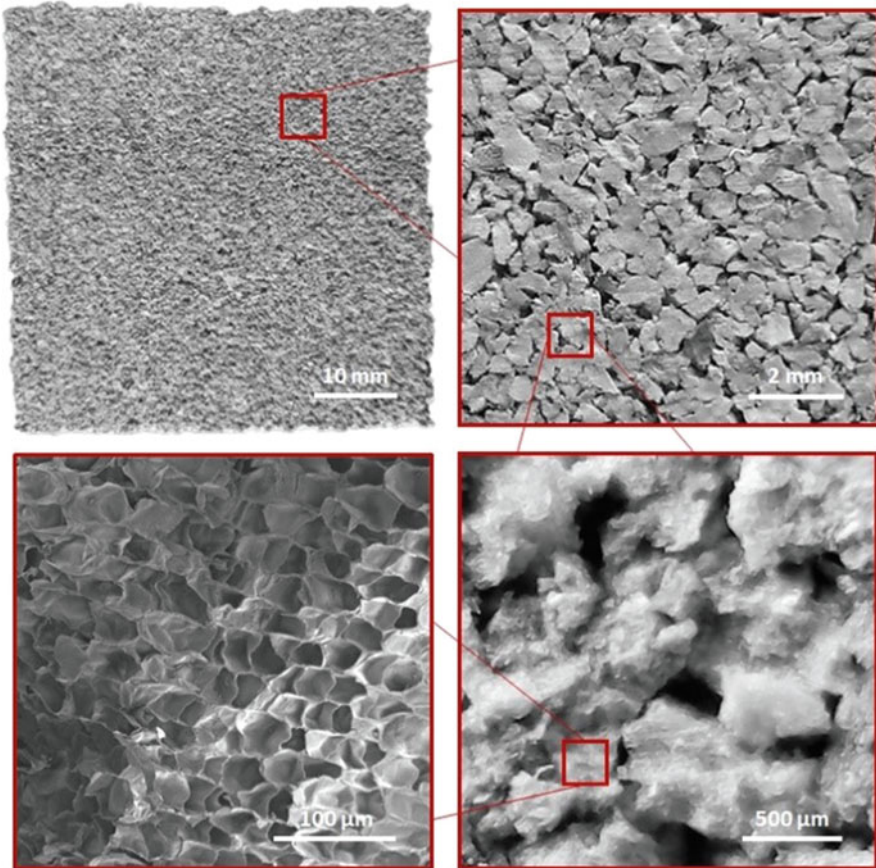


Fig. 1 Microstructural views of cork. (Gürgen et al., 2021)

forests are in the territories of these two countries. Cork production is sustainable because the cork tree is not cut down to obtain cork; only the bark is stripped to harvest the cork. The tree continues to live and grow. The sustainability of production and the easy recycling of cork products and by-products are two of its most distinctive aspects. Cork oak forests also prevent desertification and the refuge of various endangered species. Leading companies especially in the aerospace sector make investments in cork. However, there is a lack of human resources in the field since syllabuses in engineering programs focus on the technical side rather than including the environmental effects of engineering materials.

Prior to the cork use in major sectors, cork was used as bottle stoppers in the first applications. In the next periods, cork wastes were compressed into panels, and they were used as lifejackets for sailors since cork floats on water. Because cork is a kind of wooden product, cork panels were used in floor coverings. Cost-effective and recyclable materials were produced by producing cork panels from cork wastes. In

order to reinforce the cork panels, different kinds of additives such as gelatin, dextrin, casein, and polyurethane were mixed with cork granules before the molding process (Gil, 2015).

2 Cork Applications

In aerospace applications, cork is used in a laminate form. In order to produce cork laminates, stripped cork layers from the cork oaks are ground into different sizes of granules. Then, the cork granules are mixed into a polymer matrix, generally polyurethane, and molded into desired dimensions of panels. Figure 2 shows different cork panels. Although neat cork panels are ready for installation in aerospace applications, these panels are also used with elastomer coatings, metal coverings, or rubber granules. Elastomer coatings protect the cork panels from external conditions such as humidity, sharp impacts, and heavy loadings. Metal covers are used for producing sandwich cork composites. Rigidity and stiffness are increased by using metal skins on the cork panels. These sandwich structures are generally used in flooring applications as well as prefabricated houses. Rubber-mixed cork granules are common in civil engineering applications. Rubber/cork panels are used for increased flexibility especially for floor coverings.

Cork laminates are applied in aerospace structures for the isolation of vibrational and thermal loadings. In aircraft, cork laminates are bonded on the mating surfaces of brackets to suppress the vibrations in the joints. Boeing 737 and combat helicopter Atak are some of the platforms using cork-covered brackets from the aircraft industry. Air vehicles are subjected to unavoidable vibrational loadings during flights, and therefore, the structures are reinforced by vibration isolators to lower the vibrations. The joints such as brackets are important application areas because the undesired vibrations may unfasten the joints and may lead to the disassembly of

Fig. 2 Cork panels in different thicknesses



Fig. 3 Cork cover on a bracket



components. Figure 3 shows a cork cover bonded on a bracket. Apart from aircraft applications, space vehicles take advantage of cork composites both for suppressing undesired vibrations and insulating the vehicle from heat sources. In solid rocket boosters, engine skirting, nose cone, frustum, forward and aft skirt, external tank attach ring covers, and assembly and tunnel covers are applied with cork panels (Fig. 4). These sections are protected by composite laminates from heat and vibrations. In addition to these loadings, cork panels are also used for impact protection against space debris. Due to the viscoelastic behavior of cork, it provides quite good anti-impact properties according to early studies (Gürgen et al., 2021).

3 Conclusions

Due to its environmentally friendly properties, cork is a good choice for engineering applications. In addition to sustainable properties, cork exhibits good mechanical and thermal behavior. This natural material provides excellent vibration and thermal insulations and very low density as well. For this reason, the aerospace industry benefits from cork composites as isolators against vibrational and thermal loadings. In air vehicles, joints such as brackets are covered with cork panels not to unfasten the assemblies under vibrations. On the other hand, cork is used as a thermal insulator shield in space vehicles. Heat-affected sections near the space engines are protected with cork panels. Moreover, the nose cone of space shuttles is insulated with cork laminates to protect the vehicle from the heat generation that emerges due to the frictional interaction at high-speed flight in the atmosphere.

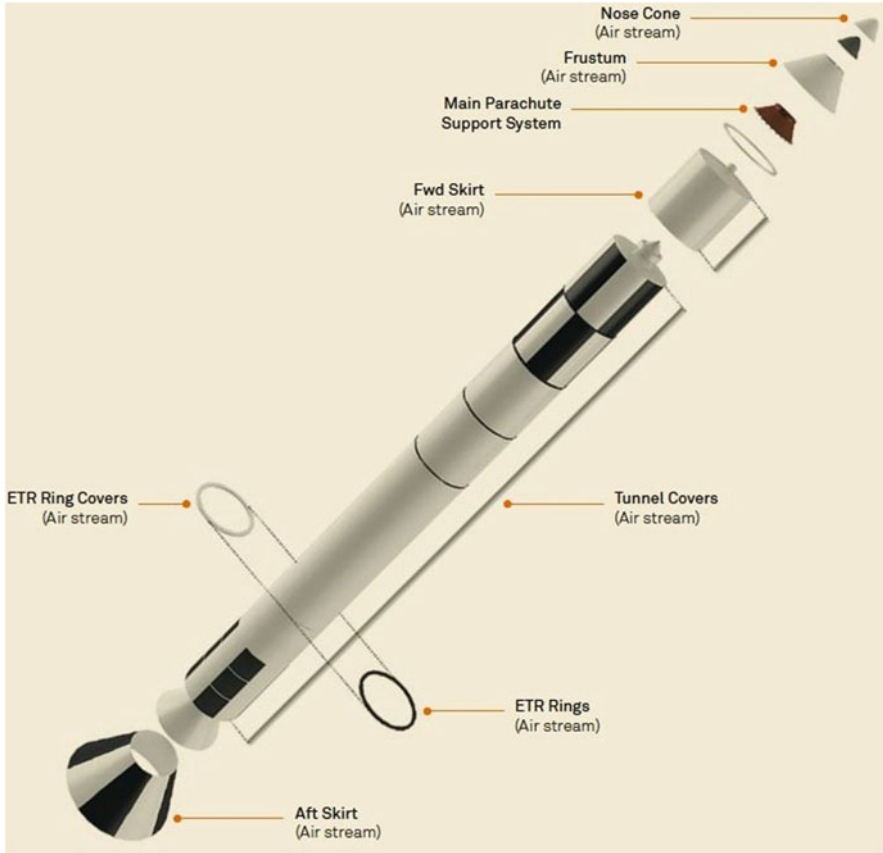


Fig. 4 Cork application areas in a space vehicle. (Amorim, 2021)

References

- AMORIM. (2021). *Ablative thermal protection* [Online]. Available: <https://amorimcorkcomposites.com/en-us/materials-applications/aerospace/>. Accessed on 11 Jan 2021.
- Gil, L. (2009). Cork composites: A review. *Materials*, 2, 776–789.
- Gil, L. (2015). Cork. In *Materials for construction and civil engineering*. Springer.
- Gürgen, S., Fernandes, F. A., De Sousa, R. J. A., & Kuşhan, M. C. (2021). Development of eco-friendly shock-absorbing cork composites enhanced by a non-newtonian fluid. *Applied Composite Materials*, 28, 165–179.

Low-Velocity Impact Resistance of Nylon 6.6 Nanofiber-Reinforced Epoxy Adhesives Used in Aircrafts



Musa Yılmaz and Mürsel Ekrem

Contents

| | | |
|-----|---|----|
| 1 | Introduction | 8 |
| 2 | Method | 9 |
| 2.1 | Production of Nanofibers | 9 |
| 2.2 | Surface Treatment of Adherent Plates | 9 |
| 2.3 | Preparation of Single-Lap Bonded Joints | 10 |
| 2.4 | Low-Velocity Impact Tests | 11 |
| 2.5 | Tensile Tests | 12 |
| 3 | Results and Discussion | 12 |
| 3.1 | Analysis of Fracture Surfaces | 12 |
| 3.2 | Non-Impact Single-Lap Joints | 13 |
| 3.3 | Single-Lap Joints with Impact at Different Temperatures | 14 |
| 4 | Conclusions | 15 |
| | References | 15 |

Nomenclature

| | |
|-------|---|
| N6.6 | Nylon 6.6 |
| CFREC | Carbon fiber-reinforced epoxy composite |
| GNPs | Graphene nanoparticle |
| SEM | Scanning electron microscope |

M. Yılmaz

Department of Transportation Services, Sorgun Vocational School, Yozgat Bozok University, Yozgat, Türkiye

M. Ekrem (✉)

Department of Mechanical Engineering, Faculty of Engineering, Necmettin Erbakan University, Konya, Türkiye

e-mail: mekrem@erbakan.edu.tr

1 Introduction

Fiber-reinforced polymer composites are preferred especially in contemporary applications of aerospace, automotive, and defense industries, thanks to their high specific strength and modulus (Babu et al., 2013). In general, by adding nano-reinforcement, multifunctional structures can be obtained by fully customizing the mechanical, electrical, and thermal properties of the material (Ekrem, 2019b; Fiedler et al., 2006; Thostenson et al., 2005). Carbon-based nano-reinforcements are a popular method in the synthesis of advanced materials. Carbon fiber-reinforced polymer composite materials show superior properties compared to other conventional fiber-reinforced composite materials with excellent strength, low specific gravity, toughness, high fatigue, high-temperature wear, and high oxidation resistance (Allix et al., 1995; Ladeveze & Ledantec, 1992). Nylon 6.6 (N6.6) stands out among other polyamides due to its high hardness, wear resistance, toughness, and thermal deformation values (Düzçükoğlu et al., 2015). It is also widely used to obtain composite materials with higher mechanical properties by mixing various fibers (Zhao et al., 2006).

Electrospinning, which is the process of forming nanofibers along an electrically charged jet from a polymer solution or melt, is the most widely used and most developed method in terms of the reproducibility of the process, as well as the production of long and continuous nanofibers (Fong et al., 1999; Yıldırım et al., 2020). Nanofibers are used both in the improvement of composite materials (Gojny et al., 2005) and in the development of adhesives by hybridization (Ekrem, 2019a; Yılmaz, 2019).

Adhesive bonding is a method with advantages such as low weight, uniform stress distribution, waterproofing, and galvanic corrosion prevention, which allow the joining of different materials without damaging the components (Arenas et al., 2013; Nemati Giv et al., 2018).

In this study, single-lap adhesion joints were formed by using carbon fiber-reinforced epoxy composite and aluminum 2024-T3 (AA2024) alloy plates with pure epoxy adhesive and Nylon 6.6 nanofiber-reinforced epoxy adhesive. N6.6 nanofiber produced by the electrospinning method was used to increase the applied load and to improve the damage mechanisms by reinforcing the epoxy resin. Single-lap joints produced in accordance with the ASTM D1002-10 standard were first subjected to a low-velocity impact at different temperatures (-50 , -20 , 0 , 23 , and 50 °C) and at a nondestructive speed of 1.04 m/s. After low-velocity impact, tensile tests at room temperature were applied to the samples, and the effect of impact at different temperatures on the adhesion joints was investigated.

2 Method

2.1 Production of Nanofibers

Nylon 6.6 nanofibers were produced using the electrospinning method to improve the damage behavior by reinforcing the epoxy adhesive, which is the thermoset polymer used in single-lap joints. For this purpose, firstly, 3 ml of chloroform and 7 mL of formic acid were added into a beaker to dissolve 1 g of N6.6 polymer in granular form and mixed in a magnetic stirrer at 400 rpm for 1 day until a homogeneous solution was formed. Nanofiber production was started by drawing 5 ml solution from this prepared solution into a 0.8 mm diameter and 5 ml syringe and placing it in the electrospinning device. The most suitable parameters in nanofiber production, for optimum nanofiber after literature research and repeated trials, are syringe movement speed at 0.35 ml/h, voltage at 20 kW, distance between rotating cylinder and syringe tip at 13 cm, room temperature at 23–25 °C, and relative humidity at 55%.

2.2 Surface Treatment of Adherent Plates

Aluminum alloy 2024-T3 plates were cut by laser using nitrogen gas in 101.6×25 mm dimensions according to ASTM D 1002-10 standard, the burrs were removed and surface preparation processes were started. According to the ASTM D3933-98 phosphoric acid anodizing standard, the factors that reduce the penetration of the epoxy such as dirt and oil on the surface were cleaned, and by forming a controlled oxide (Al_2O_3) layer, both corrosion resistance and homogeneous roughness were obtained. In this context, aluminum samples were first kept in a mixture of sodium hydroxide (NaOH) and boiled water for 10 min, cleaned against factors such as oil and dirt, and rinsed by keeping them in pure water heated to at least 43 °C for 10 min. Then, the etching process was performed by keeping the samples in a solution of sulphuric acid – sodium dichromate dehydrate – and distilled water heated at 65–71 °C for 10–15 min and rinsed with distilled water at room temperature again. In the last stage, surface anodization was carried out in phosphoric acid – pure water solution with phosphoric acid anodization for 20–25 min – and after samples were rinsed with pure water at room temperature for 10 min. It was dried in an oven at 80 °C for 40 min (Fig. 1).

Composite plates were prepared according to ASTM D2093-03 standard as shown in Fig. 2. In this context, the surface of the composite was abraded with 300-grit aluminum oxide sandpaper in the directions shown in the figure. After the sanding process was completed, the composite was first rinsed in acetone, and then the bonding surfaces were wiped with a clean and lint-free cloth. As a final step, it was cleaned in an ultrasonic water bath with acetone for 30 min and kept in a desiccator.

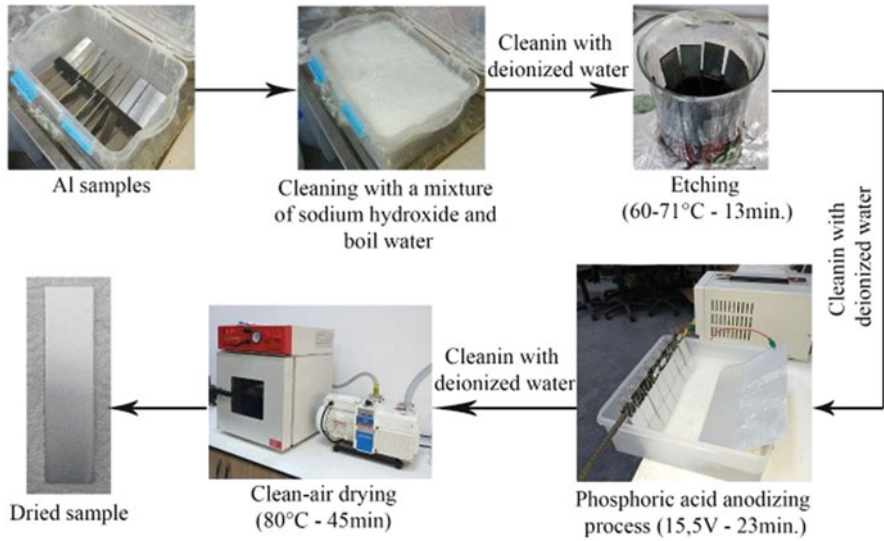


Fig. 1 Surface treatment of aluminum plates

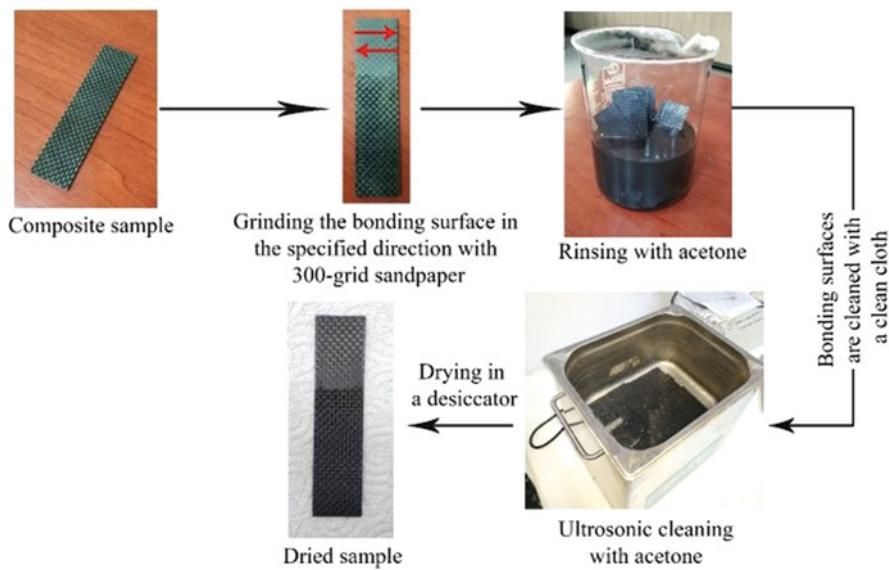


Fig. 2 Surface treatment of composite plates

2.3 Preparation of Single-Lap Bonded Joints

Firstly, epoxy adhesive was prepared for the preparation of single-lap bonding joints. In this context, a mixture of 60% epoxy resin and 40% curing agent was prepared

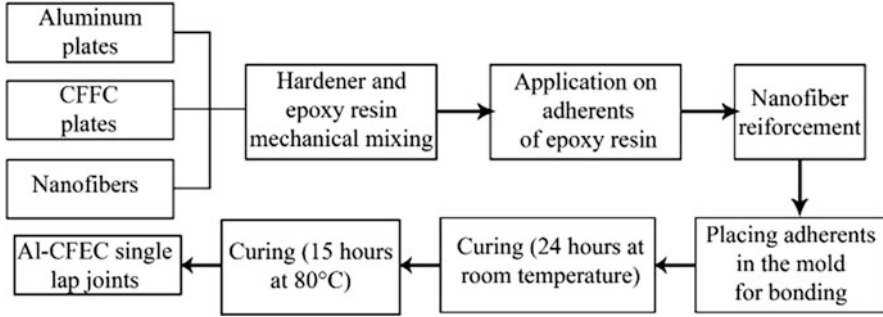


Fig. 3 Production of single-lap bonding joints

according to the manufacturer’s recommendation and mixed mechanically for 10 min. In order to remove the air bubbles formed during mixing, the adhesive was kept under 0.2 atm pressure for 10 min.

After the epoxy adhesive was prepared, it was applied to the adhesion areas of the aluminum and composite plates, the surface preparations of which were completed, and placed in the adhesion mold with the adhesion areas of both plates overlapping each other. The adhesion mold was used in all samples to obtain a mutual standard as well as 0.2 mm adhesive thickness and 20 mm adhesion length. In N6.6 nanofiber-reinforced adhesion connections, unlike pure epoxy bonding connections, the nanofibers that were pre-prepared and cut in 20 × 25mm sizes were reinforced after epoxy adhesive was applied to the adhesion areas, and the nanofiber was completely wetted with the help of a brush (Fig. 3).

After the positioning process on the mold was completed, the bonding process was completed by first curing for 24 h at room temperature and then by performing post-cure for 15 h in an oven at 80 °C.

2.4 Low-Velocity Impact Tests

Low-velocity impact tests were carried out at a speed of 1.04 m/s and an impact energy of 3 J, obtained by dropping the 5.6 kg striking head from a height of 5.46 cm. Since the postimpact loading state of the single-lap adhesion joint will be analyzed by the tensile test, height adjustment has been made to obtain the energy level where the samples will not be completely destroyed by impact. Impact mold was used so that all of the impact energy acts on the surface of the adhesion joint in the normal axis and the impact effect occurs in one axis. The low-velocity impact effect was applied to the composite side, since composite materials have better elasticity and resilience properties and are exposed to direct impact in practice.

Impact tests were carried out at five different temperatures (−50, −20, 0, 23, and 50 °C). While an oven was used to heat the samples, liquid nitrogen was used to cool the samples by spraying them onto the adhesion area with the help of a nitrogen gun.

After the conditioning process was carried out, it was followed by a thermal camera whether the desired values were reached or not.

Impact tests were tested by repeating five times in a low-velocity impact test device in Konya Technical University Mechanical Laboratory.

2.5 Tensile Tests

Tensile tests were carried out at room temperature and 2 mm/min tensile velocity of five specimens that did not break after low-velocity impact tests. Tensile tests were performed using the Shimadzu AGS-X tensile test device and Trapezium X software in the Necmettin Erbakan University Machinery Laboratory.

3 Results and Discussion

3.1 Analysis of Fracture Surfaces

In Fig. 4, macroscopic images of the adhesion joints, which were completely ruptured after low-speed impact tensile testing, are given. A mutual characteristic was observed in all adhesion joints, and it was observed that the separation in adhesion joints was not at the interface, but by breaking the adhesive, and was separated by cohesion fracture. It is also seen that the fracture paths that are expected to be observed in cohesion fracture draw zigzags. This means that since the crack could not progress in the bonding area while it was progressing, it switched to the composite sheet layer, which was weak due to sanding and returned to the adhesion area again.

In Fig. 5, postimpact 1 KX and 10 KX SEM images of single-lap joints of E and EN adhesives and observed damage types are given. As seen in Fig. 5 a and b, the damage mechanism of the epoxy resin is a flat and featureless surface. In Fig. 5 c and

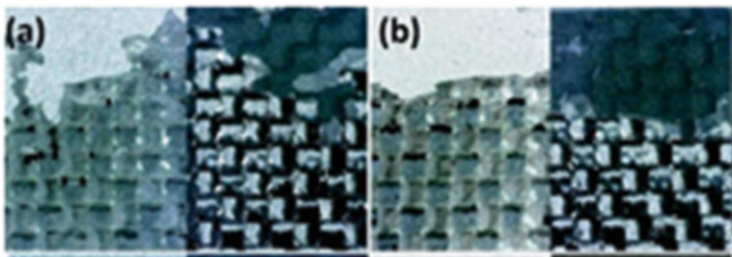


Fig. 4 Production of single-lap bonding joints

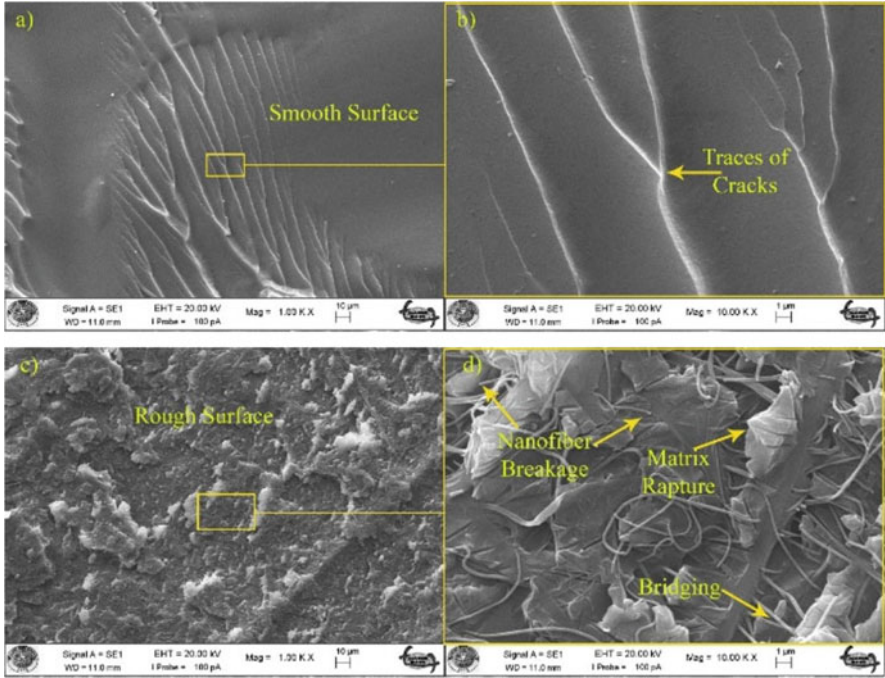


Fig. 5 Damage types observed in 1 KX and 10 KX SEM images of a single-lap joint after tensile testing (a) E-1 KX, (b) E-10 KX, (c) EN-1 KX, (d) EN-10 KX

d, a rough structure was realized in the fractured parts, and the cohesion fracture mode was realized.

When Fig. 5d is examined, the types of damage (such as nanofiber breakage, bridging, matrix rapture) that absorb energy in the adhesion joint and increase toughness are determined. The occurrence of these types of damage shows that a cohesive damage type has occurred, and the reinforcements we have made to increase the strength of the adhesive and the amount of energy required to rapture are successful.

3.2 Non-Impact Single-Lap Joints

In Fig. 6, the maximum tensile strengths are given as a result of the tensile tests of E and EN adhesives for single-lap joints without impact and at room temperature. As seen in the figure, while the maximum tensile strength of E adhesive is 3405.6 N, the max tensile force of EN adhesive is 5835.6 N, and it was determined that the nanofiber reinforcement provided an increase of 71%.

Fig. 6 Non-impact single-lap joints (*E* epoxy, *EN* epoxy+N6.6 nanofibers)

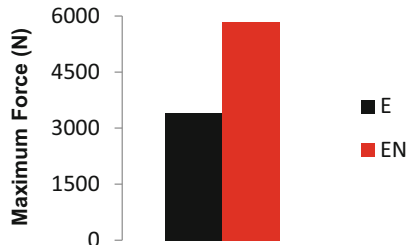


Fig. 7 Energy loading state of a single-lap bonding joint with epoxy adhesive

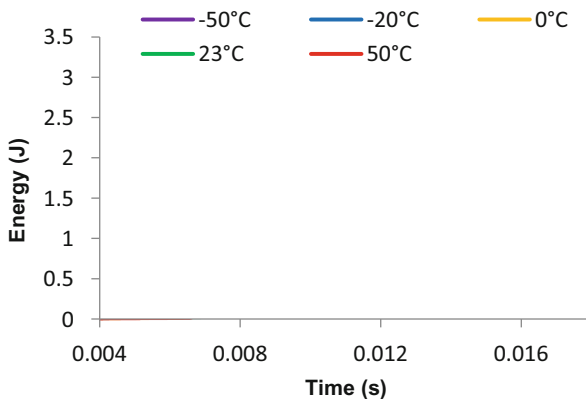
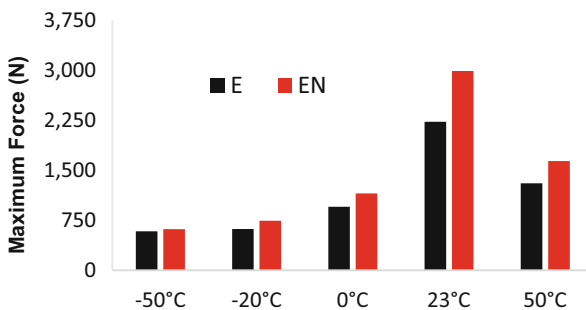


Fig. 8 Single-lap joints with impact at different temperatures max. Force



3.3 Single-Lap Joints with Impact at Different Temperatures

In Fig. 7, the 3 J impact energy/time graph of epoxy adhesive at different temperatures is given. When the graph is examined, the energy transfer times and the amount of energy returned were realized at the same time at all temperatures at a low impact speed of 1.04 m/s.

In Fig. 8 and Table 1, the maximum tensile forces of E and EN adhesives for single-lap joints obtained after low-speed impact at different temperatures are given. When the Nylon 6.6 nanofiber-reinforced epoxy adhesives were compared with epoxy, the maximum force after impact was higher at all temperatures. The

Table 1 Single-lap joints with impact at different temperatures max. Force (N) (lab measurements)

| | -50 °C | -20 °C | 0 °C | 23 °C | 50 °C |
|----|--------|--------|--------|--------|--------|
| E | 585.2 | 620.9 | 953.1 | 2230.3 | 1307.0 |
| EN | 618.6 | 744.8 | 1153.5 | 2992.7 | 1641.5 |

maximum strength of EN adhesive after impact at room temperature was 2993 N with an increase of 34%.

4 Conclusions

In this study, Nylon 6.6 nanofiber produced by the electrospinning method was reinforced with the epoxy adhesive used for joining single-lap joints of Al 2024 and carbon fiber-reinforced composite materials. Then, the maximum load-carrying capacities after a low-velocity impact of 1.04 m/s at different temperatures (-50, -20, 0, 23, and 50 °C) were investigated.

- In the 3 J postimpact energy-time graph, the energy transfer times and damped energy responses of E and EN adhesives at different temperatures are similar.
- Nylon 6.6 nanofiber-reinforced epoxy adhesive provided a 34% increase in maximum postimpact load at room temperature.

References

Allix, O., Ladeveze, P., & Corigliano, A. (1995). Damage analysis of interlaminar fracture specimens. *Composite Structures*, 31(1), 61–74.

Arenas, J. M., Alía, C., Narbón, J. J., Ocaña, R., & González, C. (2013). Considerations for the industrial application of structural adhesive joints in the aluminium–composite material bonding. *Composites Part B: Engineering*, 44(1), 417–423.

Babu, G. D., Babu, K. S., & Gowd, B. U. M. (2013). Effect of machining parameters on milled natural fiber-reinforced plastic composites. *Journal of Advanced Mechanical Engineering*, 1, 1–12.

Düzcükoğlu, H., Ekinci, Ş., Şahin, Ö. S., Avci, A., Ekrem, M., & Ünalı, M. (2015). Enhancement of wear and friction characteristics of epoxy resin by multiwalled carbon nanotube and boron nitride nanoparticles. *Tribology Transactions*, 58(4), 635–642.

Ekrem, M. (2019a). The effects of carbon nanotubes added polyvinyl alcohol nanofibers on mechanical properties of carbon reinforced composite laminates. *Sādhanā*, 44(8), 179.

Ekrem, M. (2019b). Shear strength of boron nitride nanoplatelets and nano Ag reinforced structural adhesives. *Journal of Bor*, 4(3), 128–134.

Fiedler, B., Gojny, F. H., Wichmann, M. H., Nolte, M. C., & Schulte, K. (2006). Fundamental aspects of nano-reinforced composites. *Composites Science and Technology*, 66(16), 3115–3125.

Fong, H., Chun, I., & Reneker, D. H. (1999). Beaded nanofibers formed during electrospinning. *Polymer*, 40(16), 4585–4592.

- Gojny, F. H., Wichmann, M. H., Fiedler, B., Bauhofer, W., & Schulte, K. (2005). Influence of nano-modification on the mechanical and electrical properties of conventional fibre-reinforced composites. *Composites Part A: Applied Science and Manufacturing*, 36(11), 1525–1535.
- Ladeveze, P., & Ledantec, E. (1992). Damage modelling of the elementary ply for laminated composites. *Composites Science and Technology*, 43(3), 257–267.
- Nemati Giv, A., Ayatollahi, M. R., Ghaffari, S. H., & Da Silva, L. F. (2018). Effect of reinforcements at different scales on mechanical properties of epoxy adhesives and adhesive joints: A review. *The Journal of Adhesion*, 94(13), 1082–1121.
- Thostenson, E. T., Li, C., & Chou, T.-W. (2005). Nanocomposites in context. *Composites Science and Technology*, 65(3–4), 491–516.
- Yıldırım, F., Ataberk, N., & Ekrem, M. (2020). Mechanical and thermal properties of a nanocomposite material which epoxy based and reinforced with polyvinyl alcohol nano fibers contained multiwalled carbon nanotube. *Journal of Composite Materials*, 55, 1339.
- Yılmaz, M. (2019). Low velocity impact behavior of nylon 6.6 nanofiber reinforced adhesives under different temperatures in adhesive joints of aluminium-carbon fiber reinforced composite sheets. In *The graduate school of natural and applied science* (p. 104). Necmettin Erbakan University.
- Zhao, L.-X., Zheng, L.-Y., & Zhao, S.-G. (2006). Tribological performance of nano-Al₂O₃ reinforced polyamide 6 composites. *Materials Letters*, 60(21–22), 2590–2593.

Determination of Optimum Mixing Parameter for Oil Flow Visualization



Aleyna Çolak, Mehmet Seyhan, and Mustafa Sarioğlu

Contents

| | | |
|---|------------------------------|----|
| 1 | Introduction | 17 |
| 2 | Experimental Setup | 19 |
| 3 | Results and Discussion | 20 |
| 4 | Conclusion | 21 |
| | References | 23 |

Nomenclature

| | |
|------------------|------------------|
| a | Amplitude, mm |
| Re | Reynolds number |
| TiO ₂ | Titanium dioxide |
| λ | Wavelength, mm |
| α | Angle of attack |

1 Introduction

Flow visualization has been crucial for flow analysis to understand and improve the flow characteristics particularly in complex, three-dimensional flows. Surface oil flow visualization is a relatively simple technique in which the surface of interest is covered with a thin layer of oil. The technique is easy to apply and inexpensive. When the wind tunnel is opened, the oil is carried by the airflow, and the dry pigment

A. Çolak · M. Seyhan (✉) · M. Sarioğlu
Department of Mechanical Engineering, Karadeniz Technical University, Trabzon, Türkiye
e-mail: aleyna.colak@ktu.edu.tr; mehmetseyhan@ktu.edu.tr; [sarioğlu@ktu.edu.tr](mailto:sarioглу@ktu.edu.tr)

remains on the surface. It creates a streaky pattern that indicates the flow direction and the separation or reattachment of the flow from the surface (Merzkrieh et al., 1987).

There is a lot of information and many different recipes on how to prepare an oil mixture for a particular test condition. The aim is to prepare an ideal mixture that has the appropriate combination of viscosity and surface tension. The oils generally used are kerosene, light diesel oil, and light transformer oil. The white powder-like titanium dioxide or china clay on a dark model and the black powder-like lampblack on a light model should be used that will provide a clear pattern on the model surface. The additives are used in some paints to control the size of the coagulating flocs. Oleic acid and linseed oil are widely used as they give ideal results in various paints. The mixtures and techniques have been detailed in the study of Maltby and Keating (1962).

Maltby and Keating (1962) point out the requirements for desired oil mixture. The paint should leave a pattern of pigment streaks and, at the same time, should provide good photographic quality. They agree that it is difficult to give a precise oil mixture, and trial and error methods are inevitable when using additives such as oleic acid and linseed oil. In facilities with short run times, a carrier that spreads and dries quickly, such as kerosene, should be preferred to prevent degradation of the pattern during the shutdown process. For longer duration facilities, more viscous liquids should be used (Lu, 2010).

In the literature, different oil mixtures were used to prepare a paint with consistency to leave pigment streaks indicating the flow direction. Bolzon et al. (2016) used two oil film mixtures to visualize the flow patterns and structures. The kerosene mixture consisted of kerosene, linseed oil, and talcum powder in a ratio of 5:2:1 and was designed as determining the streaklines on the models. The ethanol mixture consisting of ethanol and talcum powder in the ratio of 5:2 was used to visualize the surface shear stress patterns. Sudhakar et al. (2019) carried out a flow visualization by using a mixture of oleic acid, titanium dioxide powder, and SAE 60 grade vacuum pump oil based on a 1:5:7 ratio. Chen et al. (2012) carried out by using a mixture consisting of titanium dioxide, kerosene, and oleic acid with a ratio of 3:6:2. Various investigators have used fluorescent pigment to provide high contrast (McGranahan et al., 2003; Wei et al., 2019).

As mentioned above, there is no consensus on the mixing ratio and types of ingredients for surface oil flow visualization. In some studies, it is mentioned from an oil mixture without giving the ingredients and the mixing ratio. This study aims to determine the optimum oil mixture ratio that gives the best results. Also, it is noted that the purpose of this study is not to examine the effects of tubercles.

2 Experimental Setup

The oil flow visualization experiments were conducted in an open circuit wind tunnel with the test section dimensions of 570 mm \times 570 mm in the Mechanical Engineering Department of Karadeniz Technical University. The turbulence intensity of this wind tunnel was below 1%. Flow visualization experiments were conducted on an airfoil at 5°, 10°, 15°, and 20° angles of attacks. The wings mounted horizontally in the wind tunnel and end plates were used. The maximum misalignment error was $\pm 1^\circ$.

The airfoil model has a mean chord length of 150 mm and a spanwise length of 450 mm. The airfoil model is polished with sandpaper for a smooth surface and dyed matte black paint. Experiments were conducted on the suction side of the airfoil model, and the oil mixtures were applied to the surface with a paintbrush. While applying paint to the surface of the model may seem simple, care is needed to obtain the desired results. Maltby and Keating (1962) suggested that a proper coating can be produced if the brush moved in small circles instead of the traditional painting motion.

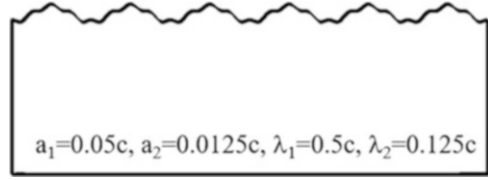
In order to determine the oil mixtures and ratios to be used in this study, the literature was examined, and similar ratios were selected. The oil mixture materials and ratios are presented in Table 1. Oil mixture A consists of titanium dioxide, kerosene, and oleic acid with a ratio of 3:6:1 instead of a ratio of 3:6:2 used in the study of Chen et al. (2012). Oil mixture B consists of titanium dioxide, kerosene, and linseed oil in the same ratio as oil mixture A. In order to examine the effect of oleic acid and linseed oil on the mixture, these mixtures were used with the same ratios. Oil mixture C consisted of kerosene, linseed oil, and talcum powder in the ratio of 5:1:3 instead of a ratio of 5:2:1 used by Bolzon et al. (2016). Oil mixture D consists of oleic acid, titanium dioxide powder, and SAE 20 motor oil based on a 1:5:7 ratio like the same ratio used by Sudhakar et al. (2019). Oil mixture E consists of ethanol and talcum powder in the ratio of 5:2 used by Bolzon et al. (2016). The purpose of using ethanol was to quicken the drying process. Since ethanol evaporates at the time the wind tunnel opened, it could not show the pattern on the model surface. Therefore, oil mixture E was not included in the Results and Discussion section.

The airfoil was created by using Eq. (1) where “ a ” refers to amplitude and “ λ ” refers to wavelength. The amplitude “ a ” refers to the half distance between a tubercle peak and trough. The wavelength “ λ ” refers to the distance from trough to trough or from peak to peak. The airfoil with leading-edge geometry was chosen to create “ a ”

Table 1 Oil mixture and ratios

| Oil mixture | No | Ratio |
|--|----|-------|
| Titanium dioxide (TiO ₂), kerosene, and oleic acid | A | 3:6:1 |
| Titanium dioxide (TiO ₂), kerosene, and linseed oil | B | 3:6:1 |
| Kerosene, linseed oil, talcum powder | C | 5:1:3 |
| Oleic acid, titanium dioxide (TiO ₂), and SAE 20 grade motor oil | D | 1:5:7 |
| Ethanol and talcum powder | E | 5:2 |

Fig. 1 The geometric details of wavy NACA 0020 airfoil



complex flow structure. In this study, the wavy model shown in Fig. 1 was utilized by using Eq. (1) which was first time proposed by Seyhan et al. (2021).

$$y_{LE} = a_1 \times \cos\left(\frac{2\pi x}{\lambda_1}\right) + a_2 \times \cos\left(\frac{2\pi x}{\lambda_2}\right) \quad (1)$$

3 Results and Discussion

In this study, flow visualization experiments are conducted at 5° , 10° , 15° , and 20° angles of attack on the NACA 0020 airfoil model using five different oil mixtures at a Reynolds number of 200,000. Oil mixtures A, B, and C were subjected to approximately 10 min, and oil mixture D was subjected to 20 min of a continuous wind tunnel. During this time, the oil moved in the direction of flow velocity dependent on boundary layer skin friction and surface tension of the oil. As a result, regions of flow will help to understand the mechanism of flow in the airfoil model.

Figure 2a shows the flow visualization on the upper surface of the airfoil for four different oil mixtures at the angle of attack of $\alpha = 5^\circ$ at $Re = 200,000$. The free stream flows from top to bottom. At the angle of attack of 5° , oil mixture A showed sharper transitions while oil mixture B of smoother transitions. Oil mixture C consisted of talcum powder insufficient to show the flow topology. Oil mixture D clearly showed the streamlines, the separation points, and the delta-shaped trailing edge flow separation.

Figure 2b shows the flow visualization on the upper surface of the airfoil for four different oil mixtures at an angle of attack of $\alpha = 10^\circ$. The leading-edge tubercles disturb the spanwise distribution of the flow field and create pairs of counter-rotating, streamwise vortices as shown in Fig. 2b. The delta-shape regions near the trailing edge formed at $\alpha = 10^\circ$ are greater than those formed at $\alpha = 5^\circ$. The delta-shape trailing edge flow separation was identified by Rostamzadeh et al. (2014) at pre-stall. At this angle, although the oil mixture C creates a streaky pattern as in other oil mixtures, the powder is insufficient to show the flow topology.

Figure 3a shows the flow visualization on the upper surface of the airfoil for four different oil mixtures at the angle of attack of $\alpha = 15^\circ$. At the angle of attack $\alpha = 15^\circ$, the airfoil model indicated the flow separation pattern known as the stall cell which is defined as a mushroom-like type of shape. The stall cell formation area formed at

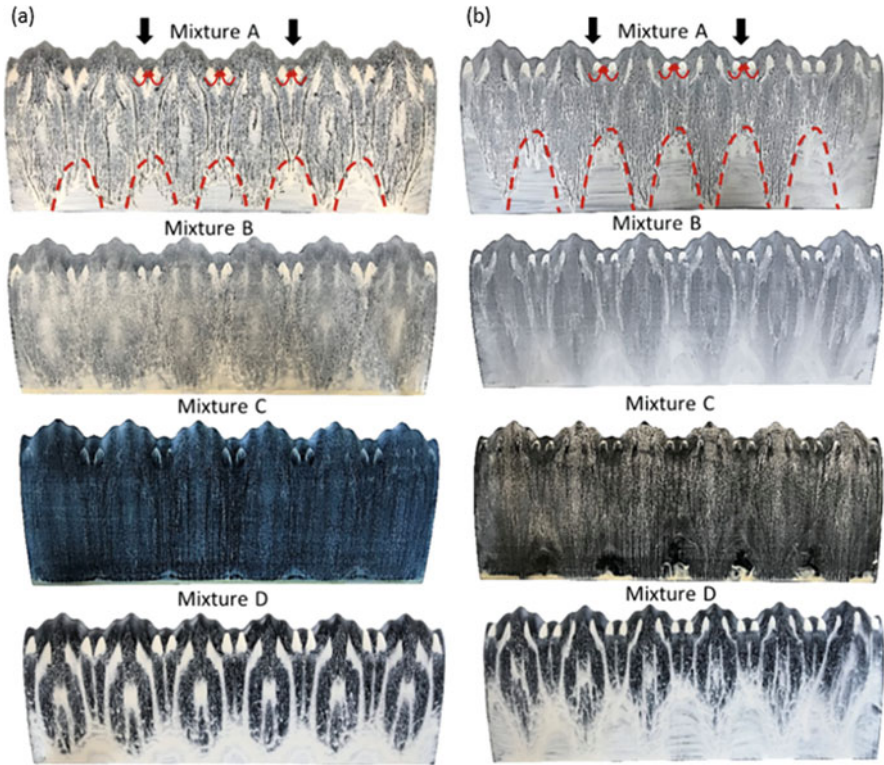


Fig. 2 Flow visualization of NACA 0020 for (a) $\alpha = 5^\circ$ and (b) $\alpha = 10^\circ$ at $Re = 200,000$

$\alpha = 15^\circ$ has greater than that formed at $\alpha = 20^\circ$. Figure 3(b) shows the flow visualization on the upper surface of the airfoil for four different oil mixtures at an angle of attack of $\alpha = 20^\circ$. The counter-rotating vortex pair formed between peaks can be seen in oil mixtures A and B. Although oil mixture C creates a streaky pattern as in the other oil mixtures and it is observed with the eyes, the powder is insufficient to show the flow topology.

4 Conclusion

In this study, a surface oil flow visualization was conducted on the leading tubercle NACA 0020 airfoil to find the optimum oil mixture. The experiments are conducted at 5° , 10° , 15° , and 20° angles of attack on the NACA 0020 airfoil model using five different oil mixtures at a Reynolds number of 200,000. After the tunnel stopped, the model in which the mixture of oil pigment was applied was taken out of the test section, and the pattern on the model surface was examined. The results obtained are listed below:

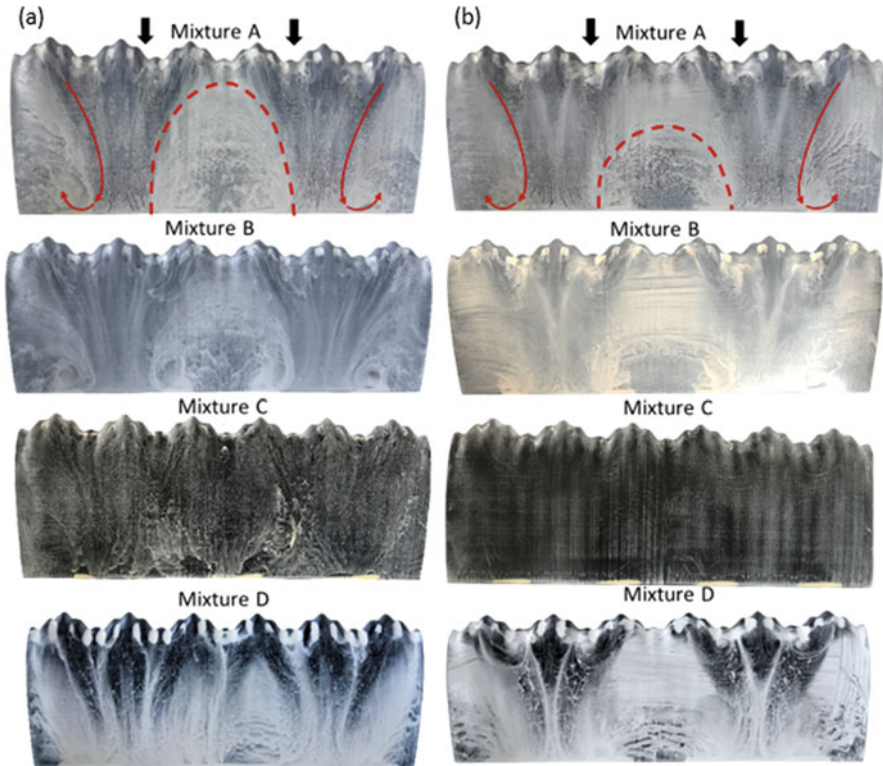


Fig. 3 Flow visualization of NACA 0020 for (a) $\alpha = 15^\circ$ and (b) $\alpha = 20^\circ$ at $Re = 200,000$

- The formation of streaks depends on the size of particles in the pigment. Additives are often used in the paint as a dispersing agent to control the size of the coagulation flocs. Oleic acid and linseed oil can be used as an additive. It is noted that they show changes in their chemical composition and oxidize when stored. As a result, it has been seen that the use of these additives requires trial and error methods.
- It has been seen that there is no definite mixing ratio, and the oil mixture can change according to the parameters of the flow.
- Some results could not be shown in the photographs as seen with the eyes. This problem can be overcome with modern digital imaging and image processing techniques.
- The purpose of using ethanol is to quicken the drying process, but ethanol evaporates when the wind tunnel is opened. Therefore, the flow structure could not be demonstrated using this ethanol mixture.
- More suitable results will be obtained if motor oil with high viscosity is used at high speeds. When linseed oil and oleic acid are compared, it is estimated that oleic acid will give ideal results at low speeds, and linseed oil will give ideal results at high speeds.

Acknowledgments The authors would like to acknowledge the financial support of this work by the Scientific and Technological Research Council of Turkey (TUBITAK) under contract number 118M592.

References

- Bolzon, M. D., Kelso, R. M., & Arjomandi, M. (2016). *Tubercles: A flow visualisation study*. Experimental Thermal and Fluid Science.
- Chen, J., Li, S., & Nguyen, V. T. (2012). *The effect of leading edge protuberances on the performance of small aspect ratio foils* (pp. 25–28). 15th International Symposium on Flow Visualization.
- Lu, F. K. (2010). Surface oil flow visualization. *European Physical Journal: Special Topics*, 182, 51–63.
- Maltby and Keating. (1962). *The surface oil flow technique for use in low speed wind tunnels* (p. 29). Flow Visualization In Wind Tunnels Using Indicators.
- McGranahan, B. D., & Selig, M. S. (2003). *Surface oil flow measurements on several airfoils at low Reynolds numbers*. 21st AIAA Applied Aerodynamics Conference.
- Merzkrieh, W., & Gersten, K. (1987). *Techniques of flow visualization*. AGARDograph No.302.
- Rostamzadeh, N., Hansen, K. L., Kelso, R. M., & Dally, B. B. (2014). The formation mechanism and impact of streamwise vortices on NACA 0021 airfoil's performance with undulating leading edge modification. *Physics of Fluids*, 26, 1–22.
- Seyhan, M., Sarioglu, M., & Akansu, Y. E. (2021). *Influence of Leading-Edge Tubercle with Amplitude Modulation on NACA 0015 Airfoil*. *AIAA Journal*, 59(10), 3965–3978.
- Sudhakar, S., Karthikeyan, N., & Suriyanarayanan, P. (2019). Experimental studies on the effect of leading-edge tubercles on laminar separation bubble. *AIAA Journal*, 57, 5197–5207.
- Wei, Z., Toh, J. W. A., Ibrahim, I. H., & Zhang, Y. (2019). Aerodynamic characteristics and surface flow structures of moderate aspect-ratio leading-edge tubercled wings. *European Journal of Mechanics, B/Fluids*, 75, 143–152.

An Assessment of Digitalization in Aircraft Maintenance



Kemal Ay and Ilkay Orhan

Contents

| | | |
|-----|--|----|
| 1 | Introduction | 26 |
| 2 | The Technologies Used During Maintenance | 27 |
| 3 | The Difficulties Encountered During Aircraft Maintenance | 27 |
| 4 | The Technological Innovations in Maintenance Operations | 29 |
| 4.1 | The Technological Evolution of Maintenance Documents | 30 |
| 4.2 | The Usage of Technology in Keeping Technical Records | 30 |
| 5 | Conclusion | 31 |
| | References | 32 |

Nomenclature

| | |
|-----|-----------------------------------|
| AML | Aircraft maintenance logbook |
| MRO | Maintenance, repair, and overhaul |
| R&D | Research and development |

K. Ay

Graduate School of Social Sciences, Anadolu University, Eskişehir, Türkiye
e-mail: kemalay@anadolu.edu.tr

I. Orhan (✉)

Graduate School of Social Sciences, Anadolu University, Eskişehir, Türkiye

Faculty of Aeronautics and Astronautics, Eskişehir Technical University, Eskişehir, Türkiye
e-mail: iorhan@eskisehir.edu.tr

1 Introduction

Maintenance and repair operations in aviation are vital for the timely and safe execution of the operation. No one will prefer to fly an aircraft that has deficiencies in maintenance or has malfunctioning systems. Before the aircraft is put on flight, it should be ensured that no condition will interfere with the flight in terms of maintenance and repair. However, no matter how careful you are, it is possible to encounter malfunctions at any time since the aircraft in question has moving parts consisting of electronic and mechanical systems. A problem to be encountered before the operation should be reported to the technical team for the solution, and the solution is expected to be provided as quickly as possible. The conditions for achieving this are possible with the healthy operation of the process. The problem needs to be solved simultaneously, such as the correct and complete reporting of the fault, the personnel having sufficient experience and knowledge, the fast and accurate demand for the needed materials, and the rapid access to the necessary documents and data. To have the required speed and accuracy, it is essential to benefit from today's technologies at the highest level possible.

Due to the complex structure of aviation, many departments have to work in harmony with each other. This requirement includes some threats to the airlines. A problem in a department will delay the whole process and cause extra costs to be billed to the airlines, depending on the scope of the situation. Even if there is no trouble in the relevant department itself, problems with communication may occur. A team that does not know when, where, and how it should be found will again disservice the flow of the process. So much so that even a mishap in the aircraft's parking position notification will cause delays.

Airlines have to constantly monitor and improve their operations to prevent or at least reduce risks. Some of these improvements should be in the form of ensuring effective communication between the departments and among themselves, creating fast and easy access to the necessary up-to-date documents, simultaneous and accurate sharing of the developed plans, and making use of technology at a high level. However, difficulties may be experienced in the integration of these innovations due to the high initial acquisition costs of these developed technologies or the difficulties of abandoning the traditional methods that have been used for a long time and adopted by the personnel.

The primary purpose of this study is to examine/research the extent to which the companies providing aircraft maintenance services in Turkey need technology and to what extent they can meet these needs. The study is limited to examining/researching the MRO providing aircraft maintenance services in hangar and line maintenance environments in Turkey and the technological possibilities they can use and use during their operations.

2 The Technologies Used During Maintenance

The technology used and its benefits to the aircraft maintenance processes were examined in the research conducted in one of the airlines providing MRO services in Turkey. In part of the airline concerned, technical personnel can instantly access the documents related to maintenance with a tablet when they need information (on the aircraft or in line maintenance). However, some of them access the required information and document if they go to the data center and use the computers. After accessing the needed data, technical personnel print them to use on aircraft. In addition, since the materials, components, and consumables to be used in maintenance are requested over the computer, it is impossible to monitor them instantly when they are transferred to the aircraft. Especially in base maintenance, the task transfer at the end of the shift is written on the maintenance cards and processed on the computer. This dual application causes severe loss of time and communication deficiencies in cases such as the technicians not providing enough detail while writing.

Since the maintenance package to be applied in the planned hangar maintenance is defined, and the malfunctions detected before the maintenance are planned and corrected until the maintenance exit, problems such as having a hard time related to task cards are not encountered in such maintenance. Using the processes more effectively and using the manpower more efficiently are essential and evaluated. However, the main problems are experienced in eliminating the problems of the aircraft that are prepared for or in operation. Unlike an aircraft maintained in the hangar or does not have a flight scheduled recently, every second is worth gold for a malfunction in an aircraft preparing for departure or having completed passenger pick-up and is waiting for departure. If such a situation cannot be eliminated, it may cause huge costs to the airlines and may cause severe damage to its brand value. Of course, malfunctions and problems are inherent in all moving vehicles such as aircraft, but in order to minimize such problems during operation, the maintenance and controls of the aircraft in the fleet should always be done meticulously, and the aircraft should be kept in a constantly airworthy condition.

3 The Difficulties Encountered During Aircraft Maintenance

The maintenance applied to the aircraft is divided into different categories according to the application times and dimensions. In the most basic sense, it is divided into line and base maintenance. Another method of distinction is planned and unplanned maintenance. Planned maintenance is classified as daily, weekly, A, B, C, and D (Bergh et al., 2013). The scope and timing of these maintenances are specific. On the other hand, failures that occur unexpectedly and need to be intervened are called unplanned maintenance. While the manufacturers publish the application forms, the

authorities inspect the requirements and intervals of these maintenance types, whether applied correctly and on time.

There are many difficulties in maintaining aircraft during operation. The most important of these is time pressure. There is usually not enough time to carry out repairs on an aircraft that has taken or will take its passengers. The maintenance process for a malfunction consists of several steps. These are detecting the malfunction, determining the necessary materials and requesting them from the relevant departments, troubleshooting, and verification test. Each of these is a process, and there is always the possibility that something could go wrong. In addition, the aircraft for which technical service is requested can be anywhere in the airport, and time is needed to reach it. In addition to the time required to reach the aircraft, delivering the aircraft to the flight on time and completing the maintenance procedure creates severe pressure. In such a difficult-to-manage environment, accessing documents or experiencing problems in supplying materials makes the process even more complex and reflects the business as time and economic costs.

On the other hand, in the base maintenance environment, the primary problem beyond time pressure is the follow-up of the works. The shift work system is generally adopted in maintenance operations, and in terms of continuity of work, task cards that cannot be completed during one shift should be transferred to the new team to ensure continuity. The deficiencies in the existing methods used in these processes can put the reliability of maintenance jobs at risk. Starting one step before the last action of the previous team brings extra cost by repeating the job, and starting one step later jeopardizes the maintenance and, accordingly, flight safety. In addition, real-time demand and tracking of materials and components demanded from different departments are a problem for MRO. It is seen that when the material cannot be tracked with a system where it is requested or coming, it is seen that the same material is asked for again and repeated orders are created, or due to the inability to monitor the inventory life, trying to bring an existing material from another location causes both time and money loss.

The biggest problems encountered during maintenance practices in aviation are experienced in the communication process and keeping records, whether in base or line maintenance. Since many departments are related to maintenance and the need to create documents about the maintenance performed in different areas, complex and risky processes may occur. Corrective actions applied to the aircraft and parts installed should be recorded following the rules, and even some of these actions should be reported to the authorities and manufacturers ([http – 1](#)). There are hefty penalties on operators and MRO companies for noncompliance with the rules. For this reason, having digital access to the platforms that different maintenance personnel may need within the scope of their authority and which they are responsible for recording, making maximum use of personnel, will contribute to the reliable recording of records and increase efficiency.

4 The Technological Innovations in Maintenance Operations

Since we are in the age of technology, digital solutions, which are being used extensively in all areas of life, are naturally also used in aircraft maintenance and are developed day by day. The innovation and digitalization goals of aircraft maintenance companies include real-time access to maintenance-related data from many points and minimizing the use of paper in maintenance processes. This is defined as “paperless maintenance,” that is, to transfer most of the processes to digital environments. These two processes, which are interconnected, can lead the industry in terms of optimization, traceability, and accessibility. Processing records on paper has many weaknesses for this industry, where speed and reliability must be high.

The information processed in a digital database can be viewed instantly by anyone with access permission. From a traceability point of view, data approaching specific values will trigger certain warnings, thanks to the ability to assign threshold values, allowing problems to be noticed before they occur. More extensive data can be stored in much smaller storage areas and transferred quickly and effectively between platforms. In addition, considering the positive effect of using less paper on our environment, it is seen that it will not be possible to stand in the way of this transformation. With this fact in mind and believing in the advantages of technology, certain MRO companies have created units that perform these tasks. With serious R&D investments, they try to gain commercial benefits by developing the software they produce both for use within their maintenance organization and in line with the needs of third-party companies. One of these companies is the MRO Lab unit ([http – 2](http://2)), created within Air France, which promises to combine paperless maintenance with business intelligence.

Should it be necessary to examine the benefits of digitalization on a few basic examples, the records of material warehouses have been added to the developed digital applications and started to be followed in real time. In this way, it is possible to instantly know which spare parts and how many are available in which warehouse. Even automatic warnings are provided when the specified critical values are lowered. In this way, situations such as human error or the inability to process data on time can be avoided. Material supply problems that may be encountered at critical moments may result in prolonged maintenance activities and increased costs.

Similarly, malfunctions that occur during the flight are written in the pilots’ flight log, and the maintenance personnel checks this book after the aircraft lands by visiting the aircraft. The corrective action is taken after the necessary preparations are completed by the maintenance team. As a result of this system, which is still used but behind the times, effective use of time is not possible, and delays may occur. However, the newly developed digital solutions created by the manufacturer can identify the faults and transfer them to the ground maintenance departments without putting a workload on the pilots. In this way, the maintenance team who is informed about the problem in advance can have the opportunity to complete the necessary

preliminary work and preparations until the plane lands. Thus, serious time savings can be achieved (Sun, 2009). The airlines and MRO centers should meticulously follow such innovations, and the rate of reliability and speed should be increased by including them in operations quickly.

4.1 The Technological Evolution of Maintenance Documents

The manufacturers publish basic reference maintenance manuals to carry out the maintenance activities of the aircraft. There are around seven maintenance manuals designed for different purposes on the aircraft (Kinnison, 2013). For example, the handbook used only for detecting and correcting faults is the fault-finding book. Another describes the maintenance practices, and another describes the wiring job. These handbooks are quite large and vary according to configuration differences even within the same aircraft type. However, malfunctions that the manufacturers cannot foresee can also be encountered in aircraft. If the maintenance team cannot find a solution to these malfunctions according to their own experience, they correct them by cooperating with the manufacturers.

For this reason, these documents are updated periodically by the manufacturers. When the Internet and computer were not widespread, these documents were used in print version, and with each update, the affected pages were changed by reprinting and updating these handbooks. This situation both made it difficult to follow up and increased the possibility of making mistakes. In addition, it was not easy to allocate so many pages to each staff member one by one and keep and use them by the staff.

Today, one of the benefits of the internet to the industry is the digitization of these documents. Manufacturers added all this data to their databases and provided access to the companies operating their aircraft. The companies have taken over the responsibility of following the revisions and corrections made due to this. In addition, the printed books, which are almost the weight of the aircraft, have disappeared, and all authorized maintenance personnel have the opportunity to access up-to-date documents from anywhere with the internet. This system, which is still not easy enough to access, has come a long way compared to its old version. Although there are still many issues that need to be corrected and improved, the spread of the Internet has brought great convenience for aviation in general. In the sector where numerous documents are used, transferring most data to digital databases has accelerated and eliminated unnecessary complexity.

4.2 The Usage of Technology in Keeping Technical Records

Aviatar, a digital solution application developed jointly by Lufthansa Technik and Honeywell companies, achieved commercial success and was sold to companies such as United Airlines, Wizz Air, and Sichuan Airlines and is actively used (Shukla

et al., 2020). The application promises to get rid of papers in general and provide more effective tracking and quick access thanks to the power of the digital world. Ultimately, since it is a software product, the application, which can be transformed to serve various purposes thanks to the updates created, provides simultaneous access from mobile devices for all authorized persons.

The starting point is to digitize the process as required by our age by eliminating the fault log in the aircraft's cockpit and the cumbersome structure it brings. The faults and information about the aircraft detected during the flight are written in the book called AML in the cockpit. This application is behind the times due to its negative aspects: it takes time to write in the flight log, the corrective action can confuse when mistakes are made, the possibility of a loss of the logbook, the need for technical personnel to come to the aircraft first to read the book and then prepare for maintenance. Created as an alternative to this application, Aviator allows authorized users to add/read data wherever and whenever they want. In addition, it offers a much more effective use thanks to its options such as application, filtering, and sorting, which prevent misunderstanding and confusion that may arise from deterioration of the paper structure or handwriting differences.

The application, which designed a different interface within the scope of the agreement with Sichuan Airlines, has been updated to monitor, analyze, and fleet optimization works of 168 v2500 and CFM56-5b engines used by the company in Airbus aircraft for 5 years. Data such as all performance values of engines, fault records, and flight hours are added to the application and are constantly monitored and controlled. As can be seen, this application, which can be redesigned for different purposes, both facilitates processes in various dimensions for its users and creates a commercial activity for its manufacturer (Meissner et al., 2019).

5 Conclusion

Digitization is undoubtedly a process that facilitates and accelerates all processes. Accessing many data with a single button gives confidence to the practitioner. However, one of the negative aspects of this is the overreliance on these applications and not paying enough attention to the processes to detect it anyway. Being aware of all the benefits of technology, maintenance personnel should make extensive use of them. But they must know that they are responsible for allocating flight safety by fully performing the necessary controls and monitoring. For this reason, in addition to the effective use of all the innovations and facilities provided, the person should also be aware that they are the most critical person to prevent problems that may arise from maintenance, with sufficient knowledge and skills.

References

- Bergh, J., De Bruecker, P., Beliën, J., & Peeters, J. (2013). *Aircraft maintenance operations: State of the art*. Faculteit Economie En Bedrijfswetenschappen, HUB Research Paper.
http-2: <https://www.afiklmem.com/en/the-mro-lab/digitalization>. Accessed on 15 May 2021
http-1: <https://www.easa.europa.eu/the-agency/faqs/occurrence-reporting>. Accessed on 15 Feb 2021
- Kinnison, H. A. (2013). *Aviation maintenance management*. McGraw-Hill Education.
- Meissner, R., Raschdorff, F., Meyer, H., & Schilling, T. (2019). *Digital transformation in maintenance on the example of a tire pressure indicating system* (pp. 1–10). 7th International Workshop on Aircraft System Technologies.
- Shukla, B., Fan, I. S., & Jennions, I. (2020). *Opportunities for explainable artificial intelligence in aerospace predictive maintenance*. In PHM Society European Conference, Vol. 5, No. 1.
- Sun, S. (2009). *ACARS data identification and application in aircraft maintenance*. IEEE Xplore.

Chip Breaking Applications and Chip Breaking Approach Using Variable Feed Rate in the Machining of Aviation Materials



Fatih Hayati Çakir

Contents

| | | |
|---|---------------------------|----|
| 1 | Introduction | 33 |
| 2 | Material and Method | 34 |
| 3 | Discussion | 36 |
| 4 | Conclusion | 37 |
| | References | 37 |

1 Introduction

Turning is one of the most basic and widely used machining methods. In the turning process, continuous chip formation can occur, especially in ductile materials. Continuous chip formation causes various problems. These include wrapping the chips around the workpiece, not being able to cool the cutting zone effectively, tool wear, and an increase in surface roughness (Stephenson & Agapiou, 2006). In order to prevent these situations from occurring, it is desirable to remove the chip from the cutting area periodically. The best method for the removal is the breaking of chips spontaneously. Among the main techniques applied for chip breaking are using high-pressure coolant, using chip breaker forms in cutting inserts, or physically removing the chips from the cutting area (Smith, 2008; Berglind & Ziegert, 2015). Although these methods are effective in some applications, they are generally insufficient in some cases due to additional cost or external hardware requirements and, in every case, not being a definitive solution. Especially low depth of cut and low feed rate magnitudes make it impossible to break chips in some cases. It has

F. H. Çakir (✉)

Eskisehir Vocational School, Eskisehir Osmangazi University, Eskisehir, Turkiye

e-mail: fcakir@ogu.edu.tr

been reported in the study that higher feed and depth of cut values are required for the chip breaking process as the cutting speed increases (Mesquita et al., 1996). The main reason for continuous chip formation is the continuous contact between the insert and the workpiece. Continuous contact causes the chips to elongate until it breaks spontaneously or due to external factors (Çakir & Çelik, 2017).

Chip breaking by using the variable feed and variable cutting speed is another way to control chips. In this application, preliminary trials are made to draw the depth of the cut and feed rate graph for determining the chip breaking zone, which is given as general information for a certain material and a specific tool. Although this graphic cutting tool is offered by manufacturers, it needs to be re-evaluated, especially for aerospace alloys.

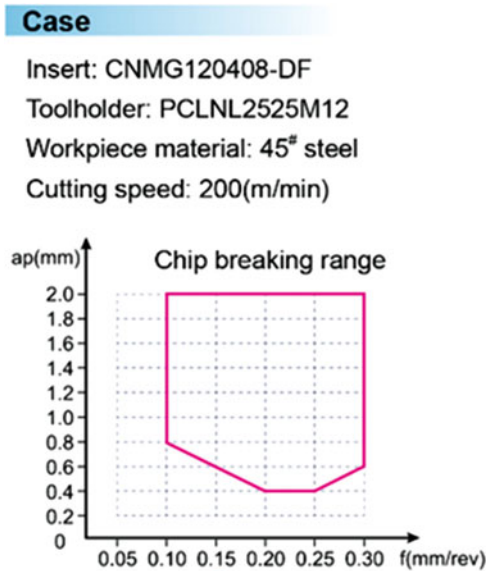
In this study, an approach that can be applied to conventional CNC-controlled turning lathes is proposed. This approach is basically based on increasing the feed rate at certain intervals in the process parameters for which chip breaking is viable. By developing CNC programs suitable for approach modeling, it is anticipated that controlled chip formation can be achieved without the need for external hardware with appropriate tools and equipment.

2 Material and Method

Continuous chip formation in machining is one of the important obstacles to unmanned production. Experimentally, different chip shapes are obtained by changing the feed and depth of cut values by making trials for a certain cutting value in a particular material. An example table is presented in Fig. 1. The presented data by the tool manufacturer is given for a general case material at a 200 m/min cutting speed. Machining parameters in which appropriate chip shapes can be obtained are added to the insert catalogs. These values are given as a feed rate and depth of cut chart for a specific cutting speed. The graphs help users to understand the chip breaking ability to cut insert and create a user-specific starting point.

In order to increase the chip, breaking zones tool manufacturers develop chip breaker forms. In this method, after the material is cut and chips begin to form, it is encouraged to rotate with a certain radius of curvature, and the bent chip is forced to make contact with the workpiece or cutting tool. As the chip flow continues, the newly formed chips force the previously formed chips and increase the effective strain. At the point where the effective strain is at its maximum, the brittle chip breaks due to the moment effect and the thermal overcooling. In order to achieve more effective chip breaking, the resulting chips must have limited flexibility. For thinner chips, the more flexible chips will not break; instead, they will bend. For example, the support effect that occurs in chips with a low feed value or pass value may cause the chip to wrap and wrap around the cutting area instead of breaking. This effect, which is theoretically planned, is effective, especially in alloys with low toughness and in alloys that become brittle due to the effect of high cooling rates, but it has less effect on alloys that have high toughness and do not lose their toughness

Fig. 1 Chip breaking zones for a cutting tool. (Toollink Co., Ltd. Chipbreaker, 2021)



due to the sudden cooling effect. It is known that chip breaker forms increase the cutting forces and increase the power requirement required for the cutting process (Lotfi et al., 2016). In addition, it has been reported by previous studies that tools that do not have any chip breaker form can effectively break chips if the correct cutting parameters are used (ÖZSOY, 2008). Figure 2 shows a numerical representation of a chip breaking with curvature the effect of the strain. A similar approach is presented in the literature (Deng et al., 2013).

The region required for chip breaking varies considerably according to the process parameters and the material used. As the cutting speed increases, the resulting chip temperature increases, and the hotter the chip shows more ductile characteristics. This situation causes the region required for chip breaking to shift to the right and upwards. In other words, higher feed rates and depth of cut values are required for chip breaking to take place. Although chip breaking is the desired situation, the required feed rate and depth of cut values in some cases may negatively affect the tool life, and it is not desired to work on these parameters for a long time (Słodki et al., 2015). In such cases, while cutting with the feed rate and depth of cut values that provide optimum cutting performance, the federate of the depth of cut can be increased to obtain chip breaking at an interval that is determined in order to prevent the chip length from exceeding a certain value, and chip breaking is provided in certain areas. In terms of application practice, control of the feed rate value is more likely than the depth of cut value in axial turning. Provided that the minimum depth of cut required for chip breaking is provided, certain cycles are created, and the feed rate value is increased to the value where chip breaking is possible, and when the chip breaking process is performed, the federate is lowered again, which is safer to

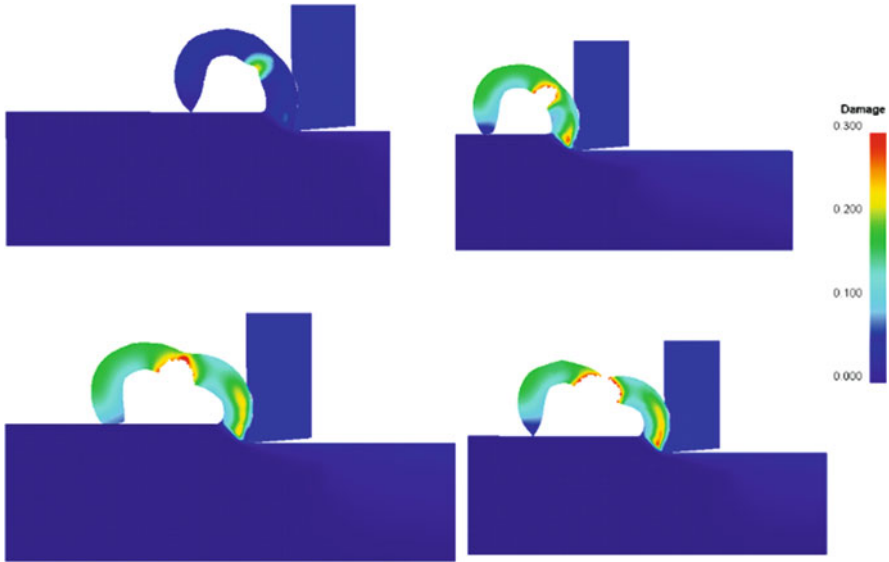


Fig. 2 Numerical representation of chip breaking process

work again. The frequency of the process and the change (amplitude) in the feed rate should be selected according to the application.

In a numerically controlled CNC program, the starting position coordinate and the end coordinate are usually defined. The advance movement between these coordinates is programmed as the feed rate value. In modern applications, such as conical cutting, the SFM value is defined in the CNC program in order to maintain the cutting speed, and the value that the spindle needs to rotate instantly is calculated and applied by the machine control system. The method suggested in this study is to provide a partial chip breaking process in areas where the feed rate is increased in places in continuous cutting processes, and thus it is possible to control the amount of chips accumulated in the cutting process. Figure 3 shows the proposed approach. The approach is increasing the feed periodically to enter the chip breaking zone and lowering again to minimize the effect of using excessive cutting parameters.

3 Discussion

Since the proposed method has the possibility of damaging the surface roughness to a certain extent, it should be analyzed well before its use in finishing turning processes. In addition, since the primary purpose of the final turning process is to achieve the desired size, the worked pass values will be relatively lower, which may mean that although the feed rate is increased, chip breakage will not result. In addition, the radius of curvature created by the chip breaker form and the support

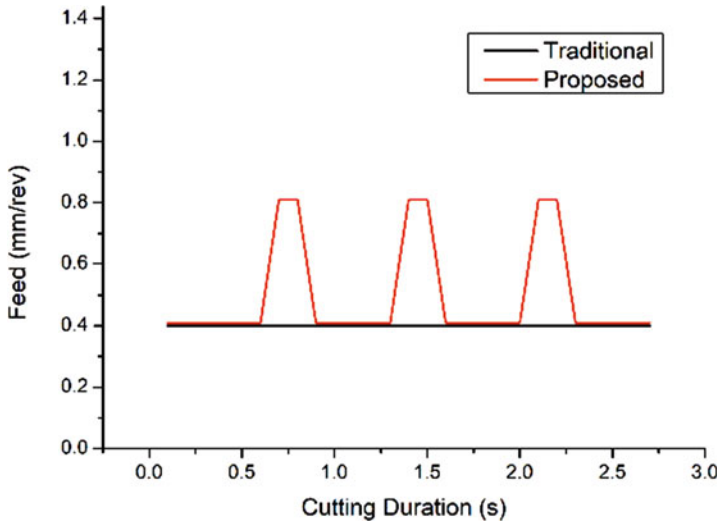


Fig. 3 Proposed feed rate for chip breaking

of the chips by hitting the material or the tool may not always work as planned, so even if the recommended method is applied, the chip formation should be carefully observed.

4 Conclusion

It is possible to obtain more controlled chips by using the method suggested in this study for chip breaking in machining. The proposed method and methodology are given considering the turning process. According to the application practice, it is suggested to apply a partial increase of the feed and depth of cut respectively in axial and face turning. Chip management is a problem encountered in many different applications of machining. With the method suggested in this study, it has been shown that the chip breaking process can be an effective tool in preventing the formation of piles of chips without the need for external equipment or specialized tools. It is thought that this approach can be adapted to CNC programming techniques and turned into a routine CAM process, and fragmented chip formation can be achieved in a controlled and continuous manner.

References

- Berglind, L., & Ziegert, J. (2015). Modulated tool path (MTP) machining for threading applications. *Procedia Manufacturing*, 1, 546–555. <https://doi.org/10.1016/j.promfg.2015.09.029>

- Çakır, F. H., & Çelik, O. N. (2017). *A new approach to chip breaking application in turning operation using variable feed rates* (pp. 188–196). Cumhuriyet Science Journal. <https://doi.org/10.17776/csj.363671>
- Deng, W. J., Xie, Z. C., Li, Q., & Lin, P. (2013). Finite element modelling and simulation of chip breaking with grooved tool. *International Journal of Simulation Modelling*, 12(4), 264–275. [https://doi.org/10.2507/IJSIMM12\(4\)5.250](https://doi.org/10.2507/IJSIMM12(4)5.250)
- Lotfi, M., Farid, A. A., & Soleimanimehr, H. (2016). A new hybrid model based on the radius ratio for prediction of effective cutting limit of chip breakers. *Proceedings of the Institution of Mechanical Engineers, Part B: Journal of Engineering Manufacture*, 230(8), 1417–1427. <https://doi.org/10.1177/0954405415586549>
- Mesquita, R. M. D., Soares, F. A. M., & Barata Marques, M. J. M. (1996). An experimental study of the effect of cutting speed on chip breaking. *Journal of Materials Processing Technology*, 56(1–4), 313–320. [https://doi.org/10.1016/0924-0136\(95\)01845-X](https://doi.org/10.1016/0924-0136(95)01845-X)
- ÖZSOY, Y. (2008). *Değişken İlerlemeli Tornalamada Talaş Kırılması ve Yüzey pürüzlülüğünün İncelenmesi*. Yıldız Teknik Üniversitesi.
- Słodki, B., Zębala, W., & Struzikiewicz, G. (2015). Correlation between cutting data selection and chip form in stainless steel turning. *Machining Science and Technology*, 19(2), 217–235. <https://doi.org/10.1080/10910344.2015.1018530>
- Smith, G. T. (2008). *Cutting tool technology: Industrial handbook*. Springer.
- Stephenson, D. A., & Agapiou, J. S. (2006). *Metal cutting theory and practice* (2nd ed.). Manufacturing Engineering and Materials Processing 68. CRC Taylor & Francis.
- Toollink Co., Ltd. Chipbreaker: Toollink Co., Ltd. (2021). <https://www.toollink.co.th/index.php/product/turning/guide-to-select-turning-tools/chipbreaker/>. Accessed 25 May 2021

SVD-Aided EKF for Nanosatellite Attitude Estimation Based on Kinematic Relations



Demet Cilden-Guler and Chingiz Hajiyev

Contents

| | | |
|---|----------------------------|----|
| 1 | Introduction | 39 |
| 2 | Mathematical Models | 40 |
| 3 | SVD Method | 42 |
| 4 | SVD-Aided EKF Method | 42 |
| 5 | Analysis and Results | 45 |
| 6 | Conclusions | 47 |
| | References | 47 |

1 Introduction

Satellite's orientation can be estimated by filtering techniques using measurements in body coordinates and reference observations. In most of the studies, the Kalman filter is proposed to be used for estimating the attitude of the satellites since it was proposed in (Lefferts et al., 1982). The dynamics of the rotational motion of the satellites is nonlinear so as to many other real-world systems. To overcome this problem, the extended Kalman filter (EKF) was proposed and used in place of linear Kalman filter to estimate the behavior of the satellite (Markley et al., 2005). Traditional approaches for satellite's attitude angles and angular rate estimation in Kalman filter design use nonlinear vector measurements since the mathematical models of the measurements are based on nonlinear models. In the linear

D. Cilden-Guler (✉) · C. Hajiyev
Faculty of Aeronautics and Astronautics, Istanbul Technical University, Istanbul, Turkiye
e-mail: cilden@itu.edu.tr; cingiz@itu.edu.tr

measurement-based approach, the attitude angles are determined by the single-frame attitude determination method (Wertz, 2002) which is based on the vector observations at each step. In literature, the SVD method is found an efficient single-frame method as it is faster than the q-method and more robust than other faster methods, such as FOAM and ESOQ (Cilden-Guler et al., 2017; Markley & Mortari, 2000; Vinther et al., 2011). Depending on the name of the single-frame method, the filter can be called a single-frame method-aided filter. The attitude angles determined by the single-frame method are used directly as measurements in the Kalman filter. Having the state measurements directly from SVD makes the model linear. The integration of the SVD supplying the linear measurements based on the vector observations with EKF is presented in (Hajiyev & Bahar, 2002, 2003; Hajiyev & Cilden, 2016) for the attitude and rate estimation purposes.

In order to model the satellite's rotational motion in the filter, the kinematics and a dynamics model can be combined. Yet, the dynamics model has inherent errors, e.g., the inertia matrix may not be well known (Crassidis et al., 2007). Therefore, kinematics model only algorithms which do not include any uncertainties.

The noisy measurements can be filtered by combining the measurements with related models. Kinematics model can be propagated using rate-integrating gyros for this purpose. There is only one problem here that might affect the estimation accuracy which is the drift on the gyros over time. In order to correct the measurements, three more terms related to gyro bias are added to the state vector for estimating them.

This chapter is organized as follows. The next section describes the mathematical model of the satellite's rotational motion. The following sections present SVD and SVD-aided EKF methods and give details about them. Simulations and results are analyzed next and finally, this chapter is concluded and summarized.

2 Mathematical Models

Kinematic equations can be derived using Euler's angles (yaw, pitch, and roll respectively) as

$$\begin{bmatrix} \dot{\phi} \\ \dot{\theta} \\ \dot{\psi} \end{bmatrix} = \begin{bmatrix} 1 & s(\phi)t(\theta) & c(\phi)t(\theta) \\ 0 & c(\phi) & -s(\phi) \\ 0 & s(\phi)/c(\theta) & c(\phi)/c(\theta) \end{bmatrix} \begin{bmatrix} p \\ q \\ r \end{bmatrix}, \quad (1)$$

where $c(\cdot)$, $s(\cdot)$, and $t(\cdot)$ are cosine, sine, and tangent functions, respectively, and p , q , r are the components of the $\bar{\omega}_{BR}$ vector of the body frame with respect to the reference frame. The transformation matrix from reference (orbit) to body coordinates can be used as,

$$A = \begin{bmatrix} c(\theta)c(\psi) & c(\theta)s(\psi) & -s(\theta) \\ -c(\phi)s(\psi) + s(\phi)s(\theta)c(\psi) & c(\phi)c(\psi) + s(\phi)s(\theta)s(\psi) & s(\phi)c(\theta) \\ s(\phi)s(\psi) + c(\phi)s(\theta)c(\psi) & -s(\phi)c(\psi) + c(\phi)s(\theta)s(\psi) & c(\phi)c(\theta) \end{bmatrix} \quad (2)$$

The transformation in the angular velocities can be achieved by using the relationship between $\bar{\omega}_{BI}$ and $\bar{\omega}_{BR}$,

$$\bar{\omega}_{BR} = \bar{\omega}_{BI} - A \begin{bmatrix} 0 \\ -\omega_o \\ 0 \end{bmatrix} \quad (3)$$

where ω_o orbital angular velocity of $\omega_o = (\mu/r_0^3)^{1/2}$. The rate gyro measurements can be modeled as

$$\omega_{BI_m}(k) = \omega_{BI}(k) + \eta_g(k) + b_g(k) \quad (4)$$

where $\omega_{BI} = [\omega_x, \omega_y, \omega_z]^T$ is the angular velocity vector of the body frame with respect to the inertial frame, b_g is the gyro bias vector, and η_g is the zero mean white noise with normal distribution with the characteristic of

$$E[\eta_{gk}\eta_{gj}^T] = I_{3 \times 3}\sigma_g^2\delta_{kj}, \quad (5)$$

where $E[\cdot]$ is the statistical averaging operator, δ_{kj} is the Kronecker delta function, and σ_g is the standard deviation of rate gyro error. The characteristic of gyro biases $b_g = [b_{g_x} \ b_{g_y} \ b_{g_z}]^T$ is given as

$$b_g(k+1) = b_g(k) + \eta_2 \times \Delta t \quad (6)$$

where η_2 is the zero mean white noise with normal distribution with the characteristic of

$$E[\eta_{2k}\eta_{2j}^T] = I_{3 \times 3}\sigma_{gb}^2\delta_{kj}, \quad (7)$$

where σ_{gb} is the standard deviation of gyro biases.

3 SVD Method

Attitude angles can be determined using two or more vectors by using a single-frame method minimizing Wahba's loss function in (9). We used Singular value decomposition (SVD) (Markley & Mortari, 2000). The loss is caused by the difference of the measurements from the corresponding reference models.

$$L(A) = \frac{1}{2} \sum_i a_i |b_i - Ar_i|^2 \quad (8)$$

$$B = \sum a_i b_i r_i^T \quad (9)$$

$$L(A) = \sum a_i - tr(AB^T) \quad (10)$$

where b_i is the measurement vector, r_i is the reference vector, and a_i is the nonnegative weight.

$$B = USV^T = U \text{diag}([S_{11} \ S_{22} \ S_{33}])V^T \quad (11)$$

$$A_{opt} = U \text{diag}[1 \ 1 \ \det(U)\det(V)]V^T \quad (12)$$

The U and V matrices are left and right orthogonal matrices defined in SVD. They express the B matrix with primary singular values (S_{11} , S_{22} , S_{33}). The Euler angle measurements can be obtained using the attitude matrix A_{opt} . The covariance matrix of the attitude angle estimation errors (P_{SVD}) is

$$P_{SVD} = U \text{diag}[(s_2 + s_3)^{-1} \ (s_3 + s_1)^{-1} \ (s_1 + s_2)^{-1}]U^T \quad (13)$$

where

$$s_1 = S_{11} \ s_2 = S_{22} \ s_3 = \det(U)\det(V)S_{33}$$

4 SVD-Aided EKF Method

The kinematics model of the satellite can be expressed as

$$x(k) = f[x(k-1)] + G(k, k-1)w(k-1) \quad (14)$$

$$Z(k) = Hx(k) + b(k) + v(k) \quad (15)$$

where $x(k)$ is the state vector, $f[\cdot]$ is the nonlinear system function, $G(k, k-1)$ is the system noise transition matrix, $w(k-1)$ is the system noise, $Z(k)$ is the measurement vector, H is the measurement matrix, $b(k)$ is the measurement bias, and $v(k)$ is the measurement noise. The process and measurement noises, $w(k)$ and $v(k)$, are normally distributed white noises. Their expected values are

$$\begin{aligned} E[w(k)] &= 0; E[w(k)w^T(j)] = Q(k)\delta(kj); E[v(k)] = 0; \\ E[v(k)v^T(j)] &= R(k)\delta(kj); E[w(k)v^T(j)] = 0. \end{aligned} \quad (16)$$

Rotational motion parameters can be estimated by using the following steps in the nontraditional extended Kalman filter (SVD-aided EKF).

The covariance matrix of the extrapolation error

$$\begin{aligned} P(k/k-1) &= \frac{\partial f[\hat{x}(k-1)]}{\partial \hat{x}(k-1)} P(k-1/k-1) \times \frac{\partial f^T[\hat{x}(k-1)]}{\partial \hat{x}(k-1)} \\ &\quad + G(k, k-1)Q(k-1)G^T(k, k-1) \end{aligned} \quad (17)$$

The covariance of the estimation error

$$P(k/k) = [I - K(k)H]P(k/k-1) \quad (18)$$

Gain of the EKF

$$K(k) = P(k/k-1)H^T [HP(k/k-1)H^T + R(k-1)]^{-1} \quad (19)$$

Innovation sequence

$$e(k/k-1) = Z(k) - H\hat{x}(k/k-1) \quad (20)$$

Extrapolation equation

$$\hat{x}(k/k-1) = f[\hat{x}(k-1/k-1)] \quad (21)$$

The estimated vector $\hat{x}(k/k)$ is found as

$$\hat{x}(k/k) = \hat{x}(k/k-1) + K(k)e(k/k-1) \quad (22)$$

Q is the covariance matrix of the process noise. R is the covariance matrix of the measurement noise and calculated by SVD as $R = P_{SVD}$ in each step because they both are the measurement error covariance matrices of the attitude angles. As the measurement covariance adapts itself by using the information from the SVD, the integrated filter becomes adaptive. By having an adaptive structure, SVD-aided EKF

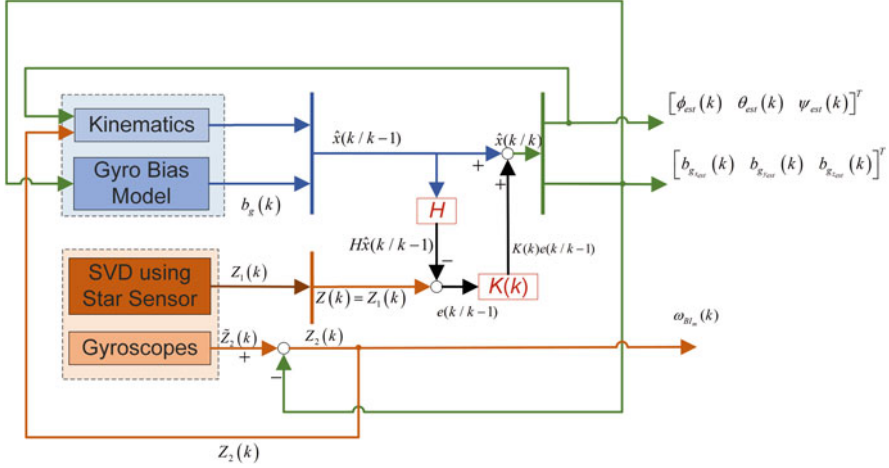


Fig. 1 Algorithm structure as a block diagram

can estimate a satellite's rotational motion parameters around the satellite's mass center.

Gyroscopes and star trackers are used as the attitude and rate sensors in this chapter. At least two vectors are measured by the star trackers, and by using those vectors in the SVD sub-step, attitude angle measurements are obtained.

The measurements can be presented as

$$\begin{aligned}
 Z_\phi(k) &= \phi(k) + v_\phi(k) \\
 Z_\theta(k) &= \theta(k) + v_\theta(k) \\
 Z_\psi(k) &= \psi(k) + v_\psi(k)
 \end{aligned} \tag{23}$$

where $Z_\phi(k)$, $Z_\theta(k)$, $Z_\psi(k)$ represent the attitude angle measurements determined by SVD method and $v_{(\cdot)}(k)$ is the measurement noises of the attitude angles. We can call the SVD measurements as $Z_1(k) = [Z_\phi(k) \ Z_\theta(k) \ Z_\psi(k)]^T$. The gyro measurements described in (4) can be expressed as $Z_2(k) = \omega_{BI_m}(k)$.

Only using the kinematics, $Z(k) = Z_1(k)$, equality is used for the measurements in the filter. This means that the measurement input vector is composed of the attitude measurements from SVD. Here, $Z_1(k)$ represents the measurements from SVD using the star tracker vector measurements, while $Z_2(k)$ represents the bias-eliminated angular velocity measurements from gyroscopes as $Z_2(k) = \tilde{Z}_2(k) - b_{g_{est}}(k-1)$ where $b_{g_{est}}(k-1)$ is the estimated gyro bias vector by the filter. The augmented state vector is

$$x(k) = [\phi(k) \quad \theta(k) \quad \psi(k) \quad b_{g_x}(k) \quad b_{g_y}(k) \quad b_{g_z}(k)]^T \quad (24)$$

The structure of the whole algorithm using the kinematics model is given in Fig. 1. As seen, the biases of the gyroscope measurements are filtered out by using the SVD-aided EKF estimations. Then, the gyroscope measurements are fed back to the kinematics model.

5 Analysis and Results

In this chapter, we considered a nanosatellite with a mass moment of inertia $J = \text{diag}([2.1 \times 10^{-3} \quad 2.0 \times 10^{-3} \quad 1.9 \times 10^{-3}]) \text{ kg}\cdot\text{m}^2$ having a star tracker and gyroscope as attitude and rate sensors. The parameters belonging to SVD-aided EKF are listed in Table 1. The states of the process are estimated without using the dynamics of the satellite's rotational motion in the filter for the system model. The mechanism updates the kinematics using the bias-eliminated gyro measurements directly (without using the dynamics). Defined vectors in (8) are implemented as b_i measurement vector which is from the star tracker outputs, r_i reference vector which is from the star catalog, and a_i nonnegative weight which is the inverse variance of the star trackers.

Figure 2 represents the estimations (a) and absolute errors of the attitude estimations (b) using star sensors on each axis. We can see from the figure that the orders of the absolute errors are around 1 arc seconds. Figure 3 shows the gyro bias estimation errors in time. The order of the errors is about 0.002 degrees per sec. Five simulations are performed for normalized root mean square error (NRMSE) and given as percentages in Table 2 for roll, pitch, yaw angles, and gyro biases about each axis. It is concluded that SVD-aided EKF can estimate the attitude angles and the bias of the gyroscopes by using only the kinematics relations.

Table 1 SVD-aided EKF parameters

| | |
|---|---|
| Initial covariance matrix of the estimation error | $P = 0.001I_{6 \times 6}$ |
| Transition matrix of the system noise | $G = I_{6 \times 6}$ |
| Covariance matrix of the system noise | $Q = 0.001I_{6 \times 6}$ |
| Measurement matrix | $H = \begin{bmatrix} 1 & 0 & 0 & 0 & 0 & 0 \\ 0 & 1 & 0 & 0 & 0 & 0 \\ 0 & 0 & 1 & 0 & 0 & 0 \end{bmatrix}$ |

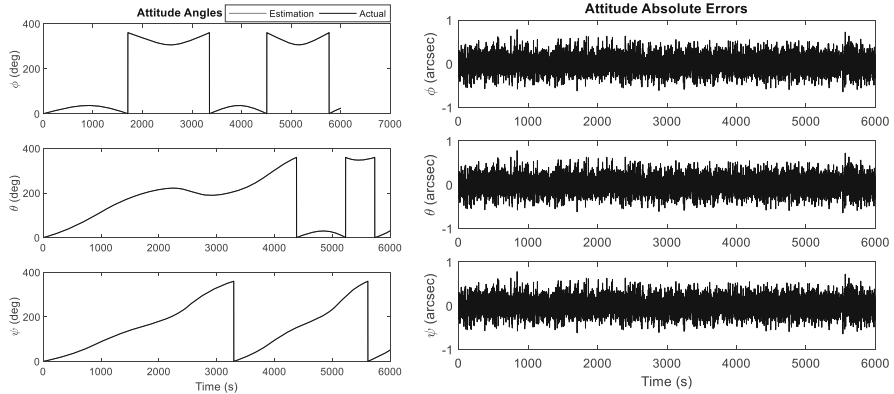


Fig. 2 Estimation (left) and estimation errors (right) of the attitude angles by the SVD-aided EKF method

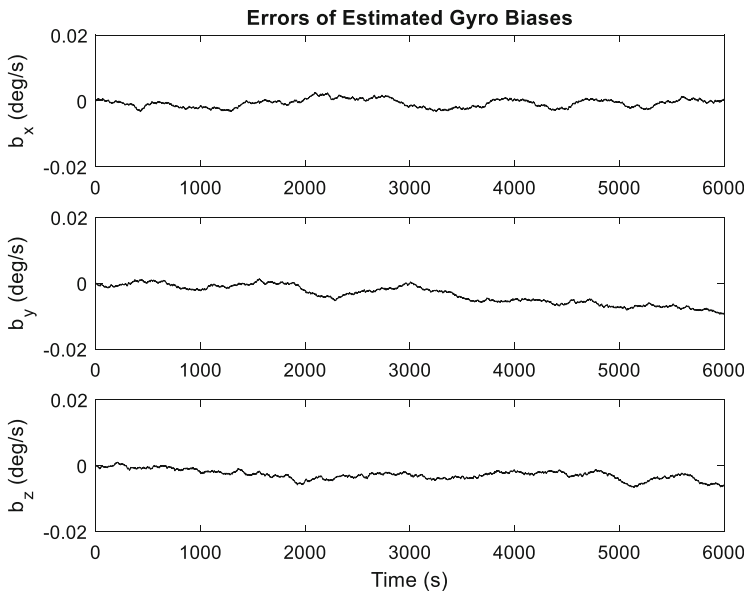


Fig. 3 Estimation errors of the gyroscope biases by SVD-aided EKF method

Table 2 NRMSE of estimations (five runs)

| NRMSE (%) | |
|-----------|--------|
| Roll | 0.0547 |
| Pitch | 0.0489 |
| Yaw | 0.0430 |
| b_x | 4.1268 |
| b_y | 1.1021 |
| b_z | 1.2511 |

6 Conclusions

In this chapter, a single-frame method-aided filter is presented to be used with only the kinematics model and not including the dynamics of a nanosatellite. Two types of sensors are placed on board as attitude and rate sensors, which are star trackers and gyroscopes. Using the star tracker measurements, attitude angles are determined by the SVD and used as input measurements in the presented filter called SVD-aided EKF. Attitude angles and the biases of the gyroscope are estimated by the presented filter. The estimated gyro biases are filtered out from the gyro measurements. After this procedure, the bias-eliminated gyro measurements are fed back to the kinematics model which is also used in the SVD-aided EKF. The whole algorithm runs recursively, and the demonstrations show that the filter estimates the attitude angles and gyro biases with high accuracy.

In further studies, it is aimed to compare the estimation accuracy of the filter using only kinematics and the filter using both the kinematics and dynamics model of the satellite under uncertainties. UKF can be used in order to compare their results with EKF in further studies.

References

- Cilden-Guler, D., Conguroglu, E. S., & Hajiyev, C. (2017). Single-frame attitude determination methods for nanosatellites. *Metrology and Measurement Systems*, 24, 313–324. <https://doi.org/10.1515/mms-2017-0023>
- Crassidis, J. L., Markley, F. L., & Cheng, Y. (2007). Survey of nonlinear attitude estimation methods. *Journal of Guidance, Control, and Dynamics*, 30, 12–28. <https://doi.org/10.2514/1.22452>
- Hajiyev, C., & Bahar, M. (2002). Increase of accuracy of the small satellite attitude determination using redundancy techniques. *Acta Astronautica*, 50, 673–679. [https://doi.org/10.1016/s0094-5765\(01\)00222-3](https://doi.org/10.1016/s0094-5765(01)00222-3)
- Hajiyev, C., & Bahar, M. (2003). Attitude determination and control system design of the ITU-UUBF LEO1 satellite. *Acta Astronautica*, 52, 493–499. [https://doi.org/10.1016/S0094-5765\(02\)00192-3](https://doi.org/10.1016/S0094-5765(02)00192-3)
- Hajiyev, C., & Cilden, D. (2016). Nontraditional approach to satellite attitude estimation. *International Journal of Robotics and Control Systems*, 1, 19–28.
- Lefferts, E. J., Markley, F. L., & Shuster, M. D. (1982). Kalman filtering for spacecraft attitude estimation. *Journal of Guidance, Control, and Dynamics*, 5, 417–429.
- Markley, F. L., & Mortari, D. (2000). Quaternion attitude estimation using vector observations. *The Journal of the Astronautical Sciences*, 48, 359–380.
- Markley, F. L., Crassidis, J. L., & Cheng, Y. (2005). *Nonlinear attitude filtering methods*. AIAA Guidance, Navigation, and Control Conference and Exhibit.
- Vinther, K., Jensen, K. F., Larsen, J. A., & Wisniewski, R. (2011). Inexpensive Cubesat Attitude Estimation Using Quaternions And Unscented Kalman Filtering. *Automatic Control in Aerospace*, 4.
- Wertz, J. R. (2002). *Spacecraft attitude determination and control, astrophysics and space science library*. D.Reidel Publishing Company.

Developing New Concepts for the Integration of Drones into the General Air Transport Management and Urban Transport



Dung D. Nguyen, Utku Kale, and Dániel Rohács

Contents

| | | |
|-----|--|----|
| 1 | Introduction | 50 |
| 2 | Operational Concept | 52 |
| 3 | Airway Network | 54 |
| 3.1 | Typical Elements | 54 |
| 3.2 | Safety Rules Applied to the Definition Airways | 56 |
| 3.3 | Safe Airspace and Airway Network Design | 58 |
| 4 | Conclusion | 58 |
| | References | 59 |

Nomenclature

| | |
|---------|--------------------------------|
| UAV/UAS | Unmanned aerial vehicle/system |
| ATM | Air traffic management |
| GPS | Global positioning system |

D. D. Nguyen (✉)

Department of Aeronautics and Naval Architecture, Budapest University of Technology and Economics, Budapest, Hungary

Department of Aircraft System Design, Faculty of Aerospace Engineering, Le Quy Don Technical University, Hanoi, Vietnam

e-mail: ddnguyen@vrht.bme.hu; dungnd@lqdtu.edu.vn

U. Kale · D. Rohács

Department of Aeronautics and Naval Architecture, Budapest University of Technology and Economics, Budapest, Hungary

e-mail: drohacs@vrht.bme.hu

Greek Letters

Δv speed, m/s

1 Introduction

Recently, science and technology are ready to develop and produce an extensive series of low-cost small remotely controlled or autonomous air vehicles as drones (generally unmanned aerial vehicles/systems – UAV, UAS, including even small pilot-less air vehicles, air taxis). The market of their civil application generated by the economy and social needs is rapidly growing. On the other hand, a severe problem blocks the rapid introduction of drones in city operations and smart city transportation. The existing air traffic management system (ATM) cannot control the predicted amount of drones operated at low altitude in the urban area between large buildings and complex environment (with, e.g., reflection), due to, e.g., (i) the limitations in the system capacity, (ii) the required workforce, (iii) the expected cost, and (iv) the required duration of the system development.

Concerning the management system, given the anticipated large amounts of drones and widely varying performance characteristics, it is far beyond the capabilities of conventional air traffic management (ATM) systems to deliver services for drones in a cost-effective manner. Traditional ATM framework is mainly established for human-crewed aircraft, while the absence of a pilot on board will pose a unique set of management issues not seen in human-crewed aircraft operations, such as avoidance collision, tracking trajectories, path planning, communication, and control. Hence, integrating drones into smart city transportation is an essential task, which requires innovative, highly automated, autonomous solutions. Numerous universities, research institutions, high-level groups, policymakers, and megaprojects deal with developing rules and methods that could support the integration of drones in air traffic management systems (EASA, 2015; EUROCONTROL, 2018; SEAR, 2020).

It seems that the most promising solutions for urban air transport management must use specially structured airspaces with predefined fixed routes or fixed corridors (Fig. 1) following the Singapore recommendation (Pathiyil et al., 2016). Here corridors mean multilane “highway” channel routes.

The Department of Aeronautics and Naval Architecture at the Budapest University of Technology and Economics has extensive practice in developing new operational concepts as (Jankovics & Kale, 2018; Rohacs & Rohacs, 2016) the integration of drones in smart city transportation systems (Nguyen, 2021; Nguyen et al., 2020; Nguyen & Nguyen, 2021).

Figure 2 shows the developed cockpit tool to support the EU-supported so-called Gabriel concept (magnetic levitation assisted take-off and landing concept of an undercarriage-less aircraft), the primary flight data, recommended flight tunnel, and side wing profiles being displayed.



Fig. 1 Recommended concepts

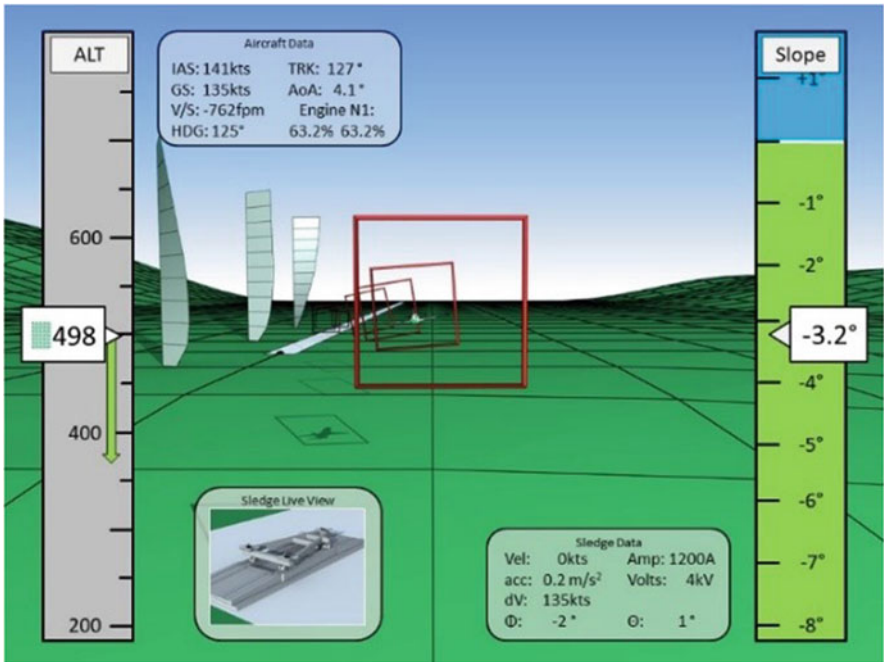


Fig. 2 Development of cockpit tools to support precision landing

In principle, the goal of safely managed UAV traffic is subject to a combination of essential services and control procedures. Thus, this chapter's motivation is to assist in the development and management of UAV operations for civil use, especially for larger drones operated at low levels.

This chapter investigates the possible integration of drones in the smart city transportation system. The proposed idea is based on the "road network" defined in 3D airspace. The drone's airway system might be constructed with typical, standard elements.

2 Operational Concept

The operational concept describes the use of the given instrument, device, or machine (here drone) by targeted users (IEEE, 1998; Cloutier et al., 2009). In drone applications, the users are the operators. In this chapter, the general objective of using drones is to diversify air freight transportation, which includes the collection and final distribution of small packages directly from senders to recipients, covering thus flights in urban areas.

Drones fly by following a predefined trajectory or corridor (Fig. 1). Each drone flies on its trajectory that might be part or follow the generally predefined trajectories with, for example, changing "lanes," heading, altitude, or speed. Drones can never meet other drones and drones moving in the opposite directions on their trajectory.

The fixed trajectories and corridors as airways can be classified upon the analogy of the road networks. The highways are corridors containing several lanes in a two-way direction. The distance between the corridors and from any surrounding infrastructure/obstacle should be at least 30 m. Major or mean airways have fixed trajectories.

High-speed delivery drones will fly within a corridor connected by nodes, such as one node in the harbor area, one node in the factory area, and another in the cargo air terminal (see Fig. 1). The predefined trajectory is desired for drones to avoid obstacles and each other. In addition, a safety puffer is defined, ensuring that drones cannot meet each other under any circumstance.

Before the flights, the operators must inform the drone air traffic management center of the planned flight and the expected target points. Upon other users' trajectories and surrounding data (e.g., static obstacles, minimum safe altitude), the automated center defines the trajectory for the given flight in a 3D virtual channel being optimized using the GIS map and opens a slot. Once the drone misses the open slot, the process should be reinitiated.

The flight is fully autonomous, but the drone continuously estimates its position and possible conflict and adapts its motion to the real flight situation. The drones' positioning is based on GPS combined with GIS mapping (Gazis et al., 1961; Pang

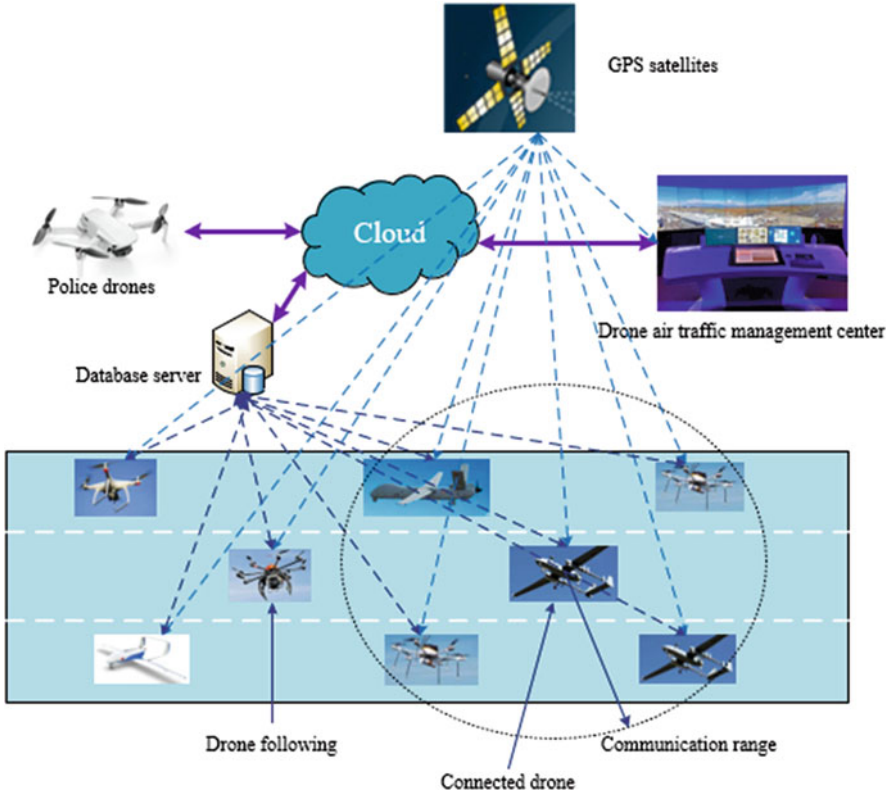


Fig. 3 General concept and system layout of the proposed autonomous drone management system

et al., 2020), using fixed-point markers in the infrastructure and active, intelligent surveillance (Fig. 3). Here GIS supports the definition of optimal trajectories based on minimizing the habitants being affected by the environmental impact or endangered by the possible emergency/accident situations.

The general concept and system layout are shown in Fig. 3. The predefined trajectory might have stops, return, or round flights. After reaching the target destination or next stop, the drone might follow the next part of the predefined trajectory of “ask” a new trajectory based on the next target point. The slots for the following parts of the flight are defined and opened automatically by the operational center.

3 Airway Network

Airway network is a better distribution of traffic flow that might reduce congestion and provide more flexibility to flight schedules and routes. Therefore, it is necessary to design an airway network to manage traffic flows better and reduce traffic congestion. Four different sectors are recommended to be used, such as the geographical sector, sectors in vertical separation (between the large buildings), sectors for vertical motion (climb/descent), and sectors for restricted areas.

3.1 Typical Elements

Elements of the airway network are simple elements of trajectories, lanes in which the aircraft might fly in one stationer flight mode as a straight flight, changing the lane, descent or climb, or coordinated turn (Figs. 4, 5, 6, 7, 8, and 9).

There are two different crossing options: (i) the straight-line crossing with no heading modification after the crossing (changing lane) (Fig. 10a) and (ii) the

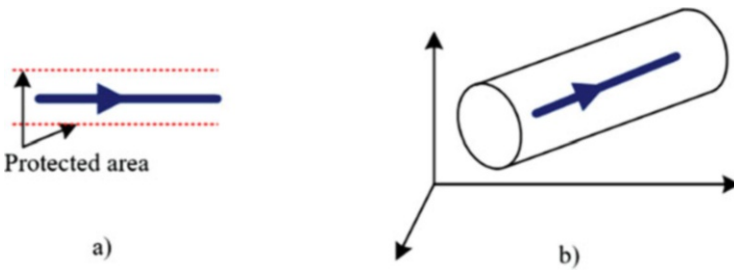


Fig. 4 One way: (a) vertical view and (b) 3D view

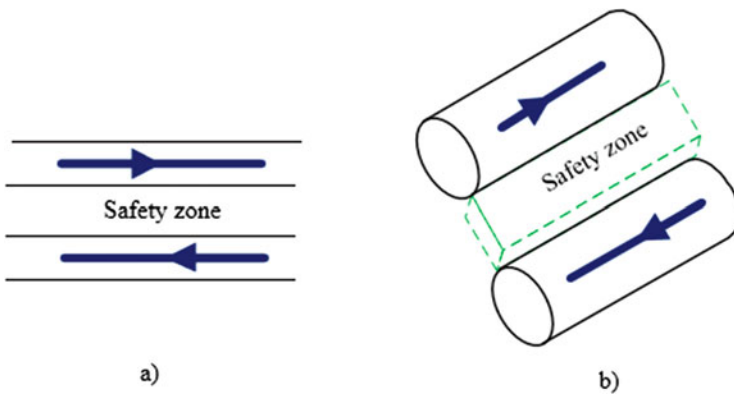


Fig. 5 Two ways: (a) vertical view and (b) 3D view

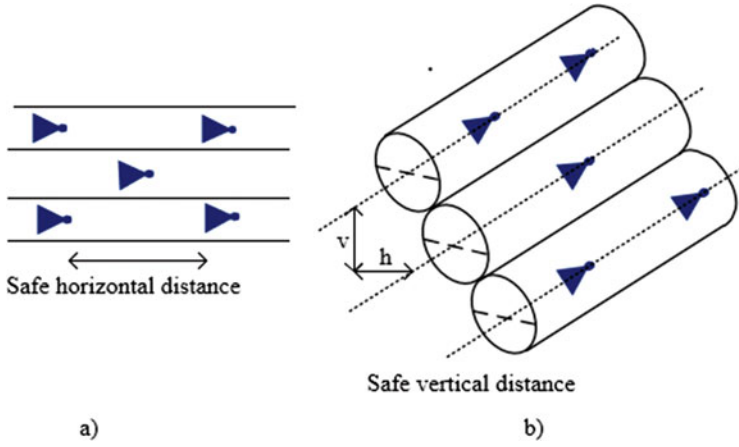


Fig. 6 Multi-lanes in one direction: (a) vertical view and (b) 3D view: v vertical safe distance, h horizontal safe distance

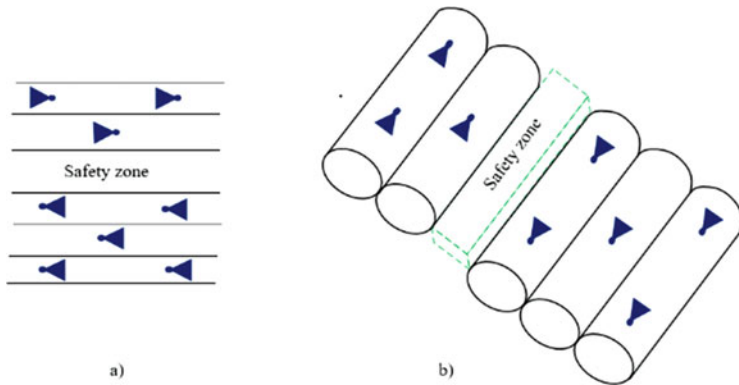


Fig. 7 Multi-lanes in two ways: (a) vertical view and (b) 3D view

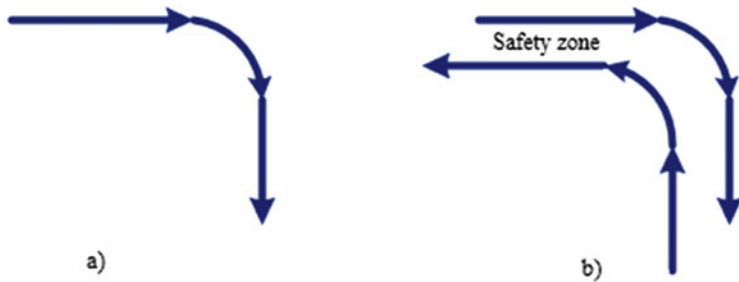


Fig. 8 Turning: (a) in one way at the same altitude and (b) in two ways at the same height

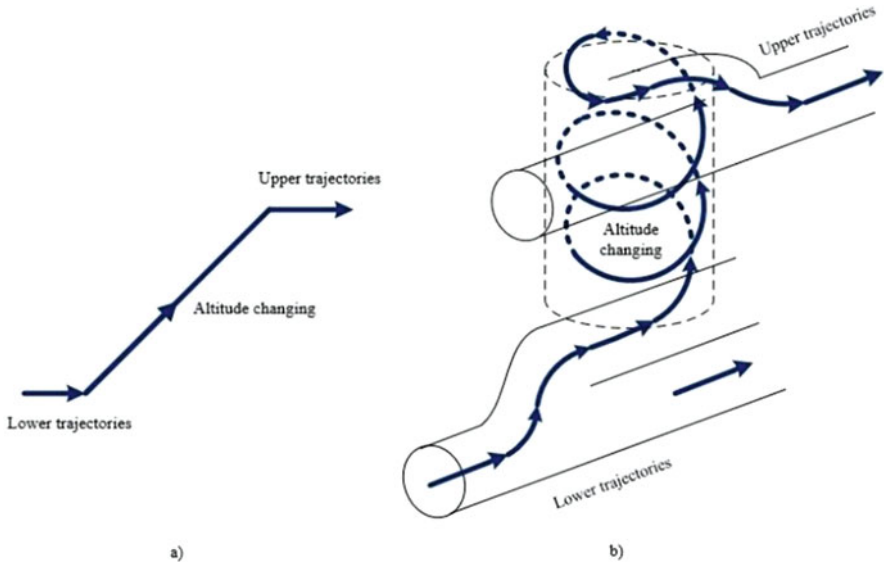


Fig. 9 Changing altitude in the same direction



Fig. 10 Crossing: (a) changing lane and (b) changing heading (in top view)

crossing with heading modification, including possibly a vertical motion due to the modified heading (Fig. 10b).

However, changing the direction (or heading) is not as straightforward. To minimize the number of potential conflicts, lanes of different headings are at different altitudes. Thus, heading modifications lead to the following six simple maneuvers, as shown in Fig. 11.

3.2 Safety Rules Applied to the Definition Airways

To define the airways, the authors investigated and evaluated several recent regulations and related works focusing on drones' safety and security aspects. The

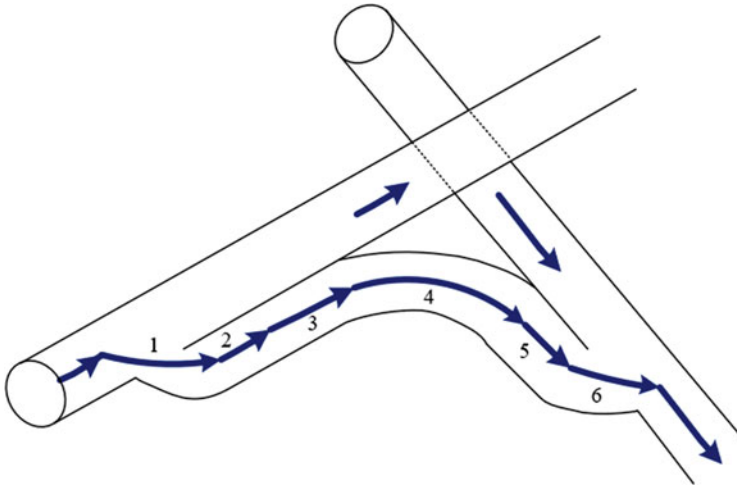


Fig. 11 Changing heading at different altitude: 1, changing to a new lane; 2, flying in the new lane; 3, increasing/decreasing the altitude; 4, turning on the same altitude; 5, flying at the new lane in the desired heading; 6, merging in the lane at the same altitude and at the desired new heading

following assumptions were made as a means to define the airway network under study and the research scope:

- Defining speed limits to 30 m/s for the corridors, 20 m/s for drones flying in fixed trajectories at a minimum of 20 m from any infrastructures (buildings), and 10 m/s for drones moving 20 m closer (but 5 m away) from the infrastructure.
- The drone’s recommended longitudinal separation in a fixed trajectory depends on the speed, difference in speeds, and the level of cooperation between the given drones. Preliminary longitudinal separation “time” should be a minimum of one second plus an additional second by every 10 m/s of flight speed sec, for the noncooperative vehicles that should be increased when the follower ($i + 1$) drone has a greater speed, Δv (m/s), being compared to the leading (i -th) drone for $\Delta v/3$ in sec. In the case of cooperative drones, the longitudinal separation time can be decreased by 30–40% (depending on the actual intensity of air turbulence) and for the case of formation flight, another 30%.
- The lateral separation (horizontal and vertical direction) is defined by figures representing the recommended typical elements of airways. As a general rule, the horizontal and vertical distance between the drones’ center of gravity heading in the same direction should be equal to 5–8 times their maximum dimensions. If drones fly in the opposite direction, a particular safe distance equal to an empty lane should be applied.
- The airways and the total network should be composed of the elements described above, and the drones might change lanes in the horizontal or vertical direction only.

- The defined trajectory as a channel for the given drone is fixed and cannot cross any other trajectory.

3.3 *Safe Airspace and Airway Network Design*

Trajectories and, generally, airway networks are developed and designed using multidisciplinary and multi-objective optimization to minimize the total impact of drones with minimum total cost. Here total means the sum of all the effects or costs of all drones. Impact includes all the immediate-, short-, and long-term effects and externalities caused by drone operations, such as the impact on nature, built and living environment, health problems initiated by the emissions and accidents, and effects on the economy. Total cost is determined by taking into account all the costs, including, for example, the operation, production, the development and operation of all the required infrastructures, or the external cost affected by accidents.

The airway network is operated in urban areas, where accurate positioning and traffic management require special supporting rules and a built environment. Rules might be developed by the partial implementation of the road traffic rules (including even the road and traffic signs) and unique markers being integrated into the city infrastructure (see Fig. 3). The airway network (as the sectorization) is operated by passive, dynamic, and active methods. Airway network should have special zones for an emergency landing if safety and security problems are detected (see Fig. 1).

This chapter deals with the civil and commercial application of drones in urban areas – smart cities. The recommended urban drone traffic system and management might operate relatively autonomous vehicles in corridors and relatively small air vehicles (mostly with less than 60 kg take-off mass) following trajectories/channels. The corridors are far enough from the built environment to be able to react even when drones are unintentionally leaving the fixed corridors (e.g., due to malfunction). The smaller drones following the fixed trajectory may cause fewer damages and problems, limiting possible unlawful actions.

4 Conclusion

The integration of drone flights into the air traffic management system is a real challenge. This chapter presented operational concepts for drone operations in urban areas, including airspace design, recommended construction of the airways, and essential safety requirements.

These rules were suggested as a means to eliminate or mitigate the causal factors or unsafe situations. Although this study proposes the safety requirements related to drones, we derived requirements assigned to the aviation authority and the manufacturer. However, a complete analysis of the authority and manufacturer levels was

beyond the scope of this study. Thus, an analysis of the control actions, their unsafe states, and the corresponding causal factors and scenarios must be studied and developed to improve the effectiveness of these requirements. Of course, the implementation of this concept needs further theoretical and practical investigation and applying an extensive series of different methods, techniques, and solutions that were studied, improved, and developed by authors, too, as possible examples.

References

- Cloutier, R., et al. (2009). *Investigation of a graphical CONOPS development environment for agile systems engineering*. Systems Engineering Research Center.
- EASA. (2015). *Concept of operations for drones: A risk based approach to regulation of unmanned aircraft*, EASA. Available at: https://www.easa.europa.eu/sites/default/files/dfu/204696_EASA_concept_drone_brochure_web.pdf. Accessed 25 July 2020.
- EUROCONTROL. (2018). *UAS ATM integration – Operational concept*. Available at: <https://www.eurocontrol.int/sites/default/files/publication/files/uas-atm-integration-operational-concept-v1.0-release20181128.pdf>. Accessed 20 Feb 2021.
- Gazis, D. C., Herman, R., & Rothery, R. W. (1961). Nonlinear follow-the-leader models of traffic flow. *Operations Research*, 9(4), 545–567. <https://doi.org/10.1287/opre.9.4.545>
- IEEE. (1998). *IEEE guide for information technology – System definition – Concept of operations (ConOps) document* (pp. 1–24). IEEE Std 1362-1998. <https://doi.org/10.1109/IEEESTD.1998.89424>
- Jankovics, I., & Kale, U. (2018). ‘Developing the pilots’ load measuring system’, aircraft engineering and aerospace technology. *Emerald Publishing Limited*, 91(2), 281–288. <https://doi.org/10.1108/AEAT-01-2018-0080>
- Nguyen, D.-D. (2021). Cloud-based drone management system in smart cities. In R. Krishnamurthi, A. Nayyar, & A. E. Hassaniien (Eds.), *Development and future of internet of drones (IoD): Insights, trends and road ahead* (pp. 211–230). Springer International Publishing. https://doi.org/10.1007/978-3-030-63339-4_8
- Nguyen, H. P. D., & Nguyen, D. D. (2021). Drone application in smart cities: The general overview of security vulnerabilities and countermeasures for data communication. In R. Krishnamurthi, A. Nayyar, & A. E. Hassaniien (Eds.), *Development and future of internet of drones (IoD): Insights, trends and road ahead* (pp. 185–210). Springer International Publishing. https://doi.org/10.1007/978-3-030-63339-4_7
- Nguyen, D. D., et al. (2020). Intelligent total transportation management system for future smart cities. *Applied Sciences*, 10, 8933. <https://doi.org/10.3390/app10248933>
- Pang, B., et al. (2020). *A concept of airspace configuration and operational rules for UAS in current airspace* (pp. 1–9). AIAA/IEEE 39th Digital Avionics Systems Conference (DASC). <https://doi.org/10.1109/DASC50938.2020.9256627>
- Pathiyil, L., et al. (2016). *Enabling safe operations of unmanned aircraft systems in an urban environment: A preliminary study* (pp. 1–10). The International Symposium on Enhanced Solutions for Aircraft and Vehicle Surveillance Applications (ESAVS 2016).
- Rohacs, D., & Rohacs, J. (2016). Magnetic levitation assisted aircraft take-off and landing (feasibility study – GABRIEL concept). *Progress in Aerospace Sciences*, 85, 33–50. <https://doi.org/10.1016/j.paerosci.2016.06.001>
- SEAR. (2020). *European ATM master plan: Roadmap for the safe integration of drones into all classes of airspace*. Available at: https://www.sesarju.eu/sites/default/files/documents/reports/European_ATM_Master_Plan_Drone_roadmap.pdf. Accessed Feb 20 2021.

Development of Aircraft Maintenance Procedures Using Lean Tools



Tapdig Imanov, Melih Yildiz, and Elif Koruyucu

Contents

| | | |
|---|------------------------------|----|
| 1 | Introduction | 61 |
| 2 | Method | 62 |
| 3 | Results and Discussion | 63 |
| 4 | Conclusion | 64 |
| | References | 65 |

1 Introduction

Maintenance and repair organization refers to every action working toward the purpose of restoring or retaining an item to a state in which it is able to perform its aimed functionality (Vieira and Loures, 2016). According to Hill et al. (2018), MRO's business model is the integration of logistic configuration and technical capacity that count the practices of outsourcing and vertical integration of the supply chain. The worldwide airline has generated a robust financial outcome in the last decade because of many factors and thanks to MRO which was the prominent sector supporting aircraft maintenance in the aviation industry. The forecast of aviation

T. Imanov (✉)
Cyprus Science University, Girne, Cyprus
e-mail: tveyranimanov@csu.edu.tr

M. Yildiz
Department of Aeronautical Engineering, Erciyes Üniversitesi, Kayseri, Türkiye
e-mail: melih.yildiz@kyrenia.edu.tr

E. Koruyucu
Eskisehir Technical University, Porsuk Vocation School, Eskisehir, Türkiye
e-mail: elifkoruyucu@eskisehir.edu.tr

experts and researchers in the area shows that there will be a major development in Asia's aircraft market, particularly in India and China, and this area will become the largest area, almost doubling up the in-service aircraft fleet and engines, therefore the demand of repair and overhaul (MRO) (Cooper et al., 2018). The state-of-the-art Lean principles and tools for their application in the MRO organizations in the aviation sector, as well as to identify leverages for improvements in aircraft maintenance management becomes unavoidable, taking into account safety, quality, and time. To eliminate non-value adding activity from the value stream is the main purpose of the Lean philosophy that means Lean waste does not add value to manufacturing and service processes, which can manifest in a variety form, such as defect, overproduction, waiting, non-utilized talent, transportation, inventory, motion, and extra processing. From a customer point of view, value-added activities are important, and customers are wishing to pay for such activities (Glass, 2016; Sanchez & Sunmola, 2017). This study presents how to identify and categorize critical factors in the aircraft maintenance process. Engine replacement is one of the critical tasks in the MRO function. Accurately identifying and clearly prioritizing such factors helps the MRO management team develop and implement Lean tools in their organizations to improve efficiency, quality, and safety, thereby reducing maintenance downtime. Proper application of methods allows the development of appropriate maintenance procedures for specific tasks described in the airlines' maintenance program. The approach to the search method this study proposes is to use combinations of Lean and Six Sigma (LSS) methods to measure the performance indicators during the engine replacement process.

2 Method

This research is based on the application of the integrated concept of the Lean Six Sigma method to improve the maintenance processes in the MRO organization. In previous studies, the main areas of the study of the LSS application were focused on the activities of the entire organization. These results go beyond previous reports, showing that this work is expanding the use of LSS methods to the different areas or systems of aircraft maintenance and removing the restrictions on the concentration on the general activities of the MRO organizations. In this study, the main focus was on the development of maintenance procedures for optimization of the GENx-2B engine replacement on the aircraft Boeing 747-8, which does not allow the use of new equipment, due to the absence of a removal and installation procedures in the aircraft maintenance manual (AMM). Based on the positive results of the study, a missing AMM procedure was developed and written; however, because of this potential limitation, it cannot be used without the approval of the aircraft manufacturer and the equipment designer. Another limitation of this is the lack of maximum preload value at the FWD PRELOAD entry that is important for determining the values of the maximum preload at the FWD and AFT pillars of the Cobra system and

Table 1 Lean tools combined with Six Sigma methods

| | |
|---------|--|
| Define | <i>High-level process map, voice of customer (VoC), stakeholder analysis, communication plan</i> |
| Measure | Value stream mapping (VSM), data collection plan, measurement system analysis |
| Analyze | Constraint identification, non-value-added, hypothesis testing |
| Improve | 5S, Kaizen, Poka-Yoke, total productive maintenance (TPM), process flow improvement |
| Control | Plan-do-check-act (PDCA), mistake proofing, visual process control, standardized work, training plan |

the values of the deflection angles on the digital inclinometer installed on the engine stand.

Boeing has no objection to the use of equipment according to the issued no technical objection (NTO) and leaving the decision to the B747 operators. Engineering departments of the airlines or dedicated MRO organizations can develop a similar engine replacement procedure using the Cobra system, therefore addressing the intention of both manufacturers to obtain missing data and request the inclusion of this procedure in the AMM Boeing 747 for future use. It is important to note that the present evidence relies on the publication of the NTO and confirmation from the equipment manufacturer.

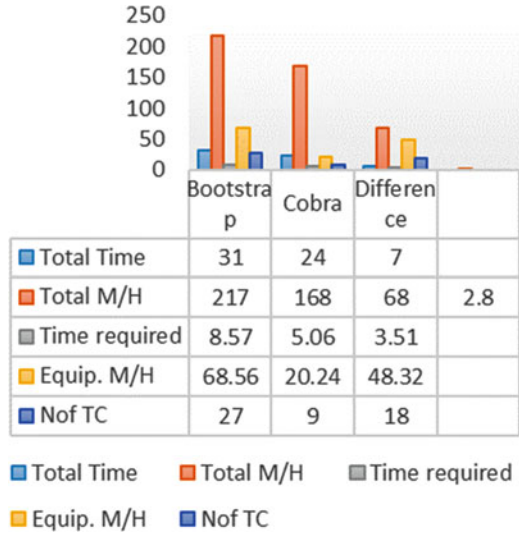
The outcome of this study shows that the combination of Lean tools with the Six Sigma methods (DMAIC) (Table 1) justifies the hypotheses envisioned to achieve the goal and expected performance during engine replacement on B747-8F aircraft with GENx-2B engines.

3 Results and Discussion

Using four maintenance staff for the Cobra system, the total of man hours (M/H) spend is equal to 20.24 h (H). Bootstrap M/H availability needs to provide eight persons which is equal to 68.56 H. The MRO's available extra M/H reached is equal to 48.32 H. Hereby the total M/H needed for engine replacement is reduced to 168 H; therefore, engine replacement time consisted of 24 h of using the Cobra system. Moreover, reduced labor required costs in the supply chain, expecting space availability in the stock, control and delivery/redelivery of bootstrap equipment to the maintenance team, transportation cost within the organization from reallocation of equipment and tools, as well as time and effort spent undergoing non-value-added tasks. Summarizing the findings of the process GENx-2B engine replacement on the aircraft Boeing 787-8F, it should be noted that the developed procedure applying HELH system using the LSS method is written as part of maintenance manual, except taking into account manufacturer limitations (Fig. 1).

Extensive results carried out show that this method improves optimizing the AMM card tasks, the goals were to minimize the time. This reduces labor costs,

Fig. 1 Result of the study



by reducing the number of MRO certifying staff and through the use of an optimized value-oriented approach while minimizing the waste (Hill et al., 2018). It will reduce aircraft down time, while increasing productivity other maintenance departments. The result of reduced downtime of the aircraft is less than 7 h under the maintenance action, therefore increasing the aircraft availability of the airlines and the financial income of the company.

The adoption of the Lean Six Sigma methods transferring to separate systems of the aircraft, such as engine replacement based on MRO context, is the first study of its kind. A similar project can be helpful to increase the area of application of maintenance and operations impacting positively on the profitability of the company. The use of standard tools was an effective approach to enable the LSS methods to identify the variables affecting performance.

4 Conclusion

In this research, the Six Sigma (SS–DMAIC) approach was used for the identification of its applicability in the development of a maintenance task card for an engine replacement on the Boeing 747-8 using PM, and the essential results can be summarized as follows:

- Engine replacement maintenance task cards decreased by 18 items.
- Total saving man hours on engine replacement consist of 68 h.
- Total saving man hours on equipment removal and installation consist of 48 h.

- Total saving time on equipment removal and installation consists of 3.51 h.
- Engine replacement time is reduced by 7 h.

References

- Cooper, T., Reagan, I., Porter, C., Precourt, C. & Wyman, O. (2018). *Global fleet & MRO market forecast commentary 2019–2029 authors*. Available Online: www.oliverwyman.com. Accessed 15 Dec 2020.
- Glass, R., Seifermann, S., & Mettemich, J. (2016). The spread of lean production in the assembly. *Process and Machining Industry, Procedia CIRP*, 55, 278–283.
- Hill, J., Thomas, A. J., Mason-Jones, R. K., & El-Kateb, S. (2018). The implementation of a Lean Six Sigma framework to enhance operational performance in an MRO facility. *Production & Manufacturing Research*, 6(1), 26–48.
- Sánchez, A. P., & Sunmola, F. (2017). *Factors influencing effectiveness of lean maintenance repair and overhaul in aviation, international conference on industrial engineering and operations management*. IEOM. July 24–25, 2017.
- Vieira, D. R., & Loures, P. L. (2016). Maintenance, repair and overhaul (MRO) fundamentals and strategies: An aeronautical industry overview. *International Journal of Computer Applications*, 135(12), 21–29.

Effect of Core Stitching on Flexural Properties of Lightweight Sandwich Composites



Çağrı Uzay

Contents

| | | |
|-----|------------------------------|----|
| 1 | Introduction | 67 |
| 2 | Materials and Method | 69 |
| 2.1 | Materials | 69 |
| 2.2 | Sandwich Manufacturing | 69 |
| 2.3 | Experimental Method | 70 |
| 3 | Results and Discussion | 71 |
| 4 | Conclusion | 73 |
| | References | 74 |

1 Introduction

Sandwiches are structural composites in which lightweight and relatively thick core materials are adhesively bonded to two separated, very thin but stiff and stronger face sheets. They have primarily emerged as a structural member in the fields of aerospace, marine, sports equipment, wind turbine, insulation, bridge and decks, and other infrastructures due to their very high flexural stiffness-to-weight ratio, acoustic, and heat insulation (Geren et al., 2021; Han et al., 2018). The characteristics of sandwich composites are the function of stiffness and strength properties of both face sheets and the core and the face sheet-to-core adhesion (Wang et al., 2015). Moreover, cellular polymer materials have a widespread application in packaging to provide energy absorption and impact load reduction. But the weakness in

Ç. Uzay (✉)

Kahramanmaraş Sütçü İmam University, Department of Mechanical Engineering,
Kahramanmaraş, Türkiye
e-mail: cagriuzay@ksu.edu.tr

through-thickness (out of plane) reinforcement between the composite laminas, including the sandwich core, is one of the most limiting issues. Because of this reason, laminar composites are much tended to delamination, crack propagation, and interlaminar shear failures (Aktas et al., 2013).

Stitching is an alternative way to increase the core materials' rigidity and strength and improve the face sheet-core interfacial strength. The process also increases the out-of-plane strength of the sandwiches and contributes to bending properties (Yalkin et al., 2015). It can also be described as a novel method providing higher through-thickness strength under compression and better energy absorption without sacrificing significant weight increase (Malcom et al., 2013), because the use of fiber yarns for the stitching process restricts the fiber-core debonding and increases the energy requirement for undesired delamination failure (Han et al., 2018). The stitching can be performed manually or by using ordinary stitching machinery. With the aid of a stitching machine, the rigid cellular polymeric foam cores can be stitched easily without the necessity of predrilling the holes. The stitch orientation and stitch quality can be controlled. Boeing developed an advanced stitching machine to produce large aircraft structures (Aktas et al., 2013). As stated by Mouritz and Cox (1999), stitching also provided to eliminate mechanical fasteners used in the fuselage and wings of a supersonic fighter aircraft, because more uniform stress distribution can be obtained and, therefore, it can be an alternative solution over the adhesive bonding or riveting. In the literature, hand stitching was carried out with both drilling holes by CNC milling machinery (Stanley & Adams, 2001) and single needle stitching tools (Potluri et al., 2003). It is understood that developments in stitching technology are required for widespread applications.

Yalkin et al. (2015) investigated the effects of perforation and stitching on the core materials with different tex yarns. The compression, shear, and bending properties of the developed sandwich structures were assessed. Malcom et al. (2013) made a corrugated core with glass fiber roving and inserted it into PVC foam. The face sheets were made of glass fibers, and the face sheets and the foam core material were stitched to each other with Kevlar. They aimed to increase shear properties and through the thickness compressive strength of the sandwich structures. Han et al. (2018) investigated the effects of stitch density on the polyurethane foam core (52 kg/m^3 , 5 mm thick) sandwiches with carbon fiber face sheets at various impact energies under low-velocity impact loads. They concluded that the decrease in stitch density led to an enlarged delamination area

In this study, the effect of core stitching on the flexural properties of low-density foam core sandwich structures was investigated. It aimed to improve the out-of-plane strength of the sandwich panels. The face sheets were made from carbon and glass fiber fabrics, respectively, and a 48 kg/m^3 density PVC foam core was used as the core material. The through-thickness reinforcement was achieved by predrilled core stitching with 600-tex fiber yarns. Three-point bending tests were conducted as per the ASTM C393 standard (ASTM, 2011) to reveal the sandwich flexural properties

2 Materials and Method

2.1 Materials

The sandwich structures were manufactured with low-density polymer foam core material and fiber-reinforced polymer composite face sheets. Moreover, 15-mm-thick PVC foam cores having 48 kg/m^3 were used. The shear strength of the core is 0.55 MPa (TDS, 2011). It is rigid and has a closed-cell structure. Such foams have advantages over the open cells with higher modulus and strength data and high resistance to environmental disturbances like water and moisture (Yalkin et al., 2015). Two different face sheets, carbon/epoxy and glass/epoxy laminates, were considered to investigate the stitching effect on sandwich structures. Woven, 3K plain fabrics with 200 g/m^2 were used to make face sheets. The objective of using woven plain fabrics is to provide better dimensional stability in both transverse and longitudinal directions than unidirectional fibers. Hence, they have almost equal mechanical properties in those directions (Dixit & Mali, 2013).

2.2 Sandwich Manufacturing

Before starting the manufacturing of sandwiches, the PVC foam cores were drilled to obtain the stitching holes. The drilling was made with a CNC milling machine with a drill diameter of 2.5 mm. The schematic of the drilled PVC foam core in a specified orientation is shown in Fig. 1.

The stitching was performed in a predetermined orientation by using 600-tex E-glass fiber yarns. The image of stitched foam core of a sandwich specimen is shown in Fig. 2. After completing the stitching, the sandwich constituents were subjected to the vacuum bagging process as presented schematically in Fig. 3. In the manufacturing process, the face sheets were co-cured with the core material. The carbon/epoxy face sheets were made of four-ply carbon fiber fabrics, whereas the glass/epoxy face sheets were made of five-ply glass fiber fabrics to obtain the same face sheet thickness values. After stacking all the layers, a perforated release film,

Fig. 1 Schematic of a stitched foam core

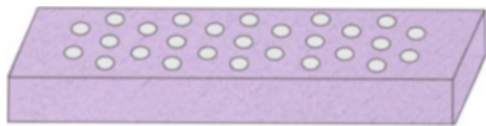


Fig. 2 Image of a stitched foam core



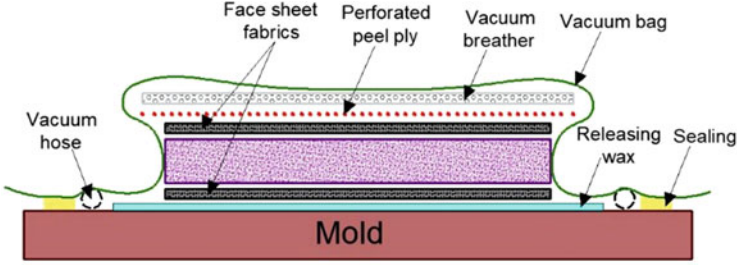
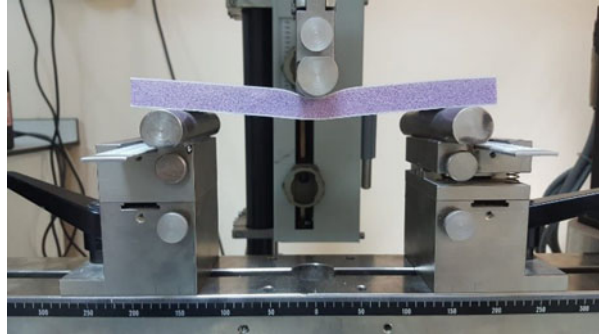


Fig. 3 Schematic of the vacuum bag process

Fig. 4 Testing of a sandwich specimen



vacuum breather, and vacuum bag were placed over the composite sandwich system, respectively. Therefore, removing excessive resin from the laminate was allowed throughout the perforated film and the breather. The sandwich panel was held inside the vacuum bag for 24 hours at room temperature under a vacuum atmosphere. The non-stitched foam cores were also sandwiched as the benchmarks.

2.3 Experimental Method

The flexural tests were carried out with three-point bending loading according to the ASTM C393 standard. The specimens are 200 mm in length and 50 mm in width. The tests were performed by using ZwickRoell Z100 (100 kN) universal testing machine. The span length was arranged as 150 mm, and the cross-head speed of the testing machine was set to 2 mm/min. The flexural load-deflection data obtained from the tests was used to reveal the bending behavior, flexural stiffness, maximum bending load, core shear strength (Eq. 1), and the maximum face sheet stress (Eq. 2). The testing sandwich specimen was shown in Fig. 4.

$$F_s^{\text{ult}} = \frac{P_{\text{max}}}{(d+c)b} \quad (1)$$

$$\sigma = \frac{P_{\max} \cdot S}{2t \cdot (d + c) \cdot b} \tag{2}$$

where F_s^{ult} and σ are the core shear and face sheet ultimate stress (ASTM C393 Standard), P_{\max} is the maximum flexural load, S is the span length in three-point bending tests, b and d are the sandwich width and thickness, c is the core thickness, and t is the face sheet thickness.

3 Results and Discussion

The results obtained from the three-point bending tests were presented comparatively for carbon/epoxy and glass/epoxy face sheets sandwiches with stitched and non-stitched foam core. Figures 5 and 6 illustrate the bending load-deflection curves of the sandwich specimens according to the type of face sheets and core modifications, respectively. Three specimens were tested for each sandwich group.

The non-stitched foam core sandwiches presented a linear straight line up to a bending load of about 400 N and 470 N for glass/epoxy and carbon/epoxy face sheets, respectively. Then the nonlinear increment reached the maximum points of bending load. It is approximately 500 N and 590 N for glass/epoxy and carbon/epoxy face sheets, respectively. After the maximum point of bending load is reached, the failure of sandwiches with glass/epoxy face sheets was carried out with a linear decreasing slope, whereas the sandwiches with carbon/epoxy face sheets provided almost a plateau between the deflections of 4 mm and 7 mm. The carbon/epoxy face sheet sandwiches then showed a sudden force drop due to the compressive failure of the upper face sheets. Carbon/epoxy face sheet sandwich provided higher linear initial stiffness than that of glass/epoxy face sheets.

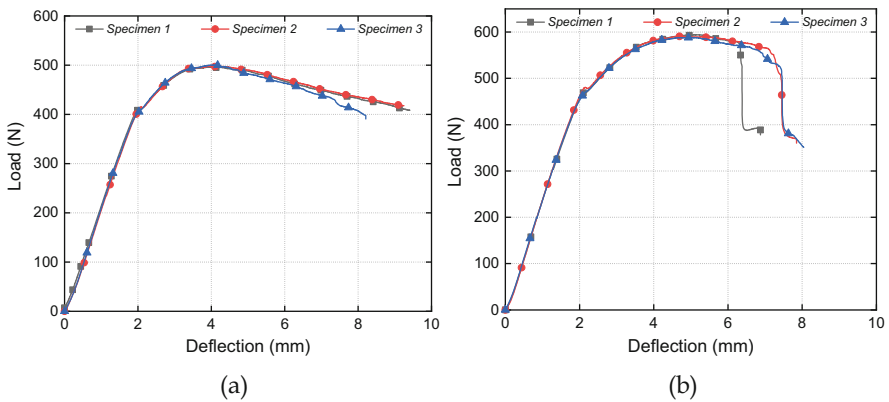


Fig. 5 Load-deflection curves of the non-stitched foam core sandwiches with (a) glass/epoxy face sheets and (b) carbon/epoxy face sheets

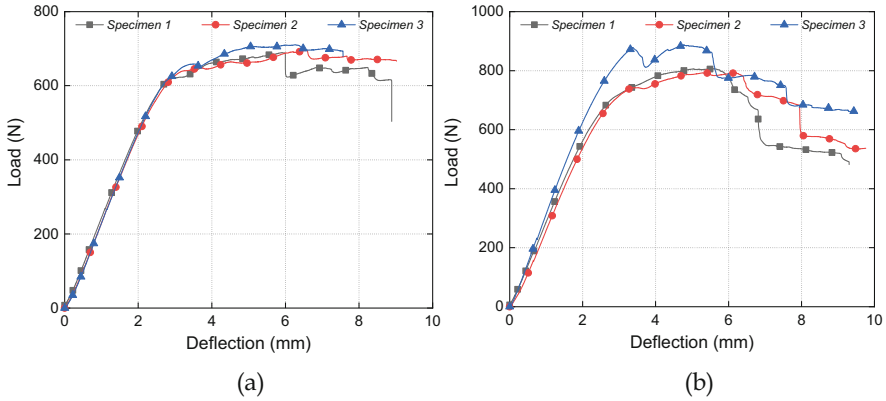
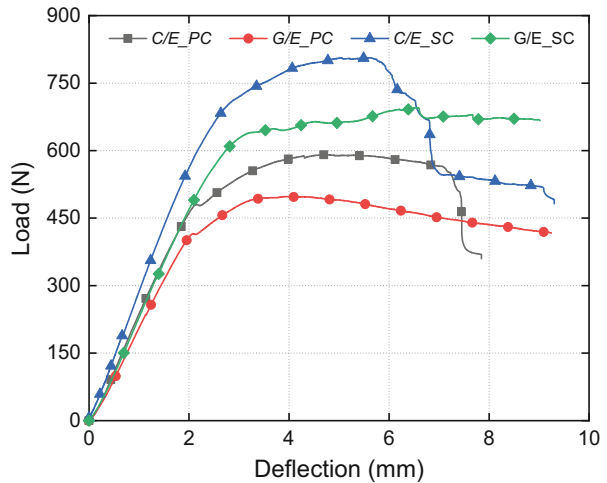


Fig. 6 Load-deflection curves of the stitched foam core sandwiches with (a) glass/epoxy face sheets and (b) carbon/epoxy face sheets

Fig. 7 Comparison of the sandwiches' flexural load-deflection curves according to face sheets and core modifications (C/E, carbon/epoxy; G/E., glass/epoxy; NC, non-stitched core; SC, stitched core)



The stitched core sandwiches increased the load-carrying capacity and initial stiffness values for both carbon/epoxy and glass/epoxy face sheets. The sandwiches with glass/epoxy face sheets first showed a linear increase to 600 N approximately, and then the force increased to the maximum value of about 700 N. Contrary to non-stitched foam core sandwiches, the core stitching prevented the load reduction and provided a large plateau. On the other hand, a force drop after a plateau was observed for the sandwiches with carbon/epoxy face sheets once the maximum bending load value (nearly 830 N) was reached.

The flexural load-deflection curves of the sandwiches were also comparatively presented in Fig. 7. As seen, the core stitching made a significant improvement in the sandwiches' load-carrying capacity. Moreover, the sandwich bending rigidity was considerably increased. The non-stitched core sandwich rigidities were obtained as

Table 1 Flexural characteristics of the sandwich panels

| Sandwich type | Max. flexural load (N) | Core shear ult. stress (MPa) | Max. face sheet stress (MPa) |
|---------------|------------------------|------------------------------|------------------------------|
| G/E_NC | 498.28 | 0.339 | 25.42 |
| C/E_NC | 591.05 | 0.402 | 30.16 |
| G/E_SC | 698.25 | 0.475 | 35.63 |
| C/E_SC | 828.78 | 0.564 | 42.29 |

216 N/mm and 230 N/mm for glass/epoxy and carbon/epoxy face sheets, respectively. The through-thickness reinforcement of the core materials increased the rigidity values up to 230 N/mm and 301 N/mm for glass/epoxy and carbon/epoxy face sheets, respectively.

The primary failure mode for the sandwiches was evaluated as core shearing. However, the non-stitched foam core sandwiches with carbon/epoxy face sheets underwent a compressive failure of upper face sheets after some amount of core crushing. The core stitching contributed to obtaining core shear failure instead of a brittle fracture of the upper face sheet due to the compressive forces. Therefore, the load acting on the upper face sheets was effectively transferred to the bottom face sheets via through-thickness reinforcement of the core materials. The core fracture was observed instead of the face sheets' fracture. Similar findings were obtained by Yalkin et al. (2015). Table 1 illustrates the maximum bending load, core shear stress, and the face sheet stress of each sandwich group. Approximately 40% increment in bending load capacity was obtained for the developed sandwiches with glass/epoxy and carbon/epoxy face sheets. The core shear ultimate stress and maximum face sheet stress values were also increased. The percent increments were similar to the increase in load capacity. The sandwiches with carbon/epoxy face sheets were subjected to higher stress values than that of glass/epoxy face sheet sandwiches due to their better resistance to flexural loads.

4 Conclusion

Core stitching is a simple manufacturing process and suitable for automation. Stitched cores can be used to develop sandwiches with very high bending rigidity to weight ratio and increased load capacity because the fiber reinforcements within the stitching holes act as resistive columns against bending forces. The stitching reinforcements provided better integrity of the face sheets to the foam cores. Therefore, the load acting on the upper face sheets was efficiently transmitted to the bottom face sheets throughout the stitched core, which provided both increased bending rigidity and load-carrying capacity. By using the stitched cores, the bending load capacity was increased by nearly 40% for both glass/epoxy and carbon/epoxy face sheet sandwiches. Moreover, an enhanced failure behavior was obtained, and upper face sheet fractures were eliminated.

Acknowledgments This study was supported by Kahramanmaraş Sütçü İmam University, Scientific Research Projects Coordination Unit under grant number 2020/9-32 M.

References

- Aktas, A., Potluri, P., & Porat, I. (2013). Development of through-thickness reinforcement in advanced composites incorporating rigid cellular foams. *Applied Composite Materials*, 20, 553–568.
- ASTM C393/C393M-11. (2011). Standard test method for core shear properties of sandwich constructions by beam flexure. In *Annual book of ASTM standards*. ASTM International.
- Dixit, A., & Mali, H. (2013). Modeling techniques for predicting the mechanical properties of woven-fabric textile composites: A review. *Mechanics of Composite Materials*, 49, 1–20.
- Geren, N., Acer, D. C., Uzay, C., & Bayramoglu, M. (2021). The effect of boron carbide additive on the low-velocity impact properties of low-density foam core composite sandwich structures. *Polymer Composites*, 42(4), 2037–2049.
- Han, F., Yan, Y., & Ma, J. (2018). Experimental study and progressive failure analysis of stitched foam-core sandwich composites subjected to low-velocity impact. *Polymer Composites*, 39, 624–635.
- Malcom, A. J., Aronson, M. T., Deshpande, V. S., & Wadley, H. N. G. (2013). Compressive response of glass fiber composite sandwich structures. *Composites Part A: Applied Science and Manufacturing*, 54, 88–97.
- Mouritz, A. P., & Cox, B. N. A. (1999). Mechanistic approach to the properties of stitched laminates. *Composites Part A Applied Science and Manufacturing*, 31(1), 1–27.
- Potluri, P., Kusak, E., & Reddy, T. Y. (2003). Novel stitch-bonded sandwich composite structures. *Composite Structures*, 59, 251–259.
- Stanley, L. E., & Adams, D. O. (2001). *Development and evaluation of stitched sandwich panels*. NASA/CR-2001-211025. Langley Research Centre.
- Technical Data Sheet (TDS). (2011). *Universal structural foam: Airex C70. 3A composites*.
- Wang, J., Chen, B., Wang, H., & Waas, A. M. (2015). Experimental study on the compression after-impact behavior of foam-core sandwich panels. *Journal of Sandwich Structures and Materials*, 17(4), 446–465.
- Yalkin, H. E., Icten, B. M., & Alpyildiz, T. (2015). Enhanced mechanical performance of foam core sandwich composites with through the thickness reinforced core. *Composites Part B Engineering*, 79, 383–391.

Environmental Impacts and Sustainability Practices of Airports



İrem Koçan and Gamze Orhan

Contents

| | | |
|-----|---|----|
| 1 | Introduction | 76 |
| 2 | The Examination of the Impacts of Airports on the Environment | 77 |
| 2.1 | Singapore Changi Airport | 77 |
| 2.2 | Munich Franz Josef Strauss Airport | 77 |
| 2.3 | Vancouver Airport | 78 |
| 2.4 | Istanbul Airport | 78 |
| 3 | Results and Discussion | 79 |
| 4 | Conclusion | 80 |
| | References | 80 |

Nomenclature

| | |
|-----------------|---|
| ACA | Airport carbon accreditation |
| ACI | Airports council international |
| APU | Auxiliary power unit |
| CAG | Changi airport group |
| CO ₂ | Carbon dioxide |
| FEGP | Fixed electric ground power units |
| ICAO | International civil aviation organization |
| IGA | Istanbul grand airport |

İ. Koçan

Anadolu University, Graduate School of Social Sciences, Eskisehir, Turkiye

e-mail: iremkoacan@anadolu.edu.tr

G. Orhan (✉)

Eskisehir Technical University, Faculty of Aeronautics and Astronautics, Department of Aviation Management, Eskisehir, Turkiye

e-mail: gozsoy@eskisehir.edu.tr

1 Introduction

Along with developing air transportation, passenger traffic is also increasing, and new airports are taking their place in the market in order to meet the increasing demand. Not only the increase in the number of airports but also the increase in ground operations and flight traffic at the airports cause some environmental problems as well as all their benefits. The main of these problems are greenhouse gas emissions, noise, water consumption, energy consumption, and waste amounts, but there are also factors such as biodiversity and wildlife.

Today, airports are aware of their environmental impacts and take various measures to reduce these impacts. Airports that want to reduce their environmental impacts follow the standards of national and international authorities such as ICAO Annex 16 (Environmental Protection – Aircraft Noise) or ICAO Airport Air Quality Manual (DOC9889).

In addition to the authorities, various organizations like ACI also guide the airports about this. With the Airport Carbon Accreditation program, it aims to reduce carbon emissions by classifying airports at six different levels – mapping, reduction, optimization, neutrality, transformation, and transition.

The aim of this study is to evaluate the environmental impacts of airports and the practices carried out to reduce these impacts.

When a literature assessment is conducted on the environmental consequences of airports and the practices that have been implemented in this regard, it is clear that sustainable practices have been implemented since the airport's establishment. At sustainable methods utilized in airports, it is noted that largely renewable energy is used.

Sukumaran and Sudhakar (2017) monitored Cochin Airport, which carries out its activities with solar energy, on a monthly basis and found a performance rate of 86.58% which is efficient enough.

In Koroneos et al. (2010) study, solar energy, geothermal energy, and biomass energy were used in uses such as heating, cooling, and lighting at Thessaloniki Airport. They found that solar energy can supply 2% of the energy used for heating, and biomass energy can supply 8% of the energy used for heating.

Benosa et al. (2018) examined the impact of techniques for reducing airport emissions on air quality in the Southern California region. It was emphasized that with the application of methods such as electrification of ground support equipment and the application of alternative aviation fuels, the region would be affected by 36% less emissions in summer and 32% in winter.

2 The Examination of the Impacts of Airports on the Environment

In this study, four airports operating in the international arena were examined. These airports are Singapore Changi Airport, Munich Franz Josef Strauss Airport, Vancouver Airport, and Istanbul Airport. The sample of the study consists of the airports selected as the best airport on a regional basis in 2020 based on the Skytrax Awards and Istanbul Airport in order to make comparisons for the national area.

Environmental impacts of selected airports were examined under the subheadings: greenhouse gas emissions, noise management, waste management, energy management and water management, and practices to reduce the impacts caused by these.

2.1 Singapore Changi Airport

According to the Airport Carbon Accreditation methodology, Scope 2 emissions are higher. Looking at the average of the last 3 years (2018, 2019, 2020), it is seen that greenhouse gas emissions decreased by 3.5% (http-1, 2021).

With its emission reduction target for 2030, Changi Airport Group (CAG) prioritizes improvements such as building design and the use of more efficient systems in the cooling of buildings, which is the biggest source of emissions.

With the use of e-waste boxes in the office, the e-waste collection rate quadrupled compared to the previous year, and a total of 5604 kg of e-waste was collected (http-1, 2021).

Electricity consumption at the airport is mostly used for air conditioning systems, terminal lighting, and baggage handling systems. It is aimed to reduce energy consumption by closing elevators, escalators, and moving walkways in nonoperational areas of the terminals.

In the 2019/2020 fiscal year, 819,439 m³ of drinking water was consumed at Changi Airport, and 782,568 m³ of wastewater was generated.

2.2 Munich Franz Josef Strauss Airport

The total amount of CO₂ was measured at Munich Airport as 147,778 tons in 2019, and a decrease was recorded compared to previous years (http-2, 2021). To reduce carbon emissions, Munich Airport carries out its pushback operations with electric vehicles called PHOENIX.

Munich Airport also monitors the amount of noise generated with 16 fixed monitoring points placed around it. Munich Airport landing fees are calculated

according to the noise levels of the aircraft, which affects the type of aircraft used by the airlines. This method encourages airlines to use quieter aircraft.

Munich Airport recycled 9666 tons of waste in 2019, reaching the highest amount compared to previous years ([http-3, 2021](#)).

The airport is working on the replacement of lighting with energy-saving LED lighting and meets almost all heating and cooling requirements based on waste heat. Thus, it decreased the amount of energy per passenger in 2019 and reached 4.88 kWh/passenger ([http-3, 2021](#)).

The airport uses stored rainwater in fire training courses to reduce water consumption. Water-saving faucets to reduce drinking water consumption are used.

2.3 Vancouver Airport

Vancouver Airport aims to reduce its emissions by using electric vehicles in its ground operations and encouraging its employees to use public transportation or bicycles. With such practices, airport emissions were reduced by 5% in 2020 ([http-4, 2021](#)).

With its ground run-up enclosure facility, it aims to reduce the noise caused by engine starts in the environment. This facility reduces noise by directing the sound coming from residential areas with its aerodynamic design and sound-absorbing panels. Also, for aircraft with a maximum takeoff weight of more than 34,000 kg, prior confirmation is required between 00:00 and 06:00 regardless of actual take-off weight ([http-5, 2021](#)).

To reduce the use of waste; targets such as reducing single-use plastics, carrying out studies to supply less packaged goods, and increasing the number of central waste sorting stations were set.

It has been converted to energy-efficient LED lighting to reduce the energy consumed for lighting. In this way, 801,410 kWh of energy was saved.

Vancouver Airport, which reduced its total water use by 47% in 2020, has conducted various studies on the use of rainwater. One of these is collecting rainwater from the roof of the airside operation building and using it for non-potable uses (emergency firefighting and vehicle washing). It is estimated that it saves about 620 m³ of drinking water per year ([http-6, 2021](#)).

Apart from this, the wildlife team directs wildlife animals that may negatively affect the airport operation in different areas.

2.4 Istanbul Airport

Aiming to reduce carbon emissions, Istanbul Airport prefers electric luggage-carrying vehicles. In order to reduce the effects of direct greenhouse gas emissions

caused by the construction of Istanbul Airport, afforestation studies were carried out to create sinks.

Istanbul Airport has made it mandatory for aircraft to be connected to FEGP since aircraft APUs generate high levels of noise.

Istanbul Grand Airport (IGA) which built and operates Istanbul Airport aims to reach the Zero Waste Target in 2023. Nonhazardous wastes are reused when necessary, reducing the amount of waste, thus saving labor, energy, and fuel.

Istanbul Airport aims to reduce energy consumption in line with ISO 50001 Energy Management System standards. Public transportation is encouraged at Istanbul Airport, priority parking spaces are reserved for low-emission vehicles, and advantageous parking spaces are reserved for vehicles that will share cars ([http-7, 2021](#)).

In order to reduce water consumption, local plants that consume less water are selected in landscape areas, and 100% water savings are achieved by using treated wastewater in irrigation. Wastewater generated as a result of vehicle washing is filtered and returned to the system ([http-8, 2021](#)).

In addition to this, while the wildlife management unit works on identifying and minimizing bird and aircraft collision risks, it also analyses the changes that can be made in the take-off-landing directions of the aircraft.

3 Results and Discussion

While each selected airport follows international standards, it also creates and implements its own environmental policy. Beyond policy-making, Istanbul Airport and Vancouver Airport have established special units in order to better manage environmental issues. All airports follow the Airport Carbon Accreditation (ACA) program initiated by ACI.

The most detailed information on all topics was obtained in the Munich Airport reports, but the numerical data on the noise occurring at Vancouver Airport and Istanbul Airport could not be reached.

When greenhouse gas emission amounts are examined; the lowest amount is seen at Vancouver Airport. Then, it is seen that Munich Airport has reduced its emissions from 2017 to 2019. Istanbul Airport does not have data before 2019, but when compared to 2019, it has been concluded that it causes less emissions than Changi Airport.

It has been concluded that Munich Airport, which shares detailed information on water consumption, uses less amount of drinking water than Vancouver Airport. In addition, it has been learned that Changi Airport, which has shared only 2019 data, realizes both drinking water consumption and wastewater discharge in lesser amounts than Munich Airport.

When the total amount of waste is compared, it is seen that Changi Airport is the airport that generates the least waste.

When the energy consumption of airports is examined, it is seen that the electricity consumption per passenger is less at Munich Airport and has decreased since 2017. There is not enough information about Istanbul Airport. Since Vancouver Airport shares its data in different energy units, comparisons cannot be made.

Considering the practices carried out by airports to reduce their environmental impact, it is seen that Vancouver Airport and Istanbul Airport do more work than other airports.

While Munich Airport and Vancouver Airport performed the most practices in terms of greenhouse gas emissions and noise, it was observed that Changi Airport did fewer practices, and sufficient information could not be reached on noise.

The practices carried out by Istanbul Airport on waste, energy, and water management stand out compared to other airports.

Apart from the topics mentioned, Istanbul Airport and Vancouver Airport also worked on different subjects such as wildlife and biodiversity and shared the details in their reports.

4 Conclusion

It is seen that airports around the world are aware of their environmental impacts and implement different practices in order to reduce these effects. When greenhouse gas emissions are compared, the lowest amount is seen at Vancouver Airport, and the highest amount is seen at Changi Airport. When the total amount of water consumption and the amount of wastewater discharge in 2019 are examined, it is seen that the lowest amount is at Changi Airport. In terms of waste, Changi Airport was the airport that generated the least amount of waste. When electricity consumption is compared, it is seen that Istanbul Airport and Vancouver Airport do not share data, and among other airlines, the electricity consumed per passenger is the least at Munich Airport.

Common aspects seen in the practices can be shown as electrification of the vehicles used, the use of energy-saving lighting and batteries, alternative fuel studies, turning off the auxiliary power unit to reduce the effects of noise and emissions, reuse of wastewater, and various activities to raise awareness of employees and passengers about the environment.

References

- Benosa, G., Zhu, S., Kinnon, M. M., & Dabdub, D. (2018). Air quality impacts of implementing emission reduction strategies at Southern California airports. *Atmospheric Environment*, 185, 121–127.
- http-1: <https://gallery.changiairport.com/>. Accessed 9 May 2021.
- http-2: <https://www.munich-airport.com/press-electric-elephant-de-ices-aircraft-10750331>. Accessed 10 May 2021.

- http-3: <https://report2019.munich-airport.com/services/downloads.html>. Accessed 11 May 2021.
- http-4: <https://www.yvr.ca/en/media/news-releases/2019/partnership-to-advance-the-availability-of-sustainable-aviation-fuel-in-canada>. Accessed 14 May 2021.
- http-5: <https://www.yvr.ca/en/about-yvr/noise-management/monitoring-and-abatement>. Accessed 15 May 2021.
- http-6: <https://www.yvr.ca/en/about-yvr/environment/water-conservatio>. Accessed 7 May 2021.
- http-7: <https://www.igairport.com/sites/sustainability/tr/birimler/sosyal-ekoloji-yonetimi/genel-bilgi>. Accessed 19 May 2021.
- http-8: <https://www.igairport.com/sites/sustainability/tr/birimler/cevre-yonetimi/yapilan-calismalar/su-yonetimi>. Accessed 19 May 2021.
- Koroneos, C., Xydis, G., & Polyzakis, A. (2010). The optimal use of renewable energy sources-the case of the new international “Makedonia” airport of Thessaloniki, Greece. *Renewable and Sustainable Energy Reviews*, 14, 1622–1628.
- Sukumaran, S., & Sudhakar, K. (2017). Fully solar powered airport: A case study of Cochin international airport. *Journal of Air Transport Management*, 62, 176–188.

Evaluating Public Transport Development Projects by Multi-criteria Methods



Omar Alharasees

Contents

| | | |
|---|--|----|
| 1 | Introduction | 83 |
| 2 | Method | 85 |
| | 2.1 Calculation | 85 |
| 3 | Results and Discussion | 88 |
| | 3.1 Sensitivity Analysis | 90 |
| 4 | Conclusion | 93 |
| | 4.1 Recommendation and Future Work | 93 |
| | References | 93 |

Nomenclature

| | |
|------|--------------------------------|
| AHP | Analytical hierarchy process |
| MCDM | Multi-criteria decision-making |
| PCM | Pairwise comparison matrix |

1 Introduction

Transport is the backbone of life. It is one of the sectors which determine the form and socio-economic development of a city (Zuidgeest & Van Maarseveen, 2006). The first step in creating sustainable transport systems is focusing on the development of passenger transport since this process must be done on a high strategic level so estimating and forecasting the network for the service to reach sustainability (Jenks et al., 2000) based on using the decision-making methods like multi-criteria

O. Alharasees (✉)

Budapest University of Technology and Economics, Budapest, Hungary

decision-making techniques (MCDM). Most of the strategic important transport development decisions are made based on capital cost limitation, administrative challenges, and other constraints (Comtois, 2009), which are often made as top-down decisions giving the authority to the operators of the service and neglecting or limiting the users' opinion such a process could give catastrophic results in the future that's why the modern sustainable development of the transportation system in any country started to consider more contribution from the public side (users and potential users) also maximizing the experts' point of view contribution (Duleba, 2019).

Due to the rising challenges in the transport world through the implementation, maintenance, and distribution of the projects and the urbanization and increase of population of the cities, the level of supply quality in the transport systems should be assessed, which is an important factor in the global field within manufacturing and of the market socioeconomics, the supply chain is prevalent in today's business model (Jenks et al., 2000). Multi-criteria decision-making MCDM is a famous and well-known branch of decision-making techniques. That deal with decision problems which requires a specific procedure under some circumstances and conditions of several decision criteria, which fits the practical strategic problems and also needs specific solutions or alternatives under a set of conditions like the situation here in public transport projects developments (Figueira et al., 2004). The MCDM approach requires that the choice or selection be made among decision alternatives or sub-criteria described by their attributes. Solving an MCDM problem involves sorting, ranking, and scoring (Mardani et al., 2015; Sabaei et al., 2015). The transportation development process is a strategic procedure that needs to identify and predict the current and future situation of the transport system, considering many different variables, and develops and chooses multiple scenarios to solve the encountered or probable problems. As multiple parameters are affecting the social life in the accommodation unit, there is a necessity to evaluate these parameters when choosing between the scenarios (Velasquez & Hester, 2013; Brunneli, 2015; Snyder et al., 2016).

This research aims to identify, analyze, and evaluate the factors in the development of the public transportation system in Budapest City by involving two types of the public, namely, experts and passengers. The current study considers the stakeholder groups by focusing on the opinion of experts on their preferences concerning the public transportation main characteristics (Duleba & Moslem, 2018). The analytic hierarchy process (AHP) is applied to build a general hierarchical model (Saaty, 2002). These decision-making models are mainly based on three levels to determine preference weights of evaluators for the (i) evaluation process, (ii) avoiding complexity, and (iii) missing data of other AHP applications. In this research, the Saaty scale has been used for scoring to illustrate the missing data using the matrices which could be calculated by a specific algorithm as well (Nakagawa & Sekitani, 2004; Duleba et al., 2012).

One of the novelties of this research is to introduce a new decision-making model for comparing the supply transport quality including the cost and environmental

impacts criteria. The process will make it easier for decision-makers to evaluate and weigh various individual aspects of public transportation from different overviews.

2 Method

There are several MCDM approaches to support decision-makers in transportation projects development from different perspectives: the experts, passengers, non-passengers, potential passengers, and governmental side also considering the main characteristics of the transport system from different overviews including the three dimensions of sustainable development; however, the analytic hierarchy process is the most popular application of MCDM applications, especially in transportation project developments and planning to reach sustainable development for the current system. Over time, numerous researchers have used the MCDM techniques and approaches in urban transportation and its development since public transportation projects need to be ranked and prioritized based on many other limitations, the MCDM is the suitable technique for the evaluation, and analyzing the data using these techniques will help and make it easier to see all stakeholder preferences including the public which lead to a sustainable transport system (Eskandarpour et al., 2015; Akdemir et al., 2018).

Budapest City has been selected because of the growing developments in the transport side (van den Berg et al., 2014) and considering that the demand side is sometimes seriously neglected. To get a more generalized view of public transportation supply quality criteria where the preferences of transport experts and passengers are considered in Budapest, the analytic hierarchy process has been applied based on a pairwise comparison (PC) questionnaire survey. A three-level hierarchical model was used in the evaluation process, (i) general, (ii) specific, and (iii) very specific, which let us gain important information on all kinds of elements in a strictly logical way by keeping the hierarchy (Saaty, 2001).

The steps of applying the AHP method could be summarized in Fig. 1. As a first step in building a three-level hierarchical model based on the basic characteristics and elements of public transportation, Table 1 shows the model with the elements of each level.

2.1 Calculation

First, we form the pairwise comparison matrices, since the AHP utilizes the special characteristics of pairwise comparison matrices (PCM). The matrix of pairwise comparisons $A = [a_{ij}]$ shown in Eqs. 1 and 2 represents the intensities of the decision-maker's preference between individual pairs of alternatives (A_i versus A_j , for all $i, j = 1, 2, \dots, n$). They are usually chosen from a given scale, the Saaty scale

Fig. 1 The process of applying AHP

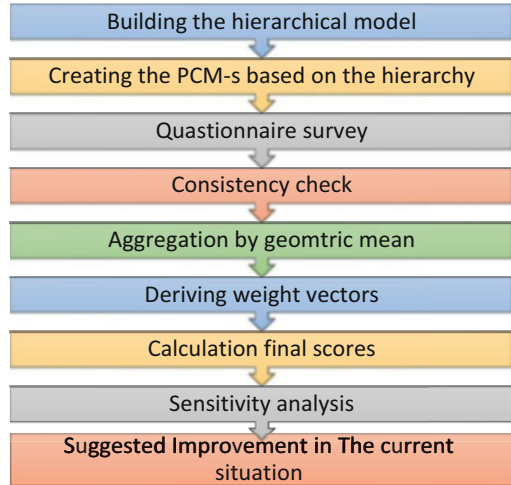


Table 1 The hierarchical model

| Level 1 | Level 2 | Level 3 |
|---|----------------------------|-------------------------|
| Supply quality | Service quality | Approachability |
| Service quality Transport quality Traceability Cost Environmental aspects | Approachability | Distance to stop |
| | Directness | Safety of stops |
| | Time availability | Comfort of stops |
| | Speed | Capacity of stops |
| | Reliability | |
| | Cleanliness and aesthetics | |
| | Transport quality | Directness |
| | Comfortability | Need for transfer. |
| | Safety of travel | Fit connection |
| | Environmental protection | |
| | Tractability | Time availability |
| | Perspiciuity | Frequency of lines |
| | Information before travel | The limited time of use |
| | Information during travel | |
| Cost | Speed | |
| Subsidies | Journey time | |
| Affordability | Awaiting time | |
| | Time to reach stops | |
| Environmental aspects | Reliability | |
| CO ₂ emissions | Dynamic timetable | |
| Noises | Delay | |
| | Comfortability | |
| | Physical comfort | |
| | Mental comfort | |

(1/9, 1/8, 1/7, 1/6, 1/5, 1/4, 1/3, 1/2, 1, 2, 3, 4, 5, 6, 7, 8, 9). Matrix A is considered consistent if all of its elements are positive, transitive, and reciprocal (Saaty, 1977).

$$A = [a_{ij}] = \begin{bmatrix} 1 & a_{12} & \dots & a_{1j} & \dots & a_{1n} \\ a_{12}^{-1} & 1 & \dots & a_{2j} & \dots & a_{2n} \\ \vdots & \vdots & \ddots & \vdots & \ddots & \vdots \\ 1 & 1 & \dots & a_{ij} & \dots & a_{in} \\ a_{1j}^{-1} & a_{2j}^{-1} & \dots & \vdots & \dots & \vdots \\ \vdots & \vdots & \ddots & \vdots & \ddots & \vdots \\ 1 & 1 & \dots & 1 & \dots & 1 \\ a_{1n}^{-1} & a_{2n}^{-1} & \dots & a_{in}^{-1} & \dots & 1 \end{bmatrix} \quad (1)$$

$$a_{ij} = 1/a_{ji}, \quad a_{ij} = a_{ij} \cdot a_{jk}, \quad a_{ij} = 1/a_{ji} \quad (2)$$

Calculate the geometric mean (see Eq. 3) of each group for each level through the pairwise comparison matrices.

$$A = \left[\sqrt[h]{\prod_{k=1}^h a_{ijk}} \right] \quad i, j = 1, \dots, n \quad (3)$$

Calculate the normalization term of the weight for a corresponding element so that the components of the weights eventually add up to 1. Then calculate the aggregated eigenvector for the final score (see Eq. 4).

$$W_{Ai} = \frac{W_j}{W} \frac{W_{ij}}{\sum_{k=1}^n W_{ik}} = \left(\frac{W_j}{W} \frac{1}{\sum_{k=1}^n W_{ik}} \right) W_{ij} \quad (4)$$

2.1.1 Questionnaire Survey

The model shows the main factors on the supply side that can affect public transportation, and we will compare them based on the Saaty scale in Table 2 (Berritella et al., 2011; Saaty & Vargas, 2012).

2.1.2 Consistency Check

Compute the consistency index (CI), where λ_{max} is the maximum eigenvalue (Saaty, 1990).

Table 2 Saaty scale (Saaty & Vargas, 2012)

| Numerical values | Verbal scale | Explanation |
|------------------|--|---|
| 1 | Equal importance of both elements | Two elements contribute equally |
| 3 | Moderate importance of one element over another | Experience and judgment favor one element over another |
| 5 | Strong importance of one element over another | An element is strongly favored |
| 7 | Very strong importance of one element over another | An element is very strongly dominant |
| 9 | Extreme importance of one element over another | An element is favored by at least an order of magnitude |
| 2,4,6,8 | Intermediate values | Used to compromise between two judgments |

Table 3 Consistency indices for a randomly generated matrix (Saaty & Vargas, 2012)

| N | 2 | 3 | 4 | 5 | 6 | 7 | 8 |
|----|---|------|-----|------|------|------|------|
| RI | 0 | 0.58 | 0.9 | 1.12 | 1.24 | 1.32 | 1.41 |

$$CI = \frac{\lambda_{\max} - n}{n - 1} \tag{5}$$

Compute the random index, RI, based on the number of criteria using the random consistency index table (Table 3).

Accept the matrix if consistency ratio, CR < 0.1, where CR is the consistency ratio because the experiential matrices most of the time is not consistent (Saaty & Vargas, 2006). CR can be determined by:

$$CR = \frac{CI}{RI} \tag{6}$$

3 Results and Discussion

After analyzing and visualizing the participants’ opinions about the development of the public transportation system in Budapest City basically by evaluating the factors and characteristics of the supply quality of the public transportation system in the city, for sure there will be some differences between the experts’ overview and the passengers’ overview although the experts have more knowledge about the transportation process and its development in a more detailed way. However, the AHP method will provide more awareness and enlightenment about public transport development based on pairwise comparisons than using simple statistical surveys.

Table 4 The supply quality (passengers' side) (study results)

| Passengers side | | | | | | |
|-----------------------|-----------------|-------------------|--------------|-----------------------|------|---------|
| Supply quality | Service quality | Transport quality | Traceability | Environmental aspects | Cost | Weights |
| Service quality | 1.00 | 1.31 | 1.78 | 0.69 | 0.22 | 13.04% |
| Transport quality | 0.76 | 1.00 | 1.98 | 0.95 | 0.21 | 12.84% |
| Traceability | 0.56 | 0.51 | 1.00 | 0.39 | 0.20 | 7.53% |
| Environmental aspects | 1.46 | 1.05 | 2.56 | 1.00 | 0.44 | 17.91% |
| Cost | 4.62 | 4.68 | 4.93 | 2.30 | 1.00 | 48.69% |
| CR = 0.017 | | | | Sum= | | 100% |

Table 5 The supply quality (experts' side) (study results)

| Experts side | | | | | | |
|-----------------------|-----------------|-------------------|--------------|-----------------------|------|---------|
| Supply quality | Service quality | Transport quality | Traceability | Environmental aspects | Cost | Weights |
| Service quality | 1.00 | 1.15 | 0.95 | 0.65 | 0.35 | 14.17% |
| Transport quality | 0.87 | 1.00 | 1.55 | 0.93 | 0.48 | 16.99% |
| Traceability | 1.06 | 0.64 | 1.00 | 0.43 | 0.57 | 13.29% |
| Environmental aspects | 1.55 | 1.08 | 2.31 | 1.00 | 0.64 | 22.50% |
| Cost | 2.90 | 2.10 | 1.76 | 1.57 | 1.00 | 33.05% |
| CR = 0.021 | | | | Sum= | | 100% |

The answers have been aggregated by using the geometric mean as mentioned in the methodology.

Based on the responses of the two groups and using the AHP method, evaluating and weighing the characteristics in each level separately, Tables 4 and 5 show the

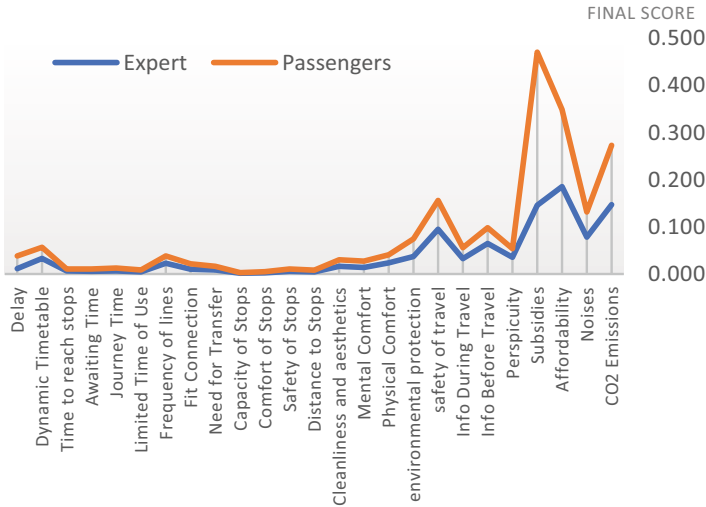


Fig. 2 The model element final score (both sides)

factors (the weights and the final score and the consistency ratio) which have been calculated for the first level, the supply quality characteristics from both sides:

We evaluated and weighed the characteristics at each level with the same process. Combining both sides in one figure shows which conflict points in the comparison and where we had big similarities in the basic component in the comparison; see Fig. 2.

The calculation shows that the cost played a very important role in the decision-making and noticeably affected the answers of the evaluators from both sides, but we can say that the experts’ opinions were more consistent than those of the normal passengers. On the experts’ side, the affordability of travel is the dominant factor from the cost criterion. What comes immediately after that is CO₂ emission from the environmental aspect criterion. On the passengers’ side, the subsidies are the dominant factor in the cost and then the affordability.

3.1 Sensitivity Analysis

Since in both cases the cost was the strongest factor affecting the evaluation process to know how deep does the cost affect the choices of other criteria, we apply sensitivity analysis (see Fig. 3) to the results to see how much a simple change in the ratio of the critical weight could affect the other weights and the final score of the characteristics. Applying sensitivity analysis to such decision-making processes is essential to ensure the consistency of the final decision. Sensitivity analysis gives the decision-maker confidence in consistency and robustness (Sun & Li, 2010). Compared with the conventional transportation evaluation methods. Through sensitivity

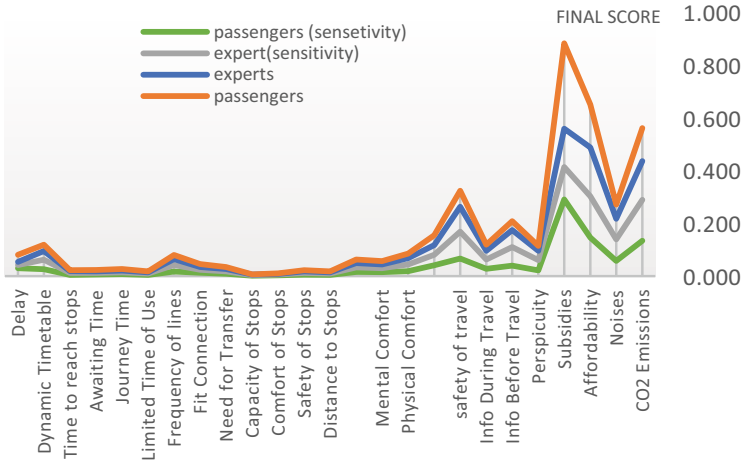
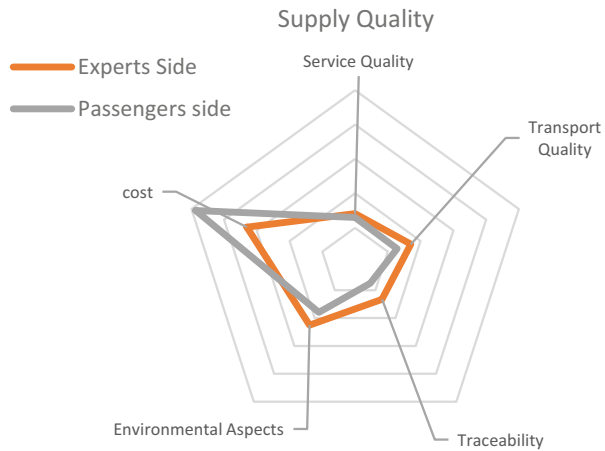


Fig. 3 Sensitivity analysis

Fig. 4 First-level element outcome in the model



analysis, different “what-if” scenarios can be visualized which is helpful to observe the impact of changing criteria to final alternative rank.

The sensitivity analysis has been taken to the critical elements in the first level only (the cost) by decreasing a very small amount of 0.05 of the weights and increasing it equally to the other remaining criteria observing the concluded changes in the model. The results show that both CO₂ emissions and safety of travel will be the most affected by the small change in the cost (neglecting the sub-criteria of the cost).

Since the cost of the transport process is the strongest and the dominant element in the evaluation from both sides (see Fig. 4), the cost may determine the level of the transport system and the type of transportation projects which will impact strongly

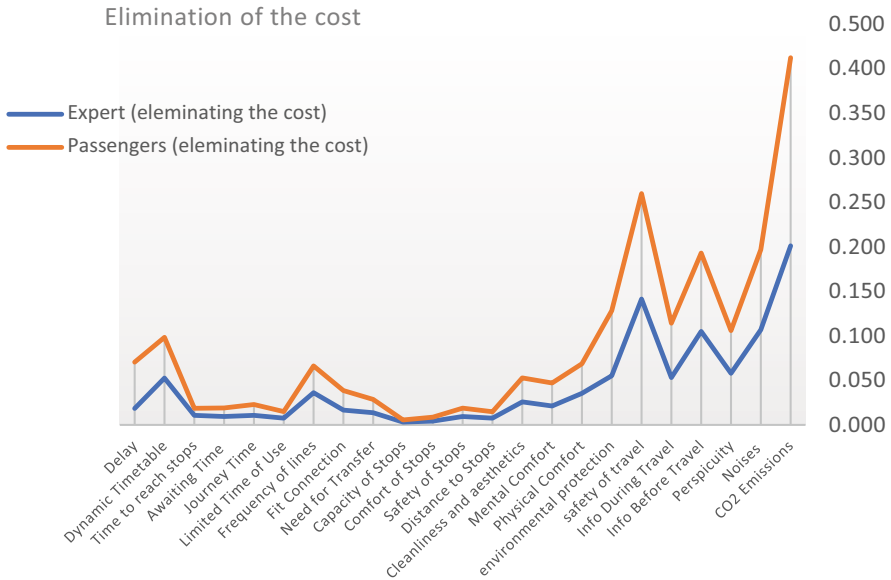


Fig. 5 The model elements excluding the cost

on the community’s economic development objectives, such as productivity, employment, business activity, property values, investment, and tax revenues.

Including the cost in the model showed how the financial issues could play a decisive role in the development. So, it could help to investigate the evaluation of the model elements by eliminating the cost-effectiveness and checking what would be the next critical characteristics by eliminating the cost-effectiveness from the first level as is shown in Fig. 5.

In general, including the cost in the model showed how the financial issues are crucial in the development especially on the passengers’ side. The distribution among the experts is also displayed in a balanced and well-distributed manner. In the first level, both the cost and the environmental aspects were the dominant factors, and in the second level, the sub-criteria of the cost and both subsidies and affordability were dominant. The CO₂ emissions from the experts’ side also were one of the decisive factors since it was in second place, yet the passengers’ side focused more on the financial issues. In the third level of the hierarchy, a conflict of the dominant factors between the two groups is obvious in the experts’ side the dynamic timetable followed by the physical comfort are the dominant and putting the frequency of lines in the third order, in the passengers’ side the dominant factors in sequence are the delay (since the passengers use the transportation in a regular way which makes them the most side affected by the delay of the trip) followed by the dynamic time table and the physical comfort in the third place.

4 Conclusion

The research outcomes revealed a priority ranking and scaling of the elements of supply quality within each level, which is a direct reflection on the transportation system of the city and trying to decrease the growing gap between the demand and supply in Budapest City, multi-criteria play a decisive role, Based on quantitative and qualitative criteria using the conventional, classic and simplified analytical hierarchical process (AHP) method for decision-making approach shows the discrepancies among the visions. The results of this survey were based on a total of 40 participants from 2 groups the experts and the passengers, and it should be mentioned that the results could vary if more participants and more groups are included.

The cost and the environmental aspects are the critical elements which requested a suggested suitable low-priced and environmentally friendly transport process which should be reached by the cooperation of all stakeholders. Another inevitable issue is to revise the issue of the safety of travel.

4.1 Recommendation and Future Work

The AHP method showed that taking different groups' preferences and more evaluator's numbers would open the discussion to new non-mentioned challenges. The research included a specific number while including more evaluators and more groups allowing a more accurate investigation.

References

- Akdemir, F., Ulvi, H., Ekiz, A., & Yılmaz, S. (2018). The use of multi-criteria assessment techniques in defining sustainable transport systems for different sized cities Ankara and rize example. In *Beyond all limits*, Ankara, Turkey, pp. 43–49.
- Berritella, M., et al. (2011). An analytic hierarchy process for the evaluation of transport policies to reduce climate change impacts. *SSRN Electronic Journal*. <https://doi.org/10.2139/ssrn.962379>
- Brunneli, M. (2015). *Introduction to the analytic hierarchy process, learning from failures*. Springer.
- Comtois, C., & S. B. (2009). *The geography of transport systems*. Routledge. <https://doi.org/10.4324/9780203884157>
- Duleba, S. (2019). An AHP-ISM approach for considering public preferences in a public transport development decision. *Transport*, 34(6). <https://doi.org/10.3846/transport.2019.9080>
- Duleba, S., & Moslem, S. (2018). Sustainable urban transport development with stakeholder participation, an AHP-Kendall model: A case study for Mersin. *Sustainability (Switzerland)*, 10(10). <https://doi.org/10.3390/su10103647>
- Duleba, S., Mishina, T., & Shimazaki, Y. (2012). A dynamic analysis on public bus transport's supply quality by using AHP. *Transport*, 27(3), 268–275. <https://doi.org/10.3846/16484142.2012.719838>

- Eskandarpour, M., et al. (2015). Sustainable supply chain network design: An optimization-oriented review. *Omega (United Kingdom)*. <https://doi.org/10.1016/j.omega.2015.01.006>
- Figueira, J. E., et al. (2004). multiple criteria decision analysis: State of the art surveys operations research & management science, methods. In *eBook*. ISBN: 0-387-23081-5.
- Jenks, M. J., Burgess, M. J. R., Acioly, C., Allen, A., Barter, P. A., & Brand, P. (2000). *Compact cities: Sustainable urban forms for developing countries*. Spon.
- Mardani, A., et al. (2015). Multiple criteria decision-making techniques and their applications – A review of the literature from 2000 to 2014. *Economic Research-Ekonomika Istrazivanja*. <https://doi.org/10.1080/1331677X.2015.1075139>
- Nakagawa, T., & Sekitani, K. (2004). A use of analytic network process for supply chain management. *Asia Pacific Management Review*. <https://doi.org/10.6126/APMR.2004.9.5.02>. airitilibrary.com.
- Saaty, T. L. (1977). A scaling method for priorities in hierarchical structures. *Journal of Mathematical Psychology*, 15(3). [https://doi.org/10.1016/0022-2496\(77\)90033-5](https://doi.org/10.1016/0022-2496(77)90033-5)
- Saaty, T. L. (1990). How to make a decision: The analytic hierarchy process. *European Journal of Operational Research*, 48(1). [https://doi.org/10.1016/0377-2217\(90\)90057-1](https://doi.org/10.1016/0377-2217(90)90057-1)
- Saaty, T. L. (2001). *Fundamentals of decision making and priority theory*. RWS Publications.
- Saaty, T. L. (2002). Decision making with the analytic hierarchy process. *Scientia Iranica*, 9(3). <https://doi.org/10.1504/ijssci.2008.017590>
- Saaty, T. L., & Vargas, L. G. (2006). Decision making with the analytic process network process. (Vol. 282). Berlin, Germany: Springer Science+ Business Media, LLC.
- Saaty, T. L., & Vargas, L. G. (2012). The possibility of group choice: Pairwise comparisons and merging functions. *Social Choice and Welfare*, 38(3). <https://doi.org/10.1007/s00355-011-0541-6>
- Sabaei, D., Erkoyuncu, J., & Roy, R. (2015). A review of multi-criteria decision making methods for enhanced maintenance delivery. *Procedia CIRP*. <https://doi.org/10.1016/j.procir.2015.08.086>
- Snyder, L. V., et al. (2016). OR/MS models for supply chain disruptions: A review. *IIE Transactions (Institute of Industrial Engineers)*. <https://doi.org/10.1080/0740817X.2015.1067735>
- Sun, X., & Li, Y. (2010). An intelligent multi-criteria decision support system for systems design. In *10th AIAA aviation technology, integration and operations conference 2010, ATIO 2010*. <https://doi.org/10.2514/6.2010-9222>
- van den Berg, L., van der Meer, J., & Carvalho, L. (2014). *Cities as engines of sustainable competitiveness: European urban policy in practice*. Ashgate.
- Velasquez, M., & Hester, P. (2013). An analysis of multi-criteria decision making methods. *International Journal of Operations Research*, 10(2), 56–66.
- Zuidegeest, M. H. P., & Van Maarseveen, M. F. A. M. (2006). Sustainable urban transport development: A modelling approach. *WIT Transactions on Ecology and the Environment*, 93. <https://doi.org/10.2495/SC060631>

Human Error Assessment and Reduction Technique in Aircraft Maintenance



Ebru Yazgan and Elif Kılıç Delice

Contents

| | | |
|-----|---|-----|
| 1 | Introduction | 96 |
| 2 | Methodology | 97 |
| 2.1 | HEART Approach | 97 |
| 3 | The Proposed HEART Approach for an Aircraft Maintenance Application | 100 |
| 4 | Discussion and Conclusion | 102 |
| | References | 103 |

Nomenclature

| | |
|-------|---|
| EPC | Error-producing conditions |
| GTT | Generic tasks types |
| HEART | Human error evaluation and reduction method |
| HEP | Human error probability |
| HRA | Human reliability analysis |

E. Yazgan (✉)

Eskisehir Technical University Faculty of Aeronautics and Astronautics, Department of Airframe and Powerplant Maintenance, Eskisehir, Turkiye
e-mail: eyazgan@eskisehir.edu.tr

E. K. Delice

Atatürk University Faculty of Engineering, Department of Industrial Engineering, Erzurum, Turkiye
e-mail: elif.kdelice@atauni.edu.tr

1 Introduction

Human error is a major contributing factor in aviation accidents and human error has been cited as the cause of 60–80% of aviation accidents (Guo & Sun 2020; Erjavac et al., 2018). Human reliability analysis (HRA) is a systematic approach to identify, quantify, and reduce the human errors of human–machine systems. Human reliability is defined as the probability of successful performance of a task and human errors are the human behaviours that fall outside the tolerance scope of a system where a person operates (Hou et al., 2021). Numerous HRA approaches have been proposed to calculate HEP and evaluate human performance and also to investigate human-related errors (HREs) such as HEART, technique for human error rate prediction (THERP), cognitive reliability and error analysis method (CREAM), standardized plant analysis risk human reliability analysis (SPAR-H), and an advanced human error assessment approach (Swain & Guttman, 1983; Hannaman & Spurgin, 1984; Cooper et al., 1996; Hollnagel, 1998; Gertman et al., 2005; Can & Delice, 2020).

The aircraft maintenance technician (AMT) is the most important part of the maintenance system that ensures the aircraft to fly for many years by performing the necessary maintenance. The slightest mistake made by the technician while performing his/her duties in aircraft maintenance poses a serious risk in terms of flight safety. Therefore, it is very important to detect the mistakes that AMT will make and to develop suggestions to prevent or correct these mistakes (Latorella & Prabhu, 2000).

There are very few studies on the use of the HEART technique in aviation. Gibson and Kirwan (2008) explain that controller action reliability assessment (CARA) is a human reliability assessment technique used to quantify human performance in the context of air traffic management (ATM). CARA involves the use of specific data for quantification, the identification and measurement of various types of air traffic controller behaviors, and the utilization of performance shaping factors (PSFs) to adjust task reliability. This method serves as a valuable tool for evaluating and quantifying human performance within the critical domain of ATM. This method serves as a valuable tool for evaluating and quantifying human performance within the critical domain of ATM. Guo and Sun (2020) propose and apply an integrated human reliability quantitative method to assess flight safety in civil aviation. They employ the improved analytic hierarchy process (IAHP) method to determine the APOA value of each EPC and then these APOA values are integrated into the HEART approach to derive the HEP of flight tasks. Chiu and Hsieh (2016) developed a latent human error analysis process to explore the factors of latent human error in aviation maintenance tasks and to provide an efficient improvement strategy for addressing those errors. They used HFACS and RCA to define the error factors related to aviation maintenance tasks and established a new analytic process for investigating latent human error and provides a strategy for analysing human error using fuzzy TOPSIS. Hybrid human error assessment (HHEA) is proposed in order to reduce the subjectivity of experts' judgements by calculating assessed proportion of affect (APOA) of error-producing conditions (EPCs) on human error

probability (HEP) integrating HEART and analytic network process (ANP) method (Yazgan & Delice, 2021).

2 Methodology

This section discusses the HEART approach.

2.1 HEART Approach

Among HRA approaches, HEART approach advanced by Williams (1988) is the most commonly used one. HEART considers the types of potential human errors, the estimated probability of such errors being made, factors that may influence this probability (e.g., time pressure, stress, poor working environment, and low morale), prevention ways of identified human errors in the design, and additional mitigating controls that can be needed for reducing their impact (Can & Delice, 2020).

There are three key elements in the HEART approach (Gibson & Kirwan, 2008):

2.1.1 Generic Task Types

In the HEART technique, a specific task is compared with generic tasks types (GTTs), of which there are eight qualitative descriptions (from A to M) and additional one (if none of the eight descriptions are appropriate for the task) (Akyuz & Celik, 2016). Definitions of GTTs and their nominal human unreliability values are given in Table 1.

2.1.2 Error-Producing Conditions

In addition to GTTs, HEART also uses EPCs. HEART includes 38 different EPCs. The impact of EPCs can change the predicted reliability of task performance. The EPCs are shown in Table 2. EPCs are factors that are predicted to negatively impact human performance and therefore increase the likelihood of overall human error associated with a GTT.

Table 1 GTTs (Williams, 1988)

| Generic tasks | | Nominal human unreliability (GTT) |
|---------------|--|-----------------------------------|
| A | Totally unfamiliar, performed at speed with no real idea of likely consequences | 0.55 (0.35–0.97) |
| B | Shift or restore the system to a new or original state on a single attempt without supervision or procedures | 0.26 (0.14–0.42) |
| C | Complex task requiring a high level of comprehension and skill | 0.16 (0.12–0.28) |
| D | Fairly simple task performed rapidly or given scant attention | 0.09 (0.06–0.13) |
| E | Routine, highly practised, a rapid task involving a relatively low level of skill | 0.02 (0.007–0.045) |
| F | Restore or shift a system to original or new state following procedures, with some checking | 0.003 (0.0008–0.0035) |
| G | Completely familiar, well-designed, highly practised, routine task occurring several times per hour, performed to highest possible standards by a highly motivated, highly trained and experienced person, totally aware of implications of failure, with time to correct a potential error, but without the benefit of significant job aids | 0.0004 (0.00008–0.009) |
| H | Respond correctly to system command even when there is an augmented or automated supervisory system providing an accurate interpretation of system stage | 0.00002 (0.000006–0.00009) |
| M | Miscellaneous task for which no description can be found (nominal 5th–95th percentile data spreads were chosen on the basis of experience suggesting log normality) | 0.03 (0.008–0.11) |

2.1.3 Calculation Method

HEART uses a simple calculation method to combine GTT HEP and EPC values. It also allows modification of the strength of effect of EPCs through a weighting process.

The HEP is calculated with Eq. (1) as follows:

$$\begin{aligned}
 \text{HEP} = & \text{GTT} \times [(\text{EPC}_1 - 1) \times \text{APOA}_1 + 1] \times [(\text{EPC}_2 - 1) \times \text{APOA}_2 + 1] \\
 & \times \dots \times [(\text{EPC}_n - 1) \times \text{APOA}_n + 1]
 \end{aligned}
 \tag{1}$$

where

GTT = the human error probability associated with a GTT (5th–95th percentile boundaries)

EPC = the maximum affect associated with an EPC

APOA = is the assessed proportion of affect value between 0 and 1, where 0 is a no effect and 1 is a full affect.

Table 2 EPCs (Williams, 1988)

| EPCs | | Maximum predicted nominal amount |
|------|---|----------------------------------|
| 1 | Unfamiliarity with a situation which is potentially important but which only occurs infrequently or which is novel | ×17 |
| 2 | A shortage of time available for error detection and correction | ×11 |
| 3 | A low signal-to-noise ratio | ×10 |
| 4 | A means of suppressing or overriding information or features which is too easily accessible | ×9 |
| 5 | No means of conveying spatial and functional information to operators in a form which they can readily assimilate | ×8 |
| 6 | A mismatch between an operator’s model of the world and that imagined by the designer | ×8 |
| 7 | No obvious means of reversing an unintended action | ×8 |
| 8 | A channel capacity overload, particularly one caused by simultaneous presentation of nonredundant information | ×6 |
| 9 | A need to unlearn a technique and apply one which requires the application of an opposing philosophy | ×6 |
| 10 | The need to transfer specific knowledge from task to task without loss | ×5.5 |
| 11 | Ambiguity in the required performance standards | ×5 |
| 12 | A mismatch between perceived and real risk | ×4 |
| 13 | Poor, ambiguous, or ill-matched system feedback | ×4 |
| 14 | No dear direct and timely confirmation of an intended action from the portion of the system over which control is to be exerted | ×3 |
| 15 | Operator inexperienced (e.g., a newly qualified tradesman, but not an “expert”) | ×3 |
| 16 | An impoverished quality of information conveyed by procedures and person–person interaction | ×3 |
| 17 | Little or no independent checking or testing of output | ×3 |
| 18 | A conflict between immediate and long-term objectives | ×2.5 |
| 19 | Not enough information to allow completeness or accuracy checks to be undertaken | ×2.5 |
| 20 | A mismatch between the educational achievement level of an individual and the requirements of the task | ×2 |
| 21 | An incentive to use other more dangerous procedures | ×2 |
| 22 | Little opportunity, such as rest breaks, to exercise mind and body outside the immediate confines of a job | ×1.8 |
| 23 | Unreliable instrumentation used to communicate information leading to lack of trust and person performing the task ignoring information | ×1.6 |
| 24 | A need for decision making which is beyond the capabilities or experience of the person performing the task | ×1.6 |
| 25 | Unclear allocation of role and responsibility | ×1.6 |
| 26 | No obvious way to keep track of progress during an activity | ×1.4 |
| 27 | Task requirement exceeds the physical capabilities of the person performing the task | ×1.4 |

(continued)

Table 2 (continued)

| EPCs | Maximum predicted nominal amount | |
|------|--|--|
| 28 | Person performing the task is unaware of its significance and their contribution to corporate objectives | ×1.4 |
| 29 | High-level emotional stress | ×1.3 |
| 30 | Evidence of ill-health amongst operatives, especially fever | ×1.2 |
| 31 | Low workforce morale | ×1.2 |
| 32 | Information displayed and how this is applied within procedures or working practices is not fully understood | ×1.2 |
| 33 | A poor or hostile environment (below 75% of health or life-threatening severity) | ×1.15 |
| 34 | Prolonged inactivity or highly repetitious low mental workload tasks | ×1.1 for first half-hour ×1.05 for each hour thereafter |
| 35 | Disruption of normal work–sleep cycles | ×1.1 |
| 36 | Pressure from someone else to increase the speed or pace at which a task is performed, beyond an individual's preferred pace and capability | ×1.06 |
| 37 | Additional team members over and above those necessary to perform task normally and satisfactorily | ×1.03 per additional man |
| 38 | Age of personnel performing perceptual tasks requiring the ability to interpret or become aware of something through the senses (sight, hearing, taste, smell, or touch) | ×1.02 |

3 The Proposed HEART Approach for an Aircraft Maintenance Application

In this section, a proposed HEART approach for aircraft maintenance application for the training aircraft of Cessna 172 Series aircraft type is introduced.

Step 1: Select of Aircraft Maintenance Application

In the first step, an aircraft maintenance practice affecting flight safety is selected. In this study maintenance practice of elevators, the most critical of the primary aircraft flight controls, in which a pilot controls the direction and attitude of an aircraft in flight, is selected in the training aircraft of Cessna 172 Series aircraft type by taking expert opinions.

Step 2: Determine Tasks Related to Selected Maintenance Application

In this step, the main tasks and sub-tasks of the selected maintenance practice are determined according to aircraft maintenance manual (AMM). AMM is the main book on aircraft maintenance, including information about systems, disassembly of systems consisting of aircraft parts, maintenance practices, settings, checks refuelling, part replacement, operating limits, tests, cleaning, painting, etc.

Elevator maintenance considered in this study is performed in the hangar. In this step, it is to define the task related to the selected critical aircraft maintenance

Table 3 HEP values for elevator maintenance application

| Task | Task name | GTTs | EPCs | APOA | HEP |
|------|---|------|------------------------------------|-----------------|----------|
| 1. | Elevator remove | | | | |
| 1.1 | Disconnect the push-pull channel from the elevator trim-tab horn | D | EPC33– EPC34 | 0.3–0.3 | 9.69E-02 |
| 1.2 | Remove the bolts that attach the tube assembly to the aft bell crank | E | EPC33– EPC34 | 0.3–0.3 | 2.15E-02 |
| 1.3 | With a support for the elevator installed, remove the bolts from the elevator hinge brackets and remove the elevator half | F | EPC2– EPC27– EPC30– EPC33 | 0.5–0.4–0.3–0.3 | 2.31E-02 |
| 2. | Elevator install | | | | |
| 2.1 | Attach the tube assembly of the elevator to the aft bell crank | F | EPC2– EPC21– EPC23– EPC33 | 0.5–0.3–0.3–0.3 | 2.89E-02 |
| 2.2 | Attach the elevator to the horizontal stabilizer at the hinge points with the bolts | F | EPC2– EPC21– EPC23– EPC33 | 0.5–0.3–0.3–0.3 | 2.89E-02 |
| 2.3 | Connect the push-pull channel (opening down) to the elevator trim-tab horn | F | EPC2– EPC21– EPC23– EPC33 | 0.5–0.3–0.3–0.3 | 2.89E-02 |
| | | | Mean of HEP value | | 3.80E-02 |

practice, which includes the main and sub-tasks in training aircraft. Table 3 shows the elevator maintenance practice.

Step 3: Select GTT for Selected Aircraft Maintenance Task

In this step, GTT is selected. Since there are nine qualitative descriptions of actions (from A to M) defined in the HEART method, the most appropriate GTT is nominated by decision maker (Akyuz & Celik, 2016). The experts select applicable GTT for each sub-tasks of elevator maintenance practice given in Table 3.

Step 4: Assign EPCs for Selected Aircraft Maintenance Task

After selected the GTTs, in this step the appropriate EPCs is selected by aircraft maintenance experts from the list of 38 conditions in order to calculate HEP. Experts are the same approved aircraft maintenance technicians by maintenance organization. Table 3 illustrates the selected EPCs by the consensus of technicians for elevator maintenance practice.

Step 5: Determine APOA Values

In this step, the APOA value indicating the effect of each EPC is evaluated between 0 and 1. In the traditional HEART method, the APOA calculation is done by the decision maker.

Step 6: Identify HEP Value of Each Selected Aircraft Maintenance Task

The HEP is calculated for each sub-task according to Eq. (1). HEP values of the traditional HEART for elevator maintenance practice are given in Table 3.

For example, HEP for sub-task 1.1 is calculated as shown:

$$\begin{aligned} \text{HEP}_{1.1} &= D \times [(EPC_{33} - 1) \times APOA_{33} + 1] \times [(EPC_{34} - 1) \times APOA_{34} + 1] \\ &= 0.09 \times [(1.15 - 1) \times 0.3 + 1] \times [(1.1 - 1) \times 0.3 + 1] = 9.69E-02 \end{aligned}$$

According to Table 3, it is observed that the HEP values of sub-task 1.1 is higher than the average HEP value.

4 Discussion and Conclusion

This study proposes a HEART model that can help improve the safety of aircraft maintenance operations and produce useful results in increasing the reliability of aircraft maintenance repairs and aircraft usability. The results obtained are considered to be an effective and strategic tool for AMOs to increase their performance. Decision makers can increase human performance and reliability by applying mitigation measures on critical EPCs to increase flight safety with a proactive approach in aircraft maintenance. In future study, necessary corrective and preventive actions are taken for EPCs in order to reduce probability of human error and re-calculated HEP values considered.

In this study, the HEP values of sub-task 1.1 is higher than the average HEP value. Sub-task 1.1 has highest probability of human error due to the poor environment and highly repetitious cycling of low mental workload tasks. The sub-task 1.1 is assigned as simple task performed rapidly or given scant attention. Removal of any part is a simpler task in aircraft maintenance than installation. That is, this task is considered to be repetitive tasks. However, many research studies have been conducted on repetitive tasks in work environments where employees perform the same action over and over again in a short period of time. So, repetitive tasks are considered human risk factors (Yazgan, 2018). Proposed nominal human unreliability of this task is also higher than other subtasks. Errors made while removing in aircraft maintenance may cause damage to very critical parts such as elevators, causing the aircraft to fall. Therefore, environmental and organizational ergonomic arrangements are required to reduce the technician's error due to the working environment conditions and the slackness caused by doing such repetitive tasks.

References

- Akyuz, E., & Celik, E. (2016). A hybrid human error probability determination approach: The case of cargo loading operation in oil/chemical tanker ship. *Journal of Loss Prevention in the Process Industries*, 43, 424–431.
- Can, G. F., & Delice, E. K. (2020). An advanced human error assessment approach: HEART and AV-DEMATEL. *Human Factors and Ergonomics in Manufacturing*, 30, 29–49.
- Chiu, M. C., & Hsieh, M. C. (2016). Latent human error analysis and efficient improvement strategies by fuzzy TOPSIS in aviation maintenance tasks. *Applied Ergonomics*, 54(9), 136–147.
- Cooper, S. E., Ramey-Smith, A. M., Wreathall, J., & Parry, G. W. (1996). *A technique for human error analysis (ATHEANA)* (No. NUREG/CR-6350; BNL-NUREG-52467). Nuclear Regulatory Commission, Washington, DC (United States). Division of Systems Technology; Brookhaven National Laboratory, Upton, NY (United States); Science Applications International Corp., Reston, VA (United States); NUS Corp., Gaithersburg, MD (United States).
- Erjavac, A. J., Iammartino, R., & Fossaceca, J. M. (2018). Evaluation of preconditions affecting symptomatic human error in general aviation and air carrier aviation accidents. *Reliability Engineering & System Safety*, 178, 156–163.
- Gertman, D., Blackman, H., Marble, J., Byers, J., & Smith, C. (2005). The SPAR-H human reliability analysis method. *US Nuclear Regulatory Commission*, 230, 35.
- Gibson, W., & Kirwan, B. (2008). *Application of the CARA HRA tool to Air Traffic Management safety cases*. PSAM.
- Guo, Y., & Sun, Y. (2020). Flight safety assessment based on an integrated human reliability quantification approach. *PLoS One*, 15(4), e0231391. <https://doi.org/10.1371/journal.pone.0231391>
- Hannaman, G. W., & Spurgin, A. J. (1984). *Systematic human action reliability procedure (SHARP)* (Interim report No. EPRI-NP-3583). NUS Corporation.
- Hollnagel, E. (1998). *Cognitive reliability and error analysis method (CREAM)*. Elsevier.
- Hou, L.-X., Liu, R., Liu, H.-C., & Jiang, S. (2021). Two decades on human reliability analysis: A bibliometric analysis and literature review. *Annals of Nuclear Energy*, 151, 107969. <https://doi.org/10.1016/j.anucene.2020.107969>
- Latorella, K. A., & Prabhu, P. V. (2000). Review of human error in aviation maintenance and inspection. *International Journal of Industrial Ergonomics*, 26(2), 133–161.
- Swain, A. D., & Guttman, H. E. (1983). *Handbook of human-reliability analysis with emphasis on nuclear power plant applications* (Final report No. NUREG/CR-1278; SAND-80-0200). Sandia National Labs., Albuquerque, NM.
- Williams, J. C. (1988). A data-based method for assessing and reducing human error to improve operational performance. In W. Hagen (Ed.), *IEEE fourth conference on human factors and power plants*. IEEE.
- Yazgan, E. (2018). Development taxonomy of human risk factors for corporate sustainability in aviation sector. *Aircraft Engineering and Aerospace Technology*, 90(6), 1012–1022.
- Yazgan, E., & Delice, E. K. (2021). Hybrid human error assessment approach for critical aircraft maintenance practice in the training aircraft. *The International Journal of Aerospace Psychology*, 32, 114–137. <https://doi.org/10.1080/24721840.2021.1946399>

Assessment of Environmental Performance Indicators Based on Fuel Performance in an Aircraft Engine



Halil Yalcin Akdeniz

Contents

| | | |
|---|------------------------------|-----|
| 1 | Introduction | 105 |
| 2 | Method | 106 |
| 3 | Results and Discussion | 109 |
| 4 | Conclusion | 111 |
| | References | 111 |

Nomenclature

| | |
|------------------|----------------------|
| CH ₄ | Methane |
| CO | Carbon monoxide |
| CO ₂ | Carbon dioxide |
| NO ₂ | Nitrogen dioxide |
| S ₂ O | Sulphur dioxide |
| UHC | Unburned hydrocarbon |

1 Introduction

The importance of air transportation has increased because of the time it saves us in daily life. In this context, the number of aircraft in service has increased and air transport has more than expected contributions to energy use. The researchers in thermal engineering have thus attracted the attention of aircraft propulsion systems,

H. Y. Akdeniz (✉)

Eskisehir Osmangazi University, Eskisehir Vocational School, Industrial Zone,
Eskisehir, Turkiye

especially gas turbine engines. However, several early research papers stress the need for exergy as an optimization and design tool for the development of more efficient and environmentally friendly systems during the development processes of air propulsion systems (Bejan & Siems, 2001; Roth et al., 2002; Şöhret et al., 2015).

The development of efficient and cost-effective energy systems techniques is an important challenge facing energy researchers. It becomes more important to understand the methods that degrade energy and its resources and develop a systematic approach in a world with limited natural resources and increasing global demand for energy, with a systematic approach to improve the design of energy systems and reduce environmental impacts (Ameri et al., 2009). The number of energy system environmental impact researchers has grown in the last two decades. Aircraft engine emissions are the main source of air pollution around airports, which affects air quality locally and regionally. The most significant emissions are carbon monoxide (CO), carbon dioxide (CO₂), NO₂, SO₂, and UHC which have significant effects on human health (Atılğan et al., 2013; Sahu et al., 2018).

Exergy is a prominent instrument in the field of engineering that offers advantages, such as energy system evaluation and optimization. The first and second thermodynamic laws are included in the exergetic analysis. The first law addresses the conservation of energy and forms energy changes within the system. This enables us to understand the rate of energy conversion in other forms, while in actual operating conditions the second legislation on thermodynamics explains the theoretical limitations of a system. Exergy analysis, both based on the first and second thermodynamic laws, focuses in addition to quantity on the quality of energy consumption and conversion within a system. Therefore, the irreversibility and losses of the examined system are understandable (Dincer & Cengel, 2001; Pavelka et al., 2015; Rocco et al., 2014; Şöhret et al., 2015).

In this study, the effects of different fuel types in an aircraft engine on the environmental performance indicators of the engine have been investigated. In this regard, depending on the second law of thermodynamics and with the help of GasTurb Software in some parameters, exergy-based performance measures (environmental effect factor, exergetic sustainability index, and ecological effect factor) are used.

2 Method

Exergy equilibrium for any control volume at steady state could be found as follows (Balli, 2017; Çengel & Boles, 2015):

$$\sum \dot{E}_{X_{in}} = \dot{E}_{X_F} = \dot{E}_{X_{Pr}} + \sum_{k=1}^n \dot{E}_{X_{D,k}} + \dot{E}_{X_L} \quad (1)$$

In Eq. (1), $\dot{E}x$ is the exergy rate. The subscripts F, Pr, D, and L indicate the total inlet exergy as fuel exergy, the product exergy, the exergy destruction, and exergy losses, respectively.

Performance indicators are given in Eqs. (2)–(4). The environmental effect factor can be written as in Eq. (2) (Balli, 2017):

$$EEF_{sys} = \left(\frac{W \dot{E}x_{R_{sys}}}{\psi_{sys}} \right) \tag{2}$$

The exergetic sustainability index can be written as in Eq. (3) (Balli, 2017):

$$\dot{E}xSI_{sys} = \left(\frac{1}{EEF_{sys}} \right) \tag{3}$$

The ecological effect factor can be written as in Eq. (4) (Balli, 2017):

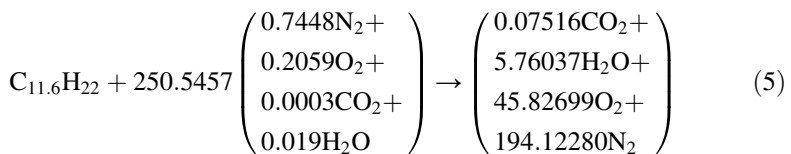
$$EcoEF_{sys} = \left(\frac{\dot{E}x_{F,sys}}{\dot{E}x_{Pr,sys}} \right) = \left(\frac{1}{\psi_{sys}} \right) \tag{4}$$

In this study, by operating an aircraft engine with three different fuels, the exergy-based environmental performance indicators of the engine were determined. Jet-A, natural gas, and AVGAS were used as fuel. The values of pressure and temperature for the reference ambient were assumed to be 101.33 kPa and 288.15 K. The inlet airflow was assumed to be 12 kg/s. The fuel flows of Jet-A, natural gas, and AVGAS are 0.270 kg/s, 0.242 kg/s, and 0.267 kg/s, respectively (GasTurb, 2021). At the end of the combustion process, complete combustion was assumed.

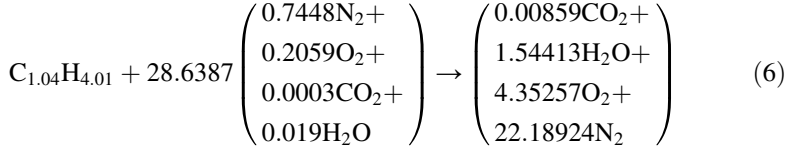
The chemical formulas for the fuels of Jet-A, natural gas, and AVGAS were taken as $C_{11.6}H_{22}$, $C_{1.04}H_{4.01}$, and $C_{7.68}H_{16.8}$, respectively. The lower heating values were taken as 43,080 kJ/kg for Jet-A, 48102 kJ/kg for natural gas, and 43,496 kJ/kg for AVGAS fuel (SAE, 2004; Topal & Turan, 2021).

Considering that the combustion energy in the combustion chamber is equal for three different fuels, the AFR (air-to-fuel ratio) values were calculated as 44.45 for Jet-A, 49.63 for natural gas, and 44.87 for AVGAS fuel. For these AFR values, When the aircraft engine is fuelled with Jet-A, natural gas, and AVGAS, the combustion equations expressed in terms of mole fractions of the gas components are calculated as in Eqs. (5)–(7), respectively.

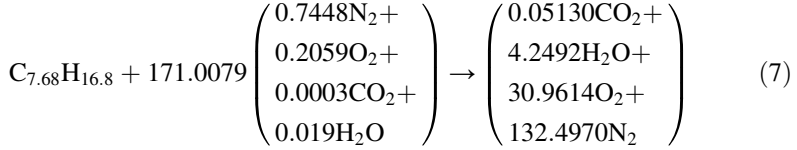
For Jet-A:



For natural gas:



For AVGAS:



After the combustion reaction, the universal gas constants (R_{gas}) of the exhaust emissions are calculated to be 0.29144847 kJ/kgK for Jet-A fuel, 0.29602385 kJ/kgK for natural gas fuel, and 0.29171912 kJ/kgK for AVGAS fuel. Based on the mass rates of the exhaust emissions, the $c_{p,g}$ values of combustion gases are calculated in terms of temperature as in Eqs. (8)–(11).

$$c_{p_{eg}}^{Jet-A}(T) = 0.99339 + \left(\frac{0.00581}{10^2}T\right) + \left(\frac{0.01853}{10^5}T^2\right) - \left(\frac{0.07384}{10^9}T^3\right) \quad (8)$$

$$c_{p_{eg}}^{NG}(T) = 1.01657 + \left(\frac{0.00441}{10^2}T\right) + \left(\frac{0.02080}{10^5}T^2\right) - \left(\frac{0.08051}{10^9}T^3\right) \quad (9)$$

$$c_{p_{eg}}^{AVGAS}(T) = 0.99476 + \left(\frac{0.00572}{10^2}T\right) + \left(\frac{0.01866}{10^5}T^2\right) - \left(\frac{0.07424}{10^9}T^3\right) \quad (10)$$

The specific heat capacity of air is a function of temperature, which can be written as follows (Balli, 2017; Çengel & Boles, 2015):

$$c_{p,a}(T) = 1.04841 - \left(\frac{3.83719}{10^4}T\right) + \left(\frac{9.45378}{10^7}T^2\right) - \left(\frac{5.49031}{10^{10}}T^3\right) + \left(\frac{7.92981}{10^{14}}T^4\right) \quad (11)$$

3 Results and Discussion

The fuel performance results on the exergy-based environmental performance indicators are illustrated in Figs. 1, 2, 3, and 4.

In the study, overall performance values for fuels have been estimated and given in Table 1.

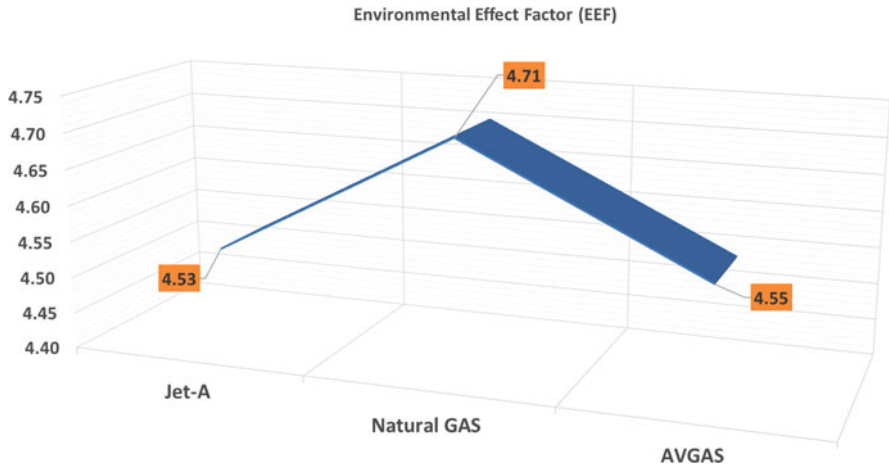


Fig. 1 Environmental effect factor (EEF) results of the fuels

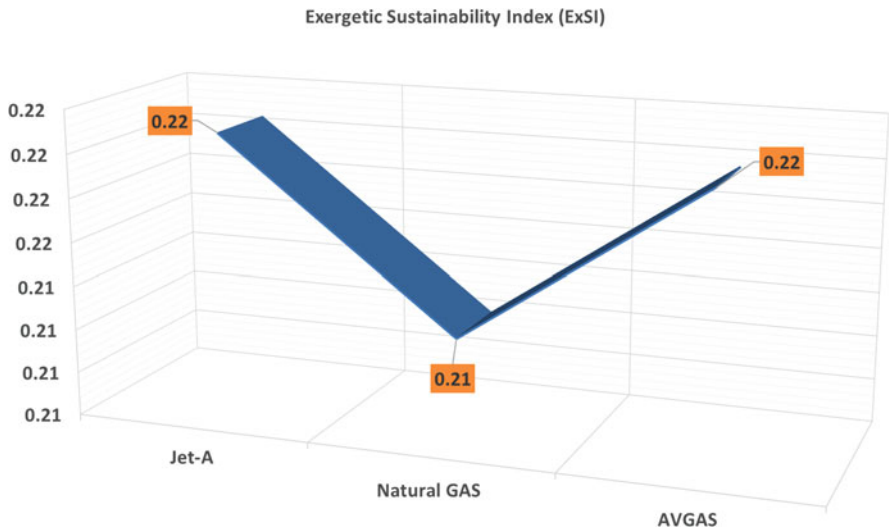


Fig. 2 Exergetic sustainability index (ExSI) results of the fuels

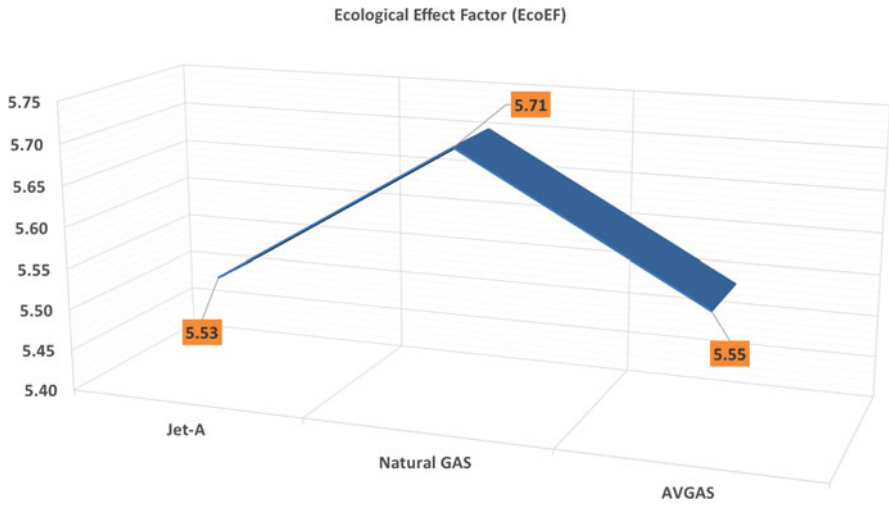


Fig. 3 Ecological effect factor (EcoEF) results of the fuels

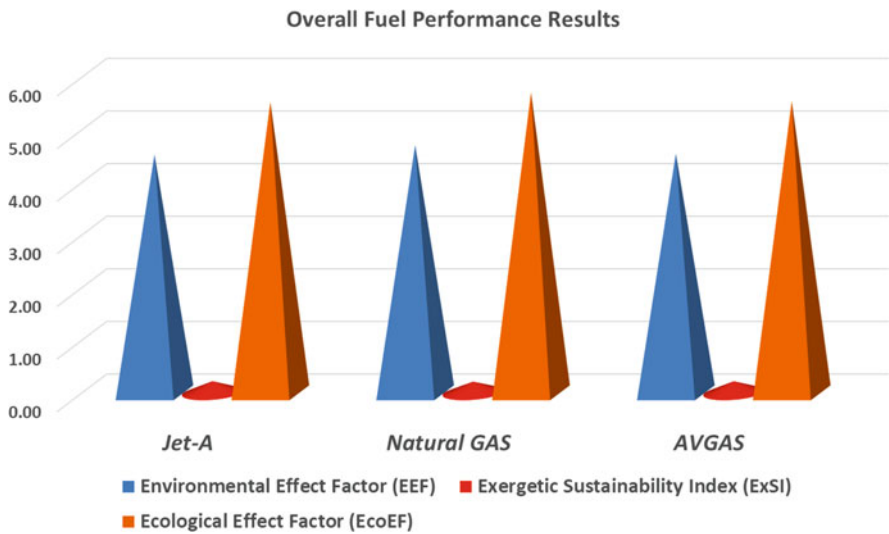


Fig. 4 Overall performance results of the fuels

Table 1 Performance results of the fuels

| Performance indicator | Jet-A | Natural gas | AVGAS |
|---------------------------------------|-------|-------------|-------|
| Environmental effect factor (EEF) | 4.53 | 4.71 | 4.55 |
| Exergetic sustainability index (ExSI) | 0.22 | 0.21 | 0.22 |
| Ecological effect factor (EcoEF) | 5.53 | 5.71 | 5.55 |

4 Conclusion

The primary results of the study can be summarized as follows:

The results of the Environmental indicator were calculated with a value of 4.53 for the Jet-A fuel, 4.71 for the Natural Gas fuel, and 4.55 for the AVGAS fuel. The results of the Exergetic Sustainability Index were obtained with a value of 0.22 for the Jet-A fuel, 0.21 for the Natural Gas fuel, and 0.22 for the AVGAS fuel. The results of the Ecological Effect Factor were estimated with a value of 5.53 for the Jet-A fuel, 5.71 for the Natural Gas fuel, and 5.55 for the AVGAS fuel.

According to the results, it can be seen that Natural Gas fuel has better environmental performance than other fuels. Also, these performance parameters are helpful to use how the aircraft engines become more environmentally for sustainable aviation.

References

- Ameri, M., Ahmadi, P., & Hamidi, A. (2009). Energy, exergy and exergoeconomic analysis of a steam power plant: A case study. *International Journal of Energy Research*, 33(5), 499–512. <https://doi.org/10.1002/er.1495>
- Atılgan, R., Turan, Ö., Altuntaş, Ö., Aydın, H., & Synylo, K. (2013). Environmental impact assessment of a turboprop engine with the aid of exergy. *Energy*, 58, 664–671. <https://doi.org/10.1016/j.energy.2013.05.064>
- Balli, O. (2017). Exergy modeling for evaluating sustainability level of a high by-pass turbofan engine used on commercial aircrafts. *Applied Thermal Engineering*, 123, 138–155. <https://doi.org/10.1016/j.applthermaleng.2017.05.068>
- Bejan, A., & Siems, D. L. (2001). The need for exergy analysis and thermodynamic optimization in aircraft development. *Exergy, An International Journal*, 1(1), 14–24. [https://doi.org/10.1016/S1164-0235\(01\)00005-X](https://doi.org/10.1016/S1164-0235(01)00005-X)
- Çengel, Y. A., & Boles, M. A. (2015). *Thermodynamics: An engineering approach* (8th ed.). McGraw-Hill Education.
- Dincer, I., & Çengel, Y. (2001). Energy, entropy and exergy concepts and their roles in thermal engineering. *Entropy*, 3(3), 116–149. <https://doi.org/10.3390/e3030116>
- GasTurb. (2021). <http://www.gasturb.de/>. Accessed 08.01.2021.
- Pavelka, M., Klika, V., Vágner, P., & Maršík, F. (2015). Generalization of exergy analysis. *Applied Energy*, 137, 158–172. <https://doi.org/10.1016/j.apenergy.2014.09.071>
- Rocco, M. V., Colombo, E., & Sciubba, E. (2014). Advances in exergy analysis: A novel assessment of the Extended Exergy Accounting method. *Applied Energy*, 113, 1405–1420. <https://doi.org/10.1016/j.apenergy.2013.08.080>
- Roth, B., McDonald, R., & Mavris, D. (2002, July 7). A method for thermodynamic work potential analysis of aircraft engines. In *38th AIAA/ASME/SAE/ASEE Joint Propulsion Conference & Exhibit*, Indianapolis, Indiana. <https://doi.org/10.2514/6.2002-3768>
- SAE Aerospace Recommended Practice. (2004). *Procedure for the analysis and evaluation of gaseous emissions from aircraft engines* (SAE ARP1533 Rev A).
- Sahu, M. K., Choudhary, T., Kumari, A., & Sanjay, R. (2018). *Thermoeconomic, sustainability and environmental damage cost analysis of air cooled CT7-7A turboprop engine*. <https://doi.org/10.4271/2018-01-0774>

- Şöhret, Y., Dinç, A., & Karakoç, T. H. (2015). Exergy analysis of a turbofan engine for an unmanned aerial vehicle during a surveillance mission. *Energy*, *93*, 716–729. <https://doi.org/10.1016/j.energy.2015.09.081>
- Topal, A., & Turan, O. (2021). Thermo-efficiencies of a tubular combustor under different inlet conditions. *International Journal of Turbo & Jet-Engines*, *38*(2), 185–192. <https://doi.org/10.1515/tjj-2018-0005>

Identification Performance Fields in Ground-Handling Operations to Corporate Performance



Ebru Yazgan, Vildan Durmaz, and Ayşe Küçük Yılmaz

Contents

| | | |
|---|--|-----|
| 1 | Introduction | 113 |
| 2 | Ergonomics Risk and Risk Assessment | 115 |
| 3 | Ergonomic Risk Factors in Ground-Handling Operations | 116 |
| 4 | Conclusion | 118 |
| | References | 118 |

1 Introduction

“Ground handling” in aviation refers to the wide variety of activities for the flight operations such as passenger services, flight operations, catering, and baggage handling (EC, 2021). As aviation industry has been grown rapidly supportive handling operational activities need to be grown as well. Increasing in traffic means the number of accidents and adverse impacts may rise even in the safest system (Luxhøj et al., 2001). For the efficiency and sustainability of airlines, airport apron area operations are significant. The operation time in this area is short and at one time several activities with different equipment have to be implemented. For those reasons, there is a high potential risk for accidents and incidents (Sari et al., 2015). The methodology in this study was determined as taxonomy. Taxonomy is a process approach to deal with risks as to the initial step of the whole management system. In this view, we have tried to embody all related ergonomic factors in a taxonomy. Taxonomy has been designed under four main groups in the view of

E. Yazgan (✉) · V. Durmaz · A. K. Yılmaz
Eskisehir Technical University Faculty of Aeronautics and Astronautics,
Department of Airframe and Powerplant Maintenance, Eskisehir, Türkiye
e-mail: eyazgan@eskisehir.edu.tr; vkorul@eskisehir.edu.tr; akucukyilmaz@eskisehir.edu.tr

sustainability management for identified fields which may impact. This taxonomy may consider as holistic picture for organization-wide risk factors by managers to reach corporate performance. In this taxonomy for aircraft ground operations, we have identified 13 risks obtained from literature and experts' opinions in aviation sector.

Human makes mistakes naturally, so the variable qualities of human resources create difficulties in managing their corporate performance. This is exactly why the sources of error must be identified and managed in a way that does not cause errors. The physical and mental workload affects the health and performance of the ground operations personnel. The level of total workload is significantly affected by environmental and organizational factors as well as mental and physical factors (Emeç & Akkaya, 2018; Can & Delice, 2017). If individual performance increases and is used for achieving corporate aims, corporate performance will also increase in view of ground-handling services.

Ground-handling operations also enable the formation and development of collaborations with aviation sector stakeholders. Managers also will be able to see to which areas they will allocate resources with this taxonomy. This taxonomy may contribute to proactive monitoring of the risk sources which about human factor. Proactive approach is important to saving sources. Also, this proactive approach will be useful in reducing the negative effects of risks arising from risk sources before accidents and breakdowns occur.

This new taxonomy, designed as a decision-making tool, may use as guide to managing risk to improving both operational and corporate performance. Then managers can also use this taxonomy to manage risks in ground operations. This tool may support to achieving their managerial decision skills for developing human resource qualifications, scheduling workload, mental and physical conditions.

To improve corporate performance on ground operations, efforts are needed to assure safe operational conditions preventing from hurting the personnel (Sari et al., 2015). Identifying the ergonomic risk factors, it is aimed to evaluate risk and try to control those activities in the phase of aircraft preparation and turnaround at ramp area.

The employees of ground-handling operations are in the front line of flight safety. They are the first to intervene on the aircraft when it arrives at an airport, they prepare the aircraft for its flight and they are the last to observe the aircraft from the outside before it takes off. So, they must have the right reflexes, the necessary knowledge, and an appropriate attitude. While some of these qualities come with experience, they are mainly acquired through adapted communications, training, awareness-raising, and actions taken by management on the subject of incident handling (Dupin et al., 2015).

The results of this study may adapt other departments of ground handling and so company can seize opportunity to identify all risk sources to deal with them before accident and/or incidents in airport. As a result, this taxonomy may contribute current literature besides supporting decision-making process of managers during managing human error especially caused by ergonomic factors in ground-handling operations.

2 Ergonomics Risk and Risk Assessment

Ergonomics is defined by International Ergonomics Association as “. . .the *scientific* discipline concerned with the understanding of interactions among humans and other elements of a system, and the profession that applies theory, principles, data and methods to design in order to optimize human well-being and overall system performance” (Middlesworth, 2018).

Ergonomic risk factors are the aspects of a job or task that impose a biomechanical stress on the worker (Iowa State University, 2021).

Ergonomic risk is vital issue and it means that risks which is associated with work environment. Job activities involving any of the ergonomic risk factors below may contribute to or result in an increased risk of strain and injury as following (UC San Diego, 2021).

- Awkward postures
- Bending
- Compression or contact stress
- Forceful exertions
- Insufficient rest breaks
- Lifting
- Lighting
- Noise
- Pushing, pulling
- Reaching
- Repetitive motions
- Static or sustained postures
- Temperature extremes
- Vibration

Ergonomic risk factors are conditions of a job, process, or operation that contribute to the risk of developing work-related musculoskeletal disorders (MSDs). This includes damaged muscles, nerves, tendons, ligaments, joints, cartilage, or spinal disks (EMC, 2021). According to Middlesworth (2018), the major workplace ergonomic risk factors to consider are as follows:

- Forceful exertions
- Repetitive/sustained awkward postures
- High task repetition

Generally, ergonomic risk factors act in combination to create a hazard. Although certain risk factors are easy to identify and it is not difficult to understand why they may be likely to create hazardous exposures, others are not as apparent or observable. Employers who already have ergonomics programs and persons who manage ergonomics programs should not have difficulty identifying risk factors in the workplace. Because these persons have training and experience, ergonomic risk factors are likely to be familiar concepts for them. Through the process of developing

and implementing their ergonomics programs, these persons have gained a good working knowledge of the ergonomic risk factors that are most likely to be present in their workplaces (Iowa State University, 2021).

Ergonomic risk assessment is proactive approach to occupational health and safety, which includes identifying the hazard, estimating the risk (likelihood and severity of harm), and making recommendations to control the risk where necessary (University of Cape Town, 2021a).

A risk assessment is the process of risk analysis and risk evaluation. Risk analysis is the use of available information to identify hazardous tasks and to estimate the risk. Risk evaluation is the process based on the risk analysis but considering other factors, such as economic and social, in which judgments are made on the acceptability of the risk.

3 Ergonomic Risk Factors in Ground-Handling Operations

In this section, significant ergonomic risk factors in ground-handling operations are briefly explained.

A taxonomy of ergonomic risk factors for ground-handling operation is developed under four main categories as scheduling workload, mental conditions, physical strength, and qualifications. Supporting subcategories of these main categories are shown in Table 1 (Luxhøj et al., 2001; Sari et al., 2015).

Scheduling workload for the ground staff is a significant element as determining the shift work, if there is a shortage of staff under the time pressure operations, individuals have potential to cause accidents and hurt themselves. Time pressure affects the performance of an individual, which in turn can place the individual in a situation of committing an error.

Table 1 Taxonomy of ergonomic risk factors

| Main categories | Subcategories |
|---------------------|---------------------------|
| Scheduling workload | Shift work |
| | Staff shortage |
| | Time pressure |
| Mental conditions | Stress |
| | Out of control |
| | Loose concentration |
| Physical strength | Vision/hearing loss |
| | Fatigue |
| | Musculoskeletal disorders |
| Qualifications | Knowledge/skills |
| | Expectancies |
| | Communication |
| | Training |

Shift work is a well-known source of occupational stress and dissatisfaction. The world is becoming a 24-hour society, and increasingly air traffic is carried on around the clock. Shift workers have an increased prevalence of sleep disturbances, fatigue, and associated stress symptoms. This entails shift work for many operators of airport facilities and ground crews including ATCs, flight line mechanics, freight warehouse workers, porters, catering, sanitation personnel, drivers, and security personnel, as well as customs officials. Shift work involves employees who, on a regular or rotating basis, work nonstandard hours. This arrangement creates a problem for many employees since nearly all bodily functions, including metabolism and patterns of wakefulness and sleepiness, follow natural rhythms regulated by a roughly 24-hour biological clock (Kushnir, 1995).

Mental workload is a concept formed by mental and perceptual activities such as calculation, decision making, remembering, and research (Delice, 2016). Mental workload or cognitive workload is the amount of mental work required to complete a task over a period of time. It generally arises from the interaction between the requirements of a task, the conditions under which it is performed, and the skills, behaviors, and perceptions of the employees (Emeç & Akkaya, 2018).

Stress is a diffuse and global negative experience accompanied by other negative emotions such as anxiety, frustration, dissatisfaction, and depression (Kushnir, 1995). In the 1980s, stress-related illnesses comprised more than 14% of all such claims (Raymond, 1988).

Physical strength of ground operations agents may be negatively affected by the aircraft movement on the ground. The noise may cause hearing from minor to permanent; dust can cause eye irritation; and fatigue may result in hurt, injury, and stress. Due to high work stress, shortage of staff and other factors such as weather and excessive working hours an individual find himself in an awkward situation. The risk of fatigue exists in all activities of ground operations before the aircraft arrival and during the aircraft on the ground (Sari et al., 2015).

Human performance may affect adversely human fatigue like sleep deprivation, circadian rhythm abnormalities, health-related tiredness, and task-induced influences (Bendak & Rashid, 2020). These adverse effects may lead to aircraft accidents.

Excessive working hours can cause musculoskeletal disorders. If the staff works in the same position for a long time, the person loses their body form and flexibility after a while and recurrent pain occurs. It is very important to make work and workplace arrangements by using ergonomic analysis methods in order to prevent health problems caused by long working hours, increased stress, irregular working environments and unsuitable environmental factors and to reduce total workloads (Adar & Delice, 2020).

Physical workload is also defined as the factors that are related to the biomechanical strains that occur in the body (Westgaard & Winkel, 1996). When any personnel work with a physical workload above their physiological capacity for a long time, it causes work accidents, faulty production, and health problems.

The physical and mental workload affects the health and performance of the ground-handling personnel. The level of total workload is significantly affected by environmental and organizational factors as well as mental and physical factors.

Qualifications: every individual has different personality traits that are out of the control of top-level management. An individual's performance level could be affected by some personal factors such as background knowledge and trained skills, expectancies, and communication abilities (Luxhøj et al., 2001). Miscommunication and misunderstanding among employees or between employee and supervisor may contribute accidents/risk occurrence during operations.

Training is especially important to increasing situational awareness. And training is one of the fundamental parts of managing ergonomic risks. Ergonomic awareness training should consist of the following (University of Cape Town, 2021b):

- Identify the signs and symptoms of work-related musculoskeletal disorders (WMSDs) and the importance of early reporting.
- Recognize workplace risk factors for WMSDs and understand general methods for controlling them.
- Recognize the employee's role in the process, employees know their jobs better than anyone else knows and are often the source of ideas to improve them.
- There should be open interaction between trainer and trainees.
- Employees need to know the procedure for reporting ergonomic risk factors and musculoskeletal disorders.

4 Conclusion

In this study, ergonomic risk factors in ground-handling operations are developed by reviewing literature (Chang & Wang, 2010; Toriizuka, 2001; Rankin et al., 2000; Reason, 2000; Reason, 1997; Fogarty, 2004) and taking experts opinions on human performance.

This study has limitations on ergonomic factors to be examined. However, risk factors affecting corporate performance depend on varies fields such as managerial decision skills, equipment and technology, human resources, investments, and communication with partners. For this reason, in future study not only ergonomic risk factors, but also organizational, human resources, sustainability risk factors, etc. can be studied. With the help of risk analysis, multi-criteria decision-making techniques will be performed.

References

- Adar, T., & Delice, E. K. (2020). Comparison of the total workload of local public transportation drivers with a new approach according to physical and mental workload criteria. *Pamukkale University Journal of Engineering Sciences*, 26(1), 254–267.
- Bendak, S., & Rashid, H. S. J. (2020). Fatigue in aviation: A systematic review of the literature. *International Journal of Industrial Ergonomics*, 76, 102928.

- Can, G. F., & Delice, E. K. (2017). A new equation for determining physical workload: A case study in a box letter manufacturing process. In *International symposium for production research*, Vienna.
- Chang, Y. H., & Wang, Y. C. (2010). Significant human risk factors in aircraft maintenance technicians. *Safety Science*, 48(1), 54–62.
- Delice, E. K. (2016). Acil Servis Hekimlerinin Nasa-Rtlx Yöntemi İle Zihinsel İş Yüklerinin Değerlendirilmesi: Bir Uygulama Çalışması. *Atatürk Üniversitesi İktisadi ve İdari Bilimler Dergisi*, 30(3), 645–662.
- Dupin, S., Thiebaut, T., & Turcot, N. (2015). *Ground handling and flight safety basics, best practices and awareness-raising, technical guide, civil aviation technical center capacity, environment, master plans department, DGAC, STAC*.
- EMC Insurance Companies. (2021). *Ergonomic risk factors, tech sheets, loss control, business life reinsurance*. <https://www.emcins.com/losscontrol/techsheet.aspx?techsheetid=566>. Accessed 31 May 2021
- Emeç, Ş., & Akkaya, G. (2018). Sağlık Sektöründe Zihinsel İş Yükü Değerlendirmesi Ve Bir Uygulama. *Ergonomi*, 1(3), 156–162.
- European Commission (EC). (2021). Air-groundhandling. *Mobility and Transport*. https://ec.europa.eu/transport/modes/air/airports/ground_handling_market_en. Accessed 21 Mar 2021.
- Fogarty, G. J. (2004). The role of organizational and individual variables in aircraft maintenance performance. *International Journal of Applied Aviation Studies*, 4(1), 73–90.
- Iowa State University. (2021). *Risk factors, environmental health and safety*. <https://www.ehs.iastate.edu/services/occupational/ergonomics/risk-factors>
- Kushnir, J. (1995). Stress in ground support personnel. In J. Ribak, R. J. Rayman, & P. Froom (Eds.), *Occupational health in aviation: Maintenance and support personnel* (pp. 51–72). Academic Press.
- Luxhøj, J. T., Choopavang, A., & Arendt, D. N. (2001). Risk assessment of organizational factors in aviation systems. *Air Traffic Control Quarterly*, 9(3), 135–174. CCC 1064-3818/95/030163-20.
- Middlesworth, M. (2018). The art and science of injury prevention. *ErgoPlus*. <https://www.ergo-plus.com/the-art-and-science-of-injury-prevention/>. Accessed 31 May 2021
- Rankin, W., Hibit, R., Allen, J., & Sargent, R. (2000). Development and evaluation of the maintenance error decision aid (MEDA) process. *International Journal of Industrial Ergonomics*, 26, 261–276.
- Raymond, C. A. (1988). Mental stress: “Occupational injury” of the 1980’s that even pilots can’t rise above. *Journal of the American Medical Association*, 21, 3097–3098.
- Reason, J. (1997). *Managing the risks of organizational accidents*. Ashgate.
- Reason, J. (2000). Human error: Models and management. *British Medical Journal*, 320(7237), 768–770.
- Sari, M., Arubusman, D. A., & Abbas, S. (2015). Airport ramp risk analysis at Halim Perdanakusuma. *Jurnal Manajemen Transportasi & Logistik*, 2(3), 275–286. ISSN 2355-4721.
- Toriizuka, T. (2001). Application of performance shaping factor (PSF) for work improvement in industrial plant maintenance tasks. *International Journal of Industrial Ergonomics*, 28, 225–236.
- UC San Diego. (2021). *Ergonomics: Risk factors*. Ergonomics, Occupational, Safety, Regents of the University of California.
- University of Cape Town. (2021a). *Module: Introduction to ergonomics, ergonomic risk factors*. Faculty of Health Sciences, School of Public Health and Family Medicine, Post Graduate Diploma in Occupational and Environmental Health.
- University of Cape Town. (2021b). *Module: Introduction to ergonomics, the process of ergonomics workplace risk assessment*. Faculty of Health Sciences, School of Public Health and Family Medicine, Post Graduate Diploma in Occupational and Environmental Health.
- Westgaard, R. H., & Winkel, J. (1996). Guidelines for occupational musculoskeletal load as a basis for intervention: A critical review. *Applied Ergonomics*, 27, 79.

Impact Performance of the Kaolin-Filled Fiber-Reinforced Polymer Facing Sandwich Structures



Durmuş Can Acer and Necdet Geren

Contents

| | | |
|---|------------------------------|-----|
| 1 | Introduction | 121 |
| 2 | Material and Method | 122 |
| 3 | Results and Discussion | 125 |
| 4 | Conclusion | 125 |
| | References | 128 |

1 Introduction

Composite materials have found their place in many industries such as aerospace, automotive, marine, and sporting goods. This is because the higher stiffness and strength values desired in these areas are achieved with lower weight compared to conventional materials (Uzay et al., 2019). Sandwich composites are based on laminated composite structures. High-strength outer thin face sheets and low-density core material are bonded together to obtain extremely high bending rigidity. Fiber-reinforced laminates or metals can be used as face sheets and woods, metal/polymeric foams or honeycomb structures can be used as core material. Sandwich structures with CFRP face sheets and PVC foam core material are known for their high strength and flexural stiffness in spite of their lightweight (Uzay & Geren, 2020).

Besides the high tensile strength of fiber-reinforced composite structures, impact damage is one of the biggest problems for the composites to the brittle nature of these types of materials. The researchers investigated the impact properties of composite

D. C. Acer (✉) · N. Geren
Çukurova University, Adana, Turkiye
e-mail: dcacer@cu.edu.tr; gerendr@cu.edu.tr

materials with different experimental and theoretical methods such as low-velocity drop weight impact (Geren et al., 2021), Charpy impact (Ghasemnejad et al., 2010) and ballistic impact (Sevkat et al., 2009), analytical models (Feli et al., 2016) and even using numerical methods such as finite element methods (Damanpack et al., 2013). Impact properties of the sandwich structures are directly affected by the face sheets and core materials. Metallic sandwiches are generally used in areas where high impact resistance is required. However, in this case, the weight of the structure increases significantly. In laminated composites, the matrix-modifying method is used to improve some mechanical properties such as impact resistance. In the matrix-modifying method, micro- or nanoparticles are mixed homogeneously into the matrix (Saghafi et al., 2018). With this method, it is possible to obtain a more resistant matrix material against impacts without significant weight gain. Argüelles et al. (2011), investigated the effect of tough and brittle matrix materials on the fracture behavior of the composite structure. They found that the tough matrix material increased the static fracture energy value by roughly 230%. Pekbey et al. (2017) modified epoxy with nano-clays and they obtain a 16.1% impact load increase in the Kevlar/epoxy composites at 21 J of impact energy. Hosur et al. (2008) constructed sandwiches with nano-clay-modified carbon fiber/epoxy face sheets and polyurethane foam core. They reported that the nano-clay added sandwich suffered less damage at the same impact energy.

In this study, it was aimed to increase the impact resistance of a polymeric sandwich structure by using modified epoxy resin with kaolin, a clay type and known for its low cost.

2 Material and Method

In this work, carbon fiber/epoxy face sheets and closed-cell PVC foam core were used for manufacturing the sandwich panels. Woven plain carbon fiber fabrics, which were used for manufacturing the face sheets of sandwiches, were procured from Kordsa Inc. in Türkiye. The physical and mechanical properties of carbon fiber fabrics used in this study are given in Table 1. Face sheets are the main load-bearing part of the sandwich structure and determine the general properties of the sandwiches (Daniel et al., 2002). Closed-cell, 10 mm thick, PVC foam was obtained from Dost Kimya and it was used as the core material. Table 2 presents the physical and mechanical properties of the core material. The sandwich production was carried out by using epoxy polymer resin and its hardener. Hexion MGS L160 epoxy and Hexion MGS H160 hardener were obtained from Dost Kimya. The mixing ratio of epoxy resin to hardener was set to 100:25 by weight. The physical and mechanical properties of the mixed compound are shown in Table 3. 5.5 μm -sized kaolin particles were used to modify the epoxy polymer matrix in various proportions such as 0% (neat), 2%, 5%, and 10%. The physical and mechanical properties of the kaolin particles used in this study are given in Table 4.

Table 1 Physical and mechanical properties of carbon fiber fabric

| | |
|------------------------------|------------------------------------|
| Weave style/pattern | Woven plain |
| Density (kg/m ³) | 1790 |
| Mass (g/m ²) | 200 |
| Fiber type/model | Warp = 3K HS CF Weft = 3K HS CF |
| Filament diameter (μm) | 7 |
| Tensile strength (MPa) | 3800 |
| Modulus of elasticity (GPa) | 240 |
| Tensile strain (%) | 1.6 |
| Carbon assay (%) | 95 |

HS: High strength, 3K: 3000 filaments per tow

Table 2 Physical and mechanical properties of PVC core

| | |
|---|------------------|
| Type | Closed-cell foam |
| Density (kg/m ³) | 48 |
| Thickness (mm) | 10 |
| Mass (g/m ²) | 480 |
| Compressive strength perpendicular to the plane (MPa) | 0.6 |
| Compressive modulus perpendicular to the plane (MPa) | 48 |
| Tensile strength in the plane (MPa) | 0.95 |
| Tensile modulus in the plane (MPa) | 35 |
| Shear strength (MPa) | 0.55 |
| Shear modulus (MPa) | 16 |

Table 3 Physical and mechanical properties of epoxy and hardener mixture

| | |
|--------------------------------------|-------------------|
| Mixed products | MGS L160/MGS H160 |
| Mixing ratio by weight | 100:25 |
| Density (kg/m ³) | 1180–1200 |
| Flexural strength (MPa) | 110–140 |
| Modulus of elasticity (GPa) | 3.2–3.5 |
| Tensile strength (MPa) | 70–80 |
| Compressive strength (MPa) | 80–100 |
| Elongation at break (%) | 5–6 |
| Impact strength (KJ/m ²) | 40–50 |

Table 4 Physical and mechanical properties of kaolin particles

| | |
|---|-----------|
| Particle size (μm) | 5.5 |
| Purity (%) | 99 |
| Density ^a (kg/m ³) | 2500–2620 |
| Modulus of elasticity ^a (GPa) | 19.6–20.4 |
| Tensile strength ^a (MPa) | 45.8–50.6 |

^aCES Selector (2021)

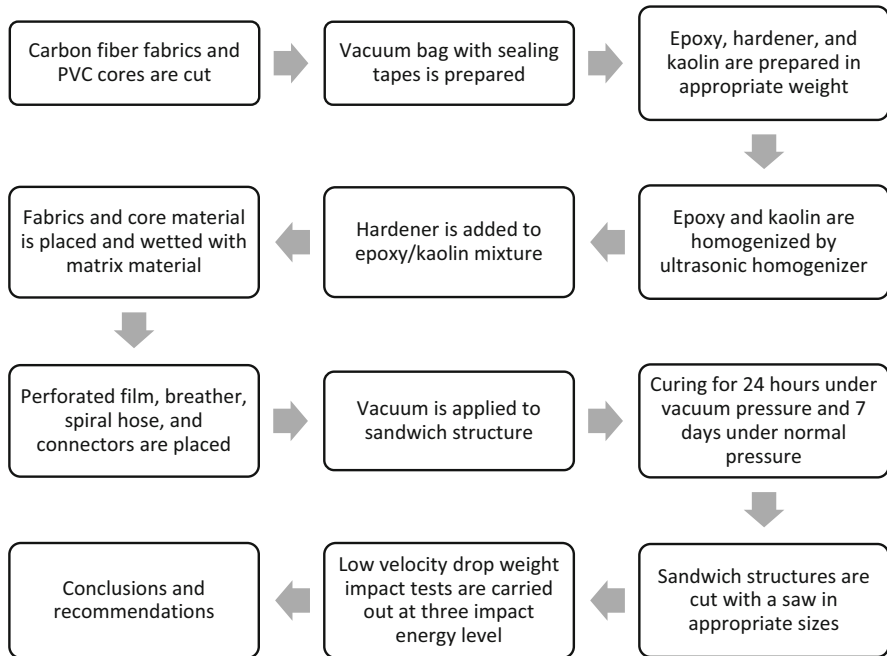


Fig. 1 Process and test steps

Table 5 Impact test conditions

| | |
|----------------------------|-------------|
| Impact energy (J) | 10/17.50/25 |
| Drop height (mm) | 203/355/507 |
| Impactor mass (kg) | 5.02 |
| Specimen dimensions (mm) | 100 × 150 |
| Impact area (mm) | 125 × 75 |
| Impactor tip diameter (mm) | 20 |

The flow chart provided in Fig. 1 represents the process and test steps. Specimen dimensions are 100 × 150 mm as suggested by ASTM D7766/D7766M–16 test standard. Four different sandwich configurations (with 0%, 2%, 5%, and 10% kaolin) were produced. These configurations were subjected to low-velocity impact testing at three energy levels, 10 J, 17.50 J, and 25 J. Impact test parameters applied in this study are given in Table 5. All tests were replicated five times. Then, the results were averaged and compared. Impact force, contact time, deformation, and energy values (absorbed and rebounded) were obtained by the test device software.

3 Results and Discussion

The load-time, energy-time, and load-displacement curves of the sandwich structures investigated in this study are presented in Figs. 2 and 3. Also, the comparative test results of the experiments are given numerically in Table 6. When the load-time figures (Fig. 2) are examined, it is observed that the load firstly rises (F1), then reduces a little, and then rises again (F2). The reason for this is that the surface layers of the sandwiches were manufactured from high-strength carbon fiber, and the core materials were manufactured from lightweight PVC foam. When the test results at all impact energies were examined, it was observed that the kaolin additive increased the impact resistance of the structure. Especially when the first contact (F1) results were examined, it was seen that the kaolin additive provided an impact load increase of up to 10.5%. This increase in the impact force indicates that the sandwich structure was hardened due to the contribution of kaolin.

When the energy-time figures (Fig. 2) are examined, it is seen that the curve first rises to the peak level which indicates impact energy, then decreases as much as the rebounded energy, and finally stabilizes. The difference between the impact energy and the rebounded energy gives the absorbed energy by the specimen. When the energy-time test results were examined, it is seen that the contribution of kaolin, especially at low impact energy (10 J), provides rebound of the impact energy to the structure rather than absorption. Since it is known that the absorbed energy causes damage to the structure (Mirdehghan et al., 2020), it can be said that the kaolin additive protects the structure against damage.

When the load-displacement curves are examined, it can be understood how many millimeters the impactor pierced the sandwich and whether the structure was punctured or not. Closed curves (Fig. 3a, b) indicate that the structure is not completely punctured, while open curves (Fig. 3c) indicate that the structure has been completely punctured. When the load-displacement results are observed, the positive effects of the kaolin particles are seen. At the 10 J impact energy level, there was 7.1% less piercing in the sandwich structure with 10% kaolin compared to the structure without kaolin.

4 Conclusion

In this study, sandwich structures containing CFRP face sheets and PVC foam core were produced. Kaolin additives in powder form were mixed into epoxy resin and they were used as matrix material in sandwich structures in four different ratios (0%, 2%, 5%, and 10%) according to the matrix weight. The low-velocity drop weight impact tests were performed at three energy levels (10 J, 17.50 J, and 25 J). Kaolin additive has exhibited significant improvement in the impact properties of the sandwich structure. The tests performed under different impact energy levels showed an increase in reaction forces (up to 10.5%) and a decrease both in absorbed energy (up to 11.3%) and indentation depth (up to 7.1%).

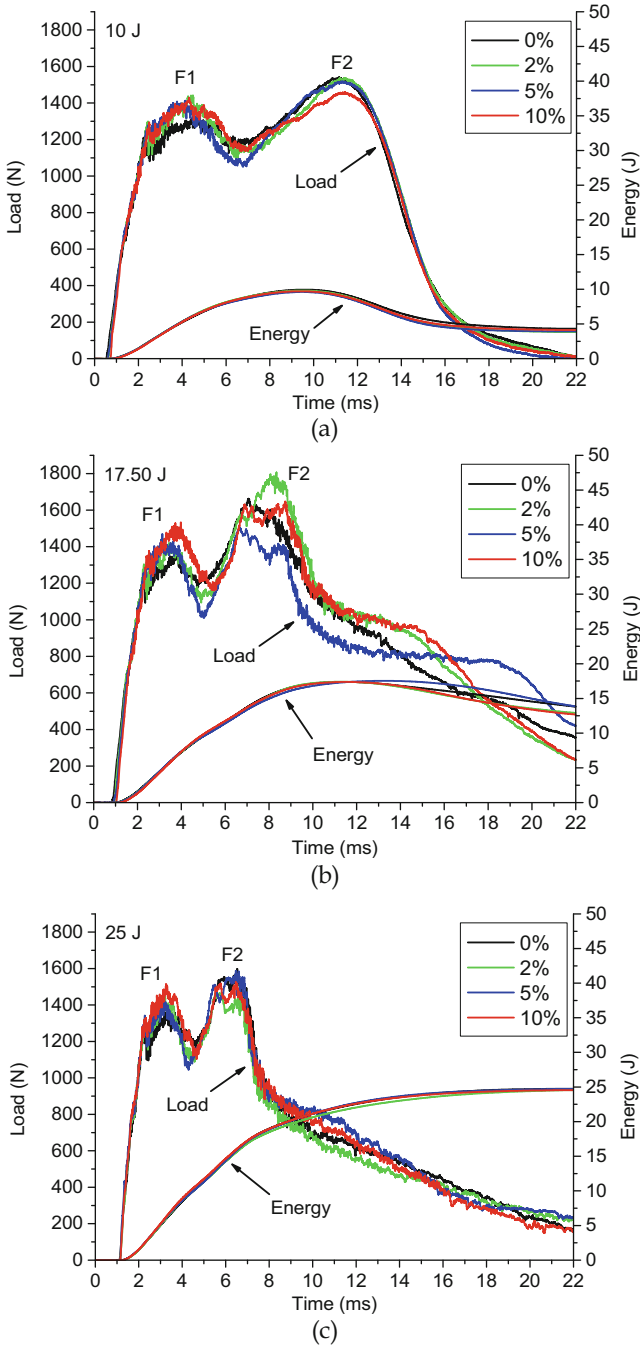


Fig. 2 Load-time and energy-time curves of the kaolin-filled sandwiches: (a) 10 J, (b) 17.50 J, and (c) 25 J of impact energy

Fig. 3 Load-displacement curves of the kaolin-filled sandwiches: (a) 10 J, (b) 17.50 J, and (c) 25 J of impact energy

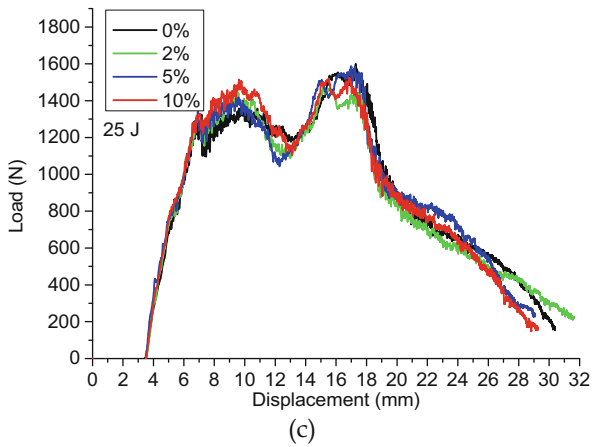
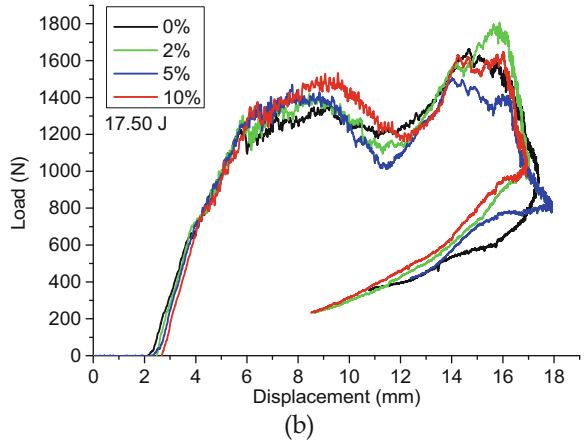
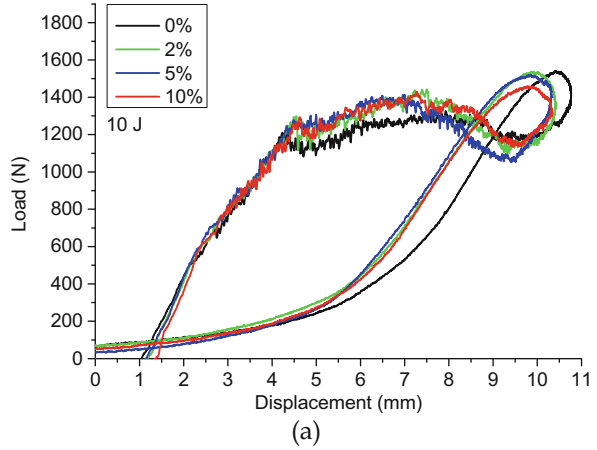


Table 6 Test results of the kaolin-filled sandwiches and percent contribution of kaolin content to impact properties

| Property | Impact energy | Neat epoxy | Kaolin content (\pm percent contribution) | | |
|-------------------------|---------------|------------|---|----------------|-----------------|
| | | | 2% | 5% | 10% |
| F1 (N) (first peak) | 10 J | 1299.4 | 1435.8 (+10.5%) | 1392.2 (+7.1%) | 1405.6 (+8.2%) |
| | 17.50 J | 1350.7 | 1392.2 (+3.1%) | 1424.7 (+5.5%) | 1489.6 (+10.3%) |
| | 25 J | 1358.7 | 1449.1 (+6.7%) | 1374.8 (+1.2%) | 1501.9 (+10.5%) |
| F2 (N) (second peak) | 10 J | 1533.9 | 1533.9 (0%) | 1516 (−1.2%) | 1456 (−5.1%) |
| | 17.50 J | 1640.5 | 1771.8 (+8%) | 1497.6 (−8.7%) | 1629.1 (−0.7%) |
| | 25 J | 1552.6 | 1464.6 (−5.7%) | 1573.6 (+1.4%) | 1508.2 (−2.9%) |
| Abs. energy (J) | 10 J | 4.32 | 3.83 (−11.3%) | 3.95 (−8.6%) | 4.13 (−4.4%) |
| | 17.50 J | 13.8 | 12.95 (−6.2%) | 13.87 (+0.5%) | 12.69 (−8%) |
| | 25 J | 24.73 | 24.56 (−0.7%) | 24.74 (0%) | 24.65 (−0.3%) |
| Inden. depth (mm) | 10 J | 9.49 | 9.01 (−5.1%) | 8.93 (−5.9%) | 8.82 (−7.1%) |
| | 17.50 J | 14.93 | 14.38 (−3.7%) | 15.2 (+1.8%) | 14 (−6.2%) |
| | 25 J | Punc. | Punc. | Punc. | Punc. |

Acknowledgments This work was supported by the Scientific Research Projects Coordination Unit (BAP) of Çukurova University, Adana, Turkey [grant number FYL-2018-10386].

References

- Argüelles, A., Viña, J., Canteli, A. F., & Lopez, A. (2011). Influence of the matrix type on the mode I fracture of carbon-epoxy composites under dynamic delamination. *Experimental Mechanics*, 51, 293–301. <https://doi.org/10.1007/s11340-010-9364-0>
- CES Selector. (2021). Retrieved from <http://www.grantadesign.com/products/ces/>
- Damanpack, A. R., Shakeri, M., & Aghdam, M. M. (2013). A new finite element model for low-velocity impact analysis of sandwich beams subjected to multiple projectiles. *Composite Structures*, 104, 21–33. <https://doi.org/10.1016/j.compstruct.2013.04.011>
- Daniel, I. M., Gdoutos, E. E., Wang, K. A., & Abot, J. L. (2002). Failure modes of composite sandwich beams. *International Journal of Damage Mechanics*, 11, 309–334. <https://doi.org/10.1106/105678902027247>
- Feli, S., Khodadadian, S., & Safari, M. A. (2016). Modified new analytical model for low-velocity impact response of circular composite sandwich panels. *Journal of Sandwich Structures & Materials*, 18, 552–578. <https://doi.org/10.1177/1099636216648489>
- Geren, N., Acer, D. C., Uzay, C., & Bayramoglu, M. (2021). The effect of boron carbide additive on the low-velocity impact properties of low-density foam core composite sandwich structures. *Polymer Composites*, 42, 2037–2049. <https://doi.org/10.1002/pc.25957>
- Ghasemnejad, H., Furquan, A. S. M., & Mason, P. J. (2010). Charpy impact damage behaviour of single and multi-delaminated hybrid composite beam structures. *Materials & Design*, 31, 3653–3660. <https://doi.org/10.1016/j.matdes.2010.02.045>
- Hosur, M. V., Mohammed, A. A., Zainuddin, S., & Jeelani, S. (2008). Processing of nanoclay filled sandwich composites and their response to low-velocity impact loading. *Composite Structures*, 82, 101–116. <https://doi.org/10.1016/j.compstruct.2006.12.009>

- Mirdehghan, A., Nosrati, H., Shokrieh, M. M., & Akhbari, M. (2020). Manufacturing and drop-weight impact properties of three-dimensional integrated-woven sandwich composite panels with hybrid core. *Journal of Industrial Textiles*. <https://doi.org/10.1177/1528083719896764>
- Pekbey, Y., Aslantaş, K., & Yumak, N. (2017). Ballistic impact response of Kevlar composites with filled epoxy matrix. *Steel and Composite Structures*, 24, 191–200. <https://doi.org/10.12989/scs.2017.24.2.191>
- Saghafi, H., Fotouhi, M., & Minak, G. (2018). Improvement of the impact properties of composite laminates by means of nano-modification of the matrix-a review. *Applied Sciences*, 8, 2406. <https://doi.org/10.3390/app8122406>
- Sevkat, E., Liaw, B., Delale, F., & Raju, B. B. (2009). A combined experimental and numerical approach to study ballistic impact response of S2-glass fiber/toughened epoxy composite beams. *Composites Science and Technology*, 69, 965–982. <https://doi.org/10.1016/j.compscitech.2009.01.001>
- Uzay, C., Geren, N., Boztepe, M. H., & Bayramoglu, M. (2019). Bending behavior of sandwich structures with different fiber facing types and extremely low-density foam cores. *Materials Testing*, 61, 220–230. <https://doi.org/10.3139/120.111311>
- Uzay, Ç., & Geren, N. (2020). Effect of stainless-steel wire mesh embedded into fibre-reinforced polymer facings on flexural characteristics of sandwich structures. *Journal of Reinforced Plastics and Composites*, 39, 613–633. <https://doi.org/10.1177/0731684420921952>

Analysis of the Airport Sustainability Plan in the Context of EONS Components



Serap Gürsel and Hakan Rodoplu

Contents

| | | |
|-----|---|-----|
| 1 | Introduction | 131 |
| 2 | Airport Sustainability Plans | 132 |
| 2.1 | Developing a Sustainability Plan | 132 |
| 2.2 | Top Drivers for Airport Sustainability | 133 |
| 2.3 | Top Aids for Airport Sustainability | 134 |
| 2.4 | Top Barriers for Airport Sustainability | 134 |
| 3 | EONS Components | 135 |
| 3.1 | Operational Efficiency | 135 |
| 3.2 | Natural Resource Conservation | 136 |
| 3.3 | Social Responsibility | 137 |
| 4 | Conclusion | 137 |
| | References | 138 |

1 Introduction

Airport administrators and all airport users experience similar problems worldwide. To provide a systematic approach to assembling and evaluating information gathered from successful airport practices can make problem solving easier. Sustainability is a main subject in aviation because of aircraft and airports. There are thousands of airports in different types in the whole world. Airport administrators want to develop sustainable practices to enhance their environmental, economic, social, and operational interests.

A number of airport administrators around the world are developing sustainability programs voluntarily or compulsorily by local ordinances. A number of countries

S. Gürsel (✉) · H. Rodoplu
Kocaeli University, Aviation and Space Science Faculty, Kocaeli, Türkiye

like the United States prepared airport sustainability plans to consolidate sustainability practices. It is known that some sustainability practices were implemented before airport sustainability plans. And the implementation of such practices is constantly evolving. Thus, it is very difficult to interpret the results of these practices that were not done systematically. Sharing the experience regarding the preparation, development and implementation of the airport sustainability plans is very important for the countries and airports that have not yet implemented these plans. Airport Council International developed EONS perspective to existing sustainability efforts. EONS is the acronym for the four factors complementing the whole for holistic airport management.

2 Airport Sustainability Plans

Airports are a crucial part of the complex international air transport system. In this way, it is ensured that passengers, cargo, and tourism travel all over the world through the facilities of the airports. Awareness of the environmental impacts of human activities has increased over the past two decades (Cowper et al., 2011).

Airports can manage sustainability in different ways. Airport administrators decide for undertaking a sustainability plan can be the result of numerous elements. The most important factors that lead to the implementation of the sustainability plan will be examined under the title of “top drivers.” Most of the airports have also undertaken airport sustainability plans because airport administrators simply believe it is the right thing. Rising energy bills, long-term energy supply, and environmental impacts of gas emissions have raised concerns among airport managers. In this direction, new sustainability practices have been started to be developed. A wide variety of sustainability practices can cause airports to lose their focus on sustainability. Therefore, sustainability plans were needed (Budd et al., 2014).

Sustainability plans keep airports to identify goals with all aviation users and stakeholders. Shared goals improve performance of airport administrators and ensure consensus to stakeholders. Airport sustainability plans are not the only way of maintaining sustainability, but they are the most organized way. Sustainability can be considered while designing an airport or can also be developed while operations are ongoing. In designing phase, airport administrators generally have outsource guidance and can decide more independent. In operational phase, sustainability plans generally include ongoing sustainability practices and can be different forms.

2.1 Developing a Sustainability Plan

Every airport must firstly develop its own definition of sustainability in the beginning of preparing a sustainability plan. While doing this, generally the sustainability practices they have applied before are taken into account. Most definition has three

dimensions: economic, social, and environmental. ACI and airport community added a fourth dimension as “operational” dimension to the definitions. Developing a sustainability plan distributes responsibilities from one person (one manager) to more than one person (the entire institution staff) in organizations. For this reason, sustainability plans help sustainability to be owned by everyone in the organization. In an airport sustainability plan, sustainability definition provides a focus for consensus-based goals. A sustainability plan is a starting point for continuous improvement. In an airport sustainability program, airport administrators have other sustainability elements like sustainable design of airport, a construction guidance, sustainability goal declaration, sustainability actions, performance measurement mechanism, other management systems, and annual sustainability application reports. Some airports implement sustainability applications on ad hoc basis instead of sustainability plans. But developing a plan is useful for setting priorities for applications.

A holistic and organized approach to sustainability planning has gained importance in the last decade. Developing sustainability practices by evaluating within the scope of EONS brings synergy to strategies and solutions. International sustainability frameworks and standards are also taken into account by airports in sustainability programs. The Global Reporting Initiative (GRI) prepared “Sustainability Reporting Guidelines and Airport Operations Sector Supplement” for airports in 2011. International Standards Organization (ISO) has many voluntary standards for sustainability such as ISO 14001 (environmental management), ISO 26000 (social responsibility), ISO 5001 (energy management), ISO 20121 (sustainable events), ISO 15392, and ISO 21000 (sustainable building construction). Other globally accepted sustainability standards are the Dow Jones Sustainability Index (DJSI) and Carbon Disclosure Project (CDP). They focus on greenhouse gases and guidance for managing sustainability (Shannon, 2017).

In sustainability practices, it is encouraged to use the management approach cycle (plan, implement, improve, and maintain) according to a perspective. By means of this method, it is possible to define the process step by step. It will also be easier to measure the performance of the process. With this method, sustainability turns into a value shared by all stakeholders. By making a sustainability plan, airports can use their resources better, bring together sustainability practices, increase communication with stakeholders, and guide sustainability-related activities. Sustainability management can be built as a stand-alone system or it can be incorporated into the existing management system (SAGA, 2010).

2.2 Top Drivers for Airport Sustainability

Developing and implementing an airport sustainability plan inside of sustainability program can be influenced by drivers, aids, and barriers. Airport administrators choose sustainability plans for several reasons. Generally specific factors that are driving airports to develop sustainability plans include worldwide awareness, airline

industry pressure, rising energy costs, environmental obligations, resource conservation, aging infrastructure, facility lifecycle costs, and enabling technologies according to SAGA. Cost reduction is the main cause, and improving environmental performance is a benefit beside that cause. Sustainability funding is another important reason for developing airport sustainability plans. It is seen that the views of the stakeholders also affect the sustainability practices.

Florida airport has an airport sustainability guidebook and airport administrator listed benefits of sustainability planning to Florida's airports. Benefits are listed below (Florida Airport Sustainability Guidebook):

- Increases the safety
- Reduces airport operational costs
- Causes more efficient use of airport facilities
- Better tackles changing energy costs
- Stretches funding
- Increases airport's operational efficiency
- Prevent environmental impacts
- Develops community support and positively impacts airport perceptions

2.3 Top Aids for Airport Sustainability

Once a sustainability plan has been prepared some aids assist the implementation. These aids consist of a variety of factors such as funding, training, analytic tools, employee engagement, and internal communications. Public demands, consultant team and planning tools, non-aviation regulatory organizations, maintenance cost savings, cost-benefit analysis, and audit results are the main aids according to airport administrators.

2.4 Top Barriers for Airport Sustainability

Financial problems are the most common reason for avoiding sustainability practices. Lack of funding and costs of new technology create the primary barrier to sustainability programs. Lack of initiative or direction, cultural bias (blocking proactive precautions), limited resources, lack of cost-benefit analysis, readiness of staff, lack of common goals between stakeholders, grandfather rights of airport users, infrastructure needs, lack of available time, old habits, and limited training opportunities are the main examples of barriers for airport sustainability.

3 EONS Components

EONS is the acronym for the four factors complementing the whole for holistic airport management (SAGA, 2010). As mentioned above, airport community adopts sustainability definition to airport operational system. EONS components gain importance according to that definition. Economic viability, operational efficiency, natural resource conservation, and social responsibility are influenced by airport sustainability initiatives. A single initiative affects not only an EONS component.

While the EONS components do not offer a specific approach to target setting or reporting, they do assist in the elaboration and analysis of an airport sustainability plan from different perspectives (Shannon, 2017).

Economic viability is the main component underlying all other components. Economic viability can be enhanced in several ways, including revenue generation, decreased costs, and success in capital expenditure projects. Financial aspects force airports to consider which projects to prioritize or pursue. Especially, the projects involving the renewal of infrastructure facilities require quite a large capital investment. Airports are also using sustainability plan to meet economic goals that will mitigate and benefit the community and stakeholders (SAGA, 2010: p.6). And there is a financial return as a result of the implementation of recycling programs, even these projects require investment in their first phase. When airports consider firstly economic viability component, the first projects they usually apply are LED lighting and recycling projects. Small airports have less funding, because of that they must think economic viability in the first place. Airports often act on financial priorities when sustainability practices are confronted with irrevocable priorities such as maintenance priorities.

Economic viability component refers to achieving the highest social return on physical and natural capital. It means the operating efficiency of airport. International Air Transportation Association released the 9th edition of the worldwide slot guidelines in 2019 and pointed out that improving airport efficiency means of promoting the sustainable development for aviation. Economic viability usually related with operational efficiency (Wan et al., 2020).

3.1 *Operational Efficiency*

Airports are places where direct and indirect activities related to flight are carried out together. In the selection and implementation of sustainability practices, operational efficiency concept should be carefully incorporated into decision processes. If airports can integrate their operational processes and sustainability processes, the probability of their sustainability plans to be successful will increase. Considering the operational efficiency concept as a priority, the developed sustainability practices are generally related to energy and climate by airport administrators. For energy saving, airport administrators use smart meters, motion-sensitive lighting, and lower

and higher temperature settings for buildings. Greenhouse gas inventories and cogeneration power plant that makes electricity from natural gas for terminal buildings can be used by airports as another options. In airport sustainability plans, operational efficiency is considered by two subclass. These are airside operational efficiency and facility operational efficiency.

Sustainability practices developed in the airside operational efficiency subclass are reducing existing approach distances, establishing automatic aircraft releases, and adopting NetGen air traffic technologies, such as direct descent. Sustainability practices developed in the facility operational efficiency subclass are tracking monthly utility charges to manage airport's consumption of energy, water, and other resources. An example is that is an initiative to partner with energy firms to maximize potential revenue generation on land that was not producing revenue benefits to offset airport operational costs and reduce fossil-fuel energy consumption. A study showed that "developing a corporate sustainability culture should be a source of competitive advantage in the long run" by Harvard Business School (Oppenheim & Stuchtey, 2015).

3.2 Natural Resource Conservation

The concept of sustainability is often primarily perceived by people only as related to the environment. Green buildings, green procurement, and environmental management systems are main sustainability practices mostly related to natural resource conservation component. Noise management programs are another sustainability example.

While environmental sustainability practices reduce environmental impacts, they also provide financial and operational benefits (Lynes & Dredge, 2010). Strategies to reduce the use of raw material resources benefit airports both environmentally and economically. Besides these strategies, strategies to reduce emissions to the atmosphere, reduce waste generation, prevent water pollution, and protect biodiversity are other options for airport administrators (Landrum & Brown Company, 2012).

Wide range of natural resource conservation practices is currently in operation at UK airports. It is expected that the number of airports using such strategies will increase over time. This data will turn into know-how with the emergence of the result data of the applications in the aviation sector. Surprisingly, however, most environmental sustainability practices are carried out at airports in areas with pollution problems such as Europe, North America, and Asia. Continuation of these practices in the same way is of great importance in terms of sustainability (Budd et al., 2014).

Many airports around the world are installing solar photovoltaic systems in order to reduce the environmental impact of energy usage and to reduce the need for traditional fossil-based fuels (Baxter et al., 2019). Thus, airports had to carry out their practices and operations in a more environmentally friendly way (Coyle et al., 2015).

3.3 *Social Responsibility*

Due to the nature of aviation, airports have to operate in a social environment. Airports are a center of interest and a source of employment for those living in the vicinity. Airport stakeholders (airport employees, aircraft owners, tenants, passengers, interact socially, operators, and service providers) interact socially at airports. Social practices usually have no costs and could be a part of management functions such as human resources. Employees of airport can participate voluntary charities and social responsibility projects. Nearly all of the social responsibility projects required little to no investment. Main social responsibility concept is maintaining a good relationship between stakeholders. Developing an airport sustainability plan with the joint effort of the stakeholders is the first step to achieve this.

4 Conclusion

Among the many methods that airport management can use to manage sustainability practices, the option to develop an airport sustainability plan is the most effective way. In addition, although the amount of benefits provided by airport sustainability plans varies from airport to airport, the emissions they provide in general will cause sustainability to be accepted as a cultural value all over the world.

Airport administrators view sustainability as a process not as an end goal. To be a sustainable airport, an airport sustainability plan should be a living process in accordance with the resources available. Airport administrators should establish a separate sustainability team to involve all stakeholders in the airport sustainability plan. With this method, airport employees and management can be integrated effectively.

Airport sustainability plans bring together airport stakeholders such as airport users, tenants, consultants, employees, regulatory organizations, and governmental bodies. Thus, stakeholders will be more willing to embrace the plan and sustainability program if they participated to develop it. And ideas came from different sources help to create a more robust product. A sustainability committee can be more useful in the early stage of sustainability planning.

Sustainability planning should first be designed as a pilot program by airports and then implemented after a familiarization process. If airports do not want to implement the sustainability plan, various implementation options are available. For example, it can use the GRI infrastructure to prioritize and support reporting efforts. Or they can use the SDGs to set their own priorities and define how they will support sustainability with them.

References

- Baxter, G., Srisaeng, P., & Wild, G. (2019). Environmentally sustainable airport energy management using solar power technology: The case of Adelaide Airport Australia. *International Journal for Traffic and Transport Engineering*, 9(1), 81–100.
- Budd, T., Budd, L., & Ison, S. (2014). Environmentally sustainable practices at UK airports. *Transport*, 168, 116–125.
- Cowper, Smith, A., & Grosbois, D. (2011). The adoption of corporate social responsibility practices in the airline industry. *Journal of Sustainable Tourism*, 19(1), 59–77.
- Coyle, J. J., Thomchick, E. A., & Ruamsook, K. (2015). Environmentally sustainable supply chain management: An evolutionary framework, marketing dynamism and sustainability. In L. J. Robinson (Ed.), *Proceedings of the 2012 academy of marketing science annual conference, May 15–20* (pp. 365–374). Springer International Publishing.
- Florida Airport Sustainability Guidebook. <https://www.fdot.gov/aviation/sustainability.shtm>. Accessed 25.05.2021.
- Landrum and Brown company. (2012). *Guidebook for incorporating sustainability into traditional airport projects*. Transportation Research Board of the National Academies, Report 80, USA.
- Lynes, J. K., & Dredge, D. (2010). Going green: Motivations for environmental commitment in the airline industry, a case study of Scandinavian Airlines. *Journal of Sustainable Tourism*, 14(2), 116–138.
- Oppenheim, J., & Stuchtey, M. (2015). *Like it or not, sustainability is good for your business*, *Fortune*, <http://fortune.com/2015/09/24/sustainability-practices-in-business-intel-unilever-walmart-dupont/>. Date of Access 23.05.2021.
- SAGA. (2010). *Sustainable aviation resource guide, planning, implementing and maintaining a sustainability programs at airports*, https://www.google.com/url?sa=t&rct=j&q=&esrc=s&source=web&cd=&ved=2ahUKEwi5y-re7P3wAhWi_7sIHYIRBdIQFjABegQIBBAE&url=http%3A%2F%2Fwww.airportsustainability.org%2Fdocument%2F9&usg=AOvVaw113a3EAdaembg48Qh8547l. Accessed 26.05.2021.
- Shannon, C. (2017). *Selecting the right sustainability framework to guide airport planning and implementation*, University of Florida, Terminal Project, <https://ufdc.ufl.edu/AA00062288/00001>. Accessed 25.05.2021.
- Wan, L., Peng, Q., Wang, J., Tian, Y., & Can, X. (2020). Evaluation of airport sustainability by the synthetic evaluation method: A case study of Guangzhou Baiyun International Airport, China from 2008 to 2017. *Sustainability*, 12, 1–18.

Optimizing Distributed Electric Aero-Propulsion Integration for a Novel Canard Aircraft Design



Omkar N. Walvekar and Satyanarayanan R. Chakravarthy

Contents

| | | |
|-----|--|-----|
| 1 | Introduction | 140 |
| 2 | Computational Methodology | 140 |
| 2.1 | Geometry | 140 |
| 2.2 | Meshing | 141 |
| 2.3 | Physics and Mathematical Model | 142 |
| 2.4 | Boundary Conditions | 142 |
| 2.5 | Numerical Methodology | 142 |
| 3 | Results and Discussion | 143 |
| 3.1 | Aerodynamic Interaction of Propellers with Main Lifting Surface | 144 |
| 3.2 | Improved Aerodynamic Performance Due to the Propeller Configurations | 148 |
| 4 | Conclusion | 149 |
| | References | 150 |

Nomenclature

- C_L Coefficient of lift
- C_D Coefficient of drag
- D Diameter, m
- L Aircraft length, m

O. N. Walvekar (✉) · S. R. Chakravarthy
Indian Institute of Technology Madras, Chennai, India

1 Introduction

In the past decade, there has been a rapid development and growth in the popularity of electric aerial vehicles ranging from unmanned aerial vehicles (UAV) to manned electric airplanes. Technological improvements in the field of battery density, optimization algorithms, and structural design have provided an impetus to these vehicles to go from academia to the commercial markets (Chan, 2002; Patterson et al., 2012). The use of distributed electric propulsion (DEP) in the design of manned electric aircraft has shown promise owing to the smaller footprint, maintenance requirements, and noise levels (Stoll et al., 2014). Its prevalence in the recent commercially viable designs, such as in the X-57, Joby S2, and Vahana (Kim et al., 2018), compels us to study the propeller configurations where, due to structural constraints, the propellers cannot be placed exactly on/ahead of the leading edge of lifting surfaces. As opposed to the conventional fuel-based propulsion systems which are constrained by scaling effects, the use of small electric motors not only allow for better reliability but also increased freedom in the design process of high-lift aerodynamic devices by allowing reduction in planform area for the same amount of lift.

This chapter aims to find an optimal configuration of propellers placed along the leading and/or trailing edge of a novel canard aircraft design to maximize its lifting capacity. The said battery-motor-propellers units can be attached to the wing main-frame with ease due to their small size, as opposed to conventional gas turbine-powered fans.

2 Computational Methodology

2.1 Geometry

The aircraft length (L) is 3 m and has been taken as the reference length for further calculations. The main wing span and root chord are 2.7 m and 0.8 m, respectively. The main-to-canard wing chord ratio is 2.5 and both wings have a taper ratio of 2.1. The propellers are circular disks of diameter 0.35 m placed normal to the fuselage axis. The domain is a cuboid of dimensions $6L \times 3L \times 3L$ with the aircraft placed at reference length from the inlet face, and centered with respect to the cross section of the domain. Four propeller configurations have been considered that are to be mounted on the leading/trailing edges of the main wing – trailing edge mounted pushers, leading edge mounted tractors, tractors with a tail rotor, and tractors with tail and tip rotors. The tail rotor is placed such that it is along the fuselage axis and behind the fuselage to alleviate the profile drag behind it.

Studies have also been conducted when the propellers have been vertically offset above the main wing's edges by a radii worth height (except the tail rotor) to study

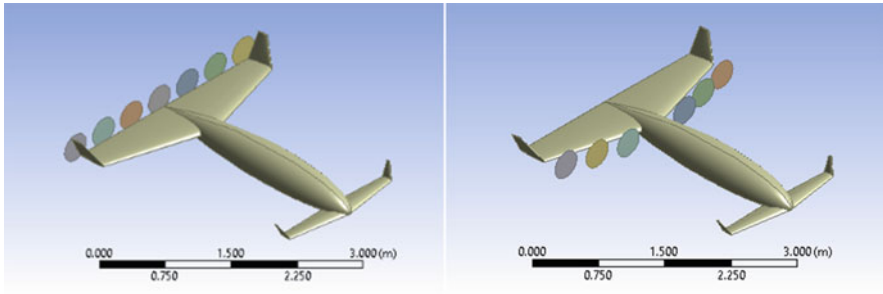


Fig. 1 Pusher (left) and tractor propeller configurations

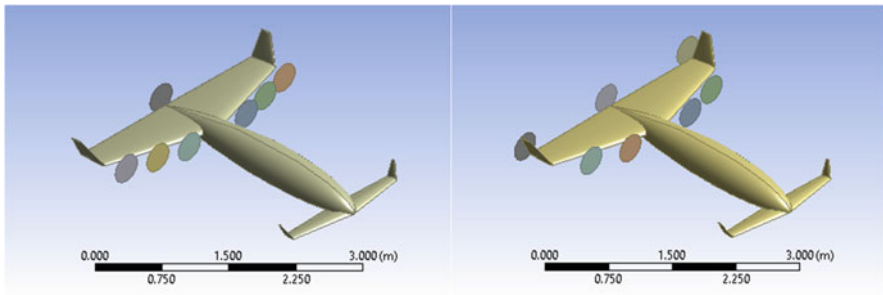


Fig. 2 Tractors with a tail rotor (left) and tractors with tail and tip rotors

the suction versus blowing effect of the propellers. The offset has been done such that the slipstream of the propeller is mainly interacting with the upper surface of the main wing. See Figs. 1 and 2 for geometries (without the vertical offset).

2.2 Meshing

A good quality mesh is essential to capture the fluid flow with sufficient accuracy while requiring the least amount of computational resources. Since the flow will encounter sharp corners in the vicinity of the aircraft, inflation layers have been set up with a nondimensionalized first-cell wall thickness (y^+) of 375, calculated using the freestream velocity and the main wing root chord length, keeping in mind the turbulence model used, which is discussed in the subsequent sections. Face-mapped meshing has been used for the aircraft surface along with a spherically coarsening mesh drawn about the center of the aircraft. A mesh independence study was performed to eliminate the dependence of the results, coefficient of drag (C_D) and lift (C_L), on the mesh size for the aircraft in the freestream placed at an angle of attack (α) of 5° , as shown in Table 1. Five meshes of different maximum tetrahedral

Table 1 Results of Mesh Independence Study

| | Mesh 1 | Mesh 2 | Mesh 3 | Mesh 4 | Mesh 5 |
|--------------------|---------|---------|---------|-----------|-----------|
| Number of elements | 363,792 | 583,903 | 983,291 | 1,683,387 | 2,987,342 |
| CD | 0.02448 | 0.02287 | 0.02202 | 0.02154 | 0.02102 |
| CL | 0.19822 | 0.20501 | 0.20864 | 0.20919 | 0.20641 |

sizes were compared for accuracy of results and the computational time required. Mesh 3 was accurately able to capture the physics of the flow while taking low computational time.

2.3 *Physics and Mathematical Model*

The fluid for this study was chosen to be air at sea level at a constant density of 1.225 kg/m^3 and viscosity of $1.7894 \times 10^{-5} \text{ kg/ms}$. The flow was assumed to be incompressible and isothermal since the expected velocities are expected to remain subsonic. The numerical technique used to simulate the fluid flow was realizable $k-\epsilon$ eddy viscosity turbulence model with enhanced wall function.

2.4 *Boundary Conditions*

The inlet of the enclosing domain allows a freestream velocity condition for the fluid at 100 km/h ($=27.7778 \text{ m/s}$) to obtain a flow of Reynolds number $\text{Re} \sim 1.47$ million for all cases. The outlet of the domain is set to a pressure outlet at zero-gauge pressure. The aircraft and other four surfaces of the domain are set as fixed no-slip walls. A constant pressure jump across the actuator disk is used to simulate the propeller slipstream. As shown in the subsequent sections, the average drag of the aircraft over non-negative α is used to calculate the required pressure jump across the actuator disk with a thrust-to-drag ratio of 1.25.

2.5 *Numerical Methodology*

The computational analysis was done using a commercially available fixed-volume method Navier–Stokes solver, FLUENT (ANSYS Inc.). Since the flow is assumed to be incompressible, a pressure-based steady-state simulation was set up, ignoring the acceleration due to gravity. The Semi-Implicit Method for Pressure-Linked Equations (SIMPLE) scheme was implemented to achieve the pressure–velocity coupling. The gradients were computed using the Least Squares Cell-Based Gradient Evaluation. Second-order discretization schemes were used for pressure, momentum, turbulent kinetic energy, and turbulent dissipation rate.

3 Results and Discussion

The airflow of an isolated actuator disk of diameter 0.5 m (D) in a viscous freestream for several pressure jumps was simulated to obtain the baseline results. A cylindrical domain of diameter $10 D$ and length $25 D$ was used for this with appropriate mesh refinement close to the disk. The CFD setup for this was same as that used in the other cases, with no swirl effects. The validation results are shown in Figs. 3 and 4. The stall characteristics of the airframe alone were studied to obtain the baseline results for the study, as shown in Figs. 5, 6, and 7. The aircraft stalls at approximately 12° , similar to the NACA0012 airfoil, on which the lifting surfaces of the aircraft are based on.

As seen in Fig. 7, the average $C_D \sim 0.04$ for $\alpha \geq 0$ for the aircraft. For the cases with propellers, the thrust requirement was calculated based on twice the average C_D and a thrust-to-drag ratio of 1.25. The wetted surface area of the aircraft is 7.1777 m^2 , giving us an imposed pressure jump across the actuator disk of 587.60 Pa and 503.66 Pa for configurations with 6 and 7 actuator disks, respectively.

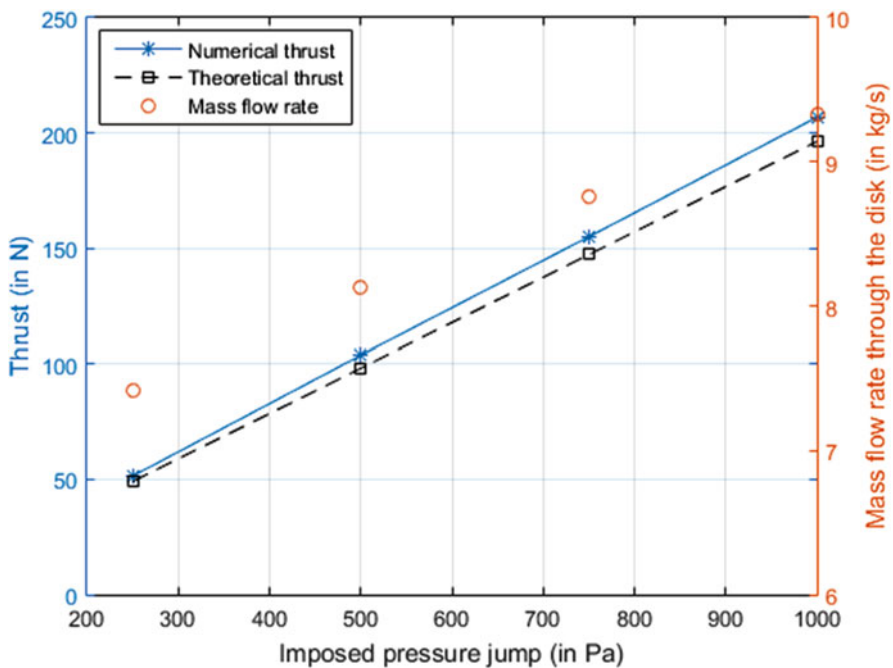


Fig. 3 Baseline data for numerical simulation of the actuator disk

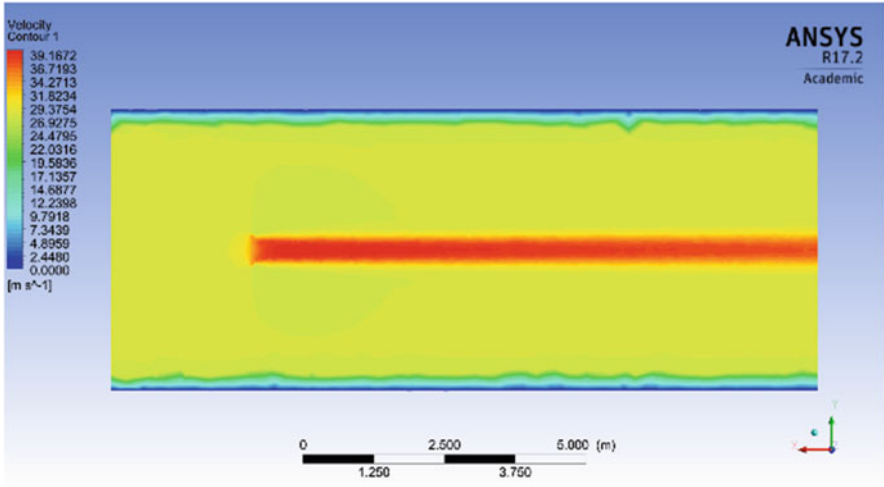


Fig. 4 Simulating isolated propeller in a freestream with 500 Pa pressure jump

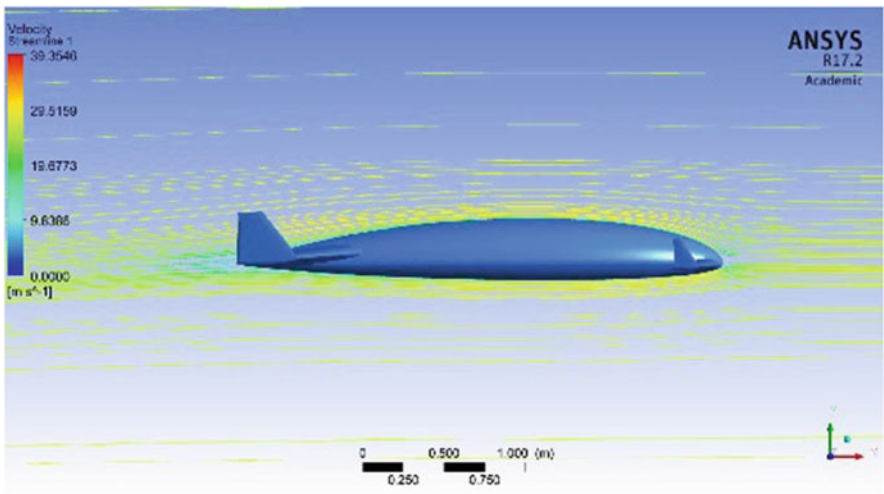


Fig. 5 Velocity streamlines for aircraft at $\alpha = 0^\circ$

3.1 Aerodynamic Interaction of Propellers with Main Lifting Surface

The combined thrust provided by all the propellers is fixed at 339.19 N. Considering this, the highest C_L and C_D of the aircraft was seen for the tractors with a tail rotor without offset, and the lowest C_L and C_D for tractors only configuration with an offset, as shown in Figs. 8 and 9. The increased dynamic pressure due to the tractor

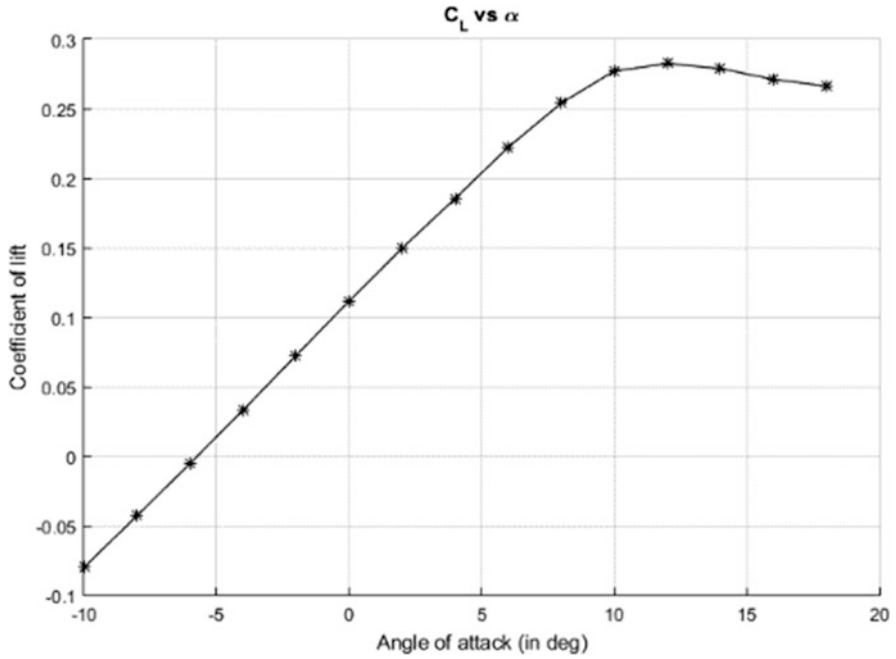


Fig. 6 Lift curve (C_L vs α) for aircraft

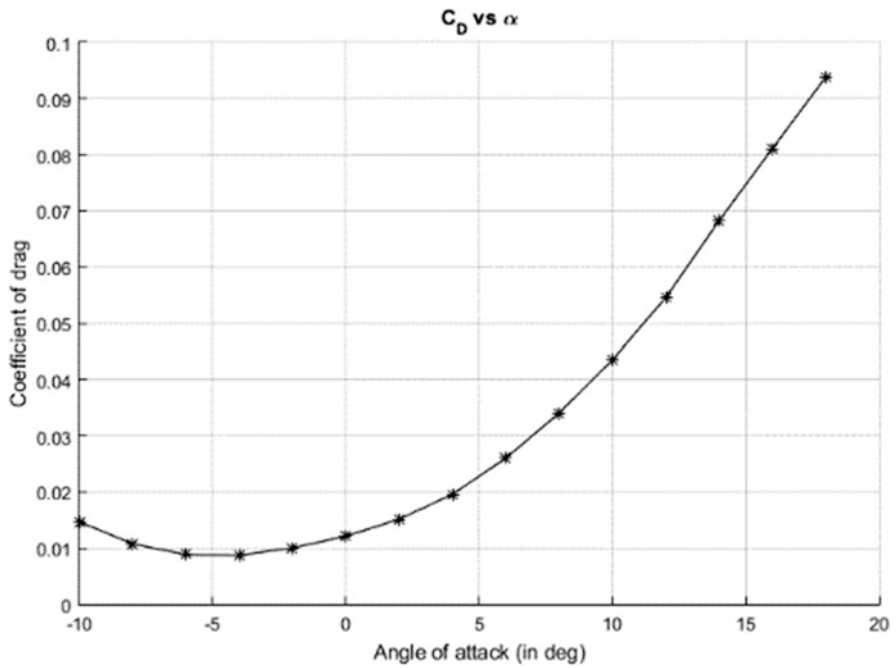


Fig. 7 Drag curve (C_D vs α) for aircraft

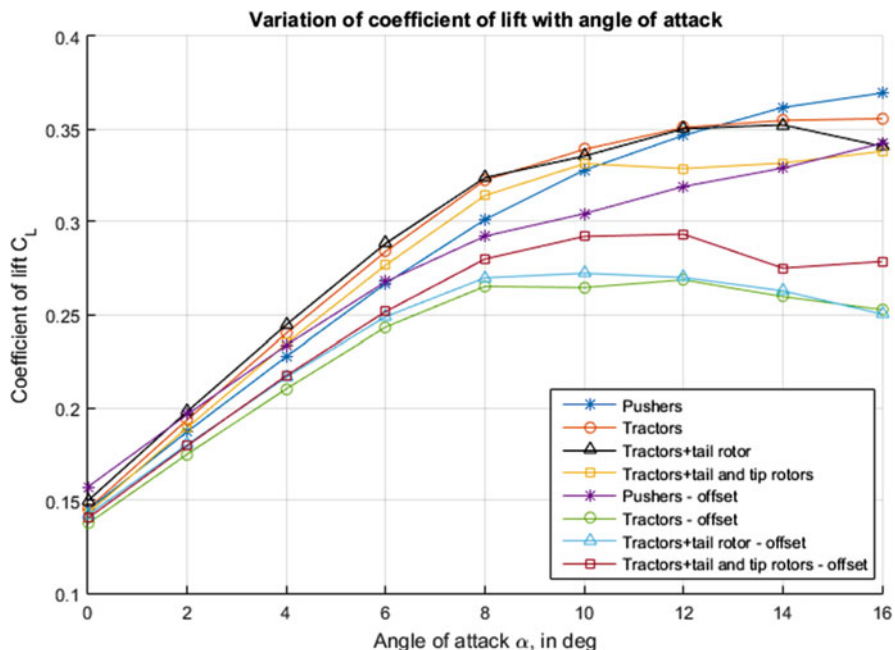


Fig. 8 Lift curves for various propeller configurations

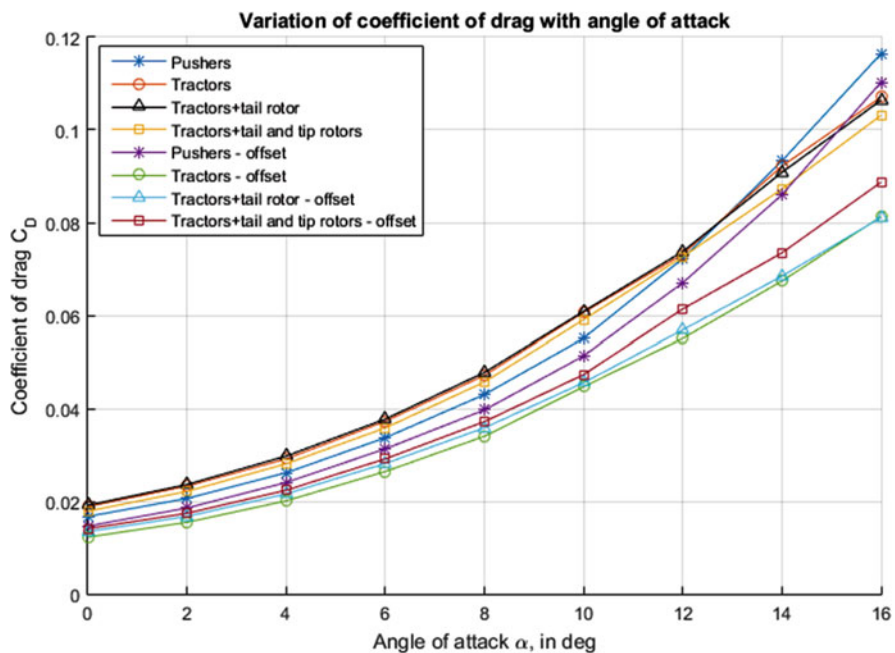


Fig. 9 Drag curves for various propeller configurations

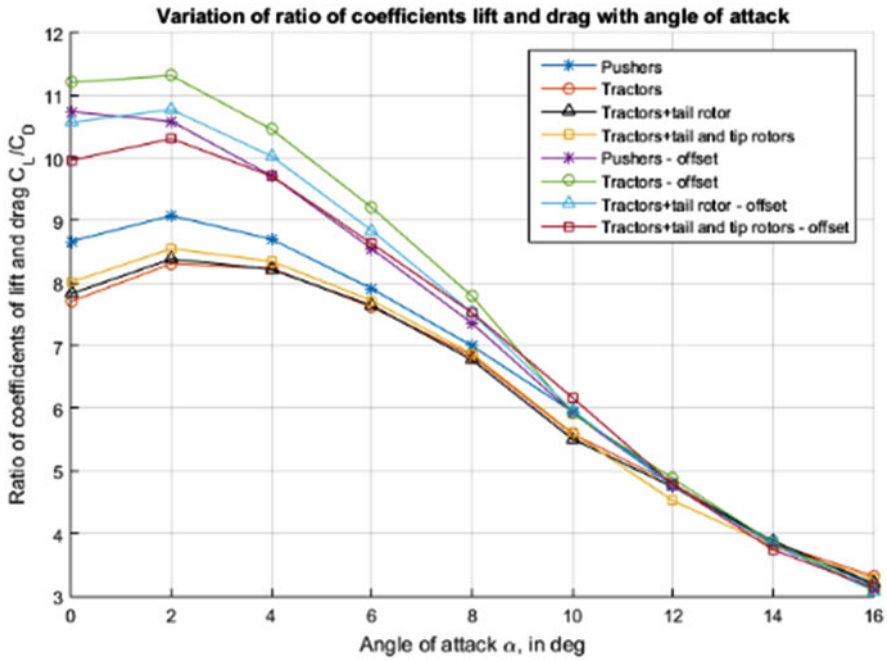


Fig. 10 Lift-to-drag curves for various propeller configurations

propellers’ slipstream increases both the lift and drag of the main wing. On the contrary, when the same propellers are vertically offset above the wing, the increased dynamic pressure primarily on the upper surface of the main wing reduces the net pressure difference between the lower and upper surfaces, thus, reducing its lifting capacity.

To see the net effect of this offset we seek the variation of C_L/C_D with α , a measure of aerodynamic efficiency, as shown in Fig. 10. It is evident that this efficiency of the aircraft decreases with α but the configurations with offset always outperform those without offset. For most nonnegative α , the highest lift is obtained by the tractors with a tail rotor followed by tractors only, tractors with tail and tip rotors, and the lowest by pushers only configuration. If the more structurally feasible offset configurations are to be implemented then the highest lift is obtained, in order, using pushers only, tractors with tail and tip rotors, tractors with a tail rotor, and lastly using tractors only. The tractor configuration with an offset, which is commonly used in many such DEP designs, does indeed have the best aerodynamic efficiency as compared to the other designs considered in this study, thus allowing for a more economical usage for commercially ferrying passengers and/or cargo. On the other hand, the pusher propeller configuration without any offset shows the least drag among any other designs, giving it the best C_L/C_D ratio despite having the poorest lifting capacity.

Such a configuration is also seen in many upcoming DEP-based designs due to availability of longer trailing edge to install the motor-propeller units, most notably seen in Lilium (Kim et al., 2018). Commercial applications not only require high payload capacity but more importantly lower drag to extend the range of the aircraft as much as possible, to improve the per mile operating cost. Hence, the configurations with offset are always better due to their higher C_L/C_D ratio. The offset configurations, in order, that offer the best aerodynamic efficiency are tractors only, tractors with a tail rotor, tractors with tail and tip rotors, and pushers only.

It is noteworthy that the addition of the tail rotor to the propeller configurations using a propeller placed at the aft of the fuselage and along its axis is able to alleviate the fuselage drag, though marginally. The high-pressure “dead-wind” zone behind the fuselage that would otherwise add to the drag of the aircraft can be mitigated using such a tail rotor. The placement of tip rotors may show additional benefits once the swirl effects due to the propeller slipstreams are considered, by reducing the losses due to tip vortices. The behavior of the lift-and-drag curves for negative angles of attack for all the configurations, with and without the offset, is pretty similar to each other and that of the airframe alone and hence does not require any detailed analysis.

3.2 Improved Aerodynamic Performance Due to the Propeller Configurations

The change in C_L and C_D due to propeller configurations as compared to the airframe alone has been calculated as given in Eqs. (1) and (2).

$$\Delta C_L = \frac{C_{L\text{with propellers}} - C_{L\text{aircraft}}}{C_{L\text{aircraft}}} * 100 \text{ (in\%)} \quad (1)$$

$$\Delta C_D = \frac{C_{D\text{with propellers}} - C_{D\text{aircraft}}}{C_{D\text{aircraft}}} * 100 \text{ (in\%)} \quad (2)$$

As evident from Fig. 11, the lifting capacity is severely deteriorated by all tractor-based configurations with an offset. At higher α we see that these configurations, in fact, perform worse off as compared to the airframe alone. Due to the reduced aerodynamic interaction of these configurations with the lifting surface, the change in drag is consequently small ($\sim 10\%$), as seen in Fig. 12. The aerodynamic effects for post-stall conditions and negative α are beyond the scope of this study.

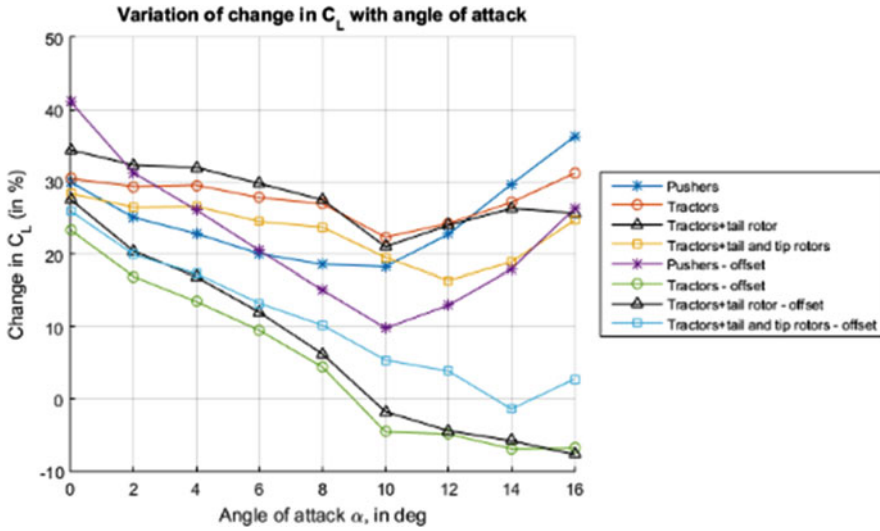


Fig. 11 Change in C_L due to propeller configurations

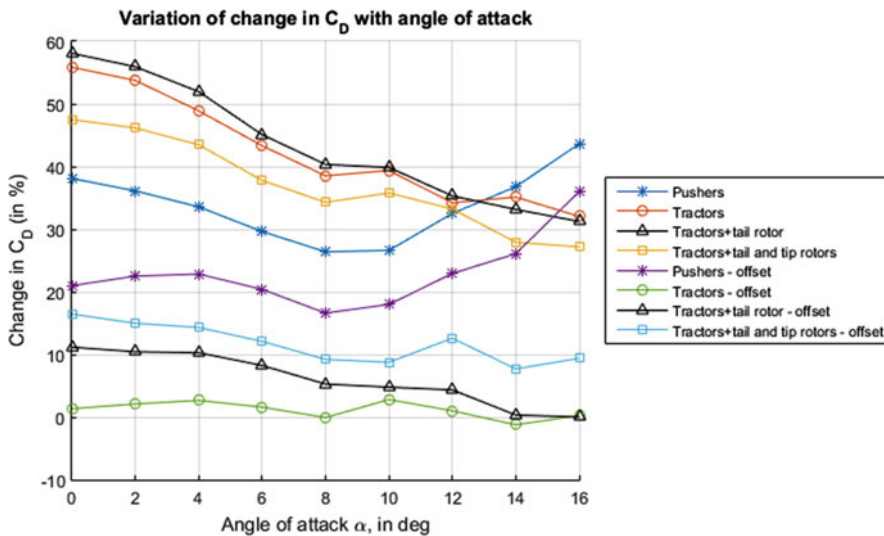


Fig. 12 Change in C_D due to propeller configurations

4 Conclusion

Numerical studies of a novel canard aircraft design were conducted to assess its aerodynamic performance in a given freestream at different angles of attack. It was found to stall and approximately 12° , similar to the airfoil its lifting surfaces are based on. Four propeller configurations were tested under same operating conditions

to find the optimal configuration for a commercially viable passenger/cargo aircraft propulsion system. Tractors with a tail rotor provided the highest increase in lifting capacity, whereas the best aerodynamic efficiency was seen for the tractors only setup with a vertical offset. The relative change in the coefficients of lift and drag due to the propulsion setups has also been compared.

References

- Chan, C. C. (2002). The state of the art of electric and hybrid vehicles. *Proceedings of the IEEE*, 90(2), 247–275.
- FLUENT, ANSYS Inc. <https://www.ansys.com/en-in/products/fluids/ansys-fluent>. Accessed on 20 May 2021.
- Kim, H. D., Perry, A. T., & Ansell, P. J. (2018, July). A review of distributed electric propulsion concepts for air vehicle technology. In *2018 AIAA/IEEE electric aircraft technologies symposium (EATS)* (pp. 1–21). IEEE.
- Patterson, M. D., German, B. J., & Moore, M. D. (2012, September). Performance analysis and design of on-demand electric aircraft concepts. In *12th AIAA aviation technology, integration and operations (ATIO) conference (2012–5474)*.
- Stoll, A. M., Bevirt, J., Moore, M. D., Fredericks, W. J., & Borer, N. K. (2014, June). Drag reduction through distributed electric propulsion. In *14th AIAA aviation technology, integration, and operations conference (2014–2851)*.

Effects of Cruise Flight Conditions on Power and NOx Emissions for High Bypass Turbofan Engine



Hakan Aygun

Contents

| | | |
|-----|------------------------------|-----|
| 1 | Introduction | 152 |
| 1.1 | System Description | 152 |
| 2 | Methodology | 153 |
| 3 | Results and Discussion | 155 |
| 4 | Conclusion | 157 |
| | References | 158 |

Nomenclature

| | |
|-----------|----------------------------|
| BFF | Boeing fuel flow |
| DLR | German Aerospace Center |
| EI | Emission index (g/kg fuel) |
| f | Fuel-to-air ratio |
| LHV | Lower heating value |
| LTO | Landing and take-off |
| \dot{m} | Mass flow rate (kg/s) |
| KN | Kinetic energy |
| M | Mach |
| T | Temperature (K) |
| P | Pressure (kPa) |
| TP | Thrust power (MW) |
| V | Velocity (m/s) |
| W | Wasted power (MW) |

H. Aygun (✉)

Department of Aircraft Air Frame and Power-Plant, Firat University, Elazig, Turkiye

e-mail: haygun@firat.edu.tr

1 Introduction

To keep global warming at 2 °C compared with preindustrial levels, the states and responsible humans should perform maximum efforts. According to recent researches, the achievement of this goal is important challenge with reduction of fuel consumption by engines, developments in aerodynamics, and weight reduction of the aircraft (Zaporozhets et al., 2020). Considering rapid depletion of energy resources due to the increasing world population, an increase in utilizing air vehicles used in military and civil fields seems to be an important problem. From 1974 to 2014, a rise in total consumed energy was calculated about 38.3% (Koruyucu, 2019). The studies that focus on the attempts regarding performance improvement of thermal systems have become hot topic due to importance of energy efficiency (Karagoz et al., 2020). The recent pandemic all around the world shows that the limited sources should be utilized more effectively (Ozturk et al., 2020). The increasing fuel consumption also affects adversely the environment. Therefore, investigation of emissions for gas turbine engines is of high importance.

In this study, with respect to flight conditions, the behavior of exhaust emissions is parametrically examined. Also, power values of the PW4000 engine are computed corresponding to flight conditions. The current study aims at contributing to the literature by measuring NO_x, CO₂ and H₂O emissions at cruise phases.

1.1 System Description

PW4000 engines have been widely used in commercial aircraft so far. These engines produce thrust value covering range of 231 kN and 271 kN and are installed at several major aircraft (Aygun & Turan, 2021). Figure 1 shows PW4000 engine and its components. Based on ICAO database shown in Table 1, EINO_x is calculated for cruise phase.

Before detailed explanation about thermodynamic analysis, pressure and temperature diagrams on component basis are given in Fig. 2. These are obtained by means

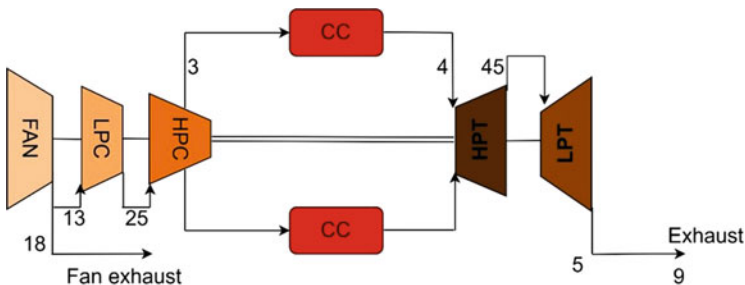


Fig. 1 Illustration of typical PW4000 engine and its components

Table 1 ICAO data for PW4000 at LTO cycle (ICAO, 2021)

| | Take-off | Climb-out | Approach | Idle |
|-------------------|----------|-----------|----------|-------|
| EINox (g/kg) | 28.1 | 22.9 | 11.6 | 4.8 |
| Fuel flow (kg/s) | 2.342 | 1.93 | 0.658 | 0.208 |
| Thrust rating (%) | 100 | 85 | 30 | 7 |

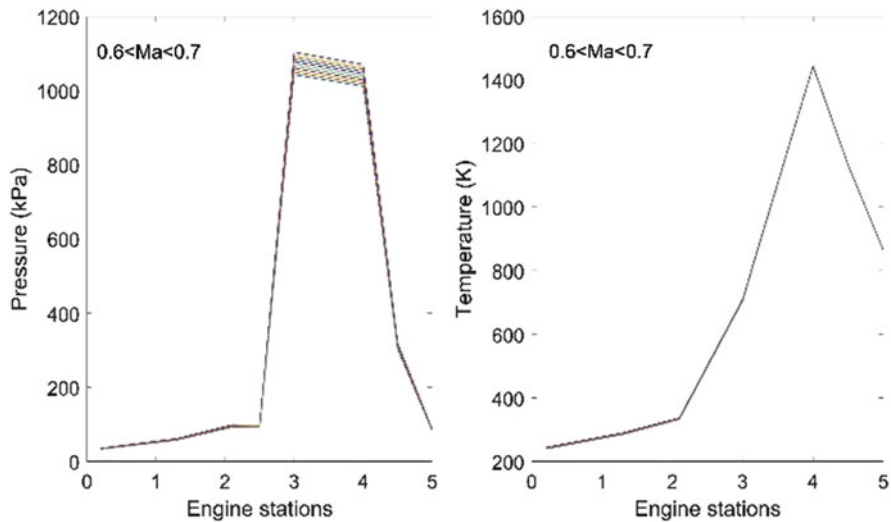


Fig. 2 P and T diagrams for main component inlet-outlet

of specific code involving parametric cycle equations for the high bypass turbofan engine.

Both energy and emission analyses require parameters given in Fig. 3. The average core mass flow decreases from 50.99 kg/s to 45.17 kg/s and the average total mass flow diminishes from 294.83 kg/s to 258.58 kg/s due to rising altitude.

2 Methodology

Main aim to carry out parametric cycle analysis is to estimate required engine parameters for thermodynamic values of component such as fuel flow and exhaust flow velocity. After calculation of fuel to air ratio from cycle equations, thanks to Eq. 1, CO₂ and NO₂ emissions are easily calculated.

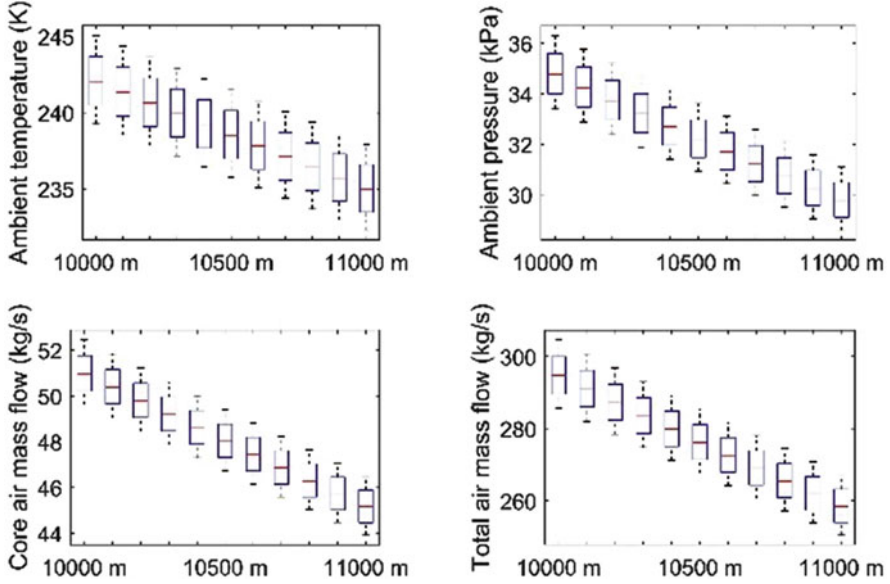
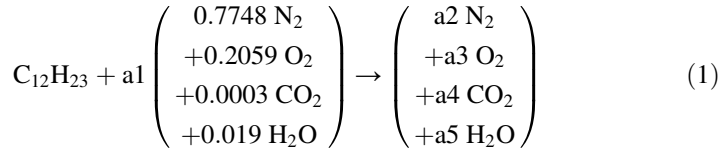


Fig. 3 Main input values for performance analysis



On the other hand, Eqs. 2, 3, 4, 5, and 6 present power relations regarding high bypass turbofan engine (El-Sayed, 2008).

$$\tau P = \tau_{\text{net}} u \quad (2)$$

$$\text{WP} = \frac{1}{2} m_a (u_{18} - u)^2 + \frac{1}{2} m_c (u_9 - u)^2 \quad (3)$$

$$\text{TP} = \frac{1}{2} m_a u_{18}^2 - \frac{1}{2} m_a u^2 + \frac{1}{2} m_c u_9^2 - \frac{1}{2} m_a u^2 \quad (4)$$

$$\eta_{\text{th}} = \frac{\text{Tu} + 0.5 \dot{m}_{13} (1 + f) (u_9 - u)^2 + 0.5 \dot{m}_{18} (u_{18} - u)^2}{\dot{m}_{\text{fuel}} \text{LHV}} \quad (5)$$

$$\eta_o = \eta_{\text{th}} \cdot \eta_p \quad (6)$$

Cruise NOx emissions are computed by employing Boeing Fuel Flow Method 2 and DLR method. For this process, after calculation of fuel flow, by using Eqs. 7, 8, and 9 NOx emission index (EINOx) for PW4000 engine is calculated (Aygun et

al., 2022). In Eq. 7, θ and δ represent relative temperature and pressure, respectively. Also, e^H denotes the humidity factor. In Eq. 9, n and t denote the number of engine and flight duration, respectively, whereas m_{ff} identifies fuel flow (kg/s). Also, subscript j represents corresponding phase.

$$EI_{NOx} = EI_{NOx,SL} \left(\frac{\delta_{amb}^{1.02}}{\theta_{amb}^{3.3}} \right)^{0.5} e^H \tag{7}$$

$$EI_{NOx} = EI_{NOx,SL} \delta_{amb}^{0.4} \theta_{amb}^3 e^H \tag{8}$$

$$E_{NOx} = \sum_j ((n_e t_j m_{ff} EI_{jNOx}) / 1000) \tag{9}$$

3 Results and Discussion

This study deals with power and emission parameters of high bypass turbofan, PW4000. By employing parametric cycle equations, some unknown parameters which are necessary in calculations of energy analysis were calculated. Figure 4 presents effects of Mach and altitude on thrust and wasted powers. As seen in Fig. 4, the higher the Mach, the higher the thrust power whereas the lower the wasted power. However, increasing altitude leads to lower both thrust and wasted power, namely, average TP is calculated as 10.53 MW at 0.6 M and 12.33 MW at 0.7 M. Furthermore, WP is averagely decreasing from 4.85 MW at 0.6 M to 3.93 MW at 0.7 M.

As for Fig. 5, increasing Mach affects favorably overall efficiency whereas rising altitude has adverse effect on it. In this context, average overall efficiency is found as

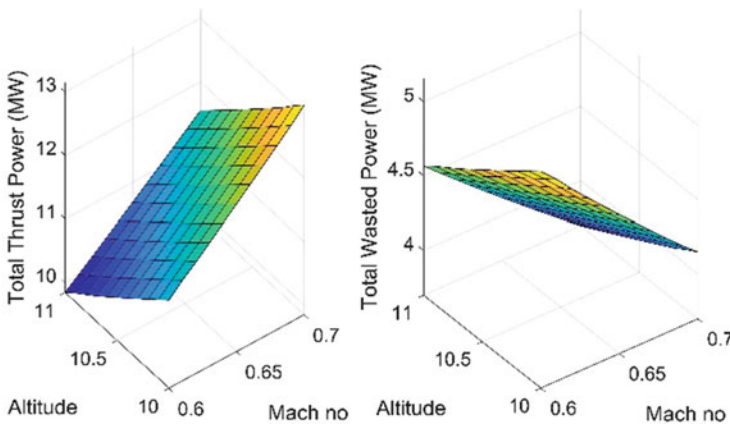


Fig. 4 Variations of total thrust and wasted powers

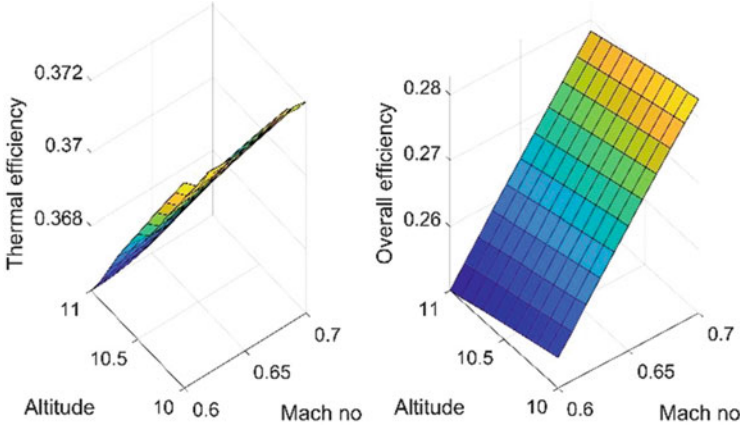


Fig. 5 Variations of thermal and overall efficiencies

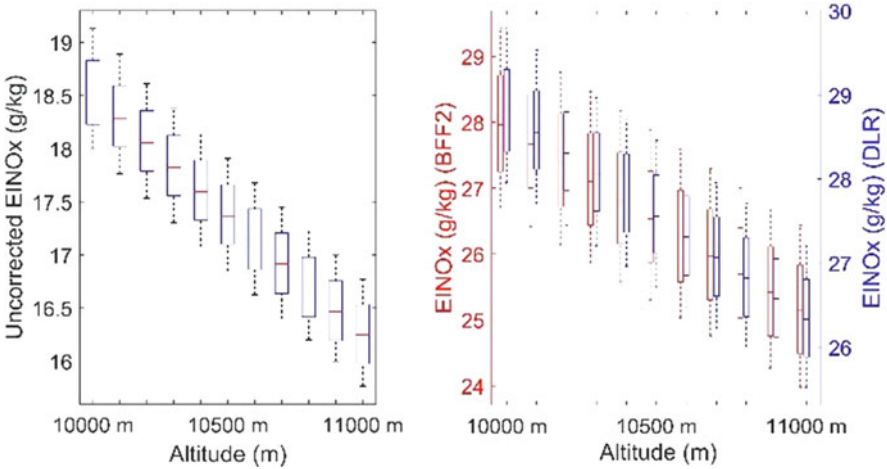


Fig. 6 EINOx emissions at cruise flight conditions (g/kg)

25.26% at 0.6 M and 28.06% at 0.7 M. Besides, thermal efficiency decreases from 36.9% at 10 km to 36.5% at altitude of 11 km.

According to NOx emission results, Fig. 6 presents uncorrected EINOx and corrected EINOx indices. EINOx calculated by DLR is higher compared with that computed by BFF2. On the other hand, each boxplot presents EINOx due to changing Mach. The average EINOx is changed from 27.99 g/kg at 10 km to 25.16 g/kg at 11 km (Fig. 6).

Figure 7 illustrates NOx, CO₂, and H₂O emissions as kg per second. As seen in Fig. 7, the CO₂ emission is calculated higher than H₂O and NOx emissions. The average CO₂ emissions is computed as 3.33 kg/s at 10 km and 2.97 kg/s at 11 km, whereas average H₂O emission is calculated as 1.307 kg/s at 10 km and 1.167 kg/s at

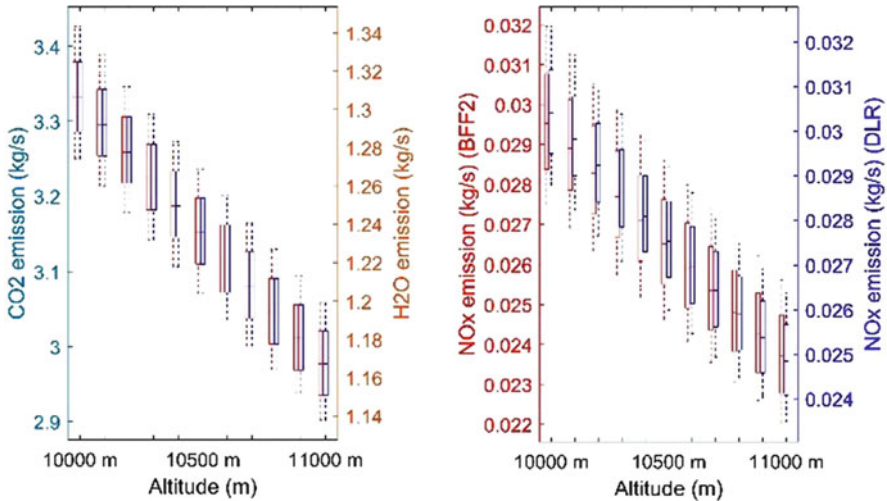


Fig. 7 NOx emissions at cruise flight conditions (kg/s)

11 km. However, NO_x emissions are relatively lower with average 0.0296 kg/s (BFF2) and 0.0304 kg/s (DLR) at 10 km, whereas it is found as 0.0237 kg/s (BFF2) and 0.0248 kg/s (DLR) at 11 km.

4 Conclusion

In this study, energy and emission analysis of PW4000 engine were carried out at different cruise flight conditions. The main aim is to reveal effects of Mach and altitude on the PW4000 power values such as thrust and wasted power and to quantify NO_x emissions as well as CO₂ and H₂O emissions by using two well-known approaches. The results of the current study could be ranked as following:

- The average thrust power of the PW4000 changes from 12.17 MW at 10 km to 10.68 MW at 11 km. It corresponds the decrease with 12.2%.
- The average overall efficiency varies between 26.9% and 26.44% in ranges of altitude 10 km and 11 km, respectively.
- Considering BFF2 method, the average cruise NO_x emission changes from 25.32 g/kg at 0.6 M to 27.89 g/kg at 0.7 M. These values are verified with DLR method that gives in relatively higher values compared with BFF2.
- CO₂ emission is the highest value ranging 3.33 kg/s and 2.97 kg/s, whereas NO_x emission is calculated 0.0295 kg/s and 0.237 kg/s in altitude ranges of 10 km and 11 km, respectively.

As next study, optimum flight phases could be scrutinized so as to find out minimum exhaust emissions by considering several flight parameters.

References

- Aygun, H. & Turan, O. (2021). Entropy, Energy and Exergy for Measuring PW4000 Turbofan Sustainability. *International Journal of Turbo & Jet-Engines*, 38(4), 397–409. <https://doi.org/10.1515/tjj-2018-0050>
- Aygun, H., Sheikhi, M. R., & Kirmizi, M. (2022). Parametric Study on Exergy and NOx Metrics of Turbofan Engine Under Different Design Variables. *Abstract Journal of Energy Resources Technology*, 144(6). <https://doi.org/10.1115/1.4052034>
- El-Sayed, A. F. (2008). *Aircraft propulsion and gas turbine engines*. CRC Press.
- ICAO. Aircraft Engine Emissions Databank [WWW Document]. <https://www.easa.europa.eu/easa-and-you/environment/icao-aircraft-engine-emissionsdatabank>. Accessed 10.02.2021.
- Karagoz, M., Uysal, C., Agbulut, U., & Saridemir, S. (2020). Exergetic and exergoeconomic analyses of a CI engine fuelled with diesel-biodiesel blends containing various metal-oxide nanoparticles. *Energy*, 214, 118830.
- Koruyucu, E. (2019). Energy and exergy analysis at different hybridization factors for hybrid electric propulsion light utility helicopter engine. *Energy*, 189, 116105.
- Ozturk, M. M., Dogan, B., & Erbay, L. B. (2020). Performance assessment of an air source heat pump water heater from exergy aspect. *Sustainable Energy Technologies and Assessments*, 42, 100809.
- Zaporozhets O., Isaienko V., & Synylo K. (2020). Trends on current and forecasted aircraft hybrid electric architectures and their impact on environment. *Energy*, 211, 118814. <https://doi.org/10.1016/j.energy.2020.118814>

Conceptual Design and Sizing of LiDAR-Equipped Solar-Powered HALE UAV for Coastal Surveillance in India



Nouman Uddin and Rajkumar S. Pant

Contents

| | | |
|----|---|-----|
| 1 | Introduction | 160 |
| 2 | Payload Specifications | 161 |
| 3 | Literature Survey of Existing UAVs | 162 |
| 4 | Mission Profile | 162 |
| 5 | Design Methodology | 164 |
| 6 | Powerplant Selection and Initial Sizing | 165 |
| 7 | Component Mass Breakdown | 165 |
| 8 | Constraint Analysis | 165 |
| 9 | CAD Model of Geometry | 166 |
| 10 | Geometry Sizing | 167 |
| 11 | Aerodynamic Analysis | 167 |
| 12 | Scheme of Payload Installation | 168 |
| 13 | Conclusions | 168 |
| | References | 169 |

Nomenclature

| | |
|---------|-----------------------------|
| LiDAR | Light detection and ranging |
| UAV | Unmanned aerial vehicle |
| CAD | Computer-aided drawing |
| OpenVSP | Open vehicle sketch pad |

N. Uddin (✉) · R. S. Pant

Aerospace Engineering Department, Indian Institute of Technology Bombay, Mumbai, Maharashtra, India

e-mail: noumanuddin1@iitb.ac.in; rpant@iitb.ac.in

1 Introduction

India is a peninsular country surrounded by oceans along its three sides, with a coastline of ~7500 km. In order to study the physical and chemical processes that shape coastal landscapes, geologists need to detect coastal topography and measure the elevation of topographical features present beneath the tree cover. Valuable inferences can be made about the factors influencing coastal climate, hydrology, and habitats, by studying results of repeat topographical surveys conducted at different times in a year or over a number of years.

In 2018, the problem statement of the 2nd National Aerospace Conceptual Design Competition (NACDeC-II) related to such an aircraft was released, which involved design of a solar-powered UAV to collect light detection and ranging (LiDAR) data while flying over ten ground stations located near the Indian coastline, as shown in Fig. 1 (NACDeC-II, 2018–19). The total range to be covered by the UAV was 3800 km, as can be seen in Table 1 that lists these ground stations along with the approximate flight distances between them.

The key performance and operational requirements for the UAV are listed in Table 2.

It was required that the UAV should be deployed from Station 1 (Porbandar), collect LiDAR data along the entire route in a nonstop flight, and finally land at Station 10 (Kolkata). Landing was not permitted at any intermediate Station or elsewhere along the route. LiDAR data was to be collected only at night (sunset to

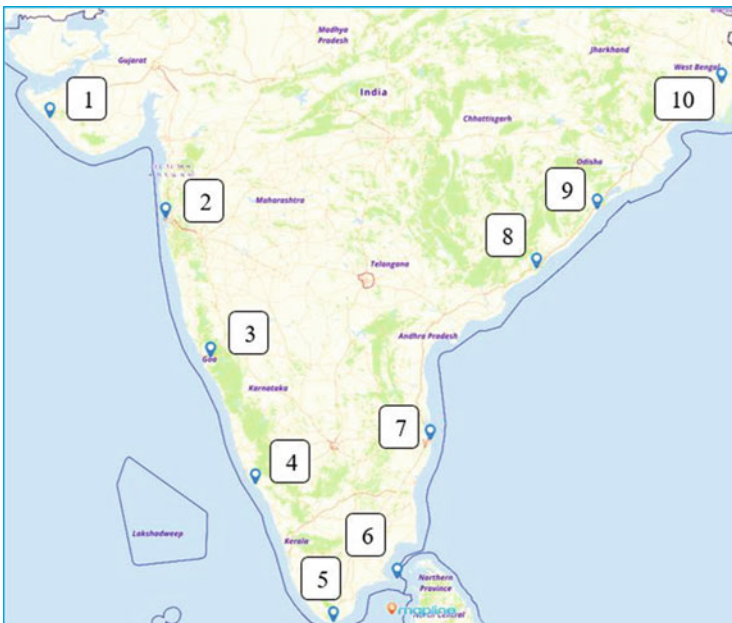


Fig. 1 Indian shoreline with ten ground stations (NACDeC-II, 2018–19)

Table 1 List of ground stations (NACDeC-II, 2018–19)

| Station number | Station name | Distance between two stations (km) |
|----------------|-----------------|------------------------------------|
| 1 | Porbandar | 0 |
| 2 | Mumbai | 440 |
| 3 | Goa | 440 |
| 4 | Kannur | 400 |
| 5 | Kanyakumari | 480 |
| 6 | Rameswaram | 245 |
| 7 | Chennai | 430 |
| 8 | Vishakhapatnam | 600 |
| 9 | Gopalpur-on-Sea | 250 |
| 10 | Kolkata | 515 |
| Total | | 3800 |

Table 2 Key mission requirements (NACDeC-II, 2018–19)

| Parameter | Value |
|---|-------|
| Operating altitude AMSL (km) | 15–20 |
| Cruising speed (m/s) | 15–25 |
| Loitering altitude AMSL (km) | 15 |
| Loitering radius (km) | 1.5 |
| Takeoff run available (km) | 1.0 |
| Operation under Indian reference atmosphere | |
| LiDAR data collection only during sunset to sunrise | |

sunrise). This gives better fidelity data, since during the daytime, high level of background light can affect the accuracy of the readings. During the daytime, the payload was to be turned off, and the UAV required to loiter over any of the ground stations at an altitude of 15 km AMSL, at which the ambient winds are expected to be low.

2 Payload Specifications

LiDAR (light detection and ranging) is a remote sensing method that uses light in the form of a pulsed laser to measure distances to the Earth's surface from an aerial platform. These light pulses, combined with other data recorded by the aerial platform, generate precise, three-dimensional information about the shape of the Earth and its surface topography. A LiDAR payload principally consists of a laser, a scanner, and a specialized GPS receiver. Airborne LiDAR system allows scientists to produce accurate shoreline maps and to easily generate digital elevation models of the land. A typical LiDAR payload is shown in Fig. 2.

Payload mass is 30 kg with diameter of 0.25 m and length of 0.7 m, and power consumption to be 500 W.

Fig. 2 LiDAR and its dimensions (NACDeC-II, 2018–19)



The remaining part of this chapter describes the design methodology followed, and presents the key results of *Vihangam*, a UAV designed to meet the abovementioned requirements.

3 Literature Survey of Existing UAVs

There are many high-altitude long endurance (HALE) UAVs available, which are designed to operate in the stratosphere. A detailed survey of literature of data related to ten such UAVs was carried out, and useful inferences were drawn about parameters. Table 3 lists down the comparative data of all these UAVs. It may be noted that AQUILA has solar cells as a source of energy while remaining UAVs have batteries as an energy source.

In addition to the above, previous studies on design of solar-powered HALE-UAVs carried out by Bhatt (2012), Najafi (2011), and Bilal (2012) were reviewed to draw useful information related to design procedure.

4 Mission Profile

Based on a critical study of the design and the mission requirements, a detailed mission profile for *Vihangam* was arrived at, as shown in Fig. 3.

The station number with subscript “L” shows the loitering station over which *Vihangam* will spend its daytime in a slow speed loiter within a loitering radius of 1 km, since collection of data was permitted only during night (sunset to sunrise). The estimated average total duration of the flight was 106 h, that is, 4.6 days, covering 3800 km (Table 4).

Table 3 Comparative data of existing solar HALE UAVs

| UAVs | AUW (kg) | Wing span (m) | Wing AR | Maximum cruise speed (km/h) | Maximum power (kW) | Max altitude (km) | Endurance (h) | Payload (kg) |
|------------|----------|---------------|---------|-----------------------------|--------------------|-------------------|---------------|--------------|
| AQUILA | 400 | 43.00 | 26 | 128 | 54.0 | 27.4 | 720 | 15 |
| CENTURION | 826 | 62.78 | 26 | 29 | 31.0 | 30.4 | 16 | 272 |
| HELIOS | 1055 | 75.28 | 31 | 43 | 31.0 | 29.5 | 24 | 330 |
| HELIPLAT | 876 | 73.00 | 33 | 71 | 30.0 | 20.0 | 3600 | 130 |
| ODYSSEUS | 500 | 74.10 | 22 | 243 | 250.0 | 27.0 | 2160 | 500 |
| PATHFINDER | 318 | 37.00 | 15 | 32 | 12.5 | 25.0 | 15 | 68 |
| + | | | | | | | | |
| PHASA 35 | 150 | 35.00 | 31 | 144 | 1.5 | 21.0 | 8640 | 16 |
| SOLARA 50 | 159 | 50.00 | 35 | 104 | 7.0 | 20.0 | 43,200 | 32 |
| ZEPHYR S | 62 | 25.00 | 33 | 58 | 3.0 | 21.0 | 600 | 5 |
| ZEPHYR 7 | 53 | 22.55 | 31 | 56 | 3.0 | 21.0 | 336 | 2.5 |

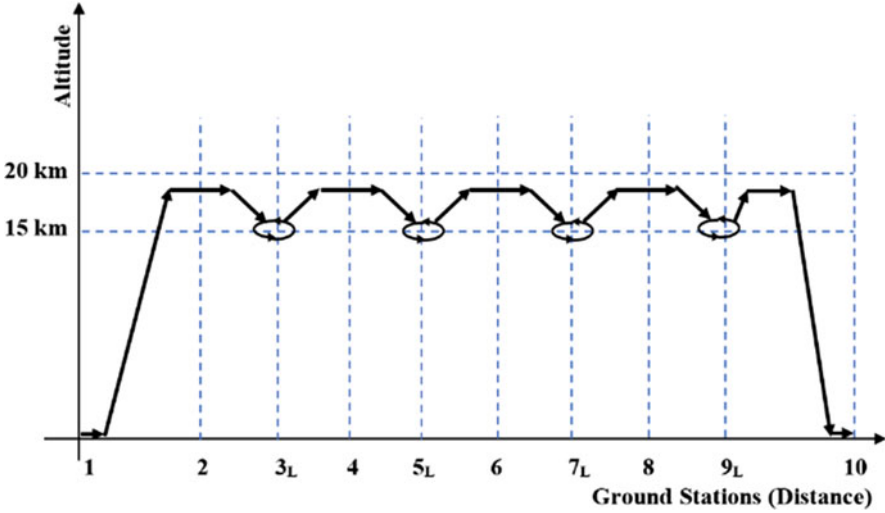
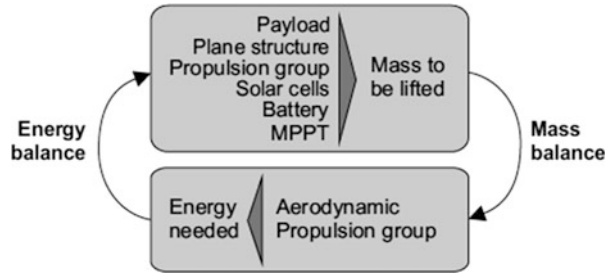


Fig. 3 Mission profile of *Vihangam*

Table 4 Distance and time during the mission (original lab measurements)

| Cruise flight | Distance covered (km) | Average speed (m/s) | Departure and arrival times |
|---------------|-----------------------|---------------------|-----------------------------|
| 1-2-3L | 880 | 20.8 | 06:18–06:58 |
| 3-4-5L | 880 | 20.8 | 18:13–06:32 |
| 5-6-7L | 675 | 15.8 | 18:12–06:30 |
| 7-8-9L | 850 | 20.0 | 17:52–06:15 |
| 9-10 | 515 | 20.8 | 18:03–01:00 |

Fig. 4 Design principle (Noth, 2008)



5 Design Methodology

The conceptual design methodology of *Vihangam* solar-powered UAV aimed to achieve two balances, viz., energy and mass balance, as shown in Fig. 4.

6 Powerplant Selection and Initial Sizing

Powerplant of *Vihangam* consists of four electrical engines powered by solar panels, rechargeable batteries, and electric motors. Solar panels made of single junction GaAs are used, which have been shown to achieve a maximum efficiency of ~30%. Li-S batteries were selected for *Vihangam*, due to their high energy density.

The average value of the solar irradiance was obtained considering all the stations for the particular month of operation from September to February. Hence, the average solar irradiance considered is $5.5 \text{ kWh/m}^2/\text{day}$.

Based on the survey of literature related to similar UAVs, the total maximum power required to maintain the flight of *Vihangam* is estimated to be ~8 kW. The solar panel area was estimated to be 58.18 m^2 , using the procedure suggested by (Noth, 2008).

7 Component Mass Breakdown

The total weight of *Vihangam* consists of the weight of airframe, payload, solar panel, batteries, avionics, and propeller system. Airframe weight was calculated using the Stender's model (Stender, 1969). Avionics weight was estimated to be 20 kg, which is typical of such UAVs. The weight of other components was estimated using standard procedures. Component mass breakdown of *Vihangam* is listed in Table 5.

8 Constraint Analysis

Constraint analysis of *Vihangam* was carried out using the procedure suggested by Raymer (2012) to meet all the performance and mission requirements. The final constraint diagram is shown in Fig. 5.

Table 5 Component mass breakdown of *Vihangam*

| Component | Mass (kg) |
|------------------|-----------|
| Airframe | 105 |
| Payload | 30 |
| Solar panel | 10 |
| Batteries | 25 |
| Avionics | 20 |
| Propeller system | 10 |
| Total | 200 |

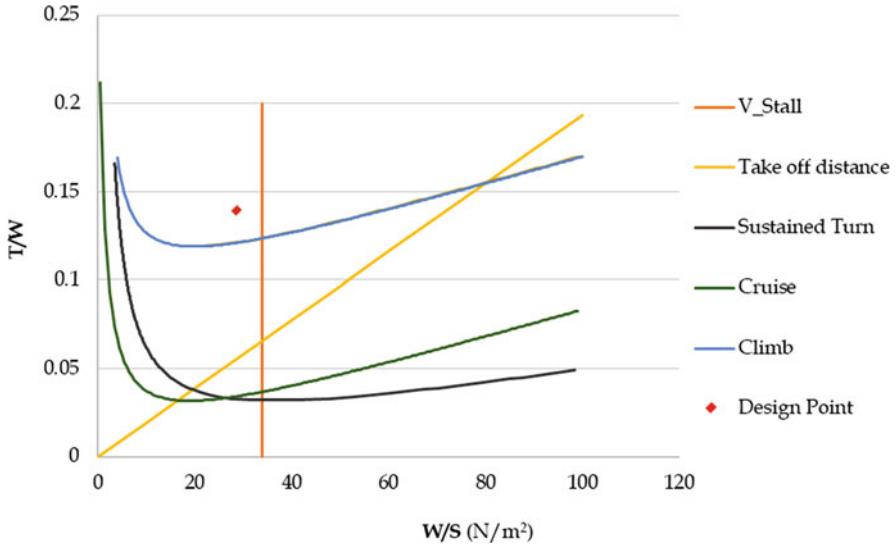


Fig. 5 Constraint diagram

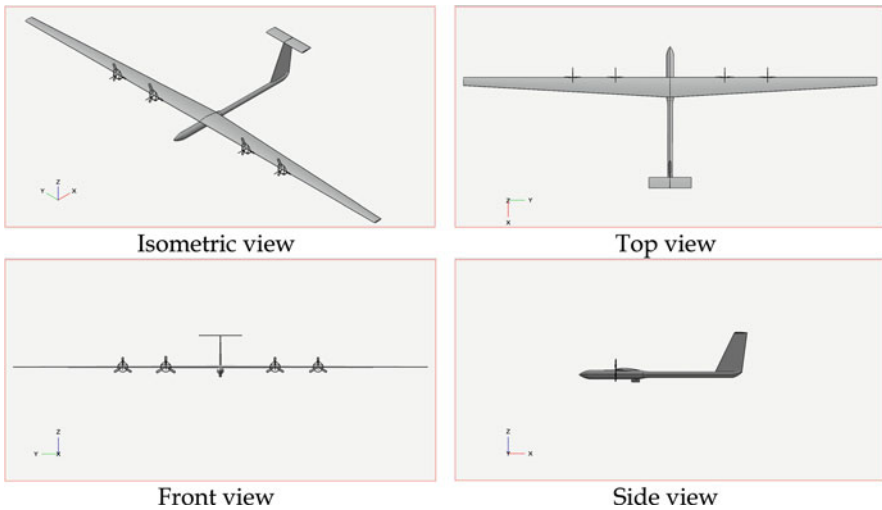


Fig. 6 Conceptual sketches of Vihangam UAV

Design point chosen was a wing loading of 30 N/m^2 and thrust-to-weight ratio of 0.14, or power-to-weight ratio of 40.38 W/kg.

9 CAD Model of Geometry

A CAD model of Vihangam was created using OpenVSP, an open-source CAD tool developed by NASA (OpenVSP, 2020), as shown in Fig. 6.

Table 6 Geometrical specifications of *Vihangam*

| Wing | | |
|---------------------------------|--------------------------|-----------|
| Layout | High wing | |
| Airfoil | NACA 2414 | |
| Thickness ratio (%) | 14 | |
| Root chord (m) | 2.020 | |
| Tip chord (m) | 0.808 | |
| Area (m ²) | 60 | |
| Span (m) | 42.42 | |
| Aspect ratio | 30 | |
| Taper ratio | 0.4 | |
| Fuselage | | |
| Length (m) | 14 | |
| Diameter (m) | 0.75 (front), 0.5 (rear) | |
| Fineness ratio | 17 | |
| Moment arm (m) | 9 | |
| Tail | Horizontal | Vertical |
| Airfoil | NACA 0008 | NACA 0012 |
| Aspect ratio | 4 | 2 |
| Planform area (m ²) | 4.713 | 5.656 |
| Span (m) | 4.342 | 3.363 |
| Root chord (m) | 1.085 | 2.278 |
| Tip chord (m) | 1.085 | 1.085 |
| Thickness ratio (%) | 8 | 12 |

10 Geometry Sizing

Geometry sizing of *Vihangam* was carried using the procedure suggested by Raymer (2012), and the results are listed in Table 6.

11 Aerodynamic Analysis

Aerodynamic analysis of *Vihangam* was carried out using OpenVSP (2020), and validated using the procedure suggested by Raymer (2012). The parasite drag coefficient and maximum lift coefficient were estimated to be 0.020 and 1.5, respectively. Oswald's efficiency factor was estimated as 0.96. The drag polar of *Vihangam* is shown in Fig. 7.

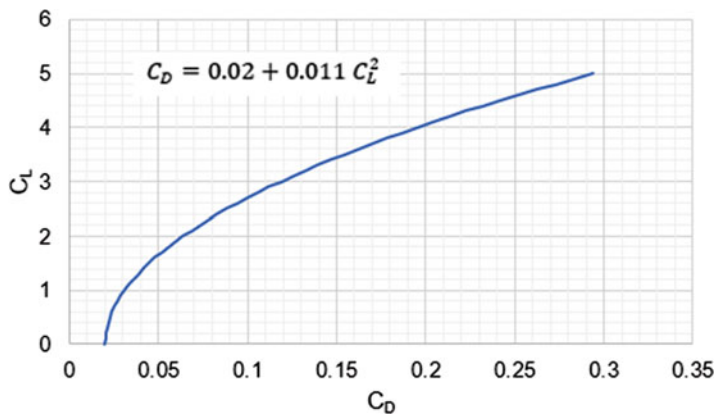


Fig. 7 Drag polar of *Vihangam*

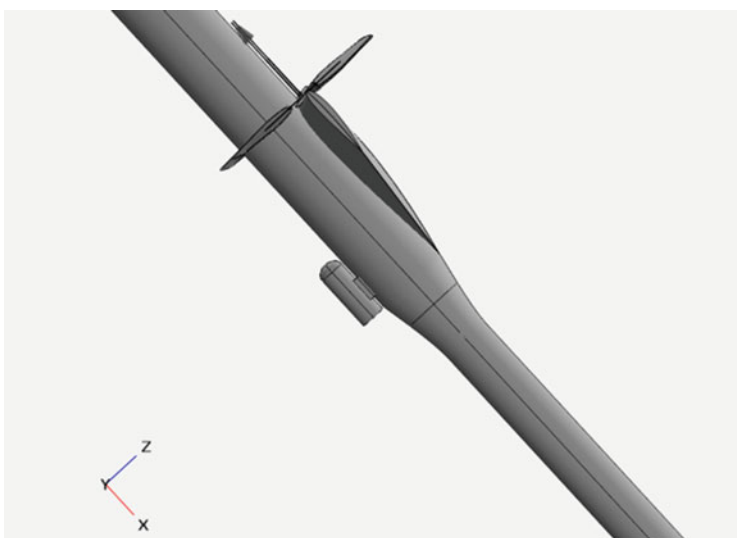


Fig. 8 *Vihangam* carrying LiDAR

12 Scheme of Payload Installation

LiDAR system should be mounted below the fuselage to carry out the surveillance task. Figure 8 shows the mounting orientation for LiDAR system.

13 Conclusions

This chapter describes the key features of a UAV named *Vihangam*, which was the result of a design exercise carried out in response to a specified problem statement for a solar-powered high-altitude long endurance mission. It was seen that *Vihangam*

was able to address all the mission and operational requirements specified in the problem statement. The methodology described in this chapter can be easily adopted for conceptual design and sizing of a solar UAVs to meet similar payload and mission requirements.

References

- Bhatt, M. R. (2012). *Solar power unmanned aerial vehicle: high altitude long endurance applications (HALE-SPUAV)*. A project presented to The Faculty of the Department of Mechanical and Aerospace Engineering.
- Bilal, A. (2012). *Design, development and fabrication of solar powered HALE UAV*. LAP Lambert Academic Publishing.
- Najafi, Y. (2011). *Design of high altitude long endurance solar powered UAV-Solar Powered Aerial Communicator (SPACOM)* (Doctoral dissertation, San Jose State University).
- Noth, A. (2008). *Design of solar powered airplanes for continuous flight* (Doctoral dissertation, ETH Zurich).
- “OpenVSP” Version: 3.21.1, 11th May 2020, NASA open source Aircraft Parametric Geometry tool. Available on <http://openvsp.org/>
- Problem statement of 2nd National Aerospace Conceptual Design Competition (NACDeC-II), 2018–19.
- Raymer, D. P. (2012). *Aircraft Design: a Conceptual Approach* (AIAA Education Series). Reston, Virginia.
- Stender, W. (1969). *Sailplane weight estimation*. Organisation Scientifique et Technique Internationale du vol à Voile.

Investigation of Heat Loss by Radiation from External Walls of Airport Buildings Depending on Different Sky Cloudiness Factor



Okan Kon and İsmail Caner

Contents

| | | |
|---|-----------------------------|-----|
| 1 | Introduction | 172 |
| 2 | Material and Method | 172 |
| 3 | Result and Discussion | 176 |
| 4 | Conclusions | 178 |
| | References | 179 |

Nomenclature

| | |
|---------------|---------------------------|
| CF | Cloudiness factor |
| G | Solar radiation |
| T | Temperature |
| ε | Emissivity |
| φ | Relative humidity |
| P | Pressure |
| σ | Stefan–Boltzmann constant |

Subscripts

| | |
|------|-----------|
| Dif | Diffuse |
| Glob | Total |
| dp | Dew point |

O. Kon (✉) · İ. Caner
Balıkesir University, Engineering Faculty Department of Mechanical Engineering, Cagis
Campus, Balıkesir, Turkiye
e-mail: okan@balikesir.edu.tr; ismail@balikesir.edu.tr

| | |
|------|------------|
| part | Partial |
| sat | Saturation |
| out | Outdoor |
| surf | Surface |
| rad | Radiation |

1 Introduction

The aim of the study is to calculate the radiation heat loss from the exterior surfaces of the airport buildings due to the different cloudiness factors of the outdoor environment for 20 cities selected from different climatic zones around the world. Average dry bulb temperatures for 20 cities, based on average relative humidity and dew point temperatures, the required sky emissivity (ϵ_{sky}) and sky temperature (T_{sky}) values were determined. In the calculations, cloudy sky atmospheric emissivity models were used, taking into account the cloudy conditions, which are the bad weather conditions. For this reason, coefficients depending on different cloudiness states are accepted. The emissivity values (ϵ_{surf}) for the surfaces of airport buildings were chosen as 0.5, 0.7, and 0.9. For the sky cloudiness factor (CF), depending on the literature, 0.0 is accepted as completely cloudless, 0.1–0.3 is slightly cloudy, 0.4–0.6 is partly cloudy, 0.7–0.9 is very cloudy, and 1.0 is completely cloudy. In the study, cloudiness factor (CF) value in calculations was accepted 0.0, 0.3, 0.6, 0.9, and 1.0. According to the Turkish Insulation Standard (TS 825), the indoor temperatures of the airport buildings are taken as 20 °C.

2 Material and Method

The sky cloudiness factor (CF):

$$CF = \left(1.4286 \frac{G_{\text{Dif}}}{G_{\text{Glob}}} - 0.3 \right)^{0.5} \quad (1)$$

Here, G_{Dif} is the diffuse radiation on the horizontal and G_{Glob} is the total radiation on the horizontal.

$\epsilon_{\text{clear-sky}}$ is the emissivity during clear-sky conditions:

$$\epsilon_{\text{clear-sky}} = 0.754 + 0.0044 \cdot T_{\text{dp}} \quad (2)$$

Here, T_{dp} is dew point temperature.

Dew point temperature is the temperature at which air begins to condense when cooled at constant pressure. In other words, it is the saturation temperature of water at partial vapor pressure.

$$T_{dp} = T_{sat, P_{part}} \quad (3)$$

$$P_v = \varphi \cdot P_{T_{out}} \quad (4)$$

Here, φ is outdoor relative humidity, P_{part} is partial pressure of water vapor at outdoor temperature, and T_{sat} is saturated water vapor pressure.

ε_{sky} is cloudy sky emissivity:

$$\varepsilon_{sky} = \varepsilon_{clear-sky} + 0.8 (1 - \varepsilon_{clear-sky}) \cdot CF \quad (5)$$

Sky temperature (T_{sky}) can be calculated through below formula:

$$T_{sky} = T_{out} \cdot [\varepsilon_{sky} + 0.8 (1 - \varepsilon_{sky}) CF]^{0.25} \quad (6)$$

Here, T_{out} is the outdoor air temperature.

External surface radiative heat loss between a building surface and sky can be calculated from below formula:

$$q_{rad} = \sigma \cdot \varepsilon_{surf} \cdot (T_{surf}^4 - T_{sky}^4) \quad (7)$$

Here, σ is Stefan–Boltzmann constant, ε_{surf} is building external surface emissivity, and T_{surf} is the airport external surface temperature (Ahmed et al., 2020; Çengel & Boles, 2012; Evangelisti et al., 2017, 2019; Dai & Fang, 2014; Li et al., 2017; Niemelä et al., 2001; Tang et al., 2004).

Among the 20 selected cities, the sky cloudiness factor (CF) value between 0.0 and 1.0 was calculated with the highest sky emissivity (ε_{sky}) value of between 0.807 and 0.962 in Lisbon (the capital of Portugal), Cape Town (the capital of South Africa), and Auckland (the city in New Zealand). These cities also have the highest dew point temperature (12 °C). Thus, the dry bulb temperature is 17.0 °C in Lisbon and Cape Town, and 15.0 °C in Auckland. The highest dry bulb temperature (T_{out}) is 17.0 °C in Lisbon and Cape Town (the capital of South Africa). Relative humidity value of Lisbon is 74%, Cape Town is 73%, and Auckland is 79%. The lowest sky emissivity (ε_{sky}) value was calculated between 0.767 and 0.954 at Beijing (the capital of China). Beijing has 13.0 °C dry bulb temperature and 55% relative humidity. This relative humidity value is the lowest humidity value. Therefore, the city with the lowest dew point temperature of 3.0 °C is Beijing. Sky temperature (T_{sky}) values in Beijing are calculated between 12.17 and 12.85 °C depending on the sky emissivity value.

Kiev (the capital of Ukraine) and Prague (the capital of Czech Republic) have the second lowest sky emissivity values. Sky emissivity was determined between 0.772

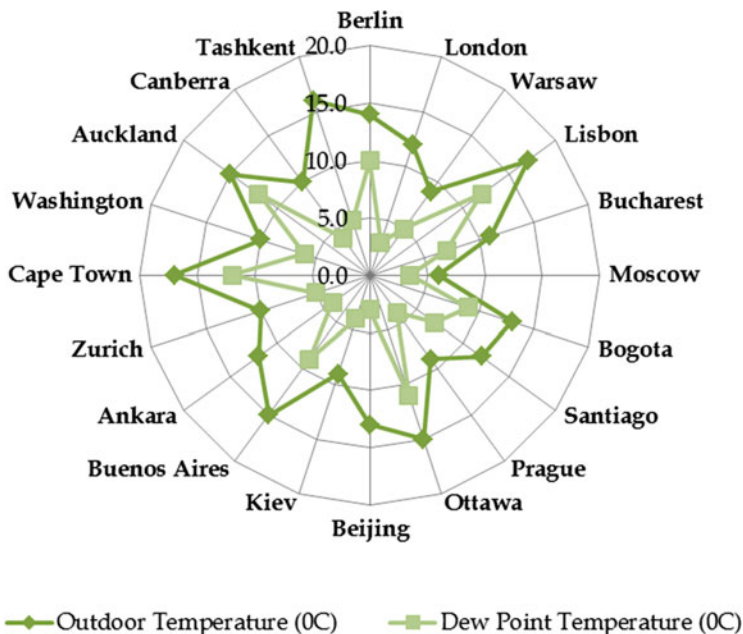


Fig. 1 The average outdoor and dew point temperatures of 20 selected cities in different climate zones in the world (www.timeanddate.com)

and 0.936 depending on different sky cloudiness factors. The dry bulb temperature in Kiev and Prague is 9.0 °C and the dew point temperature is 4.0 °C. Sky temperature values were calculated to between 8.44 and 8.90 °C depending on the sky emissivity value.

The second city with the highest sky emissivity value was calculated in Ottawa (the capital city of Canada). Sky emissivity value was found between 0.803 and 0.961 depending on different sky cloudiness factors. The dry bulb temperature in Ottawa is 15.0 °C and the dew point temperature is 11.0 °C. Relative humidity value is 75%. It was observed that the sky temperature value changed between 14.20 and 14.85 °C. In Fig. 1, average outdoor and dew point temperatures of 20 selected cities in different climate zones in the world are given. Table 1 shows the geographical characteristics of 20 selected cities in different climate zones around the world. In Fig. 2, different sky cloudiness factor (CF) related sky emissivity values of 20 selected cities in different climatic zones in the world are given.

For the 20 selected cities, the highest relative humidity value was found in Moscow (the capital of the Russian Federation) with 82%. The lowest was 55% in Beijing and Tashkent (the capital of Uzbekistan). The second highest value was determined at 79% in Polish capital, Warsaw. The second lowest was 63% in Ankara (the capital of Turkey). These values are shown in Fig. 3, the average relative humidity values of the outdoor environment for the 20 selected cities.

Table 1 The geographical properties of selected cities (ASHRAE; Evangelisti et al. 2019; www.timeanddate.com)

| City | Latitude | Longitude | Elevation (m) | Climatic characteristics |
|------------------------------|----------|-----------|---------------|--------------------------|
| Berlin | 52.47 N | 13.30 E | 51 | Mild temperate |
| London | 51.48 N | 0.45 W | 25 | Mild temperate |
| Warsaw | 52.17 N | 20.97 E | 106 | Mild temperate |
| Lisbon | 38.77 N | 9.13 W | 114 | Mild temperate |
| Bucharest | 44.48 N | 26.18 E | 90 | Mild temperate |
| Moscow | 55.83 N | 37.62 E | 156 | Snow |
| Bogota | 4.70 N | 74.13 W | 2546 | Tropical |
| Santiago | 33.38 S | 70.78 W | 474 | Dry |
| Prague | 50.10 N | 14.25 E | 365 | Mild temperate |
| Ottawa | 45.32 N | 75.67 W | 114 | Snow |
| Beijing | 39.93 N | 116.28 E | 55 | Mild temperate |
| Buenos Aires | 34.50 S | 58.42 W | 6 | Dry |
| Kiev | 50.40 N | 30.57 E | 167 | Snow |
| Ankara | 40.12 N | 33.00 E | 949 | Snow |
| Zurich | 47.38 N | 8.57 E | 569 | Mild temperate |
| Cape Town | 33.97 S | 18.60 E | 42 | Mild temperate |
| Washington (Olympia airport) | 46.97 N | 122.90 E | 61 | Mild temperate |
| Auckland | 37.02 S | 174.80 E | 6 | Mild temperate |
| Canberra | 35.30 S | 149.20 E | 580 | Mild temperate |
| Tashkent | 41.27 N | 69.27 E | 466 | Dry |

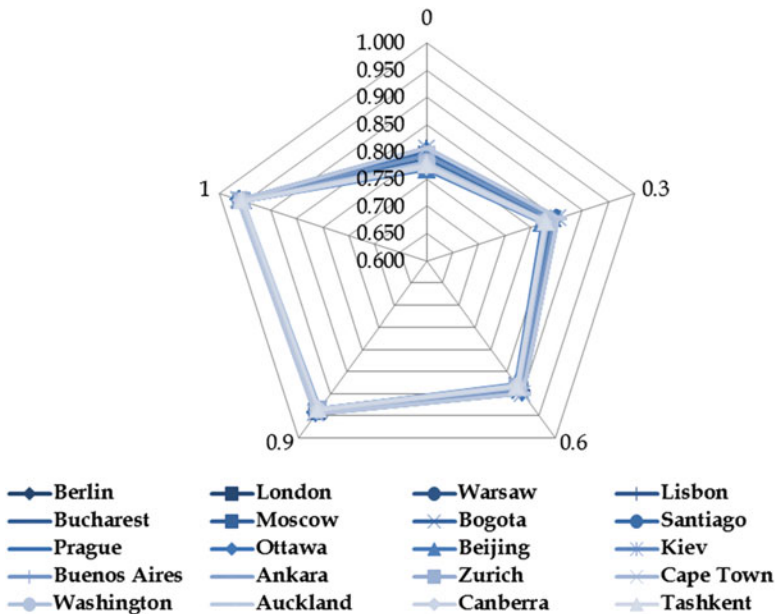


Fig. 2 The sky emissivity values depending on the sky cloudiness factor (CF) for selected cities

Fig. 3 The average relative humidity of 20 selected cities (www.timeanddate.com)

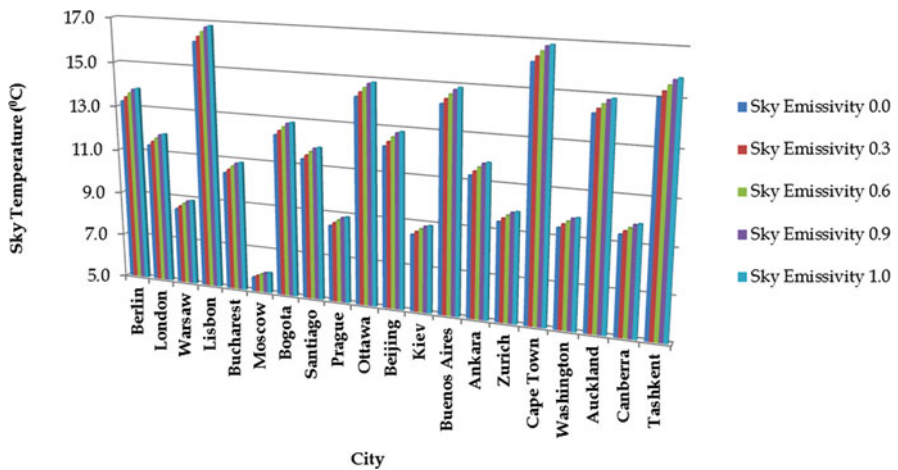
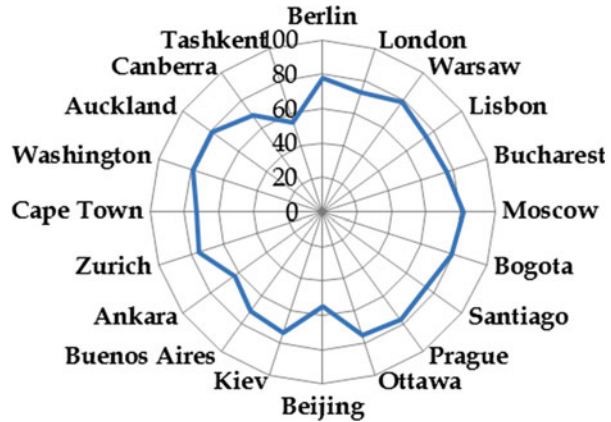


Fig. 4 The sky temperature values depending on different sky emissivity values for selected cities

3 Result and Discussion

The highest sky temperature values were calculated for Lisbon and Cape Town between 16.11 and 16.84 °C. For Auckland, it was determined between 14.22 and 14.86 °C. Depending on the sky emissivity between 0.0 and 1.0, the lowest sky temperature was recorded between 5.64 and 5.93 °C in Moscow, the capital city of Russian Federation. For the capital city of Turkey, Ankara, the sky temperature value depending on the sky emissivity value between 0.0 and 1.0 was found between 11.25 and 11.86 °C. In Fig. 4, different sky emissivity-related sky temperature values of 20 selected cities in different climate zones around the world are given.

The emissivity value (ϵ_{surf}) was chosen as 0.5, 0.7, and 0.9 for the external surface radiative heat loss calculations of the airport buildings. The highest external surface

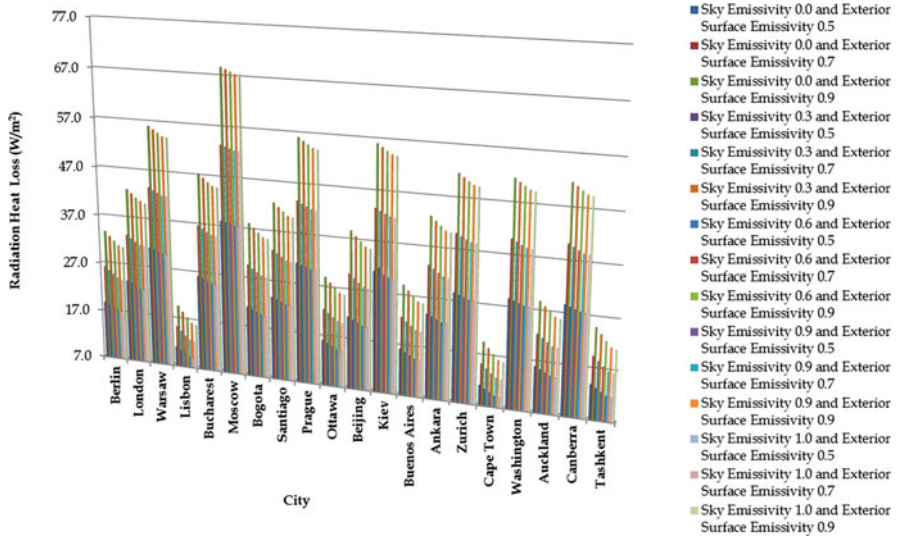


Fig. 5 The different sky and exterior emissivity-related external radiation heat loss values of selected cities

radiative heat loss was calculated in Moscow. The most important factor is that the outdoor temperature of Moscow is at the lowest value (6.0 °C). It has been determined that the sky emissivity value varies between 0.0 and 1.0 depending on the cloudiness factor, between 0.781 and 0.956. In Fig. 5, different sky and exterior emissivity-related external radiation heat loss values are given for 20 selected cities.

For Moscow, the highest external surface radiation heat loss value of the airport was calculated between 38.100 and 68.580 W/m² for a sky cloudiness factor of 0.0 and a surface emissivity value between 0.5 and 0.9. It was found between 37.880 and 68.180 W/m² for the 0.3 sky cloudiness factor and calculated between 37.650 and 67.770 W/m² for 0.6 sky cloudiness factor. It was found between 37.420 and 67.360 W/m² for the 0.9 sky cloudiness factor and calculated between 37.390 and 67.310 W/m² for the 1.0 sky cloudiness factor.

For Lisbon, the lowest external surface radiation heat loss value of the airport was calculated between 10.920 and 19.650 W/m² for 0.0 sky cloudiness factor and a surface emissivity between 0.5 and 0.9. It was found between 10.260 and 18.470 W/m² for the 0.3 sky cloudiness factor and calculated between 9.640 and 17.350 W/m² for 0.6 sky cloudiness factor. It was found between 9.070 and 16.330 W/m² for the 0.9 sky cloudiness factor and calculated between 8.874 and 15.970 W/m² for 1.0 sky cloudiness factor.

Ankara, for the sky cloudiness factor of 0.0 and the surface emissivity value between 0.5 and 0.9, the external surface radiation heat loss value of the airport was calculated between 23.900 and 43.020 W/m². It was found between 23.390 and 42.100 W/m² for the 0.3 sky cloudiness factor and calculated between 22.910 and 41.230 W/m² for 0.6 sky cloudiness factor. It was found between 22.450 and 40.420 W/m² for the 0.9 sky cloudiness factor and calculated between 22.310 and 40.160 W/m² for 1.0 sky cloudiness factor.

4 Conclusions

In the study, the following results were obtained at the end of the examinations and calculations:

- The sky emissivity value depending on the clear-sky conditions depends on the dew point temperature value. Therefore, Lisbon, Cape Town, and Auckland have the highest sky emissivity values.
- The parameter that affects the cloudy sky emissivity value the most is the sky cloudiness factor. In the study, calculations were made by assuming clear-sky conditions with 0.0–0.3 emissivity values.
- Since the parameter that most affects the sky temperature value is the outdoor dry bulb temperature, the highest value was determined in Lisbon and in Cape Town.
- As the sky cloudiness factor value increases, the sky temperature value increases.
- It was calculated that when the relative humidity value is high, the dew point temperature value is also high.
- The difference in sky temperature calculated for the value of the sky cloudiness factor value of 0.0 and the value of 1.0 was found to be the highest in Tashkent with approximately 0.80 °C. The lowest was detected in Moscow with 0.29 °C.
- As the sky cloudiness factor value increases, the airport's external surface radiation heat loss value decreases.
- As airport surface emissivity increases, external surface radiation heat loss value also increases.
- For the 0.0 value of the sky cloudiness factor, the highest external surface radiation heat loss difference depending on the 0.5 and 0.9 surface emissivity values was obtained in Moscow with 30.480 W/m². For the 1.0 value of the sky cloudiness factor, it was determined in Moscow with 29.920 W/m².
- For the 0.0 value of the sky cloudiness factor, the lowest external surface radiation heat loss difference due to 0.5 and 0.9 surface emissivity values were obtained in Lisbon 8.730 W/m². 7.096 W/m² for 1.0 value of the sky cloudiness factor was also found in Lisbon.
- The highest difference between external temperature and sky temperature (for 0.0 sky emissivity value) was determined as 0.98 °C in the capital city of Uzbekistan. The lowest was determined as 0.36 °C in Moscow.
- The difference between the external temperature and sky temperature at the sky emissivity of 1.0 (completely cloudy weather conditions) was found to be the highest in Tashkent 0.18 °C, and the lowest in the city of Auckland with 0.07 °C.
- The external surface radiation heat loss difference based on 0.5 and 0.9 surface emissivity values for the 0.0 value of the sky cloudiness factor in Ankara was calculated as 19.120 W/m². For the 1.0 value of the sky cloudiness factor, the difference was determined as 17.850 W/m².

In further studies, overall heat loss calculations of airport buildings will be made for cities in different climate zones around the world, considering convection heat transfer depending on external environmental conditions in addition to external surface radiation heat transfer.

References

- Ahmed, H. A., Yu-xin, T., Qi-chang, Y., Al-Helal, I. M., Shady, M. R., & Abdel-Ghany, A. M. (2020). Estimation of sky thermal irradiance in Arid climate under clear sky conditions. *International Journal of Thermophysics*, 41(6), 1–18.
- ASHRAE Dataset.
- Çengel, Y. A., & Boles, M. A. (2012). *Mühendislik Yaklaşımı ile Termodinamik*. Izmir.
- Dai, Q., & Fang, X. (2014). A new model for atmospheric radiation under clear sky condition at various altitudes. *Advances in Space Research*, 54(6), 1044–1048.
- Evangelisti, L., Guattari, C., Gori, P., & Bianchi, F. (2017). Heat transfer study of external convective and radiative coefficients for building applications. *Energy and Buildings*, 151, 429–438.
- Evangelisti, L., Guattari, C., & Asdrubali, F. (2019). On the sky temperature models and their influence on buildings energy performance: A critical review. *Energy and Buildings*, 183, 607–625.
- <https://www.timeanddate.com/>. Date accessed: 1 Oct 2021.
- Li, M., Jiang, Y., & Coimbra, C. F. M. (2017). On the determination of atmospheric longwave irradiance under all-sky conditions. *Solar Energy*, 144, 40–48.
- Niemelä, S., Räisänen, P., & Savijärvi, H. (2001). Comparison of surface radiative flux parameterizations: Part I: Longwave radiation. *Atmospheric Research*, 58(1), 1–18.
- Tang, R., Etzion, Y., & Meir, I. A. (2004). Estimates of clear night sky emissivity in the Negev Highlands, Israel. *Energy Conversion and Management*, 45(11–12), 1831–1843.
- TS 825. (2013). Thermal insulation requirements for buildings.

Optimal Layout Design of Multi-Rotor Vehicle Based on PSO Algorithm



Yuke Huang, Mai Bando, and Shinji Hokamoto

Contents

| | | |
|-----|--|-----|
| 1 | Introduction | 181 |
| 2 | Blade Element Momentum Theory and Modeling | 182 |
| 2.1 | Modeling from the Momentum Theory | 182 |
| 2.2 | Modeling from the Blade Element Theory | 183 |
| 3 | PSO and Parameter Configuration | 184 |
| 3.1 | About PSO Algorithm | 184 |
| 3.2 | Algorithms Principle | 184 |
| 4 | Simulation Results and Discussion | 185 |
| 4.1 | PSO Parameter Simulation | 185 |
| 4.2 | Rotor Layout Simulation | 187 |
| 5 | Conclusions | 191 |
| | References | 191 |

1 Introduction

The traditional design of multi-rotor vehicle is mostly based on the research of fluid mechanics and flight performance (ICAO, 2016). However, no unified guidelines have been formed for overall layout, although the overall structure of the rotor layout has significant influence on the aerodynamic characteristics and flight performance. As a result, the layouts of multi-rotor vehicles are greatly different in recent projects/designers. Furthermore, proper layouts depend on requirements and restrictions.

This research is based on the blade element momentum theory (BEMT) and the particle swarm optimization (PSO) algorithm to discuss the optimal layout of multi-

Y. Huang (✉) · M. Bando · S. Hokamoto
Kyushu University, Fukuoka City, Japan
e-mail: mbando@aero.kyushu-u.ac.jp

rotor vehicles. In particular, to propose rotor layout guidelines, this chapter discusses the proper PSO parameters in various requirements/conditions and the effects of the number of blades and blade angle on the lift, power, and overall weight of the rotor.

2 Blade Element Momentum Theory and Modeling

2.1 Modeling from the Momentum Theory

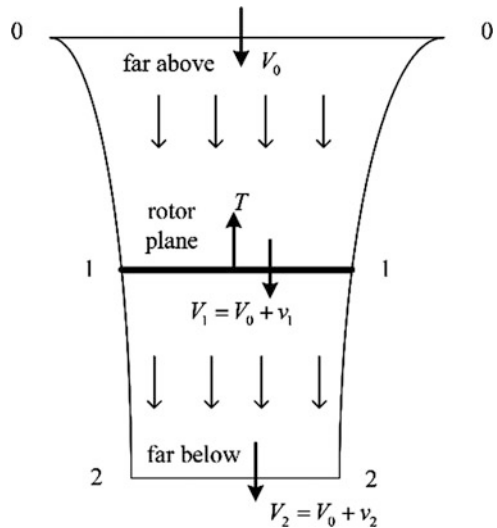
First, consider the flow before and after the rotor shown in Fig. 1.

In the 0-0 section of Fig. 1, the airflow velocity V_0 indicates the vertical ascending velocity of the rotor, and in the 1-1 and 2-2 sections, the airflow velocity increases to V_1 and V_2 , respectively. Here, v_1 and v_2 are the airflow-induced velocities.

According to the momentum theory, thrust T and power P can be expressed by rotor area and rotation speed. Each velocity in Fig. 1 can be expressed in dimensionless form with the wingtip velocity ωR ($\bar{V}_0 = V_0/\omega R$, $\bar{v}_1 = v_1/\omega R$), thrust T can be expressed in dimensionless form with $\rho\pi R^2(\omega R)^2$, the thrust coefficient can be obtained (Ryoji, 2006),

$$\begin{aligned} dC_T &= \frac{dT}{\rho\pi R^2(\omega R)^2} = \frac{2\rho(V_0 + v_1)v_1 dA}{\rho\pi R^2(\omega R)^2} \\ &= 4(\bar{V}_0 + \bar{v}_1)\bar{v}_1 \bar{r} d\bar{r} \end{aligned} \tag{1}$$

Fig. 1 The momentum theory model



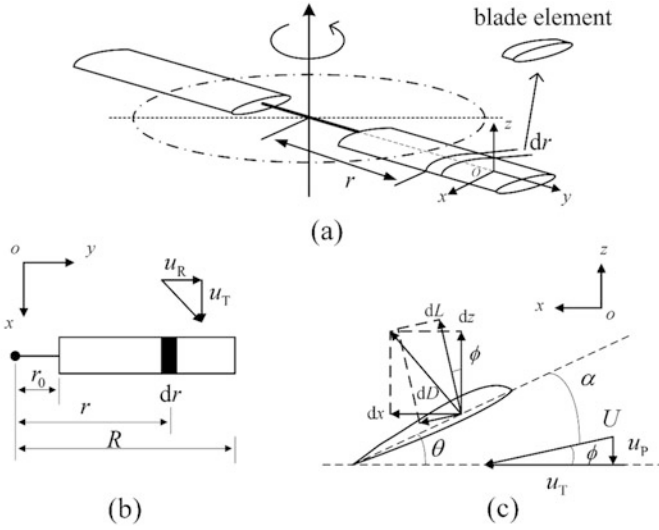


Fig. 2 The blade element theory model. (a) Overview of rotor blade, (b) an element of a blade, (c) air inflow and generated forces

2.2 Modeling from the Blade Element Theory

The essence of blade element theory is to divide the blade into infinitely small units and to establish the motion and force coordinate system of each unit.

Figure 2 is a schematic diagram of the airflow in vicinity of a blade of a rotor rotating in a vertical axis. Here, u_T , u_P , and u_R are the horizontal, vertical, and radial air inflow velocity component, respectively, and θ , α , and ϕ indicate the blade angle, the angle of attack, and the air inflow angle, respectively (Ruopeng et al., 2019).

For a rotor, “solidity” is often defined as the ratio of the area of the blade to the area of the paddle as

$$\sigma = \frac{NcR}{\pi R^2} = \frac{Nc}{\pi R} \tag{2}$$

where c is the chord length of the blade (Theys et al., 2016). Then, the differential expressions of the thrust coefficient and the power coefficient can be expressed as (Huirong et al., 2015)

$$dC_T = \frac{1}{2} \sigma C_L \bar{r}^2 d\bar{r} \tag{3}$$

$$dC_P = \frac{1}{2} \sigma (\phi C_L + C_D) \bar{r}^3 d\bar{r} \tag{4}$$

where C_L and C_D are the lift coefficient and drag coefficient of the blade, respectively.

The concept of inflow ratio is introduced here. The so-called inflow ratio refers to the ratio of the air inflow velocity in the vertical direction of the rotor to the wingtip rotational linear velocity (Yao et al., 2019). Thus, it can be expressed as follows:

$$\lambda = \frac{V_0 + v_1}{\omega R} = \lambda_c + \lambda_i = \bar{V}_1 = \frac{u_p}{\omega R} = \bar{u}_p = \frac{u_p}{\omega r} \cdot \frac{\omega r}{\omega R} = \frac{u_p}{u_T} \cdot \frac{r}{R} \approx \phi \bar{r} \quad (5)$$

Equations (1) and (3) are the expressions of the rotor thrust coefficient obtained by the momentum theory and the blade element theory, respectively (Tingting, 2018). Combining these two equations

$$\lambda(\bar{r}) = \frac{\sigma a}{16} \left(\sqrt{1 + \frac{32}{\sigma a} \theta \bar{r}} - 1 \right) \quad (6)$$

can be obtained to specify λ . Here, a is the coefficient that the lift coefficient changes with the angle of attack.

In this section, the expressions of rotor dynamic parameters are derived through the momentum theory and the blade element theory, and the inflow ratio λ is obtained. According to λ , the thrust and power of the rotor can be calculated by using numerical integration.

3 PSO and Parameter Configuration

3.1 About PSO Algorithm

Particle swarm optimization (PSO) is an evolutionary computation technique that was proposed by Dr. Everhart and Dr. Kennedy in 1995. Starting from a random solution, through the iterative calculation of particles in a certain space, the optimal solution of the model can be found. The basic idea of PSO is to share personal information to all, so that the whole can converge toward a goal from disorder to order.

3.2 Algorithms Principle

The PSO is initialized as a group of particles (random solution), and at each iteration the particles update themselves by tracking two values (individual optimal value $pbest$ and global optimal value $gbest$) (<https://www.zhihu.com/>, 2021).

$$x_i(t+1) = x_i(t) + v_i(t+1) \quad (7)$$

$$v_i(t+1) = w \cdot v_i(t) + c_1 \cdot \text{random} \cdot (x_i^{\text{pbest}} - x_i(t)) + c_2 \cdot \text{random} \cdot (x_i^{\text{gbest}} - x_i(t)) \quad (8)$$

where x and v are called particle position and velocity, and w is called the inertial factor.

4 Simulation Results and Discussion

Consider a basic requirement as that the aircraft can be hovered, and reduce the total mass of the aircraft as much as possible. Note that as the rotor size increases for a larger lift force, but the rotor and battery become heavier. In addition, an arm connecting the airframe and a larger rotor must be longer to avoid overlapping rotors but keep enough strength for larger lift force. Thus, the weight of the arm becomes heavier. For the sake of simplicity, the shape of the airframe is assumed to be a circle with a diameter of 1 m. On the other hand, a limit is set on the diameter of the rotor so that the aircraft does not become too large.

4.1 PSO Parameter Simulation

Through simulation calculation, it is found that there are two design parameters affecting the accuracy of the PSO algorithm and the calculation time. They are the number of particles and the iteration time. If the number of particles and the number of iterations are too small, the calculation does not converge and the results are unreliable. Conversely, if too large, the calculation time increases greatly. Therefore, the reasonable setting of these two parameters is important to obtain reliable solutions for a quite huge of iterations. This section explains this purpose.

Figure 3 shows typical calculation results of the minimum mass of a small octocopter (payload 20 kg). Figure 3 (a) is the configuration with the number of particles 40 and the number of iterations 200, (b) is the configuration with the number of particles 80 and the number of iterations 800. Fifty sample cases are shown in the horizontal axis, and the minimum mass values of the obtained results are the vertical axis. The yellow line represents the mass calculated by PSO for 50 samples. The blue, orange, and purple lines represent the upper limit of error of 1%, 5%, and 10% from the minimum quality, respectively. The numbers in parentheses represent the proportion of 50 samples whose quality exceeds the upper limit of error. “Average” and “standard” represent the statistical characteristics of 50 samples. “Time” represents the time required for one simulation. It can be seen from the blue line data that under the configuration of particles 40 and iterations 200, the

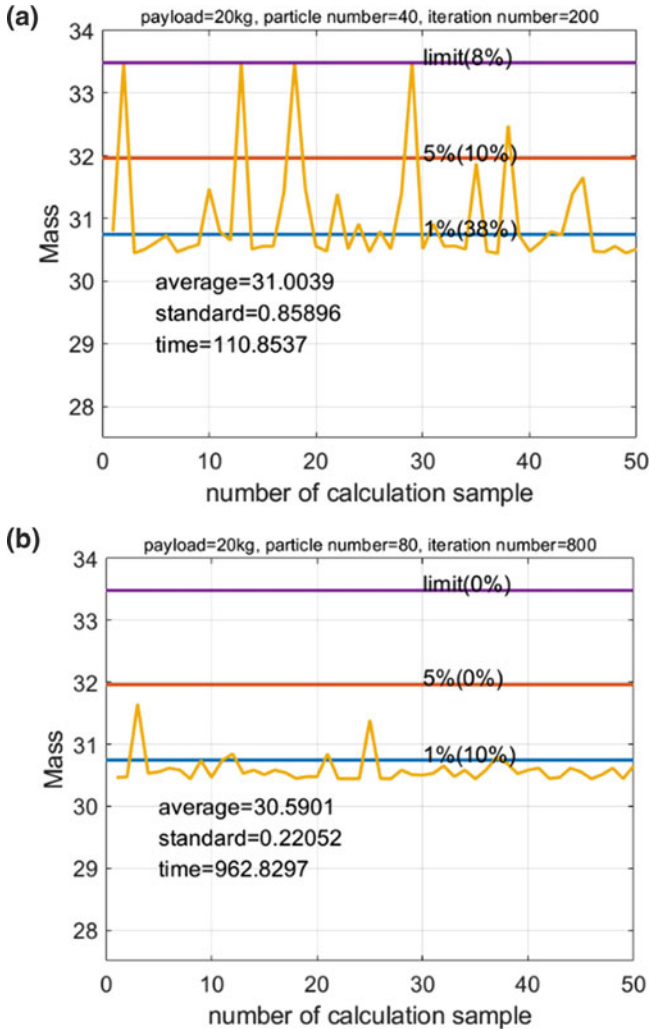


Fig. 3 PSO parameter simulation of octocopter. (a) Particle number = 40, iteration number = 200. (b) Particle number = 80, iteration number = 800

proportion of errors above 1% is 38%. Therefore, the probability of performing n times of calculation to obtain the ideal result is $(1 - 0.38^n)$. And under the configuration of particles 80 and iterations 800, the proportion of errors above 1% is 10%. Therefore, the probability of performing n times of calculation to obtain the ideal result is $(1 - 0.1^n)$. In addition, among other data not shown here, for example, particles 40 and iterations 600, the proportion of errors above 1% is 36%, particles 60 and iterations 600, the proportion is 18%. These results indicate that, for an octocopter configuration to lift up a payload of 20 kg, the number of particles 80 and the number of iterations 800 in the PSO calculation obtain accurate estimations for

the total mass with high percentages. However, the calculation of low configuration takes less time, and the calculation accuracy can also be improved by the way of multiple calculations with low configuration. For example, in Fig. 3 (a), the probability that the mass is within 1% error is $1 - 0.38 = 0.62$, and in (b) this probability is $1 - 0.1 = 0.9$. This shows that the configuration of (b) has a higher accuracy than the configuration of (a) in one calculation. However, if (a) is calculated three times, this probability becomes $1 - 0.38^3 \approx 0.95$. This probability is higher than (b), and it still takes less time than (b). It can be said that the configuration of (a) has higher computational efficiency.

In addition, through simulation calculations, it is found that there is no significant difference in the PSO parameter configuration between the small rotor (payload 20 kg) and the large rotor (payload 200 kg). It can be considered that to a certain extent, the size of the rotor does not affect the PSO calculation results.

4.2 Rotor Layout Simulation

The following is to simulate the influence of the blade number and blade angle on the rotor layout. Excluding the battery, blades, and other components, when the body mass and load are fixed (small size 20 kg and large size 200 kg), the number of rotors is 4,8, and the blade angle ($10\sim 20^\circ$) and the blade number (2,4) are changed. The blade angle here refers to the angle of the root, and the tip angle is 0. Viewing the schematic diagram vertically from above, considering the symmetry, the illustrated part is a quarter of the whole. The white circle is the rotor, the blue circle is the body, and the red line is the arm.

The first is the case of the quadcopter. The small size corresponds to Fig. 4 (a)~(c), and the large size corresponds to (d)~(e). The caption of the figure shows the blade number N , the blade angle θ , and the overall mass W of this figure. In the case of a small size of 20 kg, it can be seen from the comparison of Fig. 4 (a) and (b) that the larger the blade angle, the smaller the mass of the whole machine. It can be seen from the comparison of (a) and (c) that the larger the blade number, the larger the mass of the whole machine. In the case of large size 200 kg, the same conclusion as small can be obtained by comparing (d)~(f).

Then it is the case of the octocopter. By comparing Fig. 5(a), (b), it can be found that blade number and blade angle have similar effects on the octocopter.

In addition, if all the rotors are directly connected to the body, each arm only needs to bear the pulling force and moment of one rotor. But if the rotor and the rotor are connected to each other, then some arms need to withstand the pull and moment of multiple rotors, these arms will be thicker and the mass will be greater. This section also simulates the different connection situations of the octocopter, and the results are shown in Fig. 6. From this result, the layout in right connecting two rotors in series has a lighter weight than the layout in left.

Finally, this section calculates and simulates the influence of the blade number and blade angle on the thrust, power, and efficiency of the rotor.

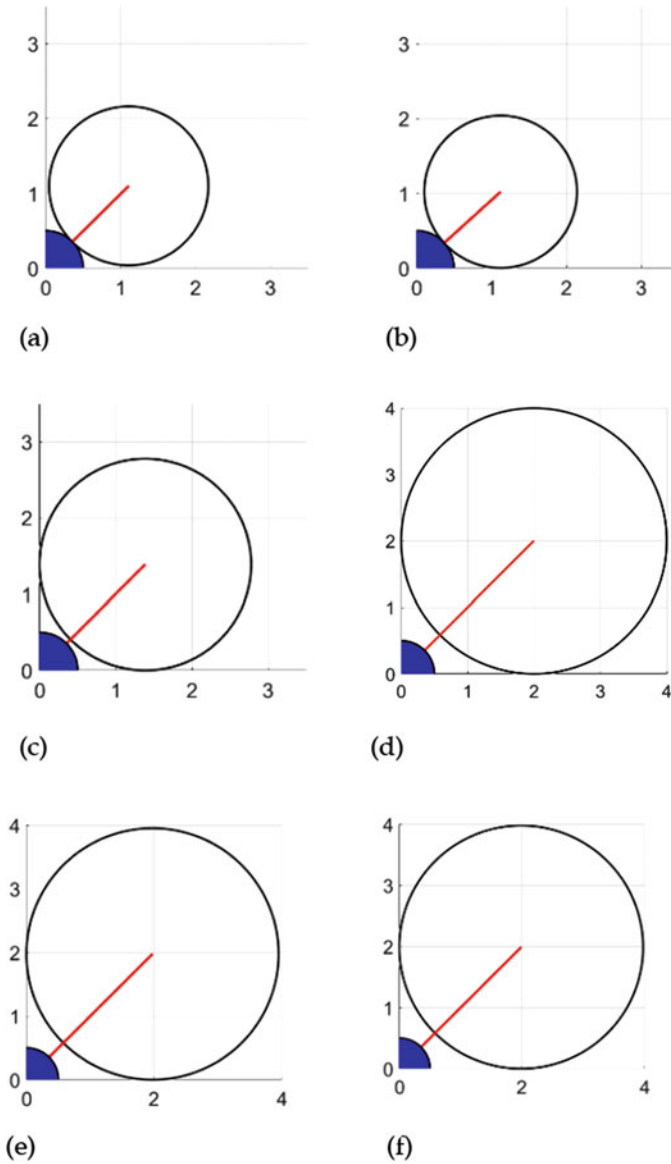


Fig. 4 Quadcopter layout simulation. (a) $N = 2, \theta = 14, W = 28.73$, (b) $N = 2, \theta = 20, W = 27.38$, (c) $N = 4, \theta = 14, W = 31.38$, (d) $N = 2, \theta = 14, W = 430.34$, (e) $N = 2, \theta = 20, W = 373.39$, (f) $N = 4, \theta = 20, W = 386.61$

Figures 7 and 8 show the efficiency FM (figure of merit) of rotors with different radii when hovering. The so-called efficiency refers to the ratio of the induced power to the total power under a certain coefficient when the rotor is working. It can be expressed as

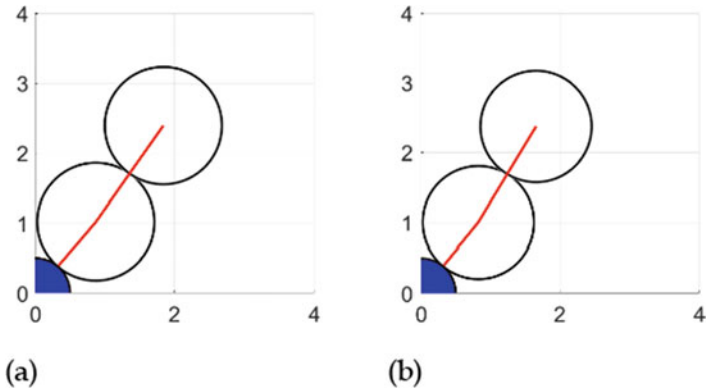


Fig. 5 Octocopter layout simulation. (a) $N = 2, \theta = 14, W = 32.80$, (b) $N = 2, \theta = 20, W = 30.02$

Fig. 6 Octocopter connection simulation

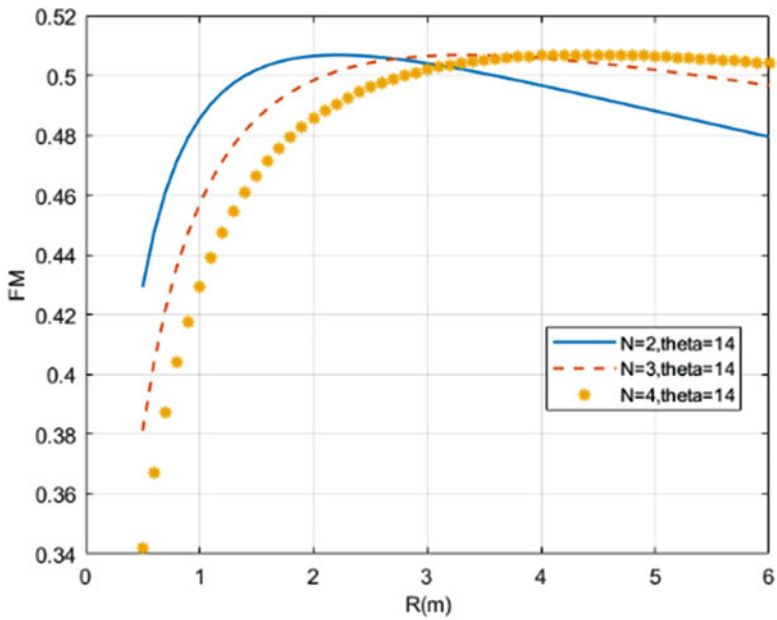
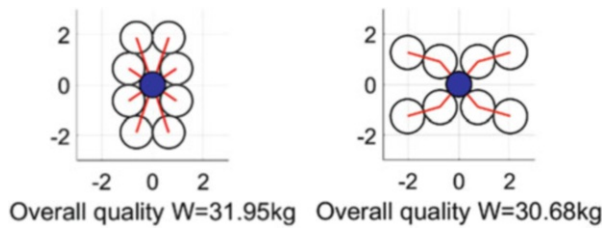


Fig. 7 FM with different blade number

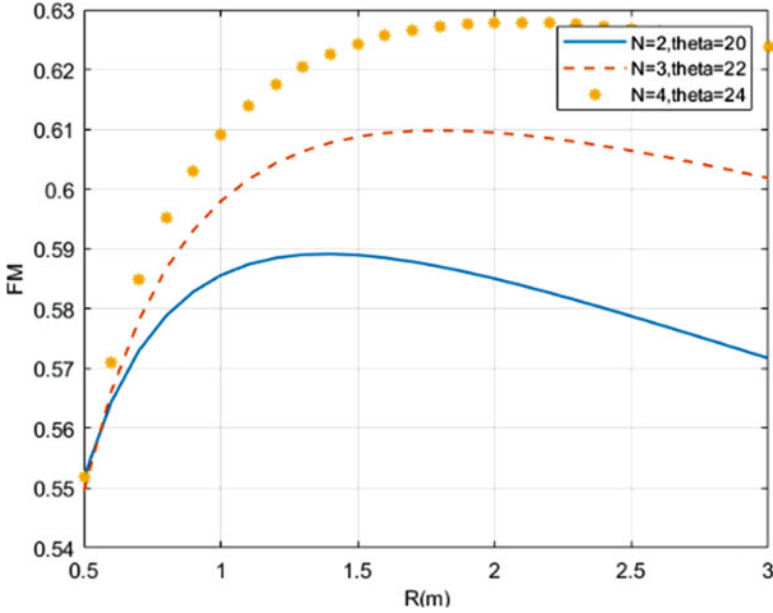


Fig. 8 FM with different blade angle and number

$$FM = \frac{P_i}{\kappa P_i + P_0} = \frac{\frac{(C_T)^{1.5}}{\sqrt{2}}}{\kappa \frac{(C_T)^{1.5}}{\sqrt{2}} + \frac{1}{2} \sigma \int_0^1 C_D(\bar{r}) \bar{r}^3 d\bar{r}} \quad (9)$$

Here, κ is the correction coefficient.

Figure 7 shows the changing law of FM under different blade number and the same blade angle. It can be seen that as the radius increases, FM first increases and then decreases. In the case of the same blade angle, the less the number of blades of a small radius propeller, the higher the efficiency. The opposite is seen in the case for a large radius propeller. The more the number of blades, the higher the efficiency. Figure 8 shows the changing law of FM when the blade angle is maximum under different blade number. Excessive blade angle will cause the blade to stall. The calculation found that different numbers of blades have different stall critical blade angles (Tao, 2019). The more the number of blades, the greater the maximum blade angle and the greater the FM.

5 Conclusions

Rotor layout is usually influenced by many factors. In this chapter, the rational selection of PSO parameters, the influence of blade angle and blade number on the rotor layout have been simulated, and the results have certain guiding significance for the rotor layout.

References

- Huirong, J., Zhicheng, D., Ming, Z., & Xueshou, P. (2015). On modeling and control of quadrotor aircraft with variable blade pitch. *Electronics Optics & Control*, 22(10), 48–55.
- ICAO. (2016). *ICAO long-term traffic forecasts*.
- Ruopeng, B., Binghe, Z., Jianyong, Z., & Miao, H. (2019). Influence of pitch angle on aerodynamic characteristics of propeller. *Journal of Drainage and Irrigation Machinery Engineering*, 37(4), 336–340.
- Ryoji, T. (2006). Aerodynamic characteristics of NACA4402 in low Reynolds number flows. *Journal of the Japan Society for Aeronautical and Space Sciences*, 54(631), 367–373.
- Tao, W. (2019). *Design and research of small coaxial double rotor UAV*. Beijing Jiaotong University.
- Theys, B., Dimitriadis, G., Hendrick, P., & De Schutter, J. (2016). Influence of propeller configuration on propulsion system efficiency of multi-rotor Unmanned Aerial Vehicles. In *2016 International Conference on Unmanned Aircraft Systems*, June 7–10, 2016. Arlington, VA, USA.
- Tingting, Y. (2018). Analysis of aerodynamic characteristics and experimental study on trapezoidal blade of Mars UAV. Harbin Institute of Technology.
- Yao, L., Rongzhao, L., & Zhiqian, W. (2019). Experimental study on the aerodynamic arrangement of small multi-rotor aircraft with high capacity payload. *Acta Armamentarii*, 40(9), 1324–1328.
- Zhihu. <https://www.zhihu.com/>. Accessed 2021.

Development of Solar Sail for Interstellar Exploration



P. Suresh, Aadesh Varne, V. C. Jishnu, U. Kushal, and Parth Borse

Contents

| | | |
|---|------------------------------|-----|
| 1 | Introduction | 193 |
| 2 | Methodology | 194 |
| 3 | Selection of the Sail | 195 |
| 4 | Material Selection | 196 |
| 5 | Control Surface Design | 196 |
| 6 | Results and Discussion | 196 |
| 7 | Conclusion | 197 |
| | References | 197 |

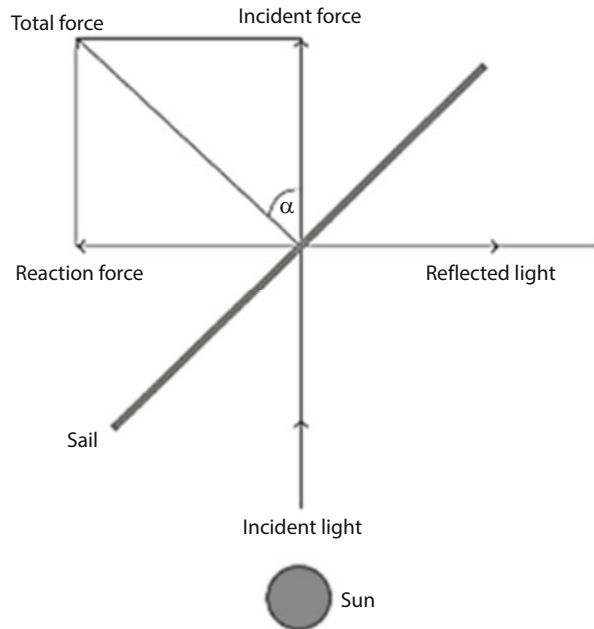
1 Introduction

The solar sail is a fuel-free system, whose momentum is determined by the immediate exchange of reflected photons. The continuous pressure of photons makes the thrust of the engine small and unable to float in space (Fig. 1). The solar sail accelerates slowly and reliably and reaches a very high speed, which is useful for interstellar exploration.

The solar sail technology is still at its developing stage. Numerous space agencies and research centers are working on various areas to develop the solar sail and are working on new set of ideas to improve the performance, control, deploy ability, etc. One of such centers is Langley Research Center (LaRC). The programs at LaRC are focusing on developing new materials and new boom technologies. Within NASA

P. Suresh (✉) · A. Varne · V. C. Jishnu · U. Kushal · P. Borse
Department of Aeronautical Engineering, Dayananda Sagar College of Engineering, Bengaluru,
India
e-mail: suresh-ae@dayanandasagar.edu; 1ds17ae002@dsce.edu.in; 1ds17ae017@dsce.edu.in;
1ds17ae023@dsce.edu.in; 1ds17ae030@dsce.edu.in

Fig. 1 A sketch of solar photons interacting with the sail (Costanza et al., 2017)



LaRC, there was recently formed the Ultralightweight and Inflatable Structures team, with research specialists in the areas of structural mechanics, structural dynamics, and control and materials research and development.

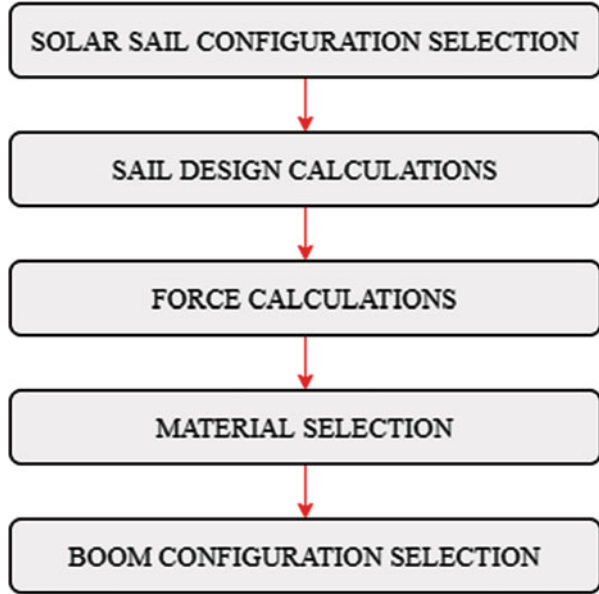
The future scope in the field of solar sail technology is vast. Various literature shows that there is no limit to the ideas and innovation for designing a solar sail. There is always a development going on in this sector. Simulation toolkits (Costanza et al., 2017) are developed to evaluate the performance of the solar sail. Based on the mission requirements, the technology is altered and improved. The study on lightweight materials too helps in designing an efficient solar sail. Solar sails are eco-friendly since they purely depend on the photon energy from the sun to propel the spacecraft.

2 Methodology

Design of solar sail will consist of configuration selection, dimensional study, force applications, boom structural design, strength analysis, etc. Configuration selection will take place by studying the research papers, differentiating the pros and cons of each configuration, and mission requirements of the spacecraft (Fig. 2).

Material selection will be done simultaneously along with the designing. Lightweight and strong composite materials will be used. Different types of materials will be required for the sail and the boom. The materials used in boom will require

Fig. 2 Methodology
(Suresh et al., 2021)



additional strength, while the materials used in sail will depend on the thickness and layering. Sail material will require very thin materials with high tensile strength.

The design of the mechanism will depend on the dimensions of the boom as well as the box dimensions of the body. The design will be analyzed and optimized as we move forward.

3 Selection of the Sail

Taking into account the required resistance and load distribution, the two best performing configurations are the continuous link and belt pedal structure. Although the tension distribution is better in the belt pedal structure, we decided to maintain permanent contact with mission. Continuous connection can make the photons falling on it evenly distributed, which is easier to achieve. Open the steering mechanism.

Depending on the destination, the size of the first-generation sail is between 100 and 200 m (Table 1). Since the structure of the sail must enable it to reach the heliosphere, we assume that the square size of the sail is 150 m (Suresh et al., 2021).

Table 1 Solar sail design specifications (Suresh et al., 2021)

| Sail design | Specifications |
|-------------------------|-----------------------|
| Sail dimensions | 150 m × 150 m |
| Catenary sag | 7.5 m |
| Sail thickness | 14×10^{-6} m |
| Billow | 0.26 m |
| Boom length | 106 m |
| No of CubeSats | 5 |
| Dimensions of 1 CubeSat | 10 cm × 10 cm × 10 cm |

4 Material Selection

Both IKAROS solar sail and Nano Sail use aluminum as the material. Due to the high strength and lightweight of carbon fiber and M5 fiber, many designs and prototypes that are still in the research stage use carbon fiber and M5 fiber as materials. Since the mission is to explore interstellar space, lightweight materials with high tensile strength must be selected (Cunniff et al., 1999). Polyester film is a highly reflective polyester film. Due to its high reflectivity and high temperature resistance, it is the most commonly used material for solar sails. Assuming a thickness of 16 μm , this is the standard thickness used in solar sail applications.

5 Control Surface Design

Control surfaces are designed to maneuver the spacecraft and to maintain the stability and control of the spacecraft. There is one control surface on each boom, 4 in total. The ratio of the total surface area of the wing to aileron is usually 10–12% and horizontal stabilizer to the elevator is 30–40% for airplanes (Sadraey, 2012).

For structural integrity, the control surface has a frame which is made up of M5 fiber and has thickness 2 mm and width of 100 mm, as shown in Fig. 3. A mylar sheet is placed on the frame which has a thickness of 14.5 μm .

6 Results and Discussion

It is understood that maximum control surface area is required for an effective maneuverability. The control surface was designed such that the distance between the gearboxes is minimum. After studying various types of gear reducers, the control mechanism was designed. Based on the torque requirements, the gear system was designed. Force considered are calculated based on the sun at orbital level of earth. For any further work, the assumptions and conditions are to be taken care of accordingly considering the limitations of this project.

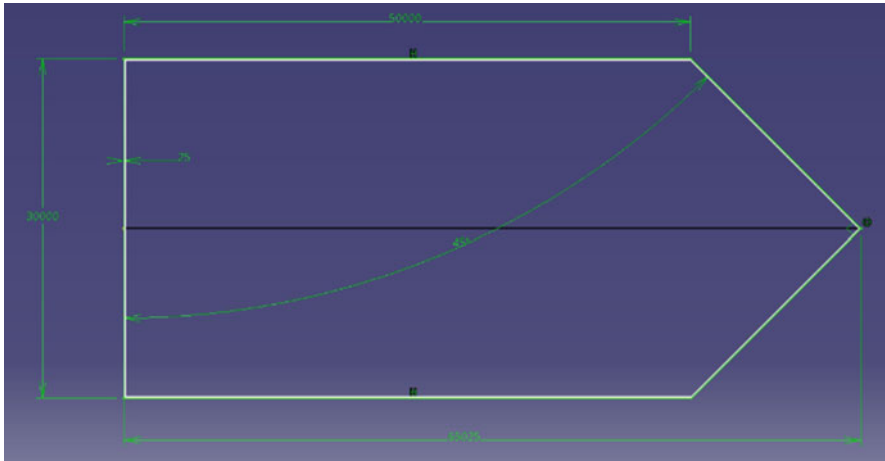


Fig. 3 Control surface design

7 Conclusion

A theoretical sail is designed under the ideal conditions. The continuous connection configuration is ideal to implement any new mechanism or improvements to the sail. The selected L-shaped boom configuration has advantages over the conventional configurations both in terms of weight and strength. The design was optimized for maximum acceleration, with an intention for an interstellar mission.

Since it is a superstructure, materials were selected based on the most optimum material available to us, until advanced materials are developed or invented for space structures and advances in engineering, manufacturing and physical technology are required.

References

- Costanza, G., Leoncini, G., Quadrini, F., & Tata, M. E. (2017). Design and characterization of a small-scale solar sail prototype by integrating niti SMA and carbon fibre composite. *Advances in Materials Science and Engineering*, 2017, 1–6.
- Cunniff, P. M., Auerbach, M. A., Vetter, E., & Sikkema, D. J. (1999). *High performance “M5” fiber for ballistics/structural composites*. Magellan Systems International.
- Sadraey, M. H. (2012). *Aircraft design: A systems engineering approach*. Wiley.
- Suresh, P., Varne, A., Jishnu, V. C., Kushal, U., & Borse, P. (2021). Configuration selection and analysis of a superstructure solar sail. *Information Technology in Industry*, 9(2), 1186–1192.

Paperless Operations in Apron: A Case Study



Eylem Turhan, Betül Kacar, İlkay Orhan, Alper Dalkiran,
and Tahir Hikmet Karakoc

Contents

| | | |
|-----|--|-----|
| 1 | Introduction | 200 |
| 2 | Approach to Paperless Processes in Apron | 201 |
| 3 | Benefits of Paperless Operations | 202 |
| 3.1 | Environmental Effects | 202 |
| 3.2 | Cost of Time | 202 |
| 3.3 | Financial Impacts | 203 |
| 4 | Certificates | 203 |
| 4.1 | EPEAT | 203 |
| 4.2 | Ecologo | 203 |
| 4.3 | Green Seal | 204 |
| 4.4 | EPA | 204 |

E. Turhan (✉)

Eskişehir Technical University, Faculty of Aeronautics and Astronautics, Eskişehir, Türkiye
Istanbul Ticaret University, Information Technology Research and Application Center, Istanbul,
Türkiye
e-mail: Eylem.turhan@eskisehir.edu.tr

B. Kacar · I. Orhan

Eskişehir Technical University, Faculty of Aeronautics and Astronautics, Eskişehir, Türkiye
e-mail: betulkacar@eskisehir.edu.tr; iorhan@eskisehir.edu.tr

A. Dalkiran

School of Aviation, Suleyman Demirel University, Keciöorlu, Isparta, Türkiye
e-mail: alperdalkiran@sdu.edu.tr

T. H. Karakoc

Eskişehir Technical University, Faculty of Aeronautics and Astronautics, Eskişehir, Türkiye
Information Technology Research and Application Center, Istanbul Ticaret University, Istanbul,
Türkiye
e-mail: hkarakoc@eskisehir.edu.tr

| | |
|--------------------------------|-----|
| 5 Results and Discussion | 205 |
| 6 Conclusions | 206 |
| References | 207 |

Nomenclature

| | |
|-----|--|
| CPM | Container pallet message |
| kWh | Annual power consumption of the printers |
| LDM | Load control messages |
| LIR | Loading instruction report |
| UCM | ULD management and control |
| ULD | Unit load device |
| USD | United States dollar |

1 Introduction

The ground operation manual (GOM) and other procedures of the airlines served are followed at the airports served over the Internet systems of the airline or directly by sharing the airline. The recording of these documents and their up-to-dateness is carried out by the Operations Department at the airports served. In addition, with the procedural changes communicated by the airlines and the requirements of the civil aviation regulations, any changes that may affect operational responsibilities or performance are simultaneously communicated to all employees in the field via “quick references” and “announcements.”

The specified documents and any documents affecting the load and balance calculations of the aircraft are kept in the trip file for the period specified under the applicable local regulations and airline requirements. The storage period of the trip file cannot be less than 3 months. If there is a flight filing cover (trip file cover) provided by the airlines, it is used first. Then, the trip file cover of the handling company is used for flight documents belonging to airlines that do not provide a trip file cover (Staff, 2005).

Operation agent is mainly responsible for coordinating the pre-arrival preparations and final control of the aircraft. The forms used in communication are printed documents (computer printouts or blank handling/airline document) and are recorded by signing between the units serving. The documents that should contain the trip file prepared for each flight are specified on the trip file cover.

Preparing a trip file and adding all relevant documents to the file belong to the operation agent. Documents specified in the trip file cover must be attached completely.

The documents that should be included in the trip file are as follows (IATA, 2021):

- LIR (loading instruction report) form signed by the responsible persons
- NOTOC (notification to captain) (if applicable)

- Fuel document (if any)
- Final load sheet including LMC (last minute change) and signed by the captain (arrival load sheet if available)
- Trip info
- Security form (if any)
- Catering document (if any)
- Passenger manifest (it is included in the trip file unless the airline specifies a different rule)
- Cargo manifest (if any)
- All arrival and departure messages

In general, documents kept in the trip file may vary depending on the airline. Any document that cannot be added to the trip file for any reason is written as a note on the trip file cover for further operational works. Destruction of stored documents may also be subject to regulation.

It is essential to understand the environmental outputs of the paper production process before investigating the unconscious and unnecessary use of paper in airports. In producing a paper starting from scratch, staff must be dealt with many environmental issues.

The paper industry is surprisingly one of the most water-consuming industries in the world. In the paper production process, which has various stages, the stage with the potential to cause the most damage to the environment is probably bleaching processes. This damage is because high-reaction chemicals such as chlorine, hypochlorite, and chlorine dioxide, which are used to bleach the color of paper, create a large amount of chlorine waste around paper factories (Dumlu, 2014). For this reason, when untreated wastewater meets nature, we are all affected as microorganisms, other living things that feed on it, plants, animals, and humans.

To reduce this effect, it is wise to focus on different ideas, make applications that will minimize the amount of paper to be used, and choose the most environmentally friendly technological tools by comparing tools according to energy consumption. In this context, various certificates worldwide encourage companies to use more environmentally friendly devices. The technological tools they will use in their offices and main buildings such as EPEAT (The Electronic Product Environmental Assessment Tool), EPA (The *Environmental Protection Agency*), GREEN SEAL, and ECOLOGO.

For this purpose, how much paper the ground-handling operator of a busy airport in Turkey consumes daily, and for what purpose they consume these papers, the connection of these papers with annual flights was examined in detail.

2 Approach to Paperless Processes in Apron

While providing load control services, the process is carried out by a general flow chart that defines the service steps and sequences. This streaming content may vary depending on the airline rules, the systems used for load control, and the contents of

the agreement made with the airline. Some of the load control process stages are described below:

- The operation agent delivers the flight plan to the captain.
- Load control messages, including dangerous goods and special cargo information, are sent by the operation agent, load control officer, or remote load control center manually or via the system (LDM, CPM, and UCM).
- The loading calculation process consists of determining the maximum load and number of passengers that can be taken on the aircraft within the operational limits of the aircraft. The handling agent must take into account the structural values, gravity, and center of gravity (CG) parameters according to the aircraft type in order for the aircraft to perform a safe flight within the scope of the airline rules. Weight and balance calculation is done for all aircraft. The operation agent, load control officer, or remote load control center handles the load and trim sheet.
- Load and trim sheet can be prepared by load master or CLC for cargo planes and passenger planes in line with the airline rules. Weight and balance calculation is done for all aircraft. Load and trim sheet is transmitted to the captain by operation agent or via the ACARS system.
- The final loading instruction form (LIR) containing the number of pieces and weights of all loads loaded on the aircraft. The operation agent delivers LIR to the loading-unloading team officer/foreman, and a verbal briefing is made about the loading details.

3 Benefits of Paperless Operations

3.1 Environmental Effects

Paperless operations require less water consumption and fewer tree felling actions. In addition, less pollution of natural resources is also one of the possible environmental consequences. Although, however, more technological solutions will offer alternative operations instead of using paper. An increase in these tools will mean fewer carbon emissions, less electricity consumption, and indirect pollution of the environment. In other words, businesses should choose the most appropriate one from these alternatives, both in terms of environment and cost (Harley et al., 2020).

3.2 Cost of Time

It will not be easy to give an average period, as documents that need to be filled out at airports can be filled in different periods according to various factors. Accordingly, we can estimate the time spent by a person working in the selected department in a day to fill out the necessary documents in the range of 30 min to 1 h. Furthermore,

when we perform the same process with a technological device such as a tablet and a smartphone, the mistakes can automatically be corrected since we will have the opportunity to automate many processes. Also, one will have the opportunity to see and control the form filled out by his/her colleague without physically talking with her/him. These advantages allow the process to be considerably shortened.

3.3 *Financial Impacts*

The maximum amount of paper that can be received in a single package in enterprises is 500 pages. The price of one of these parcels is 20–30 Turkish liras on average. Information has been picked up and scratched from various websites selling office supplies in Turkey. In our research, the average amount of paper used by the department during the day is 554. Assuming that many departments and larger paper-consuming organizations at an airport, a wide range of financial items will arise, such as the amount of paper consumed daily, the electricity needed to operate the printer, the cost of maintaining it, and the recycling cost.

4 Certificates

The certificates, which support the goal of becoming greener for manufacturers and consumers, are as follows:

4.1 *EPEAT*

The Green Electronics Council manages the Electronic Product Environmental Assessment Tool Certificate Program. EPEAT's search field includes only technological devices such as mobile phones, computers and displays, imaging equipment, network equipment, photovoltaic modules and inverters, servers, and televisions (EPEAT, [n.d.](#)). EPEAT ranks the products as "Bronze, Silver and Gold."

4.2 *Ecologo*

All products with an "Ecologo" certificate must meet each of the established criteria. Ecologo has several criteria in various categories. It provides standards in materials, energy, manufacturing and operations, health and environment, product performance and use, and product stewardship and innovation (About UL | UL, [n.d.](#)). These standards are discussed in detail under headings Building and Construction, High Tech and Office Products, Mineral Exploration, Paper and Plastic, and

Renewable electricity. For example, the subheadings in the “Paper and Plastic” section are as follows:

- Plastic Film Products
- Sanitary Paper Products
- Paper Products
- Paperboard
- Recycled Plastic Products

4.3 Green Seal

Green Seal is a nonprofit organization whose aim is to transform the economy for a healthier, greener world according to its mission. The Green Seal focuses on the effects that occur throughout the product life cycle, from the production of raw materials to packaging, use, and disposal (Green Seal, [n.d.](#)). Among the categories that can be selected in the list of standards set in the certificate are

- Sanitary paper products
- Printing and writing paper
- Coated printing paper
- Paper products used for food preparation
- Paints, coatings, stains, and sealers

4.4 EPA

Unlike other certificates cited, EPA (the Environmental Protection Agency) is the state agency for human health and environmental protection that maintains its practices within the framework of adopted laws and regulations. The EPA also created the “Safer Choice” label to help people shop for safer materials. Safer Choice labels many products, including all-purpose cleaners, laundry products, and wood cleaners (US EPA, [n.d.](#)). Products that carry the Safer Choice label must meet the requirements for the below items:

- Safer chemical ingredients
- Performance
- Packaging
- Ingredient disclosure
- Volatile organic compounds

Table 1 A comparison of the printers popularly used in the offices (Save Joules – Compare Inkjet vs Laser vs Ink Tank Printers for cost-effective printing, n.d.)

| Printers | Power (W) | Cents per page | Annual electricity consumption (kWh) | Lifecycle cost (USD) |
|----------|-----------|----------------|--------------------------------------|----------------------|
| Model 1 | 740 | 1.73 | 50.11 | 7024.95 |
| Model 2 | 740 | 1.73 | 50.89 | 7925.35 |
| Model 3 | 475 | 4.19 | 19.17 | 6756.40 |
| Model 4 | 255 | 4.19 | 15.83 | 6724.65 |

5 Results and Discussion

In Table 1, different laser printer models of HP brands commonly used in offices are examined, and only the colorless output models and those with the same function were examined. Also compared features included print power, cost of each page, annual electricity consumption, lifecycle cost, and function. All the models examined in the research have the same functions, which are P: Print, C: Copy, S: Scan, F: Fax.

The results we can draw from the table are as follows: When we compare printer Models 1 and 4, we see that the energy consumed by Model 4 is relatively small compared to Model 1.

However, the cost of a page to be print from Model 4 is relatively high compared to Model 1. In addition to these values, the annual energy consumption of Model 4 is also relatively low than Model 1. Nevertheless, companies always think about their profitability first, and therefore, while it is better in terms of other features, the cost per page is suggestive in terms of businesses. On the other hand, if we compare the printer Models 3 and 4, we can assume no significant difference between these models by looking at their numerical values from the table, except for the annual energy consumption of Model 4 and Model 3. Therefore, if a company has to choose one of these models, they should have probably chosen Model 4. So, it is critically important to compare the technological products commonly used at offices and complex structures such as airports because it allows us to understand which product is more environmentally friendly, less costly, and more efficient.

In this context, various academic research has been examined. As a result of this study, we have revealed that ultrafine aerosol particles released from modern laser printers are an essential emission source. Ultrafine particles released from laser printers are secondary particles produced by nucleating volatile compounds from paper and toner (Koivisto et al., 2010). Studies in recent years have shown that these particles can damage people's respiratory tract and lungs in the office.

The article discussed a laser printer in three different models from the same manufacturer that was newly manufactured and never used was examined in an office model. The emission rates of these printers were then determined. Various measurements such as the conditioning phase, the activation phase, and the print phase were performed in emission tests, where different components were also

calculated. In the printing phase, 266, 350, and 235 pages were printed, respectively, in 10 min from three printers. At this stage, the power consumption of printers increased to over 1100 W.

Meanwhile, the first printer temporarily raised the room temperature to 29° and the other printers to above 32°. During the printing phase, water vapor was released from the toner, which increased the relative humidity in the room. When the printers were running, the relative humidity in the room was 76%, 81%, and 52%, respectively. These changes, which occur in a short time in an office environment, can affect particle accumulation in the human body working there and much more.

6 Conclusions

Time benefit is the most fundamental source of production and consumption of aviation. Therefore, using time effectively and efficiently will increase the quality of aviation service. Significant steps for adequately managing the time are identifying the aviation industry's needs, establishing the goals, and setting priorities.

Preparing a trip file and adding all relevant documents to the file belongs to the operation agent. There are too many documents that must be filled in pre-arrival, during operation, and post-departure operation. Documents specified in the trip file cover must be attached completely. Hundreds of papers are being used during daily operations. To reduce the amount of paper used, the transition to the electronic system has too many advantages, such as reducing expenses, saving time, and long-term storage of documents. It will help to decrease the ground-handling company's environmental effects. In addition to the cost reduction benefits, calculations using electronic software reduce the likelihood of human mathematical errors. It allows all data to be recorded in a much shorter time. The computer software also alerts operation agents when a number outside the expected range for a given weight or function is entered. It aims to reduce the paper reference materials used in aircraft operations and eliminate them in some aircraft. The benefits of moving from paper to electronics include improved security, increased efficiency, and lower operating costs. Switching from paper to electronic systems can change the workload. The workload can be reduced in some ways and increased in other ways. Increased workload may result from the inefficient design of software or hardware or limitations. The workload required to change electronic documents can exceed the workload required to change paper documents. Although workload can be increased with electronic documents, this negative quality is offset by other factors such as enhanced electronic search capabilities and documents typically referenced under low workload conditions. Overall, the net increase in workload can be considered acceptable. One of the most important benefits of switching from paper to electronic systems is saving paper and storage space. Thanks to the software system, documents can be stored for many years.

References

- About UL | UL. (n.d.). Retrieved May 23, 2021, from <https://www.ul.com/about>
- Dumlu, L. (2014). *Kağıt Endüstrisi Atık Sularına Uygun Arıtma Teknolojilerinin Belirlenmesi ve Türkiye'deki Mevcut Durumun Analizi* (Çevre ve Şehircilik Bakanlığı Çevre Yönetimi Genel Müdürlüğü). Retrieved from https://webdosya.csb.gov.tr/db/destek/icerikler/lutf-ye_dumlu_uzmanl-k_tez%2D%2D20191127122356.pdf
- EPEAT. (n.d.). *About EPEAT | EPEAT Registry*. Retrieved May 23, 2021, from <https://www.epeat.net/about-epeat>
- Green Seal. (n.d.). *About Us | Green Seal*. Retrieved May 23, 2021, from <https://greenseal.org/about/>
- Harley, G., Timmis, A., & Budd, L. (2020). Factors affecting environmental practice adoption at small European airports: An investigation. *Transportation Research Part D: Transport and Environment*, 88, 102572. <https://doi.org/10.1016/j.trd.2020.102572>
- IATA. (2021). *IATA ground operations manual (IGOM)* (10th ed.). IATA. Retrieved from <https://www.iata.org/en/publications/store/iata-ground-operations-manual/>
- Koivisto, A. J., Hussein, T., Niemelä, R., Tuomi, T., & Hämeri, K. (2010). Impact of particle emissions of new laser printers on modeled office room. *Atmospheric Environment*, 44(17), 2140–2146. <https://doi.org/10.1016/j.atmosenv.2010.02.023>
- Save Joules – Compare Inkjet vs Laser vs Ink Tank Printers for cost effective printing. (n.d.). Retrieved June 5, 2021, from <https://savejoules.com/inkjet-vs-laser.html>
- Staff, F. E. (2005). “Paperless cockpit” promises advances in safety, efficiency. *Flight Safety Digest*, 1–10.
- US EPA. (n.d.). *About EPA | US EPA*. Retrieved May 23, 2021, from <https://www.epa.gov/aboutepa>

Aircraft Inspection Using Drones – Benefits and Related Safety Concerns



Lidija Tomić and Olja Čokorilo

Contents

| | | |
|-----|--|-----|
| 1 | Introduction | 209 |
| 2 | Aircraft Maintenance Inspection | 210 |
| 2.1 | Aircraft Maintenance Inspection Using Drones | 211 |
| 3 | Method | 212 |
| 3.1 | HAZOP for Aircraft Inspection Using Drones | 213 |
| 4 | Results and Discussion | 215 |
| 4.1 | Innovation Benefits | 215 |
| 4.2 | Risk Assessment | 216 |
| 4.3 | Proposed Preventive Measures | 217 |
| 5 | Conclusion | 217 |
| | References | 218 |

1 Introduction

Drone technology is now on the way to changing the aviation industry as we know it. More and more airlines and MRO organizations started to test innovative solutions with a goal to not only improve their processes but also stay competitive. One of the new areas of the drone application is aircraft maintenance inspection.

Aircraft inspection process needs to be conducted at every flight cycle, but also during daily and weekly checks, and other planned maintenance works. Current process requires a long time to prepare working platform or hangar, ground support,

L. Tomić (✉) · O. Čokorilo

University of Belgrade, Faculty of Transport and Traffic Engineering, Belgrade, Serbia

e-mail: tomic.l@vakademija.edu.rs; o.cokorilo@sf.bg.ac.rs

engineers, and appropriate equipment to conduct inspection. By automating the aircraft inspection process using drones, airlines and MRO may have significant benefits.

In addition to reducing the number of workers and equipment needed to inspect the aircraft, the airline could save money, time, and, more importantly, maintain the punctuality valued by its passengers (Mainblades, 2020).

As this concept enables engineers to be on same place, looking at the same monitors, automation will enable a more objective assessment of damage as different inspectors can have different assessment.

Additionally, efficient aircraft inspection process using drones can be very useful to mitigate daily traffic disruptions caused by abnormal events such as bird-strikes or lightening-strikes which required detailed ad hoc inspections, usually within limited turnaround time.

Considering the fact that “Risk represents the effect of uncertainty of objectives” (ISO Guide 73:2009) for every new technology, it is important to previously observe possible objective-related effects, that is, to assess the different risks which may emerge from the objective being set (Tomić, Čokorilo, and Macura 2020).

This chapter provides safety risk assessment for drone-based aircraft inspection process, as a first step of new technology application approval. The aim of conducted risk assessment is identifying new and different hazards and associated risks which presents in very different environment compared to the traditional approach.

Safety risk assessment is conducted by using HAZOP methodology which is helpfulness when facing hazards that are difficult to measure, such as ones rooted in human behaviors and ones that are difficult to detect.

The chapter ends by identification of critical point in the process, which have higher risk compared with traditional aircraft inspection process, and by suggesting some of preventive measures which should be implemented in order to mitigate risks and maximize potential of this innovation.

2 Aircraft Maintenance Inspection

The aviation industry must comply with strict rules, following a set of laws and applicable technical standards. In context of aircraft maintenance, the technical documentation prescribes regular inspections that have to be performed by a certified maintenance organization and which are controlled by the Continuing Airworthiness Management Organization (CAMO) (Novak, 2020).

The current aircraft maintenance inspection process has not significantly evolved during the last 40 years despite the rapid advances in technology (Bouarfa, 2020). The critical point is not only time consuming as it requires a long time to prepare work platforms and hangars, ground support, and engineers to perform inspection, but also dangerous working environment including the great heights and aircraft’s danger zones. Different types of aircraft maintenance inspection are as follows (Aerocorner, 2021):

- Scheduled Aircraft Inspection.
- Annual Aircraft Inspection.
- 50 and 100 Flight Hour Aircraft Inspection
- Pre-flight Aircraft Inspection.
- Unscheduled Aircraft Inspection (ad hoc inspection).

In the case of ad hoc inspections caused by unforeseen situations such as bird-strikes or lightning-strikes, it usually requires moving the aircraft to the position with adequate equipment or hangars in order to do a visual check and determine whether there is damage. When the aircraft is in rotation, for airlines it means an additional delay or aircraft change (if it happened in the airline's base and if a spare aircraft is available). Damage is not always present and therefore an adequate rapid visual inspection of the aircraft by drone could be great help in mitigating the posed disruption. On the other hand, it must be kept in mind that this would only be a visual check of whether the damage is present or not, and that in the case of the presence of damage, the next step is the physical check of it by an engineer.

2.1 Aircraft Maintenance Inspection Using Drones

When EasyJet first conducted drone inspection of an aircraft, it was paving the way for innovation in the aviation industry. In 2015, the British low-cost airline caught the attention of everyone by completing an inspection of its Airbus A320 using a drone. The flying quadcopter named RISER was programmed to scan and assess the aircraft, providing a report on any damage which may require further inspection or maintenance work. Other major industry players have followed EasyJet's pioneering footsteps like American Airlines and Air New Zealand (Mainblades, 2020).

Also, world leading aircraft manufacturer Airbus has recently demonstrated the first-ever automated, drone-based, innovative aircraft maintenance tool at the MRO Americas. The automated drone (Fig. 1) is equipped with an integral visual camera, a laser-based obstacle detection sensor, flight planner software, and an Airbus' aircraft inspection software analysis tool. The drone-based aircraft inspection system is optimized for the inspection of the upper parts of the aircraft fuselage (Unify, 2018).

Following a predefined inspection path, the automated drone captures all the required images with its onboard camera. High-quality pictures are then sent wirelessly to a tablet for the operator's review in real time. They are also transferred to a PC database for detailed analysis using a software system. This allows the operator to localize and measure visual damage on the aircraft's surface. Also, developed software automatically generates an inspection report (Unify, 2018).

Fig. 1 Drone for aircraft maintenance inspection.
(Source: airbus.com)



Fig. 2 HAZOP logic

3 Method

In these research, safety risk assessment of drone-based aircraft inspection is conducted by using HAZOP methodology. There are many authors (e.g., Qike (2016)) who have used HAZOP methodology in their research within the aviation domain.

HAZOP's aim is to identify potential hazards and operability problems caused by deviations from the design, intent of both new and existing processes.

This method requires a multidisciplinary team to brainstorm deviation and discuss hazards. One of the main benefits of this method is creation of detailed and confidential record of identified hazards.

Overall, the goal is to find potential situations that would cause that element to pose a hazard or limit the operability of the process as a whole. There are four basic steps in the process:

1. Forming a HAZOP team
2. Identifying the elements of the system
3. Considering possible deviations in operability
4. Identifying any hazards or failure points

HAZOP logic covers second, third, and fourth step (Fig. 2), and following action will be access risks that emerge from identified hazards.

Table 1 Risk assessment matrix

| Risk matrix | Risk probability (P) | | | | |
|------------------|----------------------|----------------|------------|----------------|---------------------------|
| | Frequent (F) | Occasional (O) | Remote (R) | Improbable (I) | Extremely improbable (Ei) |
| Catastrophic (C) | 3 | 3 | 3 | 2 | 2 |
| Hazardous (H) | 3 | 3 | 3 | 2 | 2 |
| Major (Ma) | 3 | 3 | 2 | 1 | 1 |
| Minor (Mi) | 2 | 2 | 1 | 1 | 1 |
| Negligible (N) | 1 | 1 | 1 | 1 | 1 |

The importance of hazard identification lies in fact that well-defined hazards are the basis for safety risks measurement. Safety risk is defined as the assessment, expressed in terms of predicted probability and severity, of the consequences of a hazard, taking as reference the worst foreseeable situation and using predefined risk assessment matrix (Table 1). In reality, one generic hazard could lead to variety of risks with different probability and severity (Čokorilo, Dell’Acqua 2013).

3.1 HAZOP for Aircraft Inspection Using Drones

3.1.1 Forming a HAZOP Team

Regarding the first step, and as mentioned above, HAZOP methodology requires multidisciplinary team for brainstorming. For this research, HAZOP team consists of aircraft maintenance technicians (AMTs), airline engineers, drone engineers, safety experts, scientific researchers, and civil aircraft pilot (Fig. 3).

3.1.2 Identifying the Elements of the System

After brainstorming team is formed, there is a need to divide observed process into subcomponents. For aircraft maintenance inspection using drones, it can be divided into following subcomponents: engineers, equipment, ground support, and airline (Fig. 4).

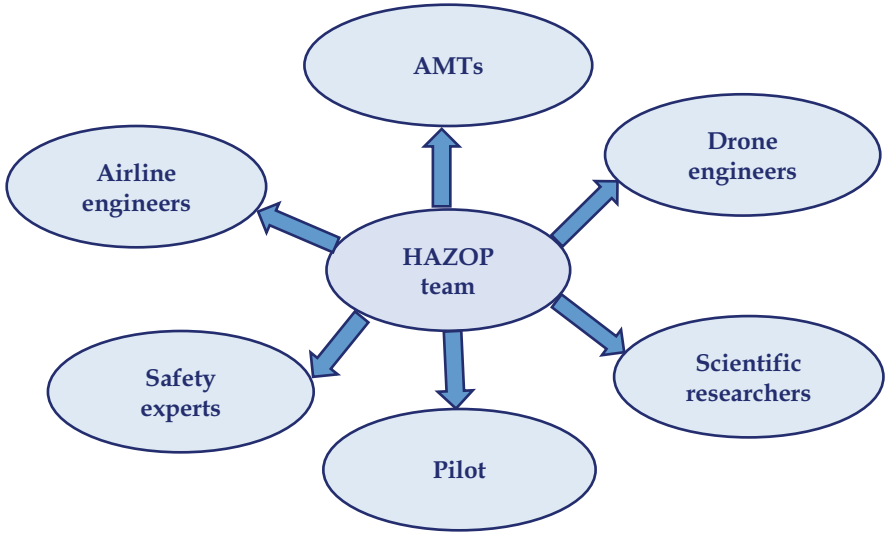


Fig. 3 HAZOP team

Fig. 4 Aircraft inspection process and subcomponents

| Process | Subcomponents |
|----------------------------------|----------------|
| Aircraft inspection using drones | ENGINEERS |
| | EQUIPMENT |
| | GROUND SUPPORT |
| | AIRLINE |

Table 2 System deviation

| |
|--|
| System deviations |
| Remote inspection |
| Data-driven decision making |
| Without ground support and appropriate equipment |
| Multi engineers involved in inspection process |
| Engineers need drone operating license |

3.1.3 Deviations in Operability

Following table (Table 2) contains deviations in operability for innovative way of aircraft inspection by using drones. It can be concluded that main differences are in the equipment that is used and in the decision-making process.

Table 3 Hazard identification

| |
|--|
| Hazard identification |
| Remote inspection |
| Not detailed inspection |
| Drone technical issue |
| Complex weather conditions (strong wind, heavy rain, snow showers, etc.) |
| Birds at airport |
| Insufficiently attached drone components |
| C2 link issue |
| Operator training (untrained drone pilot) |
| Human error |
| Aircraft on near positions |

3.1.4 Hazard Identification: HAZOP

After considering possible deviations in operability, next step is identifying any hazards or failure points.

Hazard is anything that might negatively influence the operation’s safety. The experience and imagination of the selected team are exploited via brainstorming sessions to identify related hazards. The goal of the hazard identification step is to obtain as many hazards as possible applicable, with the scope of the risk assessment.

For aircraft inspection using drones, top ten hazards identified via brainstorming with expert team are listed in Table 3.

Table above shows that there is presence of procedure’s hazards (remote inspection), equipment hazards (drone technical issue and command and control – C2 link issue), human-related hazards (operator training and error) and environment hazards (weather conditions and birds). It should be noted that hazard “Drone technical issue” covers overheating of batteries, camera breakdown, breakdown of electronics, etc.

4 Results and Discussion

4.1 Innovation Benefits

Aircraft maintenance inspection using drones have a lot of benefits. In addition to reducing the number of workers and equipment needed to inspect the aircraft, the airline could save money, time, and provide safer working environment for engineers. Also, one of the main benefits is quality of inspection process and possibility of its record and documentation. Other benefits are shown in Table 4.

Table 4 Innovation benefits

| |
|---|
| Innovation benefits |
| Save time and money required for inspection |
| Reduce number of workers |
| Safer working environment for engineers |
| Inspection record and documentation |
| Objective assessment and D3M |
| Reducing aircraft downtime |
| Saving structure of ground equipment |
| Fast ad hoc aircraft inspection |
| Inspection process can be visible to all stakeholders |

Table 5 Risk assessment

| Risk Identification | Risk assessment | | |
|--|-----------------|---|---------------|
| | P | S | Risk category |
| Loss of control over drone | R | H | 3 |
| Damage of aircraft under inspection | R | H | 3 |
| Damage of drone | O | H | 3 |
| Missing determination movement of the crack, presence of surface contamination, etc. | R | C | 3 |
| Damage of aircraft on near position | I | H | 2 |
| Damage of the property (other equipment) | I | C | 2 |
| Explosion of drone batteries | I | C | 2 |
| Injury to staff | I | C | 2 |
| Ingesting of drone by aircraft engine (a/c on near position at apron) | Ei | H | 2 |
| Inability to perform inspection | R | N | 1 |
| Obstruction of Ground Handling operations | R | N | 1 |

4.2 Risk Assessment

For hazards identified via HAZOP methodology, the next step is to identify risks emerge from it, and to access them associating appropriate probabilities (P) and severities (S).

After assessing the level of risk, the risk zone (category) is determining as green (the lowest level of risk), or yellow (moderate), or red (the highest level of risk) with aim to show how worrying this risk for organization is. Results is shown in Table 5.

Above table shows top risks identified and accessed by HAZOP team. Mentioned risks covered all three risk zones. Risks in the highest category are loss of control over drone, damage to aircraft and drone, and missing determination movement of the crack and presence of surface contamination.

Table 6 Proposed preventive measures

| |
|--|
| Proposed preventive measures |
| Define and limit safe distance from aircraft fuselage and other aircraft parts in inspection by drones |
| Ensure qualification of person operating drones |
| Equip drones with soft edge barriers |
| Develop most common drone task procedures |
| Introduce fast safety check list before each inspection |
| Define additional safety zones for aircraft on near positions |
| Develop collision avoidance system for drones |

4.3 *Proposed Preventive Measures*

Based on the identified risks, Table 6 proposes measures that should be taken so as to act proactively and prevent the risks from having a negative impact on the observed system.

In addition to the new procedures (safe distance, safety zones, and checklists) and qualification of employees, there are need for some measures regarding technical equipment (soft edge barriers on drones and collision avoidance system), all with respect to process efficiency and safety.

5 Conclusion

The results demonstrate that this innovative tendency of aircraft inspection using drones have a lot of benefits, both for MRO organizations and airlines but also for aircraft manufacturers. On the other hand, there is a lot of hazards and risks posed from this tendency. Analysis shows presence of procedure's hazards, equipment hazards, human-related hazards, and environment hazards which posed a different risk. As the highest risk category is related to loss of control over drones and possible damage both for aircraft and drones, it is recommended to work on this critical point firstly by providing adequate qualification and training for personnel who operates with drones, by introducing soft edge barrier on drones, by developing collision avoidance system, and other technical and procedure-based safety barriers in order to maximize potential of this innovation.

References

- Aerocorner. (2021). <https://aerocorner.com/blog/types-of-aircraft-inspections>. Accessed on 20 May 2021.
- Bouarfa, S., Dođru, A., Arizar, R., Aydođan, R., & Serafico, J. (2020). Towards automated aircraft maintenance inspection. A use case of detecting aircraft dents using mask r-cnn. AIAA Scitech 2020 Forum, January 6–10 2020. Orlando, Florida.
- Čokorilo, O., & Dell'Acqua, G. (2013). Aviation hazards identification using safety management system (SMS) techniques. In *16th International conference on transport science ICTS*, May 27, 2013. Portoroz, Slovenia.
- Mainblades. (2020). <https://mainblades.com/article/easyjet-makes-drone-inspection-a-reality-in-aviation-mro/>. Accessed on 13 Apr 2021.
- Novak, A., Sedlackova, N. A., Bugaj, M., Kandra, B., & Lusiak, T. (2020). Use of unmanned aerial vehicles in aircraft maintenance. In *9th International Conference on Air Transport – INAIR 2020, Challenges of Aviation Development*, March 9–11, 2020.
- Qike, W., Xusheng, G., Dengkai, Y., & Qianrui, S. (2016). Fault tree establishment of flight conflict based on the HAZOP method. In *4th international conference on machinery, materials and computing technology*, January 23–24, 2016. Hangzhou, China.
- Tomić, L., Čokorilo, O., & Macura, D. (2020). Runway pavement inspections using drone – Safety issues and associated risks. *International Journal for Traffic and Transport Engineering*, *10*(3), 278–285.
- Unify. (2018). <https://www.unify.aero/news/airbus-using-drones-to-visually-inspect-aircraft>. Accessed on 18 Apr 2021.

Sizing and Performance Analysis of a Single-Seat Tandem Helicopter



Jelena Svorcan, Aleksandar Kovačević, Lazar Popović,
and Aleksandar Simonović

Contents

| | | |
|---|----------------------------|-----|
| 1 | Introduction | 220 |
| 2 | Initial Requirements | 221 |
| 3 | Mass Estimation | 221 |
| 4 | Performance Analysis | 223 |
| 5 | Conclusions | 227 |
| | References | 227 |

Nomenclature

| | |
|-------|-----------------------------------|
| A | Area, m^2 |
| c | Chord, m |
| C | Aerodynamic coefficient |
| D | Diameter, m |
| E | Endurance, h |
| f | Equivalent wetted area, m^2 |
| FM | Efficiency |
| h | Height, m |
| m | Mass, kg |
| N_b | Number of blades |
| P | Power, kW |
| R | Range, km |
| SFC | Specific fuel consumption, g/kW/h |
| T | Thrust, N |

J. Svorcan (✉) · A. Kovačević · L. Popović · A. Simonović
University of Belgrade, Faculty of Mechanical Engineering, Belgrade, Serbia
e-mail: jsvorcan@mas.bg.ac.rs; akovacevic@mas.bg.ac.rs; asimonovic@mas.bg.ac.rs

| | |
|-----------|----------------------------|
| V | Velocity, m/s |
| κ | Correction factor |
| λ | Inflow ratio |
| μ | Forward speed ratio |
| ρ | Density, kg/m ³ |
| σ | Rotor solidity |
| Ω | Angular velocity, rad/s |
| b | Blade |
| cr | Cruise |
| do | Airfoil drag |
| e | Empty |
| f | Fuel |
| h | Hover |
| ind | Induced |
| max | Maximal |
| o | Takeoff |
| p | Progressive flight |
| par | Parasitic |
| prof | Profile |
| req | Required |
| T | Thrust |
| u | Useful |

1 Introduction

The benefits of vertical flight in urban environments are truly numerous. In addition to being able to take off and land almost anywhere as well as provide great assistance in avoiding crowds or delays, such air vehicles can also be used for deliveries, observation, or rescue missions. The first VTOL (vertical-takeoff-and-landing) air vehicle that comes to mind is certainly a helicopter (Leishman, 2006; Raymer, 2018; Yeo, 2019). Large rotors are convenient for producing thrust since induced velocities through the rotor disk can remain small (thus preserving a satisfactory value of power-to-weight ratio). On the other hand, some accompanying downsides include great rotor dimensions, noise, and forward speed limitations.

As nicely formulated by Raymer (2018), the simplest, most often employed, conventional concept implies single main rotor located near the center of gravity (CG) and a much smaller, tail rotor (that counteracts the strong torque generated by the main rotor). However, other possibilities also exist (Yeo, 2019). Tandem configuration comprising two smaller counter-rotating rotors, still abundantly investigated (as demonstrated by Mehrabi and Davari, 2020; Pena et al., 2021; Sal, 2020; Tan et al., 2019; Weishäupl and Prior, 2019; Zhang et al., 2020), apart from the decreased size, is better suited for transportation since it allows a wider range of

possible CG locations (between the fore and aft rotor). Rotor interference (and consequent efficiency loss) is their greatest disadvantage. On the other hand, the quadcopter arrangements so popular today are applicable in small sizes and in combination with electric motors and relatively cheap electronics. Additional possibilities include multicopter designs comprising a large number of small motors and rotors that are also excessively investigated (some examples are AIRBUS Vahana and Trek Aerospace FlyKart 2). However, for further development of such aircraft, advanced battery technology is required.

For these reasons, this chapter presents some basic steps of the conceptual design of a single-seat tandem configuration powered by a piston engine.

2 Initial Requirements

Every conceptual design of air vehicles begins with a good definition of initial requirements (Raymer, 2018). Here, it was most important to ensure a useful mass of $m_u = 100$ kg that roughly corresponds to a single passenger/pilot. Secondly, the range should preferably be above $R > 150$ km at the cruising speed of $V_{cr} > 100$ km/h.

Although scarce, some similar constructions have flown (e.g., AVIDRONE 210TL, LAFLAMME AERO LX300, DP-14 MULTI MISSION UAS, and DP-12 RHINO) and their basic properties can be found online. They are all unmanned, of simple design and of composite and metal structure, while differences in rotor size and design exist.

And that is why an important note must be made here. Rotor blade aerodynamics (i.e., the geometric features of rotors and blades such as rotor diameter D , blade chord c , number of blades N_b , and rotor solidity σ) must be considered from the beginning of the design process, usually by some computational method such as momentum theory (MT), blade element theory (BET), their combination – blade element momentum theory (BEMT), vortex theory, and computational fluid dynamics (CFD) approach. Also, some starting assumptions should be made.

Here, the helicopter is meant to operate at sea level (density estimated by standard atmosphere model), the blade number is $N_b = 3$, rotor tip speed is set to $V_{tip} = 170$ m/s (limitation caused by compressibility effects) while the specific fuel consumption of a piston engine is $SFC = 285$ g/kW/h. Furthermore, any rotor overlapping is neglected in this study.

3 Mass Estimation

Two important design parameters that enable the initial estimation of the required rotor diameter D and engine power P for a given takeoff mass m_o are power loading m/P [kg/kW] and disk loading m/A [kg/m²]. Although data are somewhat scattered or even unavailable for small tandem helicopters, the starting recommended values,

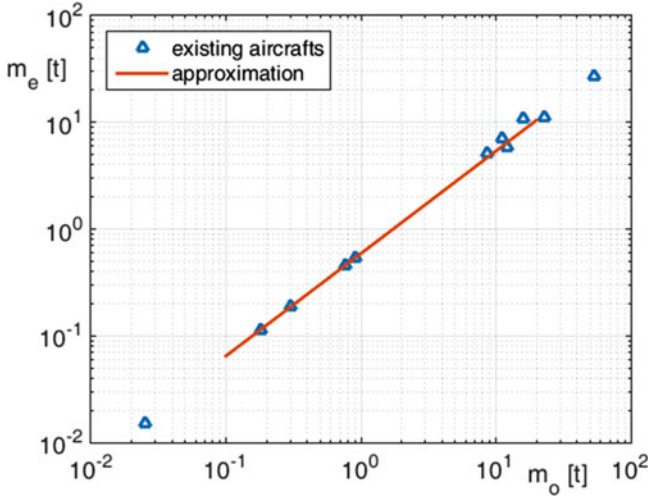


Fig. 1 Approximation of the dependence of empty on takeoff mass

provided by Raymer (2018) are $m/P = 3.6 \text{ kg/kW}$ and $m/A = 40 \text{ kg/m}^2$ (the values differ a little depending on the helicopter type, transport, or civil/utility).

So, it would seem that the only thing that remains to be done is to estimate the takeoff mass as accurately as possible. Initially, it can be assumed that the takeoff mass m_o comprises useful payload m_u , fuel mass m_f , and empty mass m_e , Eq. (1):

$$m_o = m_u + m_f + m_e \tag{1}$$

While useful payload m_u is fixed, fuel mass m_f dependent on aerodynamic quality (e.g., assumed lift-to-drag ratio is $L/D = 2.5$ and rotor efficiency $FM = 0.7$) and desired range R and SFC, the empty mass m_e is probably the hardest to accurately evaluate. From the realized air vehicles (both manned and unmanned) and freely available data, it is possible to make the following approximation, Eq. (2), that is also illustrated in Fig. 1.

$$m_e = 0.5914m_o^{0.9602} \tag{2}$$

After the mass equation is iteratively solved, it is possible to estimate the individual mass components. Although many input variables were considered (diameter D , cruising speed V_{cr} , aerodynamic quality, SFC, etc), it was concluded that useful payload m_u and range R principally dictate the mass distribution. Figure 2 illustrates the obtained relations.

In the end, the combination $(m_o, m_e) = (320 \text{ kg}, 198 \text{ kg})$ seemed the most appropriate. Furthermore, it allows for different combinations of useful payload m_u and range R spanning from $(m_u, R) = (94 \text{ kg}, 210 \text{ km})$ to $(m_u, R) = (109 \text{ kg}, 90 \text{ km})$,

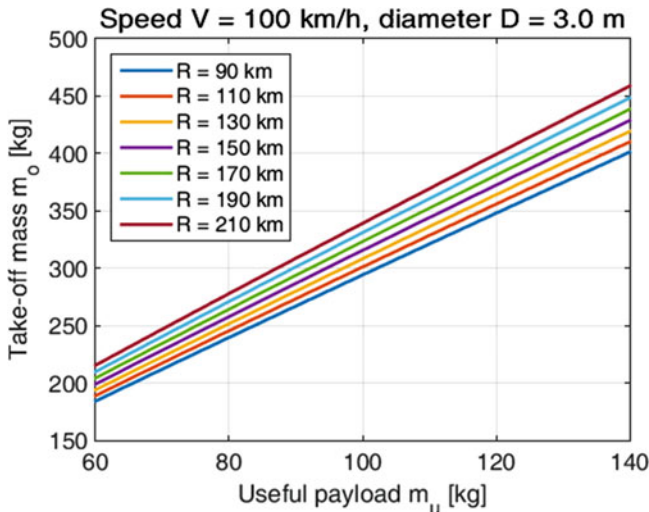


Fig. 2 Relation between the takeoff and useful payload mass for different ranges and fixed cruising speed ($V_{cr} = 100$ km/h) and rotor diameter ($D = 3$ m)

as they are inversely proportional. Also, the chosen values are in good correspondence with the values recommended by Raymer (2018) or presented by Weishäupl and Prior (2019) and Yeo (2019).

The estimated reservoir volume is then $V_f = 30 \text{ dm}^3$ for the fuel density $\rho_f = 770 \text{ kg/m}^3$.

4 Performance Analysis

After the definition of the takeoff mass m_o that directly determines the required thrust $T = 1.57 \text{ kN}$ per rotor, it is necessary to determine how much power must be consumed P_{req} in order to satisfy the initial requirements and perform the basic missions of hovering and progressive flight. The recommended value of power loading suggests that an engine of 90 kW available power should be an adequate solution for present tandem helicopter. However, this should be checked in more detail by more advanced computational methods such as the expanded MT (that includes tip losses and viscous effects).

Hover is the primary flight condition that requires more power than progressive flight at medium speeds and is the first phase to be analyzed. The required power can be estimated by Eq. (3).

$$P_{h,req} = 1.1 \left[2 \left(\frac{\kappa C_T^{1.5}}{\sqrt{2}} + \frac{\sigma C_{do}}{8} \right) \right] \rho A V_{tip}^3 \tag{3}$$

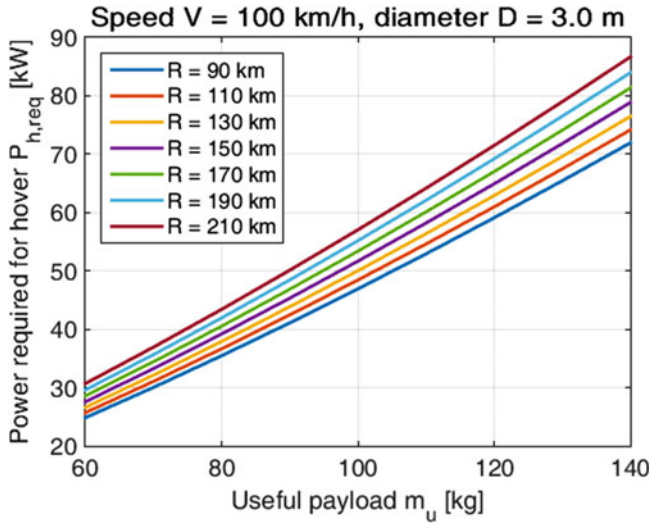


Fig. 3 Power required for hover

where ρ is the air density, A is the disk area, V_{tip} is the blade tip speed, $\kappa = 1.2$ is the correction factor that takes into account the irregular distribution of induced velocities along the rotor disk, $C_T = T/(\rho AV_{tip}^2)$ is the thrust coefficient, $\sigma = 2N_b c/(D\pi)$ is the rotor solidity, and C_{do} is the airfoil drag coefficient. The increase of 10% is made to include the transmission losses.

Figure 3 illustrates the estimated power required for hover. It can be seen that hovering with the useful payload of 100 kg requires approximately 52 kW. Similarly, it is possible to depict the rotor efficiency FM for considered flight conditions (Fig. 4).

As Eq. (4) demonstrates, power required for progressive flight $P_{p,req}$ includes more components (induced, profile, and parasitic) that account for the somewhat changed fluid flow as well as the additional drag from both the blades and the fuselage (Leishman, 2006).

$$P_{p,req} = 1.1 \left\{ 2 \left[\kappa C_T \lambda + \frac{\sigma C_{do}}{8} (1 + 4.65 \mu^2) \right] + \frac{1}{2} \frac{f}{A} \mu^3 \right\} \rho A V_{tip}^3 \quad (4)$$

where λ is the inflow ratio, μ is the forward speed ratio, and f is the equivalent wetted area of the fuselage, landing gear, rotor hubs, etc. Additional losses induced by compressibility effects and zones of reversed flow are neglected at this point.

Figure 5 presents the estimated required P_{req} and available P_a power for progressive flight of a single-seat tandem helicopter together with the contributing components of induced P_{ind} , profile P_{prof} , and parasitic power P_{par} at sea level. The excess power ΔP can be used for either climbing or accelerating as depicted in Figs. 6 and 7.

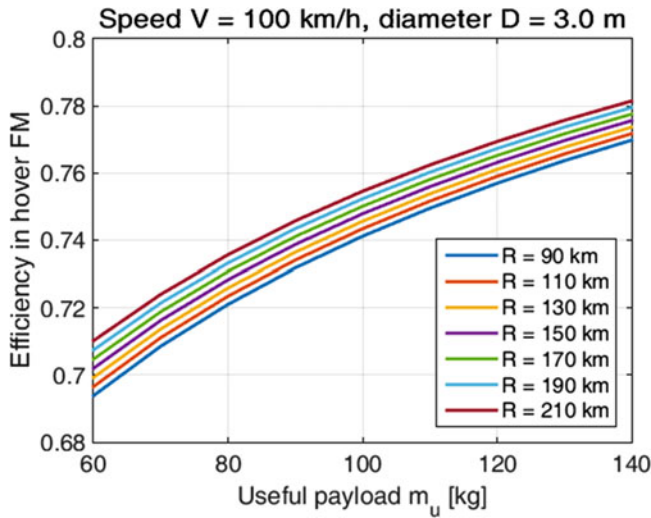


Fig. 4 Estimated rotor efficiency in hover

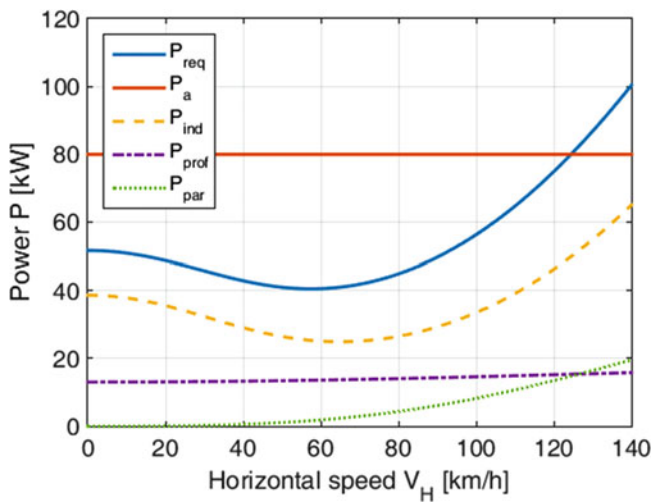


Fig. 5 Power required for horizontal flight

Furthermore, it can be concluded that the optimal speed (for the least required power and the longest endurance) is $V_{E_{max}} = 58$ km/h, while the speed of the longest range is somewhat higher $V_{R_{max}} = 90$ km/h which is sufficiently close to the initially requested cruising speed $V_{cr} = 100$ km/h. These values imply that the maximal range and endurance of $R_{max} = 129$ km and $E_{max} = 105$ min, respectively, can be achieved with the proposed single-seat tandem helicopter configuration.

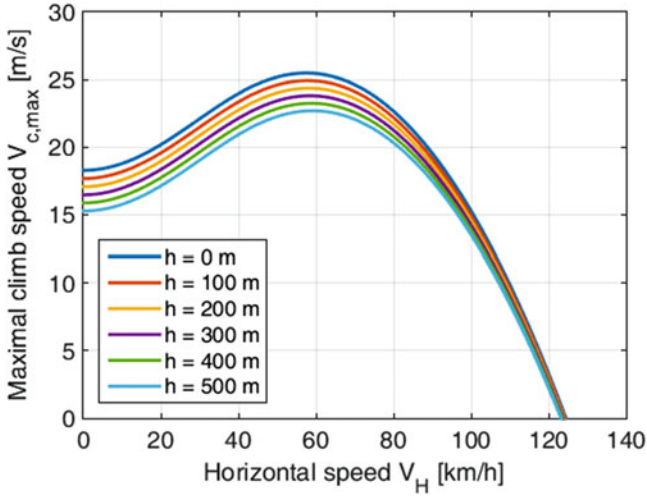


Fig. 6 Maximal climbing speeds in horizontal flight

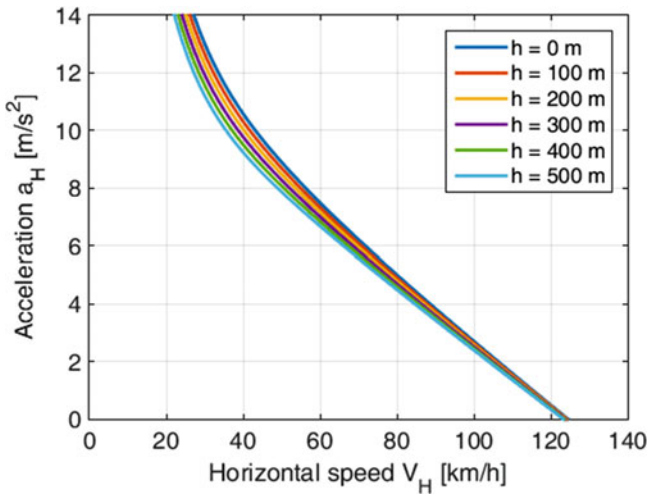


Fig. 7 Maximal acceleration in horizontal flight

Of course, in subsequent design phases, these preliminary results should be validated further by more advanced numerical methods.

5 Conclusions

In the end, it can be concluded that for the intended single-seat tandem helicopter the following characteristics are recommended:

- Takeoff mass $m_o = 320$ kg.
- Empty mass $m_e = 198$ kg.
- Rotor diameter $D = 3$ m (where the tip speed is $V_{tip} = 170$ m/s and rotor angular velocity $\Omega = 1082$ rpm).
- Rotor contains $N_b = 3$ rectangular blades whose chord is approximately $c = 15$ cm.

Further investigations should include the effects of rotor overlapping (the expected power increase amounts to 15%), the existence of fuselage and landing skids as well as more comprehensive flow investigations resembling (Mehrabi and Davari, 2020; Tan et al., 2019; Weishäupl and Prior, 2019), or flight dynamics and control analyses similar to Pena et al. (2021), Sal (2020), and Zhang et al. (2020).

Acknowledgments The research work is supported by the Ministry of Education, Science, and Technological Development of the Republic of Serbia through contract no. 451-03-9/2021-14/200105.

References

- Leishman, G. (2006). *Principles of helicopter aerodynamics*. Cambridge University Press.
- Mehrabi, A., & Davari, A. R. (2020). Outwash flow measurement around the subscale tandem rotor in ground effect. *Engineering Science and Technology, an International Journal*, 23(6), 1374–1384.
- Pena, J. M. A., Paredes, S. A. R., Martinez, J. S. V., & Aguilar-Molina, Y. (2021). A laboratory prototype tandem helicopter with two degrees of freedom. *IEEE Access*, 9, 39618–39625.
- Raymer, D. (2018). *Aircraft design: A conceptual approach*. American Institute of Aeronautics and Astronautics, Inc.
- Sal, F. (2020). Variance constrained trajectory tracking for tandem-rotor helicopters. *Aircraft Engineering and Aerospace Technology*, 92(3), 398–403.
- Tan, J. F., Zhou, T. Y., Sun, Y. M., & Barakos, G. N. (2019). Numerical investigation of the aerodynamic interaction between a tiltrotor and a tandem rotor during shipboard operations. *Aerospace Science and Technology*, 87, 62–72.
- Weishäupl, A. B., & Prior, S. D. (2019). Influence of propeller overlap on large-scale tandem UAV performance. *Unmanned Systems*, 7(4), 245–260.
- Yeo, H. (2019). Design and aeromechanics investigation of compound helicopters. *Aerospace Science and Technology*, 88, 158–173.
- Zhang, Y., Fan, W., Xiang, C., Xu, B., Ai, T., Yuan, L., & Liu, Y. (2020). An innovative aerial manipulator with tandem ducted fans: Modeling, control, and simulation. *Complexity*, 2020, 7923539.

Optimization of the Surface of Drone Propeller Manufactured in 3D Printer



Ömer Seçgin and M. Ziya Sogut

Contents

| | | |
|---|----------------------------|-----|
| 1 | Introduction | 229 |
| 2 | Drones | 230 |
| 3 | Materials and Method | 231 |
| 4 | Results | 232 |
| 5 | Conclusion | 234 |
| | References | 235 |

1 Introduction

Drones are unmanned aerial vehicles. While drones can be controlled by remote control, nowadays, they can make their own decisions and act with artificial intelligence (Al-Turjman et al., 2019).

Drones, which were previously used in the military field, are also used for commercial purposes today. Nowadays, drones are used for video shooting in the advertising and cinema industry, and for aerial support in areas where fire extinguishing is difficult and dangerous (Arslan and Delice, 2020). Various sensors are placed on the drones, effectively providing benefits in search and rescue efforts. They are also used in the agricultural sector for monitoring the harvesting time and spraying the products (Akkamiş and Çalışkan, 2020). In addition to these, drones are also used in archaeological studies (Yakar and Mırdan, 2017).

Ö. Seçgin (✉)

Technology Faculty, Sakarya University of Applied Sciences, Sakarya, Türkiye
e-mail: omerseccin@subu.edu.tr

M. Z. Sogut

Maritime Faculty, Piri Reis University, İstanbul, Türkiye

When the literature is examined, it is seen that studies on drones focus on issues such as image processing (Lee et al., 2016; Yanmaz et al., 2018; Huang et al., 2019), usage in agriculture (Mogili and Deepak, 2018; Samancı and Kardeşahin, 2018; Ahirwar et al., 2019), usage in first-aid activities (Magistretti and Dell’Era, 2019), and military potential (Wilcox, 2017).

Studies on drone production are limited in the literature. In this study, 3010 CF drone propeller was produced with a 3d printer. In additive production, a certain amount of roughness occurs on the surface of the part. If these roughnesses are too much, the quality of the product is adversely affected. In this study, the surface roughness of 3010 CF drone propellers produced by 3d printer has been optimized.

2 Drones

There are many different types of drones on the market. These can be divided into four main groups as multi-rotor, fixed-wing, single-rotor helicopter, and fixed-wing hybrid Vtol (Drone Types: Multi-Rotor Vs Fixed-Wing Vs Single Rotor Vs Hybrid Vtol, 2021). Although multi-rotor drones are common, they are not the only alternative. The single-rotor helicopter is already in manned use. But unmanned single-rotor helicopter drones are also available. These can be described as base-level drones. Generally, they can be powered by a gas engine.

Multi-rotor drones can be used in more strategic areas, because they have balance and keep hovering in a position. They generally have half an hour of flight time (Fig. 1).

Fixed-wing drones are long-range drones. They can make 16 h of continuous flight. But their landing abilities are bad. Besides, they are not able to hover. Fixed-wing hybrid Vtol drones have many propellers. This reduces the negative aspects of drones classified as “fixed-wing.”

Fig. 1 Multi-rotor drone with a camera (List of 14 Different Types of Drones Explained with Photos, 2021)



Drone bodies are usually made of plastic material. Plastic material provides lightness to the drone. Similarly, drone propellers are generally made of carbon fiber material.

3 Materials and Method

In this study, 3010 CF propeller was produced on ¼ scale. Additive manufacturing technique was used in production. Propeller fabrication work was done in FlashForge Creator 3. PLA filament with a diameter of 1.7 mm was used as the material.

The surface roughness (Ra) of the parts produced in the 3d printer was measured with Marsurf PS1. In Fig. 2, an image was given from the moment of measuring the surface roughness.

In this study, layer height, infill rate, and printing speed were determined as parameters. The parameters and their levels were given as follows (Table 1):

The experimental design was done by the Taguchi method. The experimental design was done according to the L9 orthogonal index (Table 2). Then, signal/noise (S/N) analysis was performed using the “smaller is better” formulation, and optimum levels of the parameters were determined. In addition, parameter interactions were determined by performing variance analysis.

Fig. 2 Measuring of surface roughness



Table 1 Parameters and levels

| Level | Layer height (mm) | Infill rate (%) | Printing speed (mm/min) |
|-------|-------------------|-----------------|-------------------------|
| 1 | 0.1 | 25 | 50 |
| 2 | 0.15 | 50 | 60 |
| 3 | 0.2 | 75 | 70 |

Table 2 Experimental setup and responses

| Exp. No | Parameters | | | Ra (μm) | S/N ratio |
|---------|------------|-------|----------|----------------------|-----------|
| | L. H. | I. R. | P. S. | | |
| | (mm) | (%) | (mm/min) | | |
| 1 | 0.1 | 25 | 50 | 19.593 | -25.842 |
| 2 | 0.1 | 50 | 60 | 20.610 | -26.281 |
| 3 | 0.1 | 75 | 70 | 20.277 | -26.139 |
| 4 | 0.15 | 25 | 60 | 28.493 | -29.094 |
| 5 | 0.15 | 50 | 70 | 29.753 | -29.470 |
| 6 | 0.15 | 75 | 50 | 28.337 | -29.047 |
| 7 | 0.2 | 25 | 70 | 31.093 | -29.853 |
| 8 | 0.2 | 50 | 50 | 31.440 | -29.949 |
| 9 | 0.2 | 75 | 60 | 31.330 | -29.919 |

L. H. layer height, *I. R.* infill rate, *P. S.* printing speed

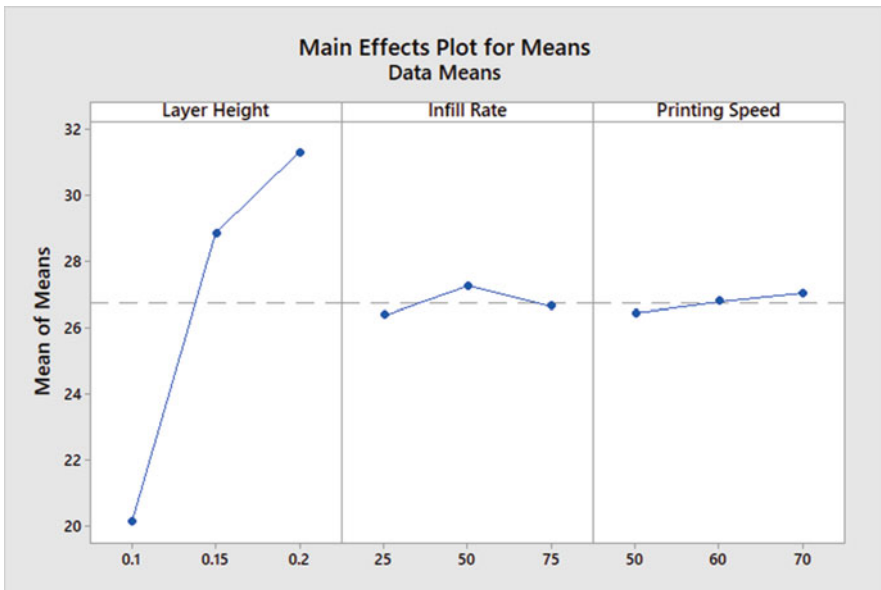


Fig. 3 Main effect plot for means

4 Results

The surface roughness of all parts produced with a 3d printer was measured. Measurement results were given in Table 2. The first section of Table 2 contains the experiment number. In the second section, the experiment parameters were given. In the last section, surface roughness (Ra) and S/N ratios were given. The main effect plot for means was given in Fig. 3.

Table 3 Response table for S/N ratios

| Level | Layer height | Infill rate | Printing speed |
|-------|--------------|-------------|----------------|
| 1 | -26.09 | -28.26 | -28.28 |
| 2 | -29.20 | -28.57 | -28.43 |
| 3 | -29.91 | -28.37 | -28.49 |
| Delta | 3.82 | 0.30 | 0.21 |
| Rank | 1 | 2 | 3 |

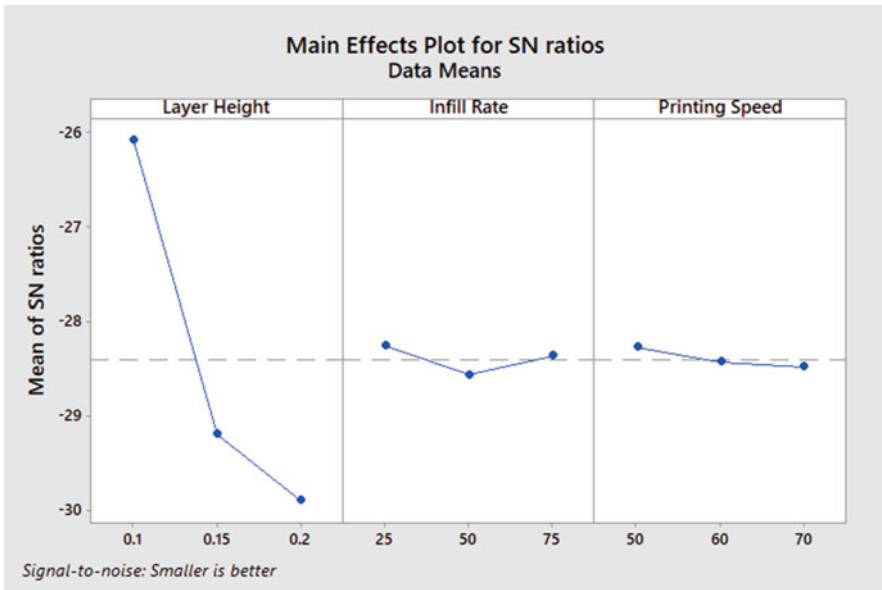


Fig. 4 S/N ratios (study results)

According to Fig. 3, when the layer height is increased from 0.1 to 0.15, the surface roughness also increases significantly. Increasing the layer height from 0.15 to 0.2 also shows an increase in surface roughness, but the increase is not as dramatic as the first.

The response table for signal-to-noise ratios was given in Table 3. The effects of parameters on surface roughness were given in the rank line. According to the rank line, the most effective parameter on surface roughness is layer height (Table 3).

S/N ratios' graphic was given in Fig. 4. According to this figure, the most important parameter on the surface roughness is the layer thickness. This is also consistent with the literature (Taşdemir, 2021). According to the S/N analysis, optimum parameter levels are 0.1 mm layer height, 25% infill rate, and 50 mm/min printing speed.

Analysis of variance (ANOVA) for SN ratios was given in Table 4. Accordingly, the most effective parameter on surface roughness is layer height ($P = 0.0000215$). In the analysis of variance, the p values of each three parameters (layer height, infill

Table 4 Analysis of variance for SN ratios

| Source | DF | Seq SS | Adj MS | F | P |
|----------------|----|--------|--------|----------|-------|
| Layer height | 2 | 24.795 | 12.397 | 46520.65 | 0.000 |
| Infill rate | 2 | 0.143 | 0.071 | 268.01 | 0.004 |
| Printing speed | 2 | 0.069 | 0.035 | 130.90 | 0.008 |
| Residual error | 2 | 0.001 | 0.000 | | |
| Total | 8 | 25.008 | | | |

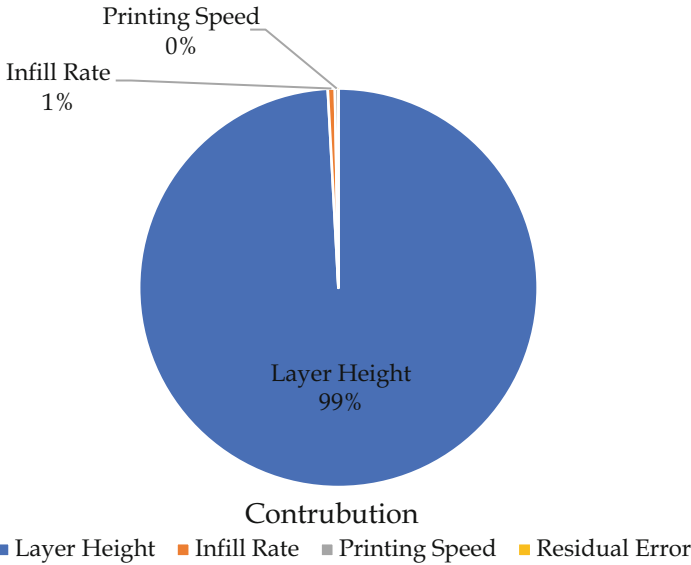


Fig. 5 Parameter’s contribution rate to Ra (original lab measurements)

rate, and printing speed) are less than 0.05. Therefore, all parameters have a significant effect on surface roughness. But, this effect ratio is very small compared to the layer height (Table 4).

In Fig. 5, the contribution ratios of the parameters on the surface roughness were given. This graphic was obtained from variance analysis. According to the graph, the most effective parameter on surface roughness is layer height.

5 Conclusion

In this study, 3010 CF propeller was produced on ¼ scale. Layer height, infill rate, and printing speed were set as work parameters. Compared to other parameters, it was seen that layer height was effective at 90%. Optimum parameter levels are 0.1 mm layer height, 25% infill rate, and 50 mm/min printing speed.

References

- Ahirwar, S., et al. (2019). Application of drone in agriculture. *International Journal of Current Microbiology and Applied Sciences*, 8(01), 2500–2505. <https://doi.org/10.20546/ijcmas.2019.801.264>
- Akkamiş, M., & Çalişkan, S. (2020). Unmanned aerial vehicles and usage in agricultural applications. *Turkish Journal of Unmanned Aerial Vehicles*, 2(1), 8–16.
- Al-Turjman, F., et al. (2019). Enhanced deployment strategy for the 5G drone-BS using artificial intelligence. *IEEE Access*, 7, 75999–76008. <https://doi.org/10.1109/ACCESS.2019.2921729>
- Arslan, N., & Delice, E. K. (2020). Drone selection for personal users with the Kemira-M method: An application. *Journal of Industrial Engineering*, 1(2), 159–179.
- Drone Types: Multi-Rotor Vs Fixed-Wing Vs Single Rotor Vs Hybrid Vtol. (2021). Available at: <https://www.auav.com.au/articles/drone-types/>
- Huang, C., et al. (2019). Learning to capture a film-look video with a camera drone. In *Proceedings - IEEE international conference on robotics and automation, 2019-May* (pp. 1871–1877). <https://doi.org/10.1109/ICRA.2019.8793915>
- Lee, E. J., et al. (2016). Early sinkhole detection using a drone-based thermal camera and image processing. *Infrared Physics and Technology*, 78, 223–232. <https://doi.org/10.1016/j.infrared.2016.08.009>
- List of 14 Different Types of Drones Explained with Photos. (2021). Available at: <https://aerocorner.com/blog/types-of-drones/>
- Magistretti, S., & Dell’Era, C. (2019). Unveiling opportunities afforded by emerging technologies: Evidences from the drone industry. *Technology Analysis and Strategic Management*, 31(5), 606–623. <https://doi.org/10.1080/09537325.2018.1538497>
- Mogili, U. R., & Deepak, B. B. V. L. (2018). Review on application of drone systems in precision agriculture. *Procedia Computer Science*, 133, 502–509. <https://doi.org/10.1016/j.procs.2018.07.063>
- Samancı, A., & Karaşahin, M. (2018). Availability of small unmanned aerial vehicle for phenotyping selection in cereal breeding nurseries. *Selcuk Journal of Agricultural and Food Sciences*, 32(3), 616–623. <https://doi.org/10.15316/sjafs.2018.144>
- Taşdemir, V. (2021). Investigation of dimensional integrity and surface quality of different thin-walled geometric parts produced via fused deposition modeling 3D printing. *Journal of Materials Engineering and Performance*, 30(May), 3381–3387. <https://doi.org/10.1007/s11665-021-05809-x>
- Wilcox, L. (2017). Embodying algorithmic war: Gender, race, and the posthuman in drone warfare. *Security Dialogue*, 48(1), 11–28. <https://doi.org/10.1177/0967010616657947>
- Yakar, M., & Mirdan, Ö. (2017). Compared problems at modeling of cultural heritages with unmanned aerial vehicles. *Journal of Geomatics*, 2(3), 118–125.
- Yanmaz, E., et al. (2018). Drone networks: Communications, coordination, and sensing. *Ad Hoc Networks*, 68, 1–15. <https://doi.org/10.1016/j.adhoc.2017.09.001>

Preparation of Smart Gels with Stiffening Behavior



Selim Gürgen

Contents

| | | |
|---|------------------------------|-----|
| 1 | Introduction | 237 |
| 2 | Materials and Method | 238 |
| 3 | Results and Discussion | 239 |
| 4 | Conclusion | 240 |
| | References | 241 |

Nomenclature

| | |
|-------|-----------------------------|
| DMA | Dynamic mechanical analysis |
| SiC | Silicon carbide |
| G' | Storage modulus |
| G'' | Loss modulus |

1 Introduction

In recent years, shear-thickening fluid has attracted much attention from the researchers. This smart fluid has been adapted to several engineering applications such as protective structures (Srivastava et al., 2011), vibration attenuation systems (Gürgen & Sofuoğlu, 2020a, b), polishing slurries (Gürgen & Sert, 2019), and cutting tools (Gürgen & Sofuoğlu, 2020a, b). Shear-thickening fluid is a nano suspension that includes colloidal particles in a chemically inert liquid. The nano

S. Gürgen (✉)

Department of Aeronautical Engineering, Eskişehir Osmangazi University, Eskişehir, Türkiye
e-mail: sgurgen@ogu.edu.tr

particles in this suspension are randomly distributed at the rest state. However, the nano particles come together to form large particle clusters when the mixture is excited. The clustering process results in a viscosity increase, thereby hindering the fluid to flow. This is due to the large particle barriers in the flow zone. By removing the loading from the mixture, nano particles are broken into individual small groups and therefore, clustering process diminishes over the suspension. At the macro level, the mixture exhibits solid-like behavior when the suspension is loaded while the suspension shows fluidic or viscous properties at the rest state. Although this smart fluid is open for integration into many fields, the fluidic behavior at the zero shear rate requires a containment of the suspension not to spill over there. Knowing this drawback in shear-thickening fluid, researchers have paid attention to solid polymers or gels rather than fluidic materials. At this point, shear-stiffening gels rise to prominence because these polymers do not require containment at the rest state. At the zero shear state, shear-stiffening gels exhibit gel-like behavior whereas the material increases its stiffness and turns into solid-like behavior upon excited.

Shear-stiffening gels have been adapted to various engineering applications just like shear-thickening fluids and the results are much efficient than shear-thickening fluid. Shear-stiffening gels exhibit more stable characteristics than shear-thickening fluids because nano particles in shear-thickening fluids are prone to settle on the bottom. In engineering applications, shear-stiffening gels were used in protective structures (Zhao & Xu, 2019). Tian and Du (2012) prepared a smart polymer gel by combining silicon oil and silicon rubber. In their study, the content of silicon oil was changed from 30% to 67%. The smart polymers were subjected to dynamic mechanical analysis and based on the measurements, the specimens show stiffer properties as silicon oil content is increased in the composition. Wang (2014) synthesized a smart polymer with shear-stiffening properties by using boric acid instead of silicon rubber. The smart polymer was employed as a matrix for magnetic particles to prepare magnetorheological gels. Furthermore, this smart gel was used as a coating on high-performance textiles to improve the anti-impact behavior of textile composites. According to the impact test results, the smart gel coating results in about 60% increase in the energy absorbing capacity of the composites. In the present work, we deal with synthesis of a shear-stiffening gel by using various chemical components. In addition to the neat gel, additive particles were included into the gel and mechanical behavior of the reinforced gel was enhanced.

2 Materials and Method

In the sample fabrication, 4 g pyroboric acid, 30 g silicone oil, and 2 ml ethanol were mixed. The mixture was rested at 240 °C for 6 h. Then, 4 wt% benzoyl peroxide (BPO) was added to the mixture at 95 °C. This procedure is followed for neat gel. In the next stage, 1 μm particle size silicon carbide (SiC) was included in the gel. SiC loading was kept at 50 wt% in the gel. In order to characterize the smart behavior of the samples, dynamic mechanical analysis (DMA) was carried out in a rheometer.

Because the gels are viscoelastic materials, dynamic shear rheology was investigated at the oscillatory shear strain of 1% and the shear frequency was varied from 0.1 to 100 Hz in the measurements.

3 Results and Discussion

Figures 1 and 2 show the dynamic shear rheology curves samples. It is obvious that both samples have a stiffening behavior. This behavior is characterized by an obvious shift from viscous state to elastic state when shear is increased on the samples. Storage modulus (G') gives the elastic part of the samples, whereas loss modulus (G'') is responsible for the viscous behavior of the samples. From the charts, loss moduli (G'') increase up to a critical point at about 20 Hz. Beyond this point, they gradually reduce for both samples. On the other hand, storage moduli (G') grow stronger for every frequency. This can be interpreted that the gels enhance their elastic response while reducing their viscous behavior after the crossover point of 20 Hz. Under shear loading, both samples behave more solid instead of viscous properties. This mechanism can be explained by the molecular networks in the gels. In the molecular network, cross-bonds of B-O link the long molecular chains at different points. Hence, short B-O cross-bonds restrict the motion of long molecular chains under increasing deformation. Due to these mechanism, the gels show

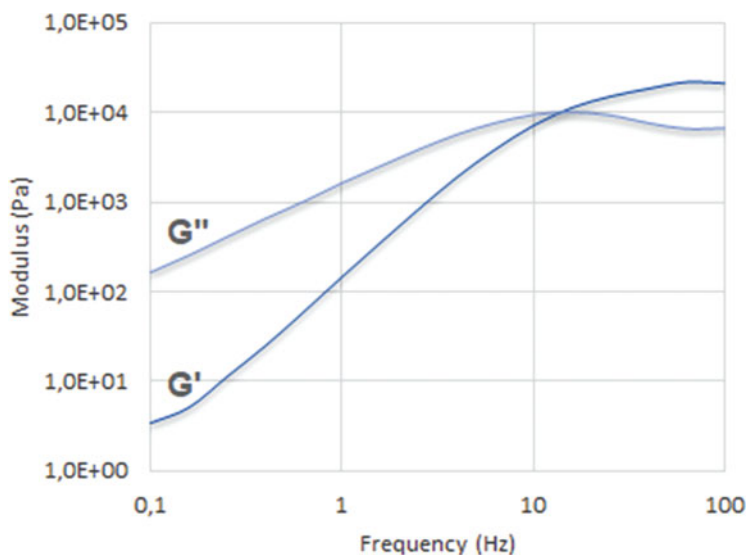


Fig. 1 Storage (G') and loss (G'') modulus for neat gel

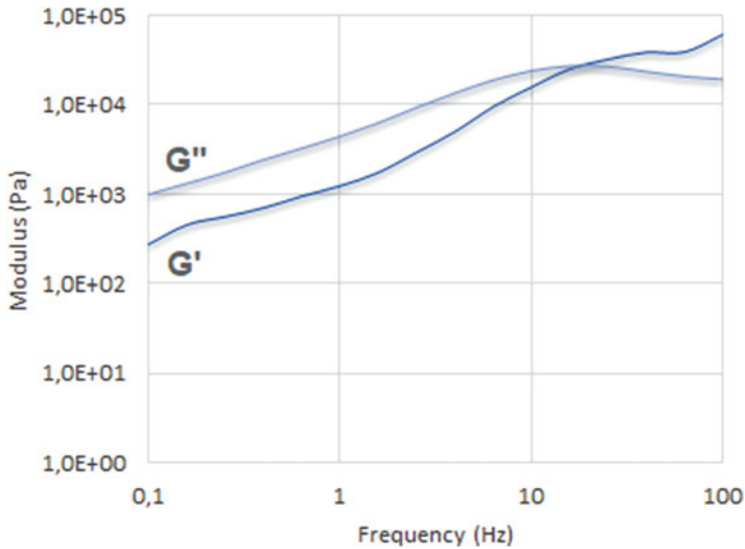


Fig. 2 Storage (G') and loss (G'') modulus for SiC included gel

increased stiffness at high shear frequencies. On the other hand, long molecular chains are more free at lower shear rates because they are not moved extensively due to low deformations. Hence, lower stiffness is observed at lower shear frequencies. In the SiC reinforced gel, stiffening introduces higher level because SiC particles locate in the molecular chain network and thereby increasing the entanglement of molecular chains. Thus, the material shows higher elastic portion. In addition to the cross-bonds, SiC particles contribute to the entanglement process.

4 Conclusion

In the present work, a smart gel having stiffening behavior under shear deformation was fabricated. In addition to the neat form, an additive, SiC particle was included in the smart gel to enhance the stiffening behavior. This shows that we can tune the elastic or viscous part of this smart material by using various amounts of SiC particles in the gel. Hence, desired level of stiffening can be tailored for different engineering applications. The most important prospective application area for this smart material is vibration damping systems. Considering the air vehicles, flutter is a big challenge for engineers and this smart gel may be adapted to anti-flutter systems in aircraft. This preliminary work will be extended to anti-vibration systems especially for aircraft systems.

References

- Gürgen, S., & Sert, A. (2019). Polishing operation of a steel bar in a shear thickening fluid medium. *Composites Part B: Engineering*, *175*, 107127.
- Gürgen, S., & Sofuoğlu, M. A. (2020a). Vibration attenuation of sandwich structures filled with shear thickening fluids. *Composites Part B: Engineering*, *186*, 107831.
- Gürgen, S., & Sofuoğlu, M. A. (2020b). Integration of shear thickening fluid into cutting tools for improved turning operations. *Journal of Manufacturing Processes*, *56*, 1146–1154.
- Srivastava, A., Majumdar, A., & Butola, B. S. (2011). Improving the impact resistance performance of Kevlar fabrics using silica based shear thickening fluid. *Materials Science and Engineering A*, *529*, 224–229.
- Tian, T., & Du, H. (2012). Study of shear-stiffened elastomers. *Smart Materials and Structures*, *21*, 125009.
- Wang, S. (2014). Multifunctional polymer composite with excellent shear stiffening performance and magnetorheological effect. *Journal of Materials Chemistry*, *2*, 7133–7140.
- Zhao, C., & Xu, C. (2019). Anti-impact behavior of a novel soft body armor based on shear thickening gel (STG) impregnated Kevlar fabrics. *Smart Materials and Structures*, *28*, 075036.

Noise and Vibration Measurement System



Anzhelika Stakhova

Contents

| | | |
|---|---|-----|
| 1 | Introduction | 244 |
| 2 | Methods and Tools for Measuring Noise and Sound Level | 244 |
| 3 | Results and Discussion | 247 |
| 4 | Conclusion | 248 |
| | References | 248 |

Nomenclature

| | |
|-----|---|
| A | Amplifier |
| ADC | Analog-to-digital converter |
| BT | Bluetooth module connected to the sensor to transmit a signal to the main board |
| BTM | Bluetooth module for receiving a signal on the main board from measuring channels |
| LCD | Module for displaying the result |
| M | Microphones |
| MCU | Microcontroller |
| V | Accelerometers |

A. Stakhova (✉)
National Aviation University, Kyiv, Ukraine
e-mail: sap@nau.edu.ua

1 Introduction

At the present stage of aviation development, the main direction of ensuring the working condition of aviation equipment is to increase the efficiency of its control. For this purpose, work on studying of a technical condition of special equipment and the analysis of its changes is carried out.

Most machine failures are expressed in increased vibration, so vibration analysis is a powerful tool for diagnosing equipment. Each fault or damage has its own type of vibration (Barkov et al., 2000). Exceeding the acceptable level of vibration during the operation of different kinds of equipment leads to a decrease in the reliability and durability of particular elements in these devices. The advent of modern vibration-measuring equipment provides the ability to make exact measurements, registration, and subsequent analysis of dynamic processes, that is, vibration signals.

It is impossible to ensure the working condition of machinery without the introduction of modern diagnostic methods and the development of new methods and systems, the use of which will significantly increase the effectiveness of control. Therefore, in the course of the work, a review and analysis of modern means of measuring vibration and noise according to the vibroacoustic parameters of the working area was carried out. The actual task of designing and research of the system of monitoring of vibroacoustic parameters of the working zone in which the influence of vibration and noise parameters is present is set.

2 Methods and Tools for Measuring Noise and Sound Level

Today, the number of devices and ancillary equipment for measuring vibroacoustic parameters is in the hundreds of types. They differ in accuracy, cost, and availability of different functionality. As a rule, firms specializing in the production of combined sanitary control devices of vibration and noise can call them both vibrometers and sound-level meters. Thus, in this chapter, the proposed system, which has high accuracy at low cost, as well as the ease of installation for measuring vibroacoustic parameters of the working area have been discussed.

For the sanitary standardization of noise and vibration, a large range of measuring instruments of varying complexity is produced. Let us review the existing means and methods of noise measurement. When developing methods of noise control and comparison of noise characteristics created by mechanisms and machines with acceptable sanitary norms, it is necessary to know its spectral composition as well as the level of its intensity.

There are two methods for measuring noise levels:

- Subjective
- Objective

When measuring by the subjective method, devices – phonometers (<https://infocom-m.ru/uk/inzhenernye-sistemy/air-and-structural-noise.html>) are used. In these devices, the pure tone of a certain frequency is compared with the measured sound or noise. Phonometers have a very limited application due to the complexity of measurements and the dependence of their results on the characteristics of hearing.

When measuring by the objective method, noise meters are used, which have become widespread for measuring noise parameters (<https://infocom-m.ru/uk/inzhenernye-sistemy/air-and-structural-noise.html>). Noise meters perceive noise with a broadband microphone. The microphone converts sound vibrations into electrical ones. Electric in turn are amplified, and then fed to the rectifier of the switch, that is, the meter. Frequency analyzers, recorders, and other devices can be connected to the output of the amplifier.

Due to the limited frequency characteristics of the sensitivity, the noise meters of the objective measurement method allow to determine only the approximate values of the noise volume levels.

Measurements of noise levels in industry are performed by noise meters of different kinds, of which the most common are the noise meter Sh-63 with an octave bandpass filter PF-1 and the noise meter Sh-3 M with 1/3-octave analyzer Liote.

The noise meter has three scales (A, B, and C), which take into account the frequency composition of the measured noise (<https://infocom-m.ru/uk/inzhenernye-sistemy/air-and-structural-noise.html>). The noise characteristic on the scale A corresponds to the volume curve 40 phon, that is, to some extent the subjective perception of the volume level and allows you to make an approximate assessment of the “trouble” or “harmfulness” of the noise. Therefore, the noise level measured on a scale A in decibels (dBA) is of great importance for the hygienic practice of industrial noise assessment (Cheremisinoff, 1996).

The noise characteristic on the B scale corresponds to a curve equal to a volume of 70 phon. To obtain the noise spectrum, the measurement must be performed on a scale of C. The linear frequency response will show a purely physical value (sound pressure level) in the range of 60–5000 Hz.

Special devices (noise analyzers) study the spectral composition of noise. Octave analyzers should often be used to measure sound pressure levels in octave bands.

The band in which the upper limit frequency is equal a twice the lower frequency (45–90, 90–180, etc.) is called the octave band. It is characterized by the average frequency (geometric mean of the upper f_1 and lower f_2 limit frequencies $f = \sqrt{f_1 \cdot f_2}$).

GM1352 digital noise meter, manufactured by Benetech (<https://gtest.com.ua/benetech-gm1352.html>). This noise meter can measure noise levels in the range of 30 to 130 dB; it has a highly sensitive capacitive microphone and can record sound oscillations in the frequency range from 31.5 Hz to 8 kHz. A distinctive feature of the noise meter Benetech GM1352 is small size, ease of use, and functionality.

Let us review the existing tools and methods for measuring sound level. A sound-level meter is a tool that determines the sound level by measuring the pressure of the noise level (De Silva, 2005). Sound enters the sound-level meter through the microphone input. Then the sound is evaluated in the device and the results are

displayed in decibels. The PCE sound-level meter meets the highest industry standards. In addition, it is light and easy to use.

PCE-428 is a class 2 sound-level meter with protocols that meets the requirements of IEC 60651 (https://pragmatic.com.ua/pce_428). This portable high-precision sound-level meter has a large backlit LCD display that displays the sound pressure level (SPL) numerically and graphically in real time. Thanks to the octave bandpass filter, even the smallest difference in frequency is detected.

The basis of any vibration-measuring instrument is a measuring transducer (vibration transducer), which converts it into an electrical signal. More often, such a transducer is called a vibration sensor.

Vibration monitoring differs from vibration control also in that when observing changes in a vibration signal, it is not necessary to carry out only quantitative measurements of parameters with a minimum total error. It is possible to carry out measurements of vibration characteristics and with a constant system error, provided that the coefficient of conversion of the vibration parameter into the controlled electrical parameter is constant over time. Therefore, when monitoring vibration measurements, it is possible to control the development in time of vibration components having frequencies up to 90–95% of the resonant frequency of the accelerometer.

If the upper limited frequency of the piezoaccelerometer is determined by its own resonance or the resonance of the sensor, taking into account the rigidity of attachment to the object, and its value is usually in the range of 1–100 kHz, then the lower limited frequency of the measured vibration depends on the electrically conductive properties of the piezoceramic element. It can be determined not only by the leakage resistance of the piezoelectric element, but also by leaks in the charge transfer circuit to the input of the matching amplifier in the measuring device. The typical lower limited frequency of a piezoaccelerometer is 0.5 Hz, but piezoaccelerometers with significantly lower limited frequencies can be manufactured to solve special problems. Typical accelerometers are most often combined with matching amplifiers in one package. There are also standards for such accelerometers, including those with power supply of the matching amplifier through the signal circuit.

Dynamic range and linearity are also important characteristics of a vibration sensor, as a such used electronic devices. A typical measurement range for the absolute vibration displacement of machines and equipment is from one to a thousand microns, that is, 60 dB. But if a vibration acceleration transducer is used, it is necessary to take into account the fact that the signal from the transducer (at the same value of vibration displacement) at the lower frequency of the measured range f_{\min} is $n = (f_{\max}/f_{\min})^2$ times less than the signal at the upper frequency f_{\max} , and this value must be added to the dynamic range of the meter. When measuring vibration displacement in the range of 2–1000 Hz, this addition to the dynamic range of the device is a very large value – 108 dB, and it is necessary to take measures to eliminate this contradiction.

3 Results and Discussion

The main goal of the project is to develop a system for monitoring vibroacoustic parameters of the working area.

The main functions of the system are constant measurement of noise and vibration parameters of the working area, analysis of measured parameters, signalling of exceeding the allowed range of measuring parameters of the working area, and display of measured data in decibels.

Based on the review and analysis of technical solutions, the main functions of the system were proposed a block diagram of the system, which is shown in Fig. 1.

The diagram shows the following:

- M1–M4: microphones (noise sensors)
- V1–V4: accelerometers (vibration sensors)
- A: amplifier
- MCU: microcontroller
- BTM: Bluetooth module for receiving a signal on the main board from measuring channels
- BT: Bluetooth module connected to the sensor to transmit a signal to the main board
- LCD: module for displaying the result

Figure 1 shows that the system has eight measuring channels: Four for vibration measurement and four for noise measurement. Each measuring channel consists of the sensor itself (M1–M4, microphone for noise measurement; V1–V4, accelerometer for vibration). The data obtained from the sensors are amplified by the operational amplifier A, such amplifiers are 8, for each of the measuring channels. After amplification, the analog signal is converted into discrete code using a single-channel ADC. The digital signal after the ADC is transmitted to the main board with a microcontroller. The board receives data from all eight measuring channels. Collecting the values obtained from the sensors, the main board uses software processing to analyze the data and transmits them to the LCD display, which in turn displays them.

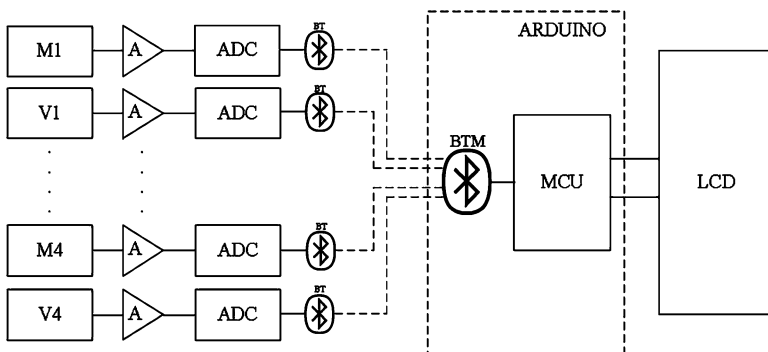


Fig. 1 Block diagram of the MVP system

A microphone is used as a sensor for each noise measurement channel. The analog signal from the microphone is amplified by an amplifier and converted into digital code by an ADC. Then the digital signal is transmitted to the main board with a microcontroller.

Similarly, an accelerometer is used for each parameter measurement channel. On each measuring channel, both for vibration parameters and for noise parameters, the analog signal received from the sensor is amplified, sampled, and transmitted to the microcontroller.

The measuring channels of the designed system transmit the measured data via a wireless connection, which simplifies their use and placement in any place in the work area and allows you to cover a larger area of the measured area. Analogs are portable devices that measure certain small planes of the working area.

As for the principles of operation, despite the large number of devices, the principle of their operation remains unchanged. The principle of measuring noise parameters is based on the received acoustic waves with the subsequent conversion of their energy by means of the most various technologies in electric potential which is directly proportional to size of a signal. As for the principle of measuring vibration parameters, vibration sensors are used, which perceive mechanical vibrations, which are also converted into the corresponding electric potential by means of various technologies.

4 Conclusion

The system of monitoring of vibroacoustic parameters of the working zone was proposed in the work, which performs the following functions: measurement of vibroacoustic parameters (vibration and noise parameters) of the working zone, analysis of measured values of vibroacoustic parameters, alarm of the user about exceeding of the allowed range of parameters of vibration and noise of a working zone, saving the measured data for a specified period of time, and display of measured data.

References

- Barkov, A. V., Barkova, N. A., & Azovtsev, A. Y. (2000). *Monitoring and diagnostics of rotary machines by vibration*. SPbSMTU.
- Cheremisinoff, N. P. (1996). *Noise control in industry: A practical guide*. Elsevier.
- De Silva, C. W. (Ed.). (2005). *Vibration and shock handbook*. CRC Press.
- <https://gtest.com.ua/benetech-gm1352.html>. Accessed on 13 Apr 2021.
- <https://infocom-m.ru/uk/inzhenernye-sistemy/air-and-structural-noise.html>. Accessed on 13 Apr 2021.
- https://pragmatic.com.ua/pce_428. Accessed on 13 Apr 2021.

A New Encryption Key Generator Design with True Random Bits



Taha Etem and Turgay Kaya

Contents

| | | |
|-----|--|-----|
| 1 | Introduction | 250 |
| 2 | ESC-50 Sound Dataset | 251 |
| 3 | Statistical Analysis | 252 |
| 3.1 | Statistical NIST Tests | 252 |
| 3.2 | Entropy Test | 253 |
| 3.3 | Number of Pixel Change Rate (NPCR) and Unified Average Changing Intensity (UACI) | 253 |
| 4 | Random Number Generator Design | 253 |
| 5 | Results and Discussion | 254 |
| 6 | Conclusions | 256 |
| | References | 257 |

Nomenclature

| | |
|------|--|
| NIST | National Institute of Standards and Technology |
| NPCR | Number of pixel change rate |
| RNG | Random number generator |
| UACI | Unified average changing intensity |

T. Etem (✉)

Computer Engineering, Cankiri Karatekin University, Cankiri, Turkiye

T. Kaya

Firat University, Electrical-Electronics Engineering, Elazig, Turkiye

e-mail: tkaya@firat.edu.tr

1 Introduction

With the development of technology, confidentiality and security have gained importance in data transfer. In addition to text, other multimedia data like sound and picture are increasing in digital media (Raghuvanshi et al., 2021). Since the image is widely used in our daily life, it has become very important to ensure its safety. For this reason, a wide variety of cryptography methods have been developed (Garcia-Bosque et al., 2017; Khan et al., 2020; Yakut et al., 2020). Cryptography is a branch of science that deals with techniques and conjecture of encryption and decryption. There are two common types of cryptography: classical method and modern method. With the increase in the power and capacity of computers, information can be transmitted quickly by encrypting (Satria et al., 2018). Testing the reliability of the encryption algorithms is also an important issue (Gong et al., 2021). As a coding science, cryptology is divided into two subdisciplines as cryptography and cryptanalysis (Etem & Kaya, 2020a; Safitri et al., 2013). Cryptography is a science used to transform data that is visible to everyone into imperceptible form. Cryptanalysis is about the analysis stages of an encrypted text and covers the methods that can be used to make the text clear (Özkaynak, 2018).

In Fig. 1, classification of cryptographic methods is represented. Symmetric key and asymmetric key encryptions that are modern cryptographic techniques are two main structures for encryption operations. The distribution of the key used here can be send through a private channel or a hidden channel as it is also used in data transmission. Since the encryption key is the basis of cryptographic applications, its selection has great importance (Etem & Kaya, 2020c; Sun et al., 2020).

Encryption keys can be generated or selected in different ways and its secrecy is the most important part of the process (Fang et al., 2021; Özkaynak et al., 2011). In order to meet this need, there are many designs of random number generators in the literature (Benssalah et al., 2014; Tuncer, 2015; Avaroglu, 2017; Kaya & Arslan Tuncer, 2019). Usability has been increased with each new random number generator design. In addition, random number generators have different usage areas such as gambling and statistical applications (Petchlert & Hasegawa, 2014). Random number generators are grouped under two main subjects as pseudo-random and true random number generators. Hybrid random number generators containing both of these components were subsequently derived (Tuna et al., 2019; Tuna, 2020; Saravanan & Sivabalakrishnan, 2021).

Hybrid systems include advantages of true and pseudo-random number generators (Yakut et al., 2019). While true random number generators are generally based on measurable data and circuits, pseudo-random number generators are generally obtained by algorithms that include mathematical operations (Avaroğlu, 2020; Coskun et al., 2019; Alçın et al., 2021). The pseudo-random number generators can be obtained with different algorithms. Their frequent usage in encryption applications is due to the fact that they are created without an external hardware and they allow high-speed operations. There are many pseudo-random number generators with different designs in the literature (Bhattacharjee et al., 2017).

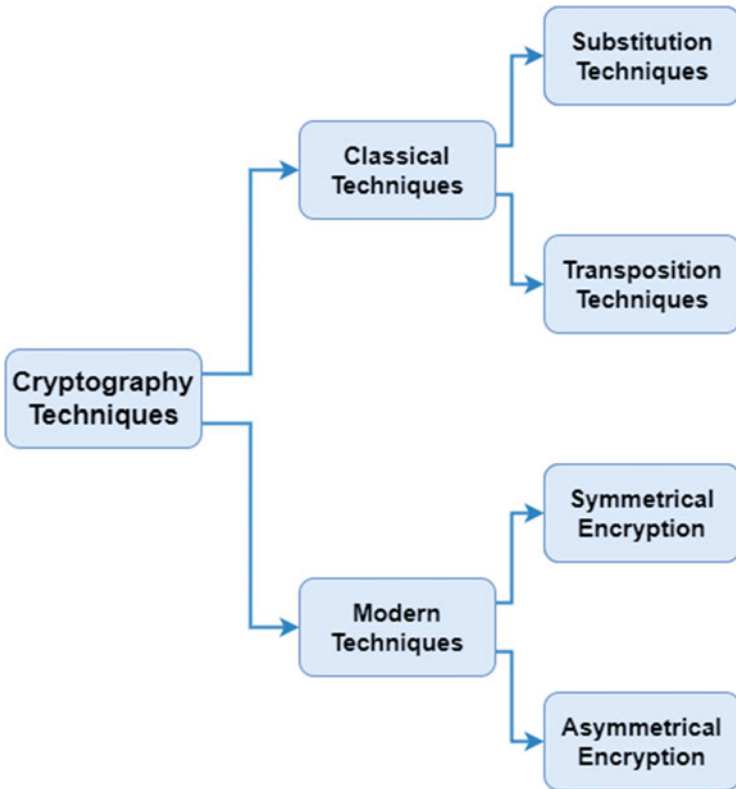


Fig. 1 Classification of cryptographic techniques

2 ESC-50 Sound Dataset

ESC-50 sound dataset consists of a variety of 50 sound class. All datasets are constructed from recordings which are publicly available. All classes are labeled in the dataset. Each sound sample has a unified format: 44.1 kHz sampling frequency, 192 Kbit/s compression rate, and 5 s long recordings (Piczak, 2015).

In ESC-50 dataset, there are 2000 labeled sounds of environmental recordings. 40 sound clips per class and total 50 classes are available in dataset. These 50 classes also have 5 major categories below:

- Urban area exterior noises
- Domestic interior sounds
- Nonspeech human sounds
- Water sounds and natural soundscapes
- Animal sounds

A sample of recordings is shown in Fig. 2.

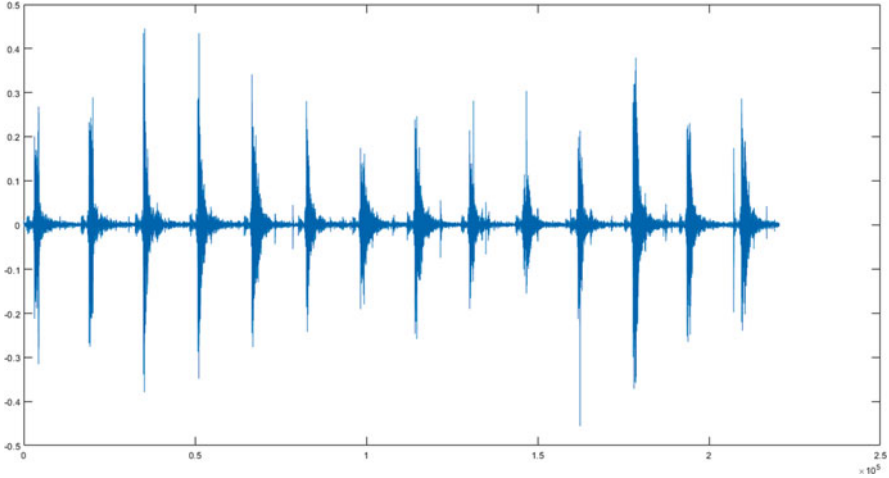


Fig. 2 Sample of sound recording dataset

In spite of the fact that one of the possible deficiencies of the environmental sound dataset is having limited number of sound clips containing in every class. This situation is generally related with sound-classifying systems. In our work, it is enough to have 2000 labeled sound clips.

3 Statistical Analysis

3.1 Statistical NIST Tests

One of the most popular tests for random numbers is the NIST-800-22 tests. The NIST-800-22 tests are internationally accepted tests in the literature (Elmanfaloty & Abou-Bakr, 2019). At least one million sample bit of random number generator is required for the NIST-800-22 tests. The NIST-800-22 tests are subjected to be complex and detailed for bit streams. In terms of reliability, the NIST-800-22 tests are considered as the most successful tests for random numbers. The NIST-800-22 tests consist of 15 different tests. In order to the bit stream subjected to the NIST-800-22 tests to be considered as accomplished, it should pass all of these tests in triumph. In the NIST-800-22 test, the results are evaluated according to the changeable P value. If the P value is accepted as 0.001 as a condition, the P value must be in the range $1 < P \text{ value} < 0.001$ for the succession (Kaya, 2019).

3.2 Entropy Test

Entropy is a type of measure in system complexity. It reflects randomness value of designed system. Its value can be calculated by Eq. (1).

$$H_m = \sum_{i=0}^n p(m_i) \log \frac{1}{p(m_i)} \quad (1)$$

Note that the equation is related with number of bits used in work. For the purpose of getting a meaningful result, generated random bits are converted in to a 8-bit matrix. So, ideal entropy value should be 8 in the calculation (Chen et al., 2020).

3.3 Number of Pixel Change Rate (NPCR) and Unified Average Changing Intensity (UACI)

Cryptographic system should be robust against information leakage attacks. Number of pixel change rate (NPCR) and unified average changing intensity (UACI) values are important metric of determining key security in encryption. They show strength of the block encryption ciphers. Differential key attack resistance of the modern iterative cryptography techniques can be evaluated. NPCR and UACI values can be calculated as below (Wu et al., 2011):

$$\Delta(i,j) = \begin{cases} 0, & \text{if } P(i,j) = T(i,j) \\ 1, & \text{if } P(i,j) \neq T(i,j) \end{cases} \quad (2)$$

$$\text{NPCR} : N(P, T) = \sum_{i,j} \frac{\Delta(i,j)}{T} \times 100 \quad (3)$$

$$\text{UACI} : U(P, T) = \sum_{i,j} \frac{|P(i,j) - T(i,j)|}{255 \times MN} \times 100 \quad (4)$$

4 Random Number Generator Design

In our design, a new random number generator is utilized as a key generator for encryption. Classical or modern cryptography systems can use this system as a key generator. The flow chart of our system is given in Fig. 3.

In the field of cryptology, the most important parameter is the encryption key (Etem & Kaya, 2020b). Generating, distributing, and hiding this key is one of the

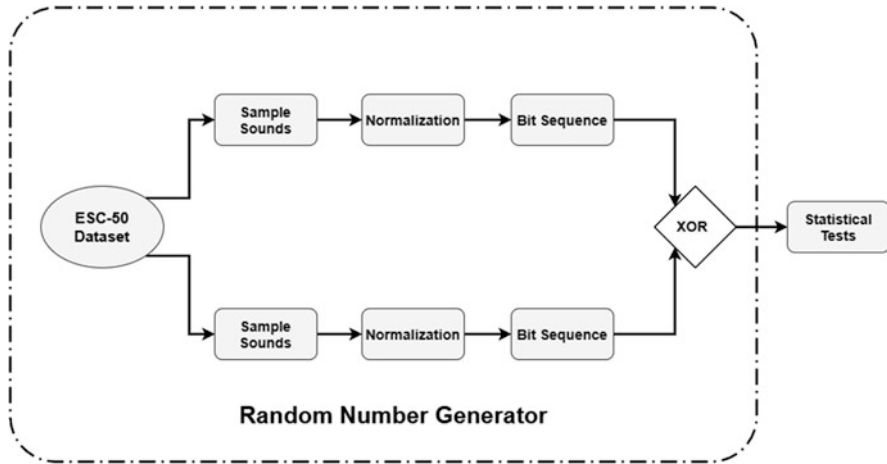


Fig. 3 Flow chart of the random number generation

biggest problems. The complexity parameters included in random number generators and their sensitivity in application process are important for the encryption. The randomness of the generators in encryption operations is closely related with the security of cryptologic studies. Random number generator designs, which have been a popular research subject in the recent years, have increased their place in the literature. The random numbers obtained are determined whether they are suitable for use in encryption applications after passing a series of internationally valid tests such as NIST-800-22.

If the key of the one encrypted data is accessed, all of the key or a part of the key can be seized as a result of the cryptanalysis. This means that all or a part of the data is captured.

5 Results and Discussion

Generated random numbers should be proved by NIST tests. In Table 1, P values of the random number generator are shown:

Generated bits are converted into 8-bit decimal values (Table 2) and they are positioned in 350×350 matrix. It is shown in Fig. 4. 8-bit form demonstrates a more meaningful result in some tests. Histogram of an image shows that how are the pixel distributions in the image. If the distributions are generally close to each other in the histogram, the resulting RNG outputs are expected to be cryptographically appropriate. Histogram results of random number generator are shown in Figs. 5 and 6.

UACI, NPCR, and ENT test results of our design are shown in Table 3. All of the test results and ideal values are given.

Table 1 NIST 800-22 test results of random number generator

| Test numbers | NIST tests | P values |
|--------------|--|-------------|
| 1 | Frequency monobit test | 0.761 |
| 2 | Frequency test within a block | 0.145 |
| 3 | Runs test | 0.586 |
| 4 | Longest run of ones in a block test | 0.387 |
| 5 | Binary matrix rank test | 0.833 |
| 6 | Discrete Fourier transform test | 0.114 |
| 7 | Non-overlapping template matching test | 0.111 |
| 8 | Overlapping template matching test | 0.690 |
| 9 | Universal test | 0.249 |
| 10 | Linear complexity test | 0.071 |
| 11 | Serial tests | 0.512/0.503 |
| 12 | Approximate entropy test | 0.319 |
| 13 | Cumulative sums test | 0.971 |
| 14 | Random excursions test (average) | 0.514 |
| 15 | Random excursions variant test (average) | 0.498 |

Table 2 Average values of random number sums

| Test | Results | Ideal values |
|------------|----------|--------------|
| 8-bit form | 127.3690 | 127.5 |
| 2-bit form | 0.5002 | 0.5 |

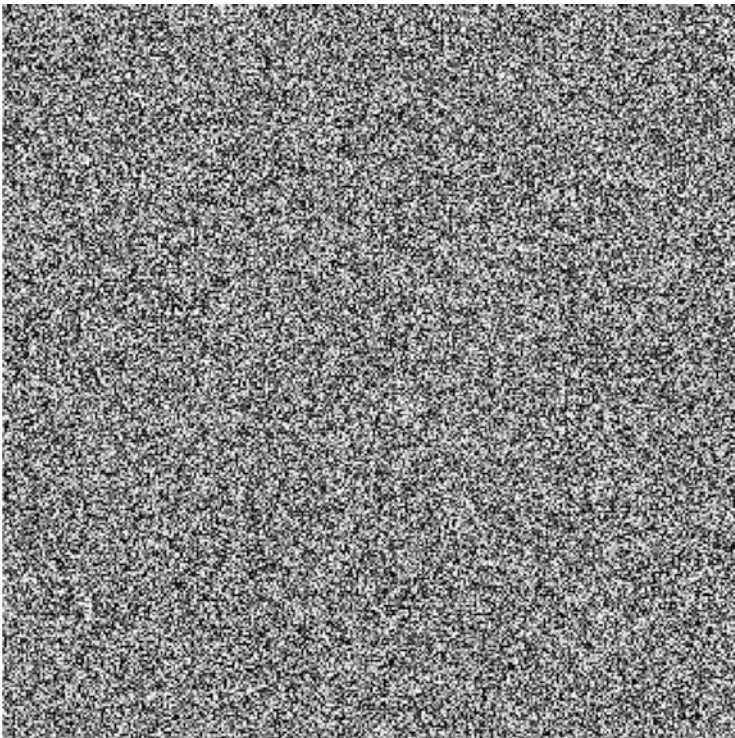


Fig. 4 8-bit matrix outlook of RNG

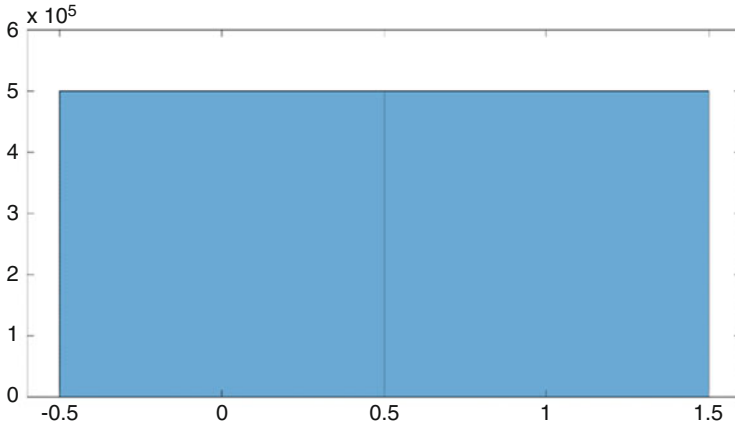


Fig. 5 Random number generator histogram

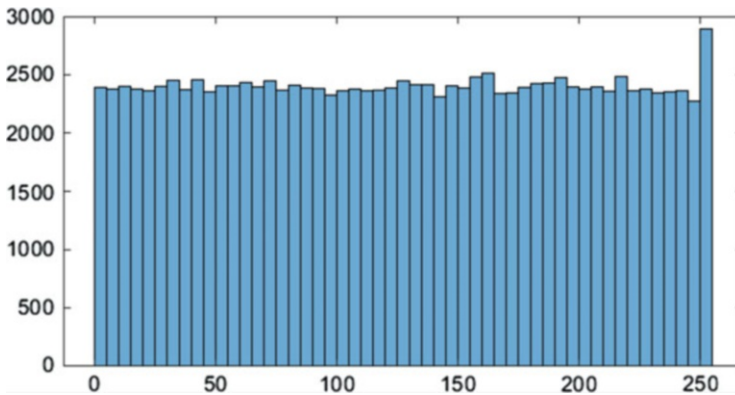


Fig. 6 8-bit matrix histogram

Table 3 ENT, UACI, and NPCR results

| Test | Results | Ideal values |
|----------|---------|--------------|
| Ent test | 7.9986 | 8 |
| NPCR | %99.609 | %100 |
| UACI | %33.463 | %33 |

6 Conclusions

In this study, a true random number generator based on ESC-50 sound dataset has been designed to be used in encryption applications. The obtained random number generator design was evaluated with the statistical NIST 800-22 tests. XOR post-processing applied to the designed system output, it has successfully passed all tests.

It was proved that random values were obtained. Encryption can be performed by using the obtained random numbers as a cryptologic key with different algorithms.

Entropy test, UACI, and NPCR values are close to the ideal values. Average values of sums are also close to the ideal values. Histogram distributions are fairly balanced. It has been shown that our study can be used in encryption applications with many different tests.

Acknowledgments This study has been produced from the doctoral thesis of Taha Etem.

References

- Alçın, M., Tuna, M., Erdogmus, P., & Koyuncu, İ. (2021). FPGA-based dual core TRNG design using Ring and Runge-Kutta-Butcher based on chaotic oscillator. *Chaos Theory and Applications*, 20–28. <https://doi.org/10.51537/chaos.783548>
- Avaroglu, E. (2017). Pseudorandom number generator based on Arnold cat map and statistical analysis. *Turkish Journal of Electrical Engineering and Computer Sciences*, 25(1), 633–643. <https://doi.org/10.3906/elk-1507-253>
- Avaroğlu, E. (2020). The implementation of ring oscillator based PUF designs in Field Programmable Gate Arrays using of different challenge. *Physica A: Statistical Mechanics and its Applications*, 546, 124291. <https://doi.org/10.1016/j.physa.2020.124291>
- Benssalah, M., Djeddou, M., & Drouiche, K. (2014, January). *Security enhancement of the authenticated RFID* (pp. 1285–1296). <https://doi.org/10.1002/sec>
- Bhattacharjee, K., Paul, D., & Das, S. (2017). Pseudo-random number generation using a 3-state cellular automaton. *International Journal of Modern Physics C*, 28(06), 1750078.
- Chen, X., Qian, S., Yu, F., Zhang, Z., Shen, H., Huang, Y., Cai, S., Deng, Z., Li, Y., & Du, S. (2020). Pseudorandom number generator based on three kinds of four-wing memristive hyperchaotic system and its application in image encryption. *Complexity*, 2020, 1–17. <https://doi.org/10.1155/2020/8274685>
- Coskun, S., Pehlivan, İ., Akgul, A., & Gurevin, B. (2019). A new computer-controlled platform for ADC-based true random number generator and its applications. *Turkish Journal of Electrical Engineering & Computer Sciences*, 847–860. <https://doi.org/10.3906/elk-1806-167>
- Elmanfaloty, R. A., & Abou-Bakr, E. (2019). Random property enhancement of a 1D chaotic PRNG with finite precision implementation. *Chaos, Solitons and Fractals*, 118, 134–144. <https://doi.org/10.1016/j.chaos.2018.11.019>
- Etem, T., & Kaya, T. (2020a). A novel true random bit generator design for image encryption. *Physica A: Statistical Mechanics and its Applications*, 540, 122750. <https://doi.org/10.1016/j.physa.2019.122750>
- Etem, T., & Kaya, T. (2020b). Self-generated encryption model of acoustics. *Applied Acoustics*, 170, 107481. <https://doi.org/10.1016/j.apacoust.2020.107481>
- Etem, T., & Kaya, T. (2020c). Trivium-linear congruential generator based bit generation for image encryption. *Firat Üniversitesi Mühendislik Bilim Dergisi*, 32(1), 287–294.
- Fang, P., Liu, H., Wu, C., & Liu, M. (2021). A secure chaotic block image encryption algorithm using generative adversarial networks and DNA sequence coding. *Mathematical Problems in Engineering*, 2021, 1–26. <https://doi.org/10.1155/2021/6691547>
- Garcia-Bosque, M., Pérez, A., Sánchez-Azqueta, C., & Celma, S. (2017). Application of a MEMS-based TRNG in a chaotic stream cipher. *Sensors (Switzerland)*, 17(3). <https://doi.org/10.3390/s17030646>
- Gong, B., Zhang, H., & Wan, L. (2021). Generating chaotic series via encryption method in fractional-order chua systems. *Discrete Dynamics in Nature and Society*, 2021(2), 1–9.

- Kaya, T. (2019). A true random number generator based on a Chua and RO-PUF: Design, implementation and statistical analysis. *Analog Integrated Circuits and Signal Processing*, 2. <https://doi.org/10.1007/s10470-019-01474-2>
- Kaya, D., & Arslan Tuncer, S. (2019). Generating random numbers from biological signals in labview environment and statistical analysis. *Traitement Du Signal*, 36(4), 303–310. <https://doi.org/10.18280/ts.360402>
- Khan, M., Masood, F., & Alghafis, A. (2020). Secure image encryption scheme based on fractals key with Fibonacci series and discrete dynamical system. *Neural Computing and Applications*, 32(15), 11837–11857. <https://doi.org/10.1007/s00521-019-04667-y>
- Özkaynak, F. (2018). Brief review on application of nonlinear dynamics in image encryption. *Nonlinear Dynamics*, 92(2), 305–313. <https://doi.org/10.1007/s11071-018-4056-x>
- Özkaynak, F., Özer, A. B., & Yavuz, S. (2011). Kaos Tabanlı Yeni Bir Blok Şifreleme Algoritması. In *IV.AĞ VE BİLGİ GÜVENLİĞİ ULUSAL SEMPOZYUMU* (pp. 1–6).
- Petchlert, B., & Hasegawa, H. (2014). Using a low-cost electroencephalogram (EEG) directly as random number generator. In *Proceedings – 2014 IIAI 3rd international conference on advanced applied informatics, IIAI-AAI 2014* (pp. 470–474). <https://doi.org/10.1109/IIAI-AAI.2014.100>
- Piczak, K. J. (2015). ESC: Dataset for environmental sound classification. In *MM 2015 – Proceedings of the 2015 ACM multimedia conference* (pp. 1015–1018). <https://doi.org/10.1145/2733373.2806390>
- Raghuvanshi, K. K., Kumar, S., Kumar, S., & Kumar, S. (2021). Development of new encryption system using Brownian motion based diffusion. *Multimedia Tools and Applications*. <https://doi.org/10.1007/s11042-021-10665-x>
- Safitri, C., Ali, H. S., & Ibrahim, J. B. (2013). A study: Cryptology techniques and methodologies. *International Journal of Science and Research (IJSR)*, 2(12), 352–357.
- Saravanan, S., & Sivabalakrishnan, M. (2021). A hybrid chaotic map with coefficient improved whale optimization-based parameter tuning for enhanced image encryption. *Soft Computing*, 0123456789. <https://doi.org/10.1007/s00500-020-05528-w>
- Satria, Y., Gabe Rizky, P. H., & Suryadi, M. T. (2018). Digital sound encryption with logistic map and number theoretic transform. *Journal of Physics: Conference Series*, 974(1). <https://doi.org/10.1088/1742-6596/974/1/012016>
- Sun, J., Li, C., Lu, T., Akgul, A., & Min, F. (2020, July). A memristive chaotic system with hypermultistability and its application in image encryption. *IEEE Access*. <https://doi.org/10.1109/ACCESS.2020.3012455>
- Tuna, M. (2020). A novel secure chaos-based pseudo random number generator based on ANN-based chaotic and ring oscillator: Design and its FPGA implementation. *Analog Integrated Circuits and Signal Processing*, 105(2), 167–181. <https://doi.org/10.1007/s10470-020-01703-z>
- Tuna, M., Karthikeyan, A., Rajagopal, K., Alcin, M., & Koyuncu, İ. (2019). Hyperjerk multiscroll oscillators with megastability: Analysis, FPGA implementation and a novel ANN-ring-based True Random Number Generator. *AEU – International Journal of Electronics and Communications*, 112, 152941. <https://doi.org/10.1016/j.aeue.2019.152941>
- Tuncer, T. (2015). Implementation of duplicate TRNG on FPGA by using two different randomness source. *Elektronika Ir Elektrotehnika*, 21(4), 35–39. <https://doi.org/10.5755/j01.eee.21.4.12779>
- Wu, Y., Noonan, J. P., & Aгаian, S. (2011, April). NPCR and UACI randomness tests for image encryption. *Journal of Selected Areas in Telecommunications (JSAT)*, 31–38. <http://www.cyberjournals.com/Papers/Apr2011/05.pdf>
- Yakut, S., Tuncer, T., & Ozer, A. B. (2019). Secure and efficient hybrid random number generator based on sponge constructions for cryptographic applications. *Elektronika Ir Elektrotehnika*, 25(4), 40–46. <https://doi.org/10.5755/j01.eie.25.4.23969>
- Yakut, S., Tuncer, T., & Özer, A. B. (2020). A new secure and efficient approach for TRNG and its post-processing algorithms. *Journal of Circuits, Systems and Computers*. <https://doi.org/10.1142/S0218126620502448>

A Case Study on Investigating Probabilistic Characteristics of Wind Speed Data for Green Airport



Ali Tatli, Ahmet Esat Suzer, Tansu Filik, and Tahir Hikmet Karakoc

Contents

| | | |
|-----|--|-----|
| 1 | Introduction | 260 |
| 2 | Method | 261 |
| 2.1 | Description of Wind Data Source and International Airport | 261 |
| 2.2 | Statistical Preliminaries Background on Parameter Estimation | 261 |
| 2.3 | Graphical Method | 262 |
| 2.4 | Empirical Method | 263 |
| 2.5 | Maximum-Likelihood Method | 263 |
| 2.6 | Extrapolation | 264 |
| 2.7 | Wind Power Density | 264 |
| 2.8 | Statistical Fitness Tests | 264 |
| 3 | Results and Discussion | 265 |
| 4 | Conclusion | 270 |
| | References | 271 |

A. Tatli (✉)

Ali Cavit Celebioglu School of Civil Aviation, Erzincan Binali Yildirim University, Erzincan, Turkiye

e-mail: ali.tatli@erzincan.edu.tr

A. E. Suzer

STM Defence Technologies Engineering Inc., Ankara, Turkiye

T. Filik

Faculty of Engineering, Eskisehir Technical University, Eskisehir, Turkiye

T. H. Karakoc

Faculty of Aeronautics and Astronautics, Eskisehir Technical University, Eskisehir, Turkiye

Istanbul Ticaret University, Information Technology Research and Application Center, Istanbul, Turkiye

1 Introduction

As an alternative solution to conventional energy sources, renewable energy sources have received more and more attention to overcome economic and environmental concerns (Bagci et al., 2021). In parallel to this considerable attention, they have seen unprecedented growth over the past years (Mahesh, 2021). There are various renewable energy sources that offer benefits to supply the increasing energy need and to negatively reduce effects on the environment, which can be addressed as wind, solar, biofuel, tidal, and wave energy (El Khchine & Sriti, 2021).

Wind energy is a major renewable energy source that continuously has grown in the energy sector (Wang et al., 2021). Over the past two decades, in particular, it has widely been utilized in satisfying the energy demand of countries (Bagci et al., 2021). The installed wind power reached the level of 651 GW by the end of 2019 and it has continued to increase in the world year by year (Suzer et al., 2021).

Accurate determination of statistical characteristics of wind distribution offers significant benefits to crucial points, including the wind behavior, wind regimes, wind speed, and wind capacity of a particular location (Bagci et al., 2021). However, the wind is uncertain, intermittent, and random variable owing to predominant factors such as local topography, surface roughness, and weather patterns (Chen et al., 2021). This fluctuating nature leads to various discrepancies such as some uncertainties, modelling errors, and significant computation errors in practice (Bagci et al., 2021). Statistical distribution functions are widely employed to model wind distribution more efficiently by minimizing theoretical computation errors (Bagci et al., 2021; Saeed et al., 2021). Numerous statistical probability distribution functions have been presented in the literature to reflect the statistical characteristics of wind distribution for a given site around the world. Each distribution function differs from degrees of accuracy, complexity, and fitness (Wadi & Elmasry, 2021).

In the research literature, the Weibull distribution, proposed by Waloddi Weibull in the 1930s, is the best-known distribution fitting well to historical wind data. Furthermore, the Weibull distribution has significant advantages of adaptability, flexibility, and simplicity (Tonsie Djiela et al., 2020). It has been used for describing the wind profile and characteristics by many researchers (Suzer et al., 2021; Wang et al., 2021; Kim et al., 2021; Boopathi et al., 2021; Wadi & Elmasry, 2021).

A number of methods, consisting of graphical, equivalent energy method, empirical, maximum-likelihood, modified maximum-likelihood, power density method, and methods of moment, are developed to estimate precisely Weibull parameters, that is, shape and scale parameters (Deep et al., 2020; Costa Rocha et al., 2012; Deaves & Lines, 1997; Justus & Mikhail, 1976). Graphical, empirical, maximum-likelihood, power density, and method of moment can be considered to be the most widely used among all methods.

Practical wind applications can need the vertical wind speed to be determined in order to model and evaluate the wind characteristics of the site (Đurišić & Mikulović, 2012). There is a mathematical relationship between wind speed and vertical height, which is referred to as extrapolation (Gualtieri & Secci, 2012). The

basic idea behind extrapolation is to use wind data from available measurement height by applying the power-law transformation to make a synthetic set of measurement data corresponding to the desired height (Đurišić & Mikulović, 2012; Gualtieri & Secci, 2012).

The primary purpose of this research is to present comparatively wind characteristics and profile of Hasan Polatkan Airport with an elevation of 787 m at various heights from the ground level, which is situated in the northwest of Eskişehir, Turkey. Wind speed at each height, composed of 10 m, 20 m, 30 m, 40 m, and 50 m, is calculated by applying the power-law equation to the wind speed. For this purpose, the rich wind dataset taken from the Meteorological Station Service is measured on an hourly basis during a period between January 01, 2010 and December 31, 2020. After the wind characteristics at each height are estimated based on widely used graphical, empirical, and maximum-likelihood estimation methods, several statistical tools are employed to make a fair comparison among the methods that help estimate the Weibull parameters. Furthermore, in the last step of the study, wind power density based on each height is computed elaborately using estimation methods and the results are compared to those of the actual wind data.

2 Method

2.1 *Description of Wind Data Source and International Airport*

Eskişehir is located in the northwestern part of Turkey. Hasan Polatkan Airport with an elevation of 787 m is situated within the border of Eskişehir. It is approximately 5 km from Eskişehir. It serves for different purposes as international and domestic flights. Its geographical coordinates are 39.813256 latitudes and 30.528400 longitudes. The code that is assigned by ICAO and IATA is LTBY and AOE, respectively.

In this study, wind speed data, taken from the Turkish State Meteorological Service, are sampled hourly for a long period between January 01, 2010 and December 31, 2020 at a height of 10 m above the ground level. The rich wind data for a period of 11 years consists of a total of over 96,354 measurements.

2.2 *Statistical Preliminaries Background on Parameter Estimation*

The wind is affected depending on a variety of factors including weather, surface roughness, terrain topography, and surface topography. However, this case can be statistically represented using a distribution function. As mentioned earlier, for this

purpose in the literature, Weibull distribution is often used in describing and modelling the wind speed distribution at a specific area.

The probability density function (PDF) for the Weibull distribution with shape and scale parameters can be formulated as in Eq. (1) in which $f(\vartheta)$ symbolizes the probability of wind velocity in the unit of m. s^{-1} , η denotes shape parameter, and μ represents scale parameter (Wang et al., 2021). Furthermore, the related cumulative density function (CDF) can be identified as in Eq. (2) (Wadi & Elmasry, 2021).

$$f(\vartheta) = \left(\frac{\eta}{\mu}\right) \left(\frac{\vartheta}{\mu}\right)^{\eta-1} \exp\left(-\left(\frac{\vartheta}{\mu}\right)^{\eta}\right) \quad (1)$$

$$F(\vartheta) = 1 - \exp\left(-\left(\frac{\vartheta}{\mu}\right)^{\eta}\right) \quad (2)$$

where $F(\vartheta)$ defines the cumulative distribution function for wind speed.

In the literature, there exist various alternative solution methods to calculate the Weibull parameters, which can be addressed as graphical, moment method, maximum-likelihood, alternative maximum-likelihood, modified maximum-likelihood, power density method, empirical, and equivalent energy method. However, in the study, several popular estimation methods, graphical, maximum-likelihood, and empirical, are employed to compute the scale and shape parameters at different heights. These estimation methods proposed to determine the Weibull parameters are presented for short in this section.

2.3 Graphical Method

Shape and scale parameters are estimated based on the cumulative distribution function of the Weibull and logarithm function. Applying the logarithm transform to the cumulative distribution function given in Eq. (2), it can be simply written as in Eq. (3).

$$\ln(-\ln(1 - F(\vartheta))) = \eta \ln(\vartheta) - \eta \ln(\mu) \quad (3)$$

In this case, Eq. (3) can be considered as in $mx + c$, the slope corresponding to the straight-line equals to shape parameter η and the intersection with y-ordinate of the line gives the scale parameter μ . The shape and scale parameters could be handled as the form in Eqs. (4) and (5).

$$\eta = m \quad (4)$$

$$\mu = \exp\left(-\frac{c}{m}\right) \quad (5)$$

2.4 Empirical Method

In this method, the shape and scale parameters are determined as follows:

$$\eta = \left(\frac{\sigma}{\bar{\vartheta}} \right)^{-1.086} \tag{6}$$

$$\mu = \frac{\bar{\vartheta}}{\Gamma\left(1 + \frac{1}{\eta}\right)} \tag{7}$$

where $\bar{\vartheta}$ denotes average wind speed in the unit of $m. s^{-1}$, σ depicts standard deviation in the unit of $m. s^{-1}$, and Γ implies well-known gamma function. It can be formulated as follows:

$$\Gamma(x) = \int_0^{\infty} t^{x-1} \exp(-t) dt \tag{8}$$

2.5 Maximum-Likelihood Method

In this method, the shape and scale parameters could be defined as follows:

$$\eta = \left(\frac{\sum_{j=1}^N \vartheta_j^\eta \ln(\vartheta_j)}{\sum_{j=1}^N \vartheta_j^\eta} - \frac{\sum_{j=1}^N \ln(\vartheta_j)}{N} \right)^{-1} \tag{9}$$

$$\mu = \left(\frac{\sum_{j=1}^N \vartheta_j^\eta}{N} \right)^{\frac{1}{\eta}} \tag{10}$$

where N depicts the number of wind speed data.

2.6 Extrapolation

In general, the meteorological wind data of a region are measured at 10 m heights from the ground level. However, it can be considered that there is a mathematical correlation between wind speed and height. Wind speed at higher altitudes can be simply obtained by applying the power-law equation to the wind speed data at 10 m height (Bañuelos-Ruedas et al., 2010; Ohunakin et al., 2011). The power-law, first proposed by Hellman, can be formulated as follows (Đurišić & Mikulović, 2012; Jung & Schindler, 2021):

$$\vartheta_h = \vartheta_r \left(\frac{\beta_h}{\beta_r} \right)^\alpha \quad (11)$$

where ϑ_h symbolizes the wind speed at a certain height β_h , ϑ_r denotes the wind speed at the reference height β_r , and α represents the surface roughness coefficient of the site.

2.7 Wind Power Density

Wind power density (W_{PD}) is essential to evaluate the wind potential and wind capacity at a location. W_{PD} can be formulated using Eqs. (12) and (13).

$$P(\vartheta) = \frac{1}{2} \rho A \vartheta^3 \quad (12)$$

$$W_{PD} = \frac{P(\vartheta)}{A} = \frac{1}{2} \rho \vartheta^3 \quad (13)$$

where ρ denotes the air intensity in the unit of $\text{kg} \cdot \text{m}^{-3}$, ϑ represents the wind speed in the unit of m , A refers to the swept area of the rotor blade in the unit of m^2 , $P(\vartheta)$ defines wind power in the unit of W , and W_{PD} expresses wind power density in the unit of $W \cdot m^{-2}$.

2.8 Statistical Fitness Tests

A method's performance can be evaluated based on basic statistical analysis tools. In the literature, there are many statistical tools such as root mean square error (RMSE), mean absolute error (MAE), mean bias error (MBE), R -squared (R^2), mean absolute percent error (MAPE), and Chi-squared (X^2). Two basic statistical indicators, RMSE and R^2 , used in this study could be formulated as follows:

$$RMSE = \sqrt{\frac{1}{N} \sum_{m=1}^N (z_m - \hat{z}_m)^2} \tag{14}$$

$$R^2 = 1 - \frac{\sum_{m=1}^N (z_m - \hat{z}_m)^2}{\sum_{m=1}^N (z_m - \bar{z})^2} \tag{15}$$

where N is the number of wind speed data, \bar{z} is the average wind speed, z_m is the measured wind speed, \hat{z}_m is the estimated wind speed, and $| |$ denotes absolute value operation.

3 Results and Discussion

This study strives to evaluate comparatively wind characteristics and regime of Hasan Polatkan Airport based on various heights above the ground level, which is situated in the northwest of Eskişehir, Turkey. Wind speed at each height, including 10 m, 20 m, 30 m, 40 m, and 50 m, is determined by applying the power-law equation to the wind data. Firstly, the wind characteristics and profile for each height are computed using well-known graphical, empirical, and maximum-likelihood estimation methods and then some statistical tools, RMSE and R^2 , are employed to make a fair comparison among the methods.

The wind data used in this study is composed of hourly observations between January 01, 2010 and December 31, 2020, time series of which are depicted in Fig. 1. The estimated Weibull parameters and basic statistical indicators related to the wind speed behavior, namely, the standard deviation and average wind speed, at 10 m, 20 m, 30 m, 40 m, and 50 m height are summarized in Tables 1 and 2, respectively. As understood from Table 1, the shape parameter of Weibull distribution at all heights fluctuates between 1.6066 and 1.9575, while the scale parameter at 10 m and 50 m heights varies from 3.3986 to 3.7147 and from 5.2089 to 5.6934, respectively.

The calculated values of mean wind speed and standard deviation by empirical and maximum-likelihood methods approximately equal to those of actual wind data for all heights. On the other hand, those for the graphical method differ substantially in comparison with the actual data for all heights.

The Weibull probability density functions that are obtained from the estimated shape and scale parameters for each height are graphed in Figs. 2, 3, 4, 5, and 6, respectively. As regards to the PDF of the estimated Weibull distribution, it can be concluded that the Weibull PDF calculated by the empirical and maximum-likelihood method for all heights exhibits a similar fitting. Furthermore, the statistical tests are conducted to evaluate whether these three methods are suitable for representing wind speed distribution or not and to model more precisely the wind speed regime of the airport, which are listed in Table 3.

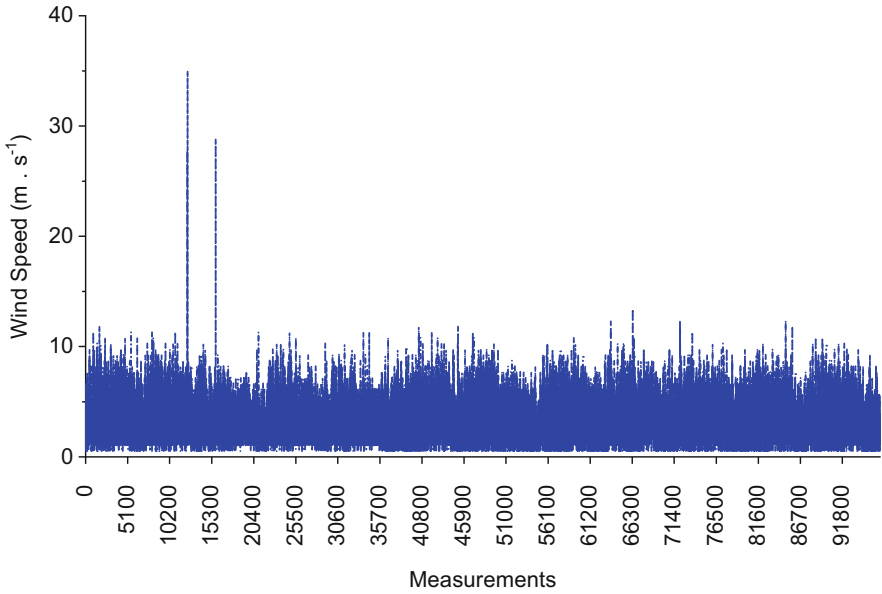


Fig. 1 Time series of hourly wind speed from 2010 to 2020 at 10 m height

Table 1 Comparison of the shape and scale parameters for each method at different heights

| Estimation methods | Distribution parameters | Height (m) | | | | |
|--------------------|-------------------------|------------|--------|--------|--------|--------|
| | | 10 | 20 | 30 | 40 | 50 |
| Graphical | η | 1.6066 | 1.6066 | 1.6066 | 1.6066 | 1.6066 |
| | μ | 3.3986 | 4.085 | 4.5487 | 4.9095 | 5.2089 |
| Empirical | η | 1.9562 | 1.9562 | 1.9562 | 1.9562 | 1.9562 |
| | μ | 3.7058 | 4.454 | 4.9599 | 5.3533 | 5.6798 |
| Maximum | η | 1.9575 | 1.9575 | 1.9575 | 1.9575 | 1.9575 |
| | μ | 3.7147 | 4.4647 | 4.9718 | 5.3661 | 5.6934 |

Table 2 Comparison of the average wind speed and standard deviation for each method at different heights (study measurements)

| Estimated parameters | Height (m) | Graphical | Empirical | Maximum | Data |
|--|------------|-----------|-----------|---------|--------|
| Average speed \bar{v} (ms^{-1}) | 10 | 3.0459 | 3.2857 | 3.2935 | 3.2857 |
| | 20 | 3.6609 | 3.9491 | 3.9585 | 3.9491 |
| | 30 | 4.0767 | 4.3976 | 4.4081 | 4.3976 |
| | 40 | 4.4000 | 4.7464 | 4.7577 | 4.7464 |
| | 50 | 4.6684 | 5.0359 | 5.0479 | 5.0359 |
| Standard deviation σ (ms^{-1}) | 10 | 3.0459 | 3.2857 | 3.2935 | 3.2857 |
| | 20 | 3.6609 | 3.9491 | 3.9585 | 3.9491 |
| | 30 | 4.0767 | 4.3976 | 4.4081 | 4.3976 |
| | 40 | 4.4000 | 4.7464 | 4.7577 | 4.7464 |
| | 50 | 4.6684 | 5.0359 | 5.0479 | 5.0359 |
| | 10 | 3.0459 | 3.2857 | 3.2935 | 3.2857 |

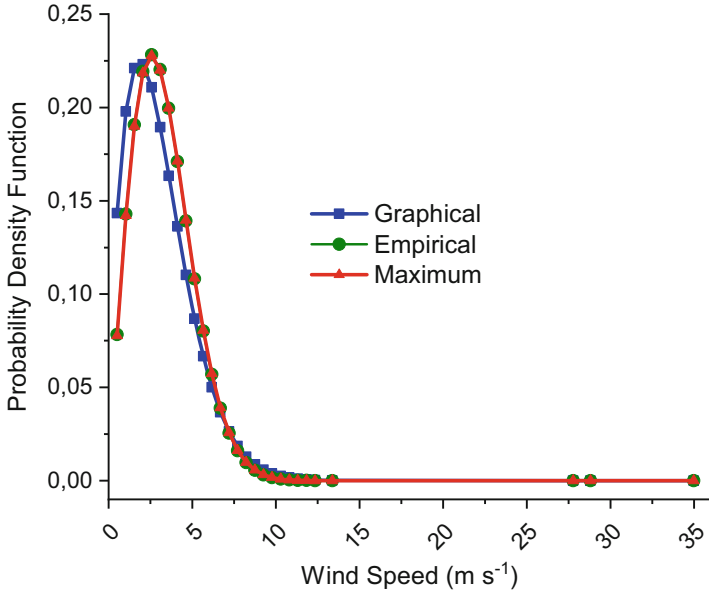


Fig. 2 Comparison of the Weibull probability density function for 10 m

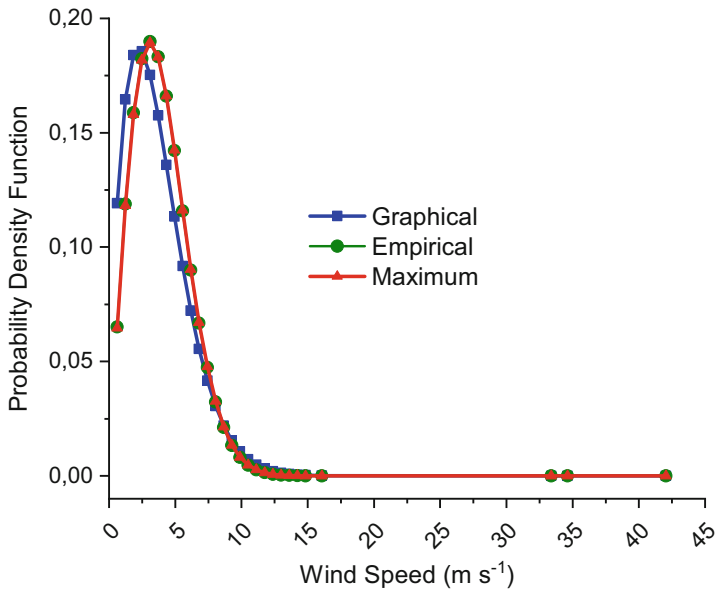


Fig. 3 Comparison of the Weibull probability density function for 20 m

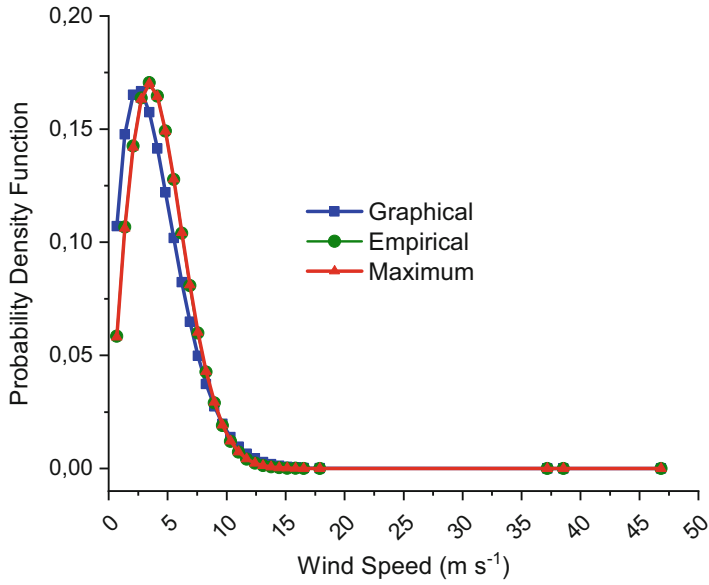


Fig. 4 Comparison of the Weibull probability density function for 30 m

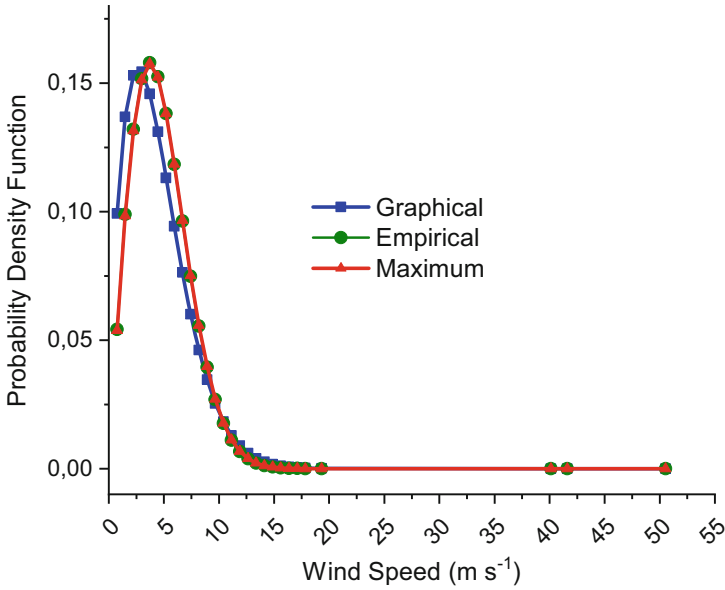


Fig. 5 Comparison of the Weibull probability density function for 40 m

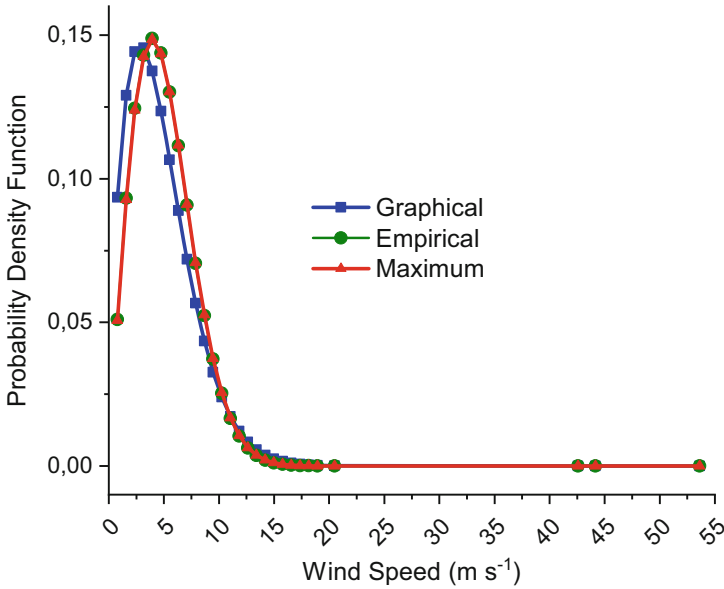


Fig. 6 Comparison of the Weibull probability density function for 50 m

Table 3 Comparative analysis of estimation methods at different heights

| Estimation methods | Statistical tools | Height (m) | | | | |
|--------------------|-------------------|------------|--------|--------|--------|--------|
| | | 10 | 20 | 30 | 40 | 50 |
| Graphical | RMSE | 0.0227 | 0.0189 | 0.0169 | 0.0157 | 0.0148 |
| | R ² | 0.9261 | 0.9341 | 0.9403 | 0.9415 | 0.9481 |
| Empirical | RMSE | 0.0133 | 0.0110 | 0.0099 | 0.0092 | 0.0086 |
| | R ² | 0.9746 | 0.9786 | 0.9802 | 0.9827 | 0.9853 |
| Maximum | RMSE | 0.0134 | 0.0111 | 0.0100 | 0.0092 | 0.0087 |
| | R ² | 0.9743 | 0.9783 | 0.9799 | 0.9827 | 0.9850 |

As can be seen from Table 3, it is observed that there is no significant discrepancy among the performance of the methods. However, irrespective of heights, the empirical method presents better ability in estimating the wind characteristics of the airport when compared to the other two methods.

Wind power cannot be entirely extracted. Thus, it is important to take into account the availability of wind power at the location. To produce the electricity and hydrogen from the wind power, in the last step, wind power density for each method based on the height is determined from the wind distribution, which is tabulated in Table 4. In the light of the data evaluation presented in Table 4, the graphical, maximum-likelihood, and empirical methods at 10 m height are observed to have a wind power density of 39.2133, 38.9768, and 39.2302 in the unit of W. m⁻², respectively, which exhibit the nearly same as the measured data of

Table 4 Comparison of wind power density for each method

| Estimated parameters | Height (m) | Graphical | Empirical | Maximum | Data |
|--|------------|-----------|-----------|----------|----------|
| Wind power density $W_{PD} W_{PD} (W \cdot m^{-2})$ | 10 | 39.2133 | 38.9768 | 39.2302 | 40.1233 |
| | 20 | 68.0828 | 67.6722 | 68.1122 | 69.5891 |
| | 30 | 94.0149 | 93.4480 | 94.0556 | 95.9932 |
| | 40 | 118.2066 | 117.4937 | 118.2577 | 120.5661 |
| | 50 | 141.1812 | 140.3298 | 141.2423 | 143.8466 |

40.1233 in the unit of $W \cdot m^{-2}$. Similarly, graphical, maximum-likelihood, and empirical methods at 50 m height are observed to have a wind power density of 141.1812, 140.3298, and 141.2423 in the unit of $W \cdot m^{-2}$.

4 Conclusion

The aim of this chapter is to present comparatively wind characteristics and the profile of Hasan Polatkan Airport at various heights from the ground level, applying the power-law equation to the wind speed. Firstly, the wind characteristics for each height are estimated based on widely used graphical, empirical, and maximum-likelihood estimation methods, as mentioned previously. Then, several statistical tools are employed to make a fair comparison among the methods. In the last step of the study, wind power density for each height is computed elaborately based on estimation methods in order to assess the potential of electricity and hydrogen generation from wind power.

The main concluding outcomes drawn from the research can be summarized as follows:

- The overall mean wind speed for 10 m, 20 m, 30 m, 40 m, and 50 m is calculated to be 3.2857, 3.9491, 4.3976, 4.7464, and 5.0359 in the unit of $m \cdot s^{-1}$, respectively.
- The standard deviation of the actual wind dataset for 10 m, 20 m, 30 m, 40 m, and 50 m is found to be 1.7712, 2.1289, 2.3707, 2.5587, and 2.7148 in the unit of $m \cdot s^{-1}$, respectively.
- The shape parameter varies from 1.6066 to 1.9575 depending on only the height, irrespective of estimation methods.
- The scale parameter varies from 3.3986 to 5.6934 depending on both the height and estimation methods.
- In the light of statistical test analysis, it is observed that there is no significant discrepancy among the performance of the methods. On the other hand, irrespective of heights, the empirical method presents better ability in modelling and estimating the wind characteristics of the airport when compared to the other two methods.

The results of the study clearly reveal that the wind speed increases as the height increases, as expected. In addition, the airport has a moderate potential to evaluate the potential of electricity and hydrogen generation from wind power.

References

- Bagci, K., Arslan, T., & Celik, H. E. (2021). Inverted Kumaraswamy distribution for modeling the wind speed data: Lake Van, Turkey. *Renewable and Sustainable Energy Reviews*, *135*, 110110.
- Bañuelos-Ruedas, F., Angeles-Camacho, C., & Rios-Marcuello, S. (2010). Analysis and validation of the methodology used in the extrapolation of wind speed data at different heights. *Renewable and Sustainable Energy Reviews*, *14*(8), 2383–2391.
- Boopathi, K., Kushwaha, R., Balaraman, K., Bastin, J., Kanagavel, P., & Reddy Prasad, D. M. (2021). Assessment of wind power potential in the coastal region of Tamil Nadu, India. *Ocean Engineering*, *219*, 108356.
- Chen, H., Birkelund, Y., Anfinsen, S. N., Staube-Delgado, R., & Yuan, F. (2021). Assessing probabilistic modelling for wind speed from numerical weather prediction model and observation in the Arctic. *Scientific Reports*, *11*(1), 7613.
- Costa Rocha, P. A., de Sousa, R. C., de Andrade, C. F., & Da Silva, M. E. V. (2012). Comparison of seven numerical methods for determining Weibull parameters for wind energy generation in the northeast region of Brazil. *Applied Energy*, *89*(1), 395–400.
- Deaves, D. M., & Lines, I. G. (1997). On the fitting of low mean windspeed data to the Weibull distribution. *Journal of Wind Engineering and Industrial Aerodynamics*, *66*(3), 169–178.
- Deep, S., Sarkar, A., Ghawat, M., & Rajak, M. K. (2020). Estimation of the wind energy potential for coastal locations in India using the Weibull model. *Renewable Energy*, *161*, 319–339.
- Đurišić, Ž., & Mikulović, J. (2012). A model for vertical wind speed data extrapolation for improving wind resource assessment using WAsP. *Renewable Energy*, *41*, 407–411.
- El Khchine, Y., & Sriti, M. (2021). Performance evaluation of wind turbines for energy production in Morocco's coastal regions. *Results in Engineering*, *10*, 100215.
- Gualtieri, G., & Secci, S. (2012). Methods to extrapolate wind resource to the turbine hub height based on power law: A 1-h wind speed vs. Weibull distribution extrapolation comparison. *Renewable Energy*, *43*, 183–200.
- Jung, C., & Schindler, D. (2021). The role of the power law exponent in wind energy assessment: A global analysis. *International Journal of Energy Research*, *45*, 8484–8496.
- Justus, C. G., & Mikhail, A. (1976). Height variation of wind speed and wind distributions statistics. *Geophysical Research Letters*, *3*(5), 261–264.
- Kim, D.-Y., Kim, Y.-H., & Kim, B.-S. (2021). Changes in wind turbine power characteristics and annual energy production due to atmospheric stability, turbulence intensity, and wind shear. *Energy*, *214*, 119051.
- Mahesh, K. (2021). A statistical analysis and artificial neural network behavior on wind speed prediction: Case study. *Theory and Practice of Mathematics and Computer Science*, *6*, 38–56.
- Ohunakin, O. S., Adaramola, M. S., & Oyewola, O. M. (2011). Wind energy evaluation for electricity generation using WECS in seven selected locations in Nigeria. *Applied Energy*, *88*(9), 3197–3206.
- Saeed, M. A., Ahmed, Z., Hussain, S., & Zhang, W. (2021). Wind resource assessment and economic analysis for wind energy development in Pakistan. *Sustainable Energy Technologies and Assessments*, *44*, 101068.
- Suzer, A. E., Atasoy, V. E., & Ekici, S. (2021). Developing a holistic simulation approach for parametric techno-economic analysis of wind energy. *Energy Policy*, *149*, 112105.

- Tonsie Djiela, R. H., Tiam Kapen, P., & Tchuen, G. (2020). Wind energy of Cameroon by determining Weibull parameters: Potential of a environmentally friendly energy. *International Journal of Environmental Science and Technology*, *18*, 2251–2270.
- Wadi, M., & Elmasry, W. (2021). Statistical analysis of wind energy potential using different estimation methods for Weibull parameters: A case study. *Electrical Engineering*. <https://doi.org/10.1007/s00202-021-01254-0>
- Wang, L., Liu, J., & Qian, F. (2021). Wind speed frequency distribution modeling and wind energy resource assessment based on polynomial regression model. *International Journal of Electrical Power & Energy Systems*, *130*, 106964.

Enhancing Flight Safety Training and Prevention of Aviation Accidents with the Use of Physics and Aeronautics



Ioanna K. Lekea and Dimitrios G. Stamatelos

Contents

| | | |
|---|---|-----|
| 1 | Introduction | 273 |
| 2 | Methodological Approach to Teaching Aeronautics to Pilots | 274 |
| 3 | Combining Theory with Practice Both in Academic Education and Flight Training | 275 |
| 4 | Conclusion | 277 |
| 5 | Future Work | 278 |
| | References | 278 |

1 Introduction

The purpose of this chapter is to present a simulation tool, which was developed and is currently into the trial phase, so as to visualize the way in which the forces exerted on the aircraft at critical events or in critical phases of the flight (e.g., during take-off or landing) can create flight hazards.

In this context, in-flight crises will be categorized according to the type of hazard they pose (structural, aerodynamic) and the degree of risk they create for the flight. The tool can be used in both academic training (aeronautics) and flight training in a

I. K. Lekea (✉)

Division of Leadership-Command, Humanities and Physiology, Department of Aeronautical Sciences, Hellenic Air Force Academy, Dekelia Air Force Base, Attica, Greece
e-mail: ioanna.lekea@hafa.haf.gr

D. G. Stamatelos

Laboratory of Strength of Materials, Division of Aeronautics, Applied Mechanics and Infrastructure, Department of Aeronautical Sciences, Hellenic Air Force Academy, Dekelia Air Force Base, Attica, Greece
e-mail: dimitrios.stamatelos@hafa.haf.gr

targeted interdisciplinary case study analysis for in-flight risk management and the discussion of flight safety issues. Thus, the aim of the simulations is to help cadets understand in an applied manner fundamental concepts, such as loading conditions, stresses, etc.

The following tasks will be carried out in the context of this chapter:

1. Preliminary investigation of whether fundamental concepts of aeronautics are well and clearly understood by the cadets in relation to their effects on flight (Hellenic Air Force Academy, Courses: Aeronautics II, Aeronautics III, for the Stream of Pilots). To this end, field research took place with questionnaires that were specifically formulated to serve our research questions and that were distributed to both cadets and flight instructors.
2. Development and testing of the scenarios that are simulated and visualized, in order to cover a range of incidents. The scenarios' specifications, along with their parameters and the technical elements, are analyzed and are fully justified.
3. Development of an educational tool (currently at the demo level) in order to visualize the forces exerted on the aircraft in a selected scenario and to analyze the possible risks for the flight. In other words, the demo concerns a specific case study and calculates the strength of a structural area of the aircraft in relation to the forces exerted in this structural area due to the special conditions of the flight.

The emerged results from the field research and the demo trials are compared with cadets' theoretical knowledge. Eventually, a new educational model for teaching flight safety and in-flight risk management is proposed.

2 Methodological Approach to Teaching Aeronautics to Pilots

The Aeronautics II and III Modules, according to the Students' Guide of the Hellenic Air Force Academy, are to be dealt in a theoretical manner. However, cadets seemed to have difficulties in understanding fundamental concepts and their relation to flight. So, a more applied approach was clearly needed in order to help future pilots understand the interrelation between aeronautics and flight safety, especially in relation to mid-air crises. To this end, academic education and flight training needed to come together in a Module, which would make cadets realize the implications of physics and flight mechanics, but in an applied way (Ören et al., 2017).

When we come to think how to effectively prepare pilots involved in a potential crisis management in mid-air, the first thought that strikes our minds is to extensively train and educate them well and in depth, so those who could find themselves in critical situations will be able to understand and describe what is happening and, also, to make decisions or act or both. Therefore, given the differences between a theoretical education and a realist training, the second point needs to be effectively and fully addressed. One thing is certain: we need to prepare pilots before the crisis

comes around, so we must start discussing the safety issues as early as possible and as in much depth as possible (Boyd, 2017; Latorella & Prabhu, 2000).

Pilots usually start discussing flight safety issues (Federal Aviation Administration, 2011) on a theoretical level during the first semester of their studies. Modules like aeronautics are not linked to flight safety, and cadets learn how to deal with mid-air crises at the practical level, without understanding how a crisis evolves and why they need to follow the particular steps described in their check list. However, can a theoretical approach be considered as a successful mean of training on safety procedures? Apparently not, trainees definitely need to know how things work on the theoretical background (physics and mechanics), but they also need to practice on decision-making and taking actions when there is no time to lose. Therefore, we need to provide pilots both with the theoretical background and the hands-on training, if we want them to be able to effectively deal with emergencies.

Given the aforementioned and the educational scope of our Academy, in order to enhance cadets' knowledge on flight safety and emergency procedures, we thought it is extremely important to plan, design, and develop the Aeronautics II and III Modules in an interactive, problem-based learning experience for educational purposes (Brodeur et al., 2002; Mohd et al., 2004), designed to provide pilots with an in-depth academic experience on dealing with critical situations related to flight safety. The idea is that using real-life and hypothetical case studies, future pilots will have the opportunity to exercise their theoretical knowledge and think by themselves how to best handle difficult situations mid-air. Also, they will be able to consider different options and think about their actions in risky situations, when there is no time to lose.

3 Combining Theory with Practice Both in Academic Education and Flight Training

The innovation of our approach to teaching aeronautics with specific reference to flight safety is that it truly brings problem-based learning as an applied, yet academic, element in flight training. Nowadays, the main educational approach to flight safety training is a mixture of providing totally theoretical knowledge in class (aeronautics) and hands-on training either by a real flight either with the use of a flight simulation (Blow, 2012; Schank et al., 2002).

Solution 1 Provide pilots with the theoretical aeronautical background in class; then by the use of appropriate documentaries or educational films, give them a view of a critical situation; and, finally, by role-playing, put them in the shoes of those who had to deal with a flight emergency.

Limitation 1 But while studying and analyzing flight manuals, rules, and safety regulations may help trainees to think of the appropriate action one should take in a critical situation, this educational approach cannot prepare pilots to deal with

complex situation in limited real time while being under stress. This is because they learn and discuss various approaches to deal with emergencies, but mainly in theory. One needs a more systematic approach to handle real-life emergencies effectively.

Solution 2 Discuss safety regulations before or after a real or simulated flight takes place during briefing or debriefing are also used in order to provide pilots with a useful framework, so as to reflect on emergencies in a more organized context.

Limitation 2 The applied approach is not missing, since a discussion and analysis of applied issues takes place and theory is combined with practice (even when the flight simulator is used). However, pilots have no access to specially developed educational materials that will help them understand the reason (aeronautics) behind the actions.

Solution 3 Use of approved and tested scenarios with limited risk for the future pilots involved during real or simulated flight to make trainees get the real feeling of an emergency situation.

Limitation 3 It is not advisable to train pilots in dangerous situations in order to show them how to deal with mid-air crises no matter how limited the danger might be. In mid-air any additional unforeseen factor might put the flight in real danger. As far as the flight simulator (Kozuba & Bondaruk, 2014; Landman et al., 2018) is concerned, this may be a better option (Byrnes, 2017; Taylor et al., 2014), but we should not forget that for the use of flight simulator, a flight officer always must be available. Therefore, trainees cannot practice virtually as frequently as they would wish.

Problem-based learning and games and simulations (Clarke et al., 2017; Doskow, 2012; Newman, 2002, Fotaris & Mastoras, 2019), on the other hand, allow us to cater for these aspects. In our new educational approach, everything will be put to the test: theoretical knowledge, different approaches, and hard choices (Helmreich, 2000). A number of developed scenarios and cases will allow pilots to work together and test how they would cooperate in difficult situations (Sun et al., 2007; Veldkamp et al., 2020; Westrum & Adamski, 2017).

We used a questionnaire to evaluate cadets' knowledge after completing Aeronautics II and III Modules, and we came to the conclusion that cadets could discuss fundamental concepts of aeronautics in a theoretical way (88%), but those concepts were not well and clearly understood in relation to the flight (63%) for the majority of the trainees. Also, 92% of the cadets requested that the two modules had a more applied approach and discuss flight with specific case studies, so that the two modules would be more interesting and targeted to flight. Among the cases cadets sought to be examined were mid-air crises (66%), human error combined with mechanical failure (18%), mechanical failure combined with harsh weather (14%), and others (12%).

Taking those results into consideration, our proposed method aims, firstly, to holistically educate (Virovac et al., 2017) future pilots on flight safety from day 1 they enter the Academy; secondly, to enhance the use of traditional techniques and

role-playing to teach the theoretical background; thirdly, to use our interactive, educational scenarios to further test the theoretical background but also to make trainees to put to test their knowledge, their ability for critical thinking and cooperation with other trainees (if the scenario has to do with flight in formation); and finally, to benefit from the mixed method of testing the theoretical knowledge per se, as well as its application in a virtual practice platform.

The benefits of our proposed method will help us provide future pilots with well-rounded training. Traditional techniques can still be used in order to provide an effective education (on the theoretical background of physics and mechanics) and applied training experience (briefing/debriefing, analysis of flight emergencies, role-playing, etc.), but trainees will also be able to use our virtual escape room (a) to test the level of their theoretical knowledge, (b) to check how stress and time limitations affect how knowledge is applied in practice, and (c) to get virtual hands-on training, and, the most complete possible education, in terms of theory and practice. Trainees will also get the best possible training, in terms of both theory and practice, whenever they feel like using our VR simulation on their personal computer (PC) or smartphone.

Trainees' evaluation will be based on their choices, decisions, and actions within the simulated emergency situation. At the end of the game, trainees will be presented with the list of options they made and how it rated against the different flight parameters that determined its payoff. Module moderators will be able to use the evaluation in a debriefing class after the game.

4 Conclusion

The main educational objectives of our scenarios and simulation on flight safety and emergency procedures are (a) to facilitate the transition between theoretical education on the subjects of flight safety and emergency procedures and (b) to enhance education and training on emergency procedures and flight safety with the application of problem-based learning techniques. Consequently, the design of our simulation is based on real-life flight emergencies, and future pilots need to study the theoretical framework (aeronautics, flight manual, and check list) before playing the game. This way they will fully understand the connection between theory and practice.

On the technical level, our scenarios support a digital simulation that can be played by one or multiple players, who will have the opportunity to fly alone or fly in formation.

The first prototype of our virtual simulator is out for testing and use during flight training since October 2020 at the 120 Air Training Wing of the Hellenic Air Force. More scenarios are prepared and are currently tested; they are further enhanced by additional reading and supporting bibliography that can be found at the end of each scenario. Also, some short tests follow each emergency scenario consisting of

multiple choice questions, true-or-false (T/F) questions, and multiple-choice questions for the trainees to answer.

Appropriate questionnaires were used to test the scenarios and the players' satisfaction from the scenarios, the questions posed, and the dilemmas they had to work out in relation to the specific mid-air crisis they had to deal with. The questionnaires were distributed to second- and third-year cadets (Stream of pilots) at the Hellenic Air Force Academy. In total, 46 questionnaires were collected (a trustworthy research sample covering the 70% of the target population) for the first assessment of the scenarios of our simulation. A briefing with the scenarios and the targets of the survey was initially held for the cadets, and then they were prompted to run the simulation. Then, the questionnaires were distributed in order to elicit their point of view regarding the scenario each cadet and the factors that influence cadets' choices.

Trainees who used the scenarios at the testing phase admitted (89%) that their understanding of how aeronautics influence the flight and the treatment of mid-air was improved with the use of a synthetic educational approach and the use of problem based learning. The simulation provided cadets with some sort of virtual experience (92%) on dealing with mid-air emergencies and making informed choices (68%) when they had no piecemeal solutions to choose from (78%). They had to think and resolve practical issues and justify their choices.

5 Future Work

Scenarios and our virtual platform will be further developed so as to cover new areas and dilemmas related to aeronautics and mid-air crises. In the future, other types of mid-air will be also included in the simulation options (overload/metal fatigue, pilot error and design flaws, loss of vertical stabilizer, propeller manufacturing defect, roof separated from fuselage, in-flight wing failure due to metal fatigue).

The schedule is to incorporate and use the tool in class as a mean of both educating and evaluating cadets (implementation period of about 18 months). We expect to use our simulation for the second- and third-year cadets in the spring term of 2022.

References

- Blow, C. (2012). *Flight school in the virtual environment: Capabilities and risks of executing a simulations-based flight training program*. School of Advanced Military Studies.
- Boyd, D. D. (2017). A review of general aviation safety (1984–2017). *Aerospace Medicine and Human Performance*, 88(7), 657–664.
- Brodeur, D., Young, P. W., & Blair, K. B. (2002). Problem based learning in aerospace engineering education. In *Proceedings of the 2002 American Society for Engineering Education annual conference & exposition* (Session 2202).

- Byrnes, K. P. (2017). Employing flight simulation in the classroom to improve the understanding of the fundamentals of instruction among flight instructor applicants. *The Journal of Aviation/Aerospace Education and Research*, 26(1), 49–63.
- Clarke, S., Peel, D., Arnab, S., Morini, L., Keegan, H., & Wood, O. (2017). EscapED: A framework for creating educational escape rooms and interactive games to for higher/further education. *International Journal of Serious Games*, 4(3), 73–86.
- Doskow, M. G. (2012). *Analysis of the impact of scenario-based training on the aeronautical decision making of collegiate flight students*. Embry-Riddle Aeronautical University.
- Federal Aviation Administration. (2011). Chapter 9. In *Aviation instructor's handbook* (FAA-H-8083-9). FAA Publications. Available online here: https://www.faa.gov/regulations_policies/handbooks_manuals/aviation/aviation_instructors_handbook/media/11_aih_chapter_9.pdf. Accessed on 06/05/2021.
- Fotaris, P., & Mastoras, T. (2019). Escape rooms for learning: A systematic review. 13th ECGBL, Odense, Denmark. <https://doi.org/10.34190/GBL.19.179>
- Helmreich, R. L. (2000). On error management: lessons from aviation. *BMJ*, 320(7237), 781–785.
- Kozuba, J., & Bondaruk, A. (2014). Flight simulator as an essential device supporting the process of shaping pilot's situational awareness. *AFOSR*, 1, 41–60.
- Landman, A., van Oorschot, P., van Paassen, M. M., Groen, E. L., Bronkhorst, A. W., & Mulder, M. (2018). Training pilots for unexpected events: A simulator study on the advantage of unpredictable and variable scenarios. *Human Factors*, 60(6), 793–805.
- Latorella, K., & Prabhu, P. (2000). A review of human error in aviation maintenance and inspection. *International Journal of Industrial Ergonomics*, 14653(26), 133–161.
- Mohd, A. A. H., et al. (2004). *A review and survey of problem-based learning application in engineering education*. Conference on Engineering Education, Kuala Lumpur, 14–15 December 2004.
- Newman, D. (2002). *Interactive aerospace engineering and design*. McGraw Hill.
- Ören, T., Turnitsa, C., Mittal, S., & Diallo, S. Y. (2017). *Simulation-based learning and education*. Springer.
- Schank, J. F., Thie, H. J., Graff, C. M., II, Beel, J., & Sollinger, J. (2002). *Finding the right balance: Simulator and live training for navy units*. RAND.
- Sun, R., Lei, W., & Zhang, L. (2007). Analysis of human factors integration aspects for aviation accidents and incidents. In *Engineering psychology and cognitive ergonomics, 7th international conference, EPCE 2007, held as part of HCI international 2007*, Beijing, China, July 22–27, pp. 834–841.
- Taylor, A., Dixon-Hardy, D. W., & Wright, S. J. (2014). Simulation training in UK general aviation: An undervalued aid to reducing loss of control accidents. *The International Journal of Aviation Psychology*, 24(2), 141–152.
- Veldkamp, A., Grint, L., Knippels, M.-C., & van Joolingen, W. (2020). Escape education: A systematic review on escape rooms in education. *Educational Research Review*, 31, 1–18.
- Virovac, D., Domitrovic, A., & Bazijanac, E. E. (2017). The influence of human factor in aircraft maintenance. *Promet – Traffic & Transportation*, 29(3), 257.
- Westrum, R., & Adamski, A. J. (2017). Organizational factors associated with safety and mission success in aviation environments. In *Human error in aviation* (pp. 475–512). Routledge.

Satellite Formation Flight Via NRM and EKF State Estimation Method



Tuncay Yunus Erkec and Chingiz Hajiyev

Contents

| | | |
|-----|--|-----|
| 1 | Introduction | 282 |
| 2 | Problem Statement | 282 |
| 2.1 | Positioning of Target and Tracker Satellites | 283 |
| 3 | Extended Kalman Filter for Satellite Relative State Prediction | 283 |
| 4 | Results and Discussion | 284 |
| 5 | Conclusion | 287 |
| | References | 287 |

Nomenclature

| | |
|------|------------------------------------|
| ECI | Earth-centered inertial |
| EKF | Extended Kalman filter |
| GNSS | Global Navigation Satellite System |
| GPS | Global Positioning System |
| NRM | Newton-Raphson method |

T. Y. Erkec (✉)

Turkish National Defence University, Hezarfen Aeronautics and Space Technologies Institute,
Yesilyurt, Istanbul, Turkiye
e-mail: terkec@hho.msu.edu.tr

C. Hajiyev

Istanbul Technical University, Faculty of Aeronautics and Astronautics, Istanbul, Turkiye
e-mail: cingiz@itu.edu.tr

1 Introduction

In space missions, both coverage and functionality limitations can be overcome by cluster satellite architecture. The use of satellites as clusters implies the coordinated movement of several spacecraft to reach a common target. Typically, satellite formation can be 10 m to 10 km between satellites, or by covering the entire Earth with several identical satellites, coverage limits can be avoided. This cluster is called a sensor mesh. Moreover, formation flight can also be used to distribute the payload on two spacecraft, depending on mission objectives (Nebylov et al., 2018).

In the literature, although the methods proposed for the relative navigation problem of spacecraft differ conceptually or applied, they are similar in terms of the limitations and difficulties encountered such as dense computational load, line-of-sight vector separation, coordinate system transformations, and sensor noise ratios (Erkeç & Hajiyev, 2019; Sever & Hajiyev, 2020).

In this study, relative satellite state vector estimates were made using the Global Navigation Satellite System (GNSS)-based actual-distance approach (pseudo-ranging approach). Estimation of the measurement data coming from the target and tracker satellite GPS was made by Newton-Raphson method (NRM). The satellite state estimation differences made were input to the extended Kalman filter (EKF) for estimation of the relative state vector as a measurement value. Thus, the sensitivity of satellite relative state vectors has been achieved. To maintain the desired geometry of the formation satellite geometry, the control signals derived from these state vectors are received as input signals to the actuators.

2 Problem Statement

The target and follower satellite orbital positions determined by the Newton-Raphson model and EKF-based algorithm architecture stand out as the state estimation. The architecture created in this context is in two stages.

First Stage

Using the “actual-distance measurement model (pseudo-ranging model)” approach with NRM based on GPS measurements, the target and tracker satellite localization state parameters were roughly estimated.

Second Stage

Using the results of the first stage, the state vectors of the satellite relative motion model are estimated. Thus, the state vector estimates of the target and tracker satellites based on the NRM were used as the measurement values for the EKF estimates of the position and velocity vectors of relative motion between satellites.

2.1 Positioning of Target and Tracker Satellites

Orbit predictions of target and tracker satellites are made with Keplerian orbital elements, considering J_2 distortion. All equations specified for locating satellites are valid for both target and follower satellites and are not specified separately.

The architecture created to find the target and follower satellites state vector estimation. Based on the position vectors defined by Kepler elements of the target and follower satellites, precise estimates are made by processing the measurement information from four GPS satellites through the Kalman filter. Thus, the position information of target and follower satellites is obtained based on the GPS-based pseudo-ranging model. In this model, nonlinear distances between GPS satellites and target and follower satellites are taken as measurement information.

The orbital equations with perturbation of target and tracker satellites are as follows:

$$\ddot{\mathbf{r}} = \begin{bmatrix} \ddot{r}_x \\ \ddot{r}_y \\ \ddot{r}_z \end{bmatrix} = \begin{bmatrix} -\frac{\mu_{\oplus}}{r^3}x - \left\{ \frac{3}{2}J_2 \frac{\mu_{\oplus}}{r^2} \left(\frac{R_{\oplus}}{r} \right)^2 \left(1 - 5 \left(\frac{z}{r} \right)^2 \right) \frac{x}{r} \right\} \\ -\frac{\mu_{\oplus}}{r^3}y - \left\{ \frac{3}{2}J_2 \frac{\mu_{\oplus}}{r^2} \left(\frac{R_{\oplus}}{r} \right)^2 \left(1 - 5 \left(\frac{z}{r} \right)^2 \right) \frac{y}{r} \right\} \\ -\frac{\mu_{\oplus}}{r^3}z - \left\{ \frac{3}{2}J_2 \frac{\mu_{\oplus}}{r^2} \left(\frac{R_{\oplus}}{r} \right)^2 \left(1 - 5 \left(\frac{z}{r} \right)^2 \right) \frac{z}{r} \right\} \end{bmatrix} \quad (1)$$

where $\mathbf{r} = [x \ y \ z]^T$ is the position vector of the satellites, x, y, z are the components of the position vector, $\|\mathbf{r}\| = \sqrt{x^2 + y^2 + z^2}$ is the Euclidean norm of the position vector, μ_{\oplus} is the universal gravitational constant, M_{\oplus} is the mass of the Earth, $\mu_{\oplus} = GM_{\oplus}$ is the standard gravity parameter of the Earth, R_{\oplus} is the average of the Earth Equatorial radius, and J_2 is the first component of the geopotential model. For the target and tracker satellites, a two-body orbit model is derived from undesired acceleration specified in the J_2 perturbation orbit model.

3 Extended Kalman Filter for Satellite Relative State Prediction

The Newton-Raphson method is used for state vector estimation of both target and follower satellites. NRM is a well-known approach to vector cost function minimization problems. The estimation architecture between the NRM method used for relative position and speed optimization of target and follower satellites and extended Kalman filter (EKF)-based satellites is shown in Fig. 1.

The relative position of target and follower satellites is roughly determined by the NRM method and entered as a measurement in the extended Kalman filter (EKF). EKF is designed using ‘‘HCW’’ equations (Hill, 2020; Clohessy & Wiltshire, 1960)

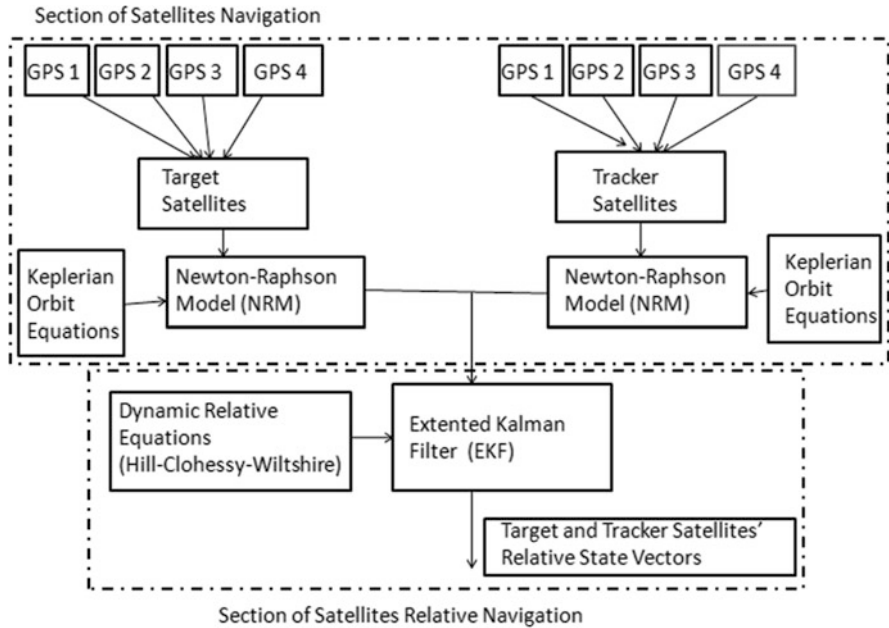


Fig. 1 Satellite relative state vector prediction diagram with extended Kalman filter

so that the relative position and velocity of the satellite can be estimated through this filter. The advantage of this method is that it is unrelated to EKF inputs for estimating relative navigation states because the positions of the target and follower satellites are determined by the NRM method and there is no correlation between them. In addition, J_2 distortion and system noise are considered to estimate the positions and relative positions of the target and follower satellites.

Using the results of the first step, the state vectors of the satellite relative motion model are estimated. Therefore, state vector estimates of target and follower satellites based on NRM were used as measurement values for EKF estimates of the position and velocity vectors of relative motion between satellites.

4 Results and Discussion

In this study close satellite formation relative state estimations are analyzed. Target and follower satellite localizations are determined with the NRM approach. NRM's outputs are input to the relative EKF between target and follower satellites. Extended Kalman filter (EKF) is an approach for nonlinear systems. EKF linearizes the system and estimates the state vectors. Initial states of the EKF are 10 m for locations and 25 m for clock bias due to actual state vectors.

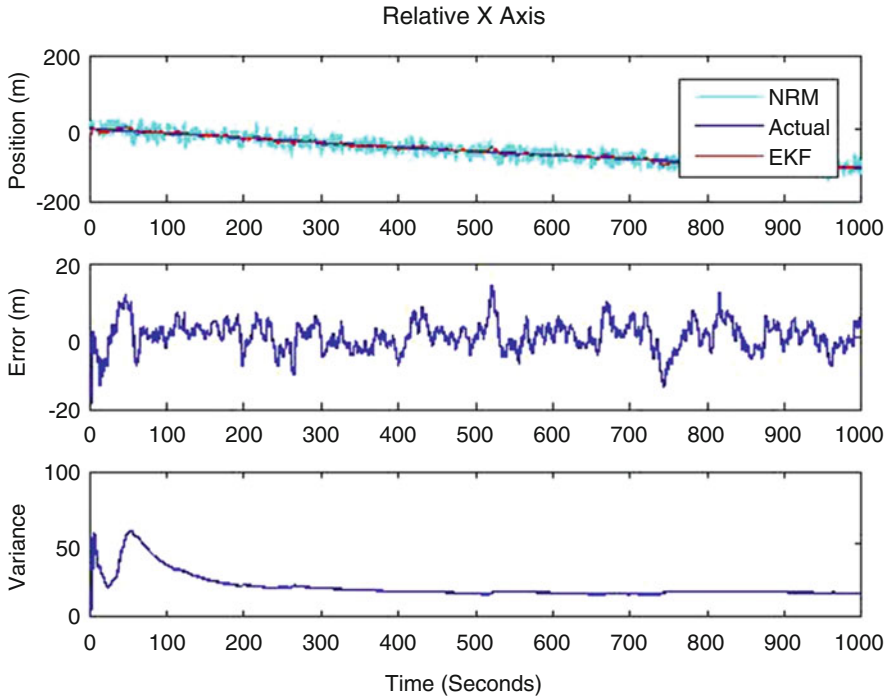


Fig. 2 Satellite relative motion *x*-axis analyses

Another approach for nonlinear systems is the Newton-Raphson method. In each iteration step, multiple computation-intensive matrix operations are performed. The Newton–Raphson method constructs a different matrix in each iterative step and thus requires performing a new set of matrix operations in each step (Sever & Hajiyev, 2020; Cheung & Lee, 2017).

NRM approach is determined to the target and follower satellites orbital vector estimations. The difference of orbit vectors is inputted to the EKF stage for estimated relative state vectors of formation architecture. The analyses of just *x* and *V_x* axes are shown in Figs. 2 and 3.

As shown in Table 1, the relative satellites states estimation algorithm has been run five times, and the average values of root mean square errors have been calculated.

As shown in Table 1, the satellite relative state vector estimates between the target and the follower satellite are roughly determined by the NRM approach. The detected drum vectors enter the EKF as the measurement value. State vector estimates become more precise and more accurate with EKF.

The designed NRM and EKF algorithms were examined through 1000 iteration steps. Errors accumulate as the target and follower satellite continue to move in orbit.

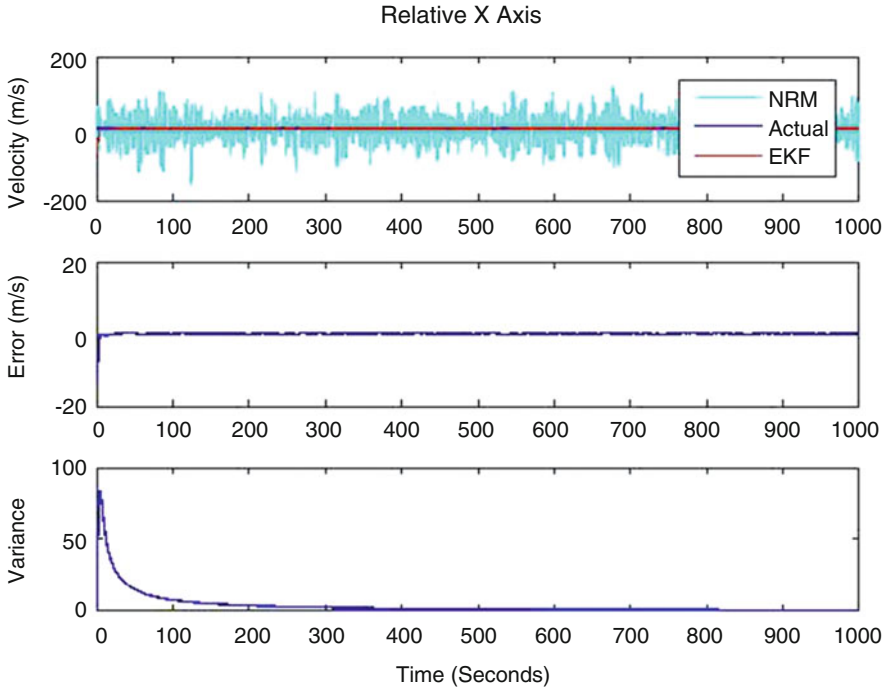


Fig. 3 Satellite relative motion V_x -axis analyses

Table 1 Relative satellite state estimation's root mean square errors for NRM and EKF approaches

| Steps | Relative position estimation errors | | | Relative velocity estimation errors | | |
|--------------|-------------------------------------|-----------|-----------|-------------------------------------|-----------------|-----------------|
| | x_R (m) | y_R (m) | z_R (m) | V_{x_R} (m/s) | V_{y_R} (m/s) | V_{z_R} (m/s) |
| 200th steps | 4.92 | 4.65 | 10.1 | 1.841 | 1.012 | 6.200 |
| 400th steps | 4.861 | 4.06 | 9.07 | 1.507 | 2.830 | 4.072 |
| 600th steps | 4.729 | 3.88 | 8.47 | 0.783 | 1.202 | 0.998 |
| 800th steps | 4.614 | 3.62 | 7.56 | 0.728 | 0.758 | 0.967 |
| 1000th steps | 4.6036 | 3.64 | 7.03 | 0.666 | 0.612 | 0.910 |

To prevent this, a satellite control part is required. Provides intersatellite sharing of information on the inter-satellite link requirement, target, and follower satellite orbit, and relative vector parameters, which are the characteristic requirements of GPS-based satellite formation architecture.

It is an undeniable fact that cluster satellite architecture will gain great importance in future space studies. The method presented in this study is a guide for other researchers in terms of developing relative vector estimation methods for the conservation of near satellite formation geometry.

5 Conclusion

In this chapter, relative satellite state vector estimates were made using the Global Navigation Satellite System-based pseudo-ranging approach. Estimation of the measurement data coming from the main and tracker satellite GPS was made by the Newton-Raphson method. The satellite state estimation differences made were input to the extended Kalman filter for the estimation of the relative state vector as a measurement value.

The designed NRM and EKF algorithms were examined through simulations. The simulation results show that relative state vector estimates between the target and the follower satellite are roughly determined by the NRM approach. The detected drum vectors enter the EKF as the measurement value. State vector estimates become more precise and more accurate with EKF.

Errors accumulate as the target and follower satellite continue to move in orbit. To prevent this, a satellite control part is required.

References

- Cheung, K., & Lee, C. (2017). *A new geometric trilateration scheme for GPS-style localization*. IPN Progress Report, pp. 42–209.
- Clohessy, W., & Wiltshire, R. (1960). Terminal guidance systems for satellite rendezvous. *Journal of Aerospace Sciences*, 27(9), 653–658. Published online: 30 Aug 2012.
- Erkeç, T. Y., & Hajiyev, C. (2019). Traditional methods on relative navigation of small satellites. In *2019 9th international conference on recent advances in space technologies (RAST)*, Istanbul, Turkey, pp. 869–874.
- Hill, G. W. (2020). Researches in the lunar theory. *American Journal of Mathematics*, 1(1), 5–26. (Original work published 1878).
- Nebylov, A., Medina, A., & Knyazhsky, A. (2018). Verification of the relative distance measurement method for pico-satellites in constellation, IFAC papers on line. *International Symposium on Artificial Intelligence, Robotics and Automation in Space (i-SAIRAS)*, 51(12), 100–105.
- Sever, M., & Hajiyev, C. (2020). Satellite localization correction with extended Kalman filter. In *International symposium on electric aviation and autonomous systems*, 22–24 September 2020, Kyiv, Ukraine.

Evaluating the Effects of a Morphed Trailing Edge Flap for Aeroacoustics Applications



Joseph C. Watkins and Abdessalem Boufferrouk

Contents

| | | |
|-----|------------------------------|-----|
| 1 | Introduction | 290 |
| 2 | Method | 291 |
| 2.1 | Geometry | 291 |
| 2.2 | Mesh | 291 |
| 2.3 | Solver Method | 292 |
| 3 | Results and Discussion | 294 |
| 4 | Conclusion | 296 |
| | References | 297 |

Nomenclature

| | |
|--------------------|---|
| CFD | Computational fluid dynamics |
| f_{\min} | Minimum frequency obtained in simulation (Hz) |
| FFT | Fast Fourier transform |
| FWH | Ffowcs Williams-Hawkings method |
| t_{end} | Flow time at end of simulation (s) |
| t_{start} | Flow time at beginning of simulation (s) |
| U_{∞} | Free stream velocity (m/s) |
| Δt | Numerical time step (s) |
| Δx | Smallest element size in flow direction (m) |

J. C. Watkins (✉) · A. Boufferrouk
University of the West of England, Bristol, UK
e-mail: abdessalem.boufferrouk@uwe.ac.uk

1 Introduction

The aim of this project is to investigate the effectiveness of morphing as a technology for noise reduction on high-lift devices, primarily the noise generated by the gap between a wing and an extended trailing edge flap (TEF). Morphing has been recently studied in many papers (e.g., Kimaru & Boufferrouk, 2017), and this particular paper adds to some previous work morphing TEFs (Evans et al., 2016; Loudon et al., 2018). Aircraft engine noise has been reduced significantly through innovations such as the mass production of high bypass ratio turbofan engines (e.g., the Rolls-Royce Trent engine line), leading to airframe noise becoming a much larger contributor to overall aircraft noise than it used to be. This study uses the 30P30N aerofoil, with no leading-edge slat, to analyse the far field aeroacoustic noise propagation from the flap cove region, and any other characteristic noise sources. Further analysis assesses whether this noise can be reduced by morphing the region linking the main wing and the flap, to create one continuous smooth surface.

The leading-edge slat on the 30P30N aerofoil geometry is not included in this study not only to simplify the problem but also because not all aircraft utilize a leading-edge slat, and so, innovations in flap noise reduction techniques can be applied to a wider range of aircraft.

Projects such as this have increased in relevance recently because residential areas surrounding airports are becoming increasingly more densely populated. Past research has shown the damaging effects of loud noise near residential areas by disturbing sleep, causing stress, damaging surrounding ecosystems and reducing wildlife populations. The 30P30N aerofoil is widely used for studying the aeroacoustics of high-lift devices, along with various reduction techniques. The full 30P30N aerofoil geometry is shown in Fig. 1.

Murayama et al. (2014) tested the 30P30N aerofoil in the 2×2 m JAXA wind tunnel test section. They placed a series of unsteady pressure transducers on the surface of the wing to analyse the near-field sound propagation, and an array of microphones on the walls of the test section to assess the far-field noise. They concluded that the 30P30N aerofoil has multiple narrow broadband peaks across all angles of attack tested, which decreased in amplitude as the angle of attack was

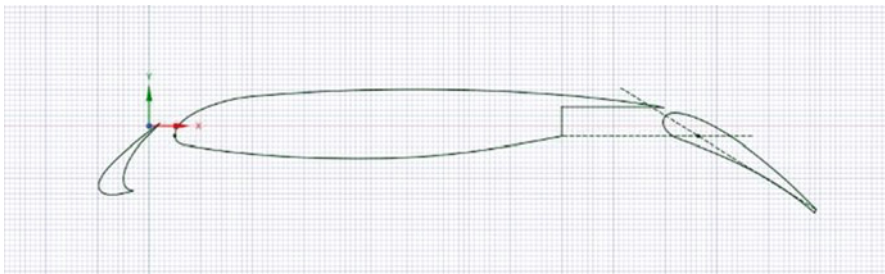


Fig. 1 30P30N high lift aerofoil configuration

increased. Similarly, they found that broadband noise for this aerofoil configuration is at its highest when at low angles of attack (i.e., 0° and 3.5°). Using data from the near-field pressure transducers around the aerofoil geometry, they demonstrated that the highest contributor to the overall wing section noise originates from the leading-edge slat. More recently, research work by R. Ilário da Silva et al. (2020) investigated the aeroacoustic effects of using various designs of fillers for the cove regions on the slat and the flap of the 30P30N aerofoil. Their results showed that there was no significant change in lift-to-drag ratio except for the full slat cove filler if used, which resulted in an improved lift-to-drag ratio. The acoustic results showed that the full-cove filler configuration reduced the overall broadband noise across a wide spectrum by 4–5 dB, and they almost eliminated the tonal noise generated by the sharp trailing edge of the slat. More research is still required to isolate the flap noise and create noise reduction techniques for the noise generated by the secondary cove region for the trailing-edge flap. This chapter investigates the use of a morphing trailing edge flap for noise abatement.

2 Method

2.1 Geometry

This study uses ANSYS Fluent, a cell-centred computational fluid dynamics (CFD) software, using a 2D planar geometry. The effects of fully morphing the trailing edge flap of the 30P30N aerofoil to the main body are investigated. This is done using a series of B-splines that traced the external contours of the conventional design to produce a smooth continuous surface from the trailing edge of the main body to the leading edge of the flap, both along the upper and lower surfaces. Testing is carried out at an 8° angle of attack, with two different flap deflections at 5° and 15° . The conventional and the morphed configurations are shown in Fig. 2 at a 15° flap deflection. The same technique is also applied to the 5° case.

The computational domain boundaries are respectively located at 13 chord lengths in front, above and below the aerofoil, and 25 chord lengths behind, to enable the wake flow to develop fully. A C-shaped domain is also used because triangular elements are used, with a sharp trailing-edged geometry. This produced a mesh with low skewness (average 0.15) and high orthogonal quality (average 0.98).

2.2 Mesh

Meshing is done using a hybrid approach, with structured inflation layers near the wall and unstructured mesh in the outer domain. The first layer height (FLH) is calculated using the chord length of 0.45 m, and a target y^+ of 1. This is to create a mesh with appropriately small near-wall element size to capture the turbulent

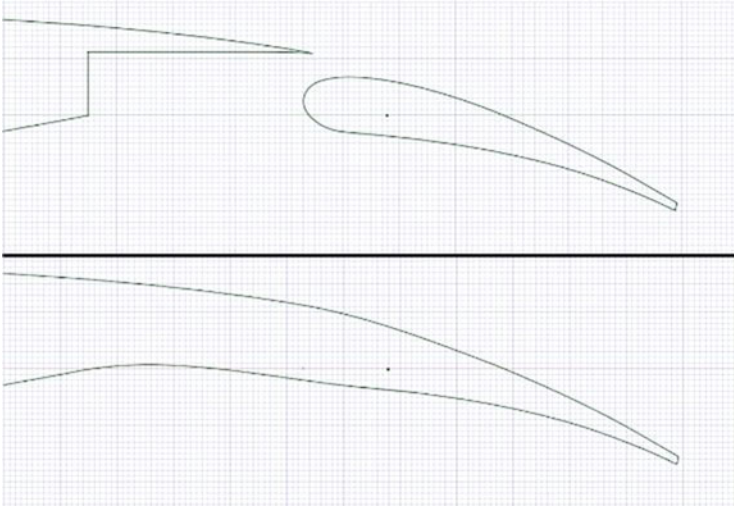


Fig. 2 15° flap deflection for conventional (above) and morphed (below) configurations

boundary layer accurately. The total number of layers is calculated using Blasius' turbulent boundary layer height equation. The FLH used for testing is 6.45×10^{-6} m, with 45 inflation layers and a geometric growth rate of 1.2.

The rest of the domain element size is determined by a wall element size of 9.7×10^{-4} m and a small element growth rate of 1.03 to an outer domain size of 0.4 m. This gradually phases out the acoustic pressure waves in such a way that they are captured accurately by the receiver but are phased out before reaching the domain boundaries. This reduces the impact of the waves reflecting off the boundaries and being detected twice by the receiver. The final mesh and domain can be seen in Fig. 3. The same mesh parameters are used across all configurations. The maximum wall y^+ across all meshes used is 1.2, and there are around 200,000 elements.

The CFD simulations were validated (not shown) against the results of Murayama et al. (2014) in terms of lift and pressure coefficients; good agreement was found. Discussion of the validation is detailed in a follow-up full-length article to this work.

2.3 Solver Method

The computational acoustic analogy used consists of, firstly, allowing the simulation to run as steady for around 1000 iterations; this acts as a good initialization for the transient simulation to speed up convergence. Following this, the simulation is changed to transient, with a time step calculated using Eq. (1), where the courant number is 1, flow velocity is 30 m/s and Δx is the smallest mesh element size. This

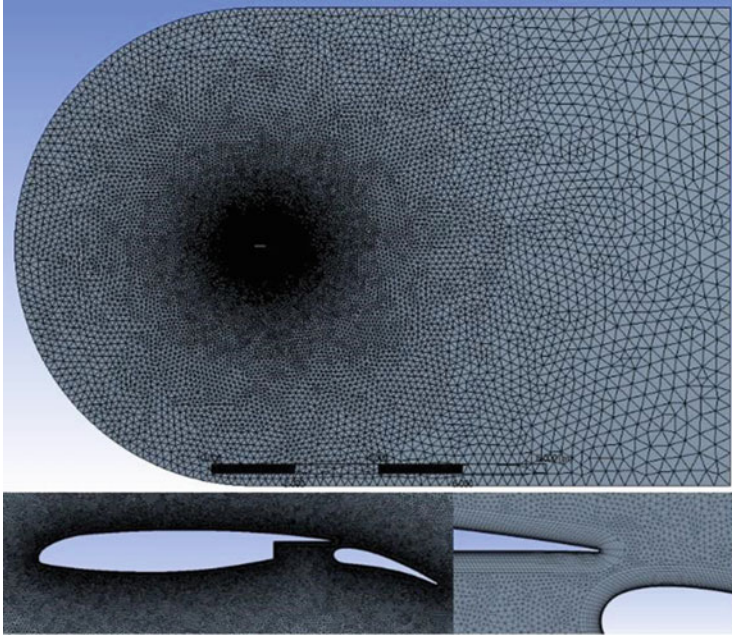


Fig. 3 Domain mesh and geometry configuration for conventional flap at 15° flap deflection

resulted in a time step of around 5.8×10^{-5} s (varying slightly for different configurations due to small mesh differences).

$$\text{Time step } (\Delta t) = \frac{\text{Courant number} \times U_{\infty}}{\Delta x} \quad (1)$$

The simulation is then run until a statistically steady state has been achieved (this is defined as the flow having no overall uptrend or downtrend in specific parameters such as lift and drag coefficient). Next, data sampling for time statistics is turned on to obtain comparable pressure and aerodynamic parameters averaged over time. In addition to activating the Ffowcs Williams-Hawkings (FWH) acoustic model with a reference pressure of 2×10^{-5} Pa (the lower threshold of human hearing), the source correlation length is set to 0.53 m, which was also used by Kamliya Jawahar et al. (2021) whose wind tunnel acoustic data is used for validation of the acoustic analogy used in this paper. The receiver is located at 1.5 m below the leading edge of the aerofoil. This is because according to the ISO (International Organization for Standardization), the near-field ends at a point defined as a wavelength of sound, or equal to a distance of three times the largest geometric dimension (ISO 12001, 1996).

The coupled pressure-velocity coupling scheme is used for all unsteady simulations, along with a second-order upwind scheme for all flow variables. Meanwhile, the PRESTO! solution method is used for pressure to achieve greater accuracy for

pressure fluctuations by not interpolating at the boundaries but solving instead, although this is more computationally expensive (ANSYS Fluent user guide). The simulation run time, with acoustics model activated, is determined using Eq. (2); this is based on running five periods for the corresponding minimum obtained frequency, as advised in ANSYS Fluent theory manual (ANSYS, 2019).

$$(t_{\text{end}} - t_{\text{start}}) = \frac{5}{f_{\text{min}}} \quad (2)$$

3 Results and Discussion

The acoustics results were validated against experimental data by Kamliya Jawahar et al. (2021) with good agreements found. Again, full discussion of the acoustic validation will be presented in a follow-up full-length article. At 5° flap deflection, the aerodynamic performance of the morphed configuration is slightly better than the conventional, with 7% more lift generated, and negligible differences in drag. This resulted in lift-to-drag ratios of 18 and 16 for the morphed and the conventional configurations, respectively. When the flap deflection is increased to 15°, the differences in aerodynamic performance between the two configurations are very small. However, the aerodynamic lift generation of the conventional flap configuration (with the gap) improves by 39% as the flap deflection is increased, whereas the morphed flap only increases its lift performance by around 3%. The conventional configuration sees a much greater increase in drag over the morphed configuration as the flap deflection is increased (8% drag increase for the morphed, and 32% increase in for the conventional between 5° and 15° flap deflections). This is likely due to the additional trailing edge vortices from the main body, and the cove regions causing more flow separation and a greater turbulent boundary layer.

The acoustic noise generation of both configurations at 5° flap deflection is shown in Fig. 4 in a sound pressure level (SPL) versus frequency plot. SPL plots are created by carrying out a fast Fourier transform (FFT) on pressure data.

The main feature is the initial low-frequency tone which peaks for both configurations at around 250 Hz, with a similar amplitude of 60 dB. This wide-frequency band peak is caused by the vortex shedding from the trailing edge of both aerofoils. The shedding vortex is large and rotates at a lower frequency, creating a loud low-frequency noise. Both aerofoils vortex shedding from the trailing edge noise characteristics are very similar because the overall chord length and angle of attack are the same. After 1000 Hz, however, the morphed configuration is much quieter. On average, the broadband noise generation of the morphed configuration across the wide spectrum of frequencies is around 25% quieter than the conventional. This increased broadband noise generation is likely due to increased flow separation caused by the cove region on the conventional flap design. The flow separation

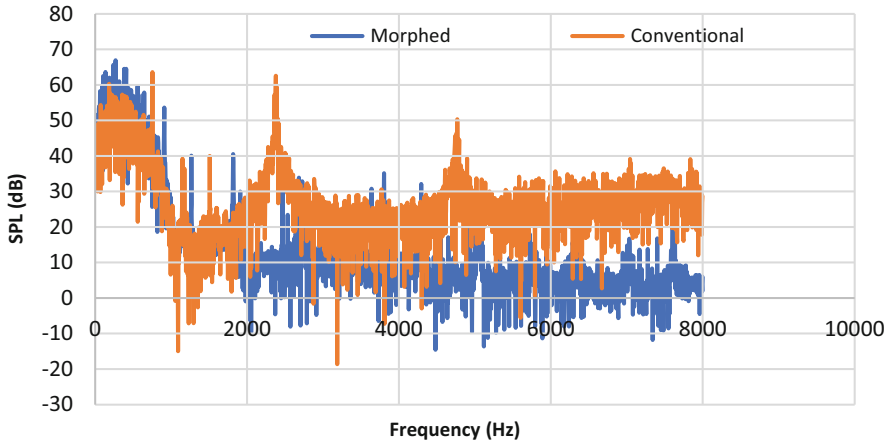


Fig. 4 SPL vs frequency plot for morphed and conventional designs at 5° flap deflection

region often has smaller eddies which can rotate across higher frequencies, generating a broadband type of noise.

There are also two distinct tonal peaks produced by the conventional configuration at 2400 and 4800 Hz, with an amplitude of 62 dB and 50 dB, respectively. These tonal peaks are not present in the morphed configuration. The expected cause for these tonal peaks in the conventional flap design is likely to be the additional sharp trailing edge of the main body of the 30P30N geometry, as also highlighted by Peng et al. (2018). This results in a sharp release of turbulent kinetic energy from the trailing edge from the cove region, thus generating tonal noise. As the flap deflection is increased to 15° , the disadvantages observed in the conventional design decrease, and the two configurations have more similar noise characteristics across the frequencies tested. Figure 5 shows the SPL versus frequency at 15° flap deflection for both configurations.

Like the 5° deflection results, there is a distinctly loud, low-frequency peak at 350 Hz for both configurations, peaking slightly higher than at 5° , up to 70 dB for both. Again, this is likely caused by the large eddy vortex shedding in the wake. The broadband noise generation of the conventional design is now nearly at the same level as that of the morphed configuration. However, at the highest frequencies beyond about 7000 Hz, the conventional configuration begins to be quieter than the morphed design. The two distinct tonal peaks are still mildly present in the conventional design at 15° but have a much smaller amplitude. This effect is similar to what Murayama et al. (2014) reported in that as the angle of attack of the 30P30N aerofoil increases, whose effect is analogous to a trailing edge flap deflection, the narrow broadband peaks are significantly reduced.

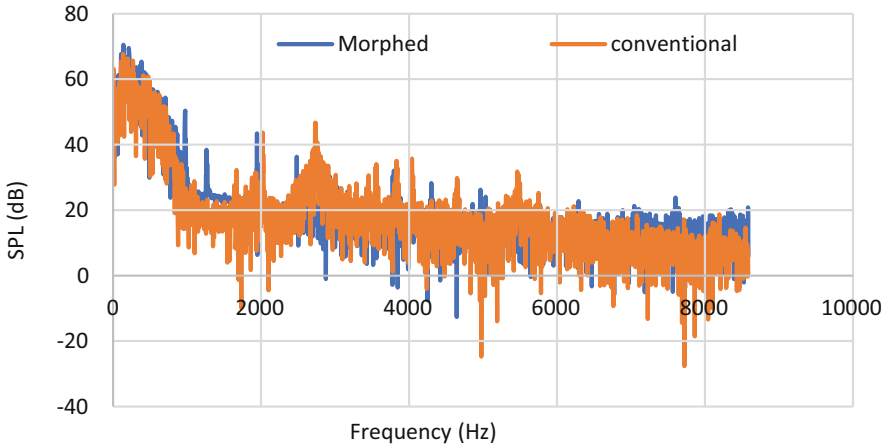


Fig. 5 SPL plot for morphed and conventional configurations at 15° flap deflection

4 Conclusion

The research presented in this chapter illustrates how a morphed trailing edge flap can affect the acoustic noise as well as aerodynamic performance when compared with a conventional trailing edge flap. Using an FFT of pressure data to produce SPL plots, results show that the morphed configuration holds significant benefit over the conventional configuration at low flap deflections, where there is 25% less broadband noise and no tonal peaks when compared with the conventional design. In addition to aeroacoustic benefits, the morphed configuration sees a 12% increase in lift-to-drag ratio over the conventional. These advantages of the morphed configuration, however, decrease when the flap deflection is increased. The distinct tonal peaks in the conventional gapped flap design are reduced significantly, and broadband noise generation is nearly at the same level as the morphed configuration, except at the highest frequencies where the conventional design is slightly quieter beyond approximately 7000 Hz.

These results demonstrate promising attributes of a morphed trailing edge flap, which should be investigated further. Key future work includes testing a wider range of deflections for the flap and a wider range of angles of attack for the main wing. The simulation of the leading edge slat and whether a practical mechanical mechanism can be developed so that if the technology is proven to be effective, it can be applied to aircraft in real flight conditions.

References

- ANSYS. (2019). *Ansys fluent theory guide*. ANSYS, Inc.
- Evans, C., Harmer, M., Marks, O., Tiley, S., Willis, T., Boufferrouk, A., & Yao, Y. (2016). Development and testing of a variable camber morphing wing mechanism. In *International symposium of sustainable aviation (ISSA)*, Istanbul, Turkey, 29 May – 1 June 2016.
- ISO 12001. (1996). *Acoustics – Noise emitted by machinery and equipment – Rules for the drafting and presentation of a noise test code (ISO 12001:1996)*.
- Kamliya Jawahar, H., Alihan Showkat Ali, S., & Azarpeyvand, M. (2021). *Aeroacoustic analysis of slat tones* (pp. 5650–5663(14)). InterNoise21.
- Kimaru, J., & Boufferrouk, A. (2017). Design, manufacture and test of a camber morphing wing using MFC actuated smart rib. In *8th International conference on mechanical & aerospace engineering, Prague, 22–25 July 2017* (pp. 791–796). IEEE.
- Loudon, K., Boufferrouk, A., Coleman, B., Hughes, F., Lewis, B., Parsons, B., Cole, A., & Yao, Y. (2018). Further development of a variable camber morphing mechanism using the direct control airfoil geometry concept. In *International symposium of sustainable aviation*, Rome, Italy, 9–11 July 2018.
- Murayama, M., Nakakita, K., Yamamoto, K., Ura, H., Ito, Y., & Choudhari, M. (2014). Experimental study on slat noise from 30P30N three-element high-lift airfoil at JAXA hard-wall low speed wind tunnel. In *20th AIAA/CEAS aeroacoustics conference*, Atlanta, GA, 16–20 June 2014.
- Peng, T., Yao, Y., & Zhu, Q. (2018). *Slat broadband noise prediction of multi-element 30P30N airfoil by a hybrid RANS-LES method*. Paper presented at 53rd 3AF International Conference on Applied Aerodynamics.
- R. Ilário da Silva, C., Azarpeyvand, M., Alihan Showkat, S., & Kamliya Jawahar, H. (2020). Aerodynamic and aeroacoustic performance of high-lift airfoil fitted with slat cove fillers. *Journal of Sound and Vibration*, 479, 115347.

Modelling of Bird Strike for the Pilot Cabin Window in Side-By-Side-Seated Aircraft



Mustafa Zeki Yilmazoglu and Mehmet Berkay Luleci

Contents

| | | |
|-----|---|-----|
| 1 | Introduction | 300 |
| 2 | Engineering Approach | 300 |
| 3 | Literature Research | 301 |
| 3.1 | Bird Strike Test | 301 |
| 3.2 | Analysis Methods and Selection | 301 |
| 3.3 | Transparent Wood | 302 |
| 4 | Analysis | 302 |
| 4.1 | Preprocess | 302 |
| 4.2 | Post-Process | 305 |
| 5 | Experimental Study of Transparent Wood Production | 309 |
| 5.1 | Delignification of Wood | 310 |
| 5.2 | Chemical Bleaching of Wood | 310 |
| 5.3 | Impregnation of Certain Chemicals into Wood | 311 |
| 5.4 | Drying Process | 312 |
| 6 | Conclusion | 312 |
| | References | 313 |

M. Z. Yilmazoglu (✉)

Gazi University Faculty of Engineering, Department of Mechanical Engineering, Maltepe,
Ankara, Turkiye

e-mail: zekiyilmazoglu@gazi.edu.tr

M. B. Luleci

Turkish Aerospace Headquarter, Fethiye District, Ankara, Turkiye

1 Introduction

With the Second World War, thanks to the development of jet engines, the aircraft's ability to reach high speeds and altitudes made it necessary to have an isolated area inside the aircraft for passengers and pilots. Thus, cockpit window structures began to be developed. The basic expectation from windshield structures is that they are resistant to cracks and breakages that may occur due to internal-external pressure difference, sudden temperature changes, or bird strikes. In this chapter, window and frame structure designs for aircraft in the "community aircraft" status were discussed, and design trials were carried out depending on the geometries of the determined aircraft models. There are standard tests, such as the bird strike test, to test the cockpit window and frame to meet certain standards. In line with the standards, the models designed in CatiaV5R20 were simulated by finite element analysis in ANSYS software and the bird hitting the pilot window. It is thought that a lighter and/or more durable model can be obtained with the changes to be made in the solid model in accordance with the design criteria. Coating a transparent wood material on the glass to increase resistance to bird strikes will be considered as a second case study. Transparent wood is a material that is formed as a result of making the wood transparent after certain chemical processes. According to researches, transparent wood is much more durable and lighter than glass. Besides, the thermal conductivity coefficient is very low. Due to these features, it is expected to have a high potential for use in the aviation industry.

2 Engineering Approach

There are many standards and certificates in aviation as in many sectors. These certificates determine aviation requirements. The Federal Aviation Administration (FAA) has published some of its standards regarding windshields in the Federal Aviation Rules (FAR). According to FAR (Sections 25,775(b) and 25,775(c)), windshields and frames must withstand hitting 4-pound (1.8 kg) birds. While examining the geometry of the windshield, the behavior of the structure was tried to be learned by applying the "bird crash test." The Beechcraft B200 model was used as the windshield geometry. The windshield structure of a B200 work drawn very close to the original is isolated. To better understand the windshield design of the B200 and to make the design more similar to the original, it was desired to examine the Beechcraft B200 aircraft. The Beechcraft B200 aircraft, which is in the inventory of the General Directorate of Maps of the Ministry of National Defence, was examined at the Land Aviation Command in line with the permissions obtained. The right windshield piece, which became unusable due to a crack, was donated by the Land Aviation Command for the project. The model dimensions have been updated according to the values obtained as a result of the measurements of the three-dimensional model.

3 Literature Research

3.1 *Bird Strike Test*

One of the biggest problems faced by airplanes in today's aviation industry is bird strikes. As a result of this situation, many accidents occur with loss of material, sometimes even life. With the development of the aviation industry, the time for aircraft to be noticed by birds is significantly reduced due to their increasing speed and decreasing noise. The purpose of bird strike analysis is to learn the designs of glass and frame structures better and to reveal a more durable structure depending on the design parameters. The majority of aircraft and bird strikes occur near airports when aircraft take-off or landing (when the aircraft is traveling at 150 knots) position. These strikes usually occur at the front of aircraft and in areas where the aircraft's jet engines are located. The situation studied is the scenario where the bird hits the windshield structure. Because it would be financially costly to see the effects of bird strikes, operating in a test environment, these effects require advanced engineering software in a computer environment. After the design made according to the results obtained is approved, the prototype stage is started, and the scenario simulated in the computer environment is also applied in real life. Thus, prototype costs and time spent are significantly minimized.

3.2 *Analysis Methods and Selection*

There are many finite element analysis methods for numerical modelling with problematic bird strikes. Lagrange method, Euler method, ALE method, and smoothed particle hydrodynamics method are some of them. The Lagrange method works with nodes. In this method, the nodes move with the material. This method is an excellent analysis method for solids (Gülcan, 2019). Niering used this method to simulate bird strikes on the engine fan blades (Niering, 1990). Euler's method is mostly used in the analysis of fluid bodies. In the Euler method, the nodes forming the network are fixed in space. In this solution network, material points are progressing. The Euler method gives good results in large-scale deformation problems, as the mesh includes both the existing material and the regions; it will be in the next time step. However, since the bird strike problem includes both solid and fluid problems, the Euler method alone cannot give the desired results. The ALE method is a mixture of the Lagrange and Euler methods. The solution network can act in this method when necessary. Hanssen et al. reported that the ALE method was consistent with the experimental results (Hanssen et al., 2006). The SPH method is a method without nodes. SPH method is preferred for problems in which very serious deformations occur after impact. Unlike classical finite elements, particle structure is used in SPH method, not network structure (Riccio et al., 2018). Among these methods, the SPH method was chosen for the analyses.

3.3 *Transparent Wood*

The studies carried out in the last 5–6 years are about giving a new mission to wood, which has been used as a building material throughout history. This mission is to make wood transparent due to its strength and thermal resistance. Cellulose and hemicellulose are optically colorless, while lignin is dark in color and has an extremely complex structure (Yano et al., 2005). The starting point of the production of transparent wood is to separate the lignin, which gives the dark color and opaque feature to the wood, from the wood as a result of some chemical processes and to impregnate the wood with the right chemical/s not to damage the mechanical properties of the wood. In the study of Fink et al., it was shown that it is possible to produce transparent wood by chemical bleaching followed by the incorporation of the polymer (Fink, 1992). After these processes, the wood material is made transparent by heat treatment. Transparent wood has much better mechanical properties compared to natural wood, and its thermal conductivity coefficient is much lower. This natural composite material stands out with its lightness.

4 Analysis

Bird strike analysis is essentially a collision analysis and is studied under open dynamics due to a collision time of less than 1 s. There are several software programs that calculate these states, such as LS-DYNA, PAM-CRASH, ABAQUS, PW/WHAM, MSC/Dytran, DYNA3D, and PAM-SHOC. In this study, analyses were performed in ANSYS-LS DYNA.

4.1 *Preprocess*

4.1.1 *Modelling the Bird Model*

The IBRG (International Biodegradation Research Group) has set standards for bird models to be used in impact tests and has proposed three different models by measuring the biometric characteristics of real birds. These are flat-end cylinder, hemispherical-end cylinder, and ellipsoid. To fix the weight of the bird geometry as 1.8 kg in the calculations, the flat-ended cylinder model was chosen from the suggested geometries. Bird geometry measurements were determined according to formulas used (Marulo & Guida, 2014).

$$D = \sqrt[3]{(2W/\pi\rho)} \quad (1)$$

Fig. 1 Model geometry of bird

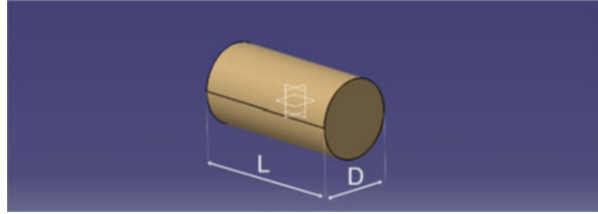


Table 1 Material properties of bird

| | |
|--------------------------|------|
| Gruneisen coefficient | 0.28 |
| Parameter C1 (m/s) | 1480 |
| Parameter S1 | 1.92 |
| Parameter quadratic S2 | 0 |
| Maximum tensile pressure | 0 |

$$L = 2D \tag{2}$$

According to FAA requirements, the weight of the bird is $W = 1.8$ kg. Since the bird was modelled according to the SPH method, its density is found to be $\rho = 950$ kg/m³ due to the void between the particles. As a result of these processes, the diameter and length of the cylinder are $D = 0.106$ m and $L = 0.212$ m, respectively (Fig. 1).

4.1.2 Modelling of Bird Material

The bird strike problem can be solved with an analogy of the pressure fluid problem, and fluid laws can be used in bird models to be used in the analysis. The hydrodynamic response of the bird substitute fluid is modelled using equations of state. The Mie-Grüneisen equation of state was used to model the bird material (Table 1).

4.1.3 Windshield Model Geometries

The windshield structure can be examined under two main headings. These are lath-frame and glass structures. The slats and frames are the skeletal system of the windshield structure. With a simple logic, since the loads on the structure are divided by the number of laths, the number of laths is directly proportional to the durability. However, the lath design and the number of laths must be designed and determined appropriately. It is extremely important to the safety of flight because of its potential to obstruct the view. The geometry of the windshield of the reviewed Beechcraft B200 is divided in the middle by a single lath. Since the number of slats here is a design parameter for us, dynamic analyses have also been carried out on windshield structures with and without slats. These are sized to B200 model dimensions to keep the remaining design parameters constant. The Gulf G-500-inspired design is used

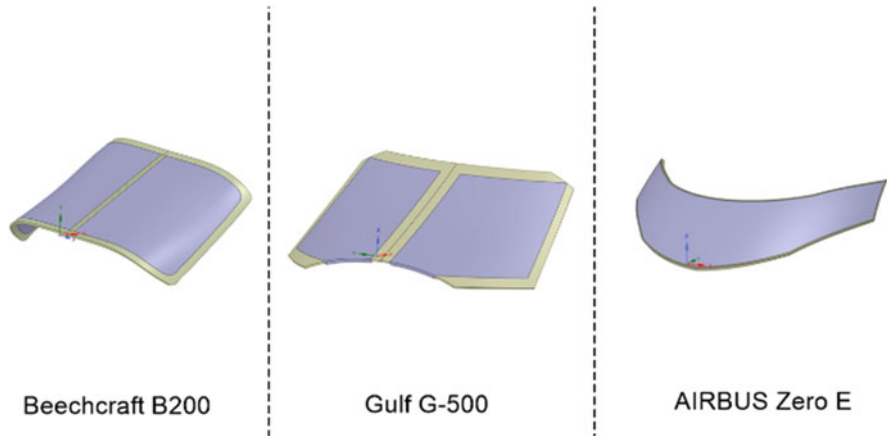


Fig. 2 Windshield geometries

Table 2 Mechanical properties of glass and Al-5083 H-166

| | Glass | AL5083-H166 |
|---|-------|-------------|
| Density ($\text{kg}\cdot\text{m}^{-3}$) | 1186 | 2700 |
| Elastic modulus (GPa) | 3.2 | |
| Tangent modulus (MPa) | 230 | |
| Poisson's ratio | 0.4 | 0.3 |
| Yield strength (MPa) | 68 | |
| Ultimate strength (MPa) | 78 | |
| Failure strain | 0.067 | |
| Bulk modulus (MPa) | | 58,330 |
| Initial yield stress (MPa) | | 167 |
| Shear modulus (MPa) | | 26,920 |

for the multi-slat model geometry, and the Airbus Zero E model-inspired design is used for the slatless model geometry. In the designs, the frame thickness is 11 mm and the glass thickness is 20.8 mm (Fig. 2).

4.1.4 Modelling of Windshield Material

Aluminum alloys are generally used in the lath and frame structures of aircraft. According to market research, aluminum 5000 and 7000 series alloys are widely used in aircraft. In this study, properties of Al5083-H116 alloy were used. The mechanical properties of Al5083-H166 are taken from the work of Sharma and Sharma (2014) (Table 2).

4.2 Post-Process

Since the deformation of the glass in case the bird strike, the stiffness behavior of the glass material is assumed to be flexible. The connections between the glass and the frame are also defined as friction, and the friction coefficient is assumed to be a very high value, such as 0.95, and the dynamic coefficient is given as 0.6. Fixed support is defined for the surfaces of the frame. Thus, different velocity values are defined for the bird geometry and the deformation scenarios that would occur in the glass are analyzed. A linear network structure is used. Due to the SPH method, a particle mesh is assigned to the bird geometry at 5-mm intervals. Quadratic elements are used as much as possible in frame and glass structures. To ensure the freedom of the results from mesh number, different mesh numbers are considered for the analysis. The velocity of the bird geometry is defined 64.4 m/s (Dar et al., 2013). The resulting deformations were compared with the study of Dar et al., and it is concluded that the values are in good agreement.

4.2.1 Analysis Results Based on Geometries

As stated above, three different explicit analyses were carried out in this study, where the design parameter is the number of laths. Model geometries used are models inspired by Beechcraft B200, Gulf G-500, and Airbus Zero E models. The maximum deformations of three different models are shown in the graphs below. As can be seen from the figures, the deformations of the multi-slat and non-slatted model are very close to each other. This is due to the geometry difference between the models. It was concluded that geometries with flat lines are more durable than geometries with sharp lines (Figs. 3, 4, 5, and 6).

Based on these results, new designs are conducted by considering the flat geometry design. In these design trials, deformations depending on the number of laths are investigated in parallel with the previous analyzes (Figs. 7, 8, and 9).

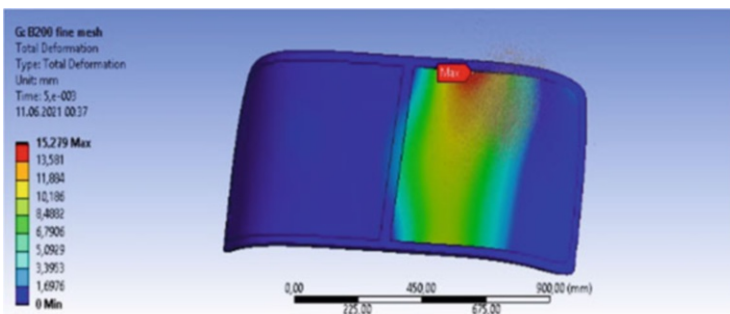


Fig. 3 Total deformation of the Beechcraft B200

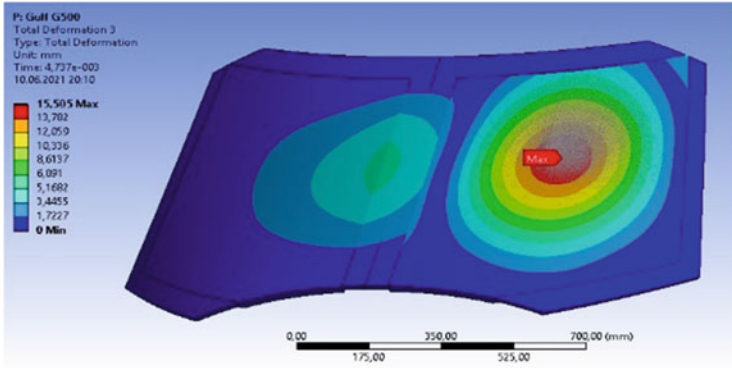


Fig. 4 Total deformation of the Gulf G-500

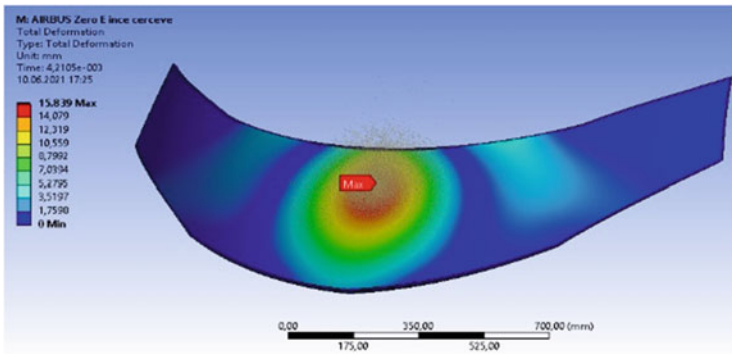


Fig. 5 Total deformation of the AIRBUS Zero E

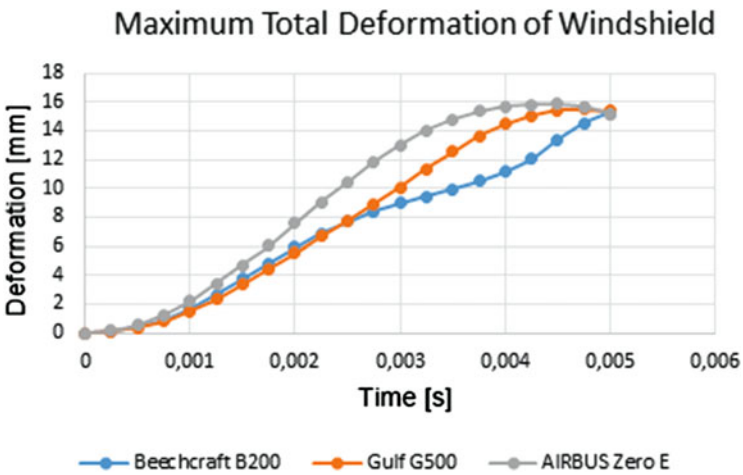


Fig. 6 Maximum total deformation of windshield

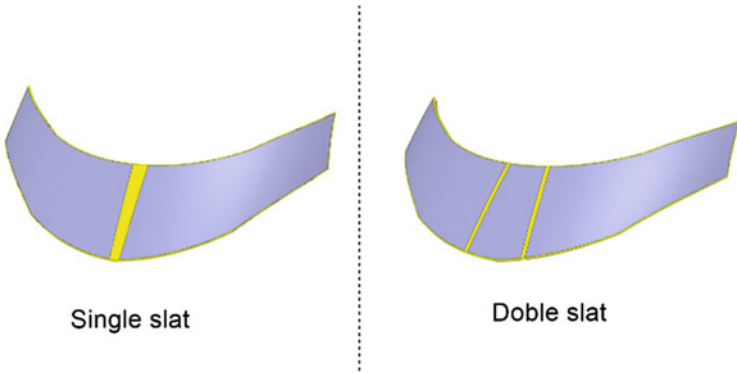


Fig. 7 New designs

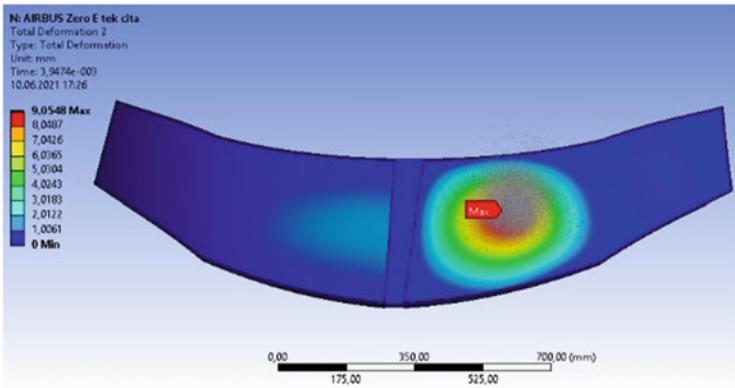


Fig. 8 Single-slate design

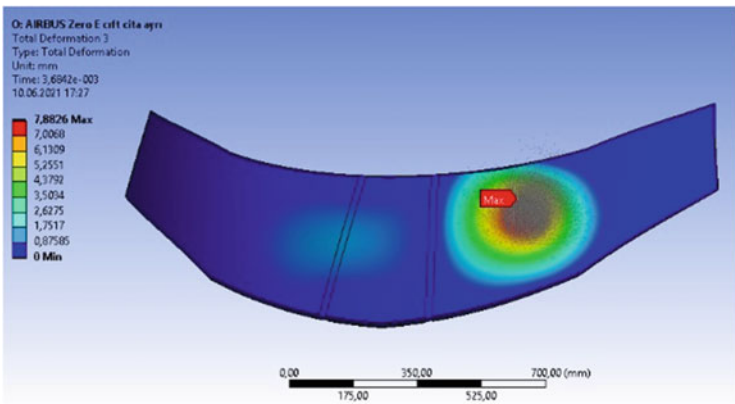


Fig. 9 Double-slate design

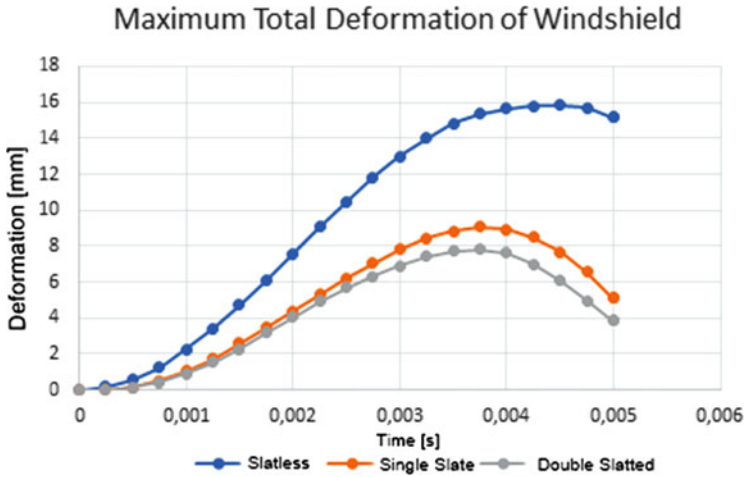


Fig. 10 Maximum total deformation of windshield

According to the results obtained, it is concluded that the maximum total deformation decreased as the number of laths increased in this geometry. Obtained deformation results are given in Fig. 10.

4.2.2 Transparent Wood Integration for Cockpit Windshield

According to the researches, transparent wood material has a high potential for use in the aviation industry, thanks to its excellent mechanical properties, low thermal conductivity, and light weight. In this study, the place of use is to place it as an external layer on the cockpit glass, to provide less damage to the glass. In the analysis, natural wood is defined in the same dimensions on the glass structure, and bird strike analysis is repeated. The mechanical properties of the wood are taken from the study of Wood handbook: wood as an engineering material (Green et al., 1999).

According to the analysis results, the deformation of the model with 3-mm wood veneer is less than the deformation of the model without wood veneer (Fig. 11). It is thought that if linden wood, which is defined as a covering material, is used as transparent wood, the deformation that will occur in the glass will be reduced even more.

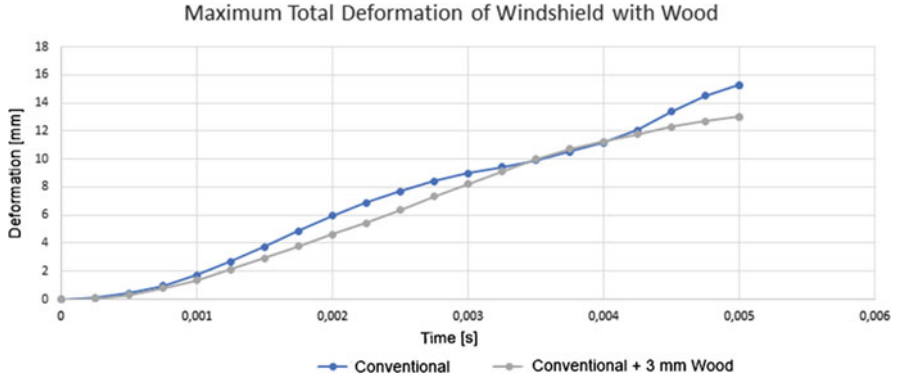


Fig. 11 Maximum deformation on wood-covered and non-wood-covered windshields

Fig. 12 A piece of balsa wood 50 mm × 50 mm



5 Experimental Study of Transparent Wood Production

Transparent wood production basically consists of four processes. Those are delignification of wood, chemical bleaching of wood, impregnation of certain chemicals into wood, and drying of wood. In these studies, 50 mm × 50 mm balsa is used as wood material. The thickness of the wooden plate is 2 mm (Fig. 12).

5.1 Delignification of Wood

The process of removing lignin from the wood is called delignification. Delignification was performed using NaOH, Na₂SO₃, and H₂O₂ in the study by Zhu et al. In this process, NaOH and Na₂SO₃ are used to dissolve most of the lignin. Wooden pieces cut in a certain order and thickness are placed in these solutions and boiled. The duration of this process varies according to the thickness of the wooden plate. As the thickness increases, the duration of this process also increases. Delignification takes 12 h. Then, three times rinsing with deionized hot water is carried out to purify the wooden plate from the solutions in which it is immersed (Fig. 13).

5.2 Chemical Bleaching of Wood

The second process is known as chemical bleaching. To remove the remaining lignin on the wood plate, the wood plate is soaked in H₂O₂ solution. In this process, without mixing, the wooden plate is kept in a boiling state until it turns milky white. As soon as the yellow color of the wood plate appears to have disappeared, the samples are removed from the solution and rinsed with cold deionized water. Thus, the lignin in the wood is eliminated.

The delignified wooden plate is kept in ethanol until it is passed to the next process. In the experiment of Zhu et al., sodium hydroxide solution (NaOH) was prepared as 2.5 molar, sodium sulfide solution (Na₂SO₃) 0.4 molar, and hydrogen peroxide solution (H₂O₂) 2.5 molar (Figs. 14 and 15).

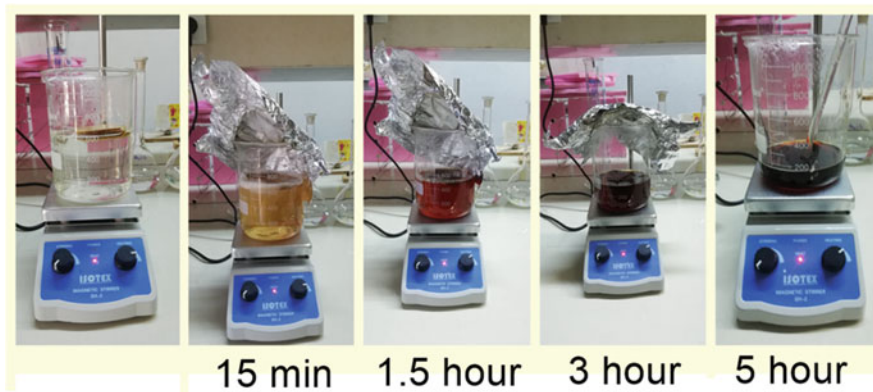


Fig. 13 Delignification process

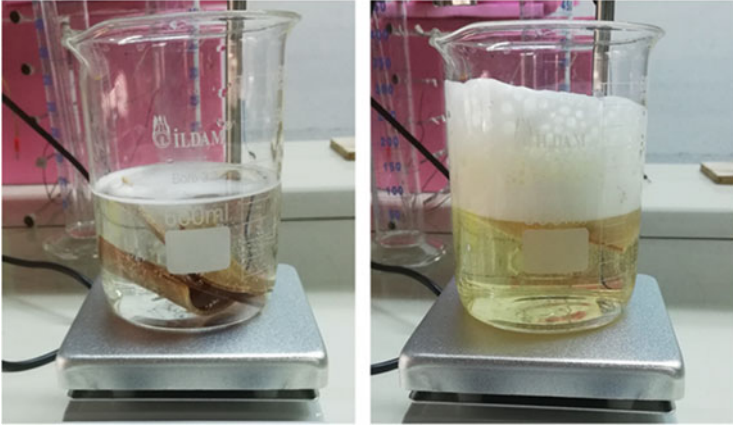


Fig. 14 Chemical bleaching process

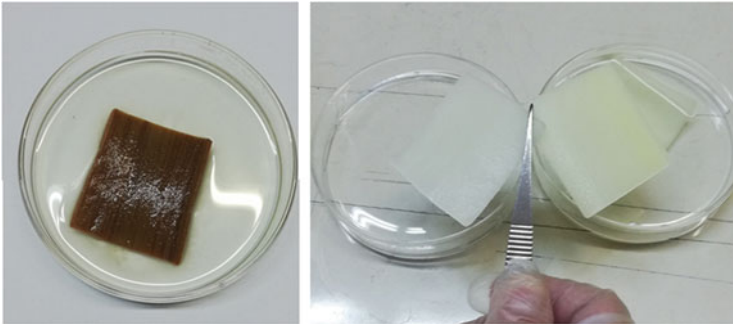


Fig. 15 Before after compare between chemical bleaching process

5.3 Impregnation of Certain Chemicals into Wood

The milky white wood, which is separated from the lignin in it, passes into the impregnation stage. Impregnation is the process of impregnating the wood with various chemical substances with different methods. With this process, it is aimed to increase the service life of the wood by protecting the wood from pests such as fungi, insects, and maggots. The role of impregnation in the production of transparent wood is to provide the material with both transparent properties and increase its mechanical properties by feeding the cavities of the ligninized wood plate with colorless epoxy resin and hardener (Zhu et al., 2016). In the study Zhu et al. used #300 epoxy resin and #21 cycloaliphatic hardener of the Aeromarine brand. These substances are mixed in a ratio of two to one and poured into the delignified wood. Li et al. performed the impregnation process using methyl methacrylate in their study (Li et al., 2017). In this study, impregnation will be done by using both materials, and the differences between them will be examined. To remove the gaseous ethanol

inside the wood plate and to allow the epoxy hardener mixture to penetrate the wood plate better, the wood plate is left in a vacuum environment (Xu et al., 2012). In the study of Zhu et al., the vacuum environment was set to 200 Pa. Vacuum is applied to the perforated wooden plate on which the epoxy-hardener mixture is poured in the petri dish in 5-min periods. After 5 min of vacuum, the valves of the vacuum chamber are opened, and the ethanol gases inside the wooden plate are discharged. This process is repeated three to four times in a row.

5.4 Drying Process

The purpose of this process is to ensure that the wooden boards whose impregnation process is finished dry and become transparent by heat treatment. Zhu et al. applied a drying at 30 °C for 12 h. It is known that different temperatures and application times are different in different studies.

6 Conclusion

In this study, the glass and frame structures of a few aircraft with community aircraft status are structurally examined. In line with the developed engineering approach, a new design was put forward based on the bird strike test results. Bird geometry is modelled using the SPH method. ANSYS-LS DYNA is used for the explicit analysis solution. According to the results obtained, it is concluded that flat geometries gave better results than sharp geometries. In addition, it was deduced that the deformation of the glass is inversely proportional to the number of laths. Since the number, shape, and position of the slats can affect the viewing angle negatively, it is beneficial to create them according to requirements. Besides, the case of using a different structure according to the results obtained with the TRIZ approach is also discussed. This structure is thought of as transparent wood. In order to better analyze the optical and mechanical properties of the transparent wood material, production experiments of the material have been carried out. In line with the studies carried out, a low percentage of transparency has been added to a wooden plate of determined dimensions, and studies in this direction continue.

Acknowledgments This study was supported by TUSAŞ Lift Up Program and Gazi University Scientific Research Projects FHD-2021-7099 projects.

References

- Dar, U. A., Zhang, W., & Xu, Y. (2013). FE analysis of dynamic response of aircraft windshield against bird impact. *International Journal of Aerospace Engineering*, 2013, 171768.
- Fink, S. (1992). Transparent wood – A new approach in the functional study of wood structure. *Holzforschung*, 46, 403–408.
- Green, D. W., Winandy, J. E., & Kretschmann, D. E. (1999). Mechanical properties of wood. In *Wood handbook: wood as an engineering material*. Forest Products Laboratory.
- Gülcan, O. (2019). Kuş Çarpmaları ve Uçaklara Etkileri Üzerine Bir Gözden Geçirme Çalışması. *Mühendis ve Makina*, 60(696), 192–220.
- Hanssen, A. G., Girard, Y., Olovsson, L., Berstad, T., & Langseth, M. (2006). A numerical model for bird strike of aluminium foam-based sandwich panels. *International Journal of Impact Engineering*, 32(7), 1127–1144.
- Li, Y., Fu, Q., Rojas, R., Yan, M., Lawoko, M., & Berglund, L. (2017). Lignin-retaining transparent wood. *ChemSusChem*, 10(17), 3445.
- Marulo, F., & Guida, M. (2014). Design criteria for birdstrike damage on windshield. *Advances in Aircraft and Spacecraft Science*, 1(2), 233.
- Niering, E. (1990). Simulation of bird strikes on turbine engines. *Journal of Engineering for Gas Turbines and Power*, 112, 573–578.
- Riccio, A., Cristiano, R., Saputo, S., & Sellitto, A. (2018). Numerical methodologies for simulating bird-strike on composite wings. *Composite Structures*, 202, 590–602.
- Sharma, R., & Sharma, S. (2014). Birdstrike simulation of an aircraft wing. *International Journal of Aerospace and Mechanical Engineering*, 1, 1–5.
- Xu, J., Zhai, C., Zheng, B., Li, H., Zhu, M., & Chen, Y. (2012). Large efficiency improvement in nanoporous dye-sensitized solar cells via vacuum assistant dye adsorption. *Vacuum*, 86(8), 1161–1164.
- Yano, H., Sugiyama, J., Nakagaito, A. N., Nogi, M., Matsuura, T., Hikita, M., & Handa, K. (2005). Optically transparent composites reinforced with networks of bacterial nanofibers. *Advanced Materials*, 17(2), 153–155.
- Zhu, M., Song, J., Li, T., Gong, A., Wang, Y., Dai, J., et al. (2016). Highly anisotropic, highly transparent wood composites. *Advanced Materials*, 28(26), 5181–5187.

Impact of Covid-19 on Air Traveler Behavior



Volkan Yavas and Rustem Baris Yesilay

Contents

| | | |
|---|------------------------------|-----|
| 1 | Introduction | 315 |
| 2 | Method | 317 |
| 3 | Results and Discussion | 317 |
| 4 | Conclusion | 320 |
| | References | 320 |

1 Introduction

The aviation industry, which had to struggle with various events, such as economic crises, terrorist incidents, and wars throughout its history, has also taken its share from epidemics. In addition to being one of the most important factors in the global spread of epidemics, it is also known that it is one of the sectors most negatively affected by the consequences of these epidemics. With the Covid-19 pandemic, the aviation industry has experienced approximately 50% seat supply, 3 million passenger loss, in 2020 compared to the previous year. It has lost \$400 billion in potential passenger revenue, and the most striking change has been a 60% drop in passenger numbers (ICAO, 2021).

The aviation industry has not been exposed to such a big impact, except for the world wars. The effects of Sars, 2003, or September 11 events, which the sector struggled with in previous periods, took place in a more limited geography and in a more limited period. Due to the Covid-19 pandemic, the industry has been exposed to a very long-lasting and devastating effect globally. And it is stated that the

V. Yavas · R. B. Yesilay (✉)

Ege University Aviation Higher Vocational School, Izmir, Turkiye

e-mail: volkan.yavas@ege.edu.tr; rustem.baris.yesilay@ege.edu.tr

estimated time for the sector to return to 2019 levels is 2023–2025 (Garrow & Lurkin, 2020).

In the normalization process of aviation, besides health-related measures and travel restrictions, regaining passenger confidence is critical. According to the research conducted by the International Air Transport Association (IATA) in 11 countries on passenger confidence in 2020, only about 25% of the passengers state that they can return to their flights immediately, while the majority reveals their uneasiness (IATA Economics, 2020). Apart from such external factors in the aviation sector, there are legal, technical, operational, etc. obstacles to normalization. In addition to these obstacles, it should be taken into account that there are some hidden psychological and sociological effects.

A study on passenger behavior in the field of tourism after the H1N1 virus in 2012 revealed that tourists can continue to travel if they know the mask, distance, and hygiene rules and believe that those rules are for their protection. However, it was mentioned that both airline companies and airports should take more health and hygiene practices/interventions on behalf of passengers rather than personal precautions (Lee et al., 2012, p. 96).

In a similar study investigating the effects of epidemic diseases such as swine flu and H1N1 on travel in 2013, it was found that the behavior changes of passengers and the pandemic affect each other, and it is stated that passengers think that the most cost-effective way to protect themselves from the pandemic is to isolate themselves; it is also emphasized that the behavioral changes of the passengers are observed more intensely in the beginning days of the pandemics (Fenichel et al., 2013, p. 9). The study also states that ending/reducing air travel is an initiative that has much lower-than-anticipated benefits on pandemics and their spread.

Brugger (2020) mentioned that there is a need for clear answers about the procedures to be applied, as well as the concerns of the passengers about the risk of Covid-19 contamination, and the importance of following a correct communication path with the cooperation of all industry stakeholders by understanding and trusting the passenger for the solution. As in the rest of the world, some passengers highlight their health concerns, while others highlight the negative aspects of their living standards. According to the results of a study shared by IATA, 68% of passengers state that travel restrictions negatively affect their quality of life, 84% will avoid traveling if there is a possibility of quarantine, and 57% will return to travel in less than 2 months (IATA, 2021).

Although the risk in air transportation is low or similar to an ordinary indoor area. It is emphasized in the studies that air transport has an effect on the 2002–2003 SARS, 2009 influenza A/H1N1, and 2012 MERS outbreaks. In addition, while it is stated that it may have an impact on future epidemics, it is emphasized that it is possible to prevent this effect with the successful cooperation of all stakeholders, from air transport passengers to airlines, from aircraft manufacturers to authorities (Kulczyński et al., 2017, p. 133).

In this symposium paper, as seen in similar examples in the literature, the effect of epidemic diseases on passenger behavior constitutes the research question. In the period called “normalization” after Covid-19, passengers’ thoughts about their

health and their attitudes to use the airline were investigated in Turkey. For this purpose, a field study was conducted, and data were collected using a scale (1–5) to evaluate the changing passenger behaviors during and after the Covid-19 period. It is thought that this study on the effect of Covid-19 on passenger behavior will be one of the pioneering studies as it will reveal the effect of epidemics, which is one of the factors affecting consumer behavior in the aviation industry.

2 Method

Field research method was used in the study, and data were collected with a questionnaire with the intention of getting the opinions of individuals in Turkey about traveling by plane after Covid-19. In this context, the sample of the study is all individuals who live in Turkey and have the potential to choose the plane while traveling after Covid-19. The draft questionnaire was filled by three faculty members with the intention of preliminary evaluation, and the questionnaire was finalized in line with their suggestions and criticisms. The questionnaire developed for this research was applied online between April and May 2021. Since there was no face-to-face answer collection opportunity within the scope of the Covid-19 pandemic and measures, the answers were collected through the “Online Form” created in MS Office 365 program. Five hundred six of the individuals accessed by non-probability sampling methods, “easy sampling” and “snowball sampling,” answered the questionnaire.

The questionnaire used in the research consisted of questions based on a Likert-type scale, which are frequently used in many fields such as social sciences and education (Turan et al., 2015), containing multiple options, and prioritized and “ordered” questions, since their coding and measurement are relatively easy. In questions based on the Likert scale, “1” represents the negative end, while “5” represents the positive end. In the questionnaire, there are questions such as age, gender, education level, and monthly household income to collect descriptive data for the respondents. Answer 3 was taken as the indifference value. It is assumed that any value below 3 in the questionnaire is negative, and scores above 3 are positive. The following questions were prepared to evaluate the Covid-19 risk perceptions and their intention to travel by plane of the individuals participating in the survey. Data were analyzed with the SPSS v25 program, descriptive statistics were obtained, and cross tables were created.

3 Results and Discussion

Before moving on to the findings of the research, it will be important to convey the participant characteristics. To summarize, 55.5% of the participants are between the ages of 22 and 41, that is, Y generation members. While an equal distribution is

Table 1 Transportation options in terms of Covid-19 contamination risk

| If you have to travel under pandemic conditions, can you rank the following transport options "in accordance with Covid-19 contamination risk"? (%) | | | | | |
|---|-----------------|--------|---------|------|--------|
| | The most unsafe | Unsafe | Neutral | Safe | Safest |
| Public transport | 75.7 | 10.5 | 5.5 | 3.2 | 5.1 |
| Special vehicle | 6.5 | 2.2 | 1.8 | 5.5 | 84.0 |
| Airline | 15.6 | 17.6 | 36.0 | 24.1 | 6.7 |
| Railway | 26.5 | 25.7 | 34.0 | 9.5 | 4.3 |
| Intercity bus | 54.0 | 25.3 | 10.7 | 5.9 | 4.2 |

Table 2 Perception of the contamination risk of Covid-19 while traveling by air by age groups

| There is a contamination risk of Covid-19 while traveling by air | | | | | |
|--|-----------------------|--------------|---------------|-----------|--------------------|
| | Strongly disagree (%) | Disagree (%) | Undecided (%) | Agree (%) | Strongly agree (%) |
| 18–21 | 2.9 | 7.2 | 33.3 | 46.4 | 10.1 |
| 22–41 | 1.4 | 5.7 | 23.1 | 58.7 | 11.0 |
| 42–56 | 2.4 | 13.7 | 21.8 | 49.2 | 12.9 |
| 57+ | – | 9.4 | 21.9 | 56.3 | 12.5 |
| Total | 1.8 | 8.1 | 24.1 | 54.5 | 11.5 |

observed in terms of gender, Bachelor's level stands out in education level. Again, while 43.9% of the participants constitute the majority by having a flight frequency at least once a year, it is seen that the household income shows a relatively equal distribution among the given options, so it does not make an effective difference in the result.

With the question "If you have to travel under pandemic conditions, can you list the following transportation options in terms of Covid-19 Contagion Risk," the survey participants were asked to evaluate the five different transportation options in Table 1, from the safest to the most unsafe.

With the question "I have the risk of contaminating COVID-19 when traveling by air," it was aimed to measure the risk perceptions of the participants of contaminating Covid-19 while traveling by air. It can be stated that with 70.9% as a sum of "agree" and "strongly agree," women have an anxiety level five points higher than the average value of 66%, and men, with 61.4%, have an anxiety level approximately five points lower than the average value.

It is evaluated that the lowest risk perception by age groups is in the "18–21 age group" with the value of 56.5% as the sum of "agree" and "strongly agree." The risk perception of other age groups is 69.8% for 22–41, 62.1% for 42–56, and 68.8% for 57+, and all of them have a higher risk perception compared to the 18–21 age group (Table 2).

Table 3 Perception of the contamination risk of Covid-19 while traveling by air by education level

| There is a contamination risk of Covid-19 while traveling by air | | | | | |
|--|-----------------------|--------------|---------------|-----------|--------------------|
| | Strongly disagree (%) | Disagree (%) | Undecided (%) | Agree (%) | Strongly agree (%) |
| High school | 2.9 | 11.8 | 23.5 | 50.0 | 11.8 |
| Short cycle | 1.4 | 9.6 | 38.4 | 39.7 | 11.0 |
| Undergraduate | 0.7 | 8.4 | 24.5 | 53.8 | 12.5 |
| Graduate | 4.1 | 5.7 | 15.6 | 65.6 | 9.0 |
| Total | 1.8 | 8.1 | 24.1 | 54.5 | 11.5 |

Table 4 Perception of the contamination risk of Covid-19 while traveling by air, according to the frequency of traveling by air

| There is a contamination risk of Covid-19 while traveling by air | | | | | |
|--|-----------------------|--------------|---------------|-----------|--------------------|
| | Strongly disagree (%) | Disagree (%) | Undecided (%) | Agree (%) | Strongly agree (%) |
| At least once a week | – | 25.0 | 12.5 | 37.5 | 25.0 |
| At least once a month | 3.3 | 13.3 | 30.0 | 50.0 | 3.3 |
| At least one time in 3 months | 1.6 | 7.9 | 19.0 | 63.5 | 7.9 |
| At least one time in 6 months | 2.6 | 6.4 | 23.1 | 60.3 | 7.7 |
| At least once a year | 1.4 | 8.6 | 24.3 | 53.2 | 12.6 |
| Rarely | 3.0 | 7.6 | 22.7 | 53.0 | 13.6 |
| Total | 1.8 | 8.1 | 24.1 | 54.5 | 11.5 |

It is seen that the lowest risk perception in terms of education level is in associate degree graduates with 50.7% as the sum of “agree” and “strongly agree” (Table 3). These are followed by high school 61.8%, undergraduate 66.3%, postgraduate 74.6%, and secondary school graduates 100%. Considering that only four participants among the respondents are secondary school graduates, the result obtained here can be neglected, and therefore it can be considered that the risk perception of undergraduate and graduate graduates is high.

According to the frequency of traveling by air, the lowest risk perception is in the group traveling by airline “at least once a month” with 53.3% as the sum of “agree” and “strongly agree,” and those who travel “at least once a week” with 62.5% (Table 4). From these results it can be stated that as the frequency of travel decreases, the rate of risk perception increases.

Finally, when the total household income (monthly) is taken into account, the highest income groups “10,000–14,999 TL” and “15,000+ TL” as the total of “agree” and “strongly agree” are 71.9% and 69.3%, respectively. It is seen that they have the highest risk perception. Risk perception in other income groups is lower by percentage values.

4 Conclusion

As of 2021, the normalization process continues after the pandemic, in which the aviation industry has come to a standstill and seriously took damage, like in many other sectors around the world. Although there are various economic, legal, and political efforts and supports in order for the sector to continue from where it left off in 2019 or to reach a similar point, the biggest obstacle to normalization is the return of demand, namely, consumer behavior. At this point, consumer behavior and attitudes and thoughts toward air transport become decisive. In this study, the attitudes of passenger behaviors during the Covid-19 process were conveyed by considering demographic characteristics. Undoubtedly, although many people around the world are aware of the seriousness and threat of this disease and the aviation sector also carries out the normalization process with various measures, it is very difficult to provide a standard in human behavior, and in parallel, the heterogeneous risk perception of passengers in the Covid-19 process in Turkey appears to be dispersed. Although there is a difference in age, in other words, generation, gender, education level, and household income seem to have different results for the participants in the risk of contracting Covid-19. These results reveal the importance of acting with a thought beyond the standard solution proposals in order to convince passengers or increase their confidence in the normalization process of the aviation industry. It also highlights the need for different applications that can positively change passenger behaviors and even perceptions of airports and other service providers, especially airlines.

There are several limitations in the study. First, due to the pandemic process and the bans implemented within the scope of pandemic measures in Turkey, face-to-face contact could not be achieved with the participants, and the data were obtained from online platforms. On the other hand, even if an airline travel restriction is applied at least once in the participant profile, it is thought that collecting the data before or after any flight at an airport will allow a more effective research. In addition, the findings obtained in quantitative research can be supported by qualitative research methods such as interviews, etc. This will enable us to gather much more realistic data about the period and provide more important clues to the sector.

References

- Brugger, P. (2020). *COVID-19: Restoring passenger confidence amid the crisis*. <https://blog.aci.aero/covid-19-restoring-passenger-confidence-amid-the-crisis/>. Online: 02.05.2021.
- Fenichel, E. P., Kuminoff, N. V., & Chowell, G. (2013). Skip the trip: Air travelers' behavioral responses to pandemic influenza. *PLoS One*, 8(3), e58249.
- Garrow, L., & Lurkin, V. (2021). How COVID-19 is impacting and reshaping the airline industry *Journal of Revenue and Pricing Management*, 20(1), 3–9, <https://doi.org/10.1057/s41272-020-00271-1>

- IATA. (2021). *Air traveler response to COVID-19 an 11-country survey: Wave V*. <https://www.iata.org/contentassets/bc49a433b047432cbbfe77840d218ba9/covid-survey-march2021-briefing.pdf>. Online: 04.05.2021.
- IATA Economics. (2020). *IATA Economics' Chart of the Week: Passenger confidence is fundamental to the recovery in air travel*. <https://www.iata.org/en/iata-repository/publications/economic-reports/Passenger-confidence-is-fundamental-to-the-recovery-in-air-travel/>. Online: 04.05.2021.
- ICAO. (2021). *Effects of novel coronavirus (COVID-19) on civil aviation: Economic impact analysis*. <https://www.icao.int/sustainability/Documents/COVID-19/ICAO%20COVID%202021%2001%2007%20Economic%20Impact.pdf>. Accessed 04.05.2021.
- Kulczyński, M., Tomaszewski, M., Łuniewski, M., & Olender, A. (2017). Air transport and the spread of infectious diseases. *World Scientific News*, 76, 123–135.
- Lee, C. K., Song, H. J., Bendle, L. J., Kim, M. J., & Han, H. (2012). The impact of non-pharmaceutical interventions for 2009 H1N1 influenza on travel intentions: A model of goal-directed behavior. *Tourism Management*, 33(1), 89–99.
- Turan, İ., Şimşek, Ü., & Aslan, H. (2015). Eğitim Araştırmalarında Likert Ölçeği ve Likert-Tipi Soruların Kullanımı ve Analizi. *Sakarya Üniversitesi Eğitim Fakültesi Dergisi*, (30), 186–203.

The Feasibility of Hydrogen Fuel Cells as a Solution Toward Zero Emissions in General Aviation Aircraft



Jonathan Charman and Abdessalem Boufferrouk

Contents

| | | |
|-----|---|-----|
| 1 | Introduction | 324 |
| 2 | Method | 324 |
| 2.1 | PEMFC Model | 325 |
| 2.2 | Mass of the Cessna 172 | 326 |
| 2.3 | Finalizing the Model | 326 |
| 3 | Results and Discussion | 326 |
| 3.1 | Like for Like Cessna Scenario | 327 |
| 3.2 | One-Pilot Scenario | 327 |
| 3.3 | The Increase of Mass for Fuel Tanks | 328 |
| 4 | Conclusion | 329 |
| | References | 330 |

Nomenclature

| | |
|------------------|--|
| A | Coefficient of Tafel equation |
| B | Coefficient for mass transport voltage loss |
| CH ₄ | Methane |
| E | Voltage before losses (V) |
| F | Faraday's constant (96485 C) |
| \overline{h}_f | Enthalpy of formation per mole |
| i | Current density (mA.cm ⁻³) |
| i_0 | Exchange current density at electrode (mA.cm ⁻³) |
| i_l | Limiting current density (mA.cm ⁻³) |
| i_n | Internal current density (mA.cm ⁻³) |

J. Charman (✉) · A. Boufferrouk
University of the West of England, Frenchay Campus, Bristol, UK
e-mail: abdessalem.boufferrouk@uwe.ac.uk

| | |
|-------------|---|
| n | Number of electrons |
| p_x | Pressure with respect to x , such as H_2O |
| R | Universal gas constant ($8.314 \text{ J.K}^{-1}.\text{mol}^{-1}$) |
| r | Area specific resistance ($\Omega.\text{cm}^{-3}$) |
| \bar{s}_f | Entropy of formation per mole |
| T | Temperature in kelvin (K) |
| V | Voltage (V) |

1 Introduction

From 1880 to 2012, the average global temperature has risen by $0.85 \text{ }^\circ\text{C}$ (IPCC, 2013) due to greenhouse emissions, and by 2100, it is predicted to have risen by $1.5 \text{ }^\circ\text{C}$ (IPCC, 2018). Although these emissions are heavily identified in relation to the amount of carbon dioxide (CO_2) produced and released into the atmosphere, it is not the only contributing factor. Tackling these emissions requires short-term and long-term solutions, but what if we can just remove emissions completely?

Recently, the UK government introduced a bill to achieve net-zero carbon emissions by 2050 (UNFCCC, 2021). The aerospace sector is a key area for such a target. Recent aerospace technologies researched include fully electric and hybrid aircraft (Xie et al., 2021), morphing wings (e.g., Kimaru and Bouferrouk (2017), Evans et al. (2016), and Loudon et al. (2018)), and green hydrogen either as a standalone fuel or when used in fuel cells (Kadyk et al., 2019). The aim of this chapter is to provide quantifiable data looking into the feasibility of replacing current propulsion techniques with hydrogen fuel cells (HFCs) on current general aviation short-range aircraft. The potential and limitations of HFCs will be identified so that a clear picture can be presented in the context of general aviation industry in its pursuit of zero-emission target. It is crucial to highlight that this study does not include design considerations but to gauge a reasonable approximation of HFC functions on a general aviation aircraft.

2 Method

The full description of the mathematical model has already been explained by many researchers and in a greater depth than what can be covered here. Suffice to say, Eqs. (1) and (2) sum up these characteristics, voltage losses, effect of pressure, and also temperature. A more thorough investigation of this model is presented in the textbooks by Larmine and Dicks (2000) and Barbir (2013).

$$E = \left(\frac{\Delta \bar{h}_f}{nF} - \frac{T \Delta \bar{s}_f}{nF} \right) + \frac{RT}{nF} \ln \left(\frac{p_{H_2} p_{airO_2}^{1/2}}{p_{H_2O}} \right) \quad (1)$$

$$V = E - (i + i_n)r - A \ln\left(\frac{i + i_n}{i_0}\right) + B \ln\left(1 - \frac{i + i_n}{i_1}\right) \tag{2}$$

The aircraft modelled for the simulation was the Cessna 172—a popular short-range aircraft, first produced in 1956 and still produced today (Dowling, 2017). It was assumed that valid and meaningful data would already be present in terms of pilot operating handbooks (POH) and other information to use in the model.

The simulation itself was developed using Simulink with integrated MATLAB functions to allow quick analysis and ease of visualizing the developed model. To ensure all tests were comparable to the original Cessna 172, a maximum flight time was developed from the Cessna 172 (POH, 1978), allowing the model to compare the same journey of the conventional Cessna 172 aircraft under different conditions.

The Simulink model itself had two major components to model, the PEMFC and the mass of the Cessna 172. In addition, three different types of hydrogen were used. These were hydrogen gas at 350 bar, hydrogen gas at 700 bar, and liquid hydrogen at 5 bar.

2.1 PEMFC Model

The assumptions made for the PEMFC need to be addressed. Due to COVID-19 restrictions, lab work for developing a small-scale prototype was not possible. Instead, values were assumed from literature including real-case scenarios used in practice. The assumptions are summarized in Table 1.

With these values and Eqs. (1) and (2), the voltage could be obtained for the PEMFC for the three types of fuel conditions. The challenging parts of the PEMFC model was the fact that the current density, i , is not constant and, in this case, can be

Table 1 Assumptions used for the PEMFC model

| Parameter | Assumed value | Justification |
|---------------------------------|------------------------------------|---|
| Operating temperature | 353 kelvin (K) | PEMFCs are usually operated between 323 and 393 K (Larmin & Dicks, 2000) |
| FC individual cell mass | 0.102 kg | From breaking down the Toyota Mirai HFC stack (Kane, 2014) |
| Limiting current, i_1 | 1000 mA.cm ⁻³ | Typical value given (Larmin & Dicks, 2000) |
| Internal current density, i_n | 3 mA.cm ⁻³ | Typical losses experienced (Larmin & Dicks, 2000) |
| Fuel consumption rate | 0.8 Nm ³ /1 kW produced | Value produced by Air Liquide (Air Liquide, 2021) |
| Pressure of the reactants | Pressure is constant | Since no physical model can be produced, it is reasonable to assume no losses |
| Oxygen partial pressure | 0.21 | Percentage of oxygen in the air |

between 0 and $996 \text{ mA}\cdot\text{cm}^{-3}$. A graph showing the trend as i increased was produced, and a reasonable value around 60% was taken, giving a value of $500 \text{ mA}\cdot\text{cm}^{-3}$.

2.2 *Mass of the Cessna 172*

Concerning the mass of the modified Cessna 172 with PEMFC installed, a number of considerations were required. The Cessna 172 uses a Lycoming 160-bhp engine (POH, 1978), this was swapped out for an electric motor of 120 kW under the assumption that one could simply swap the engines and observe the mass change. The new mass of the electric motor was 63.5 kg, based on Fehrenbacher et al. (2011).

It was also assumed that two PEMFCs would be used since normal operating power is between 1 and 100 kW. The mass from the storage tanks was the most challenging. There has been lots of research done involving storing hydrogen in its gaseous state at both 350 and 700 bar. For both pressures, the worst-case scenario was assumed to be 6% which was the world-leading percentage in 2014 (Toyota, 2017, 2021). For the best-case scenario, 13% was chosen as this was the highest value found that was achieved (Mitlitsky et al., 2000). For the likely cases, hydrogen at 350 bar, 11.3% was chosen (Mitlitsky et al., 2000); then for hydrogen at 700 bar, an average between the best and worst cases was used, producing a value of 9%. There was a major challenge in trying to find mass percentages for liquid hydrogen storage, so only one case was simulated, at approximately 6% (Michel et al., 2006).

2.3 *Finalizing the Model*

With all the assumptions and modifications accounted for, the Simulink model was then finalized. The model was validated (not shown) using existing data from other HFCs, e.g., using hydrogen at 700 bar. Bosch HFCs produced 120 kW from a stack of 400 cells (Bosch, 2021) and the Toyota Mirai produced 113 kW from 370 cells for version 1 (Toyota, 2017) and 128 kW from 330 cells for version 2 (Kane, 2014). The simulation produced 120 kW from 362 cells which is within the expected range.

3 **Results and Discussion**

The simulation produced two sets of results under two carefully designed scenarios. The first scenario compared the original Cessna 172 model with the modified PEMFC Cessna 172 and allowed direct comparison to highlight the major

differences and benefits. The second scenario involved a singular pilot flying the aircraft and removing “dead weight” including unused seats. This gave a different perspective from the first scenario and showed the capabilities of HFCs when compromise is considered.

3.1 Like for Like Cessna Scenario

The first test scenario involved direct comparison of the original Cessna 172 and the modified PEMFC-powered Cessna. Table 2 summarizes these findings.

The test aircraft only used 25 kg of hydrogen compared to the original, demonstrating that a reduction by nearly 75% was achievable. However, the overall mass of aircraft has increased, ranging from 7% to just over 32% from the best case to the worst case, respectively. Since all the scenarios showed an increase in mass, the aircraft would not be able to fly since the maximum take-off weight (MTOW) of the Cessna 172 is 1043 kg for the 160-bhp/120-kW model (POH, 1978). It goes to show that by increasing the weight percentage (wt%), the overall weight of the aircraft decreases due to a reduction in the fuel tank mass.

3.2 One-Pilot Scenario

This test scenario was run to evaluate the Cessna 172 with the greatest modification without changing the amount of fuel. This meant the same distance would still be covered. The test involved a singular pilot flying the aircraft with no baggage, and any empty seats were removed. Tables 3, 4, and 5 show the results obtained from the test runs.

Reading through Tables 3, 4, and 5, it can be seen that four of the seven test runs would allow the Cessna 172 to fly, while the other three exceeded the maximum take-off weight (MTOW). Those three were all from Table 3. Additionally, the

Table 2 Summary of results for first test scenario

| | Case scenario | Maximum weight (kg) | Percentage difference compared to original Cessna 172% |
|------------------|---------------|---------------------|--|
| Cessna 172 | Original | 1043 | N/A |
| Hydrogen 700 bar | Worst | 1379 | +32.2 |
| | Likely | 1247 | +19.6 |
| | Best | 1115 | +6.9 |
| Hydrogen 350 bar | Worst | 1380 | +32.3 |
| | Likely | 1150 | +10.1 |
| | Best | 1116 | +7.0 |
| Liquid hydrogen | Only case | 1365 | +30.9 |

Table 3 Worst-case scenarios for gaseous hydrogen at 350 and 700 bar and the liquid-only case

| Assessed parameters | <i>Worst case</i> | | <i>Only case</i> |
|------------------------------|-------------------|--------------|------------------|
| | Hydrogen gas | Hydrogen gas | Liquid hydrogen |
| Pressure (bar) | 350 | 700 | 5 |
| HFC mass (kg) | 72.92 | 72.52 | 85.57 |
| Cell stack no. | 362 | 358 | 484 |
| HFC efficiency | 66.1% | 66.3% | 59.3% |
| kW produced | 120.2 | 120.2 | 120.1 |
| Tank mass (kg) | 490.0 | 490.0 | 462.8 |
| Weight percentage (wt%) | 6 | 6 | 6.3 |
| Cessna 172 total mass (kg) | 1164 | 1163 | 1136 |
| New mass/old mass difference | +11.6% | +11.5% | +8.9% |
| Energy density (Wh/kg) | 213.5 | 213.7 | 219.0 |
| Flyable? | No | No | No |

Table 4 Likely case scenario for gaseous hydrogen at 350 and 700 bar

| Assessed parameters | <i>Likely case scenario</i> | |
|------------------------------|-----------------------------|--------------|
| | Hydrogen gas | Hydrogen gas |
| Pressure (bar) | 350 | 700 |
| HFC mass (kg) | 72.92 | 72.52 |
| Cell stack no. | 362 | 358 |
| HFC efficiency | 66.1% | 66.3% |
| kW produced | 120.2 | 120.2 |
| Tank mass (kg) | 260.2 | 358.1 |
| Weight percentage (wt%) | 11.3 | 9 |
| Cessna 172 total mass (kg) | 934 | 1031 |
| New mass/old mass difference | -10.5% | -1.2% |
| Energy density (Wh/kg) | 360.8 | 279.1 |
| Flyable? | Yes | Yes |

highest attained energy density was just over 400 Wh/kg. This was surprising as the expected amount was to be around 550 Wh/kg (Thomas, 2009). The reason for this drastic difference is down to how the energy density is calculated. In this chapter, the mass of the fuel, tank, and PEMFC was taken into account and could be the result of such a large difference.

3.3 *The Increase of Mass for Fuel Tanks*

The studied cases have highlighted the beneficial areas of using PEMFCs on aircraft but also clearly show the limitation this technology brings. Overall, PEMFC reduced the amount of fuel required to be carried on the aircraft by 75%. This is because FCs

Table 5 Best-case scenario for gaseous hydrogen at 350 and 700 bar

| Assessed parameters | <i>Best-case scenario</i> | |
|------------------------------|---------------------------|--------------|
| | Hydrogen gas | Hydrogen gas |
| Pressure (bar) | 350 | 700 |
| HFC mass (kg) | 72.92 | 72.52 |
| Cell stack no. | 362 | 358 |
| HFC efficiency | 66.1% | 66.3% |
| kW produced | 120.2 | 120.2 |
| Tank mass (kg) | 226.2 | 226.2 |
| Weight percentage (wt%) | 13 | 13 |
| Cessna 172 total mass (kg) | 900 | 899 |
| New mass/old mass difference | -13.7% | -13.8% |
| Energy density (Wh/kg) | 401.8 | 402.4 |
| Flyable? | Yes | Yes |

have a different efficiency than standard combustion engines, so less fuel is needed for the same distance and power.

However, there was an added weight penalty to the aircraft overall. In the first scenario, all test results showed that no matter the type of hydrogen used, the modified Cessna would not be able to take off as the mass exceeded the MTOW. Also, only four of the seven tests in the second scenario would allow Cessna to successfully take off.

The reason for this gain in mass is largely due to the mass of the storage tanks. The tanks were seen to weigh between 226 kg (including fuel mass) and 490 kg. This is the major limiting factor of using HFCs in aircraft, despite the advantage of a large mass to ensure that the structural of the tank can withstand both the extreme pressures of the gaseous hydrogen and the extreme temperatures. The tank masses were the major factor in determining if the aircraft was too heavy to fly.

4 Conclusion

The main aim of this chapter was to provide quantifiable evidence of how feasible HFCs are when used on a general aviation aircraft. This has been met by showing, with compromises and modification, that a Cessna 172 can fly with one pilot, in four out of seven test scenarios. In addition, using PEMFCs reduces on-board fuel by 75% for the same duration of flight on the Cessna 172.

It is shown that swapping the current combustion propulsion for PEMFC technology causes a large increase in weight from the fuel tanks, which would prevent the aircraft from flying due to exceeding the MTOW. This indicates that one major drawback of using HFCs is the added mass of storing the hydrogen on board. However, improving the wt% dramatically improves the feasibility of using PEMFC on the Cessna 172 model, as seen from the one-pilot scenario.

References

- Air Liquide. (2021). *Fuel cell*. Available at: <https://energies.airliquide.com/resources-planet-hydrogen/fuel-cell#:~:text=PEM%20fuel%20cells%20consume%20about,for%20every%20100%20miles%20covered>
- Barbir, F. (2013). *PEM fuel cells: Theory and practice* (2nd ed.). Academic Press.
- Bosch. (2021). *Fuel-cell stacks: The recipe for success in mass manufacturing*. <https://www.bosch.com/stories/fuel-cell-stack/>
- Dowling, S. (2017). The plane is so good it's still in production after 60 years. *BCC Future*. Available from: <https://www.bbc.com/future/article/20170302-the-plane-so-good-its-still-in-production-after-60-years>
- Evans, C., Harmer, M., Marks, O., Tiley, S., Willis, T., Boufferrouk, A., & Yao, Y. (2016). Development and testing of a variable camber morphing wing mechanism. In *International symposium of sustainable aviation (ISSA)*, Istanbul, Turkey, 29 May – 1 June 2016.
- Fehrenbacher, J., Stanley, D. L., Johnson, M. E., & Honchell, J. (2011). *Electric motor and power source selection for small aircraft propulsion (2011)*. College of Technology Directed Projects. Paper 33.
- IPCC. (2013). *Climate change 2013: The physical science basis. Contribution of Working Group I to the fifth assessment report of the intergovernmental panel on climate change*. Cambridge University Press.
- IPCC. (2018). *Global warming of 1.5°C*. In Press.
- Kadyk, T., Schenkendorf, R., Hawner, S., Yildiz, B., & Römer, U. (2019). Design of fuel cell systems for aviation: Representative mission profiles and sensitivity analyses. *Frontiers in Energy Research*, 7, 35.
- Kane, M. (2014). *Toyota Mirai fuel cell sedan priced at \$57,000 – Specs, videos*. Available from: <https://insideevs.com/news/323973/toyota-mirai-fuel-cell-sedan-priced-at-57500-specs-videos/>
- Kimaru, J., & Boufferrouk, A. (2017). Design, manufacture and test of a camber morphing wing using MFC actuated smart rib. In *8th International conference on mechanical & aerospace engineering, Prague, 22–25 July 2017* (pp. 791–796). IEEE.
- Larmine, J., & Dicks, A. (2000). *Fuel cell systems explained*. Wiley.
- Loudon, K., Boufferrouk, A., Coleman, B., Hughes, F., Lewis, B., Parsons, B., Cole, A., & Yao, Y. (2018). Further development of a variable camber morphing mechanism using the direct control airfoil geometry concept. In *International symposium of sustainable aviation*, Rome, Italy, 9–11 July 2018.
- Michel, F., Fieseler, H., & Allidieres, L. (2006). *Liquid hydrogen technologies for mobile use*. World Hydrogen Energy Conference.
- Mitlitsky, F., Weisberg, A. H., & Myers, B. (2000). *Vehicular hydrogen storage using lightweight tanks*. U.S DOE Hydrogen Program Review, Lawrence Livermore National Laboratory, Livermore, CA
- Pilot's Operating Handbook (POH). (1978). *Cessna Skyhawk – Cessna Model 172N*. Available from: <https://wayman.edu/files/Cessna-172N-POH.pdf>
- Thomas, C. E. (2009). *Fuel cell and battery electric vehicles compared*. Available from: https://www.energy.gov/sites/prod/files/2014/03/f9/thomas_fcev_vs_battery_efs.pdf
- Toyota. (2017). *Toyota Mirai – Fuel cell vehicle brochure*. Available from: <https://www.toyota.co.uk/new-cars/new-mirai/>
- Toyota. (2021). *2021 Mirai – Full specs*. Available from: https://www.toyota.com/mirai/features/mileage_estimates/3002/3003
- United Nations Climate Change (UNFCCC). (2021). *The Paris agreement*. <https://unfccc.int/process-and-meetings/the-paris-agreement/the-paris-agreement>
- Xie, Y., Savvarisal, A., Tsourdos, A., Zhang, D., & Gu, J. (2021). Review of hybrid electric powered aircraft, its conceptual design and energy management methodologies. *Chinese Journal of Aeronautics*, 34(4), 432–450.

Conceptual Design of Piezoelectric-Based Energy Harvesting Seats for Commercial Aircraft



Erfan Salami, Azadeh Salami, Elham Montazer, and Fairuz I. Romli

Contents

| | | |
|-----|--|-----|
| 1 | Introduction | 332 |
| 2 | Literature Review | 332 |
| 2.1 | Mechanisms of Harvesting Energy | 332 |
| 2.2 | Piezoelectric Technology | 334 |
| 3 | Methodology | 335 |
| 3.1 | Artificial Piezoelectric Material | 335 |
| 3.2 | Proposed Location of Piezoelectric | 335 |
| 3.3 | Experimental Evaluation | 336 |
| 4 | Results and Discussion | 337 |
| 5 | Conclusions | 339 |
| | References | 340 |

E. Salami (✉)

Department of Electrical Engineering, University of Malaya, Kuala Lumpur, Malaysia

Center for Research in Industry 4.0, Faculty of Engineering University of Malaya, Kuala Lumpur, Malaysia

A. Salami

Faculty of Industrial and Mechanical Engineering, Qazvin Branch, Islamic Azad University, Qazvin, Iran

E. Montazer

Department of Electrical Engineering, University of Malaya, Kuala Lumpur, Malaysia

F. I. Romli

Department of Aerospace Engineering, Faculty of Engineering, University Putra Malaysia, Selangor, Malaysia

1 Introduction

The decreases in energy consumption of portable electronic devices have attracted the concept of harvesting renewable energy from the human surrounding. The energy harvesting is a process in which the energy is taken from the environment and converted into usable electric power.

One method of power harvesting is to use piezoelectric materials (PZT), which form transducers that can interchange electrical energy and mechanical strain or force. Therefore, these materials can be used as mechanisms to transfer ambient motion (usually vibration) into electrical energy that may be stored and used to power other devices (Fan et al., 2017).

Additionally, the planes appear clean and efficient from the ground. The planes dump a significant number of dangerous pollutants into the atmosphere every day. According to American Aviation, pollution contributes to 2% of the greenhouse gases which leads to global warming (Ariff et al., 2015). A fully laden A380, according to its engine maker Rolls-Royce, uses as much energy as 3500 family cars, equivalent to 6 cars for each passenger (The Economist, 2006). This is also influenced by the demand for powering up portable electronic devices such as laptops, smartphones, tablets, etc. in today's world.

A significant amount of research has been devoted to developing and understanding power-harvesting systems. These studies demonstrate the feasibility of using piezoelectric devices as power sources (Erfan Salami et al., 2016).

2 Literature Review

2.1 *Mechanisms of Harvesting Energy*

2.1.1 Electromagnetic Vibration Energy Harvesters

Generally, there are types of styles of electromagnetic energy harvesters in terms of relative displacement. Electromagnetic energy harvesters have high-output current level at the expense of low voltage. They need no external voltage supply, and no mechanical constraints are required but rely mostly on their size. Moreover, because of the use of separate permanent magnets, it is tough to integrate electromagnetic energy harvesters with the MEMS fabrication method (Erfan Salami et al., 2019).

2.1.2 Piezoelectric Vibration Energy Harvesters

It is the ability of the materials to get an electrical potential in response to applied mechanical stress. In piezoelectric energy harvesting, ambient vibration causes structures to deform and leads to mechanical stress and strain, which is regenerate

to convert attributable to the piezoelectricity. Piezoelectric energy harvesters are either d33 mode or d31 mode. In theory, with constant dimensions, piezoelectric energy harvesters' victimization PZT-5A has the foremost quantity of output power (Zhu, 2011).

2.1.3 Electrostatic Vibration Energy Harvesters

Electrostatic energy harvesters are supported variable capacitors. There are two sets of electrodes within the variable capacitor (Table 1). One set of electrodes are mounted on the housing, whereas the opposite set of electrodes are attached to the inertial mass. Mechanical vibration drives the movable electrodes to maneuver with relation to the fixed electrode which changes the capacitance (Fig. 1).

The capacitance varies between most and minimum values. If the charge on the capacitor is unnatural, the charge can move from the capacitor to a device or the load because the capacitance decreases. Thus, energy is converted to electrical energy.

Table 1 Comparison of vibration energy-harvesting techniques (Minazara et al., 2008)

| | Electrostatic | Electromagnetic | Piezoelectric |
|----------------------------|---|--------------------------|--------------------------|
| Complexity of process flow | Low | Very high | High |
| Energy density | 4 mJ cm ⁻³ | 24.8 mJ cm ⁻³ | 35.4 mJ cm ⁻³ |
| Current size | Integrated | Macro | Macro |
| Problems | Very high voltage (needs charging source) | Very low output voltage | Low output voltage |

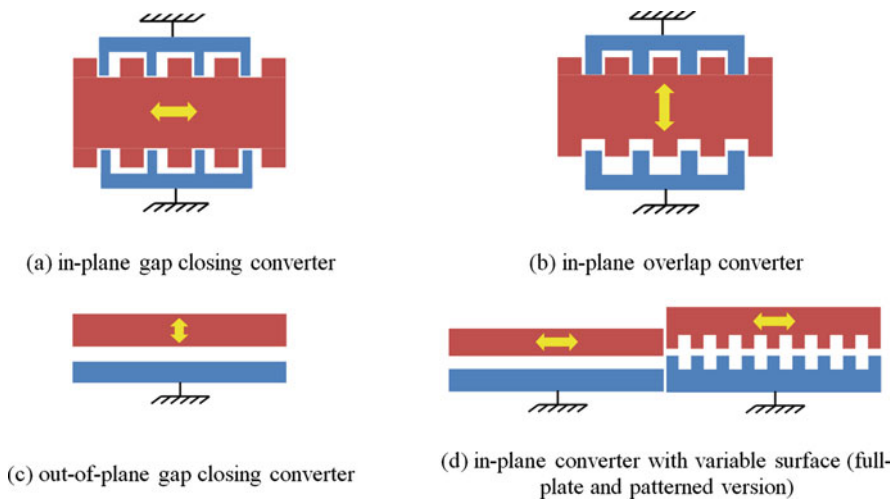


Fig. 1 Types of electrostatic energy harvesters. (a) In-plane gap closing. (b) In-plane gap overlap. (c) Out plane gap closing. (d) In-plane with the variable surface (Boisseau et al., 2012)

2.2 Piezoelectric Technology

2.2.1 What Is Piezoelectricity?

Piezoelectricity is the ability of certain materials to generate an AC voltage once subjected to mechanical stress or vibration or to vibrate once subjected to an AC voltage or both (Fig. 2). The foremost common piezoelectric material is quartz. Certain ceramics, Rochelle salts, and varied alternative solids additionally exhibit this impact (Gibilisco, 2012). The piezoelectric effect was discovered in 1880 by French physicists Jacques and Pierre Curie. The word piezoelectric effect suggests electricity ensuing from pressure. It is a Greek word that means to squeeze or press.

The piezoelectric effect exists in two domains, the first is the direct piezoelectric effect that describes the material's ability to transform mechanical strain into electrical charge; the second form is the converse effect, which is the ability to convert an applied electrical potential into mechanical strain energy (Minazara et al., 2008; Erfan Salami et al., 2020). The direct piezoelectric effect is responsible for the material's ability to function as a sensor, and the converse piezoelectric effect is accountable for its ability to function as an actuator.

2.2.2 What Is Piezoelectricity Effect?

The piezoelectric effect which is a reversible process is the linear electromechanical interaction between the mechanical and the electrical state in crystalline materials.

The direct piezoelectric effect is the internal generation of electrical charge resulting from an applied mechanical force.

The reverse piezoelectric effect is the internal generation of a mechanical strain resulting from an applied electrical field.

2.2.3 Piezoelectric Generator Principle

The vibration energy-harvesting principle using piezoelectric materials is illustrated in the Fig. 3. The conversion chain starts with a mechanical energy source which is

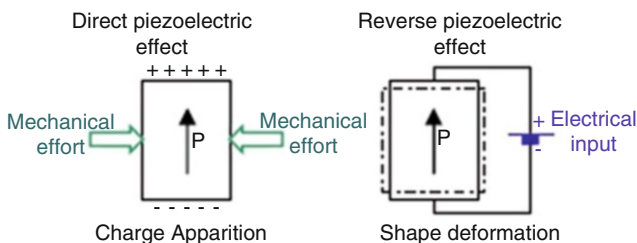


Fig. 2 Electromechanical conversion via piezoelectricity phenomenon (Minazara et al., 2008)

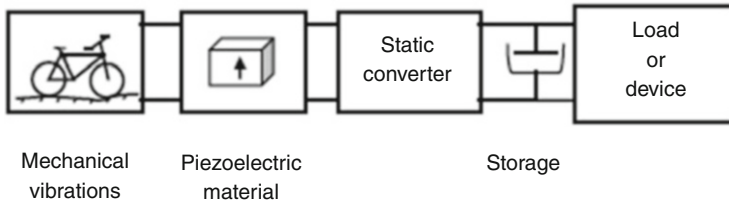


Fig. 3 General diagram of generator-based vibrations energy harvesting using piezoelectric material (Minazara et al., 2008)

Table 2 PZT, 560×10^{-12} C/N means that 1 N applied strain produces 560×10^{-12} C electrical charge (Thakur & Kumar, 2020)

| Material | D33 (10^{-12} C/N) |
|--------------------|-----------------------|
| Quartz | 2.3 |
| BatiO ₃ | 90 |
| PbTiO ₃ | 120 |
| PZT | 560 |
| PZN-9PT | 2500 |

the bike. Its vibrations are converted into electricity via piezoelectric elements. The electricity produced is thereafter formatted by a static converter before supplying to a storage system or the load (Shu & Lien, 2006).

3 Methodology

3.1 Artificial Piezoelectric Material

The piezoelectric materials such as PZT (lead zirconate titanate) present advantageous characteristics (Table 2).

3.2 Proposed Location of Piezoelectric

The piezoelectric is placed in the bottom and back cushions of the airplane seats (Fig. 4). There are challenges faced before this design which is safety hazards due to electrocution, and the piezoelectric is not operating under constant pressure.

3.2.1 Concept Generation

Three concepts are generated after being evaluated by using QFD, morphological chart, and Pugh evaluation matrix. According to the Pugh evaluation matrix, Concept 3 is chosen for having the best rating.

Fig. 4 Proposed location of piezoelectric (own reference)

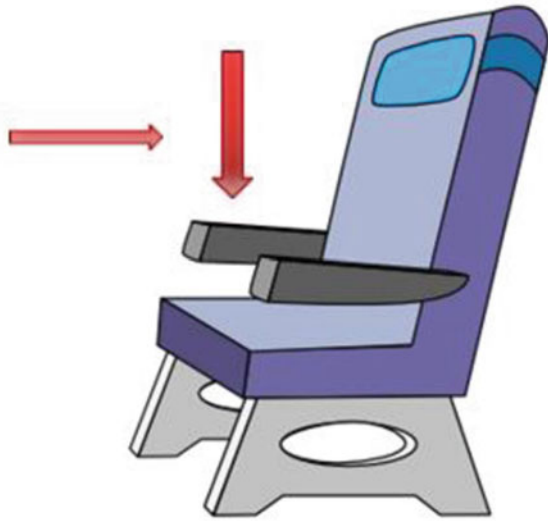


Figure 5, Concept 1, illustrates where the piezoelectric will be placed on its designed stand which is placed under the seat cushion. For Concept 2, four layers of piezoelectric materials are generating electric voltage; once the passenger sits on the seat, more voltage from piezoelectric will be extracted. For Concept 3, the piezoelectric materials will be fixed both under the seat cushion in between the yellow layer shown in Fig. 5 and the back cushion as illustrated by striped lines.

3.3 *Experimental Evaluation*

A data collection is done during the experiments of the project. The piezoelectric is connected as a complete circuit to produce electricity. The complete circuit is included when the capacitor is discharged to charge up again. To cover up this discharge, the controller is used to switch the piezoelectric as the main electricity in aircraft. The data collected are based on the weight that can produce a certain amount of power and the duration of time taken for one passenger.

The procedure of the experiment is the piezoelectric calibrated to identify the maximum amplitude. The weights used are from 0.2 to 10 N. Piezoelectric is connected to a voltmeter for the display of the voltage. The weights are applied to piezoelectric starting from 0.2 N. The stopwatch is used to record the time of piezoelectric before it discharges. The voltage is recorded from the maximum positive voltage and maximum negative voltage. The experiment is repeated several times with an increase of weights until it reaches 10 N. The table tabulated is for weight vs. time and weight vs. voltage.

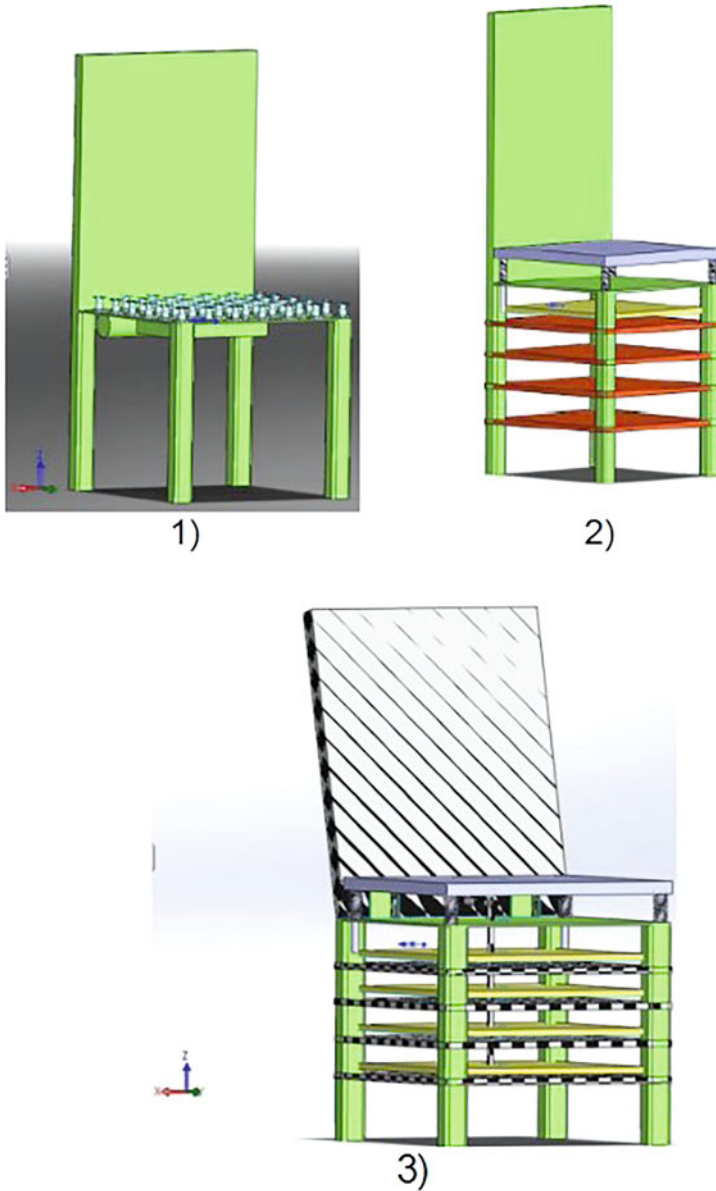


Fig. 5 Concepts 1, 2 and 3; proposed CAD designs for the energy harvesting seat

4 Results and Discussion

The result of piezoelectric shows how much power is produced based on the weight of one passenger. The time taken is analyzed to know the duration of piezoelectric can produce electricity. The data was analyzed by mathematical model software

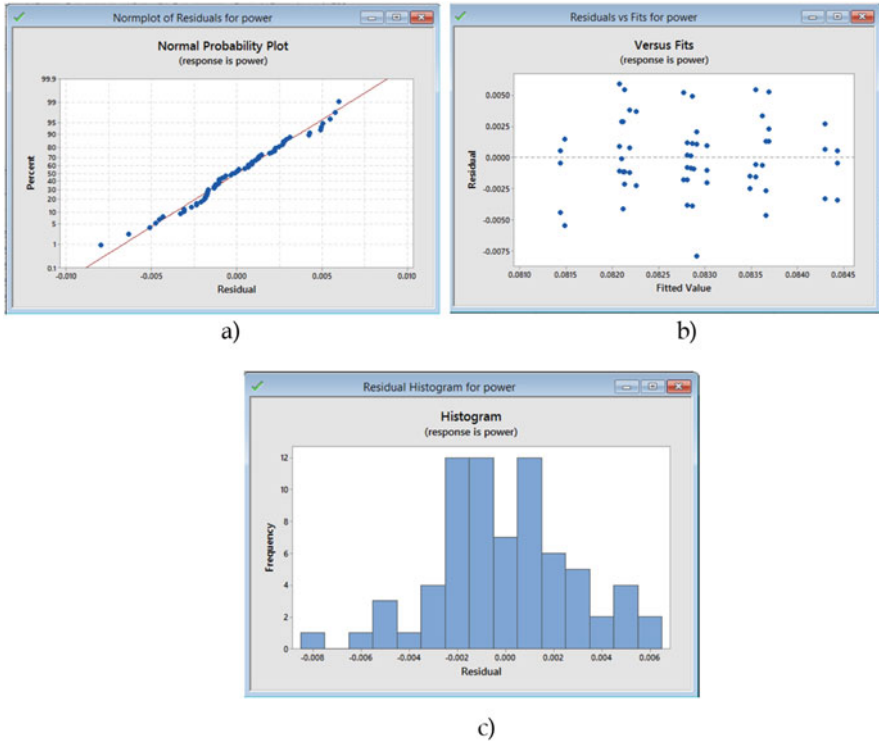


Fig. 6 Experiment data. (a) Normal probability plot. (b) Residual vs. fitted value. (c) Residual vs. frequency (analysis of this study)

which is called Minitab17. By using the software, a more accurate result and percentage of error can be seen, the intersection between the data and production of persistence data (Fig. 6). The data is analyzed based on how much power can be generated using the data obtained from voltage and time. The data of the power is preferred for the result because the power can be generated in one cycle before the piezoelectric discharge can be determined. Rapid Prototyping (3D printing) which is often used to validate a design concept or to test a product's performance (Salami et al., 2020) is the next approach considered by the authors for further validation and proposed design optimization.

From the experiment, the piezoelectric can be charged to 9 V after 20 N of the load is applied 1777.8 times. From the capacitor with 10,000 μF , 16 V capability the piezoelectric to produce 0.0045 V for each load is 2 N load. The power of piezoelectric that can be produced for one piezoelectric is 0.081 W. Each 1 N of weight will produce 0.001 V. The storage of the piezoelectric is dependent on the capacitor used. From the modelling result and validation of results, the histogram for both results is almost the same as with a normally distributed graph (Fig. 7).

The residual for both results showed a large difference in which the modelling result shows the highest is 12 Hz. The graph of versus fits for each result shows a

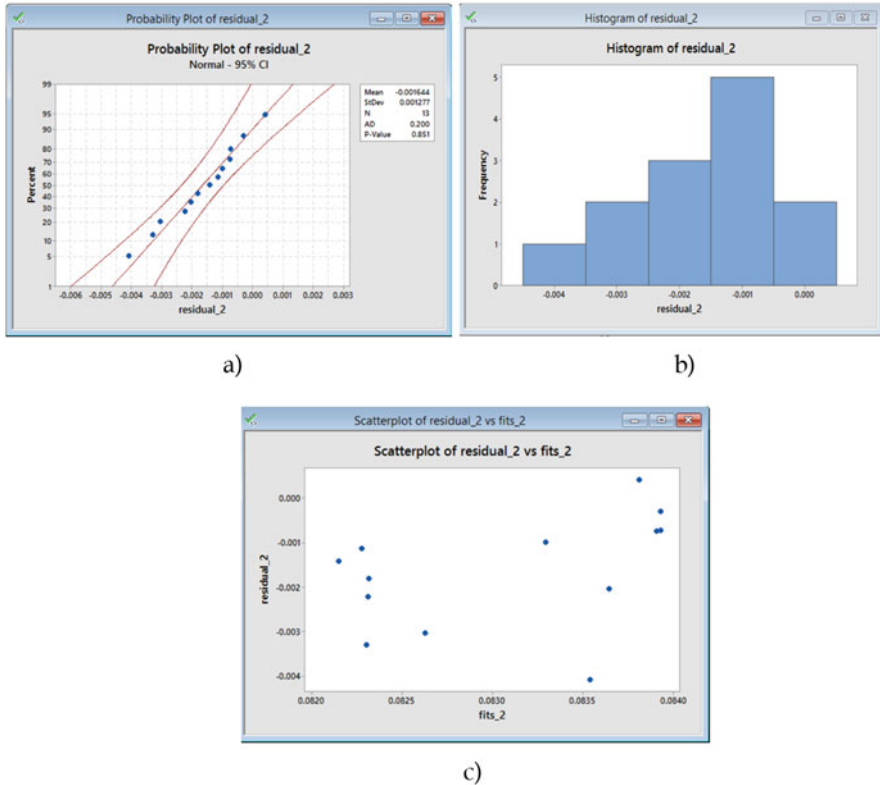


Fig. 7 Validation of results. (a) Residual vs. percent. (b) Residual vs. frequency. (c) Residual vs. fitted value (analysis of this study)

large difference. For the modelling result, the graph shows the random dots. The ideal result for this is when the graph shows the random dot, and the color is red. The normal probability fits for each result showing a linear line. The modelling result shows that the accurate linear line compared to the validation result shows some of the dots are out of the linear line.

5 Conclusions

A conceptual design for airplane seats is proposed in this chapter. This concept is chosen based on the feedback from the consumers which are the customers and manufacturers that want a lightweight, low cost, low maintenance, comfort, and low manufacturability. A future recommendation that can be carried on is by using a more flexible material and cheaper for piezoelectric. The use of super capacitors in

storing more voltage can also be used to make it more efficient in different applications. The device can be implemented in cinemas, MPH (multipurpose halls), conference halls, and seats and for the flooring of the metro stations.

References

- Ariff, O. K., Salami, E., & Romli, F. I. (2015). *Key parameters of air breathing two-stroke combustion engines for integration into small scale UAVs*. Paper presented at the 53rd AIAA Aerospace Sciences Meeting.
- Boisseau, S., Despesse, G., & Seddik, B. A. (2012). Electrostatic conversion for vibration energy harvesting. In *Small-scale energy harvesting* (pp. 1–39). InTech.
- Fan, K., Liu, Z., Liu, H., Wang, L., Zhu, Y., & Yu, B. (2017). Scavenging energy from human walking through a shoe-mounted piezoelectric harvester. *Applied Physics Letters*, *110*(14), 143902.
- Gibilisco, S. (2012). *piezoelectricity*. DEFINITION. Retrieved from <https://whatis.techtarget.com/definition/piezoelectricity>
- Minazara, E., Vasic, D., & Costa, F. (2008). *Piezoelectric generator harvesting bike vibrations energy to supply portable devices*. Paper presented at the Proceedings of International Conference on Renewable Energies and Power Quality (ICREPQ'08).
- Salami, E., Ganesan, P., Ward, T. A., Viyapuri, R., & Romli, F. (2016). *Design and mechanical analysis of a 3D-printed biodegradable biomimetic micro air vehicle wing*. Paper presented at the IOP Conference Series: Materials Science and Engineering.
- Salami, E., Ward, T. A., Montazer, E., & Ghazali, N. N. N. (2019). A review of aerodynamic studies on dragonfly flight. *Proceedings of the Institution of Mechanical Engineers, Part C: Journal of Mechanical Engineering Science*, *233*(18), 6519–6537.
- Salami, E., Ward, T. A., Montazer, E., & Ghazali, N. N. N. (2020). Nanoindentation analysis comparing dragonfly-inspired biomimetic micro-aerial vehicle (BMAV) wings. *International Journal of Bio-Inspired Computation*, *16*(2), 111–120.
- Shu, Y., & Lien, I. (2006). Analysis of power output for piezoelectric energy harvesting systems. *Smart Materials and Structures*, *15*(6), 1499.
- Thakur, A. K., & Kumar, D. (2020). Aerodynamic stability on piezoelectric multi Rotor UAV with numerical case learning. *European Journal of Molecular & Clinical Medicine*, *7*(7), 1558–1568.
- The Economist. (2006, June 8). *Aircraft emissions*. Retrieved from <https://www.economist.com/special-report/2006/06/08/the-skys-the-limit>
- Zhu, D. (2011). Vibration energy harvesting: Machinery vibration, human movement, and flow induced vibration. *Sustainable Energy Harvesting Technologies – Past, Present and Future*, *1*, 22–54.

Effects of Flow Pulsation on Shock Wave/Boundary Layer Interaction in Supersonic Isolator



Sardar Nafis Bin Ali, Abu Baker Siddque Rimon,
and A. B. M. Toufique Hasan

Contents

| | | |
|---|---|-----|
| 1 | Introduction | 342 |
| 2 | Model Description | 343 |
| 3 | Numerical Method | 343 |
| | 3.1 Boundary and Operating Conditions | 344 |
| | 3.2 Validation of Numerical Method | 345 |
| 4 | Results and Discussion | 345 |
| 5 | Conclusion | 346 |
| | References | 348 |

Nomenclature

| | |
|-----|--|
| h | Pressure outlet height (mm) |
| f | Frequency of the cycle for the oscillation of Mach number (Hz) |
| M | Free stream Mach number |
| L | Separation length (mm) |
| R | Percentage relative difference of separation length between increasing and decreasing states |
| x | Cartesian axis direction |
| y | Cartesian axis direction |

S. N. B. Ali · A. B. S. Rimon · A. B. M. T. Hasan (✉)
Bangladesh University of Engineering and Technology (BUET), Dhaka, Bangladesh
e-mail: toufiquehasan@me.buet.ac.bd

Greek Letter

τ Shear stress (Pa)

Subscripts

p Primary
s Secondary
ps Primary separation
pr Primary reattachment
ss Secondary separation
sr Secondary reattachment
sep Separation
inc Increasing
dec Decreasing
w Wall

1 Introduction

Ferri in 1939 made the first observations of shock wave/boundary layer interaction (SWBLI) during testing of an airfoil in a high-speed wind tunnel (Ferri, 1940). The flow field considerably altered when the shock wave interacts with the boundary layer. Wagner (2009) has analyzed the unstart process of a scramjet in an isolator. The experiment was done to predict the effect of shock wave/boundary layer interaction (SWBLI) inside the isolator for unstart process at Mach 5. Koo and Raman (2012) revealed that the large eddy simulation (LES) can predict fully started flow. They also concluded that LES is able to capture the large-scale features of the unstart process remarkably well, exhibiting unstart flow nearly identical to experiment.

In scramjet engine, the efficiency of compression and the combustion process largely depends on the flow condition and separation characteristics inside the inlet isolator. Inlet isolators are designed for a fixed Mach number flow entry. During taking off or landing, acceleration or deceleration or during changing altitudes or during transient atmospheric conditions flights can face fluctuating Mach number in inlet isolator rather than facing designed constant Mach number entry. This fluctuating Mach number creates complex off-design conditions which depend on the rate of fluctuation. Accordingly, the study of such fluctuating flow field is necessary. In our present study, a computation on the effect of pulsating flow on the shock wave with turbulent boundary layer interaction in supersonic inlet isolator is performed to examine the dependency of shock wave/boundary layer interaction (SWBLI) parameters on frequency and hysteresis characteristics using computational fluid dynamics.

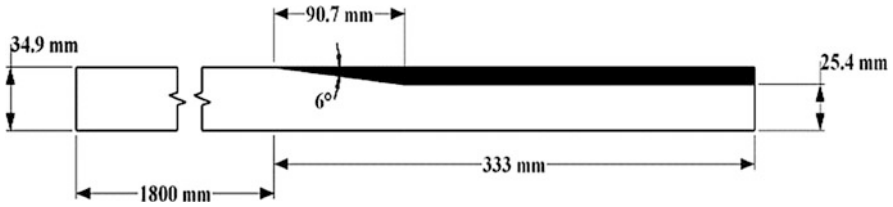


Fig. 1 Geometry of inlet isolator (all dimensions are in mm)

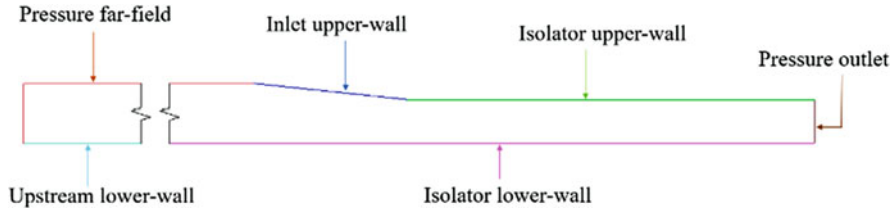


Fig. 2 Different sections of inlet isolator with prescribed boundary conditions

2 Model Description

Figures 1 and 2 show the dimensions and different sections of the geometry of supersonic isolator. There are six boundaries in our geometry. Flow enters at pressure far field at 0° angle of attack. Upstream lower wall is 1.8 m long which is much longer than our main focused portion of inlet isolator geometry. The upstream lower wall is so long in order to develop the desired boundary layer thickness and momentum thickness. The wedge angle is 6° . Pressure outlet has a height of 25.4 mm. All distances and dimensions are normalized with respect to this height. The geometry reference is taken from Koo and Raman (2012).

3 Numerical Method

Three governing equations, Navier-Stokes equation (continuity and momentum equations) in averaged form and Energy equation, are used to solve our 2D compressible flow. The matter of grid generation is a significant consideration in CFD. Quadrilateral cells are used for this model. Total number of cells in the mesh is 244,800. Structured mesh has been used in the geometry. Computational domain is shown in Fig. 3.

Density-based solver is used. As the flow field varies with time, transient computation is conducted. For capturing all of our complicated flow phenomena, Stress-Omega model of Reynold stress is used for our viscous model. Air is treated as an ideal gas in our computation. Specific heat and thermal conductivity of air is kept constant, and viscosity of air is varied with variation of temperature as per Sutherland’s law.

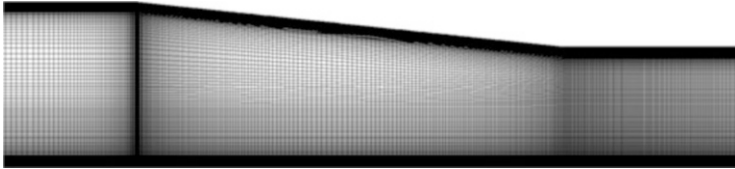


Fig. 3 Computational domain with mesh structure

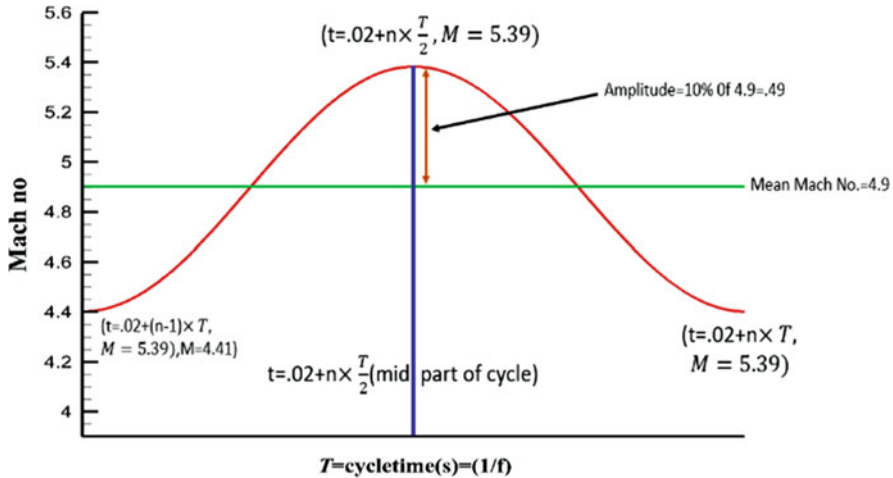


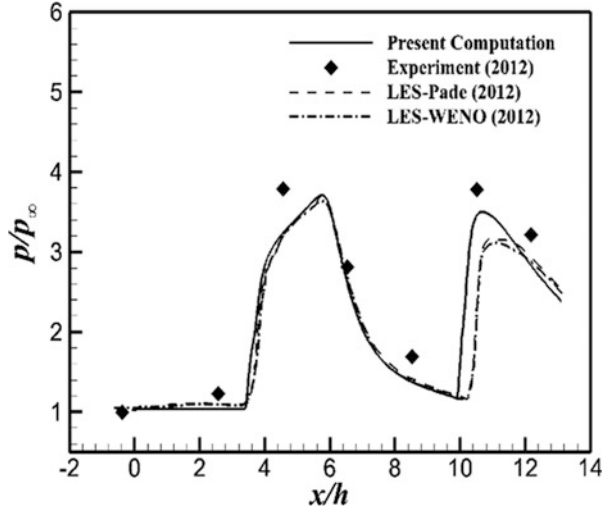
Fig. 4 Mach number variation with flow time

3.1 Boundary and Operating Conditions

In our study, the flow is set to be zero-pressure gradient flow. Wall boundary conditions are kept adiabatic. Total pressure is 2517 KPa. Total temperature is 335 K. At entrance, Mach number is varied sinusoidally with respect to time as per the formula, $M(t) = 4.9 - 4.9 \times 0.1 \cos(2\pi ft)$ as shown in Fig. 4. Static pressure and temperature are isentropically related with total pressure and temperature, respectively. The walls are stationary, and no slip condition is imposed on wall to develop boundary layer. The wall temperature is constant and adiabatic condition is maintained at all walls. So, wall temperature is related with freestream static temperature and total temperature by recovery factor according to $\frac{T_0}{(1+0.89 \times \frac{\gamma-1}{2} \times M^2)}$. There is no heat transfer. Hence, outlet total temperature is considered the same as freestream total temperature.

In the simulation, the Mach number at inlet varies sinusoidally. The pulsation can be divided into two parts: increasing part and decreasing part. The Mach number increases from 4.41 to 5.39 and then decreases from 5.39 to 4.41. But the time period of the cycle is varied by the changing the frequency. The frequencies are kept as 10, 20, 50, and 100 Hz.

Fig. 5 Wall pressure distribution along the isolator lower wall obtained from present computation and experiments and different LES calculations by Koo and Raman (2012)



3.2 Validation of Numerical Method

The performance of the present computational method is verified against available results obtained from Koo and Raman (2012). The flow configuration is based on the scramjet inlet experiment performed at the University of Texas (Wagner et al., 2010). The experiment is performed for Mach number 4.9. From Fig. 5, it is observed that our present computation has aligned well with experimental and LES data.

4 Results and Discussion

The separation characteristic is observed for the same frequency and the same Mach number in increasing and decreasing states to study hysteresis phenomenon. Then the obtained separation location, reattachment location, and separation length are compared for different frequencies to identify frequency dependency (Fig. 6).

In Fig. 7a–c, we can see the primary separation location and reattachment location and primary separation length vary very significantly with the frequencies. Figure 7d represents hysteresis behavior for primary separation length. So, hysteresis behavior and frequency dependency is found in all primary separation characteristics.

The secondary separation location and reattachment location shows similar changes as primary separation and reattachment location in Fig. 8a, b. But in the case of secondary separation length in Fig. 8c, the length can be seen to change in different pattern compared to primary separation length. The percentage relative separation length in increasing and decreasing state of cycle represents the hysteresis effect. The changes don't follow any pattern. But it can be seen that the hysteresis effect is higher for the primary separation length than the secondary separation length.

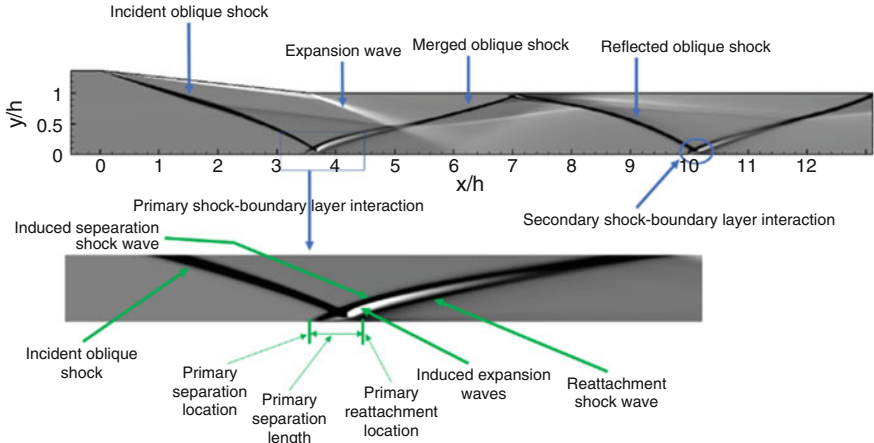


Fig. 6 Identification of different Shock boundary interaction phenomenon of our computational result (for $M = 4.9$)

5 Conclusion

In this study, flow field and the separation characteristics in the supersonic isolator are observed under the pulsation of Mach number. At first, the flow field properties and separation characteristics are observed for same frequency but for different Mach number. The inlet flow is increased from 4.41 to 5.39 and then decreased to 4.41. The flow field properties varied with the increasing and decreasing state of the cycle. Thus, hysteresis phenomenon is observed. The hysteresis phenomena is similar in behavior for all the frequency. But the value is different in different cases. The properties are then compared with the different frequencies but with the same Mach number. The properties show frequency dependencies. The range and value of the properties change in gradual manner with the frequency changes.

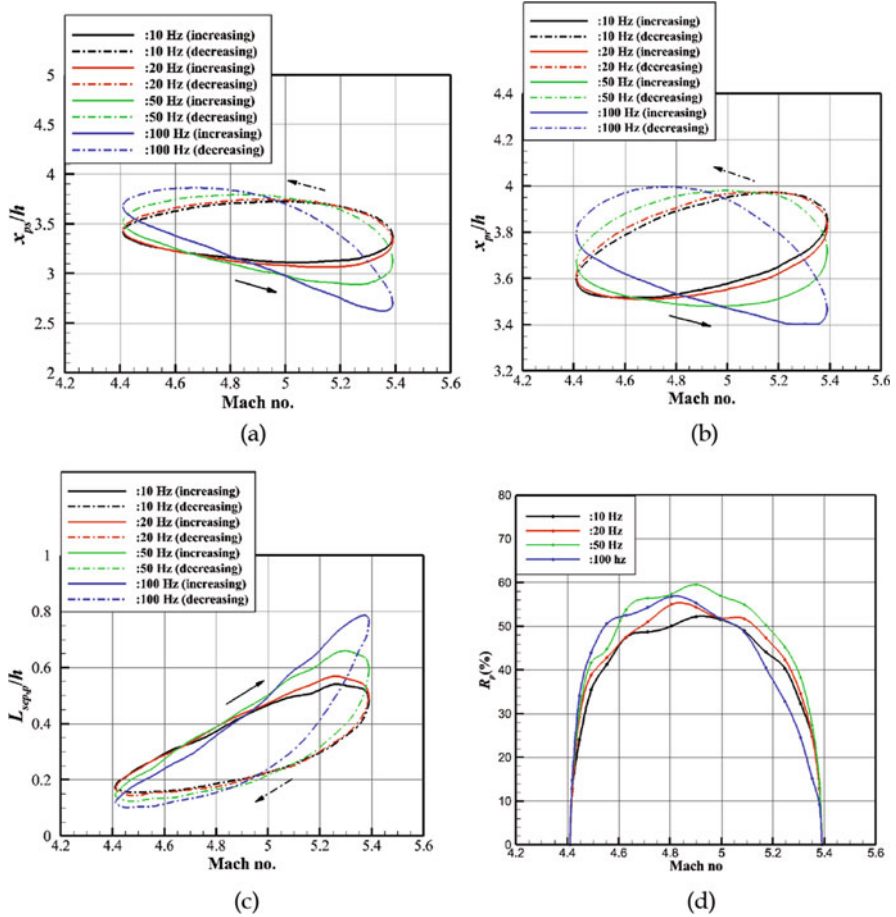


Fig. 7 Normalized (a) primary separation location, (b) primary reattachment location, (c) primary separation length, and (d) percentage relative primary separation length for different frequencies

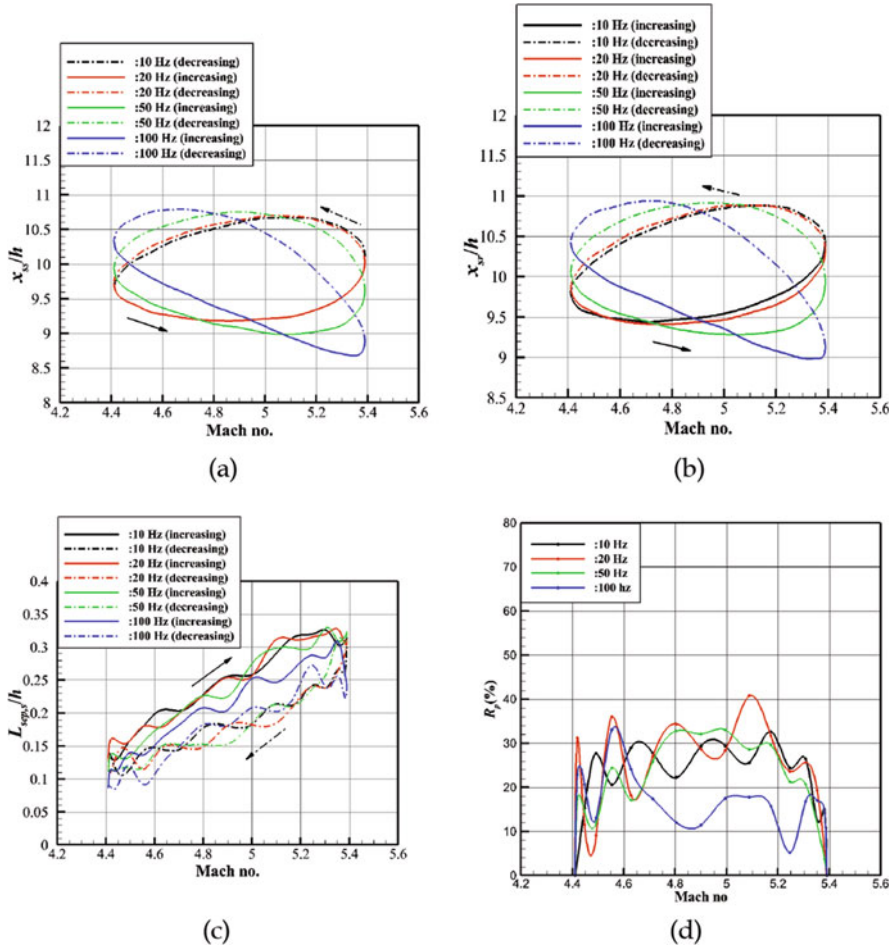


Fig. 8 Normalized (a) secondary separation location, (b) secondary reattachment location, (c) secondary separation length, and (d) percentage relative secondary separation length for different frequencies

References

Ferri, A. (1940). *Experimental results with airfoils tested in the high-speed tunnel at Guidonia*.
 Koo, H., & Raman, V. (2012). Large-eddy simulation of a supersonic inlet-isolator. *AIAA Journal*, 50(7), 1596–1613.
 Wagner, J. L. (2009). *Experimental studies of unstart dynamics in inlet/isolator configurations in a Mach 5 flow*. The University of Texas.
 Wagner, J. L., Yuceil, K. B., & Clemens, N. T. (2010). Velocimetry measurements of unstart of an inlet-isolator model in Mach 5 flow. *AIAA Journal*, 48(9), 1875–1888.

Effect of Bypass Mass Injection on Thrust Vectoring of a Supersonic Micro-Nozzle: A DSMC Investigation



Maruf Md. Ikram, Abu Taqui Md. Tahsin, and A. B. M. Toufique Hasan

Contents

| | | |
|-----|------------------------------|-----|
| 1 | Introduction | 350 |
| 2 | Methodology | 351 |
| 2.1 | Problem Statement | 351 |
| 2.2 | Numerical Method | 352 |
| 2.3 | Validation | 352 |
| 3 | Results and Discussion | 352 |
| 4 | Conclusion | 355 |
| | References | 356 |

Nomenclature

| | |
|-----------|-------------------------------------|
| C_d | Discharge coefficient |
| C_f | Thrust coefficient |
| f | Flow percentage (%) |
| FT | Thrust force (N) |
| Kn | Knudsen number |
| mT | Total mass flow rate (g/s) |
| Ma | Mach number |
| P | Pressure (Pa) |
| PPC | Particle per cell |
| T | Temperature (K) |
| β | Thrust vectoring angle ($^\circ$) |
| λ | Mean free path (m) |

M. Md. Ikram · A. T. M. Tahsin · A. B. M. T. Hasan (✉)
Bangladesh University of Engineering and Technology (BUET), Dhaka, Bangladesh
e-mail: toufiquehasan@me.buet.ac.bd

1 Introduction

Thrust-vectoring nozzle (TVN) technologies are designed to influence the spacecraft dynamics by generating lateral components of thrust in the nozzle flow where the conventional aerodynamic control surfaces lose their effectiveness. The concept of redirecting the thrust by actively manipulating the nozzle flow field is known as fluidic thrust vectoring (FTV). This can be achieved in two ways, (a) gas injection from a secondary source and (b) bypass mass injection. Between these two methods, bypass mass injection technique involves relatively inexpensive lightweight systems with the minimum penalty of the design parameters as it does not require additional flow control devices for secondary mass injection. Waithe and Deere (2003), considered a single- and multiple-port bypass mass injection 2D thrust-vectoring nozzle for both numerical and experimental investigations and compared the effectiveness for different nozzle pressure ratio (NPR). Similar methodology was considered by Wang et al. (2019), where a dual throat bypass mass injection thrust-vectoring phenomenon was studied for investigating a better flow adaptive capability, and an increase of vectoring angle with NPR was observed.

These studies are for continuum-scale analysis. However, such effort is rarely found in the open literature to characterize the flow structure and examine the thrust-vectoring effect in the case of supersonic micro-nozzles, although some studies had addressed the flow in micro -nozzles in the rarefied regime. Hao et al. (2005), performed an experimental study for micro propulsion in a rectangular converging-diverging nozzle. Their study suggests that the molecular-scale behaviour prevents the occurrence of the shock wave due to higher viscous effect. This study was extended by Saadati and Roohi (2015), for different working fluids and reported the similar generic behaviour. Sebastião and Santos (2014), considered an array of micro-nozzles and analysed the effect of surface curvature. Furthermore, Darbandi and Roohi (2011), carried out an unstructured grid-based micro-nozzle investigation and analysed the effect of particle surface collision scheme variation.

In the field of space craft miniaturization, thrust vectoring with bypass mass injection can play a leading role. Present study addresses this application by considering a thrust-vectoring nozzle with bypass mass injection for five different bypass widths (2–12 μm) and two different outlet pressures ($P_{\text{out}} = 10$ and 40 kPa). To the best of authors' knowledge, this is the first time thrust-vectoring effect for supersonic micro-nozzle in rarefied regime is being acknowledged. Parametric investigations were carried out to investigate different performance parameters, i.e. total mass flow rate, secondary flow percentage, thrust force, thrust vectoring angle, specific impulse and the thrust coefficient. Present study suggests the highest vectoring angle occurs for $P_{\text{out}} = 40$ kPa at 6- μm bypass width.

2 Methodology

2.1 Problem Statement

Two different computational domains are considered for the present numerical study considering nitrogen as the working fluid. The baseline nozzle is a planar convergent-divergent (CD) micro-nozzle that is shown in Fig. 1a with no bypass section. For thrust-vectoring purpose, a rectangular bypass channel of variable height is added to the baseline nozzle for inducing the secondary flow that opens into the diverging section at right angle as shown in Fig. 1b. The mid-plane of the bypass channel starts and ends at a distance of 10 and 120 μm from the inlet. The dimensions of the geometry are given in Table 1. All the dimensions are in μm . A specified pressure ($P_{in} = 101.325 \text{ kPa}$) and temperature ($T_{in} = 300 \text{ K}$) are maintained at the inlet, while two different outlet pressures ($P_{out} = 10$ and 40 kPa) are applied at nozzle outlet. For each of the outlet pressures, five different bypass channel dimensions (2, 6, 8, 10, and 12 μm) are considered. The nozzle and the bypass channel walls are completely diffusive with a fixed wall temperature (T_w) of 300 K.

Fig. 1 Converging-diverging (a) baseline micro-nozzle and (b) thrust-vectoring micro-nozzle with imposed boundary conditions

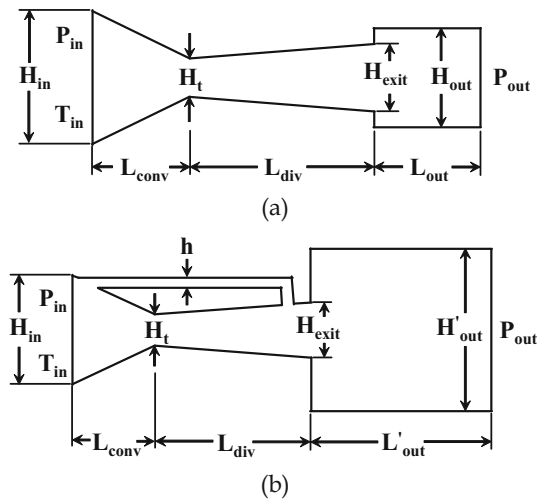


Table 1 Dimensions of the geometry

| H_{in} | H_t | H_{exit} | H_{out} | H'_{out} | h | L_{cov} | L_{div} | L_{out} | L'_{out} |
|----------|-------|------------|-----------|------------|------|-----------|-----------|-----------|------------|
| 68 | 20 | 34 | 50 | 100 | 0–12 | 50 | 95 | 55 | 110 |

2.2 Numerical Method

Present study is carried out for the rarefied condition due to higher mean free path (λ) to characteristic length ratio alternately known as Knudsen number (Kn). In the rarefied condition, Navier-Stokes equation-based continuum approach analysis is invalid due to the violation of local flow equilibrium assumption. This non-equilibrium flow is captured through the Boltzmann equation-based direct simulation Monte Carlo (DSMC) method. No time counter (NTC) collision partner selection model is used along with the variable hard sphere (VHS) binary collision model corresponding to the nitrogen (N_2) gas. In this study, mathematical modelling was executed in the open-source CFD software openFoam in the dsmcFoam+ solver. To meet the necessary requirements for time step, mesh cell size and the number of DSMC particle per cell (PPC), guidelines specified by Saadati and Roohi (2015), are strictly adhered to. For the present work, the domain was subdivided into 150×150 mesh size in the main nozzle body with ten times refined mesh in the bypass section and its projection on the main nozzle. A time step of 4×10^{-11} s with greater or equal to 12 PPC is considered to reduce the statistical error. The simulation was first allowed to reach the steady state, and then the time averaging scheme was employed to the latest step for a sample size of 36×10^6 .

2.3 Validation

For validating the present numerical modelling in dsmcFoam+ solver, a convergent-divergent micro-nozzle with a rectangular cross section and a throat size of $20 \mu\text{m}$ was considered and validated against the study of Hao et al. (2005). The variation of the nozzle mass flow rate for different outlet pressures, obtained from the present computational model and that of Hao et al. (2005), is shown in Fig. 2. Such comparison reveals a suitable agreement between these two models. To ensure further accuracy, the present model was also validated against the numerical study of Saadati and Roohi (2015). Table 2 shows the comparison of the thrust force, obtained from the present model and that of the Saadati and Roohi (2015), that ensures sufficient accuracy for subsequent studies.

3 Results and Discussion

The centreline pressure variation is described in Fig. 3a and b. For both outlet pressures, the baseline nozzle and the vectored nozzle with $h/H_t = 0.1$ have identical pressure profiles. This can be attributed to the lower secondary momentum flux inclusion for $h/H_t = 0.1$ bypass channel nozzle that gets dissipated in the boundary layer and doesn't affect the main nozzle flow. For $P_{\text{out}} = 10 \text{ kPa}$, the

Fig. 2 Comparison of mass flow rate between the present model and Hao et al. (2005)

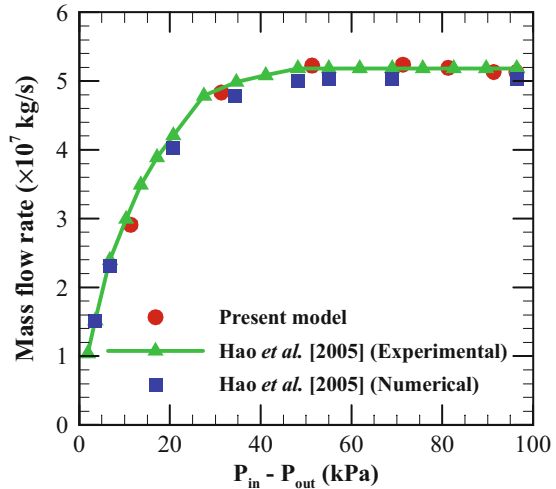


Table 2 Comparison of thrust force (N) between the present model and Saadati and Roohi (2015)

| P_{out} (kPa) | Thrust force (N) | | % Error |
|-----------------|----------------------|--------------------------|---------|
| | Present model | Saadati and Roohi (2015) | |
| 5 | 1.71 | 1.70 | 0.59 |
| 10 | 1.72 | 1.73 | 0.58 |
| 20 | 1.57 | 1.59 | 1.26 |
| 30 | 1.25 | 1.27 | 1.57 |
| 70 | 0.54 | 0.55 | 1.81 |

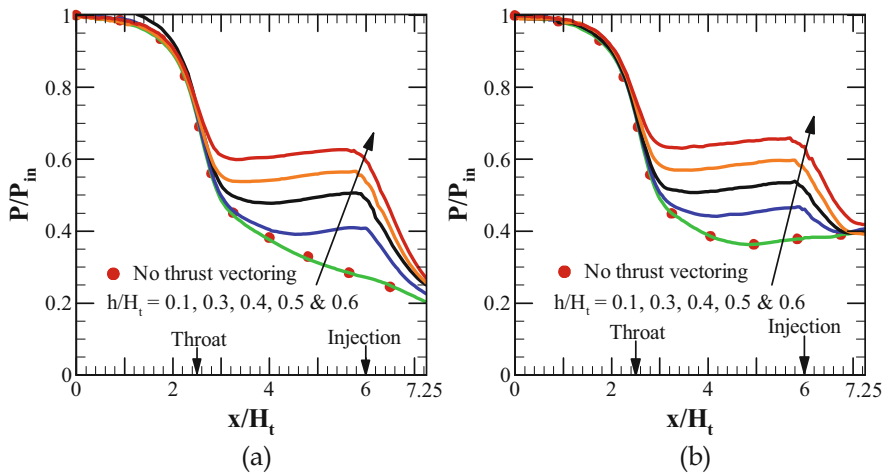


Fig. 3 Variation of pressure distribution for (a) $P_{out} = 10$ kPa and (b) $P_{out} = 40$ kPa along the centreline for different bypass dimensions

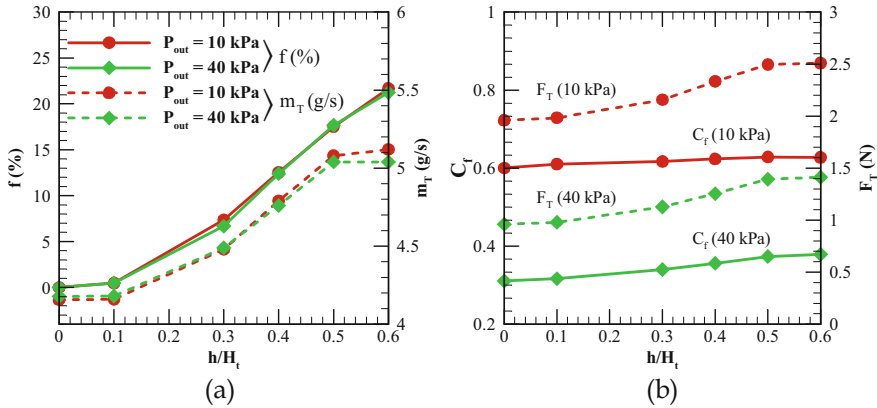


Fig. 4 Variation of the (a) total mass flow rate and the secondary flow percentage and (b) thrust force and the thrust coefficient with different bypass dimensions for $P_{out} = 10$ and 40 kPa

pressure continues to decline up to the nozzle exit for these two cases, whereas for $P_{out} = 40$ kPa, fluid pressure reaches to its lowest extremity at $x/H_t = 4.85$ and then increases. For the other bypass widths, increasing pressure bumps are observed. The pressure has a slight rising tendency in this region followed by further declination. Now in the case of $P_{out} = 40$ kPa, the pressure declination following the bump region first hits its lowest extremity and again rises unlike the pressure distribution for $P_{out} = 10$ kPa where it continues to go down beyond the bump region.

The variation of the total mass flow rate and secondary flow percentage with the bypass channel width is shown in Fig. 4a. The total mass flow rate increases with the bypass width as higher bypass width provides larger flow area to the secondary flow. Similar reasoning causes a gradual increase of flow percentage. Both of the plots signify that the total mass flow rate and the flow percentage have weak dependency on the outlet pressure except at $h/H_t > 0.5$ where the total mass flow rate for $P_{out} = 10$ kPa is higher than that of $P_{out} = 40$ kPa. Variation of the thrust force and the thrust coefficient are shown in Fig. 4b for different bypass widths. Total thrust force is continuously increasing as the bypass channel widens due to higher total mass flow rate. For all the cases, $P_{out} = 10$ kPa reports higher thrust force. This is caused by an earlier supersonic zone development for $P_{out} = 10$ kPa that induces a higher momentum development and leads to greater thrust force. Similar reasoning elevates the thrust coefficient for $P_{out} = 10$ kPa that that of $P_{out} = 40$ kPa.

Variation of the thrust-vectoring angle is presented in Fig. 5a. Two alternate behaviours are noticed in the figure. Thrust-vectoring angle for $P_{out} = 10$ kPa is continuously increasing. This is due to higher mass flow percentage with the increase of bypass width. Vectoring angle for $P_{out} = 40$ kPa has two distinctive features. Firstly, it shows greater vectoring angle than that of $P_{out} = 10$ kPa up to $h/H_t = 0.4$. Secondly, the thrust vectoring angle for $P_{out} = 40$ kPa peaks at $h/H_t = 0.3$ beyond which the vectoring angle decreases. Figure 5b shows the variation of specific impulse. Specific impulse is increasing with bypass dimension for both of

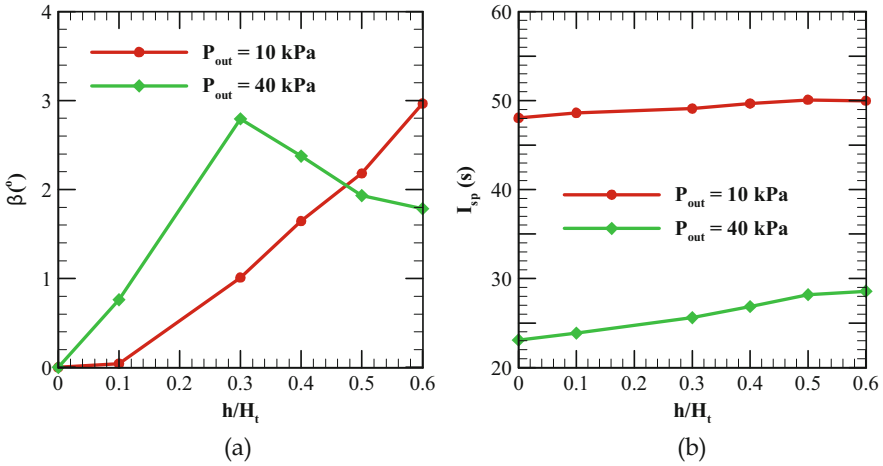


Fig. 5 Variation of the (a) thrust-vectoring angle and (b) specific impulse with different bypass dimensions for $P_{out} = 10$ and 40 kPa

the outlet pressures. This implies higher thrust-to-weight ratio of the vectored nozzle. Vectored nozzle substantiates higher increment rate of the thrust force than the mass flow rate that increases the specific impulse. Between the two outlet pressures, $P_{out} = 10$ kPa reports higher specific impulse as it has higher thrust force.

4 Conclusion

The findings of the present computational study can be summarized as follows:

- Secondary injection introduces pressure bump in the diverging section.
- Total mass flow rate and the secondary flow percentage increase with the bypass channel width with a weak dependency on outlet pressure.
- For all the bypass dimensions, thrust force corresponding to $P_{out} = 10$ kPa is greater than that of $P_{out} = 40$ kPa and increases continuously with the bypass channel width.
- Higher thrust force for $P_{out} = 10$ kPa results in higher thrust coefficient.
- For $P_{out} = 10$ kPa, thrust-vectoring angle increases continuously, whereas for $P_{out} = 40$ kPa, the thrust-vectoring angle peaks at $h/H_t = 0.3$.

References

- Darbandi, M., & Roohi, E. (2011). Study of subsonic–supersonic gas flow through micro/nanoscale nozzles using unstructured DSMC solver. *Microfluidics and Nanofluidics*, *10*(2), 321–335.
- Hao, P. F., Ding, Y. T., Yao, Z. H., He, F., & Zhu, K. Q. (2005). Size effect on gas flow in micro nozzles. *Journal of Micromechanics and Microengineering*, *15*(11), 2069.
- Saadati, S. A., & Roohi, E. (2015). Detailed investigation of flow and thermal field in micro/nano nozzles using Simplified Bernoulli Trial (SBT) collision scheme in DSMC. *Aerospace Science and Technology*, *46*, 236–255.
- Sebastião, I. B., & Santos, W. F. (2014). Numerical simulation of heat transfer and pressure distributions in micronozzles with surface discontinuities on the divergent contour. *Computers & Fluids*, *92*, 125–137.
- Waithé, K., & Deere, K. (2003). An experimental and computational investigation of multiple injection ports in a convergent-divergent nozzle for fluidic thrust vectoring. In *21st AIAA applied aerodynamics conference* (p. 3802). American Institute of Aeronautics and Astronautics.
- Wang, Y., Xu, J., Huang, S., Lin, Y., & Jiang, J. (2019). Computational study of axisymmetric divergent bypass dual throat nozzle. *Aerospace Science and Technology*, *86*, 177–190.

Research on Starting Optimizing Control and Active Load Fluctuation Control of More Electric Auxiliary Power Unit



Jiaming Zhang, Tianhong Zhang, Lingwei Li, and Xinglong Zhang

Contents

| | | |
|---|--|-----|
| 1 | Introduction | 358 |
| 2 | Structure of MEAPU | 359 |
| 3 | Modelling of MEAPU | 360 |
| 4 | Variable Substitution Optimal Control Method | 362 |
| 5 | Active Load Fluctuation Suppression Control Method | 363 |
| 6 | Results and Discussion | 363 |
| 7 | Conclusions | 365 |
| | References | 366 |

Nomenclature

| | |
|-------|---|
| AEA | All electric aircraft |
| ALFSC | Active load fluctuation suppression control |
| APU | Auxiliary power unit |
| MEA | More electric aircraft |
| MEAPU | More electric auxiliary power unit |
| SG | Starter generator |
| VSOC | Variable substitution optimal control |

J. Zhang · T. Zhang (✉) · L. Li · X. Zhang
College of Energy and Power Engineering, Nanjing University of Aeronautics and Astronautics,
Nanjing, China
e-mail: samuelz@nuaa.edu.cn; thz@nuaa.edu.cn; cepe_llw@nuaa.edu.cn;
zx1008@nuaa.edu.cn

1 Introduction

All electric aircraft (AEA) using power by wire technology was proposed in the aviation field to improve aircraft performance and reduce fuel consumption and harmful gas emissions (Rosero et al., 2007). All electric aircraft are aircraft whose hydraulic, pneumatic, and mechanical systems are entirely replaced by electrical systems (Jones, 2002; Feiner, 1993; Weale & Whitely, 2004). Because it is a systematic project to transform the traditional aircraft into an AEA, rather than simply replace the hydraulic, pneumatic, and mechanical systems with the electric system, the concept of more electric aircraft (MEA) is proposed (Verschoor, 2005).

It is necessary to provide enough electric power for the AEA/MEA. However, the energy density of the most advanced battery is only 1/18 of aviation fuel (Hepperle, 2012). Therefore, the more feasible scheme is to use high-power density SG to generate electric energy for MEA/AEA. The B787 of Boeing company adopts the more electric technology with a 250 kVA variable frequency AC SG on each engine. In order to meet the electricity demand of the aircraft, the APU on B787 uses two 225 kVA SGs (Qin & Yan, 2015).

In many researches, the traditional aero-engine model is adopted instead of establish a model of more electric engine, and the output power of the traditional aero-engine is assumed to be equal to the electric power in numerical value (Cheng et al., 2012). Most of them use TURBOMATH program of the Cranfield University for modeling and performance calculation (Felder et al., 2011). Their research mainly focuses on the AEA/MEA and lacks the research on modeling and control of more electric engine (Cheng et al., 2013). Some researches analyze the more electric engine, but there is no detailed modeling and control analysis (Morioka et al., 2011).

Compared with the traditional APU, the SG in the starting process of MEAPU is controllable. Therefore, the starting process can be optimized by controlling the SG and the fuel flow of MEAPU.

The primary function of MEAPU is to provide electric power for the AEA/MEA. In order to ensure the stability of electric generation, MEAPU should stay at 100%. So, it is necessary to suppress the speed fluctuation of MEAPU when load is fluctuation.

Therefore, this chapter establishes the MEAPU model, including the SG and APU. On this basis, the variable substitution optimal control method is proposed to realize the optimization control of the starting process. In the power-generation process, the active load fluctuation suppression control is proposed for the load fluctuation.

2 Structure of MEAPU

The traditional APU is a micro-gas turbine engine, in which the compressor, burner, and turbine constitute the core engine. Some APUs have load compressor and gearbox. The high-pressure gas produced by the load compressor is supplied to the main engine of the aircraft for auxiliary starting or the aircraft as the air source of the environmental control system. The gearbox is connected with generators to generate electricity as the auxiliary power for the aircraft. For APU without a load compressor, the high-pressure gas is usually generated directly from the core compressor for the main engine or aircraft to use (Huang et al., 2008). The anti-surge and cooling of APU are realized by bleeding and air injection. The structure diagram of traditional APU is shown in Fig. 1.

In order to provide electric power for MEA/AEA, it is necessary to reform traditional APU. Compared with the traditional APU, the load compressor is removed, and the starter generator is directly connected with the shaft without a gearbox in the MEAPU. The performance of the starter generator is controllable, so it can adjust the speed and shaft power of the APU to a certain extent, so there is no need for anti-surge bleeding. At the same time, because MEAPU adopts a lubricating oil system using electric power and an electric cooling system, there is no need for lubricating oil cooling and compartment cooling. The structure of the MEAPU is shown in Fig. 2.

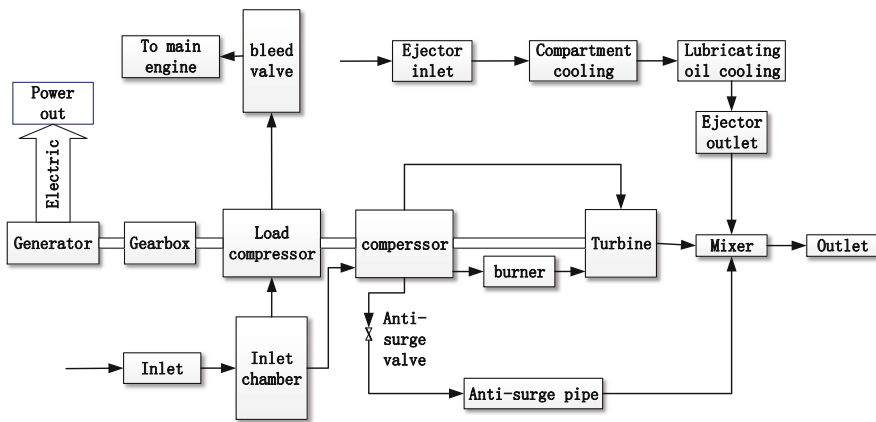


Fig. 1 The structure diagram of traditional APU. (Own drawing)

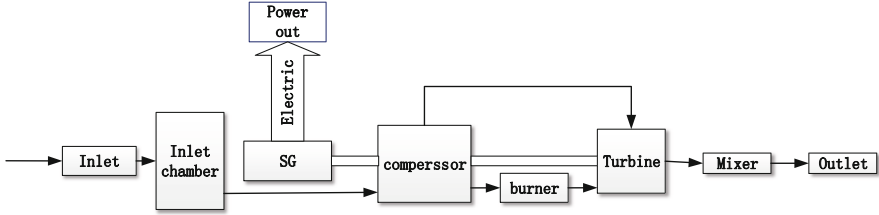


Fig. 2 The structure diagram of MEAPU. (Own drawing)

3 Modelling of MEAPU

In order to establish the model of MEAPU, the following assumptions are first made:

1. MEAPU model is a one-dimensional model, regardless of the different parameters of the same cross-section.
2. MEAPU calculation does not consider the viscous and inertial forces of the gas, nor the thermal inertia and volume effects.
3. The total pressure loss of each pneumatic part of MEAPU is the fixed value.
4. The degradation of MEPAU performance over time is not considered.

Because it is a well-known method to establish an aero-engine component level model, the component characteristics, working equations, and iterative solutions are no longer introduced in this chapter.

However, the usual compressor and turbine characteristics only include the characteristics above idle. In order to study the starting process, it is necessary to extrapolate the characteristics. Based on the low-speed region similarity principle of turbomachinery, the low-speed characteristics of compressor and turbine are extrapolated by using the following equations (Munson et al., 2013):

$$W_{\text{comew}} = K_w W_{\text{corref}} (n_{\text{comew}}/n_{\text{corref}})^q \quad (1)$$

$$\pi_{\text{comew}} = \left(K_\pi \left(\frac{n_{\text{comew}}}{n_{\text{corref}}} \right)^m \left(\pi_{\text{corref}}^{\frac{k-1}{k}} - 1 \right) + 1 \right)^{\frac{k}{k-1}} \quad (2)$$

$$\eta_{\text{comew}} = K_\eta \eta_{\text{corref}} (n_{\text{comew}}/n_{\text{corref}})^n \quad (3)$$

where n_{corref} is the corrected speed corresponding to the lowest speed line of the original characteristic and W_{corref} , π_{corref} , and η_{corref} is the corrected flow rate, pressure ratio, and efficiency corresponding to n_{corref} . K_w , K_π , and K_η are correction factors which should be determined manually. n_{comew} is the corrected speed to be extended, and W_{comew} , π_{comew} , and η_{comew} are the corrected flow rate, pressure ratio, and efficiency corresponding to n_{comew} . k is the adiabatic index, compressor is 1.4 and in turbine is 1.33. According to this equation, by selecting the appropriate power exponent q , m , and n , the characteristic of compressor and turbine at low speed can be extended.

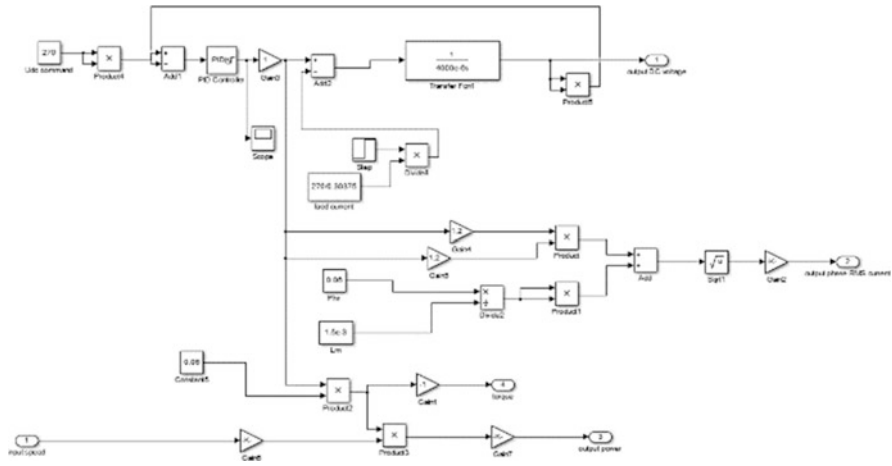


Fig. 3 Model of starter generator

SG is another important component of MEAPU, which is the primary embodiment of the concept of “more electricity.” Compared with the load compressor, the power of the SG can change abruptly according to the load demand. The power of the traditional APU is mainly extracted from the load compressor in the form of air extraction through the bleed valve, while a part of the energy is used for generating power after deceleration by the gearbox. The typical power-generation power in traditional APU is about 40 kW (Wang et al., 2020). The difference is that MEAPU adopts SG to generate electricity and extract electric power, and all power is supplied to SG to generate electricity. The SG modeled in this chapter is 240 kVA double-winding asynchronous AC SG (Pu et al., 2019). For the SG, the voltage, torque, and speed have the following relations:

$$T\omega = \frac{1}{2}C \frac{du_{dc}^2}{dt} + \frac{u_{dc}^2}{R_L} \tag{4}$$

The model of SG in SIMULINK TOOLKIT is shown in Fig. 3.

In the starting process, the power supply of the SG comes from the battery system. Assuming that the electric energy provided by the battery system does not change with the energy consumption of the battery during the starting process, which means it can provide enough electric energy for the MEAPU to start, then the SG can output constant torque to accelerate the rotor. In power generation, closed-loop control is used to keep the voltage stable. When the power load changes, the power-generation voltage is stable at 270 V, and the output torque (negative value) of SG changes.

4 Variable Substitution Optimal Control Method

In the starting process, the bleed valve of the load compressor of the traditional APU is closed, and the starter drives the APU. The starter usually runs in an open-loop mode, which cannot be controlled during the starting process. There is no loaded compressor in MEAPU, and the SG is completely controllable in the starting process. Therefore, the optimal control can be achieved by torque control of the SG and fuel flow control of the MEAPU.

The optimization objective is to shorten the starting time. After ignition, the torque is provided by the SG and the turbine, so the acceleration time is affected by the fuel flow W_f and the torque of SG M_{ST} . Therefore, the acceleration time t can be expressed as an equation of fuel flow and starting generator torque as follows:

$$t = f(W_f, M_{ST}) \quad (5)$$

To shortening starting time and ensure no surge and over-temperature, the constraint conditions are as follows:

$$I = \begin{cases} SM > SM_{\min} \\ T_{41} < T_{41, \max} \end{cases} \quad (6)$$

where SM is the surge margin of the compressor and T_{41} is the temperature before the turbine.

During the starting process, the fuel flow W_f and the torque of the SG M_{ST} jointly affect the rotational acceleration, thus affecting the surge margin. At the same time, the fuel flow W_f and the inlet flow rate W_{in} affect the T_{41} . Therefore, the fuel flow W_f and the torque of the SG M_{ST} are taken as the iteration variable of Newton iteration, and a new balance equation is set as follows:

$$\frac{SM - SM_{\min}}{SM_{\min}} = \varepsilon_4 \quad (7)$$

$$\frac{T_{41} - T_{41, \max}}{T_{41, \max}} = \varepsilon_5 \quad (8)$$

There are three balance equations and iterative variables in the MEAPU model. The variable substitution optimal control model is formed with the above two balance equations and iterative variables.

5 Active Load Fluctuation Suppression Control Method

More than 60% of the power output of the traditional APU is through the bleed air from the load compressor. Because the rate of bleed airflow cannot change suddenly, the power provided by the core engine will not change suddenly too. However, in MEAPU all power output is generated by the SG, and the power demand of the SG can change suddenly due to the sudden change of electric load. The power that it needs to provide to the SG will also change suddenly, which leads to speed fluctuation.

In general, speed closed-loop control is used to realize speed control for MEAPU. However, because APU is an inertial load, the speed change has a large lag compared with the torque change caused by the SG. Using speed feedback to adjust the fuel rate will inevitably lead to a large deviation of speed, which is also a disadvantage for the power-generation regulation of SG.

In SG, the frequency converter of SG can monitor the generation voltage and load current. Once the load changes, the voltage and current change immediately. Using the voltage and current, its output power can be calculated. Therefore, the power of SG can be introduced as a reference, combined with the speed closed-loop control to realize the active load fluctuation suppression control.

Using the MEAPU model, the fuel flow open-loop test method was adopted to obtain the fuel flow rate under different speeds and loads; the results is shown in Table 1.

Taking Table 1 as the interpolation table, the active load fluctuation suppression controller is established as shown in Fig. 4.

6 Results and Discussion

The torque of SG and fuel flow during the starting process of the starter generator are taken as the control variables to minimize the starting time meanwhile avoiding surge and over-temperature. The VSOC method is used to optimize the starting process and its results are shown in Fig. 5.

In Fig. 5, the SG stops working after the MEAPU reaches 60% of the designed speed. When the MEAPU accelerates to 90% of the designed speed, the SG starts to

Table 1 Fuel flow at different speed and load (g/s)

| Load | Speed | | | | |
|---------|-------|-------|-------|-------|-------|
| | 90% | 95% | 100% | 105% | 110% |
| 0 kVA | 20.50 | 24.9 | 29.44 | 31.34 | 33.52 |
| 60 kVA | 28.53 | 34.16 | 39.46 | 14.14 | 42.82 |
| 120 kVA | 36.74 | 42.91 | 48.72 | 51.39 | 52.98 |
| 180 kVA | 44.90 | 52.03 | 58.01 | 60.64 | 63.37 |
| 240 kVA | 53.21 | 61.37 | 67.68 | 70.22 | 72.76 |

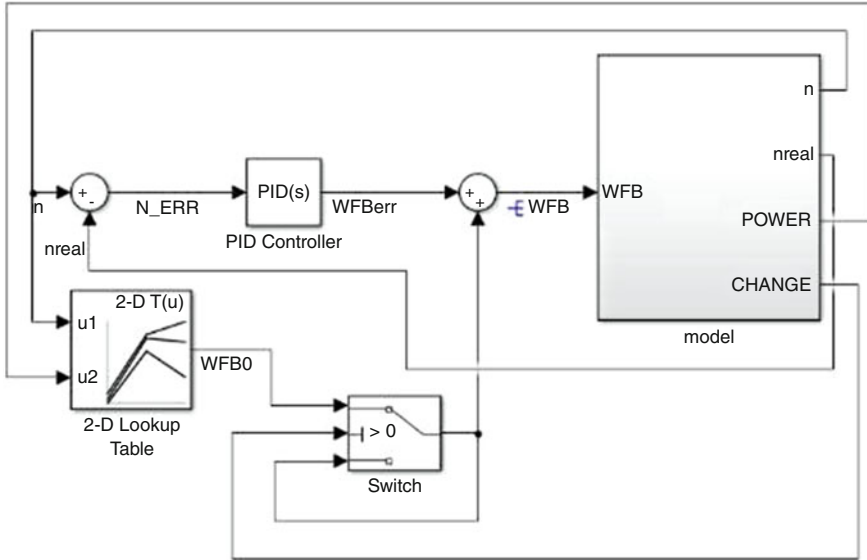


Fig. 4 Active load fluctuation suppression controller

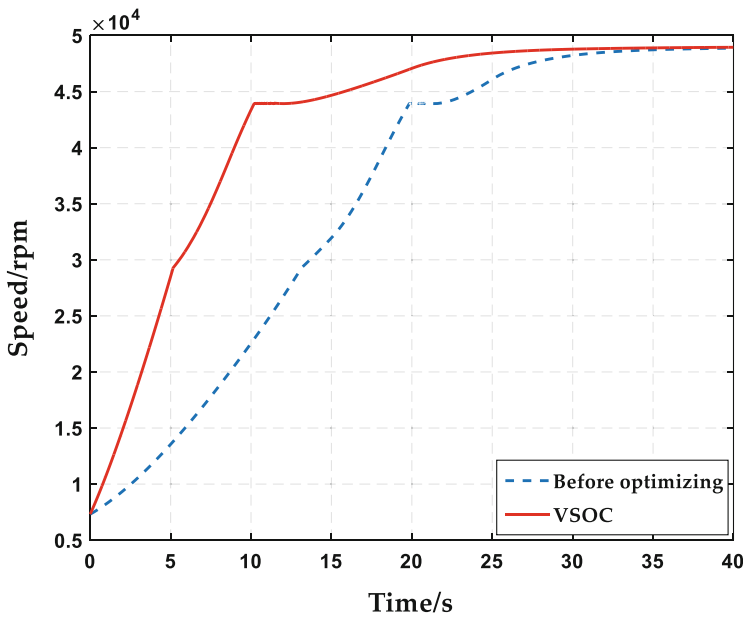


Fig. 5 The results of starting process

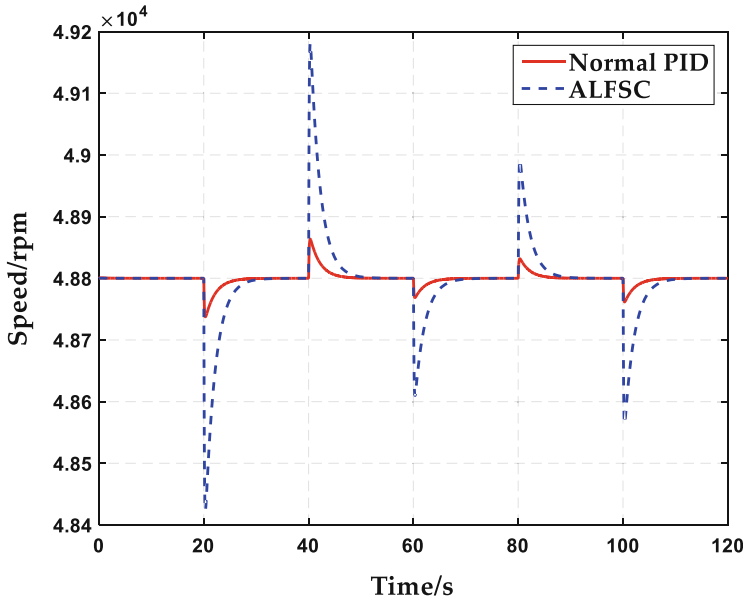


Fig. 6 The results of ALFSC

generate electricity. After optimization, the starting time is shortened by 10 s without surge and over-temperature.

The results of active load fluctuation suppression control are shown in Fig. 6. The load fluctuations of 240 kVA, -240 kVA, 120 kVA, -120 kVA, and 150 kVA are given at 20 s, 40 s, 60 s, 80 s, and 100 s, respectively. Compared with no optimization, the use of ALFSC can reduce speed fluctuations by up to 80%.

7 Conclusions

In order to study the control of the MEAPU, the structure of the MEAPU is studied firstly. Based on this structure, a MEAPU model consists of an auxiliary power unit and a starter generators is established.

Based on the model, in the starting process, a variable substitution optimal control (VSOC) method is proposed, and the starting time is shortened by 10 s without over-temperature and surge.

An active load fluctuation suppression control method is used in the generation progress, which suppresses the speed fluctuation caused by the sudden load of more than 80%.

Acknowledgments The author thanks Professor Tianhong Zhang for the research support and guidance he provided for the research.

References

- Cheng, Y. L., Georgios, D., Panagiotis, L., & Riti, S. (2012). Turboelectric distributed propulsion system modelling for hybrid-wing-body aircraft. In *48th AIAA/ASME/SAE/ASEE Joint Propulsion Conference & Exhibit Atlanta*, July 30–August 1, 2012, Atlanta, Georgia, USA.
- Cheng, Y. L., Georgios, D., Panagiotis, L., & Riti, S. (2013). Thermal cycle analysis of turboelectric distributed propulsion system with boundary layer ingestion. *Aerospace Science and Technology*, 27, 163–170.
- Feiner, L. J. (1993). Power—by—wire aircraft secondary power systems. In *Proceedings of 12th AIAA/IEEE digital avionics systems conference, 1993*. Institute of Electrical and Electronics Engineers.
- Felder, J. L., Kim, H. D., Brown, G. V., et al. (2011). An examination of the effect of boundary layer ingestion on turboelectric distributed propulsion systems. In *49th AIAA Aerospace Sciences meeting including the New Horizons Forum and Aerospace Exposition*, January 4–7, 2011, Orlando, Florida, USA.
- Hepperle, M. (2012). *Electric flight – Potential and limitations, energy efficient technologies and concepts of operation*, October 22–24, 2012, Lisbon, Portugal.
- Huang, G. P., Liang, D. W., & He, Z. Q. (2008). Comparison of technical characteristics of APU and micro turbine engines for large aircraft. *Journal of Aerospace Power*, 2, 383–388.
- Jones, R. I. (2002). The more electric aircraft—Assessing the benefits. *Journal of Aerospace Engineering*, 216(5), 259–269.
- Morioka, N., Oyori, H., Kakiuchi, D., & Ozawa, K. (2011). More electric engine architecture for aircraft engine application. In *Turbo Expo: Power for land, sea, and air*, June 6–10, 2011, Vancouver, British Columbia, Canada.
- Munson, B. R., Okiishi, T. H., Huebsch, W. W., et al. (2013). *Fundamentals of fluid mechanics* (7th ed.). Wiley.
- Pu, F. F., Liu, H. Z., Huang, W. X., & Xu, H. J. (2019, May 24). *A topological structure of a double winding asynchronous motor for AC/DC starter/generator*. CN201610258896.2.
- Qin, H. H., & Yan, Y. G. (2015). *Power system for more electric aircraft*. Beihang University Press.
- Rosero, J., Ortega, J., Aldabas, E., & Romeral, L. (2007). Moving towards a more electric aircraft. *IEEE A&E Systems Magazine*, 22(3), 3–9.
- Verschoor, M. (2005). The more electric architecture revolution. *Aerotech Magazine*, 1(1), 3–7.
- Wang, J. Q., Zhao, H. H., & Zhang, Y. (2020). Flight test of steady and transient characteristics of APU. *Aeronautical Science & Technology*, 31(9), 41–46.
- Weale, D., & Whitely, C. (2004). Power takes flight. *Power Engineering*, 18(3), 32–36.

Computational Analysis of Re-entry Space Vehicle at Supersonic and Hypersonic Speed



Jignesh Vala, Mehul K. Rana, Ayushi Mistry, Amit Parmar, Pritkumar Kathesiya, and Makadi Mahmmadsamad

Contents

| | | |
|-----|--|-----|
| 1 | Introduction | 368 |
| 1.1 | Aerodynamic Heating | 369 |
| 1.2 | Drag | 369 |
| 2 | Methodology | 369 |
| 2.1 | Design Selection | 369 |
| 2.2 | Apollo AS-202 | 370 |
| 2.3 | SpaceX Dragon Capsule | 370 |
| 3 | Analysis of Three-Dimensional Bodies | 371 |
| 3.1 | Geometry | 371 |
| 3.2 | Meshing | 372 |
| 3.3 | Setup | 373 |
| 4 | Results and Discussion | 374 |
| 5 | Conclusion | 376 |
| | References | 376 |

J. Vala (✉) · M. K. Rana

Gujarat Technological University, Sardar Vallabhbhai Patel Institute of Technology,
Department of Aeronautical Engineering, Vasad, Anand, Gujarat, India
e-mail: jigneshkumarvala.aero@svitvasad.ac.in; mehulrana.aero@svitvasad.ac.in

A. Mistry · A. Parmar · P. Kathesiya · M. Mahmmadsamad
Department of Aeronautical Engineering, Sardar Vallabhbhai Patel Institute of Technology,
Vasad, Anand, Gujarat, India

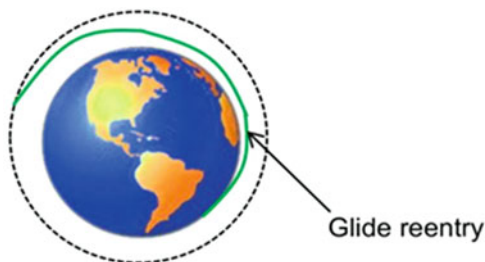
1 Introduction

Re-entry capsules are used for space applications with high withstand capacity of heating during re-entry phase. A re-entry capsule consists of a blunt body, and the aft body is straight or rounded base, for example, Dragon capsule and Apollo capsule. A bow shock forms ahead of the vehicle. Apart from the blunt-shaped nose, the most recent re-entry vehicles are equipped with heat shields to avoid damage of the capsule and get safe landing without injury. This space vehicle concept came from the obstacles, meteors and asteroids re-entry in atmosphere (Fig. 1) (Mehta, 2008).

For re-entry types based on the re-entry strategy, there are three categories of re-entry: (1) ballistic re-entry, (2) skip re-entry, and (3) glide re-entry, and out of these, glide re-entry is more preferable than other types. Because in glide re-entry, vehicles with lifting surfaces capable of producing high lift can have controlled deceleration as the vehicle descends. Here the re-entry begins with very shallow flight path angle and high angle of attack, and also drag is less compared to other re-entry types. Atmospheric entry or re-entry denotes that it is going to be reused or remodelling of the material equipment. It is a very crucial part of system to work on re-entry. As it produces high amount of friction and heat due to aerodynamic forces, the material tends to lose its stability or factor of safety in sustaining heat (Mehta, 2006). The heat shield design and its material shape and properties are helping capsules to safely re-enter into the atmosphere for further operations.

In re-entry vehicles, during re-entry phase, the thermal loads play a major role. Re-entry capsules run into high drag, high temperature and chemically reacting flow. Computational fluid dynamics (CFD) is mostly used to simulate these flows, as high enthalpy and low density associated with the flight conditions are difficult to reproduce in wind tunnels or shock tunnels at each re-entry trajectory point. Wind and shock tunnel tests are difficult and not economical to use. CFD is more economical approach for studying such flows. Therefore, CFD is mostly used as an analysis tool in the design of hypersonic vehicles. CFD is also used as a research tool to understand the complicated hypersonic effects. The two main factors affecting the re-entry vehicle during the atmospheric re-entry are aerodynamic heating and atmospheric drag.

Fig. 1 Glide re-entry
(Mehta, 2008)



1.1 Aerodynamic Heating

During atmospheric re-entry, the vehicle is moving through air at high speeds; shock wave is generated. While moving through the shock, the flow particles lose their kinetic energy which is converted to internal energy. Internal energy is only function of temperature; this rise in internal energy causes the temperature to increase. This temperature is directly affecting the body by convection process. Due to this process, the heat generated is transferred to the external surfaces of the vehicle. To protect the internal structure of the vehicle from the elevated heat on the external surfaces, thermal protection system is required. The purpose of the thermal protection system is to absorb or reject the energy released due to aerodynamic heating (Vinu et al., 2017).

1.2 Drag

It is the resistive force acting on the body in the direction of the flow when the body is moving through the fluid. This drag force is mainly responsible for decelerating the re-entry vehicle (Vinu et al., 2017).

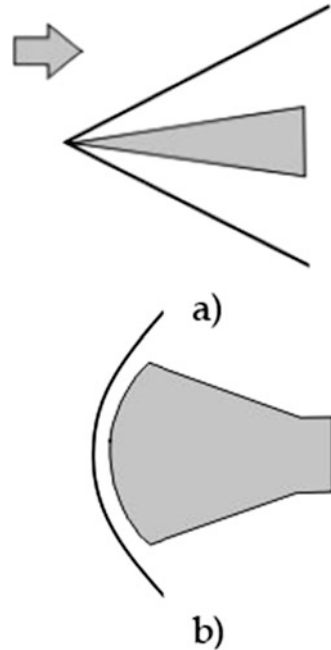
2 Methodology

CFD analysis can be divided into few parts: (1) create a required model of re-entry vehicle in particular software, (2) import the geometry into a meshing program, (3) analyse the meshed geometry in a CFD program by setting the methods, environmental condition and design parameters, and (4) calculate the results.

2.1 Design Selection

During re-entry strong shock wave is generated. Shock wave is a type of propagating disturbance that moves faster than the local speed of sound in the medium depending on the vehicle's shape; the shock wave can either be attached or detached. If the vehicle is sharp, the shock wave may attach to the tip and transfer a lot of heat, causing localized heating at the attachment point. If the vehicle is blunt, curved shock is formed in front of the body, and curved shock is strong shock because it consists of both normal and oblique shocks, but the shock is not directly attached to the body, and it cannot directly affect the body (Fig. 2) (Harshavardhana et al., 2014). So, the blunt body is more preferable than sharp body in space vehicle. The

Fig. 2 Comparison of the flow behaviour over two-dimensional. (a) Sharp body and (b) blunt body at high speeds (Harshavardhana et al., 2014)



flow behaviour over three-dimensional body such as the Dragon and Apollo capsules at supersonic and hypersonic speed is analysed.

2.2 *Apollo AS-202*

The Apollo-Saturn 202 (AS-202) mission was an unmanned suborbital flight to test the Saturn 1B launch vehicle and the Apollo Command and Service Modules. The AS-202 flight test was performed as part of the Apollo program (Rathnavel et al., 2020). The objectives of the flight were to verify the structural integrity, launch loads, stage separation and heat-shield at high-re-entry velocity.

2.3 *SpaceX Dragon Capsule*

Dragon is a class of reusable spacecraft developed and manufactured by American aerospace manufacturer SpaceX, a reusable cargo spacecraft. These are one of the best examples of the very efficient aerodynamic design used in re-entry vehicle (Figs. 3 and 4) (Harshavardhana et al., 2014).

Three-dimensional modelling is done in CATIA v5 software using given dimensions, and a detailed component design is neglected to reduce complexity and easy

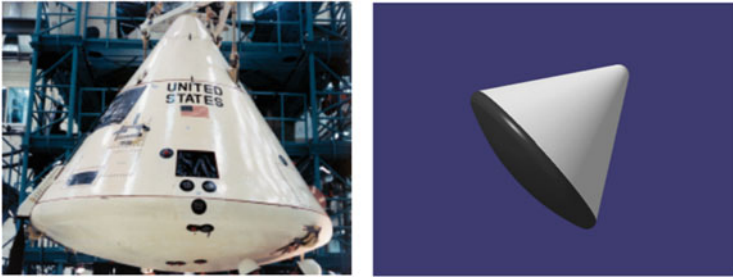


Fig. 3 The design of Apollo AS-202 capsule (Mehta, 2008)



Fig. 4 The design of SpaceX Dragon capsule (Mehta, 2006)

simulation. Geometry must be solid and defect less when it is imported in ANSYS design Modeller from the CATIA v5 software. Three-dimensional geometry is prepared by using drawing or drafting, and shaft tool is used in CATIA part design.

3 Analysis of Three-Dimensional Bodies

3.1 Geometry

Here, ANSYS Fluent is used to simulate the flow behaviour. The geometry is designed in CATIA v5 and it is imported in ANSYS (Fig. 5). The geometry is enclosed by the cylindrical domain. Then, the geometry is subtracted from the domain.

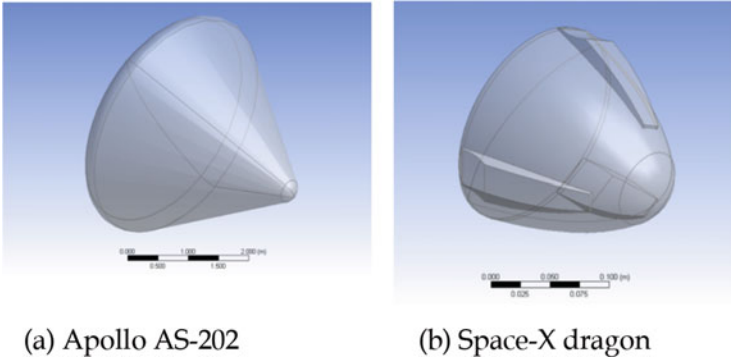


Fig. 5 (a) Apollo AS-202 and (b) SpaceX Dragon (Terry & Barber, 2007)

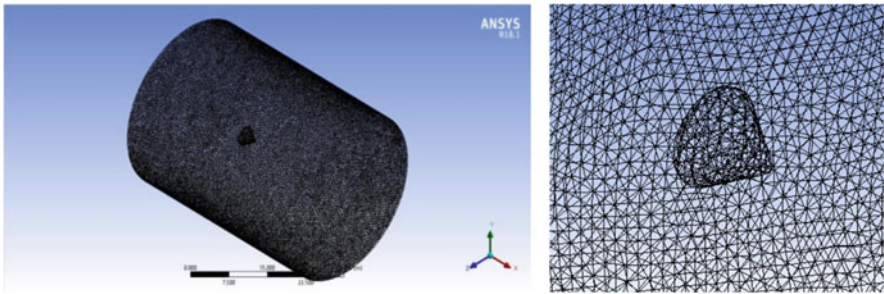


Fig. 6 Apollo AS-202 capsule (Terry & Barber, 2007)

3.2 Meshing

After importing the geometry, mesh is generated. Mesh generation is the process of dividing continuous geometric space into discrete geometry and topological cells. The domain is discretized in small elements. Here, the Tetrahedron patch conforming method and body sizing was also done for the mesh. Face sizing is done by using different element size to get a reliable result at the surface of the capsule. Mesh data for Apollo AS-202 and SpaceX capsule – 253,050 nodes, 1,445,811 elements, and 116,240 nodes, 637,345 elements – are generated, respectively (Figs. 6 and 7).

The quality is identified by minimum orthogonal quality and maximum aspect ratio. For Apollo AS-202 capsule meshing size is very fine, i.e. $1.01516e-01$ and $3.73909e+01$, respectively, and for SpaceX Dragon capsule, i.e. $8.86550e-02$ and $4.68671e+01$, respectively (Table 1).

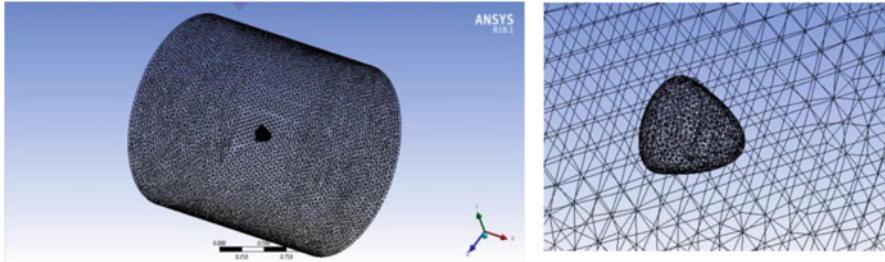


Fig. 7 SpaceX Dragon capsule (Terry & Barber, 2007)

Table 1 Boundary condition values of SpaceX Dragon Capsule (Walpot et al., 2012)

| | | |
|------------------|----------------------------------|--------------------|
| Inlet condition | Type | Pressure far-field |
| | Mach number | 1.5, 2.5, 5.0, 8.0 |
| | Flow direction in (X, Y, Z) | (1, 0, 0) |
| | Backflow turbulent intensity (%) | 5 |
| Outlet condition | Type | Pressure outlet |
| | Gauge pressure (Pa) | 0 |
| | Backflow pressure specification | Static pressure |
| | Backflow turbulent intensity (%) | 5 |
| Wall condition | Type | Pressure far-field |
| | Mach number | 1.5, 2.5, 5.0, 8.0 |
| | Flow direction in (X, Y, Z) | (1, 0, 0) |
| | Backflow turbulent intensity (%) | 5 |

3.3 Setup

Numerical setup is done by in ANSYS Fluent. Here, realizable k-epsilon (two equations) model is used which exhibits superior performance for flow involving rotation, boundary layer under strong adverse pressure gradients, separation and circulation. Air is used as a material for flow domain which satisfied ideal gas properties. Pressure boundary condition is applied at inlet and outlet surface of enclose with different Mach number as shown in Table 1. Simple solution method and coupled solution method are used for supersonic and hypersonic speeds, respectively, with second-order upwind scheme to get spatial discretization for better accuracy.

4 Results and Discussion

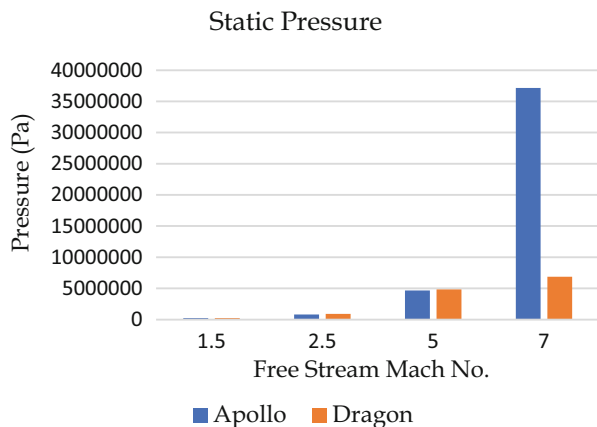
Contour has been given based on supersonic speed and hypersonic that generates curved shock in front of the body. So, shock layer term is introduced. Shock layer is defined as the flow field between the shock wave and the body. For hypersonic speed the shock layer is quite thin as compared to supersonic speed that is the main characteristics of hypersonic flow. So, shock layer is merged with viscous boundary layer at hypersonic speed, and also the viscosity is a main factor for friction. Due to influence of friction within the boundary layer, very-high-temperature region is formed near the body, and also at hypersonic speed, detachment distance is decreased compared to supersonic speed.

Variation in different flow properties is given in the form of contour (Fig. 8). Bow shock consists of both normal and oblique shock is shown in the figures. Normal shock is generated in front of the body, and oblique shock is generated above and below portion of the bow shock. A flow property is highly discontinuous across normal shock but in oblique shock gives continuous variation, and also the flow becomes subsonic after passing through the normal shock and becomes supersonic after passing through the oblique shock. Strong shock produces high entropy rise that is called normal shock region, and weaker shock produces low entropy rise that is called oblique shock region.

Here, in velocity contour above and below portion of the shock gives high variation in velocity that means flow is supersonic (red colour introduces high value), and in pressure contour high static pressure rise across normal shock and high-pressure loss takes place (Fig. 9).

So, the flow is no longer isentropic. Flow particles are passing through the normal shock; it loses their kinetic energy, and that kinetic energy is converted into internal energy. This rise in internal energy increases temperature because the internal energy is only a function of temperature. It is shown in temperature contour (Fig. 10). When re-entry vehicle Mach number increase, the shock tries to attach the body, and

Fig. 8 Static pressure variation in Apollo AS-2 capsule and SpaceX Dragon capsule (Vinu et al., 2017)



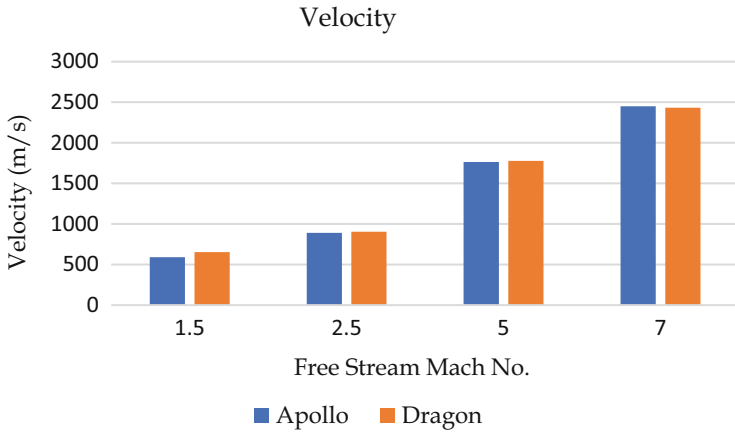


Fig. 9 Velocity variation in Apollo AS-2 capsule and SpaceX Dragon capsule (Vinu et al., 2017)

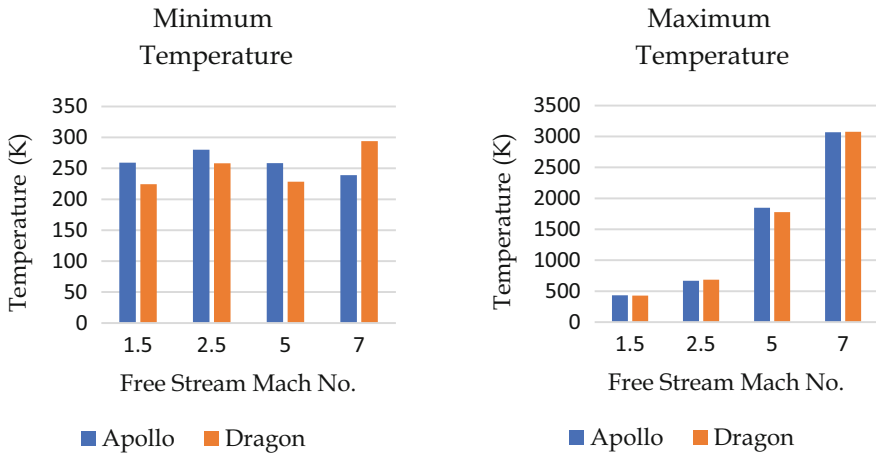


Fig. 10 Temperature variation in ApolloAS-2 capsule and SpaceX Dragon capsule (Vinu et al., 2017)

detachment distance decreases and there are more chances of high drag and heating also at high speed the vehicle is directly affected by the force convection between flow particles and body. The variation of flow properties on Apollo AS-202 and SpaceX Dragon with respect to different Mach numbers are given in above graph. From the above graph, pressure, velocity and temperature are properties that continuously increase with increase in Mach number.

5 Conclusion

By analysing the all-flow properties of both capsules, variations in all-flow properties are very high in Apollo AS-202 capsule as compared to the Dragon capsule. So, SpaceX Dragon capsule is more reliable. Below significant and important results are drawn from the present research study, when speed increases from supersonic to hypersonic at that time the shock tries to attach the body and becomes the strongest shock and that is called normal shock. Due to normal shock created ahead of re-entry vehicle, the flow properties become highly discontinuous, such as high static pressure rise, high temperature rise, high total pressure loss, adverse pressure gradient or back flow and rotational and high entropy rise. These properties can affect the body in different ways. High-temperature problem creates high aerodynamic heating problem, and adverse pressure gradient can decrease the speed of vehicle by high increase in drag. So, to compensate the high drag, aerodynamic body is used, and to withstand high heating, we provide thermal protection system or heat shield.

From the simulated methods of supersonic and hypersonic flow over capsule, the Dragon capsule is far more efficient as compared to Apollo due to the following reasons:

- The aerodynamic shape and fineness ratio
- Blunt nose and shock pattern
- Aerodynamic heating
- Boundary layer growth
- Axisymmetric flow and well-defined boundary
- Total pressure loss
- Temperature gradient near the wall
- Detachment distance

The capsule design is improved from the re-entry of natural objects such as asteroid, comets, meteorites, meteors, etc. and can re-enter safely with less damages.

References

- Harshavardhana, N. S., Sanjana, K., Sai Sharan, K., & Srinivas, G. (2014). Computational flow analysis of hypersonic reentry blunt body using fluent and gambit. *International Journal of Scientific & Engineering Research*, 5(5), 262–269.
- Mehta, R. (2006). Numerical simulation of supersonic flow past reentry capsules. *Shock Waves*, 15, 31–41. <https://doi.org/10.1007/s00193-005-0003-0>
- Mehta, R. (2008). Computations of flow field over Apollo and OREX reentry modules at high speed. *Indian Journal of Engineering and Materials Sciences*, 15, 459–466.
- Rathnavel, S., Balaji, K., Kumar, P. S., Sathesh, R., & Sankaran, K. (2020). Investigation of computational flow field over a re-entry capsule at high speed. *FME Transactions*, 48, 551–556. <https://doi.org/10.5937/fme2003551R>

- Terry, J., & Barber, T. (2007). CFD and experimental study of an inflatable re-entry vehicle model at Mach 3 conditions. *Acta Astronautica*, *61*(10), 854–865.
- Vinu, R. G., Chandran, K., & Deepak, G. (2017). Flight analysis of wedge and blunt nose re-entry capsules. *International Journal of Engineering Trends and Technology*, *49*, 181–185. <https://doi.org/10.14445/22315381/IJETT-V49P229>
- Walpot, L. M., Wright, M. J., Noeding, P., & Schrijer, F. (2012). Base flow investigation of the Apollo AS-202 Command Module. *Progress in Aerospace Sciences*, *48*, 57–74.

Sensor Fault Detection, Isolation, and Accommodation Applied to B-747



Akan Guven and Chingiz Hajiyev

Contents

| | | |
|-----|--|-----|
| 1 | Introduction | 380 |
| 2 | Method | 380 |
| 2.1 | Kalman Filter for Estimation of Lateral States of the B-747 Aircraft | 381 |
| 2.2 | Statistical Test for Fault Detection | 381 |
| 2.3 | Sensor Fault Isolation Algorithm | 382 |
| 2.4 | Reconfigured Kalman Filter | 382 |
| 3 | Results and Discussion | 383 |
| 3.1 | Sensor Fault Simulation Results with Reconfigured Kalman Filter | 383 |
| 3.2 | Reconfigured KF for Roll Rate Sensor Fault | 383 |
| 3.3 | Reconfigured KF for Roll Angle Sensor Fault | 384 |
| 3.4 | Root Mean Square Error Evaluation | 385 |
| 4 | Conclusion | 386 |
| | References | 386 |

Nomenclature

| | |
|------|------------------------------|
| OLKF | Optimal linear Kalman filter |
| RKF | Reconfigured Kalman Filter |
| RMSE | Root mean square error |
| SF | Sensor fault |

A. Guven (✉) · C. Hajiyev
Istanbul Technical University, Faculty of Aeronautics and Astronautics, Istanbul, Turkiye
e-mail: akan.guven@itu.edu.tr; cingiz@itu.edu.tr

1 Introduction

Based on Kalman filtering technique, fault accommodation is variously analyzed in the literature. Sensor fault detection and isolation based on Kalman filtering technique is referenced in various studies.

Kalman filter innovation sequence mean is based as an approach to detect and isolate aircraft sensor and control surface faults. A faster converging Kalman filter for sensor fault detection and isolation is brought (Fang et al., 2018). The faults are detected by the acknowledged threshold by the Kalman filter statistical sequence and isolated in a shorter time with initialization of the covariance matrix, and using an EKF compared to classical KF. The precedence of covariance matrices Q_{k-1} and R affects the Kalman filter operation. A method to carry out R_k is obtaining a series of measurements by keeping the system in steady state. Therefore, it is manageable to gain an order of magnitude of the measurement noise covariance after its mean has been deleted. On the other side, the selection of Q becomes a hard duty. Supposing R_k are predefined, an adaptation based on innovation term covariance is suggested to estimate Q_{k-1} at each sample time (Silva et al., 2018). Sensor fault detection and isolation is well performed based on the statistical function of Kalman filter innovation sequence (Hajiyev & Caliskan, 2005).

Only one faulty sensor at a time, roll rate and roll angle fault sensor conditions are examined. An Optimal KF is used to detect and isolate the sensor faults, and reconfigured KF is used to accommodate faults. The estimation results are assessed via root mean square error method, and reconfigured KF application has dominated estimation results compared to the conventional optimal KF method as granted by having less error magnitude.

2 Method

Aircraft EoM assumptions are pointed according Newton's Second Law;

Outer forces are thrust, gravity, aerodynamic forces, and engine moments; aerodynamic moments are the external moments. Equations of those outer forces which are also named external forces are and the equations of outer moments are based on aerodynamic coefficients (Xu, 2011).

Equations of motion (EOM) is derived on the following assumptions:

- The aircraft is rigid and the earth is flat and nonrotating. Constant aircraft mass during flight.
- Symmetry in the X_bZ_b plan which means the moments of inertia I_{xy} and I_{yz} are equal to zero. Symmetry in the X_bZ_b plan which means the moments of inertia I_{xy} and I_{yz} are equal to zero.

2.1 Kalman Filter for Estimation of Lateral States of the B-747 Aircraft

The trimmed model of LTI Boeing-747 aircraft is in steady-state flight; the lateral axis is simplified which is performed in the simulation that has four main states (x) that are consist of sideslip angle (β), yaw rate (r), roll rate (p), and roll angle (ϕ) and two inputs (u) that include rudder deflection (δr) and aileron deflection (δa). To run the simulation of the entire model, the system matrices below are calculated after the aircraft is linearized on an operating point via Taylor expansion and state space representation in Eqs. 1 and 2:

System Transition Matrix

$$A = \begin{bmatrix} -0.08895 & 0.06282 & -0.9795 & 0.04362 \\ -2.419 & -0.6024 & 0.3438 & 0.01244 \\ 1.491 & -0.2827 & -1.19 & -0.2719 \\ 0 & 1 & 0.05824 & 0 \end{bmatrix} \quad (1)$$

Control Distribution Matrix

$$B = \begin{bmatrix} 0 & 0.01024 \\ -0.1967 & 0.09127 \\ -0.0138 & -0.5503 \\ 0 & 0 \end{bmatrix} \quad (2)$$

System performance of the estimation or estimation error is dedicated by the covariance matrix. K is the value of the Kalman filter gain matrix, and P is considered as estimation error covariance. The noise covariance is directly proportional to the measurement noise, and Kalman gain matrix K is going to diminish at the moment reliability that is not steady on the measured output y during the new iteration to compute the next state \hat{x}_k .

To get accurate results from the Kalman filter, the values that are given, dynamic model and probabilistic data values, must be pertinent. Therefore, a proper model must match the probabilistic model to express changes in dynamics of the aircraft and environment circumstances. Kalman filter needs to have aircraft's initial condition state and initial covariance matrix predictions.

2.2 Statistical Test for Fault Detection

The states of the Boeing-747 model are estimated through a linear optimal KF. Two hypotheses in Eqs. 3 and 4 are introduced (Hajiyev & Caliskan, 2005):

$$H_0 = \text{No sensor fault} \quad (3)$$

$$H_1 = \text{Sensor fault occurrence on the system} \quad (4)$$

Innovation approach is utilized on the detection of sensor fault conditions. Establishing detection of sensor failure by altered mean of the innovation sequence of Kalman filter can be gathered. The normalized innovation sequence of the OLKF is used to determine which sensor exceeds the 3σ value.

This statistical function has χ^2 distribution with s degree of freedom where s is the dimension of the measurement vector. The level of significance α and threshold value $\chi_{\alpha, Ms}^2$ can be determined from the quantile table of the χ^2 distribution. Therefore, when the hypothesis H_1 is correct, the statistical value of β_k will have higher value compared to the threshold value $\chi_{\alpha, Ms}^2$, i.e.,

$$H_0 : \beta_k < \chi_{\alpha, Ms}^2, \forall k \quad (5)$$

$$H_1 : \beta_k > \chi_{\alpha, Ms}^2, \forall k \quad (6)$$

2.3 Sensor Fault Isolation Algorithm

Fault isolation process is responsible to bring out which sensor is faulty. Kalman filter-normalized innovation value is used to distinguish and isolate the faulty sensor.

Statistics property of KF-normalized innovation sequence value of the faulty sensor is assumed to be more affected compared to the remaining sensors. Meanwhile the fault has an influence on the variance of the innovation sequence. The process of decision-making is run to isolate the faulty sensor. For initial case, roll rate sensor's KF-normalized innovation function value has reached 3σ level between the time interval of $t = 300$ s till $t = 700$ s, which means fault occurred and the remaining sensor KF innovation function values seem normal. Therefore, the faulty sensor is isolated successfully by this approach.

2.4 Reconfigured Kalman Filter

The reconfigurable Kalman filter is regarded as an active fault-tolerant control system as in a reconfigurable control system; the faulty measurement channels are ignored and disabled, so its data is not used by filter algorithm. The symbol n is the number of states, and N is the number of measurement channels. The issue is the filter has to predict n states which is the full state, yet there is just $N - 1$ measurement channels that are available to obtain the incoming data for calculations. In this study, the simulations performed with basic cases and reconfigurable Kalman filter are

analyzed. The algorithm starts with disregarding the faulty measurement channel by deleting it. As a result, there is $N - 1$ states remaining at the moment simulation proceeds; the algorithm estimates N states from remaining measurement channel values.

Regulations are needed inside the OLKF algorithm to evaluate the reconfigurable technique. When a fault occurs, one channel is disabled, and the corresponding row has to be deleted from the $C_k N \times n$ -dimensional system measurement matrix. Therefore, C_k dimensions are altered as to $(N - 1) \times n$. Further, the correlated element of the faulty state has to be deleted from the v_k , N -dimensional measurement noise vector. Thus, v_k changes to $(N - 1)$ dimensional. After those adjustments, as a result, the normalized innovation also reduces its measurement channel number from four to three elements.

3 Results and Discussion

3.1 *Sensor Fault Simulation Results with Reconfigured Kalman Filter*

The technique has been executed in one state parameter for two cases which are the roll rate and roll angle sensor faults. The fault is accepted as it has started from the beginning of the iterations, and thus, faulty measurement channels are out of order over the whole simulation time span. Measurement noise increment fault is implied at time interval $t = 300$ to $t = 700$ s at lateral sensors. All types of fault are measurement noise increment fault at roll rate and roll angle for approximately 14.8 degrees per second and 9.16 degrees, respectively.

An optimal KF is used to detect and isolate the sensor faults and reconfigured KF proceed for fault accommodation. The first part of the figures illustrates the Kalman filter state estimation values and real state values as compared. The second part demonstrates the estimation error according to actual values of the Boeing-747 aircraft. And the last section demonstrates the error variance through iterations. The OLKF is not accurate after the fault took place and RKF rectifies values.

3.2 *Reconfigured KF for Roll Rate Sensor Fault*

In the case of when just one parameter is disabled, the reconfigured Kalman filter has good estimation values of roll rate sensor. Essential parameters to assess estimation performance are roll rate estimation values, the evolution of the error value, and the error variance along with the iterations and the absolute value of the stationary error. Performing the RKF, the estimations are calculated as following the real values.

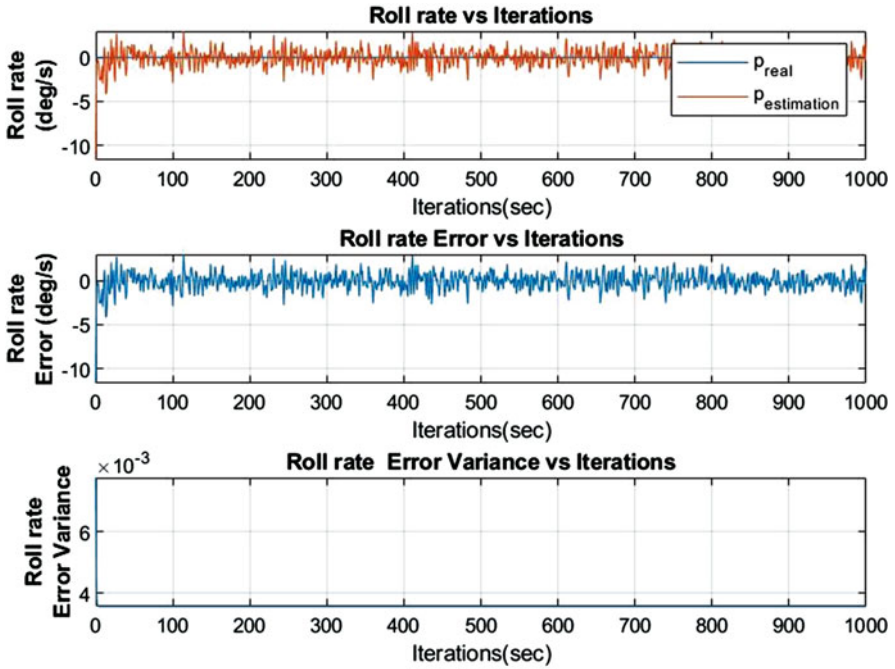


Fig. 1 Roll rate evolution results via RKF in the case of roll rate SF

In Fig. 1, the faulty measurement values are reconfigured by RKF algorithm and enhanced. The estimation values (red line) got closer to real value (blue line). Therefore, the fault is accommodated firmly.

3.3 Reconfigured KF for Roll Angle Sensor Fault

The measurement noise-increment fault took place at time $t = 300$ s till $t = 700$ s where the fault is exerted on both roll rate and roll angle sensors, the reconfigurable Kalman filter estimates even if there is no any input measurement data from faulty sensor measurement channels. The estimation values are getting closer to the stationary value which means steady-state flight values are conserved by the aircraft.

Both Figs. 1 and 2 illustrate the faults that are accommodated well and reached better estimation in spite of adverse faulty sensor measurements.

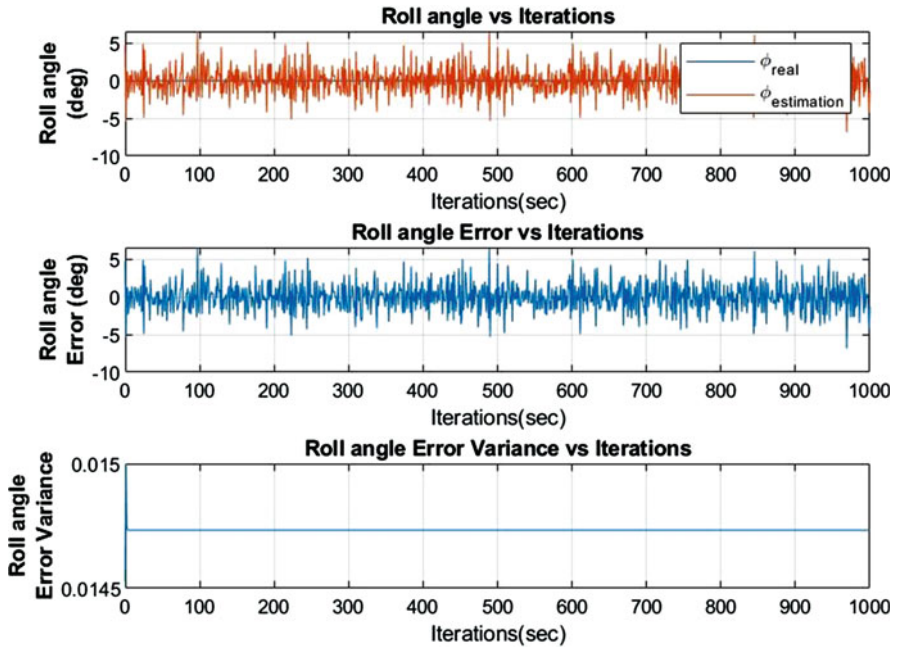


Fig. 2 Roll angle evolution results via RKF in the case of roll angle SF

Table 1 Root mean square error comparison for the sideslip angle sensor faulty case

| Lateral states | OLKF RMSE value | RKF RMSE value |
|----------------|-----------------|----------------|
| Sideslip angle | 2.1705 | 0.9940 |
| Yaw rate | 3.7693 | 1.7487 |
| Roll rate | 3.1349 | 0.9793 |
| Roll angle | 3.1226 | 1.4390 |

Table 2 Root mean square error comparison for the roll rate and roll angle double sensor fault case

| Lateral states | OLKF RMSE value | RKF RMSE value |
|----------------|-----------------|----------------|
| Sideslip angle | 2.5252 | 1.2190 |
| Yaw rate | 3.7927 | 1.9490 |
| Roll rate | 3.5726 | 1.7989 |
| Roll angle | 5.3753 | 1.7864 |

3.4 Root Mean Square Error Evaluation

Root mean square error method is performed to approve the results and that proves the estimations of RKF is better, and RMSE values can be seen in Tables 1 and 2.

4 Conclusion

Optimal linear Kalman filter (OLKF), fault detection, fault isolation, and adaptive Kalman filter algorithms are implied on selected bank angle and roll rate sensors of the Boeing-747 aircraft. The OLKF carries out satisfying estimation values if there is no fault on the system. On contrary, faulty case includes a measurement channels that seems to be broken, so the reliability of the filter estimations transforms to less accurate.

Two scenarios of fault in roll rate sensor and roll angle sensor fault are examined. Subsequently the fault detection process takes place and detects if a fault exists. The second stage consists of the fault isolation procedure which compares the statistics of the rate of sample and theoretical variances to distinguish the faulty sensor. At the last stage, the reconfigured Kalman filter algorithm runs and enhances the estimations to accomplish fault accommodation. This method is convenient to improve better results for sensor value estimations and open to develop sensor fault detection for flight control systems as auxiliary beacon for future studies.

References

- Fang, H., Tian, N., Wang, Y., Zhou, M., & Haile, M. A. (2018). Nonlinear Bayesian estimation: From Kalman filtering to a broader horizon. *IEEE/CAA Journal of Automatica Sinica*, 5(2), 401–417.
- Hajiyev, C., & Caliskan, F. (2005). Sensor and control surface/actuator failure detection and isolation applied to F-16 flight dynamic. *Aircraft Engineering and Aerospace Technology*, 77(2), 152–160.
- Silva, J. G., Limaverde Filho, J. O. D. A., & Fortaleza, E. L. F. (2018). Adaptive extended Kalman filter using exponential moving average. *IFAC-PapersOnLine*, 51(25), 208–211.
- Xu, G. X. (2011). Nonlinear fault-tolerant guidance and control for damaged aircraft. Doctoral dissertation.

Acoustic Emission and Acousto-Ultrasonic Monitoring in High-Temperature Environments



Luke Pollock and Graham Wild

Contents

| | | |
|-----|------------------------------------|-----|
| 1 | Introduction | 388 |
| 2 | Thermal Effects | 389 |
| 2.1 | Baseline Methods | 390 |
| 2.2 | Analytical Modelling | 391 |
| 3 | Sensors and Actuators (S&As) | 392 |
| 4 | Conclusion | 394 |
| | References | 395 |

Nomenclature

| | |
|------|--|
| AEs | Acoustic emissions |
| AUs | Acousto-ultrasonics |
| BSS | Baseline signal stretch |
| DF | Data fusion |
| DT | Digital twin |
| FBG | Fibre Bragg grating |
| GWs | Guided waves |
| IVHM | Integrated vehicular health monitoring |
| LDVR | Laser Doppler vibrometer |
| ML | Machine learning |
| OBS | Optimal baseline selection |
| PZT | Lead zirconate titanate |
| RUL | Remaining useful life |
| S&As | Sensors and actuators |

L. Pollock (✉) · G. Wild
University of New South Wales, Canberra, NSW, Australia
e-mail: L.Pollock@adfa.edu.au; G.Wild@adfa.edu.au

SHM Structural health monitoring
TRL Technology readiness level

1 Introduction

Acoustic emission (AE)- and acousto-ultrasonic (AU)-guided wave (GW) technologies have been presented as very realizable methods for the in situ monitoring of aerospace materials, structures and systems (Pollock & Wild, 2021; Rose, 2014; Giurgiutiu, 2007). AEs being defined as emissions released natively, typically from a transient event such as crack growth, impact or from an environmental load. In contrast, AU emissions are characterized as being induced in the material, structure or system via an actuator, typically an ultrasonic transducer. Whilst the governing behaviour of AE/AU is virtually identical, a distinction is made in this paper to allow for discussion pertaining to the various methods in which such emission can be excited in high-temperature environments (Rose, 2014). Of the various GW emissions that may exist, Lamb waves are of particular interest due to their ability to traverse large distances and strong tendencies to interact with damage (Rauter & Lammering, 2015). Due to their extensive application, Lamb waves are the primary focus of this work.

The interrogation of AE/AU in situ aids towards fulfilling the four main levels of a comprehensive structural health monitoring (SHM) system:

- Level I: The ability to detect damage
- Level II: The ability to determine the location of damage
- Level III: The ability to characterize the extent of damage
- Level IV: The ability to quantify the damage and provide remaining useful life (RUL) assessments

Unlike alternative methods, AE/AU can fulfil all four levels and are hence a viable tool towards the creation of SHM. Progressing further, beyond the interrogation of materials and structures alone and towards the monitoring of systems, enables the creation of integrated vehicular health monitoring (IVHM). IVHM provides an encompassing view of the overall health of the vehicle of which SHM can be considered a part. Individual systems can be effectively monitored, particularly with the use of AEs by examining modal characteristics. The application of machine learning (ML) algorithms to large datasets for healthy, baseline operation and damaged operation provides the ability to formulate system prognostics and RUL assessment.

IVHM is an effective tool for improving the reliability and performance of aerospace vehicles, particularly for high-risk environments. Development of hypersonic vehicle technologies has accelerated greatly over the past several decades, particularly due to security concerns. Whilst the field has seen deployment of experimental vehicles (~TRL 5), mass production has been delayed, partly owing

to the low reliability of some systems (Pollock et al., 2021). The extreme environments in which these vehicles operate introduce large uncertainties and sensitivities of which the use of IVHM can aid in overcoming. Prior to implementation, environmental factors must be considered upon IVHM techniques, of which temperature changes are most notably dominant (Andrews et al., 2008). The operation of vehicles at speeds in excess of Mach five introduces extreme aerodynamic heating that requires consideration and modelling to compensate for in IVHM. High temperatures can also be encountered in subsonic environments, most notably in propulsion systems which have recently been shown as the most common cause of fatigue failure (Pollock et al., 2021).

This chapter aims to outline the challenges associated with the deployment of AE/AU-based IVHM in high-temperature environments as well as the potential methods of overcoming them. Consideration is given for how AE/AU can be performed, including for indirect measurement. A short summary of past works into high-temperature AE/AU is provided as well as a discussion regarding potential avenues for future work.

2 Thermal Effects

Early works towards the understanding of thermally induced variations to Lamb wave behaviour focused primarily upon experimental observation. Blaise and Chang (2001) observed reductions in wave amplitudes and phase velocities at temperatures of $-90\text{ }^{\circ}\text{C}$. Lee et al. (2003) studied thermal effects on piezoelectric transducer-acquired Lamb waves, indicating how the effects of temperature showed dominance to the presence of damage. Amplitude was generally demonstrated as decreasing with increasing temperature. Several methods were proposed to overcome the effects with particular emphasis given towards identifying thermally independent features that could be used for analysis. Works conducted by Lu and Michaels (2005), Michaels and Michaels (2005) and Konstantinidis et al. (2006) attributed the variation in the response of the signals to changes in the physical properties of the materials and hence, dispersion characteristics. Stressed plates that would arise from thermal gradients have likewise been shown to exhibit changes in dispersion behaviour (Pei & Bond, 2016).

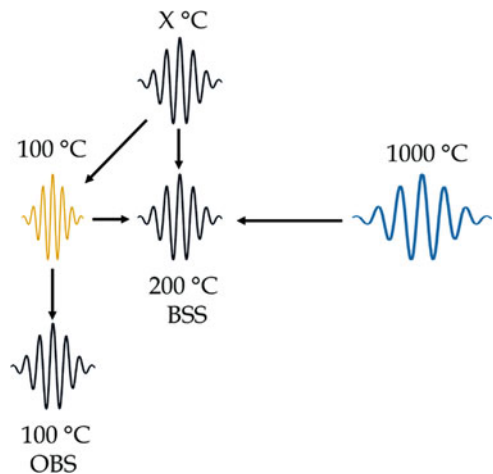
Whilst a suitable body of literature exists that explores the thermal effects on Lamb wave propagation, little work has been completed at temperatures of interest ($>1000\text{ }^{\circ}\text{C}$). Within this higher temperature range, it is expected that additional phenomena may be encountered that have not been considered in previous work. Materials for use in this temperature range including nickel-based superalloys, titanium aluminides and ceramic matrix composites (CMCs) exhibit phenomena such as viscoelastic behaviour and creep that has not been characterized or modelled (Ashby et al., 2018). Moreover, accumulation of creep damage results in higher void content and cracking that can further influence AE/AU behaviour and further engenders reflection-transmission responses (Ashby et al., 2018).

2.1 Baseline Methods

In overcoming thermal effects, the most commonly adopted approaches have utilized optimal baseline selection (OBS) or baseline signal stretch (BSS) (Fendzi et al., 2016). The use of OBS relies upon sufficient baseline data from which the most alike baseline is determined from any number of suitable criteria such as least squares error. In comparison, BSS creates a model from acquired baseline data to estimate the change in response. Hence, whilst BSS requires less data to apply, the selection of suitable modelling methods is of paramount importance. More recently, it has been demonstrated that a combination of OBS and BSS is the most effective method for thermal compensation (Liu et al., 2016). A comparison between OBS and BSS is illustrated in Fig. 1.

A variety of compensation methods have been studied, each with their own merits. Gandhi and Michaels (2010) calculated dispersion curves under the influence of changing physical properties by applying a small linear perturbation to a reference curve. The proposed method was a highly efficient and accurate alternative in comparison to complete recalculation. Clarke et al. (2010) combined OBS and BSS to create a compensation method that required less baseline signals. Fendzi et al. (2016) applied an ordinary least square regression to the thermally induced amplitude factor and phase shift. The two fitted parameters were extracted through application of a Hilbert transform with the model indicating good overall results. Liu et al. (2016) completed similar work by compensating phase shift using a Hilbert transform and amplitude via an orthogonal matching pursuit. The model proved capable up to $\pm 18^\circ\text{C}$ of the baseline signal temperature. Recent work undertaken by Sun et al. (2019) presented an algorithm for Lamb wave compensation across a thermal gradient. Hilbert transform and Levenberg-Marquardt optimization algorithms were used to extract amplitude and phase information from which a model was constructed to estimate compensation parameters.

Fig. 1 The difference between the BSS (interpolation) and OBS (nearest neighbour) methods



2.2 Analytical Modelling

Efforts have likewise been made towards analytical modelling to remove the need for the collection of large baseline datasets. One such model developed by Dodson and Inman (2013) is presented below. Similar to the original theory developed by Lamb (1917), the elastic displacement of an infinite, isotropic, and homogenous plate is considered with a traction-free boundary condition. However, the physical properties of the plate are given as a function of the temperature change θ and unlike in Lamb's work are not considered to be constant (Eq. 1).

$$(\lambda_T + \mu_T)u_{j,ij} + \mu_T u_{i,ij} + \rho_T f_i = \rho_T \ddot{u}_i \quad (1)$$

where λ_T and μ_T are the first and second temperature-dependent Lamé's constants, respectively. The temperature change θ is taken as the difference between the current temperature T and that of a reference temperature T_0 . The half-thickness of the plate h with respect to the thickness at the reference temperature h_0 is then determined by considering the linear coefficient of thermal expansion α (Eq. 2).

$$h(\theta) = h_0(1 + \alpha\theta) \quad (2)$$

Likewise, the density of the material with respect to the density at the reference temperature can be determined (Eq. 3).

$$\rho(\theta) = \frac{\rho_0}{(1 + \alpha\theta)^3} \quad (3)$$

The variation in Young's modulus and Poisson's ratio were empirically derived by Augereau et al. (2007) for aluminium 6061-T6 over a temperature range of 20–220 °C as given below (Eqs. 4 and 5).

$$E = 77.59 - 27.03 \cdot 10^{-3} \cdot T - 13.78 \cdot 10^{-6} \cdot T^2 \quad (4)$$

$$\nu = 0.317 + 54.79 \cdot 10^{-3} \cdot T + 6.5 \cdot 10^{-9} \cdot T^2 \quad (5)$$

This temperature range, evidently much lower than that being considered as 'high' for the purposes of this work, is a major limitation of the proposed model. Hence, it is noteworthy that whilst the presented analysis provides a useful analytical framework, empirical models for the temperature-dependent behaviour of materials at higher temperatures are required. Solution of Eq. 1 by application of a Helmholtz decomposition yields the traditional Rayleigh-Lamb equation and indicates that the fundamental behaviour is independent of temperature. Hence, the change in response of the medium to elevated temperatures is solely a product of the change in physical properties. As such, the variation in behaviour may be determined from the p and q constants (Eqs. 6 and 7):

$$p = \sqrt{\frac{\omega^2}{C_L^2(\theta)} - k^2} \quad (6)$$

$$q = \sqrt{\frac{\omega^2}{C_T^2(\theta)} - k^2} \quad (7)$$

where ω is the angular frequency of the Lamb wave, C_L and C_T are the longitudinal and transverse wave velocities respectively, and k is the Lamb wave number. Taking the derivative of p and q with respect to temperature provides the following relationships (Eqs. 8 and 9):

$$p \frac{\partial p}{\partial T} = k \frac{\partial k}{\partial T} - k_L \frac{\partial k_L}{\partial T} \quad (8)$$

$$q \frac{\partial q}{\partial T} = k \frac{\partial k}{\partial T} - k_T \frac{\partial k_T}{\partial T} \quad (9)$$

where k_L and k_T are the longitudinal and transverse wave numbers, respectively. Finally, the group velocity C_G may be calculated as follows from the phase velocity C_P (Eq. 10).

$$\frac{\partial C_G}{\partial T} = \frac{\partial C_P}{\partial T} \left(1 - \frac{k}{C_P} \frac{\partial C_P}{\partial k} \right) + k \left(\frac{\partial^2 C_P}{\partial k \partial T} \right) \quad (10)$$

Results of the analytical modelling identified two frequencies of interest for the antisymmetric wave mode that corresponded to no change in the group velocity. These frequencies, identified in Figs. 2 and 3, are temperature independent and hence, satisfy Lee et al. (2003) earlier proposed compensation method. Modelling of the thermal variation in phase response of Lamb waves via numerical solutions to the Rayleigh-Lamb equation likewise demonstrates a strong dependence upon temperature. Using the empirical relationships from Augereau et al. (2007), dispersion curves and AEs are computed for aluminium 6061-T6 at 25 °C and 500 °C as shown in Fig. 3. As is evident, the change in temperature has a large impact upon the dispersion curves which induce shape and time delay changes to the acquired AEs.

3 Sensors and Actuators (S&As)

Whilst a strong fundamental understanding of AE/AU behaviour is of paramount importance for the interrogation of a structure, there is likewise a requirement for suitable S&As that may be employed at high temperatures. The lack of ability to detect or actuate an emission renders any IVHM system redundant and hence,

Fig. 2 Group velocity sensitivity reproduced from Dodson and Inman (2013)

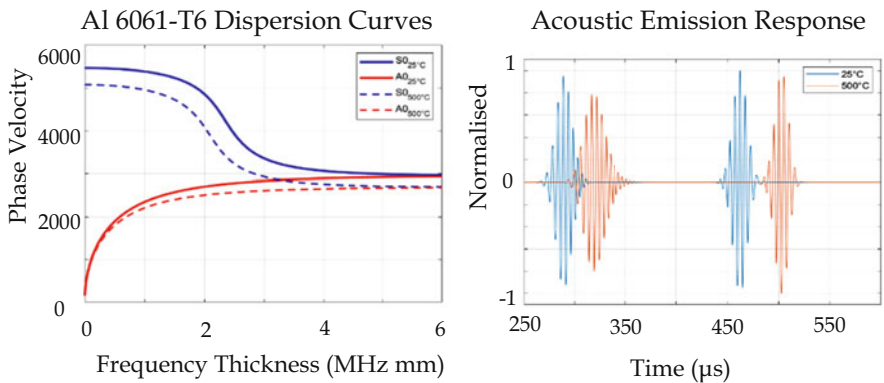
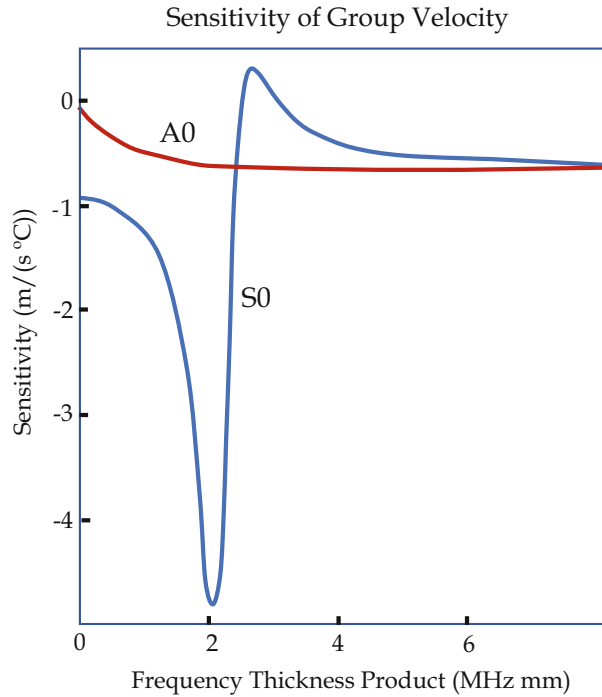


Fig. 3 Thermal effects upon Lamb wave propagation

comparable research is required. Development of suitable S&As may be considered an even more difficult task as the current technology is woefully inadequate for such extreme environments. Piezoelectric lead zirconate titanate (PZT) transducers are the most common due to their ability to function as both sensor and actuator as well as their capability to produce circularly crested waves (Giurgiutiu, 2007). Despite advances towards high-temperature PZTs, the current maximum operational limit

of such devices remains below 600 °C and hence, may only be suitable for the less extreme thermal areas of a structure (Stevenson et al., 2015).

Possibly the only contact sensor technology currently capable of operating in such extreme environments is that of a fibre Bragg grating (FBG). FBGs function as a wavelength specific mirror that is etched into an optical fibre cable. Whilst conventional silica fibres have been demonstrated up to 1200 °C, single crystalline sapphire in fibre form has been shown capable up to a temperature of 2050 °C (Habisreuther et al., 2015). Manufacturing of such fibres is not without challenges however, and further work is required to ensure that sensor readings do not drift over time in high-temperature environments (Willsch et al., 2009).

Non-contact technologies such as laser Doppler vibrometers (LDVRs) (Xiao & Yu, 2019) and high-power laser pulse actuators (Hosoya et al., 2018) show potential promise. However, a direct line of sight to the surface is required. Moreover, sufficient space is required between surface and sensor or actuator to limit thermal radiation. Hence, in the application of AE monitoring, the use of silica or sapphire FBGs may prove sufficient; however, there does not yet exist a suitable method for the ultrasonic transduction required for AU methods.

4 Conclusion

Ultimately, it is evident that further work is required towards both the understanding of AE/AU behaviour at high temperatures as well as for the development of S&As capable of enduring such extreme environments. Alternative methods to overcome physical limitations may see the application of non-contact technologies; however, digital twin (DT) techniques may prove equally useful. The development of a suitably accurate DT model renders the ability to gather numerical and simulation data. Environmental inputs to the DT can be sourced from sensor networks and used to predict the system response. Moreover, whilst few S&As exist that are suitable for the extrema conditions, instrumentation may be employed in a reasonable proximity to the region of interest following which an appropriate data fusion (DF) algorithm may be applied. A combination of experimental and numerically simulated data from the DT model combined using a DF technique such as a Kalman filter or neural network aims to enhance the reliability of the IVHM system without the need for direct contact monitoring.

Moreover, the use of ML may be used to aid in the selection of suitable baseline for thermal compensation and with adequate data may also aid in overcoming the viscoelastic and creep responses of the material. More work is evidently required to fully realize the potential applications of AE/AU IVHM in which the possibility for complete implementation has the potential to drastically increase the reliability of systems operating in extreme environments.

References

- Andrews, J. P., Palazotto, A. N., DeSimio, M. P., & Olson, S. E. (2008). Lamb wave propagation in varying isothermal environments. *Structural Health Monitoring*, 7, 265–270.
- Ashby, M. F., Shercliff, H., & Cebon, D. (2018). *Materials: Engineering, science, processing and design*. Butterworth-Heinemann.
- Augereau, F., Laux, D., Allais, L., Mottot, M., & Caes, C. (2007). Ultrasonic measurement of anisotropy and temperature dependence of elastic parameters by a dry coupling method applied to a 6061-T6 alloy. *Ultrasonics*, 46, 34–41.
- Blaise, E., & Chang, F. (2001). Built-in diagnostics for debonding in sandwich structures under extreme temperatures. In *Proceedings of the 3rd international workshop on structural health monitoring*, Stanford, California, USA, pp. 154–163.
- Clarke, T., Simonetti, F., & Cawley, P. (2010). Guided wave health monitoring of complex structures by sparse array systems: Influence of temperature changes on performance. *Journal of Sound and Vibration*, 329, 2306–2322.
- Dodson, J., & Inman, D. (2013). Thermal sensitivity of Lamb waves for structural health monitoring applications. *Ultrasonics*, 53, 677–685.
- Fendzi, C., Rebillat, M., Mechbal, N., Guskov, M., & Coffignal, G. (2016). A data-driven temperature compensation approach for structural health monitoring using lamb waves. *Structural Health Monitoring*, 15, 525–540.
- Gandhi, N., & Michaels, J. E. (2010). Efficient perturbation analysis of lamb wave dispersion curves. In *AIP conference proceedings* (pp. 215–222). American Institute of Physics.
- Giurgiutiu, V. (2007). *Structural health monitoring: With piezoelectric wafer active sensors*. Elsevier.
- Habisreuther, T., Elsmann, T., Pan, Z., Graf, A., Willsch, R., & Schmidt, M. A. (2015). Sapphire fiber Bragg gratings for high temperature and dynamic temperature diagnostics. *Applied Thermal Engineering*, 91, 860–865.
- Hosoya, N., Yoshinaga, A., Kanda, A., & Kajiwara, I. (2018). Non-contact and non-destructive Lamb wave generation using laser-induced plasma shock wave. *International Journal of Mechanical Sciences*, 140, 486–492.
- Konstantinidis, G., Drinkwater, B. W., & Wilcox, P. D. (2006). The temperature stability of guided wave structural health monitoring systems. *Smart Materials and Structures*, 15, 967.
- Lamb, H. (1917). On waves in an elastic plate. *Proceedings of the Royal Society of London. Series A, Containing Papers of a Mathematical and Physical Character*, 93, 114–128.
- Lee, B., Manson, G., & Staszewski, W. (2003). Environmental effects on lamb wave responses from piezoceramic sensors. *Materials Science Forum*, 440–441, 195–202.
- Liu, G., Xiao, Y., Zhang, H., & Ren, G. (2016). Baseline signal reconstruction for temperature compensation in lamb wave-based damage detection. *Sensors*, 16, 1273.
- Lu, Y., & Michaels, J. E. (2005). A methodology for structural health monitoring with diffuse ultrasonic waves in the presence of temperature variations. *Ultrasonics*, 43, 717–731.
- Michaels, J. E., & Michaels, T. E. (2005). Detection of structural damage from the local temporal coherence of diffuse ultrasonic signals. *IEEE Transactions on Ultrasonics, Ferroelectrics, and Frequency Control*, 52, 1769–1782.
- Pei, N., & Bond, L. J. (2016). Higher order acoustoelastic Lamb wave propagation in stressed plates. *The Journal of the Acoustical Society of America*, 140, 3834–3843.
- Pollock, L., & Wild, G. (2021). *Spectral domain analysis of acousto-ultrasonic tone burst lamb wave emissions in uncured pre-preg carbon fiber composites*. AIAA, ASCEND.
- Pollock, L., Wild, G., Abdelwahab, A. K., & Murray, J. (2021). The need for aerospace structural health monitoring: A review of aircraft fatigue accidents. *International Journal of Prognostics and Health Management*, 12. <https://doi.org/10.36001/ijphm.2021.v12i3.2368>
- Rauter, N., & Lammering, R. (2015). Impact damage detection in composite structures considering nonlinear lamb wave propagation. *Mechanics of Advanced Materials and Structures*, 22, 44–51.
- Rose, J. L. (2014). *Ultrasonic guided waves in solid media*. Cambridge University Press.

- Stevenson, T., Martin, D., Cowin, P., Blumfield, A., Bell, A., Comyn, T., & Weaver, P. (2015). Piezoelectric materials for high temperature transducers and actuators. *Journal of Materials Science: Materials in Electronics*, 26, 9256–9267.
- Sun, H., Yi, J., Xu, Y., Wang, Y., & Qing, X. (2019). Identification and compensation technique of non-uniform temperature field for Lamb wave-and multiple sensors-based damage detection. *Sensors*, 19, 2930.
- Willsch, M., Bosselmann, T., Flohr, P., Kull, R., Ecke, W., Latka, I., Fischer, D., & Thiel, T. (2009). Design of fiber optical high temperature sensors for gas turbine monitoring. In *20th International conference on optical fibre sensors* (p. 75037R). International Society for Optics and Photonics.
- Xiao, W., & Yu, L. (2019). Nondestructive evaluation with fully non-contact air-coupled transducer-scanning laser Doppler vibrometer Lamb wave system. In *Nondestructive characterization and monitoring of advanced materials, aerospace, civil infrastructure, and transportation XIII* (p. 109711G). International Society for Optics and Photonics.

Explicit Dynamic Finite Element Simulation of Plate Impacts for Damage Localization



Luke Pollock, Noemi North, and Graham Wild

Contents

| | | |
|-----|---|-----|
| 1 | Introduction | 398 |
| 2 | Finite Element Analysis (FEA) Simulations | 399 |
| 2.1 | Setup | 399 |
| 2.2 | Results and Discussion | 400 |
| 3 | Acoustic Emission (AE) Localization | 403 |
| 4 | Conclusion | 404 |
| | References | 404 |

Nomenclature

| | |
|------|------------------------------|
| AEs | Acoustic emissions |
| BVID | Barely visible impact damage |
| CFL | Courant-Friedrich-Levy |
| FEA | Finite element analysis |
| FRPs | Fibre-reinforced polymers |
| NDT | Non-destructive testing |
| SHM | Structural health monitoring |

L. Pollock (✉) · N. North · G. Wild
University of New South Wales, Canberra, NSW, Australia
e-mail: L.Pollock@adfa.edu.au; N.North@student.unsw.edu.au; G.Wild@adfa.edu.au

1 Introduction

The aim of this work is to examine the potential application of explicit dynamic finite element analysis (FEA) simulations using the software package LS-DYNA for the interrogation of acoustic emissions (AEs) released from low-velocity impacts for the purposes of acoustic source localization. Low-velocity impacts most commonly occur in aerospace structures from tool drops, runway debris (Kumar & Rai, 1993) or in-flight debris such as hail (Fawcett & Oakes, 2006) and can have severe effects upon the mechanical performance of fibre-reinforced polymers (FRPs) (Mustapha et al., 2016; Saeedifar et al., 2018).

The possible result of a low-velocity impact is the formation of barely visible impact damage (BVID) that can be difficult to detect in visual inspections, requiring advanced non-destructive testing (NDT) (Dutton et al., 2004). Figure 1 showcases the damage mechanisms for the creation of BVID. As shown, the radius of damage increases through the thickness of the structure such that the impacted side of the panel exhibits very little visual indentation. Conversely, the rear of the panel visually exhibits high levels of damage. Whilst the detection of BVID on the rear of the panel can be more easily performed, limitations regarding access to this region constrain detection capabilities.

Alternative methods for detection include the development of structural health monitoring (SHM) systems that are capable of real-time detection of impact events such that their source may be localized and damage quantified. Several methods exist for the development of SHM; however, AE monitoring presents as one of the best techniques due to the strong tendency of the AE to interact with damage and its ability to propagate over large distances (Dafydd & Sharif Khodaei, 2020; Rauter & Lammering, 2015).

BVID is of particular concern in the use of FRPs as it acts as a major damage initiation source (Dutton et al., 2004; Defense., 2002). Compression forces induced during impact are carried through-thickness by the typically brittle composite matrix. Such forces initiate damage via matrix cracking that under compression loading results in delamination and the formation of sub-laminates that are prone to buckling (Wronkiewicz-Katunin et al., 2019). As a result, the occurrence of BVID is often

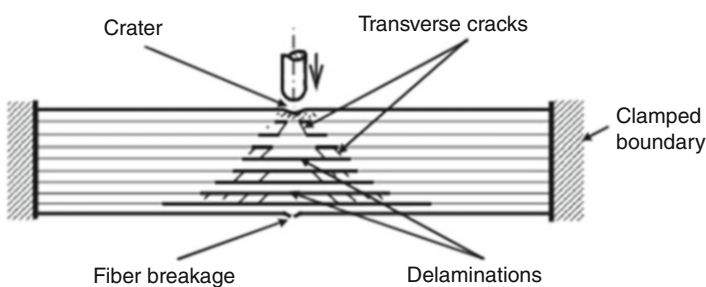


Fig. 1 A depiction of the mechanisms behind the formation of BVID resulting from low-velocity impacts in FRPs (Azouaoui et al., 2010)

characterized by reduced flexural and compression strength of the composite. Any such damage to the FRP may likewise act as an initiation point for corrosion, reducing the life of the structure (Dutton et al., 2004).

2 Finite Element Analysis (FEA) Simulations

2.1 Setup

To inform the development of a SHM system, an explicit dynamic FEA model can be used to simulate low-velocity impacts and the AEs released from such events. This work has employed the use of LS-DYNA developed by Livermore Software for such analyses. LS-DYNA is particularly well suited for the analysis of AE events in structures due to its use of the Courant-Friedrich-Levy (CFL) criteria that determines the time step size from the amount of time required for a stress wave – or acoustic wave – to propagate through the smallest mesh element (Fig. 2).

Whilst very useful and powerful, CFL requires intensive development of the structural mesh to ensure that the quality and total time of the simulation is well controlled. A single element of poor quality may produce an unnecessarily small time step size and hence, a very long time to solve the simulation. Likewise, by employing explicit time integration, several assumptions are made that allow for generally good convergence as well as low-memory requirements. Hence, LS-DYNA presents as an excellent tool for the study of highly transient events such as impact for the analysis of AEs.

Whilst the goal of this work is the development of SHM for the detection of BVID in FRPs, thus far only preliminary studies have been conducted for impacts upon an aluminium plate. Performing such preliminary studies allows for validation of the model before progressing to complex materials such as FRPs. A 10-mm-

Fig. 2 The CFL criteria used to determine the speed of sound and time step in a variety of elements

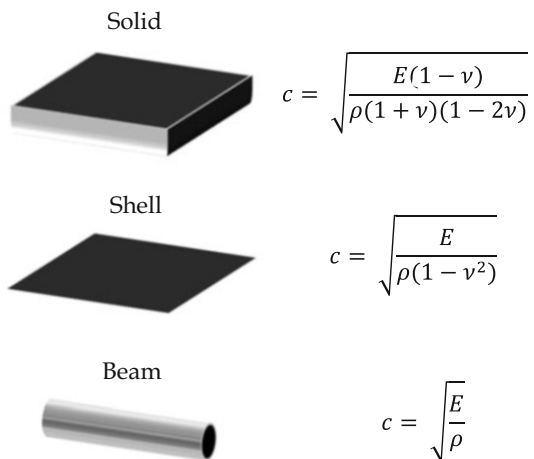
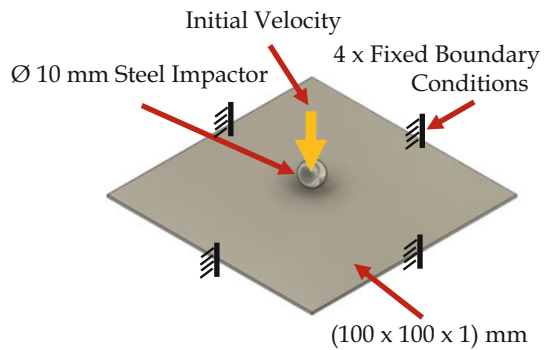


Table 1 A summary of the impact trials

| Energy (J) | Velocity (m/s) |
|------------|----------------|
| 2.50 | 34.88 |
| 5.00 | 49.32 |
| 7.50 | 60.41 |
| 10.0 | 69.76 |
| 12.5 | 77.99 |
| 15.0 | 85.43 |
| 17.5 | 92.28 |
| 20.0 | 98.65 |

Fig. 3 The model setup for the impact simulations on the aluminium plate

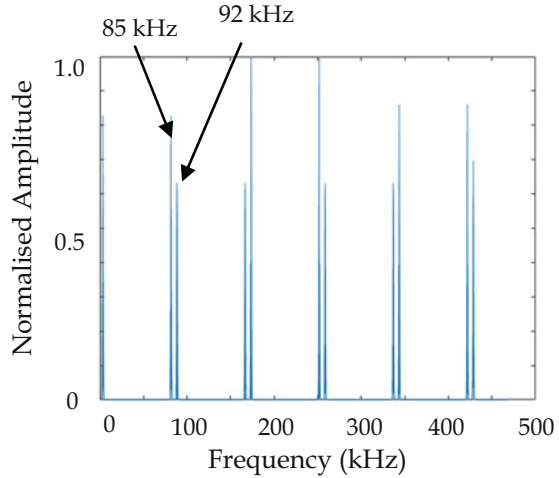
diameter spherical steel projectile has been used as the impactor for a variety of impacts between 2.5 J and 20 J. The mass of the projectile is 4.11 g, resulting in velocities for the trials as highlighted in below in Table 1.

The plate has been fixed at all four edges with the projectile in the centre. A brief depiction of the simulation setup, including boundary conditions, is shown in Fig. 3.

2.2 Results and Discussion

Prior to performing the impact analysis, the projectile was replaced with a simple impulse force input such that the resonance characteristics of the plate could be observed. Assessment of the resonance characteristics of the plate functions to both provide confidence in the quality of the simulation and a damage metric for future analysis. The results of the impulse response are shown in Fig. 4.

Fig. 4 Resonance response of the plate under an impulse



As evident, two resonances can be clearly observed, occurring at 85 kHz and 92 kHz. The quality of the resonant response of the plate indicates that the model has converged well. Following the impulse response, the impact trials were performed. An arbitrary node on the plate, located approximately three quarters along the diagonal from the location of impact, was taken as the test location. The out-of-plane displacement or through-thickness displacement of this node was examined under the influence of the impact. As the nodal response is directly measured, no analysis has been performed regarding coupling of acoustic sensors.

To ensure that the response of the plate under the impact was controlled for all energy levels, a two-step post-processing routine has been implemented. Firstly, as the projectile has been offset from the surface of the plate by a small distance, a time delay Δt results between each trial because of the difference in time required for the impact to occur. As such, each of the time signals have been translated to account for this Δt such that the displacement response $x(t)$ of the node is non-zero. This can be represented mathematically as follows (Eq. 1).

$$\Delta t := x(\Delta t) \neq 0 \mid (x(t) = 0 \mid t < \Delta t) \tag{1}$$

Following this translation, the signals are detrended to remove any constant or linear displacement offsets. To accomplish this, a high-pass filter has been applied to the signals. It was observed that a cut-off frequency of 2.5 kHz worked well to detrend the signal with little warping in the response. A depiction of the time domain signals for an impact of 2.5 J and 20 J are shown in Fig. 5 following the post-processing. As can be observed, the amplitude of the response is much larger for the 20 J impact. Interrogation of the time domain AE signals as depicted can be used to localize the source of the impact. Whilst this localization has not yet been performed, methods to accomplish this are discussed in the following section.

Fig. 5 Time domain AE signals for 2.5 J and 20 J impacts

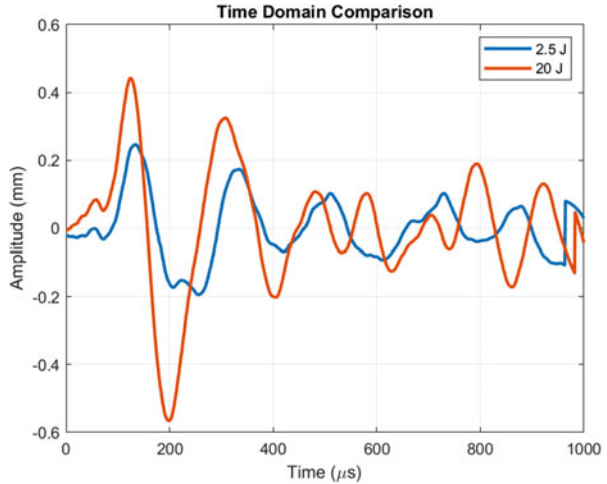
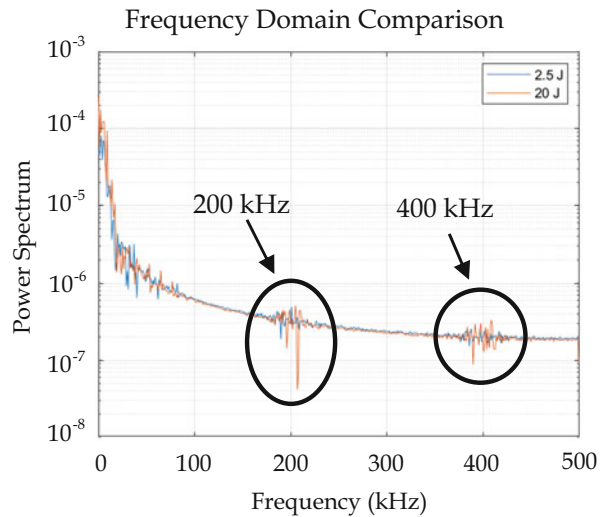


Fig. 6 Frequency domain AE signals for 2.5 J and 20 J impacts



The acquired AE signals are likewise analysed in the frequency domain as shown in Fig. 6. As can be observed, there are obvious, broadband excitations that occur at central frequencies of approximately 200 kHz and 400 kHz with frequency bands of approximately 50 kHz. Whilst there is frequency information below the 100 kHz range, the response is not well defined and would require further processing to render any useful information.

Moreover, whilst the impacts have excited the same frequency responses in the plate, the higher energy impact has resulted in stronger excitations. This behaviour is expected and hence, indicates a well-behaved model with good convergence. Finally, to showcase the modal properties of the impact as well as the permanent

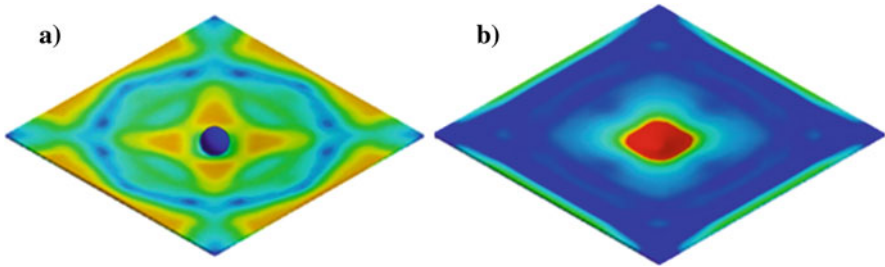


Fig. 7 von Mises equivalent stress from (a) projectile impact and (b) plastic deformation post-20 J impact

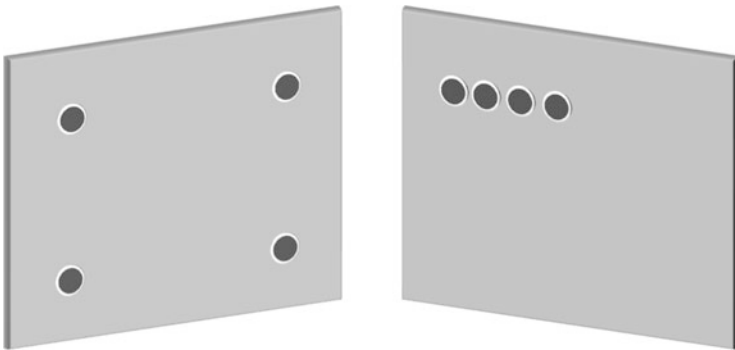


Fig. 8 Sensor configurations on a plate for (a) a sparse array and (b) a phased array

damage from the aluminium projectile, von Mises equivalent stress and plastic strain contour plots are shown in Fig. 7.

3 Acoustic Emission (AE) Localization

By utilising either a phased or sparse array – as shown in Fig. 7 – multiple time domain AE signals may be captured from the low velocity impacts upon the plate. There exists a variety of methods that may then be used to localize the source of the AE and hence, to localize the impact and possible location of BVID. There likewise exists the possibility of further interrogating the content of each AE to possibly yield useful information in an effort to characterize and quantify the damage event.

One such method to localize the source of the AE is through the application of a cross-correlation to calculate the time delay $\tau_{a, b}$ between adjacent sensor elements, following which a multilateration may be performed. The equations for determining the time delay and location via multilateration are shown below in Eqs. 2 and 3, respectively. Methods for localization of AEs is an ongoing area of study.

$$\tau_{ij} = \max \mathcal{F}^{-1} \left[\overline{X_a[k]} \cdot X_b[k] \right] \quad (2)$$

$$\tau_{ij} c_{Pf_0} = \sqrt{(x_s - x_a)^2 + (y_s - y_a)^2} - \sqrt{(x_s - x_b)^2 + (y_s - y_b)^2} \quad (3)$$

X_a and X_b represent the Fourier transformation of adjacent AE signals. Likewise, \mathcal{F}^{-1} is the inverse Fourier transformation and the overbar symbol denotes the complex conjugate. The phase velocity at the peak frequency component c_{Pf_0} is used for the multilateration to determine the AE source (x_s, y_s) by knowing the location of the acquired AE signals (x_{alb}, y_{alb}). A minimum of three sensors are required to localize an AE upon a 2-dimensional plane.

4 Conclusion

Thus far, preliminary work has been conducted towards understanding the mechanics of AE propagation resulting from low-velocity impacts. The results presented indicate that the proposed modelling tool of LS-DYNA has the capability to accurately depict such impact events as well as the emissions that result from them.

Work is hence being planned for the development of impacts upon FRP materials. Due to the complex damage mechanics involved with impacts upon such materials, a series of experimental tests will likewise be performed to aid in the validation of the model. Furthermore, the formation of fast and slow axes owing to the orthotropic nature of the FRP specimen will create greater difficulties in localizing the AE signal. To minimize this difficulty, the proposed specimen will use VTM 264 carbon prepreg with a quasi-isotropic layup.

References

- Azouaoui, K., Azari, Z., & Pluvinaige, G. (2010). Evaluation of impact fatigue damage in glass/epoxy composite laminate. *International Journal of Fatigue*, 32(2), 443–452. <https://doi.org/10.1016/j.ijfatigue.2009.09.005>
- Dafydd, I., & Sharif Khodaei, Z. (2020). Analysis of barely visible impact damage severity with ultrasonic guided lamb waves. *Structural Health Monitoring*, 19, 1104–1122.
- Defense., U. D. o. (2002). *Military handbook–MIL-HDBK-17-1F: Composite materials handbook, volume 1—Polymer matrix composites guidelines for characterization of structural materials*. US Department of Defense.
- Dutton, S., Kelly, D., & Baker, A. (2004). *Composite materials for aircraft structures*. American Institute of Aeronautics and Astronautics.
- Fawcett, A. J. & Oakes, G. D. (2006). Boeing composite airframe damage tolerance and service experience. In *Composite damage tolerance & maintenance workshop, 2006*.
- Kumar, P., & Rai, B. (1993). Delaminations of barely visible impact damage in CFRP laminates. *Composite Structures*, 23, 313–318.

- Mustapha, S., Ye, L., Dong, X., & Alamdari, M. M. (2016). Evaluation of barely visible indentation damage (BVID) in CF/EP sandwich composites using guided wave signals. *Mechanical Systems and Signal Processing*, 76, 497–517.
- Rauter, N., & Lammering, R. (2015). Impact damage detection in composite structures considering nonlinear lamb wave propagation. *Mechanics of Advanced Materials and Structures*, 22, 44–51.
- Saeedifar, M., Najafabadi, M. A., Zarouchas, D., Toudeshky, H. H., & Jalalvand, M. (2018). Barely visible impact damage assessment in laminated composites using acoustic emission. *Composites Part B: Engineering*, 152, 180–192.
- Wronkiewicz-Katunin, A., Katunin, A., & Dragan, K. (2019). Reconstruction of barely visible impact damage in composite structures based on non-destructive evaluation results. *Sensors*, 19, 4629.

Macro cognition for Preparedness in Aviation



Maria Papanikou, Utku Kale, András Nagy, and Konstantinos P. Stamoulis

Contents

| | | |
|---|---|-----|
| 1 | Introduction | 407 |
| 2 | Macro cognition for Preparedness | 409 |
| 3 | Mapping of Systemic Macro cognition | 410 |
| 4 | Conclusion | 412 |
| | References | 413 |

1 Introduction

Innovation is a driver for transitions and change management. Past transitions have aided aviation in reaching advanced knowledge over safety risks, creating foresight. During the last decade, organizations adjust or transit in a much more digitalized way of doing things, signifying an information-driven transition. Industry 4.0, commonly referred to as the Fourth Industrial Revolution, reflects the shift to increasingly advanced technologies and “smart” industries (e.g., digital

M. Papanikou (✉) · K. P. Stamoulis
Amsterdam University of Applied Sciences, Faculty of Technology, Amsterdam, The Netherlands
e-mail: m.papanikou@hva.nl; k.stamoulis@hva.nl

U. Kale
Budapest University of Technology and Economics, Department of Aeronautics, and Naval Architecture, Budapest, Hungary
e-mail: kale.utku@kjk.bme.hu

A. Nagy
University of Dunaújváros, Department of Mechanical Engineering, Budapest, Hungary
e-mail: nagy.andras@uniduna.hu

manufacturing). This shift comes with drivers and barriers at the management level (e.g., strategy and resource management) and at the workforce level (e.g., lack of qualification, knowledge, understanding of interfaces, employee readiness) (Stentoft et al., 2020). As Neumann et al. (2021) note, the focus so far has only briefly mentioned the role of organizational factors. The organizational context hence requires a better understanding of such transitions.

For example, and as in other contexts (Ferrari et al., 2020), human-data interactions (HDI) and overreliance on machine-related information (McDonnell et al., 2018; Victorelli et al., 2020) have become of seminal importance to the aviation domain. Furthermore, Ton et al. (2020) report that there is little expert knowledge on application-specific aspects such as failure behavior of components in prognostics. Studies hence emphasize the need to understand “the black boxes” in transformation (Sgarbossa et al., 2020) and the situational awareness of decision-makers (Giacotto et al., 2021).

Over the decades, advances in technical systems have become so separated from humans that there are documented concerns regarding human-related data. These are overlooked in industrial advancements (McDonnell et al., 2018). Foresight is hence under question since the negative transfer of (past) knowledge may endanger future system success as the organizations drift away from learning. Softer approaches of education problematizing, including organizations and practitioners (Ison, 2008), are confined to strategic levels, and human factors can be ignored (Ton et al., 2020). Research (Golightly et al., 2018) reports problems affecting the deployment of new technologies in predictive maintenance due to issues of knowledge gaps and human-machine interface, among other higher-level organizational factors of strategy and culture. In aviation, for example, the cultural shift airport collaborative decision-making (A-CDM) requires, data management, responsibility allocation, and the complexity of the required collaboration (Netto et al., 2020) and communication (Zuniga & Boosten, 2020) need addressing. As a wide range of teams and systems collaborate in this process (e.g., ground handling, air traffic control, aircraft operators), emphasis is placed on the importance of information flow, management, and processing.

Gaps are, therefore, observed in the understanding of higher levels of cognition within an advanced technological environment, involving hybrid, complex and multidisciplinary teams, and potentially overloaded users. The organizational “collective memory” comprises of experiences and tacit rules, aiding the operator to recall the learning from operational and safety issues and protecting it in the future (ESReDA, 2020). Due to the emerging interactions among users, teams, and ultimately of systems, the current chapter places emphasis on the need for such systemic considerations enabled by macrocognition. To this end, the chapter proposes a systemic-driven mapping focusing on a greater understanding of macrocognition in an information-driven environment.

2 Macro cognition for Preparedness

Aviation is characterized as a system of systems. Human performance in high-risk industries is an emergent behavior of a domain – a systemic web of interactions between complex systems and their users. Foresight requires a deep understanding of decisions, emergent interactions, and complexity that can affect the future (ESReDA, 2020). Systems thinking in aviation, however, involves different theories that assume different “boundaries of analysis” of the aviation system (Richardson & Midgley, 2007). Systemic analysis in aviation follows a legacy of systems engineering thinking, lacking a broader investigation. The term “systemic” is commonly confused with systematic or within-system approaches that center on a system of interest. Systems thinking, as such, has been developed according to scientific silos and lead to underexplored “softer” fields in areas such as safety and the impeccable increase of systematic approaches in others such as the technological one.

Commonly, a static structure of the aviation domain and a confined problem space is assumed. The focus remains on the latest developments such as predictive maintenance, single-pilot operations, and collaborative platforms, yet addressing either only microcognitive concerns or technical characteristics. For this reason, we posit that foresight requires a greater understanding of systems collectively and these to be studied in their natural setting. This approach is known as naturalistic decision-making (NDM) and addresses macrocognition. Macrocognition is linked to knowledge creation, as knowledge is the product of schemas and cognitive structures that precede data and information processing (Cacciabue & Hollnagel, 1995; Fiore et al., 2010). The cognitive functions within the macrocognition movement that originated in the 1980s include decision-making in natural settings, where pressure and dilemmas prevail and involve situation assessment, planning, adaptation, problem detection, and coordination (Klein et al., 2003). This paradigm addresses the background of micro-level symptoms such as inattention and lack of situational awareness. We posit that this paradigm is of importance in advanced technologies that pose the emphasis on a different, evolving set of knowledge, attitudes, and skills for systems’ users and operators since it includes developing teams, a highly technological context, and thus a broader inclusion of cognitive functions (Klein et al., 2003). Such thicker descriptions can be helpful in complex-adaptive systems such as aviation.

We, therefore, draw on Simon’s (1991) conceptualization of human cognition relating to their information environments and that humans cannot simply choose between fixed alternatives as part of their decision-making process. Within unexplored interactions, schemas – the collective memory – are being developed, processing and interpreting information to fit the pattern (Axelrod, 1973). Hence, prior knowledge is critical as it activates information processing (Widmayer, 2004). Specifically, these schemas are formulated both by technical – explicit and tacit knowledge (Mortier & Anderson, 2017). Therefore, the role of macrocognition encompasses the broader collective memory and information processing of the aviation systems required for foresight.

Systems are hence characterized as information processing machines, also researched as decision-making and communication systems (Egelhoff, 1991), with emergent macrocognitive structures. The system's evolving knowledge leads to its schemas and cognitive networks, a collective memory, and ultimately performance (Obrenovic et al., 2015). The advanced systems in aviation, within and between organizations and their operators/users, rely on a heavy load of information and data and have timely responses and reactions that require and promote a nexus of cognitive functions.

These systems also require communication among them as they are synergetic in terms of operations and collective in terms of a common goal (safe performance), which co-comprise the broader aviation system. Their users also share common characteristics and face problems that underpin technological advancements. For example, as it has been mentioned, cockpit operators – whether these will be on the air and/or on the ground – are going through a change in terms of their knowledge (e.g., from tacit to explicit, reskilling). In addition, A-CDM airports involve multiple users that collaborate yet are largely underexplored. Finally, predictive maintenance shifts the levels of knowledge and practice to real-time monitoring and prediction methodologies requiring a different set of skills and knowledge, thus creating a new cognitive structure. These systems will also transform organizationally. Knowledge comes from the organizations, and as they become data-driven, explicit knowledge will affect information processing. Such examples illustrate the complexity therein and the adaptation required to aid foresight. With the current focus on the interactions between the human (operators, users) and the automation/new technology, the analysis is being stripped of context. Attempts to merely control the system will create new interactions and implications, which initially require understanding.

3 Mapping of Systemic Macrocognition

Aiming to address the underexplored areas comprising high-change scenarios, we propose a broader analysis presented in the concept mapping (Fig. 1). Because complex systems involve nonlinearity and dynamic space, the conceptual mapping is intended as an initial guide for systemic considerations of macrocognition. Following the systemic approach, Fig. 1 maps systems at an interconnected level of analysis, considering users within a broader nexus of cognitive structures and functions. The mapping's arrows are iterative to showcase the interconnectedness, as the evolving cognitive structures feedback and feedforward due to their interacting nature as explained. The double-sided arrows indicate these interactions among cognitive structures, the transfers of information, and the dynamic relationship between top-down and bottom-up approaches. Specifically, higher levels of the cognitive system indicate the involvement of the organizational long-term cognitive structure, comprising of both the evolving explicit and tacit knowledge. The flows of information, and the results of interactions between and within organizational teams, affect the cognitive structures. The flow between systems and within a system as an

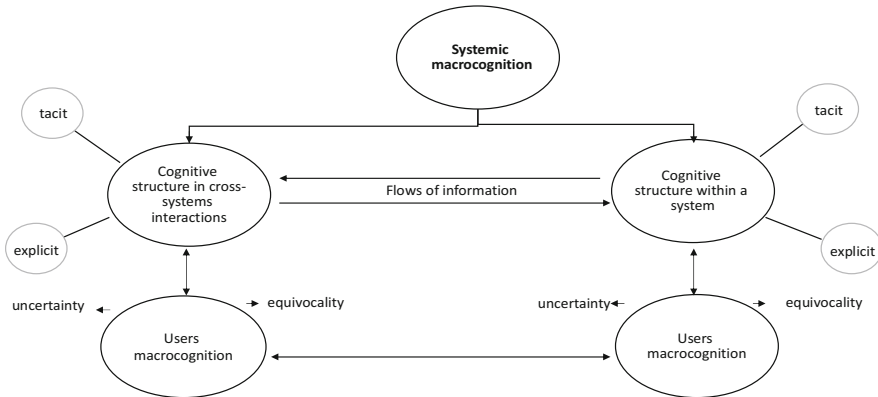


Fig. 1 Concept mapping of the systemic macrocognition architecture (own edition)

organization of processes, resources, and assets are essential for inter-domain teams, systemic relationships, and flows of information.

At a theoretical level, there are considerations for multidisciplinary and interdisciplinary research and the communication and engagement of various fields. In order to understand the emergent behavior of the aviation domain following change, in particular, what the implications might be for system effectiveness and therefore safety, the analysis needs to include knowledge of what drives this change (i.e., it is the result of which interaction, and how this change is affecting current or is creating new interactions). However, human factors are currently approached as a control problem, following the reductionist path of system decomposition. A static equilibrium is created, a static problem space of the observer (Ashby, 1957). This tradition of aviation cognitive studying now has implications for knowledge gaps and knowledge transfer, and hence preparedness and foresight.

Aviation holds a mix of explicit and tacit knowledge. Manuals, training files, performance documentation, and data management involve explicit knowledge, skills, experience, etc. and tacit knowledge. Hence parts of aviation’s knowledge are external, and the rest is internalized to the users of its systems. The technological advancements in aviation have implications for both knowledge aspects. On the one hand, it is unclear how the users of new technologies will be able to capture the required knowledge. On the other hand, it is unclear what kind of tacit knowledge is being built and required to support the new technologies. Despite notions that technology focuses on creating explicit knowledge – and hence relying less on tacit aspects that are less controllable – the collective information processing within and between systems can affect the individual’s information processing. It will ultimately create a different set of explicit and tacit knowledge. It is unclear how foresight will be created to support future developments. This research gap in aviation includes the context of high automation, big data technologies, and higher levels of information processing which is further developing. For this reason, the

current chapter proposes that microcognitive studies are supported by the inclusion of a systemic, emerging macrocognitive perspective.

Since highly advanced technological systems create a more significant information load among users of different methods that collaborate, the naturalistic decision-making focus of macrocognitive is proposed. For this reason, the systems that include those users are conceptualized as cognitive structures driving information processing and affecting the capacity of the users.

Hence, the mapping shows that the systemic view can be applied to understand within and across systems interactions. The analysis can, in addition, focus on the organizational level – alone or in combination with other studies. Specific methods can be used for the intra organizational analysis, and multiple investigations are advised in complex cases. For example, in maintenance, there can be various modes of safety management (e.g., early adaptation to lack of safety management systems), different resources and lack of readiness (e.g., SMEs, Stentoft et al., 2020), and new implementations (e.g., predictive maintenance). Bottom-up and top-down analyses on integrating old and new maintenance technologies are required. At the management level, aspects of measures, indicators, and intra-organizational processes, policies, and tacit and explicit knowledge can be explored. At the bottom level, skills, knowledge (tacit and explicit), and experience (behavioral characteristics) can be targeted. Structural and technological (e.g., data, sensors) aspects can be examined incorporating workgroups and job (re)design aspects.

Despite the advanced technologies, little knowledge is being captured and shared among aviation systems. Since advanced information systems and data banks prevail – and will growingly do so – explicit and tacit knowledge should be explored concerning cognitive functions. However, boundaries can differ depending on the interaction with other systems (e.g., a weak or strong interaction). Under this observation, the role of feedback loops should be re-evaluated and explore whether feedback loops can be useful in the systemic analysis or may lead to reverting the analysis back to pairings. Furthermore, the human capabilities should be understood in context, i.e., the changing environments, and in greater depth, since past changes and their effect are still under analysis and exploration. Before greater and more fundamental changes are introduced, we need to better understand the change effects on systems' users and their macrocognition to aid foresight.

4 Conclusion

This chapter discussed why human and organizational factors should be addressed for foresight and the effective deployment of new technologies and structures. It is argued that a systemic view under macrocognition should be adopted. Macrocognitive studies can explore the knowledge transfers in the changing context. In addition, macrocognitive studies can complement microcognitive studies by producing insights from operators' dominant information-processing models and revealing areas in need of transformation and intervention. To this end, we proposed

a systemic mapping under macrocognition through assessments and interventions that can capture shifts and reveal and close gaps in a naturalistic setting. However, certain limitations should be noted, since organizational (and safety) culture aspects, and resources may become barriers to change. Future research should apply novel tools through an open systemic view in settings with different challenges. The macrocognitive profile of organizations and their members should be researched and how microcognitive and, common, systematic approaches can be complemented through novel mixed methodologies.

References

- Ashby, W. R. (1957). *An introduction to cybernetics*. Chapman & Hall Ltd. <http://pcp.vub.ac.be/books/IntroCyb.pdf>
- Axelrod, R. (1973). Schema theory: An information processing model of perception and cognition. *The American Political Science Review*, 67(4), 1248–1266.
- Cacciabue, P. C., & Hollnagel, E. (1995). *Expertise and technology*. Taylor and Francis.
- Egelhoff, W. G. (1991). Information-processing theory and the multinational enterprise. *Journal of International Business Studies*, 22(3), 341–368.
- ESReDA. (2020). Enhancing safety: The challenge of foresight. In *European safety, Reliability & Data Association, EUR 30441*. European Safety and Reliability Data Association (ESReDA) and EU/EC Joint Research Center (JRC).
- Ferrari, B., Junior, D. P. D. S., & Pereira, R. (2020). Systemic view of human-data interaction: Analyzing a COVID-19 data visualization platform. In *Proceedings of the 19th Brazilian symposium on human factors in computing systems*, 26–30 Oct 2020, Diamantina, Brazil.
- Fiore, S. M., Smith-Jentsch, K. A., Salas, E., Warner, N., & Letsky, M. (2010). Towards an understanding of macrocognition in teams: Developing and defining complex collaborative processes and products. *Theoretical Issues in Ergonomics Science*, 11(4), 250–271.
- Giacotto, A., Costa Marques, H., Pereira Barreto, E. A., & Martinetti, A. (2021). The need for ecosystem 4.0 to support maintenance 4.0: An aviation assembly line case. *Applied Sciences*, 11(8), 3333.
- Golightly, D., Kefalidou, G., & Sharples, S. (2018). A cross-sector analysis of human and organisational factors in the deployment of data-driven predictive maintenance. *Information Systems and e-Business Management*, 16(3), 627–648.
- Ison, R. (2008). Systems thinking and practice for action research. In P. W. Reason & H. Bradbury (Eds.), *The sage handbook of action research participative inquiry and practice*. Sage Publications.
- Klein, G., Ross, K. G., Moon, B. M., Klein, D. E., Hoffman, R. R., & Hollnagel, E. (2003). Macrocognition. *IEEE Intelligent Systems*, 18(3), 81–85.
- McDonnell, D., Balfe, N., Pratto, L., & O'Donnell, G. E. (2018). Predicting the unpredictable: Consideration of human and organisational factors in maintenance prognostics. *Journal of Loss Prevention in the Process Industries*, 54, 131–145.
- Mortier, T., & Anderson, D. (2017). Understanding tacit knowledge in decision making. In D. Jaziri-Bouagina & G. L. Jamil (Eds.), *Handbook of research on tacit knowledge management for organizational success*. IGI Global.
- Netto, O., Silva, J., & Baltazar, M. (2020). The airport A-CDM operational implementation description and challenges. *Journal of Airline and Airport Management*, 10(1), 14–30.
- Neumann, W. P., Winkelhaus, S., Grosse, E. H., & Glock, C. H. (2021). Industry 4.0 and the human factor—A systems framework and analysis methodology for successful development. *International Journal of Production Economics*, 233, 107992.

- Obrenovic, B., Obrenovic, S., & Hudaykulov, A. (2015). The value of knowledge sharing: Impact of tacit and explicit knowledge sharing on team performance of scientists. *International Journal of Management Science and Business Administration*, 1(2), 33–52.
- Richardson, K. A., & Midgley, G. (2007). Systems theory and complexity: Part 4-the evolution of systems thinking. *Emergence-Mahwah-Lawrence Erlbaum*, 9(1/2), 166.
- Sgarbossa, F., Grosse, E. H., Neumann, W. P., Battini, D., & Glock, C. H. (2020). Human factors in production and logistics systems of the future. *Annual Reviews in Control*, 49, 295–305.
- Simon, H. A. (1991). Bounded rationality and organizational learning. *Organization Science*, 2(1), 125–134.
- Stentoft, J., Adsbøll Wickstrøm, K., Philipsen, K., & Haug, A. (2020). Drivers and barriers for Industry 4.0 readiness and practice: Empirical evidence from small and medium-sized manufacturers. *Production Planning & Control*, 32, 811.
- Ton, B., Basten, R., Bolte, J., Braaksma, J., Di Bucchianico, A., van de Calseyde, P., & Stoelinga, M. (2020). PrimaVera: Synergising predictive maintenance. *Applied Sciences*, 10(23), 8348.
- Widmayer, S. A. (2004). *Schema theory: An introduction*. <http://chd.gse.gmu.edu/immersion/knowledgebase/strategies/cognitivism/SchemaTheory.htm>. Accessed on 10 Apr 2020.
- Victorelli, E. Z., Dos Reis, J. C., Hornung, H., & Prado, A. B. (2020). Understanding human-data interaction: Literature review and recommendations for design. *International Journal of Human-Computer Studies*, 134, 13–32.
- Zuniga, C., & Boosten, G. (2020). A practical approach to monitor capacity under the CDM approach. *Aerospace*, 7(7), 101.

Simulation of a 6DOF Nonlinear Missile



Kutaibah Srour and Sohayb Abdulkerim

Contents

| | | |
|-----|--|-----|
| 1 | Introduction | 416 |
| 2 | Method | 416 |
| 2.1 | Translational Equations | 417 |
| 2.2 | Rotational Equations | 417 |
| 2.3 | Simulation Using MATLAB and Calculations | 417 |
| 3 | Results and Discussion | 418 |
| 4 | Conclusion | 423 |
| | References | 423 |

Nomenclature

| | |
|---|--|
| $F_{A_{x_b}}, F_{A_{y_b}}, F_{A_{z_b}}$ | Components of aerodynamic force, N |
| $F_{g_{x_b}}, F_{g_{y_b}}, F_{g_{z_b}}$ | Components of gravity force, N |
| $F_{p_{x_b}}, F_{p_{y_b}}, F_{p_{z_b}}$ | Components of thrust force, N |
| I_x, I_y, I_z | Moments of inertia, Kg.m^2 |
| LA, MA, NA | Components of aerodynamic moment vector (roll, pitch, and yaw, respectively), N.m |
| LP, MP, NP | Components of aerodynamic moment vector (roll, pitch, and yaw, respectively), N.m |
| m | Mass of a particle or body, Kg |
| p, q, r | Components of the angular rate vector (roll, pitch, and yaw, respectively), rad/s |

K. Srour (✉) · S. Abdulkerim
Gaziantep University, Gaziantep, Turkiye
e-mail: karim@gantep.edu.tr

| | |
|-----------------------------|---|
| $\dot{p}, \dot{q}, \dot{r}$ | Components of angular acceleration (roll, pitch, and yaw, respectively), rad/s^2 |
| u, v, w | Components of absolute linear velocity vector, m/s |
| $\dot{u}, \dot{v}, \dot{w}$ | Components of linear (translational) acceleration, m/s^2 |

1 Introduction

The design process of missile controller is generally made through several phases. The first phase is inferring the equation of motion, (EOM) which is always a set of nonlinear, time invariant, and coupled differential equations. In the second phase, the resulted model is solved (De Marco et al., 2007). Normal procedures to solve these questions are impossible. Therefore, there are several approximations to find the solution. Nonlinearization process is a method in which the model is reduced and decoupled into two sets of equations for longitudinal motion and for lateral and directional one. For these two sets, it is possible to use state space method or transfer function, TF, method which allows manipulating the controller design process by MATLAB, which is valid only about specific flight condition about which the linearization made. An alternative scheme is to use modern utilities by MATLAB, to simulate the complete set of equations using Simulink tool (Da Silveira & Carrara, 2015). The resulted model will be valid for the whole flight envelope.

This chapter is focused on the first and second phases and to develop a flight simulator for missiles.

2 Method

The missile flight simulation model is based on mathematical formulas that represent the dynamic movement of the missile caused by the forces and moments acting on the missile. The mathematical tool used is the EOM, which describes the relationship between the forces acting on a missile and the resulting movement of the missile. The purpose of examining missile dynamics in flight simulation is to understand these mathematical relationships. The three-degree-of-freedom model uses the translational EOM. The 6DOF model also uses the rotational EOM. The inputs to the EOM are the forces and moments acting on the missile. The output is the acceleration of the missile generated by forces and moments.

A mathematical program is required to convert the rate of change vector to a vector related to the inertial frame. If you know the rate of change of the vector for the rotating frame (Belkacem & Bachir, 2019), the general formula used to calculate the rate of change of the vector for the inertial frame is

$$\left(\frac{dB}{dt}\right)_{\text{inert}} = \left(\frac{dB}{dt}\right)_{\text{rot}} + (\omega \times B) \quad (1)$$

2.1 Translational Equations

The basis of the translational EOM is $\mathbf{m}\dot{\mathbf{v}}, \mathbf{N}$. As you can see from the previous explanation, \mathbf{F} includes the sum of the external forces (aerodynamics, pressure thrust, gravity) and the generated momentum thrust. Internally, it properly considers variable quality. In missile flight simulations, the usual procedure for solving the translational EOM is to calculate the sum of forces based on aerodynamic, propulsive, and gravitational data; replace the substitution with the EOM; and solve the absolute acceleration. Similar symbols, represented by the subscripts y and z , represent the components of the total force y and z , respectively (Kisabo et al., 2019).

$$\dot{u} = \frac{F_{A_{x_b}} + F_{p_{x_b}} + F_{g_{x_b}}}{m} - (qw - rv) \quad (2)$$

$$\dot{v} = \frac{F_{A_{y_b}} + F_{p_{y_b}} + F_{g_{y_b}}}{m} (ru - pw) \quad (3)$$

$$\dot{w} = \frac{F_{A_{z_b}} + F_{p_{z_b}} + F_{g_{z_b}}}{m} - (pv - qu) \quad (4)$$

2.2 Rotational Equations

Given the moments that act on the missile, they are derivatives of the angular momentum and are used to calculate the angular velocity of the missile. The angular velocity is included in the angular momentum vector \mathbf{h} . Normally, if the axis of rotation is unconstrained, the relationship with \mathbf{h} includes an inertial matrix (also known as an inertia tensor) $[\mathbf{I}]$ (Kisabo et al., 2019). This relationship is caused by

$$\dot{p} = [L_A + L_p - qr(I_z - I_y)]/I_x \quad (5)$$

$$\dot{q} = [M_A + M_p - pr(I_x - I_z)]/I_y \quad (6)$$

$$\dot{r} = [N_A + N_p - pq(I_y - I_x)]/I_z \quad (7)$$

2.3 Simulation Using MATLAB and Calculations

In this section, a brief description of simulating the set of EOM using Simulink is demonstrated. The translational equation in x -direction, Eq. (2), was modeled using block diagram, as shown in Fig. 1. In the diagrams, there are several blocks for basic mathematical operations and for integral operators resulting the velocity component

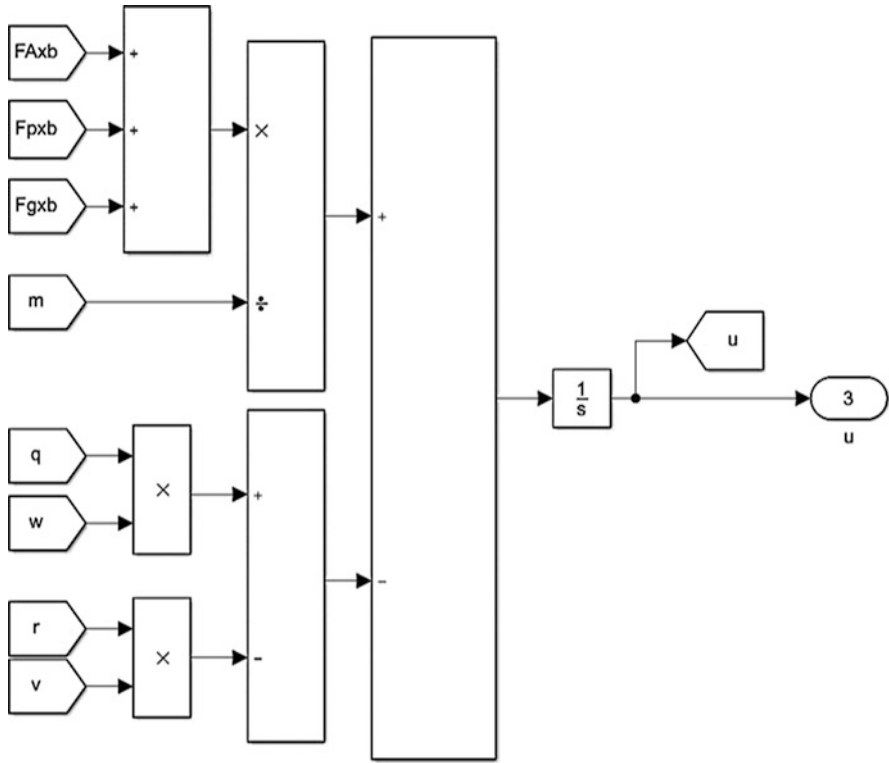


Fig. 1 Simulation block of u -velocity, Eq. (2)

in x -directions, U . The other velocity components are modeled in the same way as shown in Figs. 2, 3, 4, 5, and 6, for v -component, w -component, and rotational velocities components, P , q , and r , respectively.

3 Results and Discussion

For purposes of illustration, a particular missile configuration was investigated which was found in the literature. In this missile, torque-balanced canard was used to control the motion in addition to stabilizing tail fins which were arranged in a cruciform configuration. The full set of data describing the aerodynamics, thrust, inertia tensor, and geometry was found in a textbook of Belkacem and Bachir (Belkacem & Bachir, 2019). The data was formatted as an input data to the simulator.

The initial results of the tested missile showed that the missile was unstable. Therefore, feedback with PID controller were used to maintain stability as shown Fig. 7. In order to tune the PID controller, the Ziegler-Nicholas method was used. In

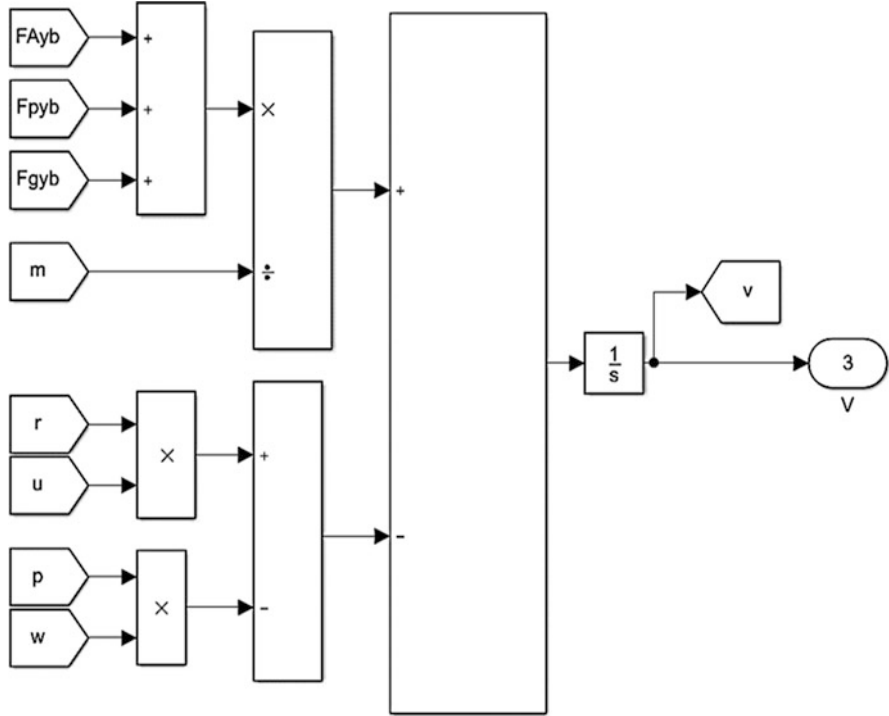


Fig. 2 Simulation block of v-velocity, Eq. (3)

fact, the Ziegler-Nichols tuning formula is based on the empirical knowledge of the ultimate gain K_u and ultimate period T_u . However, For PID controller (Hang et al., 1991).

Proportional gain $k_c = 0.6 K_u$, Integral time $T_i = 0.5 T_u$, Derivative time $T_d = 0.125 T_u$. Also it is known that

$$k_i = \frac{k_p}{T_i} \text{ and } k_d = k_p T_d$$

$$k_u = 15, T_u = 0.17$$

$$k_p = k_c = 9, T_i = 0.085, K_i = 105.88$$

$$T_d = 0.02125, K_d = 0.19125$$

For verification purposes, time series of the absolute velocities were plotted as shown in Fig. 8. The same results were found in the literature which is also depicted in Fig. 9: military handbook (missile flight simulation). The comparison is showing good agreements giving full validation of the methodology of modelling.

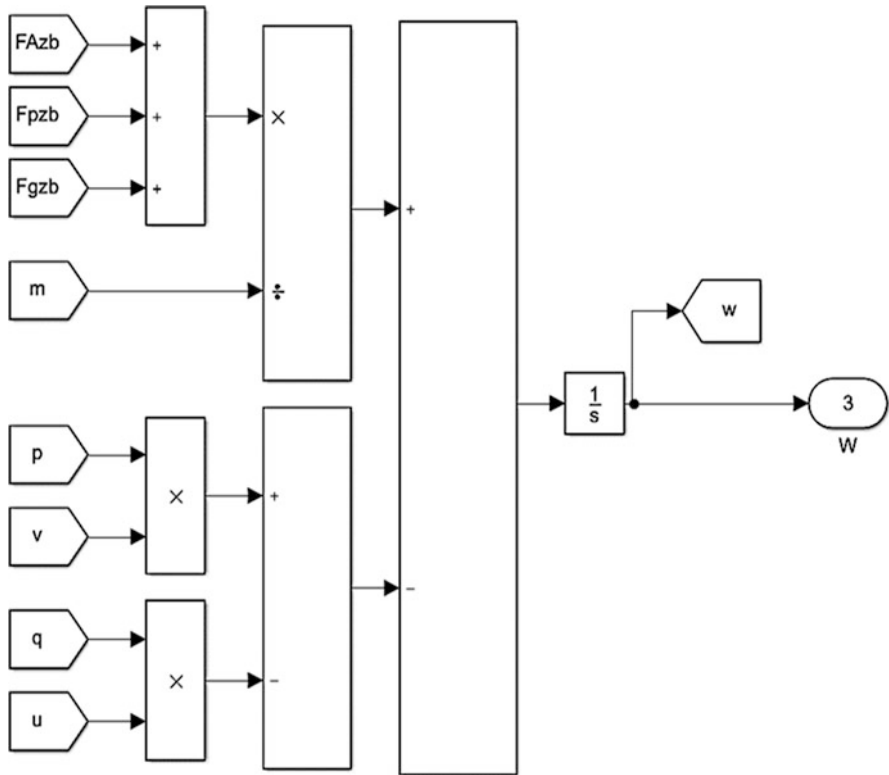


Fig. 3 Simulation block of w -velocity, Eq. (4)

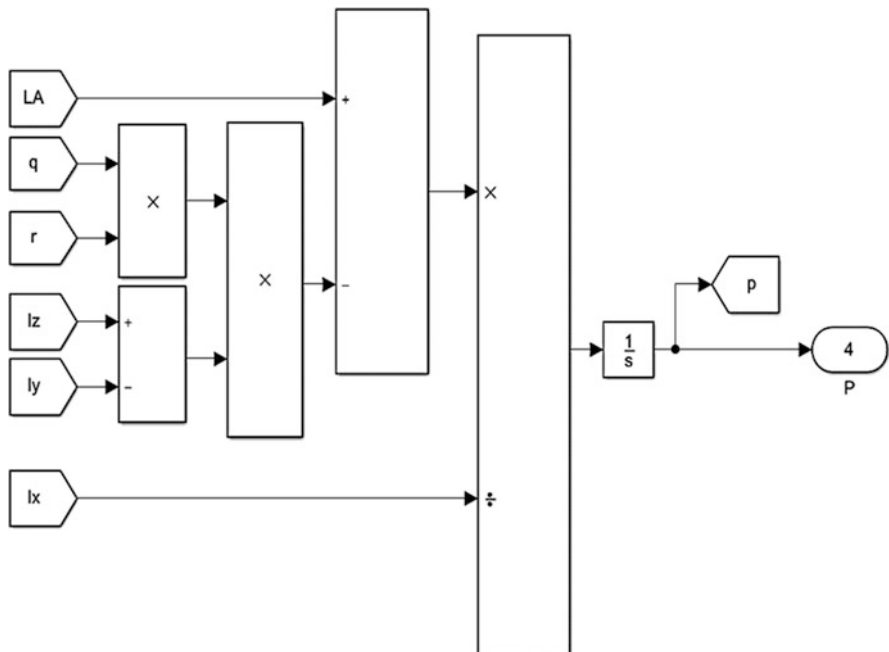


Fig. 4 Simulation block of p -angular velocity, Eq. (5)

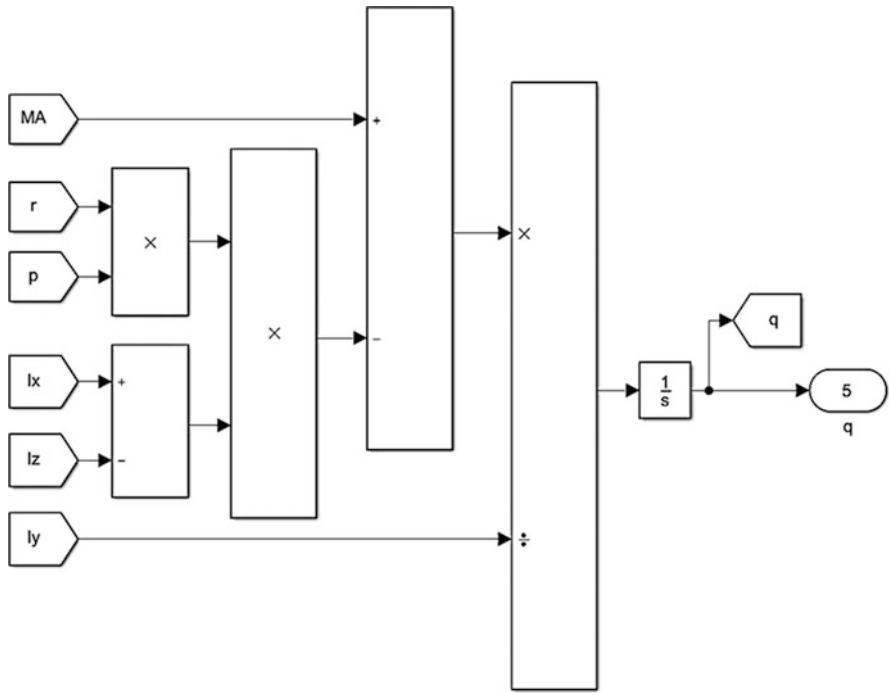


Fig. 5 Simulation block of q -angular velocity, Eq. (6)

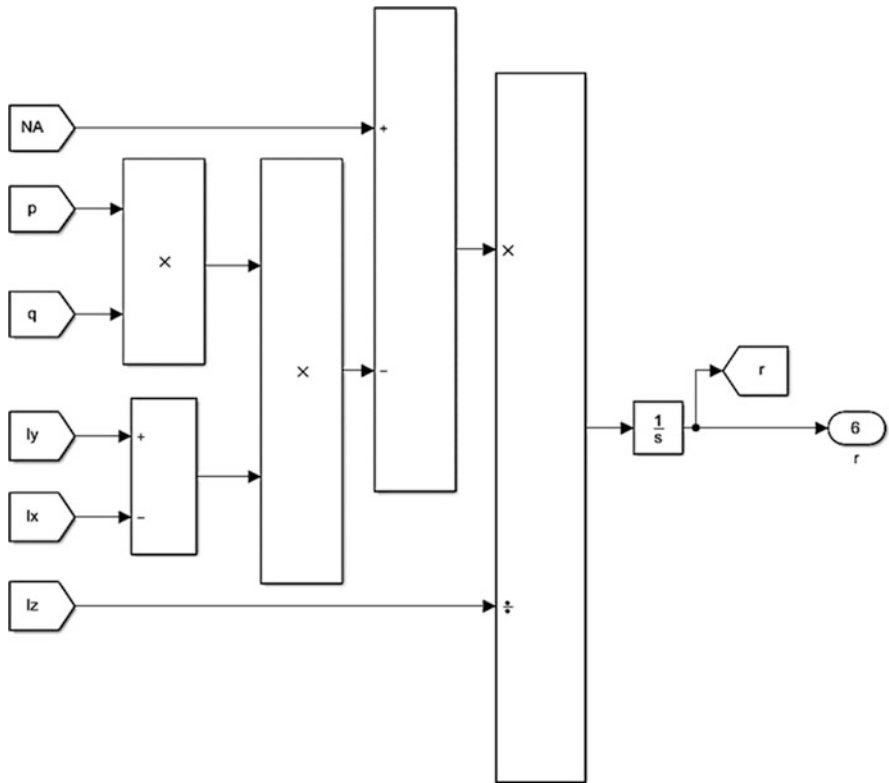


Fig. 6 Simulation block of r -angular velocity, Eq. (7)

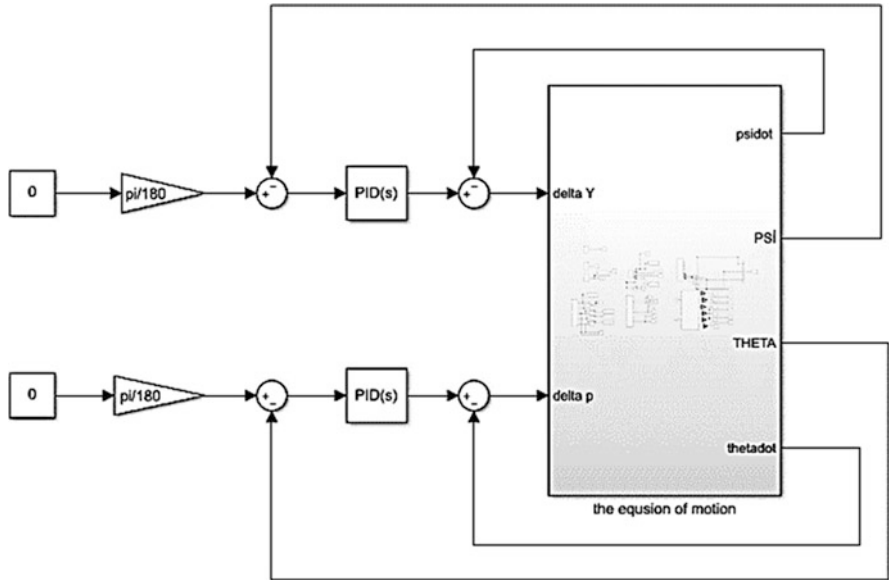


Fig. 7 Simulation block of missile model with the stabilizer

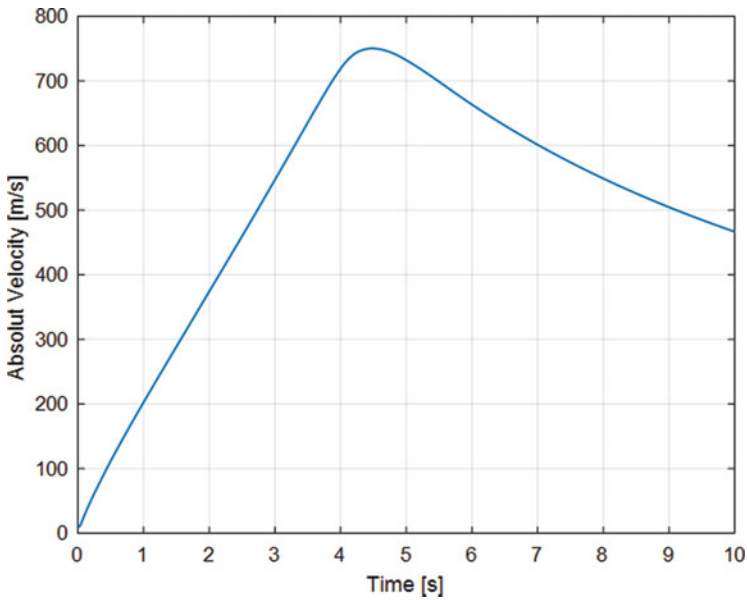
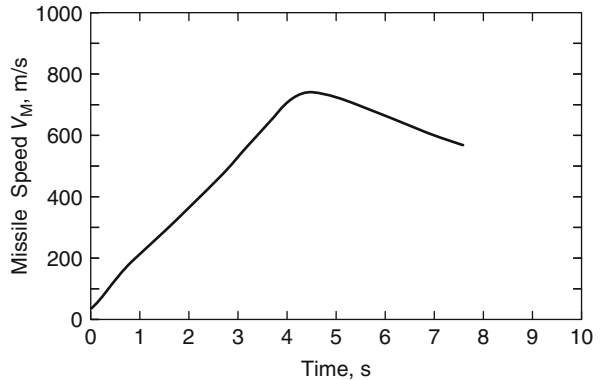


Fig. 8 Results of absolute velocity variation with time, after designing the stabilizer

Fig. 9 Results of absolute velocity variation with time, from military handbook (missile flight simulation)



4 Conclusion

In this project, flight simulator for generic missile was developed using Simulink. A canard missile was analyzed using the developed simulator. Full set of data of the case study was found in the literature in terms of thrust, inertia tensor, aerodynamics stability, and control derivatives found. For validation, the time series of the resulted absolute velocities were plotted and compared with the same result that found in the literature. The comparison showed good agreements. The simulator allowed to design a PID controller easily and to use Ziegler-Nichols method to perform the tuning process. This approach showed flexibility in modelling and controlling.

References

- Belkacem, B., & Bachir, N. (2019). *Dynamic modeling & control of large space structures: Part I* (Issue October).
- Da Silveira, G., & Carrara, V. (2015). A six degrees-of-freedom flight dynamics simulation tool of launch vehicles. *Journal of Aerospace Technology and Management*, 7(2), 231–239. <https://doi.org/10.5028/jatm.v7i2.433>
- De Marco, A., Duke, E. L., & Berndt, J. S. (2007). *A general solution to the aircraft trim problem*. <https://doi.org/10.2514/6.2007-6703>
- Hang, C. C., Astrom, K. J., & Ho, W. K. (1991). Refinements of the Ziegler-Nichols tuning formula. *IEE Proceedings D: Control Theory and Applications*, 138(2), 111–118. <https://doi.org/10.1049/ip-d.1991.0015>
- Kisabo, A. B., Adebimpe, A. F., Okwo, O. C., & Samuel, S. O. (2019). State-space modelling of a rocket for optimal control system design. *Journal of Aircraft and Spacecraft Technology*, 3(1), 128–137. <https://doi.org/10.3844/jastsp.2019.128.137>

Advanced Data Analytics and Digital Technologies for Smart and Sustainable Maintenance



Konstantinos P. Stamoulis

Contents

| | | |
|---|---|-----|
| 1 | Introduction | 425 |
| 2 | The Predictive Maintenance Approach and Building Blocks | 426 |
| 3 | Big Data Management | 427 |
| 4 | Data Analytics and Algorithmic Methods | 428 |
| 5 | Digital Twins | 429 |
| 6 | Decision Support Tools | 430 |
| 7 | Conclusion | 430 |
| | References | 431 |

1 Introduction

Optimization of aviation maintenance, repair, and overhaul (MRO) operations has been of high interest in recent years for both the knowledge institutions and the industrial community as a total of approximately \$70 billion has been spent on MRO activities in 2018 which represents around 10% of an airline's annual operational cost (IATA, 2019). Moreover, the aircraft MRO tasks vary from routine inspections to heavy overhauls and are typically characterized by unpredictable process times and material requirements. Especially nowadays due to the unprecedented COVID-19 crisis, the aviation sector is facing significant challenges, and the MRO companies strive to strengthen their competitive position and respond to the increasing demand for more efficient, cost-effective, and sustainable processes.

K. P. Stamoulis (✉)

Faculty of Technology, Amsterdam University of Applied Sciences, Amsterdam,
The Netherlands

e-mail: k.stamoulis@hva.nl

Currently, most maintenance strategies employ preventive maintenance as an industrial standard, which is based on fixed and predetermined schedules. Preventive maintenance is a long-time preferred strategy, due to increased flight safety and relatively simple implementation (Phillips et al., 2010). However, its main drawback stems from the fact that the actual time of failure and the replacement interval of a component are hard to predict resulting in an inevitable suboptimal utilization of material and labor. This has two repercussions: first, the reduced availability of assets, the reduced capacity of maintenance facilities, and the increased costs for both the MRO provider and the operator. Second, the increased waste from an environmental standpoint, as the suboptimal use of assets, is also associated with wasted remaining lifetime for aircraft parts which are replaced, while this isn't yet necessary (e.g., Nguyen et al., 2019).

The recently introduced, condition-based maintenance (CBM) and predictive maintenance (PdM) data-driven strategies aim to reduce maintenance costs, maximize availability, and contribute to sustainable operations by offering tailored programs that can potentially result in optimally planned, just-in-time maintenance meaning reduction in material waste and unneeded inspections.

2 The Predictive Maintenance Approach and Building Blocks

As the MRO providers try to address the complexity and uncertainty of the aircraft maintenance processes, the use of data-driven methods can provide meaningful information and insights into the way aircraft systems and components are operated and maintained. The rise of the so-called Industry 4.0 and the leverage of enabling technologies such as the Internet of Things (IoT) and the artificial intelligence have allowed the transition to a data-driven, proactive approach, the so-called predictive maintenance (PdM) strategy.

In literature, PdM and CBM are applied interchangeably or linked implicitly. These approaches rely both on collected data and have a lot of commonalities; however, they are focusing on different aspects: CBM in the actual condition while PdM is deploying prognostics (i.e., remaining useful life, RUL) to support the maintenance decision-making (e.g., Tinga & Loendersloot, 2014). Most authors agree on five required components to deploy a predictive maintenance approach, as illustrated in Fig. 1:

1. Hardware: sensors installed or retrofitted in physical assets or systems or components.
2. Data acquisition: data capturing and transfer between the monitored asset and the data storage and data transformation, so data can be stored in a useful form.
3. Data storage and management: platform on premises or in the cloud to ensure data storage, availability, and efficient transfer processes.

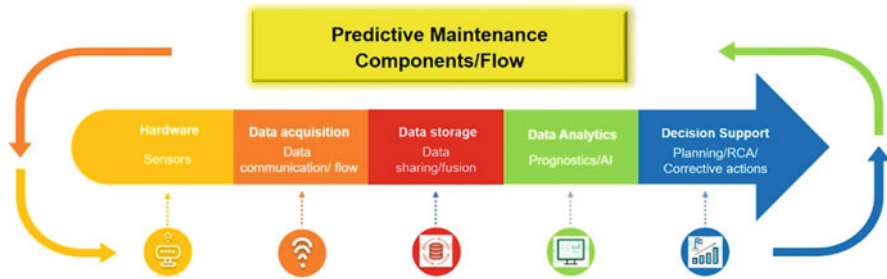


Fig. 1 Components and flow chart of PdM (own edition)

4. Data analytics: data pre-processing, so algorithms are fed with the right input and development of prognostic algorithms and models (e.g., machine learning and AI) to identify patterns or other useful information (RUL, degradation).
5. Decision support: tools used (e.g., digital twins) to determine actions based on the provided information.

Overall, added value is created by transforming the acquired data into predictions about the system condition and other relevant, meaningful information so that maintenance can be carried out when and where needed. However currently, in most cases, a few of the components or building blocks of the predictive maintenance process are in place so that developed solutions focus on these individual components and not in operationally deploy the full cycle.

3 Big Data Management

In recent decades, as every new generation of civil aircraft creates more on-wing data and fleets gradually become more connected with the ground, a lot of barriers have been removed, and an increased number of opportunities can be identified for more effective MRO operations. Today, data volumes are growing exponentially, e.g., an Airbus A350 generates and archives 50 times more data than an Airbus A320, i.e., from 12,000 parameters and 8.3TB to over 670,000 parameters and 450TB (Daily & Peterson, 2017). Therefore, data is increasingly becoming an asset for aircraft manufacturers, operators, and maintainers.

At the same time, the MRO providers underutilize their data, mainly due to data protection and focus on compliance. Other typical issues include the limited availability and low quality of historical data and the limited options in combining datasets from different operators of the same aircraft type. In addition, the availability of external data from airline operators, suppliers, and manufacturers is hampered by confidentiality and ownership issues. Last, time-consuming data preparation work is often needed to make the data quality acceptable (Pelt et al., 2019a).

Several new data capturing, manipulation, and sharing technologies are currently being developed, with the potential to change the landscape in data management. For example, data can now be organized effectively with the use of modern Big Data technologies. However, the availability, sharing, and combination of data is still an issue that has technical and legal challenges. A promising solution is the federated analytics (FA, aka federated learning) architecture which can be employed and act to combine and analyze datasets and algorithms located in different geographical locations, without compromising confidentiality or ownership (Nilsson et al., 2018; Li et al., 2020). The FA can provide an efficient data exchange environment to MRO end users without risking unauthorized exposure of their data.

4 Data Analytics and Algorithmic Methods

The key to unleash data potential and deliver meaningful insights lies in data analytics. Further, the inherent advantage of the data-driven methodologies is that they are not dependent on in-depth domain knowledge. Nevertheless, in practice, domain knowledge is required to establish what matters. Before starting the analysis and dive into specific methods and techniques, it is important to define the goal and the precise research question(s). For example, is the objective to detect abnormal behavior of an aircraft system or to predict the remaining useful life of a component? Defining first the data analysis goal helps to determine the KPIs and the variables, i.e., the input and target variables (Pelt et al., 2019a, b).

There are numerous schemes in the literature (e.g., Han et al., 2012) that can be used to classify the data analytics and algorithmic methods. In terms of technical complexity, a method can be one or any combination of the following (Apostolidis et al., 2020):

1. Fairly simple, making use of visualization techniques can be used for descriptive, exploration, monitoring, and communication purposes.
2. Simple to moderate, consisting of a wide range of statistical data mining techniques such as correlation to identify patterns and meaningful information from large pools of data.
3. Complex, using sophisticated, high-fidelity machine learning and AI algorithms for prognostics and recommendations for decision-support systems.

Overall, added value is created by transforming the acquired data into knowledge, reasoning, predictions, and ultimately, decisions and actions. Nevertheless, each problem must be approached with the appropriate, feasible, and relevant method. Then, it can be determined if the benefits outweigh the investment, taking also under consideration that the increased complexity is not necessarily an advantage. For example, complex and not transparent AI methods can create reduced confidence and certification issues, while simpler methods, more relevant with the standard practices and engineering logic, might be more attractive in certain cases.

5 Digital Twins

Digital twins (DT) are currently considered as a promising approach to address the problem of unpredictability in MRO operations. A DT is the combination of multiple state-of-the-art technologies embedded in three distinctive components, which are the physical entities, the virtual models, and the data that tie the physical and virtual entities, as illustrated in Fig. 2. However, DT is not a fundamentally new concept, as it is rooted in a wide range of conventional system simulation methodologies (Glaessgen & Stargel, 2012). Nevertheless, a conventional simulation can typically provide only a snapshot of the entity’s behavior, while a DT can extend that simulation process and yield an accurate description over time.

In literature, it is generally agreed that a DT can be considered as a detailed digital representation of the physical components of an aircraft system with the use of relevant data from various sources, such as real-time sensor data and historical maintenance data, a combination that can describe, optimize, and predict the performance behavior and the remaining useful life (URL) of an aircraft system or an MRO process with the use of simulation, prognostics, diagnostics, and analytics (Liu et al., 2018). This digital representation provides information about the current operational status of an aircraft component, with the benefit of exploring and investigating different operational and maintenance scenarios before their execution (Li et al., 2017).

A digital twin enables operators to understand, predict, and optimize the performance of their physical assets or analyze the behavior of a device after a failure or a technical issue (Apostolidis & Stamoulis, 2021). In addition, simulation models can play a crucial role in designing new maintenance practices for systems and assets which can be assessed in the virtual environment and deployed in the physical one.

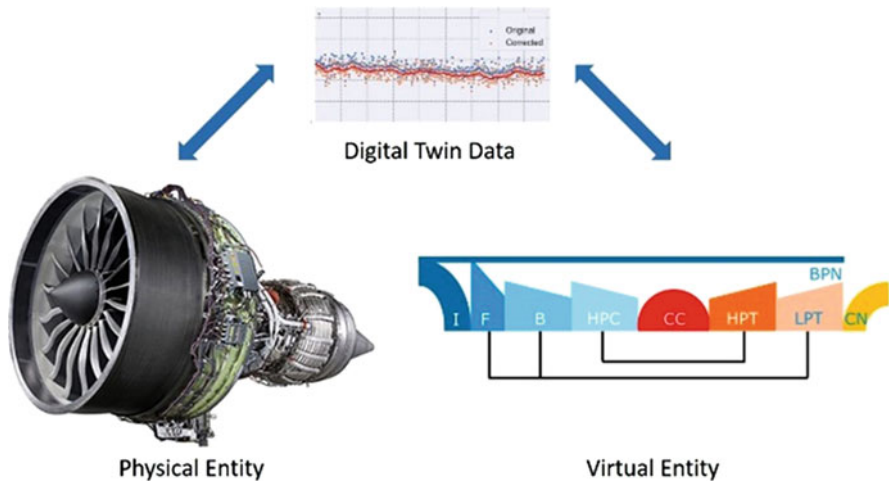


Fig. 2 An example of a digital twin (Apostolidis & Stamoulis, 2021)

This way an MRO provider can run experiments that will lead to an optimal operation of their assets. Nevertheless, various technical limitations complicated the development of effective digital twins, as it required technical maturity from a group of necessary enablers, such as the data-related and the Internet of Things (IoT) infrastructure for effective communication between the physical and the virtual entities (Wright & Davidson, 2020).

6 Decision Support Tools

The ultimate building block of a predictive maintenance flow is the application of the data analysis output into recommendations for decision-making and actions to improve the MRO efficiency. The operational deployment of predictive analytics can significantly reduce downtime, waste, and costs through labor, inventory, and material management and processes optimization without any compromise in quality and safety.

Individual case studies conducted with the use of a wide range of aviation data and analytics proved to be successful in delivering better information and prognostics, e.g., in Baptista et al. (2018); Pelt, Stamoulis, and Apostolidis (2019b); Nguyen et al. (2019); Deng et al. (2020); and Stamoulis and Apostolidis (2022) as follows:

1. Aircraft data with the use of sensors technology and effective data transfer and analytics can reveal the real-time physical status of the corresponding aircraft systems.
2. MRO-specific, AI algorithms, and simulation techniques enable faster diagnostics and prognostics, e.g., detection and assessment of hazards/defects/damages and remaining useful life (RUL) estimation.
3. Data-driven, scheduling tools can optimize fleet maintenance scheduling by determining maintenance tasks optimal slots and facilitating the decision-making.

7 Conclusion

There are a number of challenges that the aviation MRO industry is confronted with, not the least of which are related to a pressing demand for optimization in maintenance operations as well as an urgent sustainability agenda.

The operational deployment of proactive-type strategies and efficient, digital maintenance tools as discussed in the previous sections can ensure the following:

- Less unneeded maintenance and reduced waste of materials, which are currently replaced while still having remaining useful life
- Fewer operational disruptions, shorter lead times, and overall decreased downtimes

- Less deteriorated aircraft engines and systems that can operate at a higher efficiency, requiring less energy, which is translated to a better fuel consumption

Nevertheless, the current degree of operational adoption of the aforementioned enabling technologies and novel approaches in the MRO landscape is relatively low. Currently, there remain several technical and operational challenges including data challenges and human and organizational factors to be addressed to exploit the full potential of the data-driven predictive strategies and decision support tools. Moreover, as aviation is a safety-critical and highly regulated industry (e.g., in RCM-based MSG-3 standard), it is necessary to develop certification standards for the AI-based aircraft systems applications and ultimately, certifiable PdM models to render these technologies and methodologies suitable for operational deployment and real-life applications.

References

- Apostolidis, A., & Stamoulis, K. P. (2021). An AI-based digital twin case study in the MRO sector. *Transportation Research Procedia*, 56, 55–62.
- Apostolidis, A., Pelt, M., & Stamoulis, K. P. (2020). Aviation data analytics in MRO operations: Prospects and pitfalls. In *Proceedings of IEEE RAMS 2020*, Palm Springs.
- Baptista, M., Sankararaman, S., de Medeiros, I. P., Nascimento, C., Jr., Prendering, H., & Henriques, E. M. P. (2018). Forecasting fault events for predictive maintenance using data-driven techniques and ARMA modeling. *Computers and Industrial Engineering*, 115, 41–53.
- Daily, J., & Peterson, J. (2017). Predictive maintenance: How big data analysis can improve maintenance. In K. Richter & J. Walther (Eds.), *Supply chain integration challenges in commercial aerospace*. Springer.
- Deng, Q., Santos, B. F., & Curran, R. (2020). A practical dynamic programming-based methodology for aircraft maintenance check scheduling optimization. *European Journal of Operational Research*, 281(2).
- Glaessgen, E., & Stargel D. (2012). The digital twin paradigm for future NASA and US air force vehicles. In *53rd AIAA/ASME/ASCE/AHS/ASC structures, structural dynamics and materials conference, AIAA paper 2012-1818*.
- Han, J., Kamber, M., & Pei, J. (2012). *Data mining: Concepts and techniques* (3rd ed.). Morgan Kaufmann Publishers.
- IATA Maintenance Cost Technical Group. (2019). *Airline maintenance cost executive commentary*. Available online: <https://www.iata.org/contentassets/bf8ca67c8bcd4358b3d004b0d6d0916f/mctg-fy2018-report-public.pdf>
- Li, C., Mahadevan, S., Ling, Y., Wang, L., & Choze, S. (2017). A dynamic Bayesian network approach for digital twin. In *Proceedings of the 19th AIAA non-deterministic approaches conference*, Grapevine.
- Li, T., Sahu, A. K., Talwalkar, A., & Smith, V. (2020). Federated learning: Challenges, methods, and future directions. *IEEE Signal Processing Magazine*, 37(3), 50–60.
- Liu, Z., Meyendorf, N., & Mrad, N. (2018). The role of data fusion in predictive maintenance using digital twin. *AIP Conference Proceedings*, 1949, 020023.
- Nguyen, D. V., Kefalas, M., Limmer, S., Apostolidis, A., Yang, K., Olhofer, M., & Bäck, T. (2019). A review: Research and application of prognostics and health management in automotive and aerospace industries. *International Journal of Prognostics and Health Management*, 10(2).

- Nilsson, A., Smith, S., Ulm, G., Gustavsson, E., & Jirstrand, M. (2018). A performance evaluation of federated learning algorithms. In *Proceedings of the 2nd workshop on distributed infrastructures for deep learning*.
- Pelt, M., Apostolidis, A., de Boer, R. J., Borst, M., Broodbakker, J., Patron, R. F., Helwani, L., Jansen, R., & Stamoulis, K. P. (2019a). *Data mining in MRO*. Faculty of Technology, Amsterdam University of Applied Sciences.
- Pelt, M., Stamoulis, K., & Apostolidis, A. (2019b). Data analytics case studies in the maintenance, repair and overhaul (MRO) industry. *MATEC Web of Conferences*, 304, 04005.
- Phillips, P., Diston, D., Starr, A., Payne, J., & Pandya, S. (2010). A review on the optimisation of aircraft maintenance with application to landing gears. In D. Kiritsis, C. Emmanouilidis, A. Koronios, & J. Mathew (Eds.), *Engineering asset lifecycle management*. Springer.
- Stamoulis, K. P., & Apostolidis, A. (2023). *Diagnostics, prognostics & advanced maintenance technologies for aviation MRO*. Springer. in preparation.
- Tinga, T., & Loendersloot, R. (2014). Aligning PHM, SHM and CBM by understanding the physical system failure behaviour. In *Second European conference of the prognostics and health management society*.
- Wright, L., & Davidson, S. (2020). How to tell the difference between a model and a digital twin. *Advanced Modeling and Simulation in Engineering Sciences*, 7(13).

Developing Models and Methods for Autonomous Drones in Urban Air Transport



Dung D. Nguyen, Utku Kale, and Dániel Rohács

Contents

| | | |
|-----|--|-----|
| 1 | Introduction | 434 |
| 2 | Methodology | 435 |
| 2.1 | Sensor Fusion Tools Supported of Autonomous System | 435 |
| 2.2 | Following Process | 436 |
| 2.3 | Obstacle Avoidance Method | 437 |
| 2.4 | Desired Landing Orbit for UAVs | 437 |
| 3 | Results | 439 |
| 3.1 | Drone-Following Process in the Traffic Flow | 439 |
| 3.2 | Experiment Results of Drone Management System | 441 |
| 3.3 | Calculating the Desired Landing Orbits for UAVs | 442 |
| 4 | Conclusion | 444 |
| | References | 444 |

Nomenclature

r_{BI} Radius, m
 $d_{s,l}$ Distance, m

D. D. Nguyen (✉)

Department of Aeronautics and Naval Architecture, Budapest University of Technology and Economics, Budapest, Hungary

Department of Aircraft System Design, Faculty of Aerospace Engineering, Le Quy Don Technical University, Hanoi City, Vietnam
e-mail: dungnd@lqdtu.edu.vn

U. Kale · D. Rohács

Budapest University of Technology and Economics, Department of Aeronautics and Naval Architecture, Budapest, Hungary

Greek Letters

| | |
|-------------------------|------------------|
| ΔX_{pdn} | Safe distance, m |
| λ | Coefficient |

1 Introduction

With the exponential growth of numerous drone operations ranging from infrastructure monitoring to even package delivery services, the integration of UAS in the smart city transportation systems is an actual task that requires radically new, sustainable (safe, secure, with minimum environmental impact and life cycle cost) solutions.

To enable drones to be operated regularly as an integral part of the urban air transportation system, it is essential to develop technical solutions, formulate regulatory frameworks, and design management systems to safely conduct operations, both in the air and the ground.

Regarding technologies and models, researchers have focused on altitude control and trajectory tracking control problems. Several scientific reports have presented the altitude control problem in the literature. Such as authors in (Xuan-Mung & Hong, 2019b) used barometric to improve the altitude control performance of a quadcopter, while authors in (Xuan-Mung & Hong, 2019a) used a multi-loop PID controller, an infrared (IR) camera, and an IR beacon (Xuan-Mung et al., 2020). Besides, many studies have aimed to solve the trajectory tracking control problem by using backstepping (Nguyen et al., 2019), multi-loop PID controller (Kendoul, 2009), or combining a PID controller and a backstepping controller (Zuo, 2012), sliding mode control (Shah et al., 2014), extended state observer (ESO)-based robust backstepping (Xuan-Mung & Hong, 2019c), and linear quadratic regulator (LQR) (Faessler et al., 2017).

A drone management system is a sub-system of the overall unmanned traffic management system (UTM) that guarantees safe, environmentally friendly, effective, and sustainable mobility in urban/city areas. It is a sub-system only, but it has fast interconnections with air traffic management systems, including, e.g., sharing airspace, conflict/obstacle detection and resolution, and optimal trajectory control. Nowadays, new forms of transportation such as urban air transportation (drones, air taxis) must be integrated in the total transportation management (see Fig. 1 (Nguyen et al., 2020)) and harmonized with other autonomous vehicles (Hegedűs et al., 2020).

In the future, with the introduction of autonomous/connected drones and highly automated traffic management systems, the operator roles will be shifted from active control to passive observation and only expected to take active control in the case of



Fig. 1 Urban total transportation system: (I) industrial area (factories), (II) forest area, (III) urban area, IV: airport area, (1) underground, (2) road, (3) upper ground, (4) path, (5) railway, (6) highway, (7) freight transport, (8) urban air transport, (9) water transport

exceptional or emergency cases. Such a control environment should be supported with adequate data to permit the UTM to support the smart city vision.

This chapter deals with the required air traffic management and flight control for drones or a group of drones. The drones might follow fixed trajectories or predefined corridors. Several methods as sensor fusion, real-time GIS support, centralized dynamic sectorization, active management, fixed trajectory flowing models, predefined flight modes like coordinated turns, active conflict/obstacle detection and resolution, flight drone-following models, and formation flights should support the drone’s operation in smart cities.

2 Methodology

2.1 Sensor Fusion Tools Supported of Autonomous System

Autonomous systems rely on a sensor suite that provides data about themselves and sensors that sense the environment. In many cases, the autonomous system uses commercially available sensors. For pose estimation, sensors commonly used are accelerometers, gyroscopes, magnetometers, altimeters, or GPS. Sensors that sense the environment include radars and vision cameras, which provide detections of objects in their field of view. Lidars provide point clouds of returns from obstacles in the environment, and in some cases, ultrasound and sonar sensors. Some signal processing occurs in the sensor system, often including detection, segmentation, labeling, classification, and in some cases, basic tracking to reduce false alarms.

Kivelevitch et al. (2019) introduced the requirements and a possible solution for a set of tools in the perception stage in which inputs from various sensors are fused to provide a single estimation of the environment around the autonomous system. This toolset integrates sensor fusion and tracking algorithms into complete tracks, simulating sensor data, swapping trackers, testing various fusion architectures, or evaluating the overall tracking results.

Siewert et al. (2018) presented a work that focused on feasibility testing of ground electro-optical/infrared (EO/IR) and characterization of acoustic viability with the intent to expand nodes in a wireless communication network of nodes in a drone net sensor network in an air column of 1-km diameter. In this study, the active sensors, RADAR and LIDAR, were used on the ground as a secondary validation. In contrast, passive sensors competed with RADAR in terms of classification and identification performance at a lower cost.

2.2 Following Process

When the number of drones increases, severe accidents can appear in the sky, even in simple situations. The investigation of drone traffic safety and the intelligent transportation system's development requires drone-following models describing one-by-one following process in the traffic flows. The drone-following models are based on the idea that each drone can be flown under its leader, expressed by the function of safety distance or relative velocity of two drones. For example, if three drones are flying on the same route simultaneously, two of them can fly following the leader.

In the drone-following process, the drone's velocity depends on the traffic situation, namely, on the distance to the drone ahead and its velocity. This approach led to the linear models assuming that its controller controls the drone's acceleration to keep zero relative velocity to the drone ahead.

The SD model is given as follows:

$$\ddot{X}_n(t + T) = \lambda \frac{[\dot{X}_n(t)]^p}{[X_{n-1}(t) - X_n(t)]^q} [\dot{X}_{n-1}(t) - \dot{X}_n(t)] \quad (1)$$

where $X_n(t + T)$ is the acceleration of n -th drone after a reaction, $X_{n-1}(t) - X_n(t)$ is the relative distance between the $(n - 1)$ -th drone and the n -th drone, $\dot{X}_{n-1}(t) - \dot{X}_n(t)$ is the relative velocity of $(n - 1)$ -th to the n -th drones in time t , T is the delay time of a controller, λ is a weight coefficient related to the controllers, and p and q are parameters related to velocity and distance of the drone ahead.

It seems this model is well applicable to the drones flying in the desired flight path. However, the air turbulences and wind flow separated from infrastructure cause rather stochastically disturbed motion of drones. With the characteristics of advanced controllers, the controller's relative distance and actual reaction time are added to the control close-loop. This approach leads to an improved model, called the Markov model.

The Markov model is based on the approximation of the stochastic process of velocity decision. One advantage over the SD model is that the inputs of the controller are different velocities and deviations in relative distance between the drones, which can be described such as follows:

$$\begin{aligned} \ddot{X}_n[k+1] = & c_v (\dot{X}_{n-1}[k] - \dot{X}_n[k]) \\ & + c_x [(X_{n-1}[k] - X_n[k]) - \Delta X_{\text{pdn}}] + \varepsilon[k] \end{aligned} \quad (2)$$

where c_v and c_x are coefficients depending on the time, given drone and controllers, $\Delta X_{\text{pdn}} = \dot{X}(t)$ is the predefined safety distance between the drones, k is the number of steps in a chain ($t = k \cdot \Delta t$), and $\varepsilon[k]$ is the random value disturbing the process.

2.3 Obstacle Avoidance Method

Along with drone applications' spreading trend, drone collision's flight safety with buildings, helicopters, and the landscape becomes an urgent issue for civil and defense agencies. A collision avoidance system is necessary for drone flights, especially for autonomous drones in dense airspace shared with other aircraft to guarantee airspace security. Conflict detection and collision avoidance is also a valuable tool for highly automated and autonomous vehicles. There are several simulation systems for algorithms tested and designed in laboratories. The obstacle model is one of the critical parts of these systems, described as the following. Assume that each obstacle is prescribed in a cylinder with the center C_{BI} and radius r_{BI} , as shown in the following Fig. 2. The surfaces of cylinders can then be used to form constraints for obstacle avoidance. Accurately, the safe distance $d_{s,l}$ from the obstacle l is calculated from the cylinder center to its surface at the flying height.

2.4 Desired Landing Orbit for UAVs

The landing approach is one of the critical stages of the entire flight to bring the UAV to land safely at the desired location. Common landing approaches consist of the following stages: (i) heading against the direction of the wind, (ii) descending, and (iii) slowing down. However, this process will be influenced by several factors such as wind disturbance, general aerodynamic force, the traction force of an engine, and the propeller's reaction moment.

Methodologies used to determine and calculate the landing areas are based on solving the aircraft's motion equations and analytical methods. Based on the landing areas, the desired landing orbit is estimated, within which the UAV can land accurately at the desired position.

Fig. 2 Obstacle representation and safe distance calculation

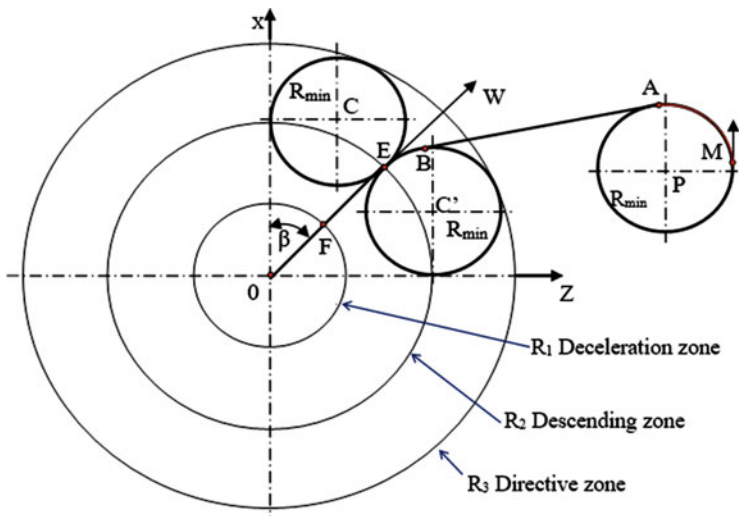
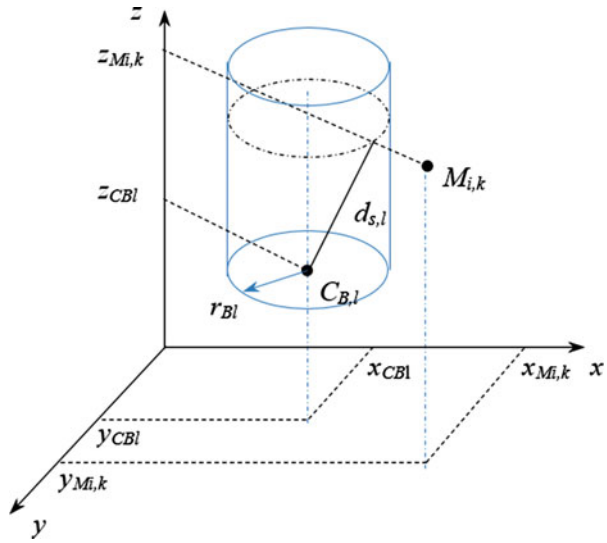


Fig. 3 The proposed UAV landing zones

The UAV landing areas include the following three zones (Fig. 3):

Deceleration zone: This is the smallest circle on the horizontal plane containing the projection of the UAV's orbit, which flies straight with the decreasing speed during the landing approach. Then, the deceleration zone's shape is a circle with a center O and radius R_1 .

Descending zone: This is the smallest circle on the horizontal plane containing the projection of the UAV’s orbit, which flies in the process of altitude reduction. This area is a circle with a center O and radius R_2 .

Directive zone: This is the smallest circle in the horizontal plane containing projections of two circles with radius R_{min} . Two circles tangent to each other at the opposite of the wind direction.

The R_{min} is the smallest rounding radius of the UAV. Thus, the directive zone is the circle with center O and the radius R_3 .

UAVs’ landing trajectories generally consist of approach, glideslope, and flare. A successful landing would depend on the selection of the landing trajectory and its implementation.

UAVs’ landing processes consist of three stages: the directive stage, the descending stage, and the deceleration stage. These stages are determined when the UAV is into each landing zones. Landing zones will be determined by knowing the radius of each region. The most common method is to investigate UAVs’ kinetic dynamics by solving the differential motion system. Therefore, UAV dynamics will be used to calculate the deceleration zone, and then the remaining landing areas will be identified by analytical methods.

3 Results

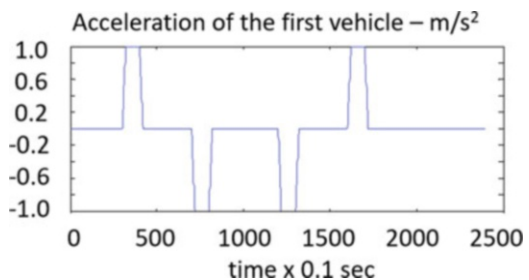
3.1 Drone-Following Process in the Traffic Flow

Drone-following models for managing drones in smart cities’ transportation management systems were introduced in previous studies (Dung, 2020; Dung & Rohacs, 2018). Such models were based on the initial idea that drones fly toward a leading drone in the traffic flow. This approach has been a novel method for managing a group of drones in smart cities.

This subsection provides the main results obtained in the simulation experiments on the SD and Markov models (see Figs. 4 and 5).

It can be noted that there is no accident and no unrealistic deceleration. The velocity of the followed drone is changed according to the speed of the drone ahead.

Fig. 4 Acceleration, deceleration of the first drone applied in verification tests



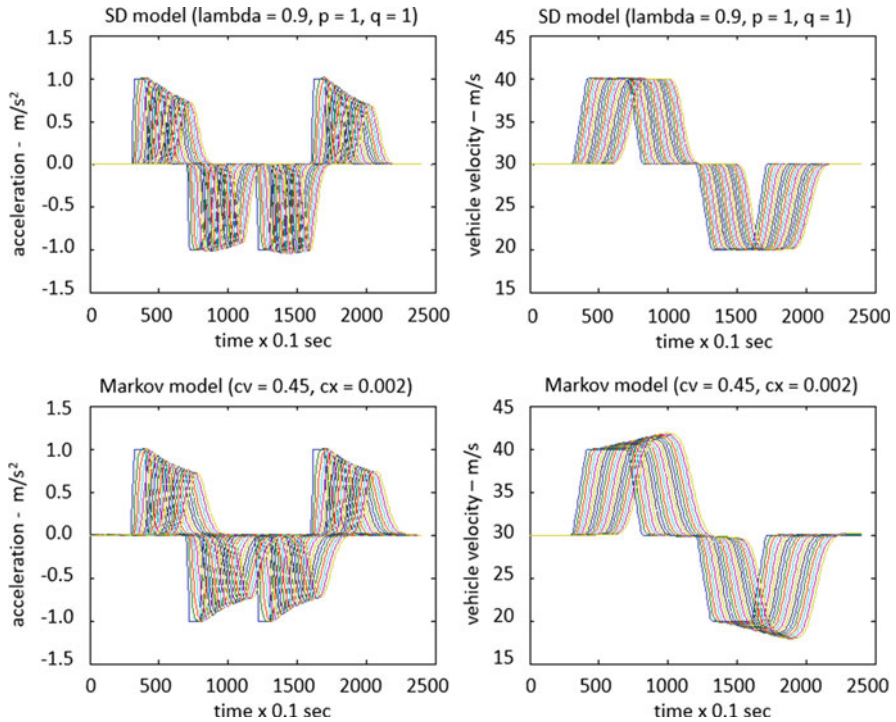


Fig. 5 Verification results for comparison of the SD and Markov drone-following models

However, the followed drone can react quickly compared to the leading drone’s reaction because of the difference in its acceleration.

Even though the SD and the Markov models are quite similar, the followed drone’s reaction in the SD model is earlier than that in the Markov model. Besides, the motion of the followed drone indicates that the stable state is slower in both models. In comparison with the SD model, the Markov model considers the changes in relative distance between drones. Moreover, the more significant the variation of the followed drone’s velocity in the Markov model, the much smaller the relative distance is between the drones.

These results verified that the developed Markov model might perform the longitudinal safety separation of drones as the SD model. In general form, the results partly validated the proposed method that is part of research aiming to integrate drones with the urban intelligent transport system. The drone-following method needs to be verified by several immediate next steps, such as the safe distance being measured in the drone directly in front and two drones beside, designing and conducting an experimental study to collect quantitative information regarding drone performance in space.

As it seems, the developing Markov model might be more accurate in the case of motion of drones in significant air turbulence and separated wind flow from the

infrastructure, and it can be used in areas where problems with GPS positioning might have appeared, especially comparing and working together with the GPS techniques or acoustic sensors, etc.

3.2 Experiment Results of Drone Management System

In experimental studies, a cloud-based managing method had been applied to drones flying in a smart city environment (Nguyen, 2021), including the physical, cloud, and control layers.

The experimental result is demonstrated in the Fig. 6. Initially, the drone was placed at a home position. When a drone received the GCS command, it took off and did a mission, visited the created waypoints. The results show that the desired trajectory and actual trajectory are correlated. The gap between the two trajectories represents GPS location because the drone receives the GPS location.

It can be observed that proportional-integral-derivative (PID) control is entirely sufficient to follow set positions at low speeds (when the drone aerodynamics changes slightly and has no wind disturbance). For initial test flights, proper tracking was achieved, even in the case of moderate errors.

It is illustrated in the Fig. 7 that a linear controller achieved the altitude flight control with the increase in the vertical speedup. The flight control unit (FCU) has



Fig. 6 The difference between desired and real trajectories (pink line: desired trajectory, blue line: real trajectory)

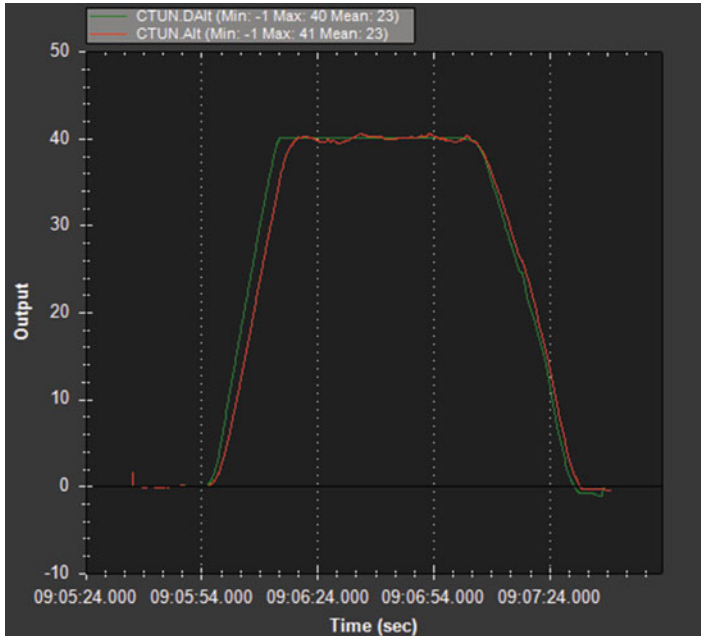


Fig. 7 The difference between desired and actual altitude of drone, green line, desired altitude; red line, actual altitude

performed extremely useful in height control despite a minor gap between the desired and actual altitudes.

During the experiments, the drone's video streamed downward, facing the camera, allowing us to observe and control the drone in a real-time environment.

These experimental results demonstrated that the proposed and applied CbDMS (cloud-based drone managing system) is a cloud solution that enables drones' management and control in a real-time environment. The monitoring efficiency can be increased by raising the regularity of refreshing GPS coordinates or adding filtering techniques (Kalman filters).

3.3 Calculating the Desired Landing Orbits for UAVs

The previous research presented the methodologies using to determine and calculate the landing stages (Rohacs & Dung, 2019). Based on the landing areas, the desired landing orbit is estimated, within which the UAV can land accurately at the desired position. The simulation results for UAV landing in the given direction are shown in the Figs. 8 and 9.

In this case, the desired landing orbit consists of two curves and two lines. At the height $H = 500$ m, the UAV completes two turning with the desired roll angle

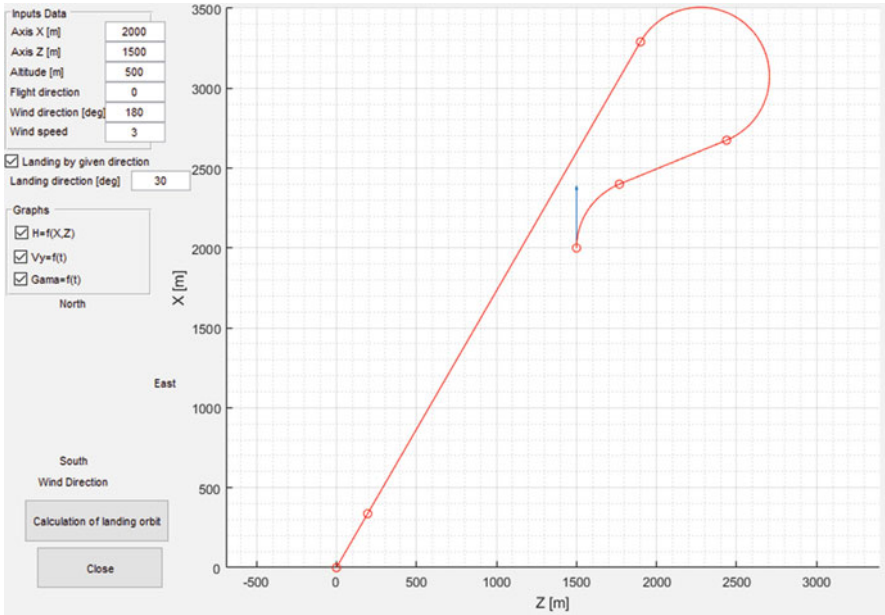


Fig. 8 The desired trajectory for UAV landing in the given direction

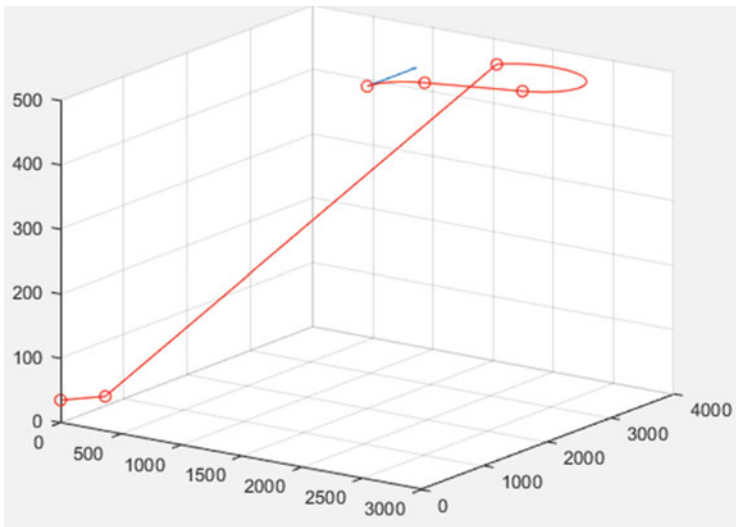


Fig. 9 The altitude of the UAV landing in the given direction

$\gamma \leq 20^\circ$. Between these two times, a straight flight takes place with speed $V = 40$ m/s. Then, the drone flies in the right orbit in the given direction, starting the step of lowering the altitude and finally straight flight at decreasing speed. The simulation

result given is reasonable and necessary to implement controlling orders. The result also shows that the landing direction is the direction from the current point of the UAV to the desired landing point, and this landing distance is the shortest one.

4 Conclusion

In this chapter, we introduced several methods for controlling and managing drone operations, such as the desired trajectory following management, following process, obstacle avoidance, and desired land orbit. By providing such a scenario, we hope to reduce much of the effort currently spent managing a large of UAV, especially drones, with every new autonomous system development project. This will enable researchers, developers, and enthusiasts to develop their autonomous systems with significantly reduced time, effort, and funding. It will also allow professionals to share best practices and best results within the organization and across organizations and disciplines. Further research is required to understand better how the proposed system could be planned, which depends on open questions linked to critical features associated with the possible significant use of drones and how sustainably they could be in life quality.

References

- Dung, N. D. (2020). Developing models for managing drones in the transportation system in smart cities. *Electrical, Control and Communication Engineering*, 15(2), 71–78. <https://doi.org/10.2478/eccc-2019-0010>
- Dung, N. D., & Rohacs, J. (2018). The drone-following models in smart cities. In *2018 IEEE 59th annual international scientific conference on power and electrical engineering of Riga Technical University, RTUCON 2018 - proceedings*. Institute of Electrical and Electronics Engineers Inc. <https://doi.org/10.1109/RTUCON.2018.8659813>
- Faessler, M., Falanga, D., & Scaramuzza, D. (2017). Thrust mixing, saturation, and body-rate control for accurate aggressive quadrotor flight. *IEEE Robotics and Automation Letters*, 2(2), 476–482. <https://doi.org/10.1109/LRA.2016.2640362>
- Hegedűs, T., Németh, B., & Gáspár, P. (2020). Challenges and possibilities of overtaking strategies for autonomous vehicles. *Periodica Polytechnica Transportation Engineering*, 48(4), 320–326. <https://doi.org/10.3311/PPTr.15848>
- Kendoul, F. (2009). Nonlinear hierarchical flight controller for unmanned rotorcraft: Design, stability, and experiments. *Journal of Guidance, Control, and Dynamics*. American Institute of Aeronautics and Astronautics, 32(6), 1954–1958. <https://doi.org/10.2514/1.43768>
- Kivelevitch, E. H., et al. (2019). Sensor fusion tools in support of autonomous systems. In *AIAA SciTech 2019 Forum*. American Institute of Aeronautics and Astronautics (AIAA SciTech Forum). <https://doi.org/10.2514/6.2019-0384>
- Nguyen, D.-D. (2021). Cloud-based drone management system in smart cities. In R. Krishnamurthi, A. Nayyar, & A. E. Hassanien (Eds.), *Development and future of Internet of Drones (IoD): Insights, trends and road ahead* (pp. 211–230). Springer International Publishing. https://doi.org/10.1007/978-3-030-63339-4_8

- Nguyen, A. T., Xuan-Mung, N., & Hong, S.-K. (2019). Quadcopter adaptive trajectory tracking control: A new approach via backstepping technique. *Applied Sciences*. <https://doi.org/10.3390/app9183873>
- Nguyen, D. D., et al. (2020). Intelligent total transportation management system for future smart cities. *Applied Sciences*. <https://doi.org/10.3390/app10248933>
- Rohacs, J., & Dung, N. D. (2019). Robust planning the landing process of unmanned aerial vehicles', *International Journal of Sustainable Aviation* , 5(1), 1. <https://doi.org/10.1504/ijsa.2019.10021483>. Inderscience Publishers
- Shah, M. Z., Samar, R., & Bhatti, A. I. (2014). Lateral track control of UAVs using the sliding mode approach: From design to flight testing. *Transactions of the Institute of Measurement and Control*. SAGE Publications Ltd STM, 37(4), 457–474. <https://doi.org/10.1177/0142331214543093>
- Siewert, S., et al. (2018). Drone net architecture for UAS traffic management multi-modal sensor networking experiments. *IEEE Aerospace Conference*, 1–18. <https://doi.org/10.1109/AERO.2018.8396716>
- Xuan-Mung, N., & Hong, S.-K. (2019a). Improved altitude control algorithm for quadcopter unmanned aerial vehicles. *Applied Sciences*. <https://doi.org/10.3390/app9102122>
- Xuan-Mung, N., & Hong, S. (2019b). Barometric altitude measurement fault diagnosis for the improvement of quadcopter altitude control. In *19th international conference on control, automation and systems (ICCAS)* (pp. 1359–1364). <https://doi.org/10.23919/ICCAS47443.2019.8971729>
- Xuan-Mung, N., & Hong, S. K. (2019c). Robust backstepping trajectory tracking control of a quadrotor with input saturation via extended state observer. *Applied Sciences*. <https://doi.org/10.3390/app9235184>
- Xuan-Mung, N., et al. (2020). Autonomous quadcopter precision landing onto a heaving platform: New method and experiment. *IEEE Access*, 8, 167192–167202. <https://doi.org/10.1109/ACCESS.2020.3022881>
- Zuo, Z. (2012). Adaptive trajectory tracking control design with command filtered compensation for a quadrotor. *Journal of Vibration and Control*. SAGE Publications Ltd STM, 19(1), 94–108. <https://doi.org/10.1177/1077546311431270>

Using a New Kerosene Flame Bench Test to Analyze at Small Scales the Fire Reaction of Fiber-Reinforced Polymer Matrix Composites



Alexis Coppalle, Eliot Schuhler, Avinash Chaudhary, and Benoît Vieille

Contents

| | | |
|-----|--------------------------------------|-----|
| 1 | Introduction | 447 |
| 2 | The Test Bench | 449 |
| 3 | The Test Protocol | 449 |
| 4 | The Tested Composite Materials | 451 |
| 5 | Results and Discussion | 451 |
| 5.1 | Temperatures at the Back Face | 451 |
| 5.2 | Mass Loss | 453 |
| 6 | Conclusion | 455 |
| | References | 456 |

1 Introduction

In the aircrafts, composite materials are now widely used. An important issue is that they may be exposed to a flame, during a malfunction of the engines or after a crash. Under such circumstances, the composite is degraded, and it loses its performances. In order to test the fire reaction of the materials, there are several standard tests specific to aeronautical applications (Mouritz & Gibson, 2006); in particular some of them use propane or kerosene impinging flames (ISO2685:1998; FAR25.856). However, they are expensive, time-consuming, and requires heavy equipment.

A. Coppalle (✉) · E. Schuhler · A. Chaudhary
CORIA, Normandy University, Saint-Étienne-du-Rouvray, France
e-mail: alexis.coppalle@coria.fr

B. Vieille
GPM, Normandy University, Saint-Étienne-du-Rouvray, France

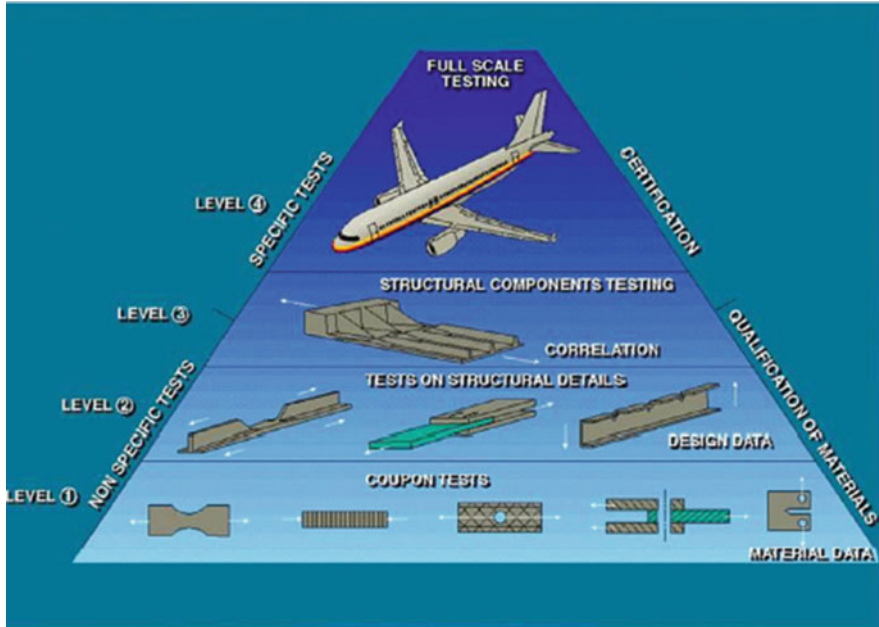


Fig. 1 From small to full scales: the testing pyramid

They can be used only for certification, and it is hard to use it for development and optimization of new products with improved fire reaction.

The performance and strength of a composite aero-structure is established incrementally through a program of analysis and a series of experimental tests conducted using specimens of varying size and complexity. The process is based on a so-called testing pyramid approach with tests at each of the following levels, as shown in Fig. 1: (i) coupon, (ii) structural detail, (iii) component, and (iv) substructure or full structure (Serra et al., 2017). The process is long and costly. Therefore, before certification, it is better to analyze and to optimize the new products at the levels 1 or 2. These are typically the aim of laboratory tests at small scales. This is often achieved with a cone calorimeter that apply a radiative flux on the sample (Stoliarov et al., 2009; Grange et al., 2018). However, the maximum thermal stress is limited to 100 kw/m^2 , which is well beyond the values encountered in real scenarios, and a direct flame impact is a more realistic thermal stress.

A new bench test was built in order to analyze at small scales, typically with sample size of a dozen of centimeters, the behavior of composites under a kerosene flame. The test bench is first described. As for examples, the tests for two carbon fiber-reinforced polymer matrix composites, a thermosetting-based (epoxy 8552) and a thermoplastic-based (polyphenylene sulfide), will be shown, and the results are discussed.

2 The Test Bench

The kerosene burner of the bench test is made of a combustion chamber fed with a spray of kerosene (0.27 g/s) and a flame tube (30 cm long and 5-cm diameter), thus providing at the exit a homogeneous flux of hot gases. The combustible to air ratio is equal to 80% of the stoichiometric value. The temperature on the flame axis is measured by thermocouples, with values equal to 1100 °C. The heat flux is measured with a Gardon-type gauge placed in front of the flame, and providing a value equal to 118 kW/m² kw/m² at 10 cm from the flame exit. The flexibility of the bench test is that the heat flux can be varied in the range 80–180 kW, by changing the distance between the flame tube exit and the sample, or the air and kerosene flow rates. The temperature of the rear face has been observed using an IR camera, and the sample mass losses monitored during tests with a load cell (Schuhler et al., 2021), as shown in Fig. 2.

The composite sample is placed between two insulation layers, and the assembly is clamped by two steel plates. In both side of the sample holder, a round aperture of 50-mm diameter is made.

3 The Test Protocol

Before each test, the temperature and heat flux measurements are carried out in the hot gas jet, at the same distance from the exit of the flame tube as the sample holder. The temperature is measured using a mobile comb of six K-type thermocouples, the spacing between each thermocouple being 8 mm, as shown in Fig. 3. After the burner ignition, a period of 15 minutes is necessary in order to reach steady conditions in temperature. For all the tests presented here, the mean value of the temperature at the center of the hot jet is about 1080 ± 30 °C. After the thermocouple comb is removed, the heat flux is measured using a water-cooled heat flux sensor

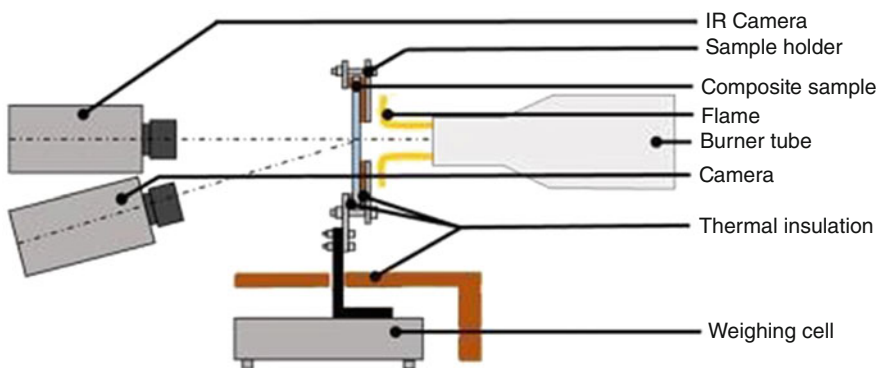


Fig. 2 Schematic view of the test bench

Fig. 3 The kerosene flame at the burner exit and view of the thermocouples used to check flame temperature

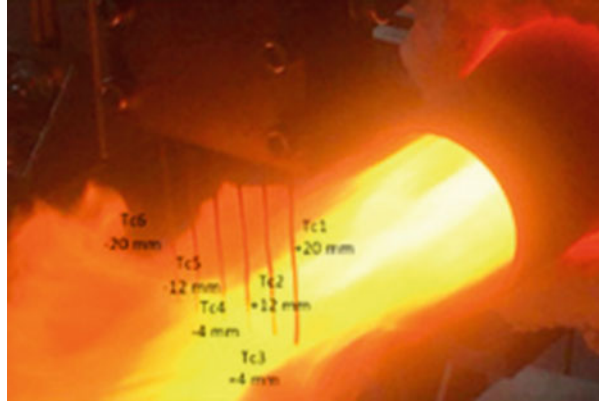


Fig. 4 View of a sample in front of the burner during a test



(Gardon, 1953; Carlomagno & Ianiro, 2014) (Captec manufacturer) inserted into a movable steel plate. The value is monitored during a few minutes, and it is well stable.

The mean value of the temperature at the center of the hot jet (1080 °C) and the heat flux (120 kW/m²) allow to reproduce the thermal stress conditions as in standard test cases (ISO2685:1998; FAR25.856).

Finally, the heat flux sensor is removed, and the sample holder is translated in front of the flame, as shown in Fig. 4.

4 The Tested Composite Materials

The composite materials studied in this work are carbon/epoxy and carbon/polyphenylene sulfide (PPS) woven-ply laminates. The samples are $70 \times 70 \text{ mm}^2$; they are cut from prepreg laminate plates.

The thermoplastic-based laminates (C/PPS) are seven plies carbon fiber-reinforced PPS prepreg laminate. The PPS resin and the carbon fibers (T300 3 K 5HS) are, respectively, supplied by Hexcel and Toray. The mass fraction of carbon fiber is 58%. The glass transition temperature of the material is $T_g = 98 \text{ }^\circ\text{C}$ and its melting temperature $T_m = 280 \text{ }^\circ\text{C}$, as measured by DSC (Blond et al., 2014). The crystallinity of PPS matrix is close to 30%. The laminates thickness is 2.2 mm, and the onset of thermal degradation is about $493 \text{ }^\circ\text{C}$.

The thermosetting-based laminates (C/epoxy) are referred to as AcF2 in (Zhang et al., 2017). The glass transition temperature is about $190 \text{ }^\circ\text{C}$, and the peak of thermal degradation is about $390 \text{ }^\circ\text{C}$.

5 Results and Discussion

5.1 Temperatures at the Back Face

For results presented below, and for both samples C-Epoxy and C-PPS, the heat flux is equal $120 \pm 5 \text{ kW/m}^2$. Figures 5 and 6 show the temperature measured with the IR camera at the center of the samples. Three different tests have been done in order to look at the reproducibility of the processes occurring degradation with the kerosene flame. This one is rather good. Some differences occur after 50 s, mainly caused by

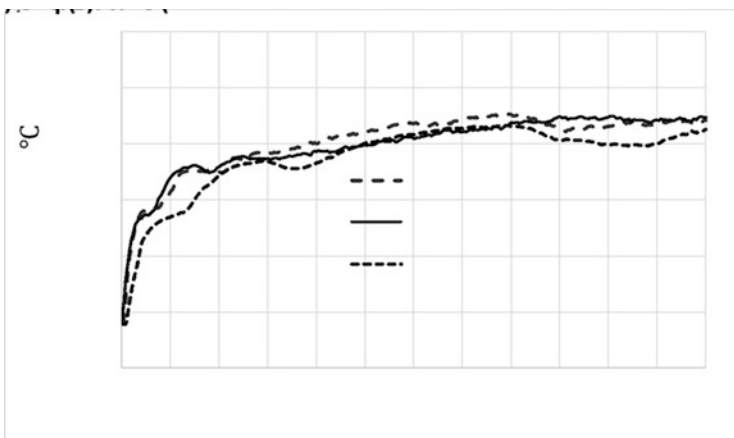


Fig. 5 C-PPS composite, temperature measured with the IR camera at the center of the back face

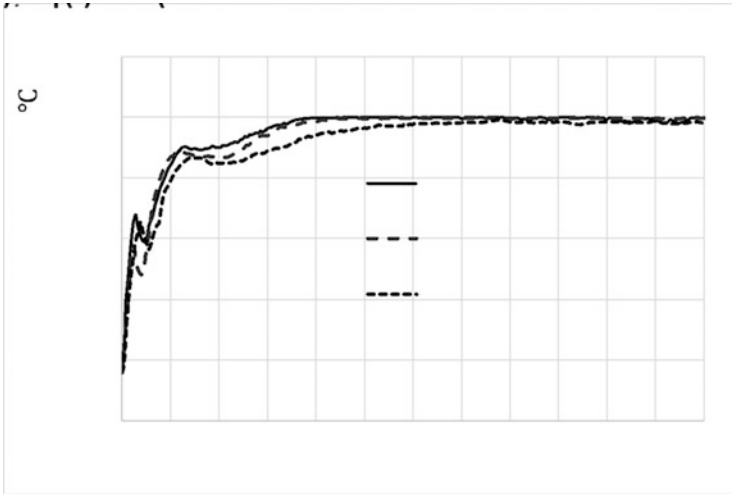


Fig. 6 C-Epoxy composite, temperature measured with the IR camera at the center of the back face

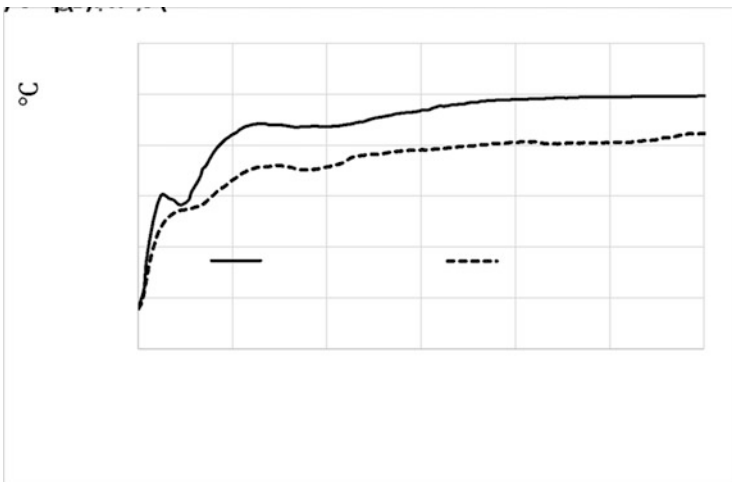


Fig. 7 Comparison between average values of temperatures measured at the center of the back face of the C-Epoxy and C-PPS samples

delamination and cracks that appear at high temperature inside the materials; these may be different from one test to another even with similar thermal stress.

On Fig. 7, the average values of the three previous tests have been reported for both C-Epoxy and C-PPS samples. The shape of the curves is more or less similar, but the temperature values for the C-PPS are lower than for the C-Epoxy. During the first seconds (<15 s), only heat transfer from the flame-side to the back-side occurs. The heating rate is very strong and about 1200 °C/s. After that, delamination is

produced inside the composites, mainly due to the high dilation of the matrix compared to the fiber plies. This causes cracks to appear, which will act as thermal barriers and which will reduce the temperature rises close to the back face. This is particularly visible for the C-Epoxy, for which a quick temperature decrease is observed. During the last period of the tests, a stabilized temperature is reached. This one is lesser for the C-PPS compared to C-Epoxy, a difference of about 100 °C. This is an interesting feature of the thermoplastic composite, which is able to act more efficiently to the heat transfer to the non-exposed surface.

5.2 Mass Loss

Mass losses are given in Figs. 8 and 9; the results are presented in percentage of the initial mass, i.e., the ratio of the mass at time t to the initial mass. The three tests carried out with the same composite (C/PPS or C/epoxy) show that the tests performed with this setup are well repeatable. The greater differences are found after 100 s for the thermosetting-based composite and after 600 s for the thermoplastic-based composite. The differences between the three tests is lesser than for the temperature measurements; however, they can be explained again by the internal damage mechanisms such as the building of cracks, delamination, and major pores that may be different from one test to another even with similar thermal stress.

On Fig. 10, the average values of relative mass losses of the C-Epoxy and C-PPS samples are reported. The speed of the mass loss is much higher for the C-Epoxy, and the final mass loss too. This has a strong influence on the residual mechanical properties. With the test bench used, no fiber ablation was observed on the exposed surface, so the mass loss is essentially due to the matrix decomposition. Since one

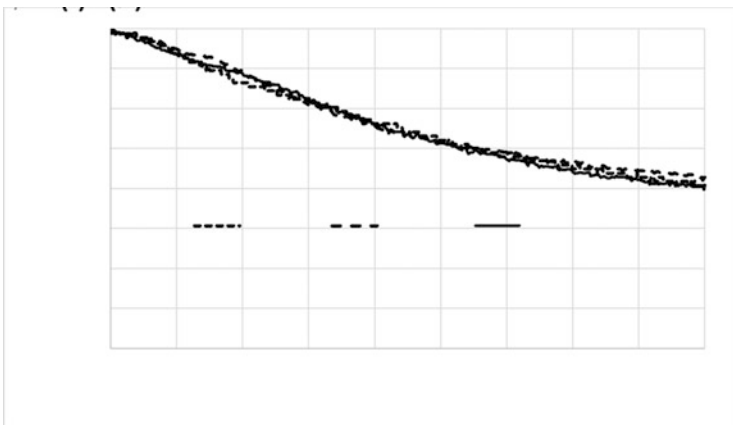


Fig. 8 C-PPS composite, relative mass loss

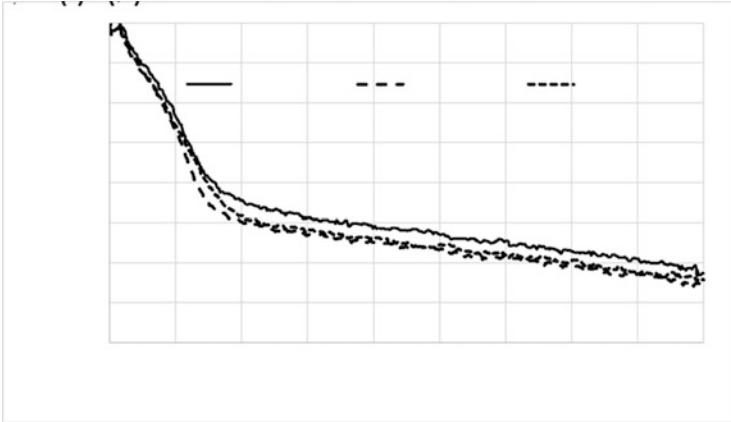


Fig. 9 C-Epoxy composite, relative mass loss



Fig. 10 Comparison between average values of relative mass losses of the C-Epoxy and C-PPS samples. Drawn lines are for highlighting the time corresponding to 50% of the final mass loss

action of the matrix in composites is to equilibrium mechanical stress between the plies, one can expect that the residual mechanical properties for the C-PPS is better to the C-Epoxy ones. The lines drawn on Fig. 10 are for highlighting the time corresponding to 50% of the final mass loss. The value for the C-PPS is about three times the value for C-Epoxy.

Figure 11 shows an example of the behavior of the C-PPS samples to three different thermal stresses, 120–140–160 kw/m^2 . As expected the relative mass loss increases with the heat flux. However, the increase of the final value between 120 and 140 kw/m^2 is not very different to the increase observed between 140 and 150 kw/m^2 . It is evident that not all the initial mass of the matrix in the composite has disappeared, even with the high flux of 160 kw/m^2 .

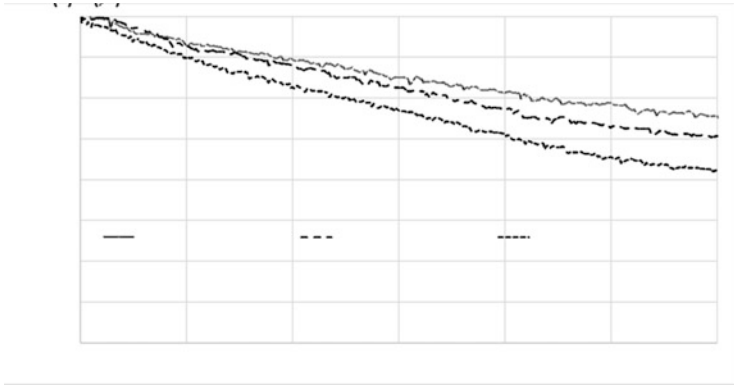


Fig. 11 C-PPS samples, relative mass loss for three thermal stresses, 120–140–160 kW/m^2

6 Conclusion

A kerosene flame test bench has been developed at laboratory scale in order to analyze and compare the fire behavior of composites, mainly for aeronautic applications. The kerosene and airflow rates can be chosen in order to produce similar thermal-stress conditions as in the standards. During the test duration, the mass loss of the sample and the temperature on the back face are measured.

With this test bench, it has been possible to analyze and compare the fire behavior of two carbon fiber-reinforced polymers, a thermosetting-based one (C/epoxy) and a thermoplastic-based one (C/PPS), with the same thickness and the same stacking sequence.

The thermosetting-based laminate is decomposed very fast and reach higher final temperature at the back face. After 15 minutes, the thermoplastic-based composite is not fully decomposed, which seems to reduce the heat transfer to the back face. Due to the reliability of the device and the repeatability of the tests, this test rig can be used to better understand and to optimize the fire behavior of thermosetting and thermoplastic-based composites used in aeronautics. In particular, it will be used in future to perform mechanical tests on composite sample when exposed to the thermal stress of the kerosene burner, as shown in Fig. 12.

Acknowledgments The work presented in this study is the result of the RIN (Réseau d'Intérêt Normand) project AEROFLAMME (Behaviour of AEROnautical Composites under FLAMme and MEchanical Loading) financed by the Normandy Region and the FEDER (European Regional Development Fund).

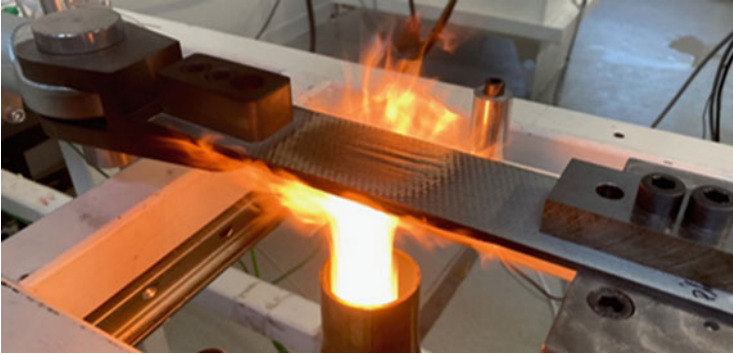


Fig. 12 Mechanical tests on a composite sample subjected to the thermal stress of the kerosene burner

References

- Blond, D., Vieille, B., Gomina, M., & Taleb, L. (2014). Correlation between physical properties, microstructure and thermo-mechanical behavior of PPS-based composites processed by stamping. *Journal of Reinforced Plastics and Composites*, 33(17), 1656–1668. <https://doi.org/10.1177/0731684414541846>
- Carlomagno, G. M., & Ianiro, A. (2014). Thermo-fluid-dynamics of submerged jets impinging at short nozzle-to-plate distance: A review. *Experimental Thermal and Fluid Science*, 58, 15–35. <https://doi.org/10.1016/j.expthermflusci.2014.06.010>
- FAR25.856: Title 14 code of Federal – test methods to determine the burnthrough resistance of thermal/acoustic insulation materials (Appendix F, Part VII), 2003.
- Gardon, R. (1953). An instrument for the direct measurement of intense thermal radiation. *Review of Scientific Instruments*, 24(5), 366–369. <https://doi.org/10.1063/1.1770712>
- Grange, N., Chetehouna, K., Gascoin, N., Coppalle, A., Reynaud, I., & Senave, S. (2018). One-dimensional pyrolysis of carbon based composite materials using FireFOAM. *Fire Safety Journal*, 97, 66–75. <https://doi.org/10.1016/j.firesaf.2018.03.002>
- ISO2685:1998(E).. Aircraft-environment test procedures for airborne equipment – resistance to fire in designated fire zones.
- Mouritz, P., & Gibson, A. G. (2006). Fire tests for composites. In *Fire properties of polymer composite materials. Solid mechanics and its applications* (Vol. 143). Springer. https://doi.org/10.1007/978-1-4020-5356-6_11
- Schuhler, E., Chaudhary, A., Vieille, B., & Coppalle, A. (2021). Fire behaviour of composite materials using kerosene burner tests at small-scales. *Fire Safety Journal*, 121.
- Serra, J., Pierré, J. E., Passieux, J. C., Périé, J. N., Christophe, B. C., & Castanié, B. (2017). Validation and modeling of aeronautical composite structures subjected to combined loadings: The VERTEX project. Part 1: Experimental setup, FE-DIC instrumentation and procedures. *Composite Structures*, 179, 224–244.
- Stoliarov, S., Crowley, S., Lyon, R. E., & Linteris, G. T. (2009). Prediction of the burning rates of non-charring polymers. *Combustion and Flame*, 156, 1068–1083. <https://doi.org/10.1016/j.combustflame.2008.11.010>
- Zhang, J., Delichatsios, M. A., Fateh, T., Suzanne, M., & Ukleja, S. (2017). Characterization of flammability and fire resistance of carbon fibre reinforced thermoset and thermoplastic composite materials. *Journal of Loss Prevention in the Process Industries*, 50, 275–282. <https://doi.org/10.1016/j.jlp.2017.10.004>

Impacts of Aircraft on Environment in Europe



Samer Al-Rabeei, Utku Kale, and Tawfik Mudarri

Contents

| | | |
|-----|--|-----|
| 1 | Introduction | 458 |
| 2 | Methodology | 458 |
| 3 | Theoretical Part | 459 |
| 3.1 | Case Studies and Findings | 459 |
| 3.2 | Facts and Figures | 459 |
| 3.3 | Pictures and Representations | 459 |
| 4 | Analysis and Comparison | 460 |
| 4.1 | Comparison Between EU and US | 460 |
| 4.2 | Comparison Between EU and Australia | 461 |
| 4.3 | Universal Indicators Followed in the USA | 461 |
| 4.4 | Universal Indicators Followed in Australia | 461 |
| 5 | Proposal Part | 461 |
| 5.1 | Findings and Observations | 461 |
| 6 | Discussions and Proposals | 463 |
| 7 | Results | 463 |
| 8 | Conclusion | 464 |
| | References | 464 |

S. Al-Rabeei (✉)

Department of Aviation Engineering Faculty of Aeronautics Technical University of Kosice,
Kosice, Slovakia

e-mail: samer.abdo@tuke.sk

U. Kale

Budapest University of Technology and Economics, Department of Aeronautics, and Naval
Architecture, Budapest, Hungary

T. Mudarri

Faculty of Mining, Ecology, Process Control and Geotechnology, Technical University
of Kosice Letná, Košice, Slovakia

1 Introduction

Aviation sector had an important role in the world over a decade due to its peculiarities. It is the fastest, safest, and most reliable transportation mode due its high mobility. This acts as one of the main catalysts for the growth of world economy. It has the ability to move people and products all over the globe quickly and safely. At present, nearly half the global population are dependent on the world's airlines for mobility. Aviation contributes to quality of life by allowing us to visit friends and relatives, to travel, to experience new places, and to explore the world.

As we look from the Economic perspectives, aviation industry is one of the fast means of transport and contributing a large share in terms of global trade, tourism, cultural exchanges, employment opportunities, and so on. By the arrival of aircrafts, the mobility of trade got much easier than before. Aviation was a revolution, and still the industry is undergoing huge innovational changes. In this chapter, we aim to find the impact made by the aircrafts across the globe regarding climate changes. Even though the share of toxic gases from aircraft are comparatively very low compared with the other factors, aviation affects the environment in many ways. People living near airports are exposed to noise from aircraft, and aircraft engines emit pollutants to the atmosphere.

In this chapter we are mainly considering the impact made by these aircrafts in the environment. This chapter describes the emission associated with commercial aviation and the health and welfare impacts that can result from those aviation emissions that degrade air quality which can in turn can cause environmental problems.

2 Methodology

The methodology part consists of details describing the purpose of the study and the related research questions and the various methods used in order to acquire the data needed for the research paper. In this part we will fix our aim to find the rate of impact made by aircrafts to the environment and the environmental hazards caused by the aircrafts apart from other factors. This chapter aims to find out the various research questions as follows:

- What is the level of impact made by the aircrafts to the environment?
- Do the regulatory policies set by different regions reduce the impact of air pollution caused by the aircrafts?

To measure the environmental impact made by aircraft, we will observe air quality, impacts on the ozone layer, contributions to climate change, waste generation, and reports general well-being made by the WHO.

To measure the environmental impact of aircraft, we will be using a history of case studies and reports. We will first focus on literal emission figures, after that on various specific case studies which include other different parameters which we can

take into consideration. Then we will look at existing solutions and regulations that various institutions have applied and measure their effectivity.

3 Theoretical Part

3.1 Case Studies and Findings

Emissions from the aviation industry are steadily increasing since the year 1990 (Abdu-Khader & Speight, 2004). Since then, they have doubled and are projected to continue rising at an even faster pace. Even reductions in average fuel burn did not help decrease total emissions. This fact illustrates the upward trend of increasingly more people using airlines as they become more accessible and crucial to many people's lives.

Apart from air pollutants emitted by aircraft travel, we also have to take into consideration the noise pollution created by the aircrafts. There are not yet any universal international regulations for aircraft emissions (European Union, 2022). They are being created by specialized UN bodies which have faced criticism for being too slow which in turn has caused a slower adaptation to the necessary regulations all over the world with some countries pushing their own in the meantime creating a chain of chaos in the atmosphere causing climate changes and other destructive environmental calamities.

Until recently, airlines and water transport were excluded from the Paris agreement, Kyoto Protocol, and similar efforts (Čabala, 2016). This has led to a worldwide delay in deciding and applying universal standards. International standards were first proposed in 2017 and are projected to come into full effect by 2028 (EDF, 2021).

3.2 Facts and Figures

In total the aviation industry contributes about 2% to the total amount of all CO₂ emissions produced across the globe (EIA, 2022).

It has a share of 12% in CO₂ emissions from when we are taking in concern regarding the total of emission rate out of all transport mediums (EIA, 2021).

3.3 Pictures and Representations

The third European Aviation Environmental Report provides an objective overview of the significant developments in response to the environmental performance of the aviation sector. European citizens are increasingly aware of the impact of aviation

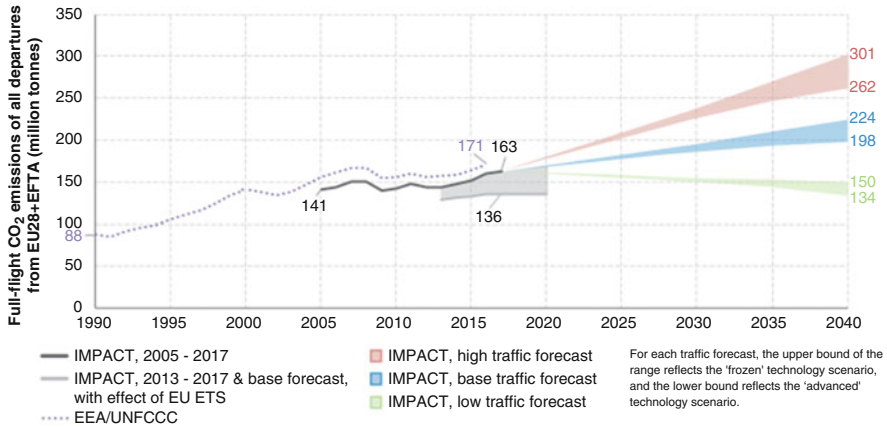


Fig. 1 Emissions in the EU over time (EU aviation report)

activities on their quality of life, and businesses must build their strategies and brand around sustainability to reduce their environmental impact and attract a growing market share. Collaboration between public and private stakeholders is essential to deliver the European Green Deal objectives (Fig. 1).

4 Analysis and Comparison

4.1 Comparison Between EU and US

Comparing emission data from the USA and EU, the USA has 10% more emissions (180MT vs 200MT). The USA also has the biggest aviation industry. Since US aviation policies are more favorable to the aviation parameters, there are no particular set of standards as we are comparing with the EU.

The EU has been working on limiting emissions by implementing the emissions trading system (ETS) (European Aviation Safety Agency, 2014). Each airline operator receives a set amount of free, tradeable emission allowances in addition to which they can buy more at an auction. This allows airlines to operate at maximum capacity without negatively affecting the environment too much and making compromises possible in special cases.

The USA has stated in 2019 that it has been implementing regulations for aircrafts too, but at a slower pace (FAA, 1970–1998).

4.2 Comparison Between EU and Australia

Compared to the EU, Australia has a relatively small aviation market which emits about 24MT (vs 180MT EU).

Similar to the EU, Australia has been making efforts for regulation since the year 2012 with the release of their Action Plan. They are also partaking in the Carbon Offsetting and Reduction Scheme for International Aviation (CORSIA) proposed by the International Civil Aviation Organization (ICAO) similarly to the EU. The start of the phased implementation is projected to be in 2021 (Hovanec et al., 2018).

There also have been efforts to make airports carbon-neutral which has already seen success in some places.

4.3 Universal Indicators Followed in the USA

Until recently, the US government didn't make any steps in regulating aircraft emissions. Until mid-2020, the market was completely unregulated. Because of that, airlines have seen an increase in fuel consumption paired with diminishing increases in fuel efficiency. It took several years and lawsuits for the US government to finally start taking action.

4.4 Universal Indicators Followed in Australia

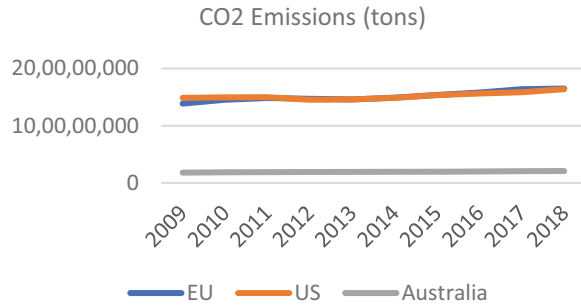
The Australian government has been implementing measures since the introduction of the 2012 Action Plan. They are also partaking in the CORSIA plan with planned implementation starting in 2021. They plan to gradually improve all parts of the aviation industry including air traffic management and airports (IAEA, 1999). They already have deployed some measures such as renewing their fleet to use the latest advances in technologies or investing into research and market development of sustainable biofuels.

5 Proposal Part

5.1 Findings and Observations

From our research and analysis, we have come to a few conclusions and projections for the future. Totally aircraft contribute only very small percentage to the total amount of human-induced emissions, 2% from recent observations. It has a share of 12% in emissions from all transport (Fig. 2).

Fig. 2 Comparison on the basis of CO₂ emissions (own elaboration)



Aircraft traffic is projected to keep increasing in volume, following the trend of over a 40% increase compared to ~2005 levels. The trend also keeps accelerating, projected to an additional 60% or more increase in traffic and emissions going into the year 2032.

Up until recently, there was little work done to implement an international standard. Many countries, including the USA, did not have any regulations regarding aircraft emissions up until now. It is crucial that countries collaborate and make an effort to unify the industry and its regulations for healthy growth.

The CORSIA scheme proposed by the ICAO is set to begin its gradual implementation in the year 2021 following complete implementation by the year 2028. Their proposals, which aims to reduce emissions and other environmental hazards from aircraft, is deemed dated by some. That is mainly because today's aircrafts are already meeting their limits which they proposed a few years by default. Their main aim is to keep aircraft emissions at 2020 levels while still allowing for growth of the industry. The main areas of optimization are novel fuels, modern aircraft, carbon-neutral airports, and carbon offset schemes (ICAO, 2019).

Currently more than 70 countries are participating including Australia, all EU member countries and recently the USA.

The initiative to increase fuel efficiency won't be enough to offset the continuously accelerating grow of the industry. Alternative methods such as biofuels from sustainable sources or significant advances in technologies are needed to make the industry carbon-neutral (Infrastructure.gov.au).

The EU has been probably the most efficient in controlling emissions and other environmental factors. It is already using its ETS to regulate emissions. It's also closely working together with international organizations to help create a plan.

Australia is also already efficient in regulating its aircraft emissions by starting implementation of the system back in the year 2012. They also have multiple voluntary running initiatives to make their airports carbon-neutral and are actively investing into research and development of alternative biofuels together with the facilities and infrastructure needed for it (International Atomic Agency, 2000).

The USA has not up until recently, despite having the biggest aviation market, been working together with the UN on its regulations plan for aircraft and shipping

markets. That resulted in an uncontrolled market for a considerable amount of time which will take some effort to clean up.

6 Discussions and Proposals

Despite long periods of no action, in the recent year’s efforts to regulate the aircraft industry have been put forward with some countries taking the lead and some falling behind.

Currently there are no universal standards and also no global ETS. Standards are being worked on and their implementation already started in some countries. A global ETS is not yet implemented (Jakubiak, 2015).

The focus currently is on the implementation of the existing CORSIA program with many (over 90% of the market) countries participating. Some countries which for example have a small aviation industry can be excluded from this program.

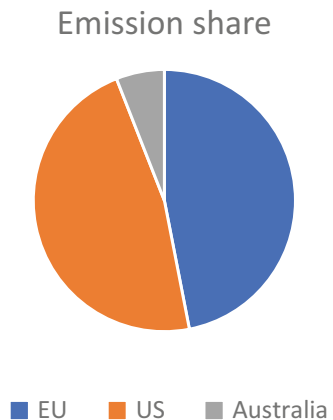
Another area of optimization is a global ETS. This system is already applied in some countries and regions. At the moment the biggest market is the EU.

To reduce other negative factors (such as noise pollution), regulations should be developed and applied. There are also no regulations except general noise regulations. These are likely not suited for a situation like an airport, where the noise is very frequent.

7 Results

The results from this research indicate that a worldwide consensus is being formed and countries are gradually implementing new regulations and innovating their technologies (Fig. 3).

Fig. 3 Graphic representation of the emission shares of EU, USA, and Australia (own elaboration)



Recent developments and discoveries in engine and biofuel technology coupled together with a global ETS alongside improvements in places such as airports, e.g., production facilities have shown that the targets set by the CORSIA project are achievable and being worked on.

Other factors (such as noise) are not being effectively regulated (except general regulations) in most places yet but are also being taken into account in the recent years with research showing them being significant factors in general well-being and therefore health.

8 Conclusion

Our conclusion is that the authorities should focus on the implementation of global systems for ease of tracking and trading emissions. After that all focus should be shifted to implementing and enforcing the so-called regulations using data from the global systems to reach the projected milestones.

References

- Abdu-Khader, M. M., & Speight, J. G. (2004). The concepts of energy, environment, and cost for process design. *International Journal of Green Energy*, 1, 137–151. (for Journal) <https://www.aircraftperformance-software/case-studies/by-solution/case-study-environmental-emissions>
- An official website of the European Union. (2022). Mobility And Transport. Aircraft noise. [Online] https://ec.europa.eu/transport/modes/air/environment/aircraft_noise_en.
- Čabala, J. (2016). Integrácia BIM a RFID technológie pri riadení stavebnej výroby. In *Oceňovanie a riadenie stavebných projektov 2016 : zborník vedeckých prác* (pp. 25–29). EuroScientia. ISBN 978-90-822990-2-1.
- EDF. (2021). Reducing aviation's climate impact. [Online] <https://www.edf.org/climate/aviation>
- EIA. (2022). Energy and the environment explained. [Online] <https://www.eia.gov/energyexplained/energy-and-the-environment/where-greenhouse-gases-come-from.php>
- EIA. (2021). Environment. Access on the Internet. [Online] <https://www.eia.gov/environment/emissions/state/>
- European Aviation Safety Agency, Part-145. Acceptable means of compliance and guidance material. [online]. 17. 12. 2014, Available at: <https://www.easa.europa.eu/sites/default/files/dfu/Annex%20II%20to%20Decision%202015-029-R%20-%20%28AMC-GM%20Part-145%29.pdf>
- FAA. (1970–1998). Study of the factor affective the sensitivity of liquid penetrant inspection. National Technical Information Service (NTIS), Springfield, Virginia 22161.
- Hovanec, M., et al. (2018). Non destructive testing in the case of aircraft wheel overhaul. In *Transport means 2018. Part III = Proceedings of 22nd international scientific conference* (pp. 1467–1472). Kaunas University of technology. [print, online]. - ISSN 1822-296X. https://www.airservicesaustralia.com/wp-content/uploads/Environment_Strategy_2011-16.pdf. 2018

- IAEA. (1999). Non-destructive testing: A guidebook for industrial management and quality control personnel. [Online]. International Atomic Energy Agency (IEIA), Vienna, Austria, January 1999. Available at: TRAINING COURSE SERIES No. 9. Non-destructive Testing: A Guidebook for Industrial Management and Quality Control Personnel. INTERNATIONAL ATOMIC ENERGY AGENCY, VIENNA, 1999. [Online] http://www.iaea.org/inis/collection/NCLCollectionStore/_Public/31/005/31005449.pdf
- ICAO. (2019). Secretariat. Introduction to LAQ. [Online] https://www.icao.int/environmental-protection/Documents/EnvironmentalReports/2019/ENVReport2019_pg97-99.pdf
- Infrastructure.gov.au. Aviation emissions. [Online] <https://www.infrastructure.gov.au/aviation/environmental/emissions/index.aspx>
- International Atomic Agency: Liquid Penetrant and Magnetic Particles Testing at Level (2000) [online]. International Atomic Energy Agency (IEIA), Wagramer Strasse 5, P.O. Box 100 A-1400 Vienna, Austria, February 2000. [Cited December 15. 2017], Available at: <https://www-pub.iaea.org/MTCD/publications/PDF/TCS-11.pdf> [Online]. [Cited February. 18. 2018], Available at: <https://www.ndeed.org/EducationResources/CommunityCollege/PenetrantTest/MethodsTech/selection.htm>
- Jakubiak, M. (2015). Environmental_impact_of_air_transport_-_case_study_of_Krakow_Airport. *LOGISTYKA*, 2, 276–283.

Hybrid Nanoparticle-Reinforced Polyurethane Composites Mechanical Behavior



Safa Ak and Mürsel Ekrem

Contents

| | | |
|---|-----------------------------|-----|
| 1 | Introduction | 467 |
| 2 | Method | 468 |
| 3 | Result and Discussion | 471 |
| 4 | Conclusion | 473 |
| | References | 473 |

Nomenclature

| | |
|--------|--|
| ASTM | American society for testing and materials |
| BNNP | Boron nitride nano palates |
| Co | Carbon nanotube |
| CNT | Carbon nanotube |
| H-BNNP | Hexagonal boron nitride nanoplate |
| RH | Relative humidity |
| PU | Polyurethane |

1 Introduction

Polyurethane is one of the most preferred adhesive types in glass, metal, and wood applications due to its high adhesion properties, resistance to moisture, high temperature, frost, and long-term durability. Adhesive bonding applications are cheap,

S. Ak (✉) · M. Ekrem

Necmettin Erbakan University, Faculty of Engineering, Mechanical Engineering Department, Konya, Turkiye

e-mail: mekrem@erbakan.edu.tr

fast, and durable when compared with traditional bonding techniques. In addition, adhesive joints enable lighter designs and provide energy efficiency. Using thermoset PU in bonding joints provides flexibility for manufactures to overcome design challenges such as impact, fatigue, and safety (Loureiro et al., 2010; Scetta et al., 2021). For these reasons, intensive studies are carried out on Pu adhesives in the academic field and industry. Improving the mechanical properties of PU will increase its usage areas (Szatkowski et al., 2017; Gao et al., 2011).

Nanoparticle addition into PU resin is one of the effective methods to improve its' performance. Nanoparticles' high-elastic modules and high surface volume ratios can provide load transfer within the polymer structure. Therefore, although they added a small percentage in resin, they significantly affect the polymer resin mechanical properties. For example, 1% CNT addition in nylon-6 increased the materials' elasticity modulus, strength, and hardness value by 115%, 120%, and 67%, respectively (Zhang et al., 2004). Most polymers have shown low strength because of the slippage mechanism in their polymer chain (Senyurt et al., 2021; Ekrem, 2019b). Appropriate ratio nanoparticle adding in polymers could lock the polymer chain slippery mechanism and provide desired mechanical properties (Ekrem, 2019a; Bahramnia et al., 2021). CNT's, which have two types as multi-walled and single-walled, are cylindrical tubes with varying diameters from angstrom level to the nanometer level, formed by each carbon atoms hexagonal bonding. They have a high aspect ratio. Therefore, they make covalent bonding with polymer chains and reduce the needed nanoparticle ratio to improve mechanical properties (Chen et al., 2012). Homogeneously distributed CNT into PU resin improves mechanical properties, increases thermal stabilization and thermal conductivity and ensures better adhesion of PU to bonding surfaces (Shokry et al., 2015). H-BNNPs are formed by layered overlapping of hexagonal structures consisting of boron and nitrogen atoms. Due to the weak Van der Waals bonds between the BNNPS layers, the layers slide easily over each other and show ductile properties. Although BNNPs are resistant to temperature and have high thermal conductivity, their electrical conductivity is very low (Rosas et al., 2005). 0.20% BNNP and 0.20% GNP by mass addition into the thermoplastic PU increased the thermal conductivity of the composite films; in addition, it has also increased strength and resistance to bending fatigue (Soong & Chiu, 2021).

2 Method

In this study, KLB 75 solvent-free thermoset PU was used, which was produced by DURATEC company. KLB 75 has superior temperature and impact resistance, and also it can cure at room temperature (Table 1). Isocyanate is preferred as the hardening compound. MWCNTs obtained from the NANOCLAY company were produced by the vapor deposition method. MWCNT diameter is between 5 and 50 nm and the length between 10 and 30 μm . The h-BNNP supplied from Bortek has a density of 2.27 g/cm^3 , the mean thickness is 100 nm, and the purity is above

Table 1 T-PU and its hardener isocyanate mixture mechanical properties

| Properties | Unit | 80 PU+ 20 isocyanate |
|-------------------------------------|-------------------|----------------------|
| Density | g/cm ³ | 1.35 ± 0.10 |
| Viscosity | mPas | 2.100 ± 300 |
| Maximum lifespan (23 °C, 100 ml) | Minute | 65 ± 15 |
| Open waiting time (23 °C, %55 RH) | Minute | 90 ± 15 |
| Solidification time (23 °C, %55 RH) | Hour | 24 |
| Full hardening (23 °C, %55 RH) | Week | 1 |

99%. Its thermal durability temperature is 1000 °C in an open atmosphere and 1400 °C in a vacuum environment.

Polyurethane and isocyanate, which used as curing agent weight ratio, were determined as 80/20. PU viscosity was reduced by adding acetone 1/10 by mass of PU. Then 0.25% MWCNT, 0.5% h-BNNP, and 0.25% CNT + 0.5% BNNP were added into PU-acetone mix. Van der Waals interaction between particles is the biggest obstacle in the formation of the homogeneous mixture. For this reason, the mixing PU viscosity was reduced by adding acetone 1/10 by mass of PU. Then 0.25% MWCNT, 0.5% h-BNNP, and 0.25% CNT + 0.5% BNNP were added into PU-acetone mix. The process was done with an ultrasonic mixer in two stages of 10 minutes. PU and nanoparticle damage resulting from overheating was prevented by two-stage mixing.

Nanoparticle-reinforced PU-acetone mixture was kept in a vacuum oven under 0.02 MPa pressure for 24 hours at 60 °C degree. In this way, it was ensured that the acetone in the mixture evaporated, and air bubbles that would adversely affect the test result were removed. Nanoparticle-reinforced PU was taken out in the vacuum oven, and then the hardener was added and mixed mechanically for 15 minutes. PU, nanoparticles, and hardener mixture were kept in a vacuum oven under 0.02 MPa pressure for 15 minutes to remove air bubbles formed due to mechanical mixing and then poured into molds and left to cure at room temperature for 24 hours. After 24 hours, samples were removed from the mold. Then they were kept at room temperature for 2 weeks to complete curing. After complete curing, the tensile test and shore hardness test were applied to determine the mechanical properties of samples. All the steps involved in producing are shown in Fig. 1.

Mold has 165-mm-length, 155-mm-wide, 5-mm-thickness bottom and top plates. Plates connected with bolt and nut are used to produce ASTM-D 638-10 standards tensile specimens. A detailed view of the mold and the molding method is illustrated in Fig. 2.

Each mold allows producing five test samples. In the study, 15 samples were produced, including five pieces neat PU, five pieces Pu 0.25% CNT, and five pieces PU + 0.25% MWCNT +0.5% h-BNNP added samples. During molding, wax was applied to the mold surfaces. It prevents samples from sticking to the mold and enables the specimen to leave the mold without any deformation. After 24 hours from the molding process, specimens were removed from the mold, and they have waited at room temperature for 2 weeks to the ultimate cure. A tensile test was

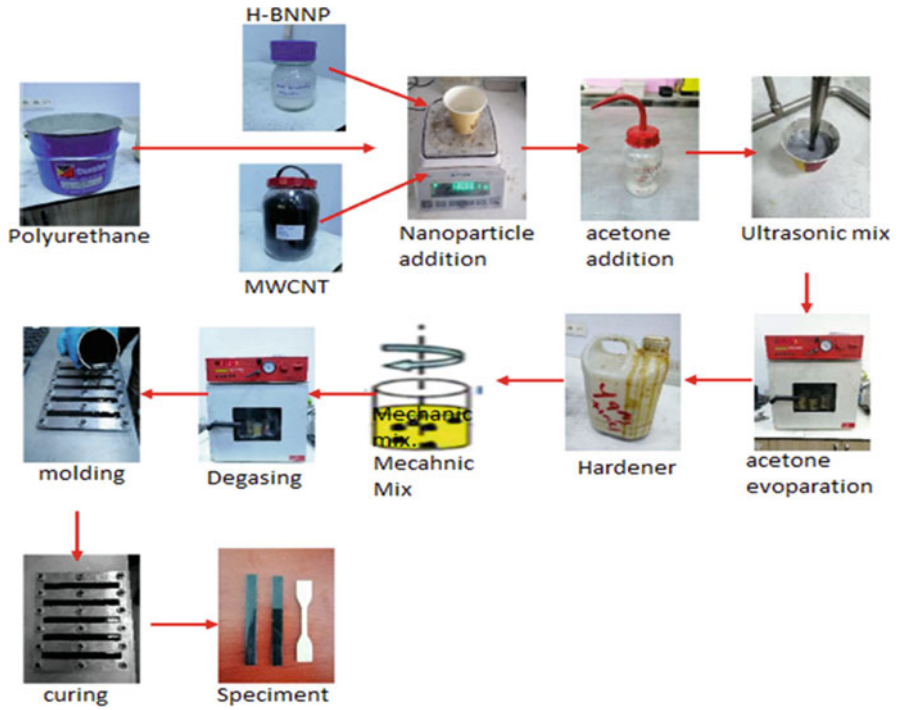
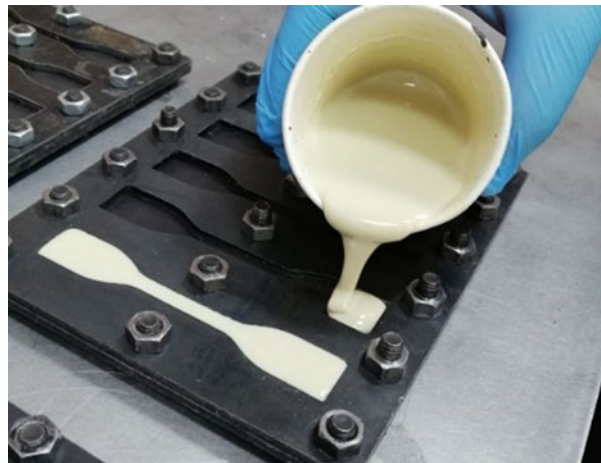


Fig. 1 Preparing of Nanoparticles doped PU samples

Fig. 2 Neat sample molding process



conducted with 5-mm/min constant jaw speed at room temperature. The test was carried out on the Shimadzu AGS-X tensile testing device in the Mechanical Engineering Laboratory of Necmettin Erbakan University. After the tensile test,

the Shore D hardness test was applied for all samples according to ASTM-D2240 standards.

3 Result and Discussion

The tensile test was applied first to raw PU samples to use them as a reference in evaluating the particle added samples test result. PU specimens' maximum tensile strength is 20.80 mPa, and the strain value is 15%. All samples' stress-strain graphs are shown in Fig. 3.

When neat PU samples were examined with reference, h-BNNPs addition into the polymer caused the maximum fracture strength to decrease by 29% from 20.8 to 14.7 MPa. Because the layered structure of the BNNP layers is sliding easily, this effect increased the ductility of the samples by 110%. Among all samples, the highest tensile strength was observed in PU + 0.25% CNT + %0.5 BNNNP (hybrid) samples. CNTs' make a bridging mechanism in polymer bonds. Due to this bridging mechanism, the breaking strength of the samples increased by 15% compared with neat PU samples. Moreover, compared to the BNNP-reinforced samples, hybrid composites exhibited 66% higher tensile strength. However, the addition of MWCNT into the PU thermoset drastically reduced the ductility properties of the samples.

Nanoparticle addition magnificently affected the thermoset PU elasticity module (Table 2). The reinforcement of h-BNNPs led to a significant reduction in the elastic modules. On the other hand, CNT incorporations with h-BNNP in PU increased elastic

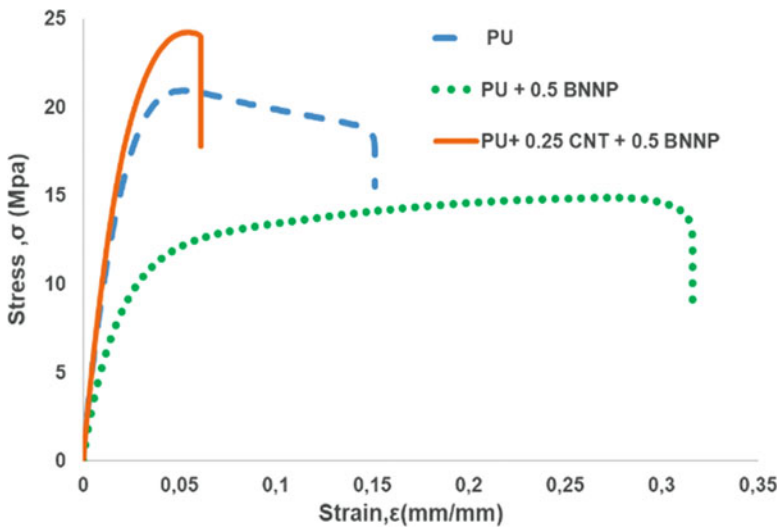
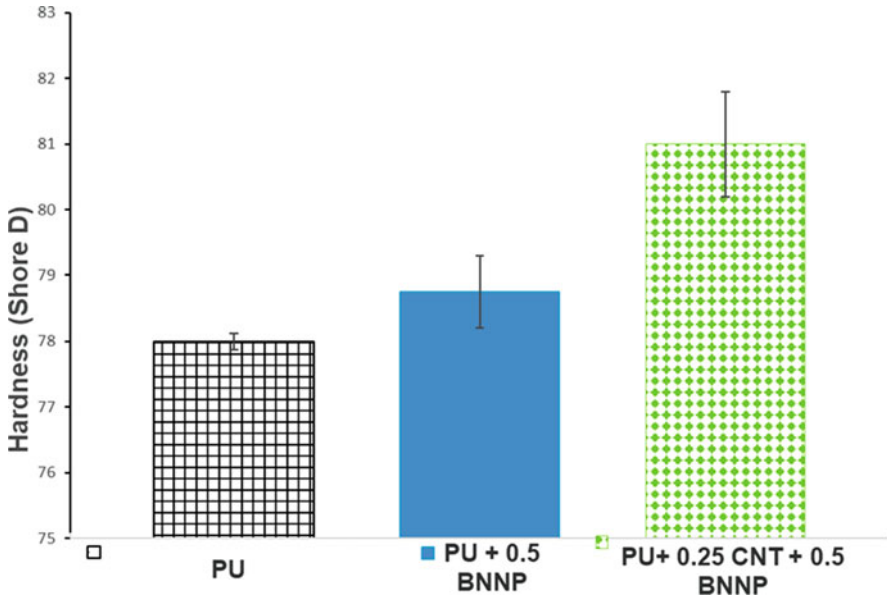


Fig. 3 PU, PU + 0.5 BNNP, and PU + 0.25 CNT + 0.5 BNNP stress-strain graph

Table 2 Hybrid nanoparticles reinforced PU composites' mechanical properties

| Samples | Max. load | Elasticity module (GPa) | Toughness (kJ/m ³) |
|------------------------|-----------|-------------------------|--------------------------------|
| PU | 565.18 | 0.908 | 1596 |
| PU+ 0.5 BNNP | 374.86 | 0.204 | 2781 |
| PU + 0.5 BNNP+0.25 CNT | 639.62 | 1.002 | 457 |

**Fig. 4** Samples hardness result

modules by 10%, from 0.908 to 1.002 GPa. This result proves that how effected small amount of MWCNT on mechanical properties. However, high elasticity, which is desired property for adhesive bonding, also brought negative brittle properties. Although h-BNNP addition reduces brittles, it also drastically reduces specimens' rigidity and tensile stress. However, CNT and h-BNNP together reduced elasticity and increased rigidity. And CNTs' stiff properties explain elasticity reduction.

Hardness test results according to ASTM-D 2240 shore D are shown in Fig. 4. CNT+ BNNP-reinforced samples' hardness test exhibited that CNTs' high-elastic modules and stiff structure increased the hardness of the sample. This result supports the highest tensile stress measured in hybrid samples.

However, in contrast to the tensile test, compared with the neat PU, adding h-BNNP increased the hardness in a small ratio. This situation indicates that the sliding mechanism between h-BNNP layers formed during the tensile test is not occurring in the hardness test or is not effective as in the tensile test.

4 Conclusion

Polymer adhesive bonding has a wide variety of using areas as the defense industry, maritime, automobile, and space. So, improving their mechanical properties is piercingly important. In this study, we aimed to enhance thermoset PU ductility and tensile stress at the same time. For this intention, we added h-BNNP and CNT + h-BNNP in PU resin and compared the result with the neat PU by an aspect of strength and elasticity.

Tensile test results exhibited that BNNP adding in the thermoset PU severely reduced the tensile stress but increased its ductility. The weak Van der Waals bond at HBNNPs layers explains this result. These layers are easily sliding over each other and reduce maximum strength. Synergistic interaction of BNNP and MWCNT was examined by adding these two nanoparticles together in PU resin. Although MWCNTs increased polymer resin tensile stress as expected, BNNPs had not increased ductility when added together with MWCNT. In summary, together addition of these two particles increased the tensile stress of PU, but ductility decreased despite the presence of BNNP.

Considering the results, MWCNT increases the tensile strength and decreases the toughness of thermoset PU. However, to fully understand the synergistic effect of nanoparticles in PU, new studies should be done by adding only MWCNT and HBNNP + MWCNT particles at different rates.

References

- Bahramnia, H., Semnani, H. M., Habibolahzadeh, A., & Abdoos, H. (2021). Epoxy/polyurethane hybrid nanocomposite coatings reinforced with MWCNTs and SiO₂ nanoparticles: Processing, mechanical properties and wear behavior. *Surface and Coatings Technology*, *415*, 127121.
- Chen, S. B., Wang, Q. H., & Wang, T. M. (2012). Damping, thermal, and mechanical properties of carbon nanotubes modified castor oil-based polyurethane/epoxy interpenetrating polymer network composites. *Materials & Design*, *38*, 47–52.
- Ekrem, M. (2019a). Hexagonal boron nitride nanoplates-nano Ag / epoxy composites: Production, mechanical and thermal properties. *El-Cezeri Journal of Science and Engineering*, *6*(3), 585–593.
- Ekrem, M. (2019b). Shear strength of boron nitride nanoplatelets and nano Ag reinforced structural adhesives. *Journal of Bor*, *4*(3), 128–134.
- Gao, X., Zhu, Y., Zhao, X., Wang, Z., An, D., Ma, Y., Guan, S., Du, Y., & Zhou, B. (2011). Synthesis and characterization of polyurethane/SiO₂ nanocomposites. *Applied Surface Science*, *257*(10), 4719–4724.
- Loureiro, A., Da Silva, L. F., Sato, C., & Figueiredo, M. (2010). Comparison of the mechanical behaviour between stiff and flexible adhesive joints for the automotive industry. *The Journal of Adhesion*, *86*(7), 765–787.
- Rosas, G., Sistos, J., Ascencio, J., Medina, A., & Perez, R. (2005). Multiple-walled BN nanotubes obtained with a mechanical alloying technique. *Applied Physics A*, *80*(2), 377–380.
- Scetta, G., Ju, J., Selles, N., Heuillet, P., Ciccotti, M., & Creton, C. (2021). Strain induced strengthening of soft thermoplastic polyurethanes under cyclic deformation. *Journal of Polymer Science*, *59*(8), 685–696.

- Senyurt, M. A., Ekrem, M., Duzcukoglu, H., & Avci, A. (2021). Effect of composite to aluminum single lap joints reinforced with graphene doped nylon 6.6 nanofibers. *Proceedings of the Institution of Mechanical Engineers Part E-Journal of Process Mechanical Engineering*, 235(5), 1269–1278.
- Shokry, S., El Morsi, A., Sabaa, M., Mohamed, R., & El Sorogy, H. (2015). Synthesis and characterization of polyurethane based on hydroxyl terminated polybutadiene and reinforced by carbon nanotubes. *Egyptian Journal of Petroleum*, 24(2), 145–154.
- Soong, Y.-C., & Chiu, C.-W. (2021). Multilayered graphene/boron nitride/thermoplastic polyurethane composite films with high thermal conductivity, stretchability, and washability for adjustable-cooling smart clothes. *Journal of Colloid and Interface Science*, 599, 611–619.
- Szatkowski, P., Pielichowska, K., & Blazewicz, S. (2017). Mechanical and thermal properties of carbon-nanotube-reinforced self-healing polyurethanes. *Journal of Materials Science*, 52(20), 12221–12234.
- Zhang, W. D., Shen, L., Phang, I. Y., & Liu, T. (2004). Carbon nanotubes reinforced nylon-6 composite prepared by simple melt-compounding. *Macromolecules*, 37(2), 256–259.

Design of Experiments for Wind Tunnel Testing of 53° Sweep Lambda UCAV Configuration



Bilal Haider, Shuhaimi Mansor, Shabudin Mat, Wan Zaidi Wan Omar, and Nazri Nasir

Contents

| | | |
|-----|-------------------------------------|-----|
| 1 | Introduction | 476 |
| 2 | Wind Tunnel Facility | 476 |
| 2.1 | JR3 External Balance | 477 |
| 2.2 | Surface Flow Visualization | 479 |
| 3 | Dynamic Oscillatory Rig | 480 |
| 3.1 | Accuracy and Data Acquisition | 483 |
| 4 | Conclusion | 484 |
| | References | 485 |

Nomenclature

| | |
|-----------------|-------------------------------------|
| C_{n_r} | Yaw damping derivative, rad-1 |
| C_{n_β} | Yaw stiffness, rad-1 |
| $t_{1/2}$ | Time to half amplitude, second |
| fMO | W/T model frequency, Hz |
| I _{zz} | Moment of inertia, kgm ² |
| K _m | Reduced frequency |
| K _s | Spring stiffness, N/m |
| UCAV | Unmanned combat air vehicle |

B. Haider (✉) · S. Mansor · S. Mat · W. Z. W. Omar · N. Nasir
School of Mechanical Engineering, Faculty of Engineering, Universiti Teknologi Malaysia,
Skudai, Johor, Malaysia
e-mail: hbilal1983@graduate.utm.my; shuhaimi@utm.my; shabudin@utm.my;
wanzaidi@utm.my; mnazrimnasir@utm.my

1 Introduction

Extreme flight condition such as high-pitch angle, α , and large angular rates are encountered during the flight of the modern UCAV wing configurations. Unsteady and highly nonlinear aerodynamics which significantly affects the stability of the aircraft is associated with the low-sweep lambda wing UCAV configurations. Low-sweep lambda wing UCAV configuration aerodynamic studies are of prime interest due to the complex vortex flow topology over the wing surface (Rockwell, 1993). The investigation and the estimation of the flow topology and stability of the modern UCAV configuration for medium- to higher-pitch angle, α persists vital to superior maneuverability and performance (Schuette et al., 2018). The aerodynamic studies can be carried out either by wind tunnel experiments or by the CFD simulation.

Different countries have established their static and dynamic wind tunnel test methods and associated experimental setups to study the aerodynamics features of the aircraft in unsteady flow fields to support the aircraft designers with reliable steady-state and dynamic test data. The experimental setup data can be used for the flight characteristics such as stability analysis and the verification and validation of the CFD simulations (Dadkhah et al., 2019).

In this work, we will discuss in detail the design of the experiments to be carried out for the low-speed wind tunnel testing of the 53° sweep lambda wing UCAV configuration. The main interests of this research are to design and develop the experimental setup to investigate the steady-state aerodynamic coefficients and the flow visualization and to design and develop a dynamic facility that will be capable to investigate the transient response of the UCAV configuration.

2 Wind Tunnel Facility

The Universiti Teknologi Malaysia Low-Speed Wind Tunnel (UTM-LST) is a closed-circuit low-speed wind tunnel facility as shown in Fig. 1. UTM-LST has a test section which is rectangular with the volume 16.5 m^3 (5.5 meters (length) \times 1.5 meters (height) \times 2.0 meters (wide)). The maximum velocity managed in the UTM-LST can be up to 82 meters per second. Before the test section as shown in Fig. 1, there is a settling chamber where the flow angularity and the turbulence level in the airflow are reduced. In the settling chamber, honeycomb and three screens are installed which acts as the turbulence filter and the flow straightener (Noor & Mansor, 2013). The flow quality of the wind tunnel is presented in Table 1.

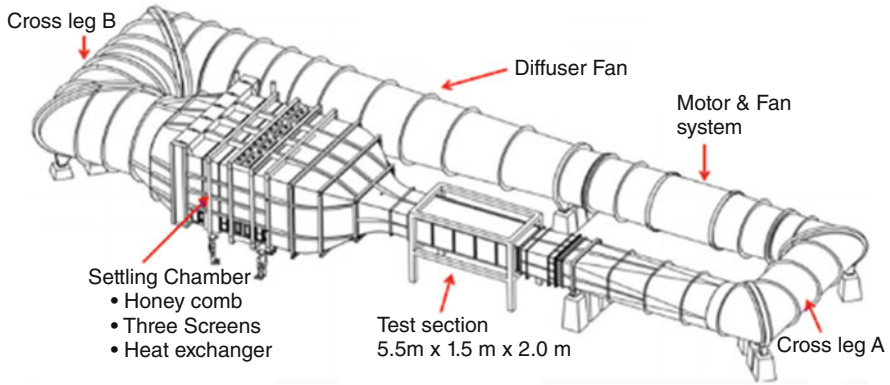


Fig. 1 Flow diagram of steady-state testing

Table 1 Test section flow quality (Elfstrom, 2007)

| Parameters | Measured values |
|---------------------------------|-----------------|
| Velocity spatial uniformity | 0.13% |
| Flow angularity, pitch | 0.13° |
| Temperature spatial uniformity | 0.16 °C |
| Flow angularity, yaw | 0.13° |
| Flow angle gradient, pitch | 0.003°/m |
| Axial wind speed gradient | 0.0003°/m |
| Flow angle gradient, yaw | 0.070°/m |
| Temperature temporal uniformity | 0.08 °C |
| Velocity temporal uniformity | 0.046% |

2.1 JR3 External Balance

The steady-state aerodynamic characteristics, lift, drag, side force, pitching moment, and yaw moment can be measured by the JR3 external balance system. The MULDICON wing model configuration is fixed on the sturt support, and the sturt support is attached to the JR3 balance sensor with the help of the flange as shown in Fig. 2.

Figure 3 shows the JR3 external balance sensor that will be used in the wind tunnel testing for the measurement of the steady-state aerodynamic characteristics (TAAH & Mat, 2019). The JR3 external balance is a portable three-dimensional six-component force and moment balance system which can measure three forces, i.e., lift, drag, and side force and three moments pitch, yaw, and rolling moments. The JR3 external balance is capable to log the aerodynamic loads at various wind direction by rotation of the wind tunnel (W/T) model via the turntable that is placed underneath the wind tunnel floor as shown in Fig. 2 for various yaw angles and by pitching of the W/T model via pitching device which is placed inside the W/T model. The accuracy of the balance is within 0.04% standard deviation. The balance load range as specified by the manufacturer is summarized in Table 2.

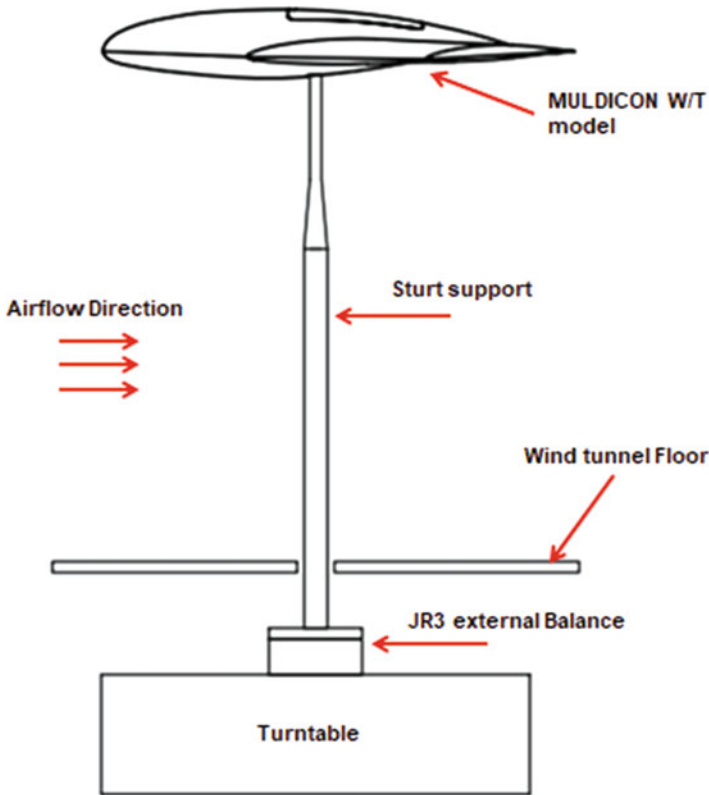
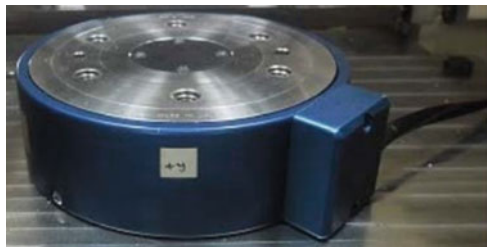


Fig. 2 Wind tunnel components

Fig. 3 JR3 external balance



All forces and moments are measured in the body axis. The loads are measured by load cells, and the calibration matrix converts them into three forces (lift, drag, and side force) and three moments (pitch, yaw, and roll). The software saves the data as both force and moments. The balance is operated using a dedicated program that also allows the user to choose a suitable sampling rate and data-averaging time. The flowchart for data reduction to the steady-state aerodynamic coefficient is presented in Fig. 4.

Table 2 Maximum allowable loads limit

| Component | Load range |
|------------------------|--------------|
| Drag, F_x | ± 1000 N |
| Side force, F_y | ± 1000 N |
| Lift, F_z | ± 2000 N |
| Rolling moment, M_x | ± 160 nm |
| Pitching moment, M_y | ± 320 nm |
| Yawing moment, M_z | ± 160 nm |

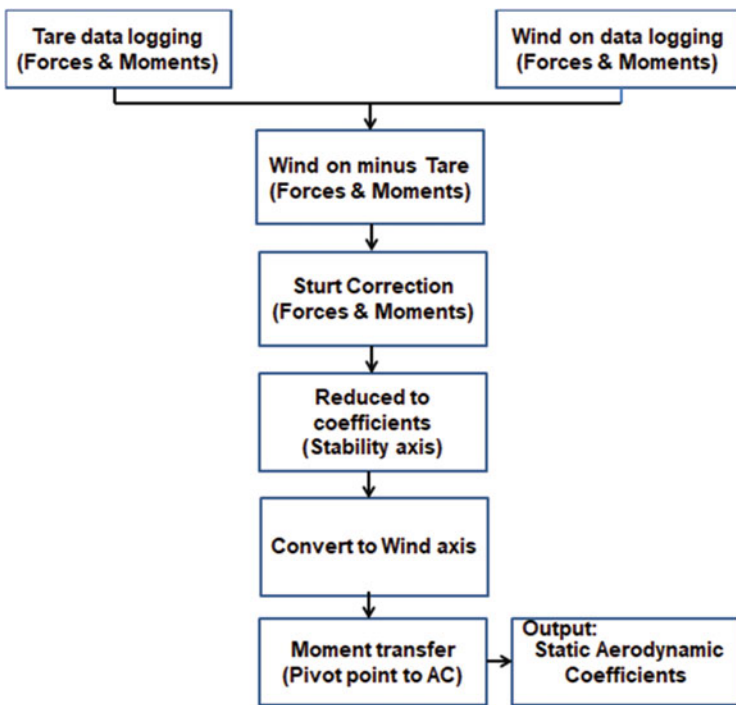


Fig. 4 Flow chart for steady-state data reduction

2.2 Surface Flow Visualization

Surface flow visualization using oil mixture will be used to study the flow pattern on the wing surface. Flow visualization for the W/T model will give a general view of flow topology. Surface flow visualization may observe the separation lines, location of boundary layer transition, characteristic unsteadiness, and the extent of separation

Fig. 5 Oil mixture application on W/T model



zones. The flow visualization data will help to correlate the vortex development with aerodynamic derivatives.

A mixture of lubricating oil 10 W-30 and titanium dioxide (TiO_2) will be used for the surface flow visualization. Oil mixture will be applied to the W/T model as shown in Fig. 5. Wind speed will create the flow pattern on the W/T model surface; hence, the surface flow topology can be visualized. Surface flow visualization will provide useful information on the apex, inner, and tip vortices formation. The flow visualization data will help to correlate the vortex development with aerodynamic derivatives. The qualitative data from the surface flow visualization will be very useful for the CFD simulation validation of the flow topology.

3 Dynamic Oscillatory Rig

To highlight the unsteady response of the tailless low-sweep lambda wing configuration experimentally at various pitch angles, α , a single degree of freedom torsional system has been developed as shown in Fig. 6. The dynamic oscillatory rig will be capable to find out the transient aerodynamic stability derivatives (C_{n_p} and C_{n_r}). The dynamic oscillatory rig facility approach to finding out the dynamic stability derivatives is very cost-effective and efficient (Rajamurthy, 1997). The

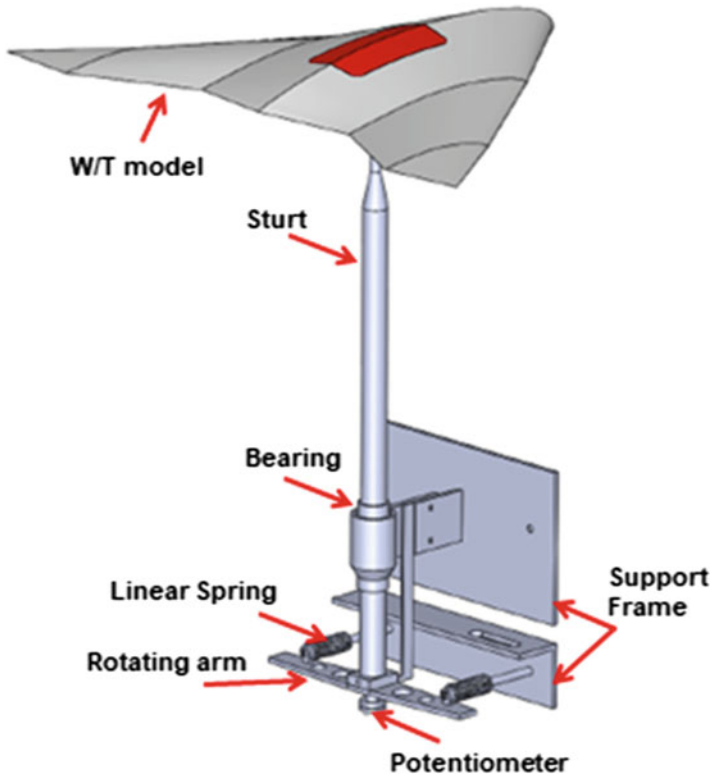


Fig. 6 Dynamic oscillatory rig facility animation

Table 3 Steady-state versus dynamic W/T testing

| Parameters | Static W/T testing | Dynamic W/T testing |
|-----------------------|--|---|
| Model motion | Model is stationary | One degree of freedom oscillation |
| Stability derivatives | Steady-state $C_{n\beta}$ and C_{nr} | Estimates both steady-state and dynamic |
| Data logging | Steady flow measurement only | Data logging regardless of flow steadiness |
| Derivatives | Derivatives are a gradient of the yaw angle, β | Derivatives are function of frequency and amplitude |
| Reynolds number | Dependent | Independent |

advantages of the dynamic aerodynamic load’s measurement to the steady-state aerodynamic load’s measurement are listed in Table 3.

The dynamic rig will be mounted under the wind tunnel test section, and the wind tunnel model will be mounted on the single sturt as shown in Fig. 6, and one-third of the sturt support will pass through the floor of the wind tunnel. Hence, the rig facility will be capable to operate freely for the yaw motion. The wind tunnel model is

Table 4 Basic design specification for dynamic rig

| Parameters | Range |
|---|---------------------------|
| Mechanical damping | Kept minimum |
| Single degree of freedom | Yaw oscillation only |
| Model weight | Lightweight (low inertia) |
| Springs | Always pre-tension |
| Moving arm deflection (yaw oscillation) | $\pm 30^\circ$ |
| Pitch angle variation (static) | $\pm 35^\circ$ |
| Noise | Low |

constrained to rotate at the pivot point to obtain the yaw oscillation motion. The combination of the flow and the wind tunnel model yaw oscillation motion will generate the unsteady condition. The springs of various stiffness will be used to vary the oscillation frequency to obtain different yaw damping derivatives (Xi-qi et al., 2006). Hence the springs of different stiffness will be selected based on the frequency of interest, based on the unsteadiness of the flow. Therefore, to capture the best possible unsteady aerodynamic loads that exist on the W/T-scaled model, a reduced frequency (K_m) technique will be implemented. The dynamic rig is designed, so the rig facility will be highly sensitive to the transient aerodynamic loads and the design specification of the dynamic oscillatory rig is presented in Table 4.

The estimated specific range of frequency of interest for the scaled model oscillation frequency $f_{MO} = 0.1\text{--}5$ Hz. Then, spring stiffness K_s will be estimated by Eq. 1. The spring selection is also subject to the capability for the W/T model to oscillate within the maximum yaw deflection of the moving arm.

$$K_s = \frac{I_{ZZ}(2\pi f_{MO})^2}{2b^2} \quad (1)$$

K_s is the spring stiffness, I_{ZZ} is the moment of inertia, and b is the arm length of the dynamic oscillatory rig facility. The springs of the stiffness between 20 and 1820 N/m are selected that correspond to the desired reduced frequency range for the dynamic testing of the low-sweep wind tunnel model. Once the dynamic rig facility is installed as shown in Fig. 7, the moving arm will be deflected at positive yaw angle before being released, and time histories for the yaw oscillation will be logged.

The W/T model is attached to the sturt support and constrained to the yaw oscillation motion only as shown in Fig. 7; the sturt support is attached to the ball bearings to reduce the friction between the sturt support and the holder during yaw oscillation motion. The sturt support is then attached to a potentiometer at the bottom as shown in Fig. 6. The potentiometer is then attached via cable to the National Instrument equipment NI-PCIe 6321 for data acquisition (DAQ), and NI-PCIe 6321 is connected to the LabVIEW software to visualize and store the measurement data. The recorded data will be sampled at 1000 Hz. Digital low pass filter will be applied

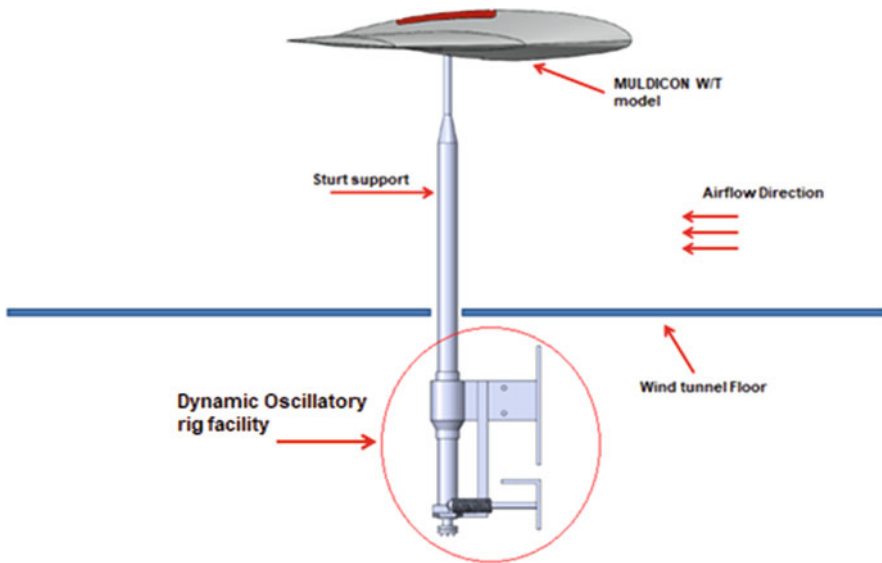


Fig. 7 Dynamic rig mounted in the wind tunnel

to the recorded data in the MATLAB, and then the filtered data will be further processed in MATLAB software. For the initial experiments, the arm will be deflected, and the data will be logged and processed for yaw angle = $\pm 10^\circ$. The processed data from the MATLAB will give the exponential decay of the oscillation amplitude where we can find out the T (period) and $t_{1/2}$ (time to half amplitude); they will be used to describe aerodynamic damping derivatives. Figure 8 shows the dynamic yaw stiffness C_{n_p} and yaw-damping derivative C_{n_r} .

3.1 Accuracy and Data Acquisition

JR3 external balance installed in the UTM-LST will provide us with the steady-state aerodynamic coefficients data including the lift, drag, side force, pitching moments, and the yaw moment coefficient data. The UTM-LST provides good flow quality as discussed in Table 1. The accuracy of the JR3 balance is within 0.04% standard deviation. The flow visualization will only provide us with qualitative data for the flow topology of the low-sweep configuration. The dynamic oscillatory rig facility will provide the yaw stability derivatives data and the side force stability derivatives data also. The dynamic stability rig facility is made highly efficient and sensitive to the aerodynamic loads by reducing the friction and the noise of the system.

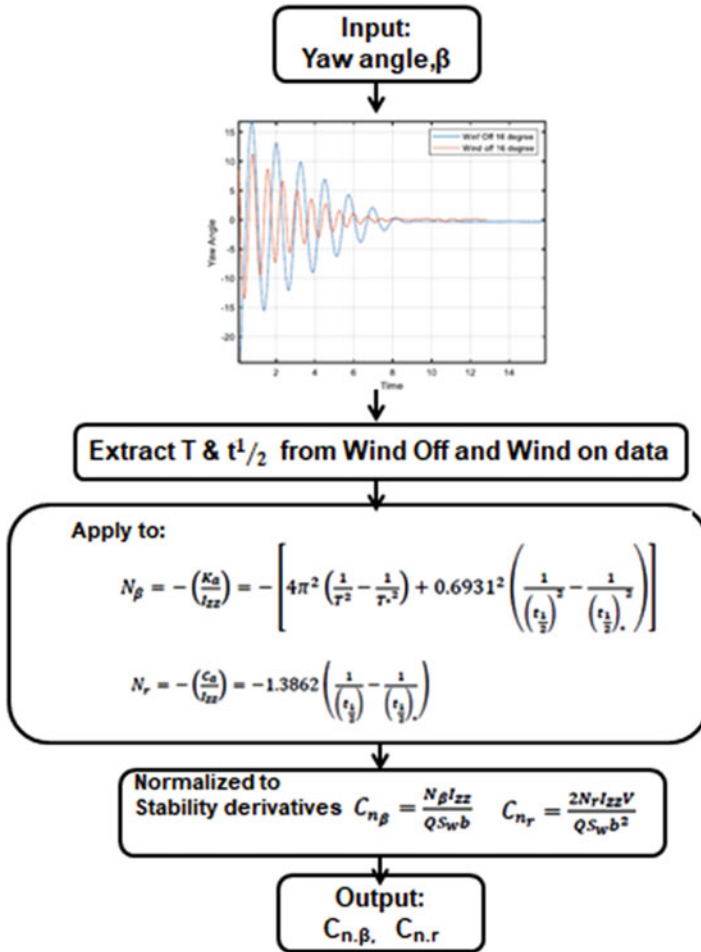


Fig. 8 Flow chart for dynamic $C_{n\beta}$ and C_{nr} estimation

4 Conclusion

The steady-state experimental setup will find out the static aerodynamic coefficients such as lift, drag, side force, yaw moment, and the pitching moment coefficients. The surface flow visualization provides the qualitative flow patterns for the flow topology of the UCAV configurations. The dynamic oscillatory rig facility will provide dynamic aerodynamic derivatives including yaw stability derivatives data and the side force stability derivative data.

References

- Dadkhah, M., Masdari, M., Vaziri, M. A., & Tahani, M. (2019). The effects of flow separation on a lambda wing aerodynamics. *Aircraft Engineering and Aerospace Technology*, 91(8), 2–5.
- Elfstrom, G. (2007). *History of test facility design expertise at Aiolos Engineering Corporation*. Paper presented at the 45th AIAA Aerospace Sciences Meeting and Exhibit.
- Noor, A., & Mansor, S. (2013). Measuring aerodynamic characteristics using high performance low speed wind tunnel at Universiti Teknologi Malaysia. *Journal of Applied Mechanical Engineering*, 3(132), 1–7.
- Rajamurthy, M. (1997). Generation of comprehensive longitudinal aerodynamic data using dynamic wind-tunnel simulation. *Journal of Aircraft*, 34(1), 29–33.
- Rockwell, D. (1993). *Three-dimensional flow structure on delta wings at high angle-of-attack- Experimental concepts and issues*. Paper presented at the 31st aerospace sciences meeting.
- Schuette, A., Vormweg, J., Maye, R. G., & Jeans, T. (2018). *Aerodynamic shaping design and vortical flow design aspects of a 53deg swept flying wing configuration*. Paper presented at the 2018 Applied Aerodynamics Conference.
- TAAH, T. M., & Mat, S. (2019). Wind tunnel testing of ice roughness effect on UTM half model. *Jurnal Mekanikal*, 42(2).
- Xi-qi, D., Wei-dong, H., & Chen, B. (2006). *Summary of the dynamic test capabilities at Caria low speed wind tunnel*. Paper presented at the 25th International Congress of the Aeronautical Sciences.

Determination of Aerodynamic Characteristics for Leading-Edge Tubercle NACA 0015 Airfoil at Low Reynolds Number



Mehmet Seyhan, Mustafa Sarioğlu, and Yahya Erkan Akansu

Contents

| | | |
|---|------------------------------|-----|
| 1 | Introduction | 488 |
| 2 | Experimental Setup | 489 |
| 3 | Results and Discussion | 489 |
| 4 | Conclusion | 491 |
| | References | 492 |

Nomenclature

| | |
|-----------|---------------------|
| a | Amplitude, mm |
| AOA | Angle of attack, mm |
| c | Chord length |
| C_D | Drag coefficient |
| C_L | Drag coefficient |
| L/D | Lift to drag ratio |
| s | Spanwise length, mm |
| λ | Wavelength, mm |

M. Seyhan (✉) · M. Sarioğlu
Karadeniz Technical University, Mechanical Engineering Department, Trabzon, Türkiye
e-mail: mehmetseyhan@ktu.edu.tr; sarioglu@ktu.edu.tr

Y. E. Akansu
Niğde Ömer Halisdemir University, Mechanical Engineering Department, Niğde, Türkiye
e-mail: akansu@ohu.edu.tr

1 Introduction

In recent years, humpback whale flippers having leading-edge tubercle have drawn attention by the researcher because of their acrobatic skills underwater in spite of its huge body size. The leading-edge structure of the flipper is widely used in the unmanned aerial vehicle (Goruney & Rockwell, 2009), wind turbine blade (Wang & Zhuang, 2017), propeller (Asghar et al., 2020), and wing (Loughnane et al., 2021) by the researchers.

A pioneering study about leading-edge tubercle airfoil was carried out by Fish and Battle (1995). Following years, Miklosovic et al. (2004) initiated an experimental study about the flipper model having a tubercle at the leading edge. They found that the tubercle form significantly delays stall angle. Aerodynamic characteristics of NACA 634-021 airfoil with leading-edge tubercle are researched by measuring drag and lift forces at Reynolds numbers of 2.9×10^4 , 4×10^4 , and 5.8×10^4 (Mehraban et al., 2021). The results indicate that the leading-edge tubercle helps to delay the stall angle. Lin et al. (2016) numerically investigated the flow characteristics of NACA 0015 airfoil having trailing edge tubercle for the application of vertical axis wind turbine (VAWT). Their findings showed that the trailing edge tubercle increases the power output of the VAWT when it compared to the baseline turbine. Lu et al. (2021) numerically desired to optimize the leading-edge tubercle form in terms of the stall, lift, and drag performance by utilizing Non-dominated sorting genetic algorithm II and response surface method-based Kriging model. They find four optimal airfoils that delay stall angle and increase the lift coefficient. In the study of Sreejith and Sathyabhama (2020), aerodynamic and flow characteristics of E216 airfoil with leading-edge tubercle were numerically studied at $Re = 1 \times 10^5$. They observed significant flow patterns such as laminar separation bubble and three-dimensional flow structure on the flow around E216 airfoil with leading-edge tubercle. Cai et al. (2017) investigated the effect of leading-edge tubercles of NACA 634-021 airfoil. While the periodic and symmetric flow pattern are observed at low angle of attacks, aperiodic and asymmetric flow pattern are obtained at high angle of attacks at the different spanwise locations. In another study of Cai et al. (2018), they numerically and experimentally researched aerodynamic characteristics of the single leading-edge tubercle for the same airfoil section. In their results, the single tubercle enhances the post-stall characteristics, while it worsens the pre-stall characteristics. Loughnane et al. (2021) investigated the influence of the tubercle geometry at the leading edge, trailing edge, and both leading and trailing edge. They performed the experimental study by measuring force with load cell and flow field with particle image velocimetry (PIV). Their results showed that the leading-edge tubercle enhances the post-stall characteristics as compared to the trailing edge tubercle model.

The aim of this study is to research the influence of the leading-edge tubercle form for the NACA 0015 airfoil with different amplitude parameters at $Re = 5 \times 10^4$.

Table 1 Specifications of the tubercle test models

| A | a_1 | λ_1 | a_2 | λ_2 |
|----|--------|-------------|---------|-------------|
| T1 | 0.025c | 0.5c | 0.0125c | 0.0625c |
| T2 | 0.025c | 0.5c | 0.025c | 0.0625c |
| T3 | 0.025c | 0.5c | 0.05c | 0.0625c |

2 Experimental Setup

This study is performed to investigate the effect of the tubercle on the aerodynamic characteristics of the NACA 0015 in a suction-type wind tunnel at $Re = 5 \times 10^4$. Force measurements were achieved with a six-axis load cell at angles of attack (AOA) between 0° and 30° . More information about the measurement system could be found in the study of Seyhan et al. (2021).

$$y_{LE} = a_1 \times \cos\left(\frac{2\pi x}{\lambda_1}\right) + a_2 \times \cos\left(\frac{2\pi x}{\lambda_2}\right) \tag{1}$$

The leading-edge tubercle model consists of two wavelengths and two amplitudes. This form can be obtained with Eq. 1. In Eq. (1), “ a ” is amplitude and “ λ ” is wavelength Eq. (1) was suggested by Seyhan et al. (2021). Specifications of three different test models are given in Table 1. The test models have chord (c) of 150 mm and spanwise of 450 mm. All models were produced with the help of a 3D printer.

Schematic views of the models are presented in Fig. 1. Test models, shown in Fig. 1, are denoted as T1, T2, T3, and baseline.

3 Results and Discussion

Results obtained from force measurements for the four airfoil models are presented in this section. Figure 2 indicates the lift coefficient (C_L) variations as a function of the angle of attacks (AOA) changing between 0° and 30° . T1 and T2 models enhanced the common stall characteristic when it is compared to the baseline model. While the stall angle of the baseline model is 9° , that of T1 is 18° . Although the T3 model produces a lower lift coefficient than the baseline model, it generally appears to increase the lift coefficient with increasing AOA from 0° to 30° and significantly delay the stall angle. According to these results, there is a strong relationship between increasing amplitude and increasing lift coefficient within leading-edge tubercle models. Up to $AOA = 7^\circ$, T1 and T2 show a similar trend with the baseline model. When the second amplitude of the tubercle geometry decreases from 0.05c to 0.0125c, lift curves of T1, T2, and T3, which are tubercle models, significantly increase.

Fig. 1 Schematic view of leading-edge tubercle models

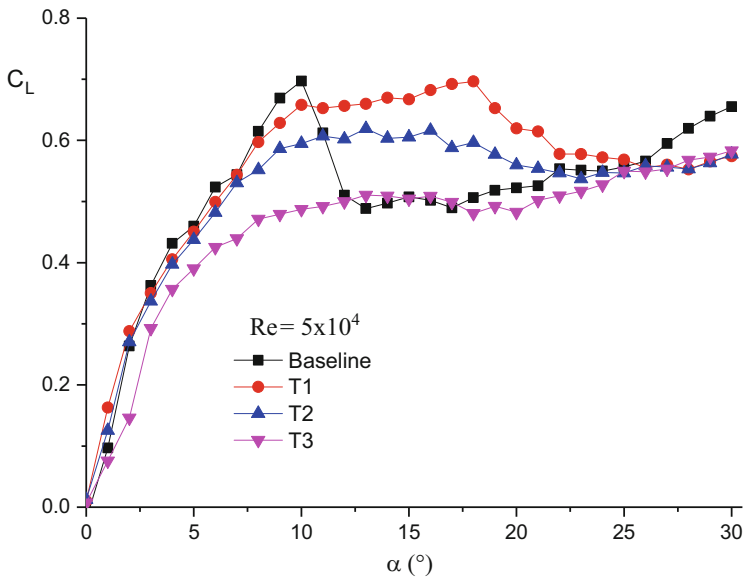
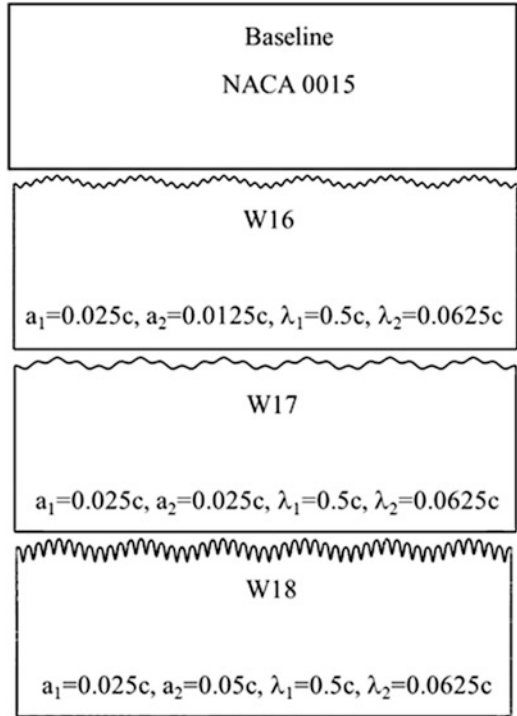


Fig. 2 Lift coefficient variation as a function of angle of attack for leading-edge tubercle models

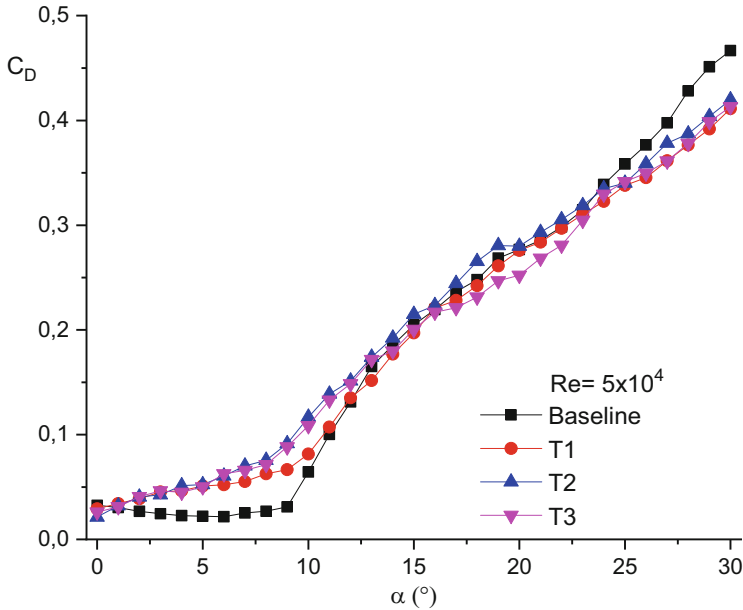


Fig. 3 Drag coefficient variation as a function of angle of attack for the leading-edge tubercle models

The drag coefficient variations versus the AOA for the baseline model, T1, T2, and T3, are presented in Fig. 3. Leading-edge tubercle models have a higher drag coefficient at the pre-stall region. After $\text{AOA} = 24^\circ$, T1, T2, and T3 have lower drag coefficient values than the baseline model.

Lift to drag ratios as a function of the AOA for the baseline, T1, T2, and T3 models were presented in Fig. 4. Lift to drag (L/D) ratios for the baseline model are higher than those of T1, T2, and T3 models up to $\text{AOA} = 11^\circ$. After this angle, L/D's of T1, T2, and T3 models are higher than that of the baseline model.

4 Conclusion

An experimental study was performed to investigate the influence of NACA 0015 airfoil models with leading-edge tubercles by measuring aerodynamic forces at low Reynolds number. Results indicate that while the leading-edge tubercles enhance the lift coefficient at the post-stall region, they increase the drag coefficient at the pre-stall region. Also, the leading-edge tubercles have delayed the stall angle significantly.

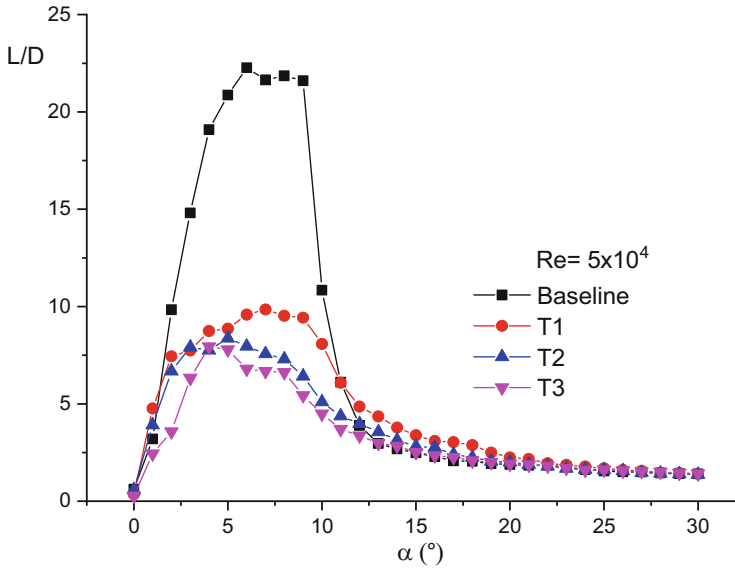


Fig. 4 Lift to drag ratios for T1, T2, T3, and baseline models

Acknowledgments The authors would like to acknowledge the financial support of this work by the Scientific and Technological Research Council of Turkey (TUBITAK) under the Contract Number of 118M592.

References

- Asghar, A., Perez, R. E., Jansen, P. W., & Allan, W. D. E. (2020). Application of leading-edge tubercles to enhance propeller performance. *AIAA Journal*, 58(11), 4659–4671.
- Cai, C., Zuo, Z., Maeda, T., Kamada, Y., Li, Q., Shimamoto, K., & Liu, S. (2017). Periodic and aperiodic flow patterns around an airfoil with leading-edge protuberances. *Physics of Fluids*, 29(11), 115110.
- Cai, C., Zuo, Z., Liu, S., & Maeda, T. (2018). Effect of a single leading-edge protuberance on NACA 634-021 airfoil performance. *Journal of Fluids Engineering*, 140(2), 21108.
- Fish, F. E., & Battle, J. M. (1995). Hydrodynamic-design of the humpback whale flipper. *Journal of Morphology*, 225(1), 51–60.
- Goruney, T., & Rockwell, D. (2009). Flow past a delta wing with a sinusoidal leading edge: Near-surface topology and flow structure. *Experiments in Fluids*, 47(2), 321–331.
- Lin, S. Y., Lin, Y. Y., Bai, C. J., & Wang, W. C. (2016). Performance analysis of vertical-axis-wind-turbine blade with modified trailing edge through computational fluid dynamics. *Renewable Energy*, 99, 654–662. Available at <https://doi.org/10.1016/j.renene.2016.07.050>
- Loughnane, F., Mongin, M., & Gunasekaran, S. (2021). Effect of airfoil-preserved undulation placement on wing performance and wingtip vortex. *AIAA Journal*, 59(5), 1598–1613.

- Lu, Y., Li, Z., Chang, X., Chuang, Z., & Xing, J. (2021). An aerodynamic optimization design study on the bio-inspired airfoil with leading-edge tubercles. *Engineering Applications of Computational Fluid Mechanics*, 15(1), 293–313. Available at <https://doi.org/10.1080/19942060.2020.1856723>
- Mehraban, A. A., Djavarehshkian, M. H., Sayegh, Y., Forouzi Feshalami, B., Azargoon, Y., Zaree, A. H., & Hassanalian, M. (2021). Effects of smart flap on aerodynamic performance of sinusoidal leading-edge wings at low Reynolds numbers. *Proceedings of the Institution of Mechanical Engineers, Part G: Journal of Aerospace Engineering*, 235(4), 439–450.
- Miklosovic, D. S., Murray, M. M., Howle, L. E., & Fish, F. E. (2004). Leading-edge tubercles delay stall on humpback whale (*Megaptera Novaeangliae*) flippers. *Physics of Fluids*, 16(5), 39–42.
- Seyhan, M., Sarioglu, M., & Akansu, Y. E. (2021). Influence of leading-edge tubercle with amplitude modulation on NACA 0015 airfoil at low Reynolds number. *AIAA Journal*, 59(10), 3965–3978.
- Sreejith, B. K., & Sathyabhama, A. (2020). Experimental and numerical study of laminar separation bubble formation on low Reynolds number airfoil with leading-edge tubercles. *Journal of the Brazilian Society of Mechanical Sciences and Engineering*, 42(4). Available at <https://doi.org/10.1007/s40430-020-2229-2>
- Wang, Z., & Zhuang, M. (2017). Leading-edge serrations for performance improvement on a vertical-axis wind turbine at low tip-speed-ratios. *Applied Energy*, 208(June), 1184–1197. Available at <https://doi.org/10.1016/j.apenergy.2017.09.034>

Comparison of GPS-Based Position Estimation Methods



Mert Sever and Chingiz Hajiyev

Contents

| | | |
|---|---|-----|
| 1 | Introduction | 495 |
| 2 | Problem Statement | 496 |
| 3 | Linear Kalman Filter-Based GPS Localization | 498 |
| 4 | Extended Kalman Filter-Based GPS Localization | 499 |
| 5 | Pre-processed LKF with Newton-Raphson Method | 500 |
| 6 | Simulation Results and Discussion | 503 |
| 7 | Conclusion | 505 |
| | References | 505 |

1 Introduction

Global Positioning System (GPS) is a commonly used instrument for estimation of localization of an object. GPS usage has expanded with the increase of autonomous systems (Wertz, 1992). Various studies have been created for GPS-based localization (Erkek & Hajiyev, 2019; Soken and Hajiyev 2010, 2012).

Global Positioning System satellites provide three-dimensional position, velocity, and time services, and many users benefit from these services using GPS-based positioning systems via devices such as phones, computers, and navigation (Maldonado et al., 1984).

M. Sever (✉)

Turkish National Defense University, Hezârfen Aeronautics and Space Technologies Institute, Istanbul, Turkiye

C. Hajiyev

Istanbul Technical University, Faculty of Aeronautics and Astronautics, Istanbul, Turkiye
e-mail: cingiz@itu.edu.tr

Nonlinear problems become more accurate with the implementation of the Kalman filters, and GPS-based positioning is a nonlinear problem. The signals received by GPS transmitters are noisy data. The purpose of the study is to decrease the errors and obtain more accurate results (Kumar and Rao 2019). GPS data can be processed by various Kalman filter methods and in this study were processed with traditional extended Kalman filter (EKF), linear Kalman filter (LKF), and LKF pre-processed with the Newton-Raphson method. Required data are taken from GPS receivers and processed with the algorithm.

Four GPS satellites were chosen for estimation and coordinates of Şükürü Saraçoğlu stadium assumed as a point. The location of the stadium was determined in Earth-centered inertial (ECI) reference frame. With using determined location, pseudo-ranging models were created due to each GPS satellite. Actual distances were summed with clock bias and random noise, where random is the Gaussian random noise with zero mean and unit variance. With this operation, GPS measurements were simulated. EKF, LKF, and LKF pre-processed with the Newton-Raphson method results have better solutions than measurement estimation and results converged to actual state vectors.

2 Problem Statement

In this study, Şükürü Saraçoğlu stadium GPS location were chosen for estimation. Pseudo-ranging method was used. Four GPS satellites were chosen. Distance between GPS satellites and location were calculated for each iteration. After measurement model were created, traditional EKF, LKF, and NRM pre-processed LKF are applied for correction of estimations:

$$D_{a(i)} = \sqrt{(x_i - x)^2 + (y_i - y)^2 + (z_i - z)^2} \quad (1)$$

$$D_{m(i)} = \sqrt{(x_i - x)^2 + (y_i - y)^2 + (z_i - z)^2} + b_i + v_i \quad (2)$$

$$L_i = \sqrt{x_i^2 + y_i^2 + z_i^2} \quad i = 1, 2, 3, 4 \quad (3)$$

where x_i, y_i, z_i represents the Descartes coordinates of the i 'th GPS satellite; $x, y,$ and z represent the coordinates of the location; v_i is white Gaussian noise with zero mean; and b is the clock bias. $L_1, L_2, L_3,$ and L_4 are distances between origin and GPS satellite. D_a is the actual distance and D_m is measured distance by GPS receiver. After calculating actual distance with Eq. (1), random zero mean Gaussian errors and clock bias were added to actual distances for simulating GPS.

The continuous-time state equation in the considered case is given by

$$\dot{x} = 0, \quad \dot{y} = 0, \quad \dot{z} = 0, \quad \dot{b} = u_s \quad (4)$$

Here u_s is the white noise with zero mean.

The state Eq. (4) can be written in the discrete-time form as

$$\begin{aligned} x(k) &= x(k-1) \\ y(k) &= y(k-1) \\ z(k) &= z(k-1) \\ b(k) &= b(k-1) + T_s u_s \end{aligned} \quad (5)$$

Here T_s is the sampling time.

We can rewrite the preceding statements for scalar equations in the state space form, yielding

$$\begin{bmatrix} x(k) \\ y(k) \\ z(k) \\ b(k) \end{bmatrix} = \begin{bmatrix} 1 & 0 & 0 & 0 \\ 0 & 1 & 0 & 0 \\ 0 & 0 & 1 & 0 \\ 0 & 0 & 0 & 1 \end{bmatrix} \begin{bmatrix} x(k-1) \\ y(k-1) \\ z(k-1) \\ b(k-1) \end{bmatrix} + \begin{bmatrix} 0 \\ 0 \\ 0 \\ T_s u_s \end{bmatrix} \quad (6)$$

This means that the systems dynamics matrix is unit:

$$\phi(k, k-1) = I_{4 \times 4} \quad (7)$$

The system noise vector is

$$W(k) = [0 \ 0 \ 0 \ T_s u_s]^T \quad (8)$$

The state space model can be written in matrix form as

$$X(k) = \phi(k, k-1)X(k-1) + W(k) \quad (9)$$

$$X(k) = [x(k) \ y(k) \ z(k) \ b(k)]^T \quad (10)$$

Equation (10) represents the state vector of the model.

3 Linear Kalman Filter-Based GPS Localization

The linear Kalman filter (LKF) is a filter that estimates X parameters for the vector of linear regression model. LKF estimation for stationary user previously studied by Hajjiyev [5]. State vectors were given in Eq. (10), and due to these state vectors, linear Kalman filter equations can be shown as following equations.

Estimation equation:

$$\hat{X}(k) = \hat{X}(k/k-1) + K(k)\hat{Z}(k) \quad (11)$$

Extrapolation equation:

$$\hat{X}(k/k-1) = \hat{X}(k-1/k-1) \quad (12)$$

Innovation sequence:

$$\hat{Z}(k/k-1) = Y(k) - H(k)\hat{X}(k/k-1) \quad (13)$$

Here the measurement $Y(k)$,

$$Y(k) = \begin{bmatrix} \frac{1}{2}(L_1^2 - L_2^2 + D_2^2 - D_1^2) \\ \frac{1}{2}(L_1^2 - L_3^2 + D_3^2 - D_1^2) \\ \frac{1}{2}(L_1^2 - L_4^2 + D_4^2 - D_1^2) \end{bmatrix} \quad (14)$$

Kalman gain coefficient matrix:

$$K(k) = P(k/k-1)H(k)^T \left[H(k)P(k/k-1)H(k)^T + R(k) \right]^{-1} \quad (15)$$

Predicted correlation matrix of estimation error:

$$P(k/k-1) = P(k-1/k-1) \quad (16)$$

Correlation matrix of estimation error:

$$P(k/k) = [I - K(k)H(k)]P(k-1/k-1) \quad (17)$$

Measurement matrix (H):

$$H(k) = \begin{bmatrix} x_1 - x_2 & y_1 - y_2 & z_1 - z_2 & D_2 - D_1 \\ x_1 - x_3 & y_1 - y_3 & z_1 - z_3 & D_3 - D_1 \\ x_1 - x_4 & y_1 - y_4 & z_1 - z_4 & D_4 - D_1 \end{bmatrix} \quad (18)$$

Measurement error covariance matrix (R):

$$R = \begin{bmatrix} (D_1 - b)^2 \sigma^2 + (D_2 - b)^2 \sigma^2 + \sigma^4 & (D_1 - b)^2 \sigma^2 + \frac{1}{2} \sigma^4 & (D_1 - b)^2 \sigma^2 + \frac{1}{2} \sigma^4 \\ (D_1 - b)^2 \sigma^2 + \frac{1}{2} \sigma^4 & (D_1 - b)^2 \sigma^2 + (D_3 - b)^2 \sigma^2 + \sigma^4 & (D_1 - b)^2 \sigma^2 + \frac{1}{2} \sigma^4 \\ (D_1 - b)^2 \sigma^2 + \frac{1}{2} \sigma^4 & (D_1 - b)^2 \sigma^2 + \frac{1}{2} \sigma^4 & (D_1 - b)^2 \sigma^2 + (D_4 - b)^2 \sigma^2 + \sigma^4 \end{bmatrix} \quad (19)$$

Here σ is the standard deviation of the distance measurement, and b is the clock bias of the GPS receiver.

4 Extended Kalman Filter-Based GPS Localization

Extended Kalman filter (EKF) is an approach for nonlinear systems. EKF linearizes the system and estimates the state vectors. State vectors of the model were given in Eq. (10).

Estimation equation:

$$\hat{X}(k) = \hat{X}(k-1) + K(k)\hat{Z}(k/k-1) \quad (20)$$

Extrapolation equation:

$$\hat{X}(k/k-1) = \hat{X}(k-1/k-1) \quad (21)$$

Innovation sequence:

$$\hat{Z}(k/k-1) = D(k) - \bar{D}(k) \quad (22)$$

$$\begin{aligned} D(k) &= [D_1(k) \quad D_2(k) \quad D_3(k) \quad D_4(k)]^T, \\ \bar{D}(k) &= [\bar{D}_1(k) \quad \bar{D}_2(k) \quad \bar{D}_3(k) \quad \bar{D}_4(k)] \end{aligned} \quad (23)$$

$$\bar{D}_i = \sqrt{\frac{(x_i(k) - \hat{x}(k-1))^2 + (y_i(k) - \hat{y}(k-1))^2}{+(z_i(k) - \hat{z}(k-1))^2}} + \hat{b}(k-1) \quad (24)$$

$$D_i = \sqrt{(x_i - x)^2 + (y_i - y)^2 + (z_i - z)^2} + b + w_i \quad i = \overline{1,4}$$

Here x_i , y_i , v_i , and z_i represent the position states of the i th navigation satellite, and x , y , v , and z represent the position states of the user; b is the clock bias of the GPS receiver and w_i random measurement noise.

Kalman gain coefficient matrix:

$$K(k) = P(k/k-1)H(k)^T \left[H(k)P(k/k-1)H(k)^T + R(k) \right]^{-1} \quad (25)$$

Predicted correlation matrix of estimation error:

$$P(k/k-1) = \phi(k, k-1)P(k-1/k-1)\phi(k, k-1)^T + Q(k-1) \quad (26)$$

Predicted correlation matrix of estimation error:

$$P(k/k) = P(k-1/k-1) - K(k)H(k)P(k-1/k-1) \quad (27)$$

Measurement matrix:

$$H(k) = \begin{bmatrix} \frac{\partial D_1}{\partial x} & \frac{\partial D_1}{\partial y} & \frac{\partial D_1}{\partial z} & \frac{\partial D_1}{\partial b} \\ \frac{\partial D_2}{\partial x} & \frac{\partial D_2}{\partial y} & \frac{\partial D_2}{\partial z} & \frac{\partial D_2}{\partial b} \\ \frac{\partial D_3}{\partial x} & \frac{\partial D_3}{\partial y} & \frac{\partial D_3}{\partial z} & \frac{\partial D_3}{\partial b} \\ \frac{\partial D_4}{\partial x} & \frac{\partial D_4}{\partial y} & \frac{\partial D_4}{\partial z} & \frac{\partial D_4}{\partial b} \end{bmatrix} \quad (28)$$

Measurement error covariance matrix (R):

$$R(k) = \sigma^2 I_{4 \times 4}, \sigma = 10 \text{ m} \quad (29)$$

5 Pre-processed LKF with Newton-Raphson Method

Newton-Raphson method is the nonlinear system approach. For each iteration, multiple matrix operations are performed for estimation. The Newton-Raphson method requires a new set of matrix calculations and constructs a different estimation in each iterative step (Cheung & Lee, 2017).

$$F(p_k) = \begin{bmatrix} f_1(x, y, z, b) \\ f_2(x, y, z, b) \\ f_3(x, y, z, b) \\ f_4(x, y, z, b) \end{bmatrix} \tag{30}$$

where $x, y,$ and z are position vectors and b is the clock bias. Each distance is proper for different sphere equation and sphere equations given in Eq. (30).

$$\begin{aligned} f_1(x, y, z, b) &= (x_1 - x)^2 + (y_1 - y)^2 + (z_1 - z)^2 - (D_1 - b)^2 \\ f_2(x, y, z, b) &= (x_2 - x)^2 + (y_2 - y)^2 + (z_2 - z)^2 - (D_2 - b)^2 \\ f_3(x, y, z, b) &= (x_3 - x)^2 + (y_3 - y)^2 + (z_3 - z)^2 - (D_3 - b)^2 \\ f_4(x, y, z, b) &= (x_4 - x)^2 + (y_4 - y)^2 + (z_4 - z)^2 - (D_4 - b)^2 \end{aligned} \tag{31}$$

The Jacobian matrix is

$$J(p_k) = \begin{bmatrix} \frac{\partial}{\partial x}f_1(x, y, z, b) & \frac{\partial}{\partial y}f_1(x, y, z, b) & \frac{\partial}{\partial z}f_1(x, y, z, b) & \frac{\partial}{\partial b}f_1(x, y, z, b) \\ \frac{\partial}{\partial x}f_2(x, y, z, b) & \frac{\partial}{\partial y}f_2(x, y, z, b) & \frac{\partial}{\partial z}f_2(x, y, z, b) & \frac{\partial}{\partial b}f_2(x, y, z, b) \\ \frac{\partial}{\partial x}f_3(x, y, z, b) & \frac{\partial}{\partial y}f_3(x, y, z, b) & \frac{\partial}{\partial z}f_3(x, y, z, b) & \frac{\partial}{\partial b}f_3(x, y, z, b) \\ \frac{\partial}{\partial x}f_4(x, y, z, b) & \frac{\partial}{\partial y}f_4(x, y, z, b) & \frac{\partial}{\partial z}f_4(x, y, z, b) & \frac{\partial}{\partial b}f_4(x, y, z, b) \end{bmatrix} \tag{32}$$

After mathematical transformations, J obtained for this problem as

$$J = \begin{bmatrix} 2(x_1 - x) & 2(y_1 - y) & 2(z_1 - z) & 2(b - D_1) \\ 2(x_2 - x) & 2(y_2 - y) & 2(z_2 - z) & 2(b - D_2) \\ 2(x_3 - x) & 2(y_3 - y) & 2(z_3 - z) & 2(b - D_3) \\ 2(x_4 - x) & 2(y_4 - y) & 2(z_4 - z) & 2(b - D_4) \end{bmatrix} \tag{33}$$

where x_i, y_i ve, and z_i ($i = \overline{1,4}$) represent the position of navigation satellites; $x, y,$ and z represent the positions of the stationary user; b is the clock bias of the GPS receiver; and D_i ($i = \overline{1,4}$) is the distance between navigation satellite and stationary user.

ΔP and new state vectors estimated by Newton-Raphson method are given in Eq. (34). NRM estimation for each iteration continues while the absolute value ΔP is greater than error tolerance of the system. When the error tolerance becomes greater than ΔP , NRM estimation of i th iteration ends and starts estimating $i + 1$ th iteration state vectors.

$$\begin{aligned}\Delta P &= -F.J^{-1} \\ P_{k+1} &= P_k + \Delta P\end{aligned}\quad (34)$$

Equation (33) represents the estimation of NRM state vectors. After estimation of NRM, LKF estimation starts.

Estimation equation:

$$\widehat{X}(k) = \widehat{X}(k/k-1) + K(k)\widehat{Z}(k) \quad (35)$$

Extrapolation equation:

$$\widehat{X}(k/k-1) = \widehat{X}(k-1/k-1) \quad (36)$$

Innovation sequence:

$$\widehat{Z}(k/k-1) = Y(k) - \widehat{X}(k/k-1) \quad (37)$$

where $Y(k)$

$$Y(k) = [x_{\text{NRM}} \quad y_{\text{NRM}} \quad z_{\text{NRM}} \quad b_{\text{NRM}}]^T \quad (38)$$

Kalman gain coefficient matrix:

$$K(k) = P(k/k-1)H(k)^T \left[H(k)P(k/k-1)H(k)^T + R(k) \right]^{-1} \quad (39)$$

Predicted correlation matrix of estimation error:

$$P(k/k-1) = \phi(k, k-1)P(k/k-1)\phi(k, k-1)^T + Q(k-1) \quad (40)$$

Estimated correlation matrix of estimation error:

$$P(k/k) = [I - K(k)H(k)]P(k/k-1) \quad (41)$$

Measurement matrix (H):

$$H(k) = I_{4 \times 4} \quad (42)$$

Measurement error covariance matrix (R):

$$R(k) = \begin{bmatrix} \beta_x & 0 & 0 & 0 \\ 0 & \beta_y & 0 & 0 \\ 0 & 0 & \beta_z & 0 \\ 0 & 0 & 0 & \beta_b \end{bmatrix} \tag{43}$$

where $\beta_x, \beta_y, \beta_z,$ and β_b are variance of the NRM estimation errors.

6 Simulation Results and Discussion

In this study stationary user localization is estimated by using GPS simulation, LKF, traditional EKF, and pre-processed LKF with the Newton-Raphson method. GPS measurement results converged to actual state vectors with the implementation of filter estimations. Estimated results compared to other estimations.

The results of stationary user localization using the Kalman filter for three different approaches are shown in Figs. 1, 2, and 3. The first part of figures gives

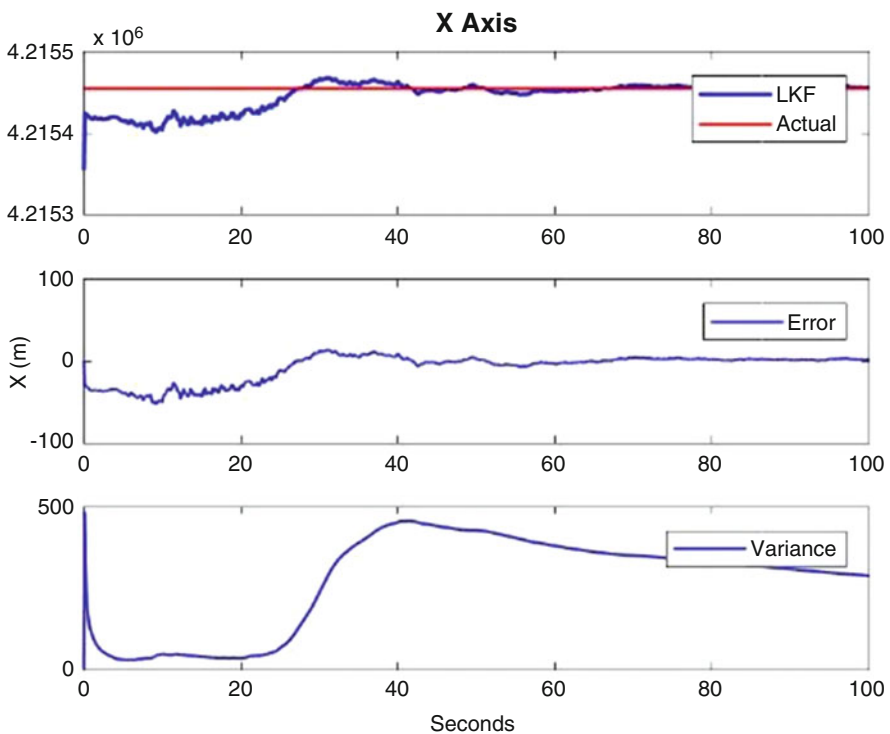


Fig. 1 LKF X axis estimation

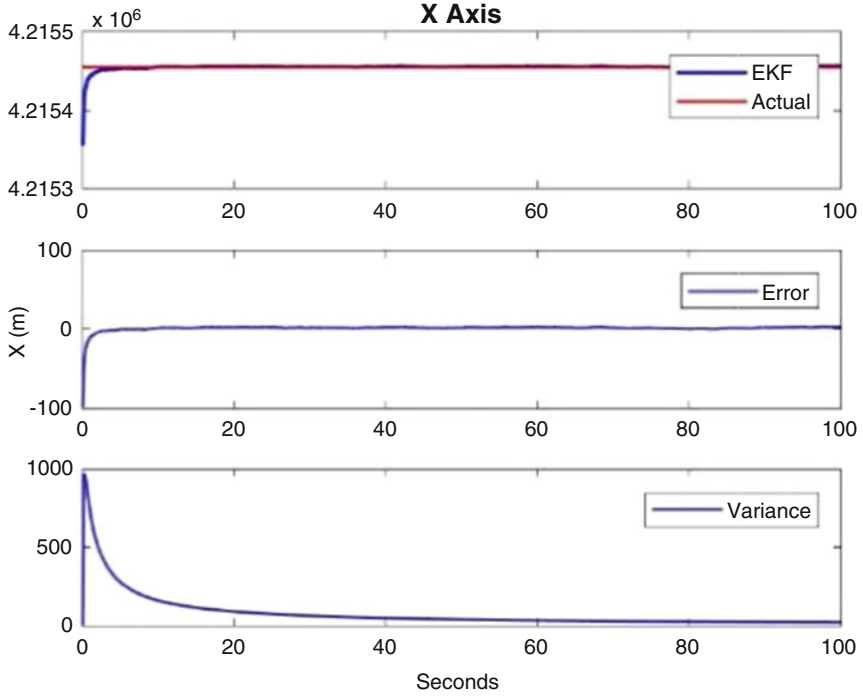


Fig. 2 EKF X axis estimation

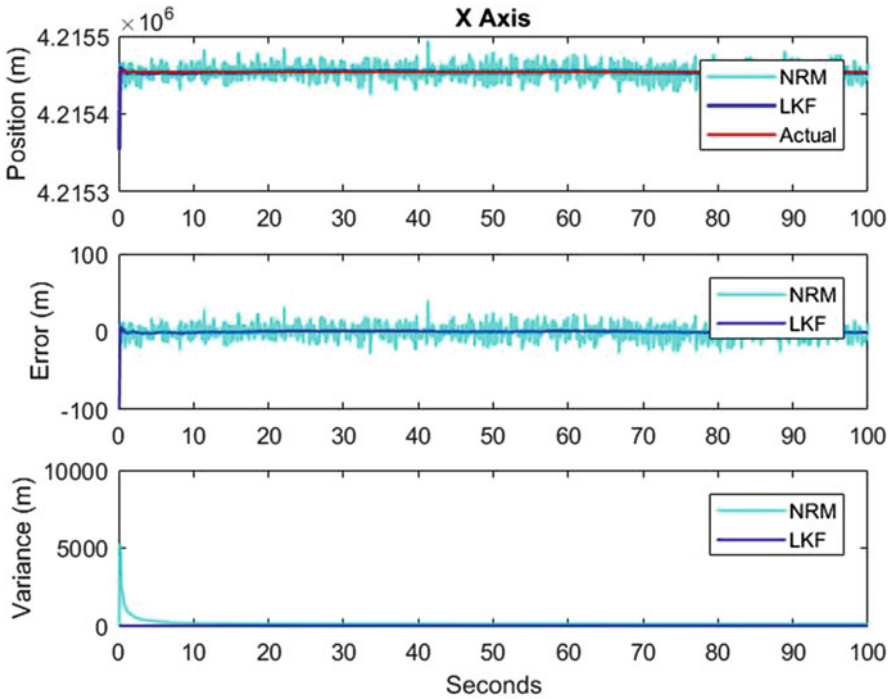


Fig. 3 NRM pre-processed LKF X axis estimation

Table 1 Root mean square errors for 500 seconds

| | X (m) | Y (m) | Z (m) | Bias (m) |
|-----------|--------|--------|--------|----------|
| EKF | 1.1659 | 1.0109 | 1.2467 | 0.7086 |
| LKF | 0.9745 | 1.0489 | 0.9617 | 0.9941 |
| NRM + LKF | 1.1023 | 1.0902 | 1.2570 | 0.8322 |

position estimation results and the actual values in a comparing way. The second part of the figures shows the error of estimation process. The last part indicates the variance of the estimation error. Linear Kalman filter estimation for X axis is presented in Fig. 2.

Extended Kalman filter estimation for X axis is presented in Fig. 2.

Pre-processed linear Kalman filter with Newton-Raphson method estimation for X axis presented in Fig. 3.

As can be seen from the graphs shown in Figs. 1, 2, and 3, all three investigated approaches give rather good results for estimating the position of a stationary user.

According to Table 1, the best estimation results were obtained LKF. Traditional EKF is the second best estimation when compared to other methods.

7 Conclusion

Three different Kalman filter approaches are used in this study for stationary user localization: traditional extended Kalman filter, linear Kalman filter, and NRM pre-processed linear Kalman filter. The Şükrü Saraçoğlu stadium’s location (Istanbul, Turkey) was estimated and compared via various types of Kalman filters. The obtained results show that LKF is the best estimation for 500 s stationary user localization. Through this research, users can determine the best position estimation approach for their own problem.

References

Cheung, K., & Lee, C. (2017). *A new geometric trilateration scheme for GPS-style localization*. IPN Progress Report, pp. 42–209.

Erkeç, T. Y., & Hajiyev, C. (2019). Traditional methods on relative navigation of small satellites. In *2019 9th international conference on recent advances in space technologies (RAST)*, Istanbul, Turkey, pp. 869–874.

Kumar, A., & Rao, G. S. (2019, May). *Unscented kalman dilter for GPS based positioning and tracking services*. International Journal of Innovative Technology and Exploring Engineering (IJITEE). (Vol. 8)

Maldonado, A. L., Bayloçq, M., & Hannan, G. (1984, June 25–27). Autonomous spacecraft navigation - extended Kalman filter estimation of classical orbital parameters. In *17th fluid dynamics, plasma dynamics, and lasers conference*.

Soken, H. E., & Hajiyev, C. (2010). Pico satellite attitude estimation via robust unscented Kalman filter in the presence of measurement faults. *ISA Trans.*, 49, 249–256.

- Soken, H., & Hajiyev, C. (2012). Robust Estimation of UAV Dynamics in Presence of Measurements Faults. *Journal of Aerospace Engineering*, 25, 1–10. [https://doi.org/10.1061/\(ASCE\)AS.1943-5525.0000095](https://doi.org/10.1061/(ASCE)AS.1943-5525.0000095)
- Wertz, J. R. (1992, April 28). *Autonomous spacecraft navigation system*. United States Patent, Patent no:5109346.

Investigation of the Accuracy of Terrestrial Radio Navigation Methods for Determining Aircraft Position



Alper Mehdi Sametoğlu and Chingiz Hajiyev

Contents

| | | |
|---|--|-----|
| 1 | Introduction | 507 |
| 2 | Mathematical Model of Aircraft Dynamics | 508 |
| 3 | Determination of Aircraft's Coordinates via Distance Measurement Method | 510 |
| 4 | Determination of Aircraft Coordinates via Distance Difference Measurement Method ... | 512 |
| 5 | Determination of Aircraft's Coordinates by Integrated Method | 513 |
| 6 | Simulation Results and Discussion | 514 |
| 7 | Conclusion | 516 |
| | References | 516 |

1 Introduction

An aircraft's position in a space is defined by three coordinates. In navigation, for aircraft's position characteristics, position surface, and position lines are used. The aircraft's position is defined by two position lines or three position surfaces or by position line and position surface. As a navigation parameter, elevation angle, azimuth angle, distance, distance difference, or sum of distances can be used (Krinetskiy, 1979; Kayton & Fried, 1997).

In general, when three geometric surfaces cross, there are a few intersecting points (Haciyev, 1999). In this case, there may be several solutions for determining

A. M. Sametoğlu
SAJEV Ozel Kucuk Prens High School, Istanbul, Turkiye

C. Hajiyev (✉)
Istanbul Technical University, Faculty of Aeronautics and Astronautics, Istanbul, Turkiye
e-mail: cingiz@itu.edu.tr

the aircraft's position. This problem can be avoided by using extra information for each position.

The error analysis in determining the coordinates of aircraft by the distance measurement method is given in Hacıyev and Üner (1998). In Erkal and Hacıyev (2004), the accuracy of the distance difference measurement method is investigated. However, these studies do not compare different types of terrestrial radio navigation techniques.

In this study, the accuracy of the distance measurement, distance difference measurement, and integrated angle measurement/distance measurement terrestrial radio navigation methods is investigated using simulations. For this purpose, the aircraft flight dynamics are simulated, and the obtained values of the coordinates were compared with the actual values. The aircraft position determination method that has better accuracy was investigated by comparing the absolute errors of the examined methods.

2 Mathematical Model of Aircraft Dynamics

The mathematical model of the aircraft's motion consists of longitudinal and lateral motion models. The longitudinal motion of the aircraft consists of forward, vertical, and pitching motions. The state vector X_u and control vector U_u of the longitudinal model can be written in the following form:

$$\begin{aligned} X_u &= [u \ w \ q \ \theta]^T \\ u &= [\delta_E] \end{aligned}$$

where u is the forward velocity (m/s), w is the vertical velocity (m/s), q is the pitch rate (degree/s), θ is the pitch angle (degree), and δ_E is the elevator deflection (degree).

The mathematical model of the longitudinal motion is given by the following differential equation:

$$\dot{X}_u = A_u X_u + B_u U_u \quad (1)$$

where A_u is the system matrix and B_u is the control distribution matrix. These matrices are (McLean, 1990)

$$A_u = \begin{bmatrix} X_u & X_w & 0 & -g \cos \gamma_0 \\ Z_u & Z_w & U_0 & -g \sin \gamma_0 \\ \tilde{M}_u & \tilde{M} & \tilde{M}_\theta & \tilde{M}_\theta \\ 0 & 0 & 1 & 0 \end{bmatrix} \tag{2}$$

$$B_u = \begin{bmatrix} X_{\delta_E} \\ Z_{\delta_E} \\ \tilde{M}_{\delta_E} \\ 0 \end{bmatrix} \tag{3}$$

The lateral motion of the aircraft consists of sideslip, roll, and yaw motions. The state vector X_y and control vector U_y of the lateral model can be written as

$$X_y = [\beta pr \varphi \psi]^T$$

$$u = \begin{bmatrix} \delta_A \\ \delta_R \end{bmatrix}$$

where β is the sideslip angle (degree), p is the roll rate (degree/s), r is the yaw rate (degree/s), φ is the roll angle (degree), ψ is the yaw angle (degree), δ_A is the aileron deflection angle (degree), and δ_R is the rudder deflection angle (degree).

The mathematical model of the lateral motion is given by

$$\dot{X}_y = A_y X_y + B_y U_y \tag{4}$$

where the system matrix A_y and the control distribution matrix B_y are (McLean, 1990)

$$A_y = \begin{bmatrix} Y_v & 0 & U_0 & g \cos \gamma_0 & 0 & L'_v & L'_p & L'_r & 0 & 0 & N'_v & N'_p & N'_r & 0 & 0 & 0 & 0 & 1 & \tan \gamma_0 & 0 & 0 & 0 & 0 & 0 & 0 & 0 \end{bmatrix} \tag{5}$$

$$B_y = \begin{bmatrix} 0 & Y_{\delta_R} \\ L'_{\delta_A} & L'_{\delta_R} \\ N'_{\delta_A} & N'_{\delta_R} \\ 0 & 0 \\ 0 & 0 \end{bmatrix} \tag{6}$$

For small side slip velocities, $v = U_0 \beta$ assumption can be made. Notations in (2), (3), (5), and (6) can be found in McLean (1990).

Additional expressions must be included in the model to determine the positions along X, Y, and Z directions:

$$\dot{x} = u \quad (7)$$

$$\dot{y} = v = U_0\beta \quad (8)$$

$$\dot{z} = w \quad (9)$$

The state vector of the mathematical model of aircraft is

$$X = [u \quad w \quad q \quad \theta \quad \beta \quad p \quad r \quad \phi \quad \psi \quad x \quad y \quad z]^T$$

The control vector of the system is

$$U = [\delta_E \quad \delta_A \quad \delta_R]^T$$

Discretizing the aircraft's mathematical model, we have

$$\begin{aligned} \dot{X} &= AX + BU \Rightarrow \dot{X}_i = \frac{X_{i+1} - X_i}{\Delta t} = AX_i + BU_i, \\ X_{i+1} - X_i &= A \cdot \Delta t \cdot X_i + B \cdot \Delta t \cdot u_i, \\ X_{i+1} &= \underbrace{(I + \Delta t A)}_{A^*} X_i + \underbrace{\Delta t \cdot B U_i}_{B^*} \Rightarrow \\ X_{i+1} &= A^* X_i + B^* U_i \end{aligned} \quad (10)$$

where X is the aircraft state vector, A^* is the system matrix, U is the control input vector, and B^* is the control distribution matrix.

3 Determination of Aircraft's Coordinates via Distance Measurement Method

In the distance measurement method, the position surface is a sphere with radius D which is the distance from the station to the aircraft. Thus, aircraft's position in a space can be found by intersecting three $D = \text{const}$ position surfaces. Since there are two intersection points when intersecting three spheres, the results of this method are uncertain. To make this method more precise, it can be integrated with extra navigation systems with low accuracy.

Three measurement stations (distance measurement stations) are located on the ground to determine the position of the aircraft. Let's assume that the ground stations are located on $O_1(x_1, y_1, z_1)$, $O_2(x_2, y_2, z_2)$, and $O_3(x_3, y_3, z_3)$ points of $O_0X_0Y_0Z_0$. Descartes coordinate system to find calculation formulas of distance measurement method (Fig. 1). l_1 , l_2 , and l_3 show the distance between the ground station's origins and the origin of $O_0X_0Y_0Z_0$ coordinate system, and D_1 , D_2 , and D_3 show the

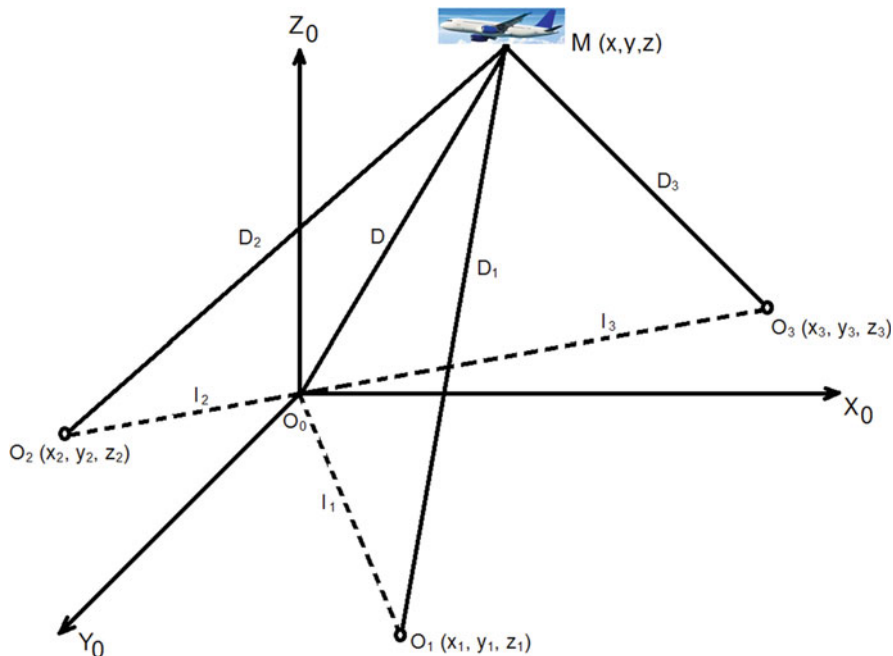


Fig. 1 Distance measurement method's scheme in determining the position of the aircraft

distances to the aircraft at $M(x,y,z)$ point. The equations for the coordinate determination can be written as

$$x = e_1 - az; \tag{11}$$

$$y = e_2 - bz; \tag{12}$$

$$(a^2 + b^2 + 1)z^2 + 2(x_1a - z_1 + y_1b - ae_1 - be_2)z - (D_1^2 - l_1^2 - e_1^2 - e_2^2 + 2x_1e_1 + 2y_1e_2) = 0 \tag{13}$$

where

$$e_1 = \frac{c_1(y_2 - y_3) - c_3(y_1 - y_2)}{(x_1 - x_2)(y_2 - y_3) - (x_2 - x_3)(y_1 - y_2)};$$

$$e_2 = \frac{c_1(x_1 - x_3) - c_2(x_1 - x_2)}{(x_1 - x_3)(y_1 - y_2) - (x_1 - x_2)(y_1 - y_3)};$$

$$a = \frac{(z - z_2)(y_2 - y_3) - (z_2 - z)(y_1 - y_2)}{(x_1 - x_2)(y_2 - y_3) - (x_2 - x_3)(y_1 - y_2)};$$

$$b = \frac{(z_1 - z)(x_1 - x_3) - (z_1 - z)(x_1 - x_2)}{(x_1 - x_3)(y_1 - y_2) - (x_1 - x_2)(y_1 - y)}$$

4 Determination of Aircraft Coordinates via Distance Difference Measurement Method

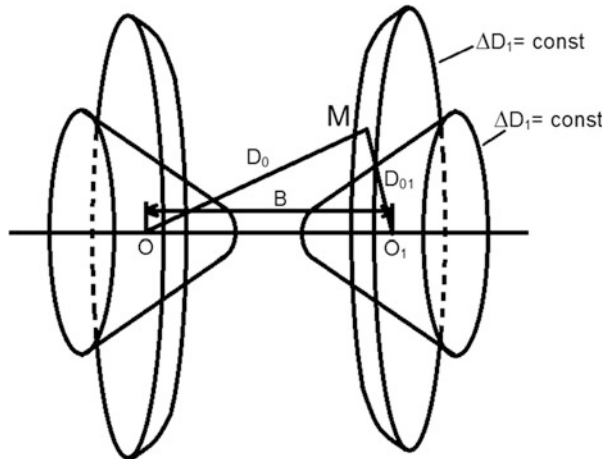
In distance difference measurement, radio navigation systems, the distances from two ground stations to aircraft are taken as navigation parameters (Krinetskiy, 1979). The measurement of ΔD distance differences allow to determine that the aircraft locates on $\Delta D = \text{constant}$ state surface. This surface is in the form of rotating hyperboloids of the two-leaf stage which has measurement stations on O and O_1 centers (Fig. 2).

The aircraft's position is found as the intersection point of three state surfaces. Therefore, the distance difference measurement radio navigation system includes four ground stations. One of these stations is the router (main station) and the others are directed (assistant stations). With the help of signals sent by the main station, three directed stations are provided to work synchronously. With the distance difference method, we derive the following expressions and get x , y , and z coordinates of an aircraft:

$$x_1x + y_1y + z_1z - D\Delta D_1 = f_1 \tag{14}$$

$$x_2x + y_2y + z_2z - D\Delta D_2 = f_2 \tag{15}$$

Fig. 2 Illustration of the state surfaces in the distance difference measurement method



$$x_3x + y_3y + z_3z - D\Delta D_3 = f_3 \quad (16)$$

Here,

$$\Delta D_1 = D - D_1$$

$$\Delta D_2 = D - D_2$$

$$\Delta D_3 = D - D_3$$

are the range differences.

$$f_1 = \frac{1}{2} (l_1^2 - \Delta D_1^2);$$

$$f_2 = \frac{1}{2} (l_2^2 - \Delta D_2^2)$$

$$f_3 = \frac{1}{2} (l_3^2 - \Delta D_3^2)$$

Via solving (14), (15), and (16) equations, the expressions required for the aircraft coordinates x , y , and z are found.

5 Determination of Aircraft's Coordinates by Integrated Method

Measurement of angle and measurement of distance methods are used at the same time in the integrated method (Haciyev, 1999). The integrated method is usually used in radiolocation systems, and it determines D distance to the aircraft, azimuth angle α , and elevation angle β . When this method is used, the coordinates of the aircraft are determined as the intersection point of the sphere state surface ($D = \text{constant}$), cone state surface ($\beta = \text{constant}$), and vertical plane suitable for $\alpha = \text{constant}$ state surface (Fig. 3). The aircraft coordinates are determined with a single point (ground station) with the help of this method without the need for difficult calculations.

The following formulas are used to calculate aircraft coordinates:

$$\begin{aligned} x &= D \cos \beta \cos \alpha \\ y &= D \cos \beta \sin \alpha \\ z &= D \sin \beta \end{aligned} \quad (17)$$

Distance, azimuth, and elevation angles are determined by radiolocation measurements. A single radiolocation station is enough for this method.

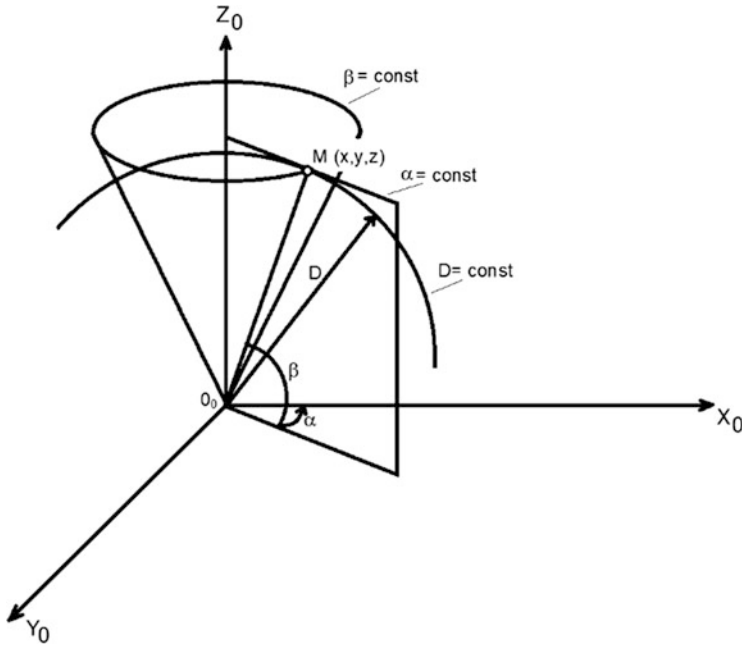


Fig. 3 Illustration of the state surfaces in the integrated method

6 Simulation Results and Discussion

The distance measurements are simulated via the equation below:

$$D_{z_i} = \sqrt{(x_i - x)^2 + (y_i - y)^2 + (z_i - z)^2} + b + \sigma_D \text{randn} \tag{18}$$

where $x_i, y_i,$ and z_i are the coordinates of the ground radio navigation stations, b is the bias in the distance measurements, and σ_D is the standard deviation of random distance measurement error, which is $\sigma_D = 10$ m in simulations.

The simulations are performed for the azimuth angle α and elevation angle β via the expressions below:

$$\begin{aligned} \alpha &= \text{ArcTan} \left[\frac{Y}{X} \right]; \\ \beta &= \text{ArcTan} \left[\frac{Z}{X} \text{Cos} \alpha \right] \end{aligned} \tag{19}$$

The simulation results and error analysis show that the distance difference method gives more accurate position results. The distance difference measurement method simulation results along the x and y axes are given in Fig. 4 and Fig. 5, respectively.

Fig. 4 Absolute error along the x -axis when using the distance difference measurement method

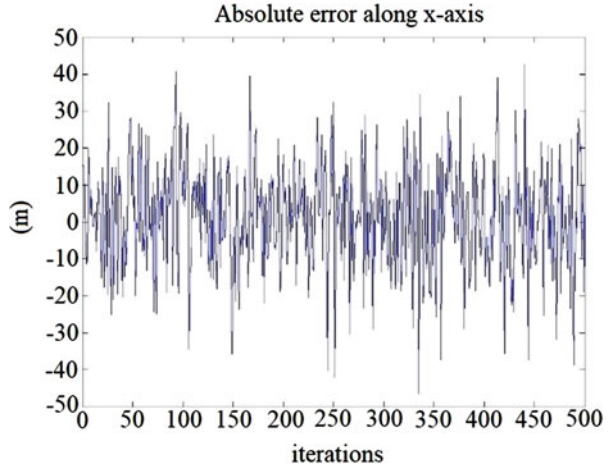
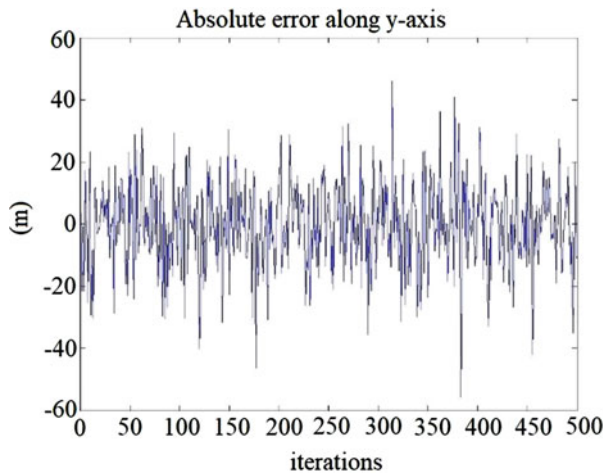


Fig. 5 Absolute error along the y -axis when using the distance difference measurement method



The aircraft position error analysis led to the result that the distance difference method is more accurate for horizontal x and y coordinates, while it is not as much as good for the vertical z coordinate. As seen from the graphs, the absolute error of horizontal x and y coordinates varies approximately between 30 m. The disadvantage of this method is that four ground stations are required for implementation.

Simulation results are also obtained for distance measurement and integrated methods. The obtained results show that the errors calculated in the distance measurement method are smaller than the errors found in the integrated angle measurement/distance measurement method. As a result, calculating the aircraft coordinates with the distance measurement method is more advantageous than the integrated method. However, to implement the distance measurement method, three

ground stations are required, whereas only one station is necessary for the integrated method.

7 Conclusion

In this study, the accuracy of the different terrestrial radio navigation methods is investigated. The distance measurement, distance difference measurement, and integrated angle measurement/distance measurement aircraft position determination methods are taken into consideration. Simulations were carried out for aircraft flight dynamics. The position values that are determined by the presented methods were compared with the actual values.

Simulation and error analysis led to the result that the distance difference method is superior and gives more accurate position results. It was observed that the distance measurement method errors were smaller than the errors of the integrated method.

The demonstrations also show that the examined aircraft position determination methods are more accurate in determining the horizontal x and y coordinates than the vertical z coordinate determination.

References

- Erkal, Y., & Hacıyev, Ç. (2004). Determination of aircraft motion parameters using GNSS based on distance difference measurement and Doppler methods and error analysis. In *Aviation advanced technologies and applications symposium* (Vol. 1) December 9–10, 2004, Istanbul, Turkey.
- Hacıyev, Ç. M. (1999). *Radio navigation*. Istanbul Technical University.
- Hacıyev, Ç., & Üner, Ü. (1998, May 11–15). Guaranteed error analysis in determining the coordinates of aircraft by measuring distances. In *2nd aeronautical symposium*, 1998, Kayseri.
- Kayton, M., & Fried, W. R. (1997). *Avionics navigation systems*. Wiley.
- Krinetskiy, Y. I. (Ed.). (1979). *Flight tests of rockets and space apparatus*. Maşinostroyeniye. (in Russian).
- McLean, D. (1990). *Automatic flight control systems*. Prentice Hall International.

Development of an Efficient Finite Element Model for the Analysis of Buckling, Debonding, and Collapse Characteristics of Composite-Stiffened Panels Under Compressive Loading



Vasileios Mantzaroudis and Dimitrios Stamatelos

Contents

| | | |
|-----|---|-----|
| 1 | Introduction | 518 |
| 2 | Theoretical Background | 518 |
| 3 | Reference Benchmark Study and Finite Element Modeling | 519 |
| 4 | Results and Discussion | 521 |
| 4.1 | Modeling Debonding with No Composite Failure | 521 |
| 4.2 | Modeling Debonding with Composite Progressive Damage Modeling | 525 |
| 5 | Conclusions | 526 |
| | References | 526 |

Nomenclature

| | |
|-------|--|
| b | Total skin width (equal to total specimen width), mm |
| d | Initial debonded length, mm |
| h | Total stringer height, mm |
| l_e | Element length in FE model, mm |
| L | Total specimen length, mm |
| L_f | Free-to-buckle specimen length, mm |
| N_e | Number of elements in cohesive zone of the CZM |
| w | Element length in FE model, mm |

V. Mantzaroudis · D. Stamatelos (✉)

Laboratory of Strength of Materials, Division of Aeronautics, Applied Mechanics and Infrastructure, Department of Aeronautical Sciences, Hellenic Air Force Academy, Dekelia Air Force Base, Attica, Greece

e-mail: dimitrios.stamatelos@hafa.haf.gr

1 Introduction

An important feature of aircraft structures is their ability to resist a certain amount of damage (damage tolerance philosophy), under a series of loading scenarios. This importance lays in the knowledge of “what is left” from the structure after the damage initiation, i.e., its residual strength and behavior under a certain loading condition. A common damage of composite aircraft structures is the debonding between the interfaces of their components that often lead to their collapse. When such structures are analyzed numerically, during the design phase, the study of such phenomena can become very time-consuming and computationally expensive. By employing commercial FE software packages, for the analysis, certain techniques are used for studying the debonding behavior, such as the VCCT (virtual crack closure technique) and the CZM methods. The VCCT methods require a considerable amount of code development, while the CZMs are much easier in their programming. However, the CZMs are built in such a way that extremely refined meshes (elements with dimensions even of tenths of a millimeter) are required. Engineering approaches for the achievement of coarse meshes by modifying certain CZM parameters have been presented in the literature, and their applicability has been verified for simple debonding scenarios only, such as the double cantilever beam (DCB), i.e., Turon et al., 2007; Harper & Hallett, 2008; Turon et al., 2010; Alvarez et al., 2014; and Gliszczynski et al., 2019. The application of this methodology has not yet been attempted to complex structure, such as stiffened panels. Therefore, this method is extended to the cases of stiffened panels, and it is presented hereafter.

2 Theoretical Background

This contribution is based on the work previously presented by Turon et al., 2007, that presented an engineering methodology to determine the maximum normal (mode I) and shear (modes II–III) traction parameters of a bilinear CZM, as a function of the mesh size. Originally, CZMs when used with the nominal maximum tractions require extremely fine meshes, which usually lead to high solution time, especially when powerful workstations are not available or when iterative calculations are required, i.e., during the preliminary design stage. The analysis of Turon et al., 2007, is focused on an essential characteristic size of specimens under debonding, the “cohesive length zone,” which expresses the length from the crack tip to the point of the – still undamaged – interface where, under single mode loading (mode I or II–III), the developed normal (for mode I) and shear (for mode II–III) traction reach their maximum values. Regarding the finite element analysis (FEA) of such problems, a minimum number of elements are required to span the cohesive zone length. Previous studies (Turon et al., 2007) propose that the cohesive zone length must be between three and five elements (referred hereafter as N_c). Turon

et al., 2007, suggested that the cohesive zone length can be adapted to the selected mesh size, by modifying the maximum normal and maximum shear traction, for the bilinear CZM, but the fracture toughness must remain constant. In this way, an engineer can avoid the highly refined meshes, usually needed for the analysis of debonding phenomena with CZMs, by modifying the maximum normal and shear tractions. The last can be obtained utilizing Eq. 1 (see Nomenclature for explanation of the parameters):

$$\text{Modified traction (normal or shear)} = \sqrt{\frac{9\pi E_{22} G_c}{32 N_e l_e}} \quad (1)$$

3 Reference Benchmark Study and Finite Element Modeling

A single-stiffener compression specimen (SSCS) previously analyzed experimentally and numerically in the literature has been selected as a reference point to study the effectiveness of the bilinear CZM implemented in ANSYS[®] software. In this approach, the maximum normal and maximum shear traction parameters are modified according to the fore-mentioned engineering methodology, so they can be suitably adapted, based on Eq. 1, to increasingly coarser meshes. More specifically, taking under consideration the buckling phenomena typically arising in SSCS configurations, the FE models developed are assessed in terms of (a) prediction of load-displacement curve, (b) prediction of the debonded length at the end of the loading, and (c) total solution duration.

Initially, the FE model is developed implementing only the ability for debonding through the previously mentioned modified CZM, to evaluate the effectiveness of this modification method, without being affected by any composite failure predictions. Subsequently, apart from the debonding behavior, composite material failure criteria with stiffness degradation (progressive damage modeling (PDM)) implemented in ANSYS[®] software, are activated to realize the overall buckling, debonding, and collapse characteristics of the panel.

The experimental results acquired from Orifici et al., 2008, for a SSCS, are used as reference. Additionally, a comparison between the results of the present contribution, with corresponding ones from other numerical methods that analyze debonding phenomena, is carried out. In detail, the results of the present contribution are compared with the results achieved by Raimondo et al., 2015, where results from a standard and a modified VCCT are available. This modified VCCT is compared with results obtained with the standard VCCT, as well as with experimental results of the same SSCS of Orifici et al., 2008. The geometric characteristics of the examined SSCS are presented in Fig. 1 and Table 1. The material properties (IM7/8552 UD), of the specimen, are documented by Raimondo et al., 2015.

Fig. 1 SSCS geometry.
(Reproduced from Orifici et al., 2008)

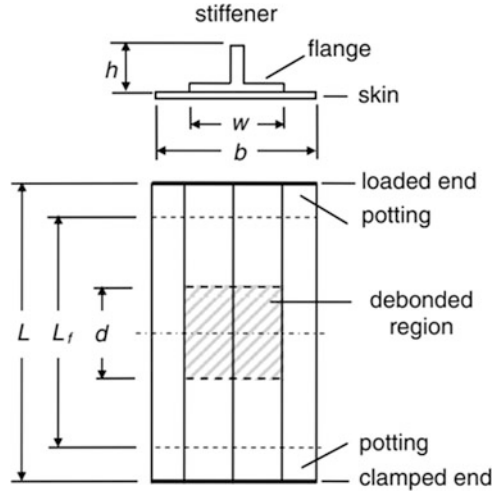


Table 1 Geometric properties and layup of the specimen (Orifici et al., 2008)

| Property | Value |
|-----------------------|--|
| L (mm) | 400 |
| L_f (mm) | 300 |
| b (mm) | 64 |
| h (mm) | 14 |
| w (mm) | 32 |
| d (mm) | 80 |
| Layup | Lamination code |
| Skin layup | [90/±45/0] _s |
| Stringer flange layup | [0 ₆ /±45 ₃] |
| Stringer web layup | [±45 ₃ /0 ₆] _s |

The skin and stringer components of the examined SSCS are modeled with layered solid-shell (SOLSH190) and layered solid (SOLID185) elements of the ANSYS[®] software library, for comparison reasons. The cohesion conditions between the skin and stringer of the SSCS are modeled with four-node surface-to-surface contact and target elements (CONTA173 and TARGE170 for each contact pair). For the skin-stringer interface that is initially bonded, a “bonded” contact type is activated, along with the definition of a CZM material, to enable possible further debonding during loading. The initially debonded part of the interface is modeled with a “standard” contact type because only interpenetration of surfaces is taken under consideration for this part. Four element lengths are examined, namely, 1.25, 2.5, 5, and 10 mm, and the respective values of the CZM maximum normal and shear tractions are calculated according to Eq. 1. The results of the modified CZM are also compared with the results obtained without using any modification to the nominal

Table 2 Material properties of the specimen

| Property | Value |
|--|-------|
| E_{11} (GPa) | 147.8 |
| $E_{22} = E_{33}$ (GPa) | 11.8 |
| $G_{12} = G_{13}$ (GPa) | 6 |
| G_{23} (GPa) | 4 |
| $\nu_{12} = \nu_{13}$ | 0.3 |
| ν_{23} | 0.45 |
| Max normal traction (mode I) (MPa) | 50 |
| Max shear traction (mode II) (MPa) | 100 |
| G_{Ic} (J/m ²) | 243 |
| $G_{IIc} = G_{IIIc}$ (J/m ²) | 514 |

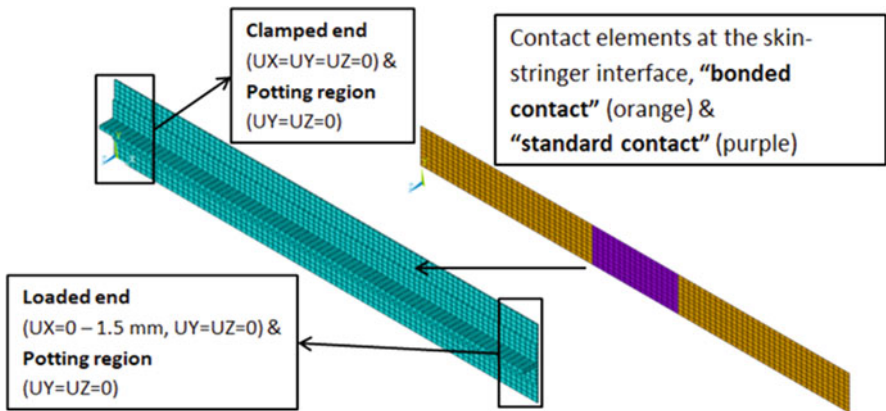


Fig. 2 The FE model of the SSCS

values of Table 2. In Fig. 2, a typical FE model of the SSCS under consideration along with the boundary conditions used is depicted.

4 Results and Discussion

4.1 Modeling Debonding with No Composite Failure

Figure 3 shows a contour plot of the out of plane displacement of the FE model when the load is fully applied to the specimen. This is also the buckling mode of the SSCS, assuming 5-mm element length for the mesh of the model. However, it is obvious that there is a considerable difference in the displacement pattern, since the debonding behavior with and without modifying the CZM is quite different. More specifically, when the modified CZ method is used, the initial debonding grows

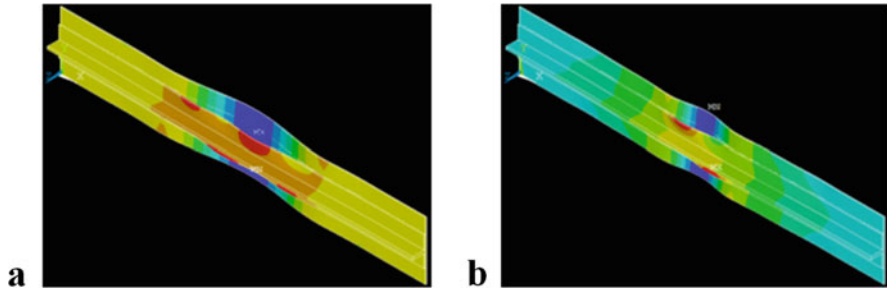


Fig. 3 Out of plane displacement contour plot at full load, when maximum traction parameters of the CZM are modified (a) and not modified (b)

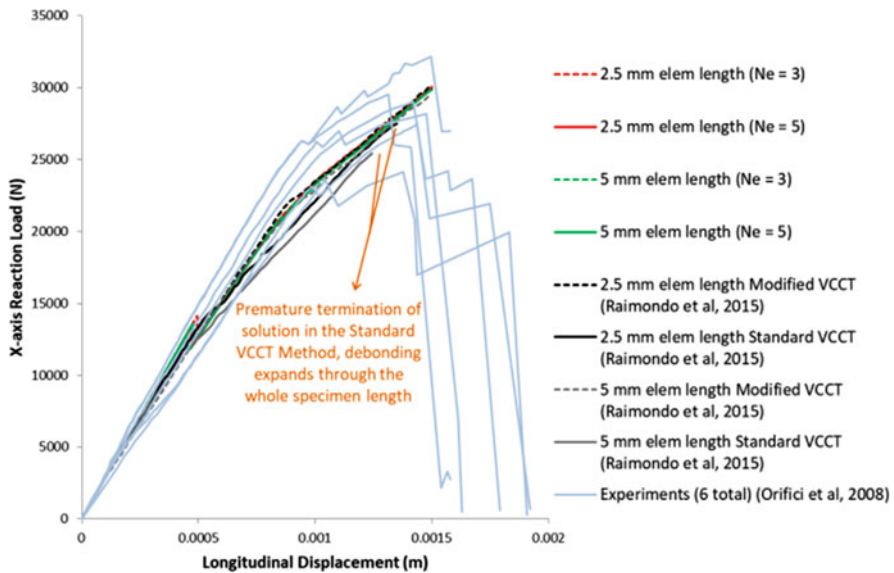


Fig. 4 Comparison of FE load-displacement results for SOLSH190 with numerical and experimental results from the literature selected, is proved; it is observed that when of the CZM is not modified, the predicted loads are much higher than the ones predicted by the modified CZM by a significant percentage of 10–12%

beyond its original length, something that does not happen when the CZM parameters are not modified.

In Fig. 4, load-displacement curves for the element type SOLSH190, when the modified CZM is applied, are compared with the respective experimental and numerical results from the literature. The numerical work by Raimondo et al., 2015, uses 2.5- and 5-mm element lengths; hence, only the results from the FE models with these element lengths are presented in this graph. The numerical results

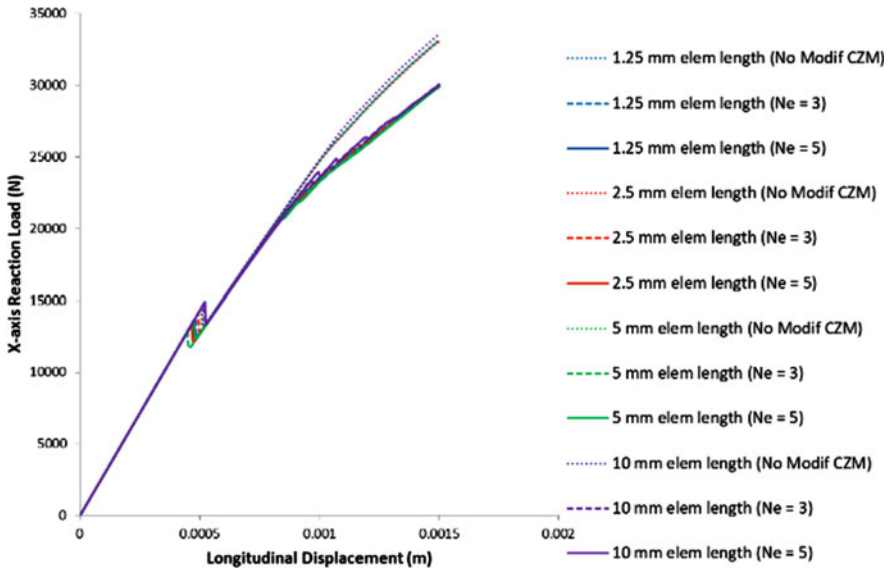


Fig. 5 FE load-displacement results with all the parameters included, for SOLSH190

are meaningful up to a longitudinal displacement of 1.5 mm, because after this value, the experiments showed intralaminar damage (fiber and matrix fracture). However, in the present FE models, the intralaminar damage is not implemented, since the focus of this work is the debonding behavior predicted by the CZM. An excellent agreement is achieved between the modified CZM used here and the modified VCCT presented by Raimondo et al., 2015, as well as with the experimental results up to the point of interest (longitudinal displacement 1.5 mm). In Fig. 5, the load-displacement curves for SOLSH190 element type, for all element lengths and values of CZM parameter N_e , are presented (it is mentioned that almost identical results are gained when the SOLID185 element type is used). Additionally, in this graph, results obtained without modifying the CZM parameters are also included. By simultaneously examining the results from Figs. 4 and 5, the necessity of the implementation of the CZM modifications, according to the mesh size.

Another important aspect of the FE model is its ability to predict the total debonded length when the load is fully applied. Figure 6 presents a comparison of the FE results obtained for 5-mm element length for both element types (SOLID185 and SOLSH190). The obtained results are compared with the respective experimental and numerical ones from the literature. The numerical results are obtained with a modified VCCT and a standard VCCT, where an excellent agreement is observed between them. It is remarkable that, when the CZM parameters are not modified, the debonding does not grow at all and retains to its initial length. However, the experimental results prove that the initial debonding length is growing during loading. Consequently, the necessity of the CZM modification method is proved.

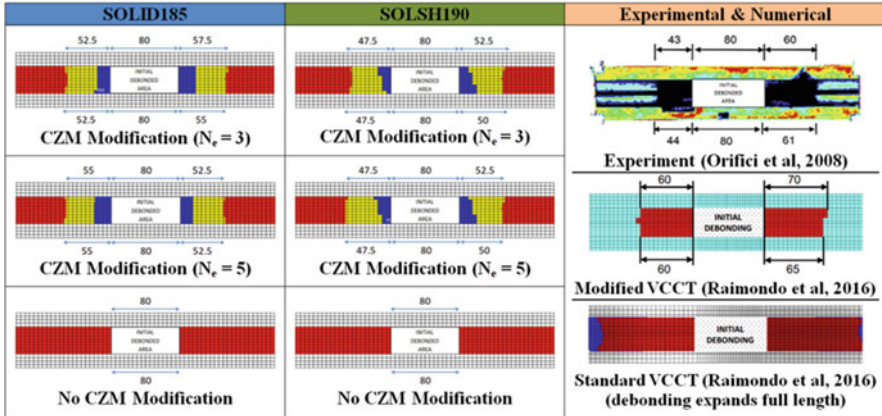


Fig. 6 Comparison of final debonding length between FEM (5-mm element length), experimental and numerical (VCCT)

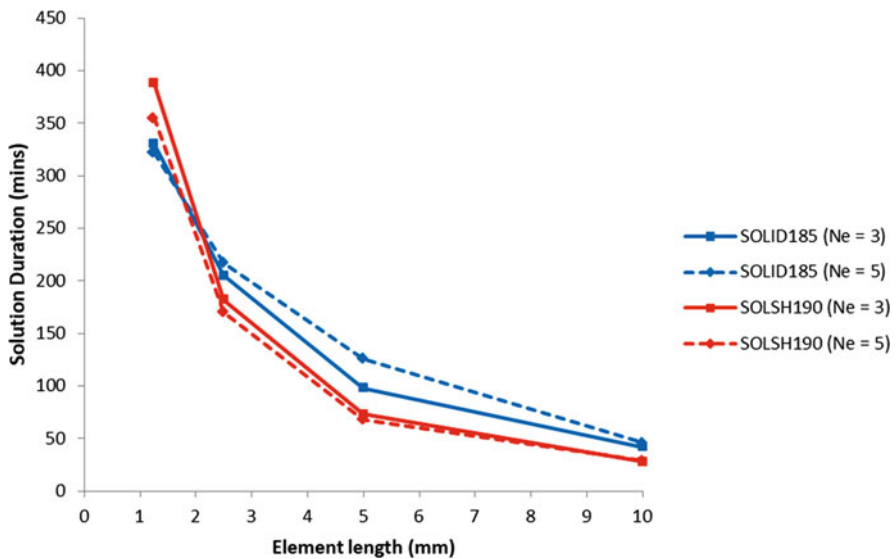


Fig. 7 Solution time versus element length

A final important feature of the developed FE models is their ability to produce accurate results with reduced solution time. This feature is essential especially when either powerful workstations are not available or iterative analyses are required. In Fig. 7 the solution time when the modified CZM is employed (both N_e parameter values and element types are included) versus the element length is presented. It is impressive that the reduction of the solution time from the finest mesh to the coarsest

one is approximately 85–90% (all calculations were performed in a Workstation with a 12-core AMD Ryzen 9 processor, 64 GB of DDR4 RAM).

4.2 Modeling Debonding with Composite Progressive Damage Modeling

The presented FEM incorporated only the debonding capability. It is now enriched with PDM capabilities, meaning activation of composite failure criteria accompanied with instant stiffness degradation. The aim is to examine the FE model's ability to simulate the actual behavior of the SSCS specimen. Hashin failure criteria are used for composite failure, accompanied with three (3) stiffness reduction factors (namely 90%, 85%, and 80% reduction), which are common degradation values for fiber and matrix failure modes. A typical load-displacement curve is shown in Fig. 8 for the SOLSH190 element type (element length of 5 mm) compared to the experimental results from Orifici et al., 2008. It is noted that the selection of the stiffness reduction factor plays an important role on the behavior of the model, but in general, all three (3) selected reduction factors yielded to results within the range of the six (6) SSCS experimental curves. Figure 9 presents a comparison of the collapse mode between the FE results and the corresponding experimental. It is obvious that the predictions of the FE models are in a satisfactory correlation with the respective experimental.

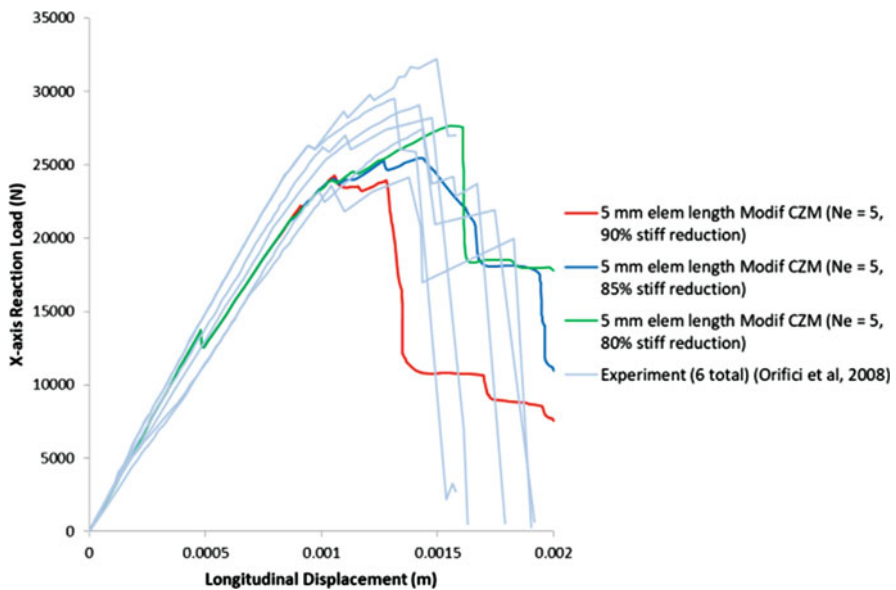


Fig. 8 FE load-displacement results for SOLSH190 incorporating modification of the CZM and PDM stiffness degradation

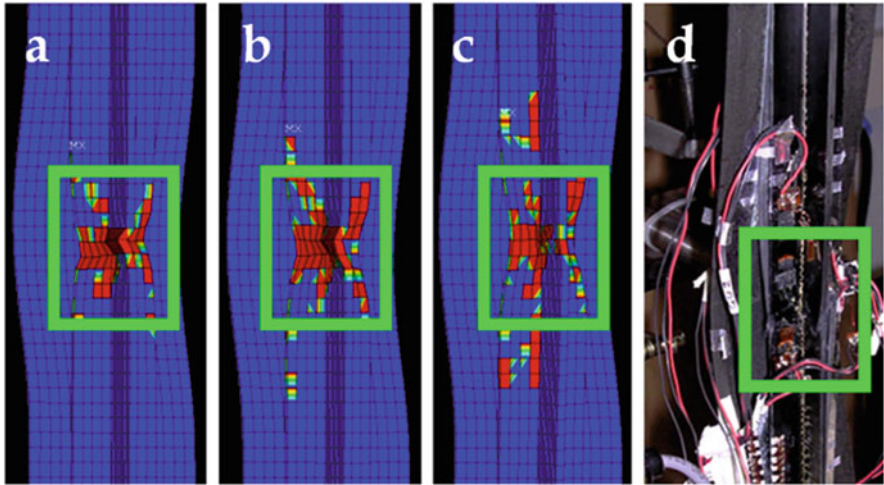


Fig. 9 Collapse mode for FEM (a, b, c) and experimental test (d) (90 (a), 85 (b), and 80% (c) stiffness reduction factor)

5 Conclusions

In this contribution, an engineering methodology from the literature, intended to properly modify the nominal maximum normal and shear tractions of bilinear CZMs, is employed to the desired mesh size of a single-stringer composite panel with initial debonding. The obtained results, as compared with the respective experimental and numerical from the literature, demonstrate the necessity and efficiency of the modified CZM. Moreover, the proved efficiency of the methodology even with coarse meshes can lead to large reductions on the solution time, without affecting the accuracy of the results. The additionally activated composite material progressive damage capabilities demonstrated the usability of the developed FEM in simulating the entire structural behavior of the specimen examined.

Further work for enhancing the present FE model could focus on more advanced theories for modifying CZM, as well as on incorporating more advanced user-programmable methods of composite material failure and degradation rules. Extension of the results in larger, more complicated structures is of interest as well.

References

- Alvarez, D., Blackman, B. R. K., Guild, F. J., & Kinloch, A. J. (2014). Mode I fracture in adhesively bonded joints: A mesh-size independent modeling approach using cohesive elements. *Engineering Fracture Mechanics*, *115*, 73–95.
- Gliszczynski, A., Samborski, S., Wiacek, N., & Rzczkowski, J. (2019). Mode I Interlaminar fracture of glass/epoxy unidirectional laminates. Part II: Numerical analysis. *Materials*, *12*, 1604.

- Harper, P. W., & Hallett, S. R. (2008). Cohesive zone length in numerical simulations of composite delamination. *Engineering Fracture Mechanics*, 75, 4774–4792.
- Orifici, A. C., De Zarate Alberdi, I. O., Thomson, R. S., & Bayandor, J. (2008). Compression and post-buckling damage growth and collapse analysis of composite stiffened panels. *Composites Science and Technology*, 68, 3150–3160.
- Raimondo, A., Riccio, A., & Scaramuzzino, F. (2015). A robust numerical approach for the simulation of skin-stringer debonding growth in stiffened composite panels under compression. *Composites Part B Engineering*, 71, 131–142.
- Turon, A., Davila, C. G., Camanho, P. P., & Costa, J. (2007). An engineering solution for mesh size effects in the simulation of delamination using cohesive zone models. *Engineering Fracture Mechanics*, 74, 1665–1682.
- Turon, A., Camanho, P. P., Costa, J., & Renart, J. (2010). Accurate simulation of delamination growth under mixed-mode loading using cohesive elements: Definition of interlaminar strengths and elastic stiffness. *Composite Structures*, 92, 1857–1864.

A Conceptual Inventory of Entropy Management About Exergetic Sustainability Based on Different Cruise Altitude for Aircraft Engines



M. Ziya Sogut, Enver Yalcin, and Tahir Hikmet Karakoc

Contents

| | | |
|---|---|-----|
| 1 | Introduction | 529 |
| 2 | Turboprop Engines | 530 |
| 3 | Entropy Management and Conceptual Inventory | 531 |
| 4 | Results and Discussion | 533 |
| 5 | Conclusion | 536 |
| | References | 537 |

1 Introduction

Although the aviation sector suffered a significant loss as a result of the global threat of COVID-19, sectoral expectations and scenarios show that the demand increase trend will continue. As a matter of fact, in addition to sectoral developments, increased aircraft deliveries since the 2000s with new route sources support the developments in this regard (Boeing, 2016).

M. Z. Sogut (✉)
Maritime Faculty, Piri Reis University, Istanbul, Turkiye

E. Yalcin
Department of Mechanical Engineering, Faculty of Engineering, Balikesir University, Balikesir, Turkiye
e-mail: eyalcin@balikesir.edu.tr

T. H. Karakoc
Faculty of Aeronautics and Astronautics, Eskişehir Technical University, Eskişehir, Turkiye
Information Technology Research and Application Center, Istanbul Ticaret University, Istanbul, Turkiye

While the sectoral competition process makes technology management valuable, on the other hand, developments in aircraft engine technologies show an improvement of over 60% in efficiency potentials since the 1960s. Turboprop and turbofan engines, which are mostly prominent in today's aircrafts, have provided significant gains in reducing environmental pollution as well as their technological advantages (Gobbi et al., 2011). It is seen that aircraft engines have an important environmental problem related to irreversibility, mostly in parallel with fossil fuel consumption. It is seen that the production of entropy due to irreversibility in engines operating on the basis of thermodynamic cycle has important impact criteria in terms of environmental sustainability.

In aircraft engines, load and power analysis, mostly used sectoral evaluation method, are considered in the context of dynamic analysis. However, the generation of power associated with the combustion process should be directly evaluated on the basis of thermodynamic principles related to the engine. This will also be the main criterion for evaluating the environmental impacts caused by fuel consumption (Parker, 2009). Fuel and combustion process, which is one of the pillars caused by the inefficiency in engines, are evaluated by direct energy and exergy analysis. These processes, which are also defined as the thermal performance effect, are also the result of exergy destruction as an environmental effect. This feature indicates the basic load of entropy, which is formed by environmental impact. Irreversibility due to the dead state in environmental conditions also represents the potential associated with fuel or combustion loss of the engine. Performance analyzes, especially in turboprop engines, can be seen as process analyzes that should be evaluated.

Altitude conditions are the main criteria that directly affect engine efficiency in different climatic conditions. However, the inefficiency of engines in their flight processes is also a potential that can be defined in this respect. In this study, firstly, the performance efficiency of a turboprop engine with different temperature values in cruise conditions is discussed with thermodynamic analyzes. Especially in different altitude conditions, the entropy characteristics of the engine due to irreversibility and the defined environmental criteria were evaluated, and a conceptual inventory criterion expressing sustainability was created.

2 Turboprop Engines

Turboprop engines are one of the engine technologies that are increasing in importance in the sector. In engine performance, they are expressed as high-performance engines at low and medium speeds (below 400 mph), with effective speed characteristics in altitude conditions. In engine dynamics, they are considered as engines that stand out with their improved speed performance efficiency as a combination of turbojet and piston engines. Compared to other engines, they have high performance between 250 and 400 mph, especially in the 18,000-ft to 30,000-ft range. However, these motors also have advantages over other motors in their low-speed profile. The optimal altitude condition of the engines depending on the

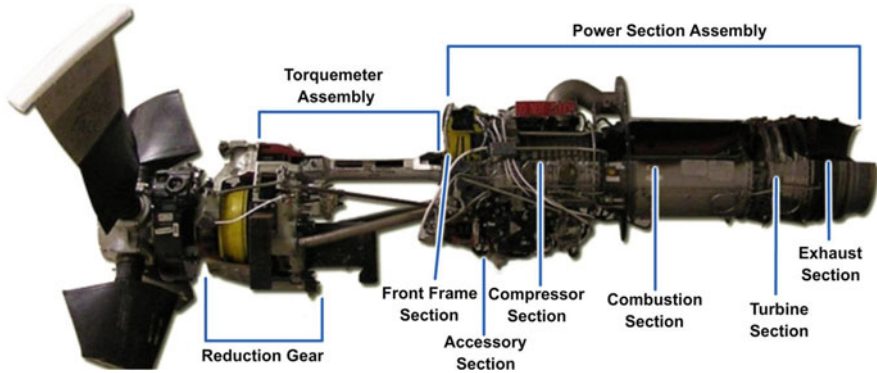


Fig. 1 A turboprop engine (CNATT; 2016)

altitude is expressed as 25,000 ft. In addition to mechanical reliability, indicators such as light weight, operational convenience, minimum vibration, and high-power generation per unit weight can be counted as manufacturing features (FAA, 2016). Although these engines, which are alternatives for unmanned aerial vehicles in recent years, are mostly preferred in low-altitude helicopters, trainers, and private planes, it is seen that this scale has increased in recent years. The propulsion effect is important in these engines, which are mostly based on the Brayton cycle in the context of the thermodynamic cycle feature. This engine and its components can be seen in Fig. 1.

In this study, the environmental performances of the engines depending on the altitude conditions were evaluated, and a conceptual inventory was developed in this context. Especially environmental conditions for engines directly affect fuel consumption and engine performance. For the reference PT6-21 engine, thermal and environmental performances due to different ambient temperatures under two different altitude conditions were examined. Depending on the environmental indicators defined in the inventory, the performances of the engine according to the altitude characteristics were examined.

3 Entropy Management and Conceptual Inventory

It is seen that many studies have been carried out in the management of fossil fuel-based environmental sustainability in the aviation sector. Although it seems small, the aviation industry is a sector that has a significant impact as a result of intense fossil fuel resource use, with a potential of approximately 3% in the fight against global climate change. In this respect, effective and efficient management of fossil fuel consumption in flight processes primarily depends on a potential determination.

As in all flight processes, environmental conditions related to altitude conditions also affect performance. Therefore, different interactions emerge when altitude-related performances are evaluated together with environmental conditions. In this respect, the first law analysis will give a quantitative result, while the second law will give real performance results depending on the nature of the environmental conditions. Therefore, it is important to establish a model framework for the performance effects of environmental parameters encountered according to the engine’s altitude conditions. In this context, a conceptual inventory has been developed in order to develop the criterion of environmental sustainability based on the thermodynamic approach. This approach is a research-level tool developed to test conceptual understandings (Lindell et al., 2007; Jorion et al., 2015). A number of key concepts related to the subject have been developed on the basis of integrity that allows for the elimination of misconceptions. Such a flow model is very important for measuring conceptual intelligibility. The intended results of this concept inventory play a role in creating the right key to environmental sustainability. Accordingly, the following equations in Table 1 are used in the thermal performance analysis of the engine.

In this study, entropy management requires an exergy-based flow. These are exergy flow, exergy destruction, and entropy generation. However, an inventory criteria were defined for entropy. These are given in Table 2.

Table 1 Equations of energy and exergy analysis (Dincer & Rosen, 2012; Cornelissen, 1997; Moran et al., 2011; Van Gool, 1997)

| Name | Equation |
|-----------------------|---|
| Mass balance | $\sum \dot{m}_{in} = \sum \dot{m}_{out}$ |
| Energy balance | $\sum \dot{E}_{in} = \sum \dot{E}_{out}$ $\dot{Q} - \dot{W} + \sum \dot{E}_{in} - \sum \dot{E}_{out} = 0$ $\dot{Q} - \dot{W} = \dot{m} \left[h_2 - h_1 + \frac{v_2^2 - v_1^2}{2} + g(z_2 - z_1) \right]$ |
| Exergy | $\sum \dot{E}x_i = \dot{E}x_k + \dot{E}x_p + \dot{E}x_{ph} + \dot{E}x_{ch}$ |
| Exergy balance | $\sum \dot{E}x_{in} - \sum \dot{E}x_{out} = \sum \dot{E}x_{dest}$ |
| Exergy work | $\dot{E}x_{work} = \dot{W}$ |
| Exergy flow | $\dot{E}x_{mass} = \sum \dot{m}\psi$ $\psi = (h - h_0) - T_0(s - s_0)$ |
| Energy efficiency | $\eta_I = \frac{\dot{E}_{out}}{\dot{E}_{in}}$ |
| Exergy efficiency | $\eta_{II} = \frac{\dot{E}x_{out}}{\dot{E}x_{in}} = 1 - \frac{\dot{E}x_{dest}}{\dot{E}x_{in}}$ |
| Improvement potential | $\dot{I}P = (1 - \eta_{Ex})(\sum \dot{E}x_{in} - \sum \dot{E}x_{out})$ |

Table 2 Entropy management criteria (Sogut et al., 2015, Sogut 2020)

| Criteria | Symbol | Equation |
|---------------------------------|----------|--|
| Exergy renewability | α | $\alpha = E_{x_{in,rev}}/E_{x_{in}}$ |
| Depletion number | D_P | $D_P = E_{x_{dest}}/E_{x_{in}}$ |
| Environmental compatibility | ζ | $\zeta = E_{x_{in,e}}/(E_{x_{in}} + E_{x_{in,abatement}})$ |
| Environmental performance index | EPI | $EPI = \left(\frac{\sum S_{gen}}{\sum E_{x_{in}}} \right) * T_0$ |
| Sustainability index | SI | $SI = \left(\frac{\sum S_{gen,e}}{\sum E_{x_{in}}} \right) * T_0$ |

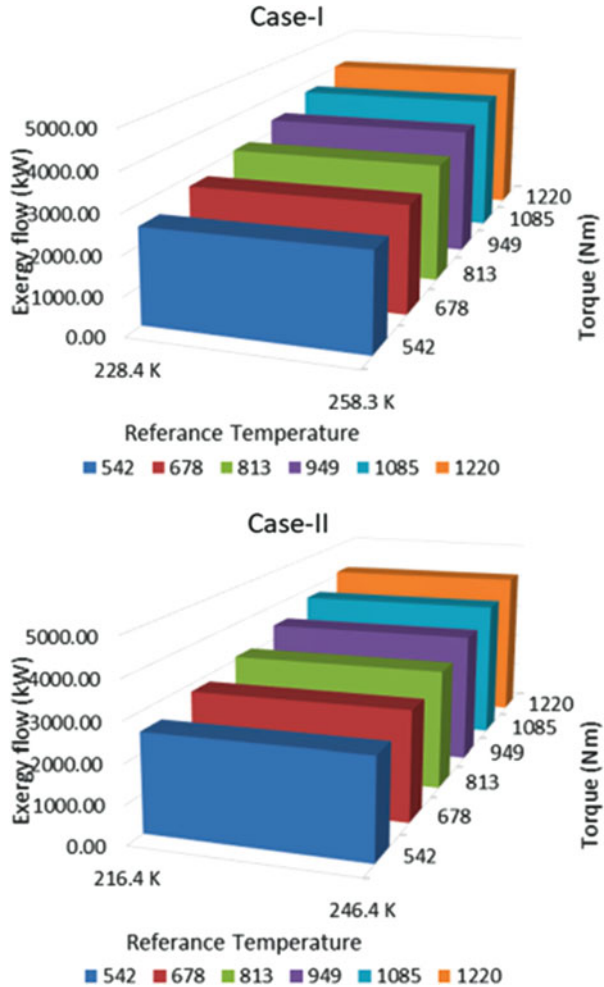
Table 3 Technical features of the reference engine (Jetprop, 2016)

| 15,000 Ft | | | | | | | |
|------------------|---------|------------------------|-----------|------------------------|-----------|-----------------------|-----------|
| Np (rpm) | Torque | Case I | | Case II | | Case III | |
| | | Temperature (-44.6 °C) | | Temperature (-14.7 °C) | | Temperature (13.6 °C) | |
| | | Air sped | Fuel flow | Air sped | Fuel flow | Air sped | Fuel flow |
| | Nm | KTAS | gph | KTAS | Gph | KTAS | gph |
| 2200 | 542.33 | 134 | 22 | 137 | 22.6 | 135 | 26 |
| | 677.91 | 160 | 24.5 | 165 | 25.1 | 168 | 28 |
| | 813.49 | 177 | 27.3 | 183 | 27.7 | 188 | 31 |
| | 949.07 | 188 | 29.9 | 195 | 30.6 | 202 | 33 |
| | 1084.65 | 200 | 32.9 | 207 | 33.6 | - | - |
| | 1220.24 | 209 | 36.2 | 217 | 36.9 | - | - |
| 21,000 Ft | | | | | | | |
| | | Temperature (-56.6 °C) | | Temperature (-26.6 °C) | | Temperature (3.4 °C) | |
| 2200 | 542.33 | 134 | 22 | 137 | 22.6 | 135 | 26 |
| | 677.91 | 160 | 24.5 | 165 | 25.1 | 168 | 28 |
| | 813.49 | 177 | 27.3 | 183 | 27.7 | 188 | 31 |
| | 949.07 | 188 | 29.9 | 195 | 30.6 | 202 | 33 |
| | 1084.65 | 200 | 32.9 | 207 | 33.6 | | |
| | 1220.24 | 209 | 36.2 | 217 | 36.9 | | |

4 Results and Discussion

The environmental effects of engines are a direct result of their energy performance in relation to the thermodynamic properties of the altitude. In this respect, first of all, the extent of the possible irreversibility of the reference engines under the defined altitude conditions is discussed. In this respect, the criterion of irreversibility has been handled according to the inventory defined above as an improvable criterion. Thermodynamic parameters according to the altitude characteristics of the reference engine in this study are given in Table 3.

Fig. 2 Exergy flow rate at cruise altitude



The thermodynamic irreversibility of the aircraft under the defined altitude conditions was investigated and studied for the defined altitude properties as Case I and Case II. For this feature, which is defined as exergy destruction in the literature, the distributions depending on both conditions are given in Fig. 2.

The total exergy flow produced at the engine’s reference values should be evaluated together with the fuel consumption. In this context, the total exergy difference for both altitude conditions was examined for maximum and minimum temperature values. For Case II data, a 15.1% higher exergy flow occurs at maximum temperature, while this value is 15.2% at minimum temperature values. The difference in total fuel consumption for both streams is 2.1%. These values should be

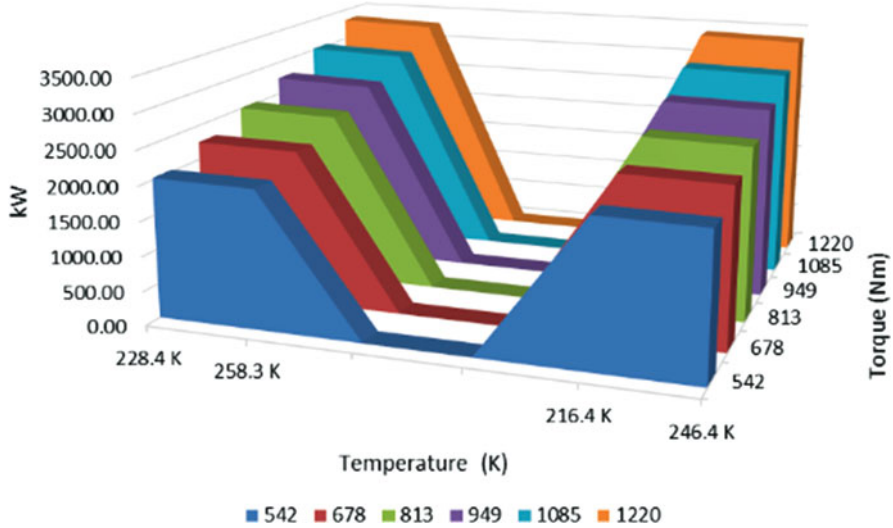


Fig. 3 Exergy destruction at cruise altitude

considered in terms of the extent of irreversibility in terms of environmental impact. In this context, the criterion defining the irreversibility of the engine for both cases, exergy destruction, was examined, and the distributions are given in Fig. 3.

Exergy destruction appears to be directly affected by altitude temperatures. In particular, the change in altitude values of exergy destruction due to torque change has been examined in maximum and minimum temperature values for both cases. For Cases I and II, there was a 34.07% improvement potential at maximum temperature changes. However, it has been observed that this rate of change has a low performance of 2.47% for low temperatures. Especially in these consumption behaviors, entropy generation also has a significant change potential. The entropy distributions of this change are given in Fig. 4.

The entropy produced is important for the evaluation of environmental sustainability potential. In this respect, the relationship between energy potential and altitude has been evaluated. When the maximum temperatures of the motor for both cases are evaluated, it is seen that the potential is 30.95% less for 228.4 K. However, in the low-temperature evaluation, this effect is 7.42% for 258.4 K. All these values make the temperature scale valuable for the determination of altitude in the entropy generation of the engine. Figure 5 shows the engine’s savings potential in the generation of entropy due to the enhancement potential.

The potential for improvement in entropy generation due to the IP potential of the engine shows a potential of 84.2% for Case I and 82.2% for Case II. All these evaluation criteria are important in terms of the effects of emission management.

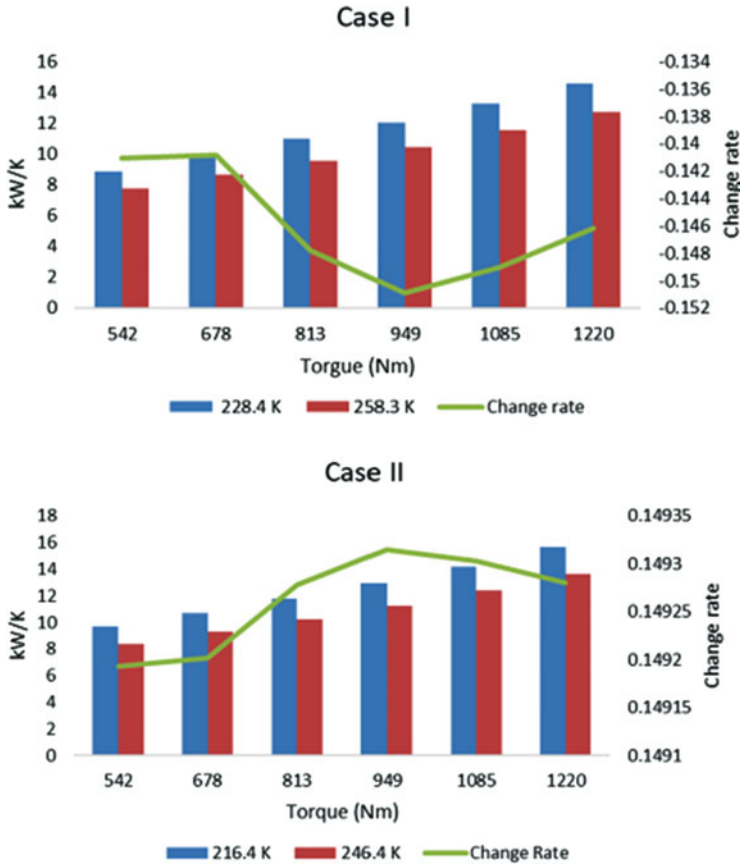


Fig. 4 Entropy generation at cruise altitude

5 Conclusion

This study is primarily based on an inventory study based on indicators based on entropy management. In this context, a performance analysis based on two defined cruise conditions was carried out on a reference turboprop engine. Especially in terms of environmental sustainability, it has been seen that the irreversibility potential of the engine due to entropy generation has a potential proportional to the altitude temperatures. It has been observed that the temperature control of the engine in terms of altitude loads affects engine performance along with entropy production. It is foreseen that the study can be improved by examining the concepts in the defined inventory for the development of manageable indicators.

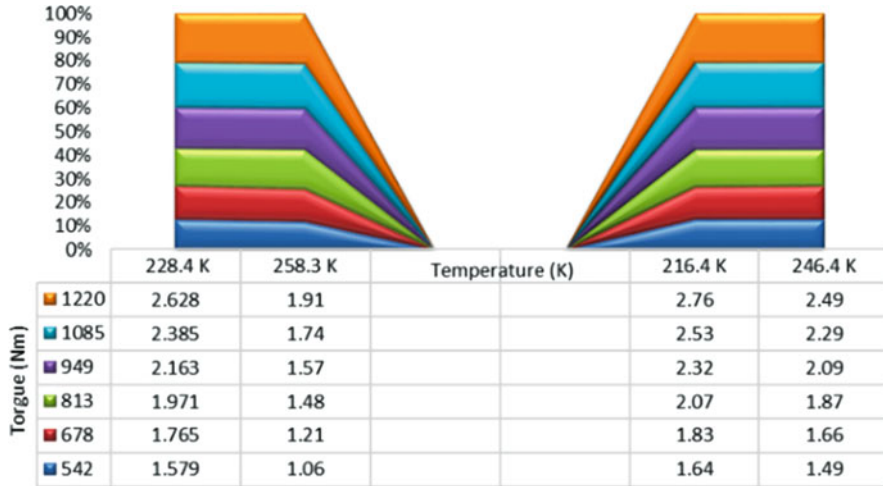


Fig. 5 Entropy production after IP effect

References

Boeing, Current market outlook 2016–2035, Boeing Commercial Airplanes Market Analysis, Seattle, WA, 98124–2207. <https://www.docdroid.net/rpHW9nm/boeing-current-market-outlook-2016-2035-pdf#page=54>

CNATT, (2016). CNATT Rate Training Manager 230 Chevalier Field Avenue Pensacola, FL 32508.

Cornelissen, R. L. (1997). *Thermodynamics and sustainable development: The use of exergy analysis and the reduction of irreversibility*. PhD Thesis, University of Twente, The Netherlands.

Dincer, I., & Rosen, M. A. (2012). *Exergy: Energy, environment and sustainable development*. Elsevier.

FAA. (2016). Chapter 14: Transition to turbopropeller-powered airplanes. In *Airplane flying handbook*. https://www.faa.gov/regulations_policies/handbooks_manuals/aviation/airplane_handbook/media/16_afh_ch14.pdf

Gobbi, G., Lightening, B., Sträter, B., & Majka, A. (2011). *Report on current strength and weaknesses of existing seaplane/ amphibian transport system as well as future opportunities including workshop analysis*. FUSETRA – Future Seaplane Traffic, Version 1.0. www.FUSETRA.eu

Jetprop. (2016). Dash34_Performance_Charts, Description and Operation of The Airplane and its systems, East 6427 Rutter Ave, Spokane, WA 99212. http://www.jetprop.com/sites/all/docs/charts/Dash34_Performance_Charts.pdf

Jorion, N., Gane, B. D., James, K., Schroeder, L., Dibello, L. V., & Pellerino, J. W. (2015). An analytic framework for evaluating the validity of concept inventory claims. *Journal of Engineering Education*, 104(4), 454–496.

Lindell, R. S., Peak, E., & Foster, T. M. (2007). Are they all created equal? A comparison of different concept inventory development methodologies. *AIP Conference Proceedings*, 883, 14–17). Syracuse, New York. <https://doi.org/10.1063/1.2508680>

- Moran, M. J., Shapiro, H. N., Boettner, D. D., & Bailey, M. B. (2011). *Fundamentals of engineering thermodynamics*. Wiley.
- Parker, R. (2009). From blue skies to green skies: Engine technology to reduce the climate-change impacts of aviation. *Technology Analysis and Strategic Management*, 21(1), 61–78.
- Sogut, M. Z. (2020). Investigation of entropy optimization related to thrust control for jet engine in atmospheric elevation. In *International symposium on sustainable aviation (ISSA)*. Universiti Putra Malaysia.
- Sogut, M. Z., Altıntaş, O., & Soner Aplaç, H. (2015). Indicators based on exergy approach for the turbofan engine. In *International symposium on sustainable aviation 2015*, 31 May, 03 June 2015, İstanbul.
- Van Gool, W. (1997). Energy policy: Fairy tales and factualities. *Innovation and technology strategies and policies*, 93–105. https://doi.org/10.1007/978-0-585-29606-7_6

Index

A

Acoustic emissions (AEs), 388, 389, 392, 394, 398, 399, 401–404
Acousto-ultrasonic (AU), 388, 389, 392, 394
Active load fluctuation suppression, 358, 363–365
Actuator disk, 142, 143
Additive manufacturing, 231
Aeroacoustics, 290–296
Aerodynamic heating, 369, 376, 389
Aeronautics, 50, 273–278, 455
Aerospace structures, 3, 398
AI, 427, 428, 430
Aircraft, 3, 8–15, 26–31, 61–65, 105–111, 131, 136, 137, 140, 185, 200, 202, 206, 209–217, 221, 240, 273, 274, 290, 300–312, 324, 325, 332–340, 358, 359, 380, 381, 425, 427–430, 437, 458–464, 476, 507, 518, 529–536
Aircraft emissions, 459, 462
Aircraft engines, 105–111, 290, 431, 458, 529–536
Aircraft inspection, 209–217
Aircraft maintenance, 26–31, 61–65, 96–102, 209–213, 215, 426
Aircraft seats, 332–340
Airport, 28, 76–80, 113, 114, 117, 131, 200–203, 205, 215, 261, 290, 316, 320, 410, 435, 461–464
Airport buildings, 172, 176, 178
Airport management, 132, 135, 137
Air transport management, 50–59
Air transportation, 76, 105, 135, 316, 434

Analytic hierarchy process (AHP), 84–86, 88, 89, 93
Apollo AS-202, 370–372, 375, 376
Attitude estimation, 39–47
Autonomous drones, 53, 434, 437, 444
Autonomous flight trajectory, ix
AVGAS, 107, 108, 110, 111
Aviation, 26, 28, 30, 33–37, 76, 96, 111, 113, 114, 131, 132, 135–137, 200, 206, 209–212, 244, 273–278, 301, 315, 316, 320, 358, 407, 425, 430, 458–463, 529, 531
Aviation safety, 273–278

B

Barely visible impact damage (BVID), 398, 399, 403
Bird strike, 210, 211, 300–312
Blade, 181–184, 187, 189–191, 221, 224, 264, 301, 488
Buckling analysis, 518–526
Boeing fuel flow method, 154
Business intelligence, 29
Bypass mass injection, 350

C

Carbon fiber, 68, 69, 122, 123, 125, 196, 231, 451
Carbon nanotube (CNT), 468, 469, 471–473
Chip breaking, 33–37
Cloudiness factor, 172–175, 177, 178

- Cluster satellites, 282, 286
- Community aircrafts, 300, 312
- Composites, 1–4, 8–12, 15, 67–73, 121, 122, 194, 238, 302, 398, 399, 447–456, 467–473, 518–526
- Computational fluid dynamics (CFD), 143, 221, 291, 292, 342, 343, 352, 368, 369, 476, 480
- Consumer behavior, 317, 320
- Control mechanism, 196
- Converging-diverging micro nozzle, 350, 351
- Core stitching, 67–73
- Cork, 1–5
- Corporate performance, 114, 118
- Covid-19, 315–320, 325, 425, 529

- D**
- Damage, 8, 9, 12, 13, 27, 58, 102, 121, 122, 125, 201, 205, 210, 211, 216, 217, 244, 302, 308, 320, 368, 376, 388, 389, 398–404, 430, 453, 469, 518, 523
- Data analytics, 425–431
- Debonding, 68, 518–526
- Depth of cut, 33–35, 37
- Digitalization, 26–31
- Digital twins, 429–430
- Direct simulation Monte Carlo (DSMC), 350, 352, 355
- Distance measurement, 499, 508, 510–512, 514–516
- Distributed electric aero-propulsion, 140–150
- 6DOF model, 416
- Drag coefficient, 167, 184, 224, 293, 491
- Drones, 50–59, 209–217, 229–234, 434–437, 439–444
- Dynamic mechanical analysis, 238
- Dynamic oscillatory rig, 480–484

- E**
- Educational tool, 274
- Efficiency, 28, 62, 113, 134–136, 147, 148, 150, 152, 155–157, 165, 167, 187, 188, 190, 206, 217, 221, 222, 224, 225, 244, 328, 329, 342, 360, 430, 431, 442, 461, 462, 468, 526, 530, 532
- Electric aircraft, 140, 358
- Electric propulsion, 140–150
- Electrospinning, 8, 9, 15
- Empty-to-takeoff mass ratio, 222
- Energy, 11, 13–15, 68, 76–80, 106, 107, 122, 124–128, 132, 134–136, 152, 153, 157, 162, 164, 201, 203, 205, 248, 332–340, 401, 402, 431, 532, 533, 535
- Energy generating, 361
- Engine, 4, 31, 62–65, 78, 106, 107, 152–154, 157, 165, 193, 221, 223, 230, 290, 300, 301, 326, 329, 332, 342, 358, 359, 363, 380, 437, 447, 464, 530–536
- Ent test, 254
- Environmental effect, 2, 202, 206, 530, 533
- Environmental impacts, 53, 76, 77, 80, 84, 106, 132, 134, 136, 434, 458, 460, 530, 535
- Environmental risks, 115
- Epoxy matrix modifying, 122
- Ergonomic risk, 114–118
- Estimation methods, 261, 262, 265, 269, 270, 282–287, 495–505
- Extended Kalman filter, 39, 43, 283–284
- Extrapolation, 43, 260, 261, 264, 498, 499, 502

- F**
- Feed rate, 33–37
- Finite element, 122, 300, 301, 398–404, 518–526
- Fire reaction, 447–455
- Flexural test, 70
- Flight safety, 28, 31, 96, 100, 102, 114, 273–278, 426, 437
- Foresight, 407–412
- FRP, 399, 404
- Fuel performance, 105–111

- G**
- General aviation, 324–329
- Global Positioning System (GPS), 52, 161, 282, 283, 287, 435, 441, 442, 495, 496, 498–501, 503
- Green airport, 265
- Ground-handling operations, ix, 113–118, 216

- H**
- HALE UAVs, 160–169
- Handling company environmental impacts, 206
- High temperature, 8, 196, 368, 376, 389, 392, 394, 452, 467
- Hover, 223–225, 230
- Human error evaluation and reduction method (HEART), 96–102
- Human factors, 114, 408, 411
- Human reliability analysis, 96

- Hybrid composite, 471
 Hydrogen, 269–271, 310, 324–329
 Hydrogen fuel cells, 324–329
- I**
 Impacts of aircraft, 458–464
 Implementation, 58, 59, 84, 132, 134, 135, 137, 278, 389, 394, 412, 426, 439, 461–464, 496, 503, 515, 523
 In flight crisis management, 273, 274
 Integrated vehicular health monitoring (IVHM), 388, 389, 392, 394
 Interdisciplinary simulation, 274
 Interstellar exploration, 193
 Irreversibility, 106, 530, 533–536
 Isolator, 3, 4, 342–346
- J**
 Jet-A, 107, 108, 110, 111
- K**
 Kalman filter, 39, 40, 283, 380–384, 386, 394, 442, 496, 498, 503, 505
 Kaolin, 122–125, 128
 Kerosene flame, 448, 450, 451
 Kinematics, 39, 40, 42, 44, 45, 47
 Knowledge, 26, 31, 88, 99, 114, 116, 118, 274–277, 350, 407–412, 419, 425, 428, 518
- L**
 Lamb wave, 388–390, 392
 Lateral state estimation, 381
 Leading-edge, 19, 20, 140, 290, 291, 293, 296, 488–492
 Lean, 61–65
 Lift coefficient, 167, 184, 488–491
 Light detection and ranging (LiDAR), 160–162, 168, 435, 436
 Low-speed wind tunnel, 476
 Low velocity, 122, 125
 Low-velocity impact, 8, 11–12, 15, 68, 124, 403
- M**
 Macro cognition, 408–413
 Maintenance, repair, and overhaul (MRO), 26–30, 61–64, 209–211, 217, 425–431
 Management, 37, 50, 52, 53, 58, 62, 77, 79, 80, 113, 114, 118, 133, 136, 137, 210, 274, 407, 408, 411, 412, 426–428, 430, 434, 435, 439, 441–442, 444, 529–536
 Measurement, 15, 39–45, 47, 63, 133, 164, 205, 213, 232, 244–248, 261, 266, 282–285, 287, 300, 302, 317, 380–384, 386, 389, 449, 453, 477, 481, 482, 489, 496, 498–500, 502, 503, 508, 510, 512–516
 Mechanical properties, 8, 69, 122, 123, 302, 304, 308, 311, 312, 453, 454, 468, 469, 472, 473
 Missile, 416–423
 Monitoring system, 244, 247, 248, 388
 More electric auxiliary power unit, 358–365
 Morphing, 290, 291, 324
 Multi-criteria decision making (MCDM), 84, 85
 Multi-rotor, 181, 230
- N**
 NACA 0015, 487–491
 NACA 0020, 20–22
 Nanosatellite, 39–47
 Natural gas, 111, 136
 Newton Raphson method, 285, 496, 500–503
 NIST 800-22 test suite, 252, 254–256
 Noise, 41, 43–45, 76–80, 86, 99, 115, 117, 136, 140, 220, 233, 244–248, 251, 282, 284, 290, 291, 294–296, 301, 380, 381, 383, 458, 459, 463, 464, 482, 483, 496, 497, 500
 NOx emission, 154, 156, 157
 Number of pixel change rate (NPCR), 253, 254, 256, 257
- O**
 Operational costs, 134, 136, 425
 Optimal linear Kalman filter (OLKF), 382, 383, 385, 386
- P**
 Paperless aircraft operations, 200–206
 Particle swarm optimization, 181, 184
 Performances, 31, 35, 50, 62–64, 76, 96, 97, 99, 102, 105–111, 114–118, 121–125, 132–134, 148, 149, 152, 154, 160, 165, 181, 193, 194, 200, 203, 204, 264, 269, 270, 294, 296, 345, 350, 358–360, 373, 381, 383, 388, 398, 409–411, 429, 434,

- 436, 440, 447, 448, 459, 476, 488,
530–533, 535, 536
- Piezoelectric, 246, 332–336, 338, 339, 389, 393
- Pilot window, 300
- Planning, 50, 85, 133, 134, 137, 409
- 30P30N high lift wing, 290
- Polyurethane, 3, 68, 122, 467–473
- Position determination, 508, 516
- Predictive maintenance, 408–410, 412,
426–427, 430
- Prevention of aviation accidents, 273–278
- Progressive damage modelling, 525–526
- Progressive flight, 223, 224
- Propeller, 140–149, 165, 190, 229–234, 278,
437, 488
- Pseudo-ranging model, 282, 283, 496
- Public transport, 83–93
- PVC foam, 68, 69, 121, 122, 125
- R**
- Radiation heat loss, 172, 177, 178
- Rate Gyro, 41
- Reconfigured Kalman filter, 382–384
- Re-entry capsules, 368
- Relative navigation, 282, 284
- Renewable energy, 76, 260, 332
- Risk assessment, 115–116, 210, 212, 213,
215, 216
- Rotor layout, 181, 182, 187–191
- S**
- Sandwich, 3, 67–73, 121, 122, 124–128
- Sandwich structures, 3, 68, 69, 121–125
- Satellite, 39, 40, 42, 44, 45, 47, 282–287, 495,
496, 500, 501
- Sensor fault detection, 380, 386
- Separation, 12, 18, 20, 54, 57, 282, 294, 342,
345–348, 370, 373, 440, 479, 488
- Shear-stiffening gel, 238
- Shock wave, 342–346, 350, 369, 374
- Shock wave/boundary layer interaction
(SWBLI), 342
- Simulation, 40, 45, 142, 143, 185–190, 194,
273–278, 287, 292–294, 296, 325, 326,
342, 344, 352, 370, 381–383, 394,
398–404, 416–423, 429, 430, 437, 439,
442, 443, 476, 480, 503–505, 508,
514–516
- Simulink, 325, 326, 361, 416
- Single lap joints, 8, 9, 12–15
- Six Sigma, 62–64
- Sky emissivity, 172–176, 178
- Sky temperature, 172–174, 176, 178
- Smart polymers, 238
- Solar sail, 193, 194, 196
- Space-X Dragon, 370–371
- Starter-generator, 359, 363
- Star tracker, 44, 45, 47
- State space model, 497
- Stationary user localization, 503, 505
- Steady-state experiments, 476, 484
- Stiffened panel, 518, 526
- Strain, 34, 35, 115, 117, 123, 239, 304, 332,
334, 335, 403, 471
- Structural health monitoring (SHM), 388,
398, 399
- Supply quality, 84, 85, 88, 89, 93
- Surface oil flow visualization, 17, 18, 21
- Surface roughness, 33, 36, 230–234, 260, 261,
264
- Sustainability, 2, 76–80, 83, 111, 113, 118,
131–137, 430, 460, 529–536
- SVD-aided EKF, 40, 42–47
- Systemic approach, 410
- T**
- Taguchi, 231
- Tandem helicopter, 223–225, 227
- Terrestrial radio navigation, 507, 508, 516
- Test bench, 448, 449, 453, 455
- Thermal protection, 376
- 3D printing, 229–234, 489
- Thrust vectoring, 350, 354, 355
- Trailing edge flap, 290–296
- Trajectory, 50, 52–54, 57, 58, 368, 434, 435,
439, 441, 443, 444
- Transparent wood, 300, 302, 308–312
- Transport experts, 85
- Traveler, 315–320
- TRIZ, 312
- True random number generators, 250, 256
- Tubercles, 18–21, 487–491
- Turbofan, 154, 155, 290, 530
- Turboprop engine, 530–531, 536
- Turkey, 26, 27, 122, 174, 176, 178, 201, 203,
261, 265, 317, 320, 492, 505
- Turning, 33–37, 55, 57, 80, 442
- U**
- UAV conceptual design, 160–169
- Unified average changing intensity (UACI),
253, 254, 256, 257

Unmanned aerial vehicles (UAV), 50, 52, 140,
160–162, 164, 166, 168, 437–439,
442–444
Urban air transport, 50, 434, 435, 444

V

Variable substitution optimal control, 358, 362
Vibration, 3, 4, 115, 237, 240, 244–248,
332–335, 531
Vibroacoustic parameters, 244, 247, 248

W

Wind, 17, 19, 20, 22, 67, 161, 215, 260–266,
269–271, 290, 293, 342, 368, 436, 437,
439–441, 476–483, 488, 489

Z

Zero-emissions, 324–329